–Universidad Autónoma de Madrid–

CHAOS AND THERMALIZATION IN COLLECTIVE AND STRONGLY CORRELATED QUANTUM SYSTEMS

CAOS Y TERMALIZACIÓN EN SISTEMAS CUÁNTICOS COLECTIVOS Y FUERTEMENTE CORRELACIONADOS

DOCTORAL DISSERTATION SUBMITTED IN ORDER TO OBTAIN THE ACADEMIC DEGREE OF DOCTOR

BY

Ángel López Corps

SUPERVISORS

Rafael A. Molina Fernández
Armando Relaño Pérez

Madrid, 2024

ACKNOWLEDGEMENTS

It's over. What? It really feels like it is, doesn't it? Yes, yes, I've always been told that completing your doctoral studies is one of those experiences you're not forgetting in your lifetime; listen, I know that story already. And yet, somehow, I *wish* it wasn't over. That difficult decisions were not expected from me; that I could keep pretending there's nothing outside of the private comfort bubble I've created, a bubble that seemed surprisingly stable for so many years. Happy times are often hard to look back on. What lies ahead, though, I do not know. What I *do* know is that none of this would've been possible without the help and support of many people. Come on, it's not like I need to emphasize how mentally draining this job can be, right?

I believe that people come into your life by chance. Statistically, it wouldn't make sense otherwise; I mean, there are 8.1 billion people on Earth (as of 2024, that is). So you need to cherish those little fortuitous encounters. In my case, I'm somewhat confident that I wouldn't be writing this had it not been because I stumbled upon the right people. None of this was premeditated. For this I want to thank Rafa and Armando, my PhD supervisors. I've never played the lottery, so it's surprising that I still managed to win such a big prize! I'm aware this is not scientifically sound, but I'm positive I couldn't have found a supervisor quite like them. Thanks to my tutor, Francesca, who always, without exception, has nice words for me.

I want to thank Cris and Laura, who have accompanied me as I walked the path of academics (this was before I even got into doing a PhD!). Thank you for your time, for understanding, for caring. Well, also thanks for Chinese food and Burger King, I guess. There are possibly no secrets with you at this point.

I'm grateful to all of my colleagues at the Instituto de Estructura de la Materia and to its group of Theoretical Condensed Matter Physics for a myriad of deep and interesting conversations. Such a nice and peaceful place to work at. Thanks to Jorge, Eduardo, Pedro, and my 'roommates' there, especially Yuriko, Álvaro and Marta. Thanks to Jesús for fun times in congresses! And thanks to Carlos and Giuseppina for being partners in crime.

Thanks to the Andalusian official *phase transitioners*, Pedro, Pepe, José Enrique, Curro, Jamil and the rest, for their hospitality and fascinating scientific discussions.

I also want to thank my friends in Prague, Pavel Cejnar and Pavel Stránský (*the Pavels*), who welcomed me at Charles University in 2022. The experience was so positive we wrote a paper in two months! And thanks to the Czech dream team, especially Jakub and Felipe. I hope our adventures can be repeated!

Thanks to the Grupo Interdisciplinar de Sistemas Complejos for having me in all of their annual workshops. Thanks to Chantal for her collaboration as I asked her to write a recommendation letter for my doctoral fellowship. Thanks to Gisela Coromines from 'la Caixa' Foundation for taking care of my asymptotically infinite number of emails and phone calls.

Thanks to Jad, who invited me, a complete stranger, to his research group in Ludwig-Maximilians Universität in Munich in 2024. Thank you for your kindness and interesting conversations about physics and all other topics.

Lastly I want to thank my parents, (really) the best parents to ever exist, Tere and Ángel, and my grandma, Pepi, for supporting me in more than one way. And thanks to Marina, whose future shines as bright as the morning sun.

読み終わるのが嫌いんだ。
面白い話など読み進めたい。
けれど、
読み進むのが怖いだ

This work has been partially supported by the Spanish grants PGC-2018-094180-B-I00, PID2019-106820RB-C21 and PID2022-136285NB-C31, funded by Ministerio de Ciencia e Innovación/Agencia Estatal de Investigación MCIN/AEI/10.13039/-501100011033 and FEDER "A Way of Making Europe". The author of this thesis acknowledges support from 'la Caixa' Foundation (ID 100010434) through the fellowship LCF/ BQ/DR21/11880024, which has financed his doctoral contract.

ABSTRACT

The fundamental understanding of the behavior of many-body quantum systems has long been a source of scientific fascination. These systems have many particles and their interactions are quite intricate, so they are frequently referred to as *complex* quantum systems. In recent years, there has been a revival in the interest for basic dynamical phenomena, such as chaos and thermalization, in these physical systems. The reason is twofold: first, unraveling new, exotic phases of matter offers incredibly interesting possibilities allowing us to push the boundaries of physics; second, simulating and controlling complex quantum systems has never been easier than it is today, when a plethora of quantum technologies platforms make it possible to test our physical theories and discover new physics otherwise not easily accessible.

Generally speaking, complex quantum systems are expected to develop chaos. Far from being a mathematical inconvenience, chaos acts as a powerful catalyst for thermal behavior: letting the system relax for sufficiently long times will lead to equilibration, and the equilibrium values of physically relevant observables are then described by thermal ensembles of statistical mechanics. The focus of this thesis, however, is on the many effects that may cause a complex system to deviate from thermalization, or even never actually reach it. The main suspects are three: integrability, many-body localization, and certain forms of symmetry-breaking and phase transitions. The problem of localization in systems of many particles has attracted a lot of attention and many fundamental questions are still under debate; even its very existence in the macroscopic world, the thermodynamic limit, is under scrutiny. All in all, many-body localization has been described as an exotic form of integrability. In comparison, phase transitions constitute a much older topic. Phase transitions mean a sudden response of a system under variation of some of its control parameters, in such a way that certain of its observable properties behave non-analytically in the thermodynamic limit. These abrupt variations of the system's behavior are in many cases due to symmetry-breaking. Thermalization can also be hampered in symmetry-broken phases, where equilibrium states do not satisfy a global Hamiltonian symmetry. Although these states do frequently equilibrate, these equilibrium values cannot be well described by standard thermal averages.

We are determined to provide some answers to these questions in this thesis, which is organized as follows:

Chapter 1 provides a general introduction to the several topics of this thesis. We have intended to maintain a pedagogical but rigorous style, in the hopes that it may successfully pass on the knowledge to younger (and older!) generations.

Chapter 2 opens up the results part of this thesis. Here we report on our analysis of the many-body localization transition in nearest and next-to-nearest neighbors spin chains. We address the existence of the many-body localized phase and propose a mechanism driving the transition. Our arguments are based on the random matrix theory and the eigenstate thermalization hypothesis.

Chapter 3 deals with the description of equilibrium states in systems with $\mathbb{Z}_2$ symmetry-breaking. The symmetry-breaking that we consider is caused by different forms of phase transitions, like ground-state and excited-state quantum phase transitions. We propose a generalization of the canonical and microcanonical thermal ensembles describing the asymptotic effective equilibrium values of observables in these systems. This is accomplished by the identification of a set of emergent conserved quantum operators in the symmetry-broken phases. We apply this theoretical framework to the problem of dynamical phase transitions, and consider equilibrium states in energy cat states, where the mean energy of a non-equilibrium state is not a well-defined quantity. In all of these cases, the usual arguments of the eigenstate thermalization hypothesis fail.

Chapter 4 presents our results on a deformed version of the quantum optical Dicke model. The deformation term added to the usual Hamiltonian is responsible for the appearance of two asymmetric, disconnected wells. As a consequence, the development of chaos becomes non-trivial, with the signatures of both classical and quantum chaos decoupling in these two wells. We start with a theoretical study of chaos in this system, where we employ Lyapunov exponents, spectral statistics, and Peres lattices. Then, we present an experimental realization of the model on a biparametric electronic platform, obtaining excellent agreement between theoretical and experimental results.

Finally, in Chapter 5 we gather the main conclusions of this thesis.

RESUMEN

La comprensión a nivel fundamental del comportamiento de los sistemas cuánticos de muchos cuerpos ha sido tradicionalmente una fuente de gran fascinación científica. Estos sistemas tienen muchas partículas y sus interacciones son altamente no triviales, de modo que frecuentemente se les llama sistemas cuánticos *complejos*. Recientemente, ha habido un renacimiento en el interés por fenómenos dinámicos básicos, como el caos y la termalización, en estos sistemas. La razón es doble: por un lado, el descubrimiento de nuevas fases exóticas de la materia ofrece posibilidades increíblemente interesantes que nos permiten ampliar los límites del conocimiento en física; por otro lado, la simulación y el control de los sistemas cuánticos complejos nunca ha sido tan fácil como lo es hoy en día, cuando tenemos a nuestra disposición una inmensidad de plataformas basadas en tecnologías cuánticas que hacen posible poner a prueba nuestras teorías físicas y también descubrir nueva física difícilmente accesible sin estos instrumentos.

En general, los sistemas cuánticos complejos desarrollan caos. Lejos de ser una inconveniencia matemática, el caos actúa como un fuerte catalizador del comportamiento térmico: si dejamos que el sistema relaje durante tiempos suficientemente largos, alcanzará el equilibrio, y los valores de observables físicamente relevantes en estados de equilibrio estarán entonces descritos por colectividades térmicas de mecánica estadística. Sin embargo, está tesis está centrada en los variados efectos que pueden hacer que un sistema complejo se desvíe de la termalización, o quizás no la alcance nunca. Los principales sospechosos son tres: la integrabilidad, la localización de muchos cuerpos, y ciertas formas de ruptura de simetría y transiciones de fase. El problema de la localización en sistemas de muchas partículas ha atraído mucha atención y muchos interrogantes fundamentales siguen estando bajo debate; incluso su misma existencia en el mundo macroscópico, el límite termodinámico, está siendo cuestionada. Con todo, la localización de muchos cuerpos se ha descrito como una forma exótica de integrabilidad. En comparación, las transiciones de fase constituyen un tema mucho más antiguo. Una transición de fase se manifiesta a través de una respuesta de un sistema a variaciones de sus parámetros de control, de forma que algunas de sus propiedades medibles se comportan de forma no analítica en el límite termodinámico. Estas variaciones abruptas en el comportamiento del sistema están debidas en muchos casos a una ruptura de simetría. La termalización puede verse comprometida en fases con

simetría rota, donde los estados de equilibrio no satisfacen una simetría global del Hamiltoniano. Aunque estos estados frecuentemente equilibran, estos valores de equilibrio no se describen por promedios térmicos estándar.

Nuestra intención es proporcionar algunas respuestas a estas preguntas en esta tesis, que está organizada como sigue:

El Capítulo 1 proporciona una introducción general a los diversos temas de esta tesis. Hemos procurado mantener un estilo pedagógico pero riguroso, con la esperanza de que pueda transmitir el conocimiento a generaciones más jóvenes (¡y también mayores!).

El Capítulo 2 abre la parte de resultados de esta tesis. Aquí presentamos nuestros análisis de la transición a la localización de muchos cuerpos en cadenas de espín con interacciones a primeros y segundos vecinos. Abordamos la existencia de la fase de localización de muchos cuerpos y proponemos un mecanismo responsable para ella. Nuestros argumentos están basados en la teoría de matrices aleatorias y en la hipótesis de termalización de autoestados.

El Capítulo 3 trata de la descripción de estados de equilibrio en sistemas con ruptura de simetría $\mathbb{Z}_2$. La ruptura de simetría que consideramos está causada por distintas formas de transiciones de fase, como transiciones de fase de estado fundamental y de estados excitados. Proponemos una generalización de las colectividades canónica y microcanónica para describir los valores de equilibrio efectivo en estos sistemas. A tal efecto, identificamos un conjunto de constantes del movimiento emergentes en fases con ruptura de simetría. Aplicamos este marco teórico al problema de las transiciones de fase dinámicas, y consideramos los estados de equilibrio en estados energéticos de tipo gato, donde la energía promedio de un estado fuera del equilibrio no es una cantidad bien definida. En todos estos casos, los argumentos usuales de la hipótesis de termalización de autoestados resultan inválidos.

El Capítulo 4 presenta nuestros resultados sobre una versión deformada del modelo de Dicke de óptica cuántica. El término de deformación añadido al Hamiltoniano usual es responsable de la aparición de dos pozos simétricos y desconectados. Como consecuencia, el desarrollo del caos se vuelve no trivial, y las trazas del caos clásico y cuántico se desacoplan en estos dos pozos. Empezamos con un estudio teórico del caos en el sistema, en el que empleamos exponentes de Lyapunov, estadística espectral y redes de Peres. Después, presentamos una realización experimental del modelo en una plataforma electrónica biparamétrica, obteniendo excelente acuerdo entre resultados teóricos y experimentales.

Finalmente, en el Capítulo 5 reunimos las principales conclusiones de esta tesis.

CONTENTS

I INTRODUCTION

1 INTRODUCTION 3

1.1 Thermalization in closed systems 3

1.1.1 Thermalization in classical systems 4

1.1.2 Thermalization in quantum systems 7

1.2 Chaos as a mechanism for thermalization 18

1.2.1 Classical chaos 18

1.2.2 Quantum chaos 25

1.2.3 Fitting the pieces: RMT $\subset$ ETH 36

1.3 Exceptions to thermal behavior 37

1.3.1 Integrability 37

1.3.2 Localization 44

1.3.3 Symmetry-breaking and phase transitions 55

II RESULTS

2 BREAKING ERGODICITY VIA DISORDER 77

2.1 Preliminaries 77

2.1.1 Hamiltonian model 77

2.1.2 Long-range spectral statistics: the power spectrum of the unfolded level spacings 78

2.2 Analysis in the $J_1 - J_2$ random model 79

2.2.1 Looking at the tails: extreme events as a function of disorder 79

2.2.2 Spectral statistics across the transition 84

2.3 Conclusions 91

3 CONSTANTS OF MOTION AND $\mathbb{Z}_2$ SYMMETRY-BREAKING 93

3.1 Motivation: discrete symmetry-breaking in fully-connected models 94

3.2 General framework 97

3.2.1 Assumptions 99

3.2.2 First result 100

3.2.3 Second result 105

3.2.4 Numerical realization of equilibrium states 111

3.2.5 Implementation in cold atom platforms 114
3.2.6 Symmetry-breaking perturbation and stabilization 117
3.3 Application to dynamical phase transitions 124
3.3.1 Classical limit of the fully-connected transverse field Ising model 126
3.3.2 Dynamical order parameters: dynamical phase transition of type I 129
3.3.3 Cusps in return probabilities: dynamical phase transitions of the type II 144
3.3.4 Watching the seeds of DPTs-II: the complex-time survival amplitude 150
3.4 Thermodynamics of energy cat states induced by ESQPT criticalities 165
3.4.1 Deformed Rabi Hamiltonian 166
3.4.2 Quantum manifestations of classically asymmetric energy wells 171
3.4.3 Engineering cat states in the spectral domain 181
3.4.4 Equilibrium dynamics in energy cat states 185
3.5 Conclusions 188
4 CHAOS IN A DEFORMED DICKE MODEL 191
4.1 Preliminaries 191
4.1.1 Deformed Dicke model 191
4.1.2 The classical deformed Dicke Hamiltonian 193
4.2 Theoretical analysis of chaos and conserved quantities 196
4.2.1 The traces of classical chaos 196
4.2.2 Signatures of quantum chaos 201
4.3 Experimental realization of the deformed Dicke model 208
4.3.1 Experimental platform 208
4.3.2 Exploring the ground-state features 211
4.3.3 Measuring chaos and phase transitions 214
4.4 Conclusions 218
III CONCLUSIONS AND BIBLIOGRAPHY
5 GENERAL CONCLUSIONS 223
BIBLIOGRAPHY 229

LIST OF FIGURES

Figure 1 Kurtosis excess as a function of the disorder strength in the $J_1 - J_2$ model 81

Figure 2 Analysis of the observable diagonal fluctuations as a function of disorder 82

Figure 3 Finite-size scaling of the kurtosis excess and analysis of the transition critical point 83

Figure 4 Level spacing distribution for disorder values $\omega \geq 4.7$ 86

Figure 5 Power spectrum of the level spacings for disorder values $\omega \geq 4.7$ 87

Figure 6 Power spectrum of the level spacings for disorder values $\omega \leq 4.7$ 88

Figure 7 General landscape of the many-body localization transition 90

Figure 8 Kurtosis excess of the diagonal fluctuations and accuracy of semi-Poisson statistics 91

Figure 9 Representation of the classical phase space of the Lipkin-Meshkov-Glick model 96

Figure 10 The three classes of symmetry-breaking equilibrium states 112

Figure 11 Preparing the different symmetry-breaking equilibrium states in the transverse-field Ising model with long-range interactions 116

Figure 12 Quantum quenches in the perturbed transverse-field Ising model 121

Figure 13 Magnetization and $\hat{\mathcal{C}}$ operator in the perturbed transverse-field Ising model 123

Figure 14 Schematic representation of the DPT-I and DPT-II phase diagram 126

Figure 15 Classical level density of the Lipkin-Meshkov-Glick model 129

Figure 16 Population probabilities following quantum quench protocols 131

Figure 17 Time evolution of the DPT-I order parameter following different quantum quenches 133

Figure 18 Finite-size scaling of the semi-classical time and the revival time following quantum quenches 134

Figure 19 Equilibrium values of observables following a quantum quench 138
Figure 20 Finite-size scaling of the long-time average of the order parameter following a quantum quench 139
Figure 21 Average energy of the state evolving in time according to the Schrödinger equation 142
Figure 22 Time expectation value of observables following a time-dependent protocol and predictions of the generalized microcanonical ensemble 143
Figure 23 Exemplification of DPT-II via rate function of parity-projected return probability 151
Figure 24 Exemplification of DPT-II via rate function of standard survival probability 152
Figure 25 Comparison of critical times of DPT-I and DPT-II 153
Figure 26 Exemplification of the mechanism of DPT-II. Contour plots of the complexified survival amplitude following a quantum quench 155
Figure 27 Complexified survival amplitude and time evolution of the survival probability rate function following a quantum quench 157
Figure 28 Finite-size scaling of the number of complex zeros of the complexified survival amplitude 158
Figure 29 Complexified survival amplitude and time evolution of the survival probability rate function for two initial states with different proportion of positive and negative parity ground-state population 159
Figure 30 Complex time survival amplitude and excited-state quantum phase transitions 162
Figure 31 Complexified survival amplitude and survival probability rate function for a quantum quench leading to the excited-state quantum phase transition spectral region 163
Figure 32 Demonstration of regular and anomalous DPTs-II from a symmetric initial state 164
Figure 33 Energies associated to the critical points of the Rabi classical Hamiltonian 167
Figure 34 Classical phase space of the deformed Rabi model for different values of the control parameter 168
Figure 35 Classical level density of the deformed Rabi model for different values of the control parameter 169
Figure 36 Signatures of ground-state quantum phase transitions in the deformed Rabi model 170

Figure 37 Diagonal expectation values of observables in the deformed Rabi model 171
Figure 38 Level-flow diagram of the deformed Rabi model 173
Figure 39 Quantum vs classical level-flow diagram of the deformed Rabi model 174
Figure 40 Behavior of $\hat{C}$ near level crossings 177
Figure 41 Allowed transitions between consecutive eigenstates of the Rabi model 179
Figure 42 Analysis of level crossings in the deformed Rabi model 180
Figure 43 Energy cat states in the deformed Rabi model 182
Figure 44 Formation of classically separated cat states in the deformed Rabi model 184
Figure 45 Relaxation dynamics in energy cat states and microcanonical description 187
Figure 46 Classical phase space of the deformed Dicke Hamiltonian 194
Figure 47 Classical chaos and Poincaré sections 197
Figure 48 Classical chaos and Lyapunov exponents 199
Figure 49 Distribution of the ratio of consecutive level spacings for different spectral and symmetry regions 203
Figure 50 Quantum chaos and Peres lattices 205
Figure 51 Onset of quantum chaos in the deformed Dicke model and adiabatic invariants 209
Figure 52 Experimental realization of the deformed Dicke model: electric circuit 211
Figure 53 Comparing experimental and numerical measurements of the ground-state properties of the deformed Dicke model 213
Figure 54 Schematic representation of the phase diagram of the deformed Dicke model 215
Figure 55 Theoretical vs experimental measurements of chaos 217

LIST OF TABLES

Table 1 Summary of spectral region considered for the analysis of chaos and thermalization in the $J_1 - J_2$ spin chain 80

Table 2 Average energy and equilibrium value of the magnetization and the $\hat{\mathcal{C}}$ operator for three different quantum protocols in the Lipkin-Meshkov-Glick model 111

Table 3 Information erasure upon crossing the excited-state quantum phase transition in the Lipkin-Meshkov-Glick model 144

Table 4 Chaotic proportion of the classical phase space in the deformed Dicke model 200

INDEX OF ACRONYMS

MBL	Many-body localization
DPT	Dynamical phase transition
ESQPT	Excited-state quantum phase transition
ETH	Eigenstate thermalization hypothesis
GGE	Generalized Gibbs ensemble
GME	Generalized microcanonical ensemble
LDOS	Local density of states
LMG	Lipkin-Meshkov-Glick (model)
ME	Microcanonical ensemble
NATS	Non-Abelian thermal state
PPRP	Parity-projected return probability
QPT	Quantum phase transition
RMT	Random matrix theory
(S)SB	(Spontaneous) symmetry breaking
TFIM	Transverse-field Ising (model)
TL	Thermodynamic limit
TPT	Thermal phase transition

LIST OF PUBLICATIONS

The scientific content of this thesis is based on the following author's original articles:

- A. L. Corps, R. A. Molina, and A. Relaño, "Signatures of a critical point in the many-body localization transition," SciPost Physics **10**, 107 (2021).
- A. L. Corps, R. A. Molina and A. Relaño, "Chaos in a deformed Dicke model", J. Phys. A: Math. Theor. **55** (2022) 084001.
- A. L. Corps and A. Relaño, "Energy cat states induced by a parity-breaking excited-state quantum phase transition", Phys. Rev. A **105**, 052204 (2022).
- A. L. Corps and A. Relaño, "Dynamical and excited-state quantum phase transitions in collective systems", Phys. Rev. B **106**, 024311 (2022).
- A. L. Corps and A. Relaño, "Theory of dynamical phase transitions in quantum systems with symmetry-breaking eigenstates", Phys. Rev. Lett. **130**, 100402 (2023).
- A. L. Corps, P. Stránský, and P. Cejnar, "Mechanism of dynamical phase transitions: The complex-time survival amplitude", Phys. Rev. B **107**, 094307 (2023).
- M. A. Quiroz-Juarez*, A. L. Corps*, R. A. Molina, A. Relaño, J. L. Aragón, R. de J. León-Montiel, and J. G. Hirsch, "Experimental observation of phase transitions of a deformed Dicke model using a reconfigurable, bi-parametric electronic platform", Eur. Phys. J. Plus (2023) 138:775.
- A. L. Corps and A. Relaño, "General theory for discrete symmetry-breaking equilibrium states", arXiv:2303.18020 [quant-ph].

*: equally contributing

Upon completion of his PhD thesis, the author's full record of publications also includes the following contributions:

- A. L. Corps, R. A. Molina, and A. Relaño, "Thouless energy challenges thermalization on the ergodic side of the many-body localization transition," Phys. Rev. B **102**, 014201 (2020).

- A. L. Corps and A. Relaño, "Distribution of the ratio of consecutive level spacings for different symmetries and degrees of chaos", Phys. Rev. E **101**, 022222 (2020).
- A. L. Corps and A. Relaño, "Constant of Motion Identifying Excited-State Quantum Phases", Phys. Rev. Lett. **127**, 130602 (2021).
- A. L. Corps and A. Relaño, "Long-range level correlations in quantum systems with finite Hilbert space dimension", Phys. Rev. E **103**, 012208 (2021).
- A. Rubio-García, A. L. Corps, A. Relaño, R. A. Molina, F. Pérez-Bernal, J. E. García-Ramos, and J. Dukelsky, "Exceptional spectral phase in a dissipative collective spin model", Phys. Rev. A **106**, L010201 (2022).
- A. L. Corps and A. Relaño, "Comment on 'Revisiting the phase transitions of the Dicke model"', Phys. Rev. A **106**, 047701 (2022).
- A. L. Corps, P. Pérez-Fernández, and A. Relaño, "Relaxation time as a control parameter for exploring dynamical phase diagrams"', Phys. Rev. B **108**, 174305 (2023).
- A. L. Corps, J. Dukelsky and A. Relaño, "Constants of motion characterizing continuous symmetry-broken phases", Phys. Rev. E **109**, 064102 (2024).
- A. L. Corps, A. Relaño and J. C. Halimeh, "Unifying finite-temperature dynamical and excited-state quantum phase transitions", arXiv:2402.18622 [quant-ph], submitted to Phys. Rev. Lett.

Part I

INTRODUCTION

1 INTRODUCTION

In this Chapter we present a comprehensive introduction to the main topics of this thesis. In Sec. 1.1 we review the overarching theme of thermalization in closed systems; the first part of this section, Sec. 1.1.1, is devoted to thermalization in classical systems, whereas the transition to the quantum world is carried out in Sec. 1.1.2. Next, we delve into one of the main mechanisms for thermalization, chaotic dynamics, in Sec. 1.2. We again begin with a brief introduction to chaos in classical Hamiltonian systems in Sec. 1.2.1, while the meaning of chaos in the quantum world and how to observe its traces is explained in Sec. 1.2.2. Some formal connections between the eigenstate thermalization hypothesis (EHT) and the random matrix theory (RMT) are reviewed in Sec. 1.2.3. Finally, in Sec. 1.3 we tackle some of the most notable exceptions to thermal behavior in complex many-body systems: integrability, in Sec. 1.3.1, many-body localization, in Sec. 1.3.2, and symmetry-breaking and phase transitions of diverse nature, in Sec. 1.3.3.

1.1 THERMALIZATION IN CLOSED SYSTEMS

It is to be suspected that thermalization is justified differently in the classical and quantum worlds. Yet, it is reassuring that the general grounds on which this phenomenon rests are paralleled in both frameworks. Loosely speaking, thermalization relies on the hypothesis that the motion of the system is sufficiently complex, disorganized, *chaotic*. The detail-oriented reader will be glad to find a bit more specific explanations in subsequent parts of this thesis. For this reason, it is natural that integrability, associated with an extensive number of constants of motion constraining the dynamics, making it predictable and easily solvable, is one of the biggest enemies of thermalizing behavior, and perhaps the best well known. Thermalization is tightly tied to the loss of information about the initial state where one chooses to prepare a physical system. A common working definition for this process in isolated quantum systems, which we adopt in this thesis, is the following:

Thermalization.– We say that a system thermalizes if, for sufficiently long times, the dynamical evolution relaxes to the microcanonical prediction and remains close to it at most later times [1], [2].

In this definition there is an implicit link between the microscopic and macroscopic properties of the system under consideration. In any physical system, the dynamical evolution depends on the initial condition, as this is the configuration from where the system departs. Yet, the microcanonical prediction refers to certain statistical, macroscopic features where the microscopic details no longer play a relevant role. For this reason, it is sometimes said that thermalization helps us to understand how the macroscopic reality emerges from microscopic laws. In particular, the thermalization process is at the heart of a solid foundation of statistical mechanics.

Although the goal of this thesis is not to understand thermalization on the classical level, we posit that the macroscopic reality is a good place to start from, as is often the case.

1.1.1 Thermalization in classical systems

In our journey, we first visit the part of the material reality that we are most used to: the macroscopic world, governed by the laws of classical mechanics [3], [4]. Most daily-life physical objects do not seem to change over time, unless they are subjected to some kind of external force or interaction. Their macroscopic state appears to be well defined and static. Why does a stone not depend on the particular configuration that its internal degrees of freedom, assumed to be point-like in classical mechanics, as they evolve in time? It is because the system has reached thermal equilibrium.

In classical mechanics the quantities that we can measure are mathematically referred to as dynamical functions. To make contact with quantum mechanics in later sections of this thesis, we will refer to these dynamical functions as *observables*, $O(\mathbf{q}, \mathbf{p})$. These depend on certain *continuous* variables that are defined on a real set called the phase space, $\mathcal{M}$. For the sake of simplicity, we will concentrate on canonical position and momentum. The state of the system of f degrees of freedom is then completely specified by indicating the full configuration of $2f$ variables $(\mathbf{q}, \mathbf{p}) \equiv (q_1, \ldots, q_f, p_1, \ldots, p_f) \in \mathcal{M}$. The details of the system are encoded in its Hamiltonian, $H(\mathbf{q}, \mathbf{p})$. One nice aspect of classical mechanics is that it allows us to determine simultaneously position and momentum, and so one can think of the system dynamics as a *trajectory* in phase space. Given an initial configuration, $(\mathbf{q}(0), \mathbf{p}(0))$, the future state of the system, $(\mathbf{q}(t), \mathbf{p}(t))$, is completely set on stone,

as the time evolution is mathematically given by the Hamilton equations of motion, which are of course deterministic:

$$\frac{\mathrm{d}\mathbf{q}}{\mathrm{d}t} = \frac{\partial H(\mathbf{q},\mathbf{p})}{\partial \mathbf{p}}, \quad \frac{\mathrm{d}\mathbf{p}}{\mathrm{d}t} = -\frac{\partial H(\mathbf{q},\mathbf{p})}{\partial \mathbf{q}}, \tag{1}$$

subjected to the conditions that $\mathbf{q}(t=0) = \mathbf{q}(0)$ and $\mathbf{p}(t=0) = \mathbf{p}(0)$. In phase space, the time-evolving trajectory will reside on a constant-energy surface compatible with the system's constraints,

$$\mathcal{S}_E \equiv \{(\mathbf{q},\mathbf{p}) \in \mathcal{M} \subseteq \mathbb{R}^{2f} \ / \ H(\mathbf{q},\mathbf{p}) = E\}. \tag{2}$$

Say, then, that we wish to compute the time average of our observable $O(t)$ over the time interval $[0,\tau]$. Our hope is that we can eventually take the limit $\tau \to \infty$, and we can associate this *time-independent* long-time average, $\overline{O}$, with the equilibrium state reached by the system after it has relaxed,

$$\overline{\langle O \rangle} \equiv \lim_{\tau\to\infty} \frac{1}{\tau} \int_0^\tau \mathrm{d}t\, O(t). \tag{3}$$

In principle, the transient short-time dynamics of $O(t)$ is immaterial to us, as we are only interested in its infinite-time behavior. But why should we have to wait for infinitely long times? The physical justification of (3) is that normally a macroscopic measurement implies a long microscopic time, and if the classical trajectories explore all available phase space in an erratic way (see below), then the value provided by a measuring apparatus will essentially coincide with (3), which, of course, is a mathematical idealization of this process. According to (3), we only need to obtain the instantaneous values of the configuration variables, $(\mathbf{q}(t),\mathbf{p}(t))$, given by (1), and then integrate the corresponding observable accordingly. Unfortunately, this is easier said than done. Classical mechanics can sometimes be merciless, and there is no guarantee that such a potentially complicated system of differential equations as (1) can be easily solved, let alone integrate (3). Think, for example, of solid state systems typically representing the material reality with reasonable accuracy. Do we realistically expect to solve a system of $\sim 10^{23}$ (the Avogadro number) coupled differential equations?! This approach is simply too naive, and unfortunately we must abandon, as it will not be useful except in the case of very simple, schematic systems.

Is there a way to circumvent this brute-force method? The answer is: *'yes, if the system is ergodic'*. Ergodicity is profound physical phenomenon closely connected to, but not implying, chaoticity (see next section for more details). A rigorous definition for ergodicity requires certain mathematical apparatus that we have decided to exclude from this thesis. Yet, broadly speaking [5], its meaning can be summarized as follows:

Ergodicity.– In an ergodic system, the trajectory of the system will get arbitrarily close to every point on the constant energy surface, $\mathcal{S}_E$, as it evolves during a sufficiently long time.

Ergodicity is quite a strong condition for a physical system to exhibit. Albeit quite simplistic, there are some paradigmatic models where full ergodicity has been proved. Among these we find the so-called Sinai billiards [6]–[8], which consist of gases composed of hard spheres constrained to a certain geometrical volume with periodic boundary conditions, and also the Bunimovich stadium [9], in which a single particle is allowed to move freely in a two-dimensional surface resembling a stadium with hard walls that are circular on the sides but straight in the middle.

In addition to this notion, Liouville's theorem [3] (as formulated in the context of dynamical systems) teaches us that the decisive factor for how much time the system will spend within a certain region of phase space is the *volume* of such subset of phase space; in other words, equal volumes in phase space are associated to equal times spent by the system in that region of phase space. If we also assume the system to be ergodic, this means that the system will cover uniformly each of the subsets where it spends a certain amount of time. Therefore, the long-time average of our observable $O(t)$ can be computed exactly as in the microcanonical ensemble of equilibrium statistical mechanics [5], $\langle O \rangle_{\text{ME}}$, i.e.,

$$\overline{\langle O \rangle} = \frac{\int\!\!\!\!\!\!\diagup_{\mathcal{S}_E} \mathrm{d}^f\mathbf{q}\,\mathrm{d}^f\mathbf{p}\,O(\mathbf{q},\mathbf{p})}{\mathcal{V}(\mathcal{S}_E)} \equiv \langle O \rangle_{\text{ME}}, \tag{4}$$

where $\mathcal{V}(\mathcal{S}_E) = \int\!\!\!\!\!\!\diagup_{\mathcal{S}_E} \mathrm{d}^f\mathbf{q}\,\mathrm{d}^f\mathbf{p}$ is the $2f$-dimensional volume of the constant energy surface (2). Experience shows that calculating the microcanonical average in (4) tends to be easier than the long-time average in (3).

Equation (4) establishes a fundamentally striking consequence: *if the system is fully ergodic, the equilibrium long-time average, which is a dynamical entity coming directly from the equations of motion, coincides exactly with the predictions of the microcanonical ensemble, which is a thermodynamic object.* When this happens, we say that the system has *thermalized*, because its equilibrium value can be captured by a thermodynamic description. Equation (4) also helps us to comprehend why the microscopic details of the initial configuration do not play a role once the system has thermalized: many initial configurations can potentially lead to the same thermalized state. This is the core of the thermalization process of classical systems and, as we will see later on, it nicely connects with that of quantum systems. The equivalence of long-time averages and microcanonical averages is commonly termed the ergodic hypothesis, a primitive form of which was invoked by Boltzmann already in 1898 in order to prove energy equipartition in his kinetic theory of gases

[10]. The ergodic hypothesis is generally believed to apply to most interacting systems, but there are some important exceptions of integrable or near-integrable interacting systems that do not thermalize. A famous example is the Fermi-Pasta-Ulam-Tsingou (FPUT) experiment, in which the behavior of a string of anharmonic oscillators was numerically investigated. The FPUT experiment was pioneering in that it showed that complex interacting systems do not necessarily exhibit a random or disorganized pattern, but that they can also exhibit quasi-periodic behavior common to integrable systems, eluding thermalization. In passing we note that the FPUT experiment has a well-deserved fame for highlighting the usefulness of using computer simulations as a tool to discover new physics, and it was the seed of a whole new field of research: nonlinear dynamics. The FPUT report was never published in a scientific journal [11].

One can intuitively grasp why in the case of integrable systems (which will be discussed in more detail in subsequent sections) thermalization, as defined above, does not take place in general. Due to their extensive number of constants of motion, the classical trajectories do not fully cover the entire available phase space defined by total energy conservation; instead, the integrals of motion impose geometrical constraints for the configuration variables $(\mathbf{q}, \mathbf{p})$ so that the motion does not take place in $\mathcal{S}_E$ but, possibly, in a subset of it, and in such a way that not all states entering the average (4) are equivalent in the probabilistic sense. By contrast, chaotic dynamics, as we will discuss later, can be understood as a strong catalyst for thermalization.

1.1.2 Thermalization in quantum systems

That unitary dynamics of closed quantum systems may also allow a system to thermalize may come as a surprise, especially since there are no true equilibrium states unless dissipation is induced, for example, by connecting the system to an external bath.

In quantum mechanics, physically measurable quantities are represented by Hermitian operators, and the microscopic details of a given system are encoded in its quantum Hamiltonian, $\hat{H}$. The Hamiltonian is itself Hermitian, and therefore it can be diagonalized (we are only concerned with finite-dimensional Hilbert spaces). To fix notation, focusing on finite-dimensional Hamiltonians which will be the main focus of this work, Hamiltonian eigenvalues (or eigenenergies, or energy levels) will be generically denoted by E_n, where $n \in \mathbb{N}$ is their level number index, while the corresponding eigenvectors (or eigenstates) are $|E_n\rangle$. They verify the eigenvalue equation $\hat{H}\,|E_n\rangle = E_n\,|E_n\rangle$, $\forall n \in \mathbb{N}$. In this thesis, we will always use the

hat notation to remind ourselves that we are dealing with an operator, $\hat{O}$, instead of a function, $O(x)$, or a scalar, O. Additionally, the states that a quantum system may assume are represented by a wavefunction in a Hilbert space, $|\psi\rangle \in \mathcal{H}$.

On a mathematical level, the building blocks of quantum dynamics are completely different than those of classical mechanics. For instance, the quantum uncertainty principle means that there exist no state $|\psi\rangle$ for which the position and momentum are well defined simultaneously, as their respective deviations are bound by the relation $\Delta p \Delta q \geq \hbar/2$. This fundamental principle applies to any pair of non-commuting quantum operators, which are often referred to as 'incompatible operators'. For this reason, formally speaking, there is no exact quantum analogue of the classical phase space, as there are no trajectories, at least in the classical sense. Suppose we prepare our quantum system in an initial state given by $|\psi(0)\rangle$. For the most part, we will not be concerned with time-dependent Hamiltonians in this thesis. For time-independent Hamiltonians, the state $|\psi(0)\rangle$ will evolve in time according to the *iconic* Schrödinger equation,

$$i\hbar \frac{\mathrm{d}}{\mathrm{d}t} |\psi(t)\rangle = \hat{H} |\psi(t)\rangle , \tag{5}$$

subjected to $|\psi(t=0)\rangle = |\psi(0)\rangle$, whose solution affords the instantaneous state of the quantum system and is of course given by

$$|\psi(t)\rangle = e^{-i\hat{H}t/\hbar} |\psi(0)\rangle = \sum_n c_n e^{-iE_n t/\hbar} |E_n\rangle , \quad t \in \mathbb{R}, \tag{6}$$

where $c_n \equiv \langle E_n|\psi(0)\rangle \in \mathbb{C}$ are the expansion coefficients of the initial state $|\psi(0)\rangle$ in the Hamiltonian eigenbasis. Here, $\hat{H}|E_n\rangle = E_n |E_n\rangle$. The complexity of the time evolution (6) is largely dependent on the number of non-zero c_n. From now onward, we set $\hbar = 1$. The instantaneous expectation value of an arbitrary observable $\hat{O}$ will be denoted as

$$\langle \hat{O}(t) \rangle \equiv \langle \psi(t)| \hat{O} |\psi(t)\rangle . \tag{7}$$

The simplest initial state that we can think of is possibly a single eigenstate of $\hat{H}$, $|\psi(0)\rangle = |E_n\rangle$. Such states are uninteresting from a dynamical point of view because they are stationary, namely the Schrödinger equation will only make them acquire complex phases and, by virtue of the orthonormality of the Hamiltonian eigenbasis, $\langle E_n|E_m\rangle = \delta_{nm}$, the expectation value of any observable is stuck in its initial value, $\langle \hat{O}(t) \rangle = \langle \hat{O}(0) \rangle$. In order to study non-trivial dynamics, the initial state $|\psi(0)\rangle$ can be, for example, an arbitrary pure state, whose decomposition in the eigenbasis of $\hat{H}$ is $|\psi(0)\rangle = \sum_n c_n |E_n\rangle$, where $\sum_n |c_n|^2 = 1$. Later on we will comment on another common way to generate out-of-equilibrium dynamics

from initial states that are linear superpositions of a Hamiltonian eigenstates that is widely used in experiments: the quantum quench. Inserting (6) into (7), the most general expression for the expectation value of an observable $\hat{O}$ is

$$\begin{aligned}\langle \hat{O}(t) \rangle &= \sum_{n,m} c_n c_m^* e^{-i(E_n - E_m)t} O_{mn} \\ &= \sum_n |c_n|^2 O_{nn} + \sum_{n \neq m} c_n c_m^* e^{-i(E_n - E_m)t} O_{mn},\end{aligned} \tag{8}$$

where we have abbreviated the expectation value of $\hat{O}$ in the eigenstates of the Hamiltonian as $O_{mn} \equiv \langle E_m | \hat{O} | E_n \rangle$. The elements O_{nn} are called *diagonal* expectation values, while the O_{mn} are referred to as *off-diagonal*, for obvious reasons.

What is the long-time average of this instantaneous expectation value? Does it coincide with the predictions of a thermal statistical ensemble, as we previously noted for the case of classical dynamics? First of all, the fate of (8) depends on whether the quantum Hamiltonian exhibits *degeneracies*, i.e., if there exist $n \neq m$ such that $E_n = E_m$. For the moment, let us assume that no such degeneracies are found in the system's spectrum. After that, we will consider the degenerate scenario.

Non-degenerate spectrum.– After some relaxation time where the system may exhibit non-generic behavior, the sum of off-diagonal terms in (8) eventually averages out to zero, and the long-time average of (8) is given by

$$\overline{\langle \hat{O} \rangle} \equiv \lim_{\tau \to \infty} \frac{1}{\tau} \int_0^\tau \mathrm{d}t \, \langle \hat{O}(t) \rangle = \sum_n |c_n|^2 O_{nn}. \tag{9}$$

In 2008, Reimann showed rigorously [12] that, under experimentally realistic conditions, (9) is a good equilibrium state because the excursions of the real-time dynamics $\langle \hat{O}(t) \rangle$ from $\overline{\langle \hat{O} \rangle}$ are exceedingly rare, and that for most times the difference $\langle \hat{O}(t) \rangle - \overline{\langle \hat{O} \rangle}$ is below the instrumental resolution limit of any observable that may be experimentally monitored. The particularly simple expression (9) shows that, *in the absence of degeneracies*, the long-time dynamics are primarily controlled by the population coefficients c_n. Since the information about the initial state is stored in these coefficients, in general different initial states will attain different equilibrium values. This constitutes a marked difference with respect to classical thermalization, where the details of the initial state are completely erased by the time evolution if the system thermalizes. It is important to emphasize that what (9) is suggesting somehow is that thermalization *should not happen* in the quantum world! This is terrible for a quantum-classical correspondence and it contradicts all we know about classical mechanics emerging from quantum mechanics in the limit $\hbar \to 0$. Luckily, not all hope is lost: we will see that thermalization in quan-

tum mechanics is best understood as a *statistical* phenomenon, manifesting in the limit of large number of particles, N.

Statistical physics teaches us that, due to quantum energy levels being quantized, the quantum mechanical counterpart of the classical microcanonical average (4) at macroscopic energy E is

$$\langle \hat{O} \rangle_{\text{ME}} \equiv \frac{1}{\mathcal{N}} \sum_{E_n \in [E-\Delta E/2, E+\Delta E/2]} O_{nn}, \tag{10}$$

where the summation is performed over a large number states, $\mathcal{N} \gg 1$, whose associated eigenvalues are contained in the energy shell ΔE. In the case of, e.g., generic many-body quantum systems, the mean distance between neighboring levels (the *level spacing*) typically decreases exponentially with N, and thus a small energy window ΔE contains a huge number of states. In other class of systems where this distance does not decrease so fast, we need to make sure that ΔE contains a reasonable number of states so that a statistical analysis is justified. The energy shell cannot be too wide in comparison to the macroscopic energy, $\Delta E/E \ll 1$. Sticking to our definition of thermalization, we wish to make (9) and (10) match. There are several ways to look at this conundrum, and while we will certainly not explore all of them, let us mention that this question is the center of much active scientific (and sometimes philosophical, too) debate.

Random eigenstates

The simplest solution to this problem comes from assuming that the eigenstates of the Hamiltonian, $|E_n\rangle$, are random vectors, i.e., its components, in a certain computational basis, are random numbers taken from a certain probability distribution. Whimsical though it may look, this way of thinking is reminiscent of (or, rather, in agreement with) the ideas of random matrix theory [13], [14], which is one the oldest and most powerful analytical tools that we have to understand quantum chaotic behavior. The essence of quantum chaos will be discussed in the next section of this thesis. For now, suffice it to say one of the defining features of quantum chaotic systems is that the the statistics of their energy levels (with some technical caveats) are in close agreement with some probability distributions coming from assuming that the Hamiltonian is so complicated that it resembles an Hermitian random matrix satisfying certain symmetry properties. Naturally, the eigenvectors of such a random Hamiltonian are random vectors. In that case, the diagonal terms O_{nn} do not vary much as a function of n. In the limit where one assumes that O_{nn} equals a certain constant, it is obvious that (9) and (10) coincide. This simplistic argument, which we will refine below, is really the essence of the

eigenstate thermalization hypothesis. It suggests that if a quantum system behaves similarly to a random matrix, i.e., if it is chaotic, then thermalization should occur. The usefulness the RMT to understand thermalization in isolated quantum systems has many precedents, but let us highlight the 1991 contribution by Deutsch [15], where he assumed that in ergodic Hamiltonians the eigenstates are basically featureless random vectors. This is an extension of Berry's conjecture, which had been formulated in 1977 and applied to semiclassical systems [16]. And indeed, in [17], [18], Santos and Rigol provided clear evidence of the onset of thermalization being accompanied by the development of quantum chaos in many-body bosonic and fermionic lattice systems without a classical analogue.

While this discussion is certainly a bit hand-waving, it will help us connect with the ETH.

Eigenstate thermalization hypothesis

In modern quantum mechanics, the ETH is the hypothesis that underlies our understanding of thermalization. Its current formulation was developed in the 1990s and it is mostly due to Srednicki [19]–[21]. Essentially, the ETH is a statement about how the expectation values of physical observables need to fluctuate about the microcanonical average for the long-time average to coincide with the predictions of statistical mechanics. Let us consider that the solutions of the eigenvalue equation $\hat{H}\,|E_n\rangle = E_n\,|E_n\rangle$ have been previously separated by symmetry sector (e.g., in lattice systems with periodic boundary conditions the momentum is conserved). The fundamental statement of the ETH can be formulated as follows [2]:

For a large class of operators, the diagonal expectation values in the Hamiltonian energy eigenbasis, O_{nn}, fluctuate around the microcanonical average at energy E_n, that is,

$$O_{nn} = \langle \hat{O} \rangle_{\mathrm{ME},E_n} + \Delta_n, \;\; n \in \{1, \ldots, D\}, \tag{11}$$

where Δ_n is some random noise and D is the system's Hilbert space dimension. The terms Δ_n are called *diagonal fluctuations*, and they are assumed to vanish on average, $\langle \Delta_n \rangle = 0$, while their deviations with respect to this mean value decrease exponentially with system size, $\langle \Delta_n^2 \rangle \propto \langle \hat{O}^2 \rangle_{\mathrm{ME}} e^{-aD}$, where $a > 0$ is some constant. In other words, the ETH relies on the natural assumption that if the fluctuations of O_{nn} around their microcanonical value decrease fast enough (exponentially) with system size, then quantum thermalization is guaranteed. As we can see, this hypothesis is really an extension of the random vector mechanism given above, whereby the diagonal expectation values behave as a smooth, almost constant function of energy. If (11) is satisfied, then it is clear that, on average, a single

diagonal term is enough to ascertain to what value the dynamics will equilibrate, as $\langle O_{nn} \rangle = \langle \hat{O} \rangle_{\mathrm{ME}}$. This is the reason why this hypothesis is called the ETH: it assumes that *every* eigenstate is thermal itself. While this may sound erroneous since isolated quantum systems, by definition, are not coupled to an external bath of any kind, the common way to interpret this self-thermalizing nature is that a number of degrees of freedom of the system act as its own heat bath.

The fact that in the above statement there is an explicit mention of how the fluctuations around the microcanonical average are suppressed as the system size increases suggests that, according to (11), one should not expect thermalization in a very small quantum system. Although this may look as a shortcoming, it is really in good agreement with our expectations of why and when statistical mechanics should work. Thermalization is then best understood as a statistical phenomenon.

The ETH can also appear quite vague in that it does not really specify to which quantum observables it applies. Some of the criticism that the ETH has attracted is partly due to this precise observation: indeed, if one is allowed to categorize any Hermitian operator as a quantum measurable quantity, i.e., an observable, then nothing prevents us from expecting certain strange observables to thermalize too. Consider, for instance, an arbitrary function of the system Hamiltonian. The operator $\hat{O} = g(\hat{H})$ *is* Hermitian, and its diagonal expectation values are given by $O_{nn} = g(E_n)$ as $[g(\hat{H}), \hat{H}] = 0$, irrespective of the functional form of g. Yet, if g is not sufficiently well-behaved, it is perfectly possible that the ETH hypothesis is violated. Of course, this example can be argued to be too artificial, and if we are let to go down this path, we may as well come up with a plethora of nonsensical Hermitian operators that do not thermalize. The main point that we wish to highlight here is that we should only expect the ETH to apply, in the first place, to *physically* relevant observables. The ETH generally accepted to apply to few-body observables in non-integrable systems, but even then the limits of where the ETH applies and where it breaks down can be blurry. In the context of lattice models, it has been argued by Garrison and Grover [22] that the ETH can hold for few-body observables that connect up to $N/2$ particles, with N being the total number of particles of the system.

Another point where the ETH statement can look sloppy, at least from a mathematical viewpoint, is that it does not clearly indicate how many of the O_{nn} must verify (11) for the observable $\hat{O}$ to reach thermal equilibrium. Real quantum systems are normally not as perfect as we would wish them to be, and the existence of certain O_{nn} that do not deviate from $\langle \hat{O} \rangle_{\mathrm{ME}}$ only by an exponentially small amount, even if they are non-integrable, is certainly not out of the question. Think, for example, of strongly correlated quantum systems with few-body interactions; in these systems, the Hilbert space dimension grows exponentially with the num-

ber of particles. In this exponentially large set of eigenstates of the Hamiltonian, we could still find, say, an exponentially small number of wave functions that do not behave as dictated by the ETH. This situation has been termed *weak* ETH [23], in contrast to the *strong* ETH, where all O_{nn} are assumed to be very close to the microcanonical average [1]. One should take note that, even in chaotic systems, the eigenstates close to the edges of the spectrum are highly non-generic and localized; it is hard to guarantee that these states will, too, be thermal in general.

But in the study of thermalization there are even more intricate questions, which we do not intend to solve here. We normally associate this phenomenon with the long-time behavior of certain, reasonable observables, while we do not pay much attention to the wavefunction $|\psi\rangle$ defining the initial state or how we have prepared the system to test if it thermalizes or not. Initial states that lead to thermalization are technically referred to as *typical*. Typicality has been an overall fruitful concept in our efforts to understand thermalization [24]–[27]. Yet, it is clear that the notion of typicality also depends somehow on the quantum system under consideration; there is no doubt that the expansion coefficients, $c_n = \langle E_n|\psi\rangle$, responsible for the Hamiltonian population distribution, retain an important degree of control of the dynamics, as (9) evidences. Paradoxically enough (as under the ETH the thermalizing nature of a single eigenstate is enough to discover what the long-time dynamics of an observable will be), quantum thermalization strongly relies on the fact that the population distribution $\{|c_n|^2\}$ generated by the initial state is sufficiently well behaved and narrow. We may ask ourselves this question: Can we expect (9) to agree with (10) if quantum states are not even remotely statistically equivalent? We venture to say that the answer is most certainly negative. Say, for example, that the $|c_n|^2$ is a multimodal distribution, strongly peaked about distinct energy values. In this case, it does not take much thought to realize that the microcanonical average as defined in (10) should be unable to capture the long-time dynamics. Some may argue that this scenario is so artificial that it is hardly relevant; however, very similar population distributions are realistically found in cat states, the macroscopic superposition devised by Schrödinger himself [28] and named after a grumpy but charismatic creature. How we may describe the long-time dynamics of observables under these states [29] is a question that we intend to answer later on in this thesis, see Chapter 3.4.

The previous discussion stimulates the following question: Does the ETH inextricably imply thermalization? This is the elephant in the room, which we can answer affirmatively only if the distribution of populated states $\{|c_n|^2\}$ is well clus-

tered around a single energy value, the mean energy of the state: $\langle E\rangle = \sum_n |c_n|^2 E_n$. Indeed, it follows from the ETH ansatz (11) that the long-time average reads

$$\overline{\langle \hat{O}\rangle} = \sum_n |c_n|^2 (\langle \hat{O}\rangle_{\mathrm{ME},E_n} + \Delta_n), \tag{12}$$

but since the diagonal fluctuations vanish exponentially as the system size increases, this implies, up to negligible corrections, that

$$\overline{\langle \hat{O}\rangle} \simeq \sum_n |c_n|^2 \langle \hat{O}\rangle_{\mathrm{ME},E_n} \text{ as } N \to \infty. \tag{13}$$

Does this equal $\langle \hat{O}\rangle_{\mathrm{ME},E_n}$, given that the microcanonical average is evaluated at energy E_n? If only c_n associated to E_n close to the mean energy value significantly contribute to the sum above (and the microcanonical average does not change a lot between neighboring eigenenergies, which should be the case unless the spectrum exhibits some sort of non-analytic behavior), then to very high precision in (13) we may approximate $c_n \simeq 0$ unless n is such that $E_n \simeq \langle E\rangle$, and thus $\overline{\langle \hat{O}\rangle} \simeq \langle \hat{O}\rangle_{\mathrm{ME}}$. An analogous reasoning shows why (10) cannot describe the thermalization process in cat states.

We can ask ourselves the converse question: Is thermalization a consequence of the ETH? Unlike the previous question, the answer is no. The ETH is a theoretical tool that certainly does a good job at bridging the gap between microscopic reversibility and the experimental observation that most real physical systems thermalize, playing much the same role that the ergodic hypothesis in classical mechanics. However, the equivalence between the ETH and the physical phenomenon that we call thermalization is excessive. In fact, even some integrable systems can satisfy the ETH in the weak sense, as shown by Müller *et al* for translation-invariant finite-range interacting quantum lattice systems [30]. Then there are examples of systems that do thermalize for most initial conditions, satisfying the weak ETH and not the strong ETH [31]. The ETH is thus a formal guiding principle that puts us on the right track, that allows us to make sense of experimental observations.

A natural question we may ask is how long must one wait to observe a quantum system thermalize. We have noted before that for sufficiently long times, the sum involving oscillating off-diagonal matrix elements in the instantaneous expectation value given by (8) can be assumed to average to zero. Nevertheless, the question still remains: How long is 'sufficiently long'? If our only means to observe thermalization in a quantum system is to wait for a period of time equivalent to the age of the Universe, we may as well disregard the entire concept as it becomes experimentally useless. And indeed, this would seem to be the case, for example, in interacting many-body systems, whose mean level distance decreases is exponentially small in system size. Before the oscillating terms $e^{-i(E_m-E_n)t}$ can be

neglected, an exponentially large time needs to have elapsed, comparable to the inverse of the mean level spacing: the Heisenberg time. This is at odds with our daily experience where it is not rare to observe physical systems thermalize within minutes! Formally speaking, all the ETH tells us is that thermalization is bound to happen; it does not really make any estimate as to *when* it should happen. This is not a shortcoming of the ETH, though: it serves its purpose, as it establishes conditions under which a system thermalizes. But for us, human beings, life is limited and time, precious. It so happens that the vast majority of physical systems, statistically speaking, are so complex and their interactions are so strong that they come close to being chaotic. And according to the RMT, the off-diagonal matrix elements of generic observables in fully chaotic systems are exponentially small in system size. To keep it short, under RMT one has that the matrix elements of $\hat{O}$ satisfy [1]

$$O_{mn} \approx \overline{O}\delta_{mn} + \sqrt{\frac{\overline{O^2}}{D}} R_{mn}, \tag{14}$$

where $\overline{O} \equiv \frac{1}{D}\sum_k O_k$, O_k are the eigenvalues of $\hat{O}$, D is the Hilbert space dimension and, importantly, R_{mn} is a Gaussian random variable with $\langle R_{mn}\rangle = 0$ and $\langle R_{mn}^2\rangle = \mathcal{O}(1)$. This implies that the off-diagonal terms ($m \neq n$) vanish approximately as fast as the decrease in mean level distance, $O_{mn} \propto 1/\sqrt{D} = \mathcal{O}(e^{-N})$, almost miraculously countering the oscillating terms $e^{-i(E_m - E_n)t}$! We can rest assured: if the system is chaotic or near-chaotic, no such infinite-time periods are effectively needed to reach equilibrium. Yet, it should be mentioned that although the RMT ansatz (14) provides a good qualitative idea of what we should expect, there many features of realistic physical systems that are not captured by the RMT (see next section for more details). As to what happens to systems where correlations are not so strong as to bring it close to chaoticity, without further mathematical assumptions this is something we would need to examine on a one-by-one basis.

What happens after the system has reached thermal equilibrium? Does it stay there forever? Our definition of thermalization does not preclude some infrequent and not very drastic deviations from the thermal value. But do physical systems satisfy this definition, once they have thermalized for the first time? Generally, we can say that yes, they do. We have already mentioned the proof provided by Reimann [12] of the long-time average being a good equilibrium state. The reader may be familiar with the notion of quantum *revivals* [32], whereby the Schrödinger equation can lead the time-evolving wavefunction $|\psi(t)\rangle$ arbitrarily close to its initial value $|\psi(0)\rangle$ as was beautifully demonstrated in the classical limit of the hydrogen atom [33]. Owing to Poincaré's recurrence theorem [34], if a system is

prepared in an 'atypical' value of an observable, such recurrences are guaranteed to occur. However, Poincaré's result is only relevant for finite systems, or even, one might say, for small systems: the recurrence time increases exponentially with the number of degrees of freedom, so for moderate systems it is so long that it can be disregarded.

Truthfully, the ETH is not only concerned with the diagonal expectation values of observables, as (11) suggests. An *off-diagonal* ETH exists which is useful to understand dynamic correlation functions. In this thesis we will not deal with these additional features, but more details will be given below.

Our discussion of thermalization and the ETH has departed from considering an initial state that generates non-trivial dynamical evolution. The key point is that the population distribution $\{c_n\}$ cannot be the trivial distribution for this to occur. Because of its importance to this thesis, we will introduce the concept of *quantum quench*, which is an experimentally relevant method to take an initial state out of equilibrium in systems whose dynamics is controlled by some control parameter.

Quantum quench.- Let us consider a quantum Hamiltonian depending on a control parameter, $\hat{H}(\lambda)$. Suppose that we use the eigenstates of the Hamiltonian at an initial value of the control parameter, λ_i, to build an initial state, $|\psi(0)\rangle = |E_0(\lambda_i)\rangle$. A quantum quench is the procedure whereby the Hamiltonian control parameter is instantaneously changed to a final value, $\lambda_i \to \lambda_f$, so the initial state evolves according to (6).

As a consequence of the quench, the initial state can potentially overlap with a huge number of eigenstates of the final Hamiltonian, $\hat{H}(\lambda_f)$. Depending on the details of the initial state itself or the final Hamiltonian, the distribution of $\{c_n\}$ can be very complex, and thus so can be the time evolution (6). Observe that the quenched state is not stationary under $\hat{H}(\lambda_f)$, as $\hat{H}(\lambda_i)$ and $\hat{H}(\lambda_f)$ have different eigenstates. All of the results discussed in this section remain valid if the initial state is quenched. Quenches will be extensively used in the results of this thesis.

Before ending this part, we will allow one final question: We know that chaotic systems are good candidates to thermalize, but does the RMT, which we still have not properly defined, imply the ETH? Is the ETH some sort of consequence or extension of the RMT? The ETH reduces to the RMT on a certain energy scale, called the Thouless energy [35] (see below), but the ETH goes beyond the RMT because it describes dynamical features outside the more restrictive range of applicability of the RMT.

Degenerate spectrum.– Suppose our quantum system is such that its spectrum exhibits degeneracies. For the sake of simplicity, let us consider the case where the degeneracies are due to the presence of a $\mathbb{Z}_2$ symmetry, i.e., an operator $\hat{\Pi}$ with only two eigenvalues and which is such that $[\hat{H}, \hat{\Pi}] = 0$. In a large class of

interacting systems, this symmetry is called *parity*, and its spectrum is $\mathrm{Spec}(\hat{\Pi}) = \{-1, +1\}$. The eigenvalues of this symmetry are then used as quantum numbers to assign to the eigenstates of the Hamiltonian, i.e.,

$$\hat{\Pi} \left| E_{n\alpha} \right\rangle = \alpha \left| E_{n\alpha} \right\rangle , \tag{15}$$

where $\alpha \in \{-1, +1\}$ and $n \in \mathbb{N}$. The system's Hilbert space can be then decomposed into symmetry sectors, so that the full Hamiltonian is simply $\hat{H} = \bigoplus_{\alpha=-,+} \hat{H}_\alpha$. Let us assume that all states of opposite parity are degenerate, i.e., $E_{n+} = E_{n-}$ for all n. Of course, the existence of degeneracies in a quantum spectrum is not necessarily derived from a symmetry, but in this thesis this physical situation will play a central role so we will work within this framework from the start.

It is clear from (8) that, in the presence of degeneracies, the term containing the off-diagonal terms does not need to average to zero in the infinite-time limit, as the degenerate states contribute with resonances that are completely static, thus surviving the long-time average. Even more: such terms carry observable matrix elements of the form O_{mn}, and there is no way to reconcile this, in general, with the microcanonical average (10), which contains diagonal elements O_{nn} alone. The consequence for thermalization is fatal: the equivalence of long-time and microcanonical averages breaks down!

More explicitly, let us consider an initial state of the form

$$\left| \psi(0) \right\rangle = \sum_{n,\alpha} c_{n\alpha} \left| E_{n\alpha} \right\rangle , \quad \sum_{n\alpha} \left| c_{n\alpha} \right|^2 = 1. \tag{16}$$

Analogously to (8), at time t the expectation value of an observable $\hat{O}$ is then

$$\langle \hat{O}(t) \rangle = \sum_{n,m} \sum_{\alpha,\beta} c_{n\alpha} c^*_{m\beta} e^{-i(E_{n\alpha} - E_{m\beta})t} O_{m\beta;n\alpha}, \tag{17}$$

where now $O_{m\beta;n\alpha} \equiv \left\langle E_{m\beta} \right| \hat{O} \left| E_{n\alpha} \right\rangle$. What is the long-time average? In answering this question, a little manipulation is convenient. This expression can be separated into different parts: (i) first, we have the diagonal terms, which are such that $n = m$ and $\alpha = \beta$; (ii) second, we have the combination $n = m$ and $\alpha = -\beta$, which are not diagonal but which give rise to degenerate contributions; (iii) and third, we have the case where $n \neq m$, where there cannot be degeneracies according to our setup. Therefore,

$$\begin{aligned} \langle \hat{O}(t) \rangle = & \sum_{n\alpha} \left| c_{n\alpha} \right|^2 O_{n\alpha;n\alpha} + \sum_{n\alpha} c_{n\alpha} c^*_{n-\alpha} O_{n-\alpha;n\alpha} \\ & + \sum_{n \neq m} \sum_{\alpha\beta} c_{n\alpha} c^*_{m\beta} e^{-i(E_{n\alpha} - E_{m\beta})t} O_{m\beta;n\alpha}. \end{aligned} \tag{18}$$

In the long-time limit, the third summation eventually averages to zero as this term contains no degeneracies, but the first two terms survive. Therefore:

$$\overline{\langle \hat{O} \rangle} = \sum_{n\alpha} |c_{n\alpha}|^2 O_{n\alpha;n\alpha} + \sum_{n\alpha} c_{n\alpha} c^*_{n-\alpha} O_{n-\alpha;n\alpha}. \tag{19}$$

If the observable $\hat{O}$ is the Hamiltonian, this expression allows us to recover the mean energy of the system, which is of course constant, $\langle E \rangle \equiv \langle \hat{H} \rangle = \sum_n [|c_{n+}|^2 E_{n+} + |c_{n-}|^2 E_{n-}]$. Likewise, the parity of the state (16) is simply $\langle \hat{\Pi} \rangle = \sum_n [|c_{n+}|^2 - |c_{n-}|^2]$. These expressions only contain diagonal terms and therefore it would appear that the measurable quantities are obtained simply considering each of the parity sectors separately. However, (19) hides important information about the *coherence* between both parity sectors. This information is revealed in the long-time average of a *parity-breaking* observable. Let us consider an operator $\hat{M}$ such that

$$\hat{M} |E_{n\alpha}\rangle = \sum_n m_n |E_{n-\alpha}\rangle , \quad m_n \in \mathbb{C}. \tag{20}$$

$\hat{M}$ is a parity-breaking operator because its expectation value vanishes under states of the same parity, $\langle E_{n\alpha}| \hat{M} |E_{m\alpha}\rangle = 0$ for all n, m. In some systems, $\hat{M}$ can represent the total magnetization along certain direction [36]. Equation (19) tells us that its long-time average is

$$\overline{\langle \hat{M} \rangle} = \sum_{n\alpha} c_{n\alpha} c^*_{n-\alpha} m_n, \tag{21}$$

which clearly depends on the coherence between opposite parity sectors.

We mentioned before that the long-time average (19) cannot match the predictions of the standard microcanonical ensemble (10). But is there a way to make this equilibrium state describable through an equilibrium ensemble other than the microcanonical? It is clear that the answer must lie somewhere beyond traditional statistical mechanics; for instance, the canonical ensemble could not do the job either, as in the thermodynamic limit it coincides with the microcanonical ensemble, which cannot describe this state. This question is central to this thesis, and we will provide answers to it in the chapters dedicated to results.

1.2 CHAOS AS A MECHANISM FOR THERMALIZATION

1.2.1 Classical chaos

The notion of chaos has originated an immense deal of interest both within the scientific community and in popular culture. Within science, chaos meant a conceptual revolution as it is at odds with the notion of the Universe as an ordered

entity which we can attempt to describe in a controlled way. Out of science, the reader is sure to have come across a number of movies and novels where chaos plays a role in one way or another; often this has to do with the idea that the effect of apparently minor events gets amplified as time goes by, the so-called 'butterfly effect'. In daily-life language, chaos is 'a state of utter confusion' [37]; even more: it is 'a state of total confusion with no order', with some synonyms being 'disarray', 'disorder', 'disorganization' or, apparently, 'anarchy' [38]. These expressions retain some of the essence of chaos, at least in principle, but they are also misleading as a physical system need not be 'disordered' for it to be chaotic: the double pendulum is a chaotic system, yet it is hard to argue that it is very complicated or convoluted. It may be shocking to know that, despite its ubiquity and relevance, there is still today not a definition of chaos that every scientist can happily accept. Despite this, its phenomenology is fairly well understood and its mathematical foundations are incredibly sophisticated. While the development of chaos in discrete systems and in dynamical systems in a broad sense is a fascinating topic, here we will focus on Hamiltonian chaos and its manifestations.

In every history of chaotic dynamics, there is one person whose mention is never missed: Edward Lorenz is commonly accepted as the discoverer of chaos. As of September 2023, his famous 1963 paper amasses some 28000 citations [39]. The way he was led to make his discovery is intimately related to one of its main signatures: the sensibility of chaotic trajectories to a small modification of the initial conditions. Lorenz was a mathematician working as a meteorologist at the Massachusetts Institute of Technology. One day, as he trying to predict the weather conditions with a digital computer, he observed that if he changed the working precision of his machine from 3 digit arithmetic to 6 digit arithmetic (though he did this inadvertently), then he would obtain completely different estimates for what the forecast would be for that day. As he eloquently recalls in his popular book [40], his hope was to replicate some previous results that he did not understand very well:

'I stopped the computer, typed in a line of numbers that I had printed out a while earlier, and set it running again. [...] The numbers being printed out ***were nothing like the old ones****. [...] I found that the new values at first repeated the old ones, but soon afterward differed by one and then several units in the last decimal place, and then began to differ in the next to the last place and then in the place before that. [...] The numbers that I had typed in were not the exact original numbers, but were the rounded-off values that had appeared in the original printout. The initial round-off errors were the culprits; they were* ***steadily amplifying until they dominated the solution****.'*

Lorenz was not the first to come to the realization that some complex dynamical systems may behave in a seemingly random and unpredictable way, even if they

are they are subject to the laws of classical dynamics, which are deterministic. Like many scientists of his time, Lorenz thought that a small change of initial conditions should imply a change in the subsequent dynamical evolution, at most, of the order of magnitude of the initial condition modification. To be fair, the fact that some systems may exhibit erratic behavior upon slight modification of initial conditions had already been pointed out by Poincaré in his 1908 essay[1] *Science et méthode* [41]:

'[...] il peut arriver que de ***petites différences*** *dans les conditions initiales en engendrent de* ***très grandes*** *dans les phénomènes finaux; une petite erreur sur les premières produirait une erreur énorme sur les derniers. La prédiction devient impossible et nous avons le* ***phénomène fortuit****.'*

The fortuitous phenomenon Poincaré mentions is chaos, though he never called it that. Poincaré was never interested in chaos, and simply dismissed it as a tedious artifact that rendered the three-body problem too complicated to solve. Anyway, we can rightfully say that Lorenz is responsible for the unexpected explosion of scientific interest in this phenomenon. Today, chaos is the subject of study of innumerable texts, among which we mention [42]–[44] and, of course, the classic [4]. One way we have come to understand chaos is as the science that deals with what *looks* random but is not. Or, as Lorenz put it , *'when the present determines the future, but the approximate present does not approximately determine the future'*.

In simple terms, a physical system is chaotic if it does not have sufficiently many constants of motion which simplify the dynamics. This is connected to the notion of integrability, which we will discuss in detail in the next section.

Classical chaos is really *deterministic chaos*. Given a dynamical system and an initial condition, its future configuration is completely determined by, e.g., the Hamilton equations of motion, if the system under consideration is treated within the Hamiltonian formalism. These constitute a system of coupled non-linear differential equations, in which no element of randomness can be found. Even more: the dynamics generated by these differential equations is reversible. Given a final configuration, we are formally allowed to go back in time to the state where we prepared the system. One may then be led to mistakenly think, as is sometimes the case, that the reason why we cannot predict the future in a chaotic system is that its equations of motion are very complicated, in contrast to integrable systems whose solution is easy to find. But some integrable systems may also be described by quite intractable differential equations, and we do not call them chaotic. It must be emphasized that the *practical unpredictability* of chaotic dynamical systems has

1 In English: *'[...] it may happen that* ***small differences*** *in the initial conditions generate very great ones in the final phenomena; a small error in the former would produce an enormous error in the latter. Prediction becomes impossible, and we have the* ***fortuitous phenomenon****.'*

a fundamental origin: it is *impossible* to come up with an algorithm capable of obtaining an approximated solution with a time-independent precision (in integrable systems this can be done). Yet, it would be unfair to say that the dynamical nature is not related to the form of the differential equations by which it abides: in classical mechanics, they are non-linear, which allows for chaotic behavior. All chaotic systems are described by non-linear differential equations, but not all non-linear differential equations need to give rise to chaos.

Lyapunov exponents.- We have mentioned that one of the strongest signatures of classical chaos can be characterized by an *exponential* divergence of infinitesimally nearby trajectories. In integrable systems, however, such separation can be, at most, algebraic. Mathematically, this is quantified by the so-called *Lyapunov exponents* [45], [46]. Consider an initial condition in phase space $\mathbf{r}(0) \equiv (\mathbf{q}(0), \mathbf{p}(0)) \in \mathcal{M}$ to which we apply a small perturbation, $\delta\mathbf{r}(0)$. In a chaotic system, the magnitude of this amplitude grows exponentially with time,

$$\|\delta\mathbf{r}(t)\| \sim \|\delta\mathbf{r}(0)\| e^{\lambda_{\mathrm{L}} t}. \tag{22}$$

Here, $\lambda_L \geq 0$ is the (largest) Lyapunov exponent, which characterizes the rate of divergence of two initial trajectories $\mathbf{r}(0)$ and $\mathbf{r}(0) + \delta\mathbf{r}(0)$. This number is defined as the following double limit:

$$\lambda_{\mathrm{L}} = \lim_{t\to\infty} \lim_{\|\delta\mathbf{r}(0)\|\to 0} \frac{1}{t} \ln \frac{\|\delta\mathbf{r}(t)\|}{\|\delta\mathbf{r}(0)\|}. \tag{23}$$

Chaotic trajectories have $\lambda_{\mathrm{L}} > 0$. Osledec showed [47] that the limit in (23) exists and equals a finite number for almost all initial configurations $\mathbf{r}(0)$ and almost all initial perturbations $\delta\mathbf{r}(0)$. Rigorously speaking, in a system of f degrees of freedom there exist exactly f Lyapunov exponents, and each of them is associated to one of the directions along which the trajectory separation can be probed. The dynamics is controlled by the largest Lyapunov exponent, and therefore this is the quantity that is commonly computed.

Mathematically, the Lyapunov exponent is completely defined by (23). A different question is how to efficiently compute this quantity. Most of the problem comes from the fact that the evolution in time of the initial perturbation, $\delta\mathbf{r}(t)$, can be quite difficult to obtain in a consistent way. To circumvent this issue, certain computationally effective algorithms have been devised. This goes on to show the vital role that numerical calculations play in the field of non-linear dynamics, where an exact solution of the differential equations is very frequently out of reach. In this thesis, we have used a common algorithm that we present below [45].

Broadly speaking, in our approach for a Hamiltonian system of f degrees of freedom we need to solve a system of $2f + (2f)^2$ differential equations, which

can be broken down into two systems of equations that we solve simultaneously. The first system consists of the $2f$ differential equations encoded in the Hamilton equations of motion: f of them correspond to the canonical positions and the remaining f equations solve the dynamics of the associated conjugated momenta. This is the *dynamical problem*

$$\frac{\mathrm{d}}{\mathrm{d}t}\mathbf{r}(t) = F(\mathbf{r}(t)), \tag{24}$$

subject to $\mathbf{r}(t=0) = \mathbf{r}(0)$. Here, F is the so-called dynamical function, whose components are given precisely by the Hamilton equations. The remaining $(2f)^2$ differential equations come from the *variational problem*,

$$\frac{\mathrm{d}}{\mathrm{d}t}\Phi(t) = D_{\mathbf{r}}F(\mathbf{r}(t))\Phi(t), \tag{25}$$

subject to $\Phi(t=0) = 1_{4f^2}$, where 1_n stands for the n-dimensional identity matrix, and $D_{\mathbf{r}}F(\mathbf{r}(t))$ is the Jacobian of the dynamical function F. The systems specified by (24) and (25) are coupled, as $\mathbf{r}(t)$ depends on $\Phi(t)$ through $D_{\mathbf{r}}F(\mathbf{r}(t))$. It can be shown that in the limit of small perturbations, $\|\delta\mathbf{r}(0)\| \to 0$, the problem can be linearized for any value of time, and at time t the perturbation is related to its initial value through $\Phi(t)$:

$$\delta\mathbf{r}(t) = \Phi(t)\delta\mathbf{r}(0). \tag{26}$$

Insertion of (26) into (23) then allows to easily compute the Lyapunov exponent. In practice, it is common to consider an ensemble of different initial separations $\delta\mathbf{r}(0)$, sometimes chosen at random according to some probability distribution, and then compute an averaged Lyapunov exponent, $\overline{\lambda}_{\mathrm{L}}$. This is because even in strongly chaotic systems there can be small stability islands [43] and thus one can still find a small number of regular trajectories: a single trajectory can give the impression that the system is not chaotic. Even though this algorithm is quite effective, it is clear from its formulation that in general we will not be able to treat systems with a very large number of degrees of freedom. We will use these ideas in Chapter 4 of this thesis.

At this point it is important to emphasize that although a positive Lyapunov exponent (23) is commonly accepted as a signature of classical chaos, in some situations it is insufficient to guarantee that the system is chaotic. The reason is that the Lyapunov exponent is best understood as a signature of *dynamical instability*, which is a necessary but not sufficient condition for chaos. Think, for example, of an inverted pendulum, where the mass is placed vertically at its highest position. Under the Hamilton equations of motion, it is clear that such a state is stationary, as it will remain static eternally. However, we know from experience that it

is very unlikely that the system will remain in that position for a very long time. Indeed, the system described is in equilibrium, but this equilibrium is unstable: a very small perturbation is enough to destroy it. The Lyapunov exponent associated to this scenario is positive, because infinitesimally close but different initial perturbations will generate trajectories that separate exponentially. Yet, the single pendulum is not chaotic, but integrable. In the case of the pendulum, no initial condition apart from the one specified above can give rise to positive Lyapunov exponents. Contrarily, the system exhibits a smooth dependence on most initial conditions, so that if they are slightly modified very similar trajectories should ensue. But this example is quite illustrative in that it shows that positive Lyapunov exponents are not enough to guarantee chaotic dynamics, much in the same way that a single zero Lyapunov exponent, technically, is not sufficient to speak of integrability either. In this sense, positive Lyapunov exponents have been found in integrable classical systems whose phase space exhibits unstable fixed points [48], a feature that is unrelated to chaos.

Chaos is related to the notions of ergodicity and mixing. As we mentioned in Sec. 1.1.1, ergodicity is the phenomenon whereby any 'typical' trajectory will eventually cover all available phase space at a given constant energy. Ergodicity means that a single initial condition is enough to describe the average behavior of the system, and it is the reason why long-time averages can be computed as microcanonical averages where all configurations are assigned equal probability of occurrence. Ergodicity is a technical term that in every-day life could be associated with the idea of randomness or disorder. Ergodicity does not necessarily imply chaos. Now, since we are so interested in pendulums, the one dimensional harmonic oscillator is an counterexample for a system that is ergodic but not chaotic: its equations of motion do not even fulfill the non-linearity condition necessary for chaos! Thus, it seems that for a system to be chaotic some property other than ergodicity is missing. This property is called mixing. Intuitively, it reflects the behavior that we expect in a glass of water when we add a droplet of ink. If we think of water and ink as subsystems, after some time has elapsed (which can be very long) both become completely 'intertwined'. A mathematical description of mixing is beyond the intended scope of this thesis, but the main idea can be summarized as follows.

Mixing.- A dynamical system is mixing if each subset of phase space gets uniformly dispersed under the system's dynamics. In a mixing system, different trajectories get arbitrarily close to one another infinitely many times.

This is equivalent to the statement that the self-correlation of a well-behaved dynamical function decays to zero after sufficiently long time. The mathematical concept of mixing was established in 1932 by von Neumann [49] and then further developed by Hopf [50], [51], but the first to consider it as an independent phe-

nomenon was thermodynamicist Gibbs, who already in 1902 stated that mixing is like *'the effect of stirring an incompressible system'*, which brings it to *'a state of uniform mixture'* [52]. Mixing is a stronger condition than ergodicity; in particular, mixing implies ergodicity. There are not many mathematically rigorous proofs of systems that are mixing. Sinai showed that the paradigmatic hard-sphere gas is mixing as, roughly speaking, a slight change in the direction of motion of any particle gets magnified as it collisions with the convex surface of another particle [53], [54]. Suffice it to say that the proof of the simplest case, that of a single particle, occupies around 70 pages.

In defining what chaos is in terms of its phenomenology, as we are attempting to do, it is important to emphasize that 'chaos' is quite a generic term that is commonly used to refer to a certain physical properties, such as the presence of positive Lyapunov exponents. Rigorously, the notion of chaos can be broken down into several classes of systems depending on their degree of 'chaoticity'. Even more, it should be noted that not all systems that are not integrable need to be chaotic, or at least not completely chaotic. In this sense, technically, 'chaos' is much of an umbrella term. The origin of this hierarchy of chaos lies in the KAM theorem, which explains how integrable systems evolve to chaoticity as perturbation terms are added to the system Hamiltonian. The KAM theorem will be briefly discussed in the next section, but for now let us say that by 'fully chaotic' system what is normally meant is a system whose Kolmogorov-Sinai entropy is positive (although other alternatives are possible).

Entropy is a way to quantify information. Information we have, or information we lose. Thus, for example, in statistical mechanics the Boltzmann equation connects the entropy of a system and the number of microstates that are compatible with the macrostate the system is in. If the number of microstates is large, so is the entropy, but if there is a single microstate then the entropy vanishes as there is no new information we can gain by performing a measurement of the state. The Shannon entropy quantifies the uncertainty in, for example, a combination of letters, words or a text. Very common words such as 'the' have a very low information entropy because they do not help us determine what the text it is found in can be. The Kolmogorov-Sinai entropy [55], [56], although formally much more involved, is a measure of the quantity of information that is carried by a certain trajectory in phase space. It can be thought of as an indicator of how much information per unit time is lost as the system evolves in time. Physical systems whose Kolmogorov-Sinai entropy is positive are called K-systems, while for integrable systems this entropy is zero. The Kolmogorov-Sinai entropy also provides an estimate of the maximum timescale beyond which the motion of a system becomes unpredictable; this time is inversely proportional to the Kolmogorov-Sinai entropy.

K-systems.- In a K-system, there are no stable orbits. Any two initial conditions will give rise to exponentially diverging trajectories.

We can see that K-systems capture our intuitive idea of what a chaotic system should be. Yet, it should be noted that the classification does not stop here, and there other classes of systems that, in a certain sense, are even more chaotic. For our purposes, the diverging nature of classical trajectories will be enough. All K-systems are mixing, and all mixing systems are ergodic.

1.2.2 Quantum chaos

Quantum mechanics as a whole is the most general theory that we have to describe the physical reality. The quantum-classical correspondence principle tells us that classical mechanics should emerge from quantum mechanics in the limit $\hbar \to 0$, essentially at sufficiently large scales roughly comparable to the De Broglie wavelength. Then, one is led to expect that the origin of classical chaos is to be found somewhere deep within quantum mechanics. Nevertheless, it became clear that the phenomenology of classical chaos cannot be mapped directly to quantum mechanics, which makes it impossible to employ our classical understanding to deduce what form chaos should take in the quantum world.

What even is quantum chaos?

One fundamental reason is that quantum dynamics is controlled by the Schrödinger equation, which is linear, and therefore cannot give rise to chaos in the classical sense. In fact, our classical understanding of chaos is tightly connected to the notion of phase space where trajectories are embedded. Yet, in quantum theory the position and momentum operators are non-commuting and thus there are no quantum states where these operators are completely determined (i.e., with zero uncertainty); this is the content of Heisenberg's uncertainty principle. If one cannot fix position and momentum, it is clear that the concept of classical trajectory does not have a quantum counterpart. The fact that there are no trajectories in quantum mechanics has several important consequences, but for our purposes, it is enough to say that one of the main signatures of chaos, the exponential sensitivity of trajectories to slight changes of initial conditions, cannot be properly defined in the quantum world. One may then think that this issue may be solved if we replace the classical trajectory with some object that is native to quantum mechanics and that specifies the state of a system: the wavefunction. Unfortunately, this will not help either because the time evolution operator, $\hat{\mathcal{U}}(t)$, is unitary, $\hat{\mathcal{U}}^\dagger\hat{\mathcal{U}} = 1$, which means that it is preserves distances and norms. The fact that the distance between

two arbitrary wavefunctions evolving under the same Hamiltonian is constant can be illustrated with the following simple example. Consider to initial conditions given by $|\psi(0)\rangle$ and $|\phi(0)\rangle$. Wavefunctions are really vectors in some Hilbert space, so similarly to vectors in real space one may define their distance through their norm,

$$d(|\psi\rangle, |\phi\rangle) = \||\psi\rangle - |\phi\rangle\|, \tag{27}$$

where $\||\psi\rangle\| \equiv \langle\psi|\psi\rangle$. At time t, the previous initial wavevectors read $|\psi(t)\rangle = \mathcal{U}(t)|\psi(0)\rangle$ and $|\phi(t)\rangle = \mathcal{U}(t)|\phi(0)\rangle$. Therefore, due to unitary dynamics, the distance at an arbitrary time t coincides with the initial distance:

$$\begin{aligned} d(|\psi(t)\rangle, |\phi(t)\rangle) &= |(\langle\psi(0)| - \langle\phi(0)|)\hat{\mathcal{U}}^\dagger(t)\hat{\mathcal{U}}(t)(|\psi(0)\rangle - |\phi(0)\rangle)| \\ &= d(|\psi(0)\rangle, |\phi(0)\rangle), \end{aligned} \tag{28}$$

so, of course, the idea of exponentially divergent trajectories, even in some quantum sense, must be abandoned.

In order to make this discussion complete, two remarks are convenient. First, it is worth mentioning that, technically, quantum mechanics can be defined within a phase-space formalism through the Wigner-Weyl transformation [57], but even within this framework trajectories cannot be properly defined as the uncertainty principle still applies. Second, the fact that the distance of two wave functions evolving under the same Hamiltonian is mathematically preserved does not really make any indication as to what happens if such Hamiltonian is only slightly perturbed. This can explored by means of the *fidelity*, which measures how 'close' two quantum states are. It should be noted, however, that the fidelity is not a distance in the space of density matrices, however. Let us consider a pure initial state $|\psi(0)\rangle$. We will let it evolve under an arbitrary Hamiltonian, $\hat{H}$, and a slightly perturbed Hamiltonian, $\hat{H}_\delta = \hat{H} + \delta\hat{V}$, where $\hat{V}$ is an Hermitian operator encoding some perturbation of $\hat{H}$ and $|\delta| \ll 1$. The time-evolved counterparts of $|\psi(0)\rangle$ are $|\psi(t)\rangle = e^{-i\hat{H}t}|\psi(0)\rangle$ and $|\psi_\delta(t)\rangle = e^{-i\hat{H}_\delta t}|\psi(0)\rangle$. Clearly, $|\psi(t)\rangle \neq |\psi_\delta(t)\rangle$, but what is about the fidelity or squared overlap

$$F(|\psi(t)\rangle, |\psi_\delta(t)\rangle) = |\langle\psi(t)|\psi_\delta(t)\rangle|^2. \tag{29}$$

Does (29) behave differently depending on the properties of the Hamiltonian $\hat{H}$? Broadly speaking, Peres found [58], [59] that if $\hat{H}$ describes the dynamics of a quantum system whose classical analogue is regular, then the overlap (29) remains approximately constant and close to unity for short times, while if $\hat{H}$ corresponds to a quantum system with chaotic classical analogue then (29) decays exponentially at short times, i.e., states $|\psi(t)\rangle$ and $|\psi_\delta(t)\rangle$ are less and less alike in an exponential

way. Note that the setting of this experiment is completely different as the classical exponential sensitivity to initial conditions refer to two trajectories evolving under the *same* Hamiltonian, so by no means does this invalidate the distance preserving property illustrated by (28). However, it goes on to suggest that even if chaos is to be redefined in the quantum world, there are indeed some dynamical traces that seem to depend on whether the quantum system is related to a classically integrable or chaotic system.

The question remains: What can we call 'quantum chaos'? [60] This has been the subject of endless debate and while we do not attempt to provide a definite answer as to whether we should be properly speaking of chaos in quantum physics, the truth is that quantum chaos [61]–[64] is a very active research field which has been proved incredibly fruitful to understand the dynamics of complex (and sometimes also simple) quantum models and it is also directly tied to paramount physical phenomena such as thermalization or decoherence [1], [2], [17], [65]. There is no doubt that it is an important phenomenon that we should not disregard. M. V. Berry, one of the protagonists of the history of quantum chaos, took fault with the use of 'chaos' as anything that could describe quantum dynamics as, strictly speaking, a quantum system cannot show any chaoticity in the classical sense. In his famous Bakerian lecture [66], which we gave as he was awarded the Royal Society prize in physical sciences, he proposed to use the term 'quantum chaology' instead:

'Quantum chaology is the study of semiclassical, but nonclassical, behaviour characteristic of systems whose ***classical motion exhibits chaos****.'*

While this definition is perfectly acceptable, it only refers to quantum systems with a well-defined classical analogue. Some of the most important quantum models studied nowadays are strongly correlated systems that are genuinely quantum in the sense that they do not approach classicality as a function of system size or of any of its internal parameters. What is about these systems?

The way we understand quantum chaos is through the statistical properties of the spectrum of a system although, as we will discuss below, alternative characterizations relying, for example, on the structure of the Hamiltonian eigenstates are also possible. The mathematical tool that allows to establish this correspondence is the RMT, which have already briefly touched on in this thesis.

Chaos in the quantum spectrum: the random matrix theory

The main idea behind quantum chaos is that it is hopeless to attempt to understand all the details of a complex many body system such as the atomic nucleus. These systems appear to be have so complicated interactions that a statistical approach

may be better suited to gain insight about their overall behavior. The following is a extract of the speech given by Wigner at a conference on neutron physics held in Gatlinburg, Tennessee, in 1956:

'Perhaps I am now too courageous when I try to guess the ***distribution of the distances between successive levels*** *[of energies of heavy nuclei]. Theoretically, the situation is quite simple if one attacks the problem in a simpleminded fashion. The question is simply what are the distances of the characteristic values of a symmetric* ***matrix with random coefficients****.'*

Together with Dyson, Mehta and others, Wigner is considered the inventor of the RMT [67]–[72]. The RMT is a mathematical theory that studies the properties of random matrices, i.e., matrices whose elements are drawn from a certain probability distribution. The mathematical aspects of the RMT are discussed in detail in the monograph by Mehta [13] and in the review by Guhr *et al* [14]. Here, we will summarize some main results.

In the theory of chaos in closed quantum systems, Gaussian ensembles have traditionally played a predominant role (but not only, see [73] for an extension of the RMT to the problem of quantum transport). According to Wigner's idea, one may replace the system's Hamiltonian with a suitably chosen *ensemble* of random matrices which, on average, describe the features of the real physical system. The general philosophy should not be so unfamiliar to us: statistical mechanics works in a very similar way, as the knowledge of the precise characteristics of a system is renounced in favor of an overall understanding. However, the RMT takes this one step further, as in statistical mechanics the form of the interactions is given by the precise physical system of interest; in the RMT, however, the interactions are also randomized! Yet, the individuality of the real system is encoded in the RMT ensembles through some geometrical constraints that define their *symmetry classes*. In the context of the Gaussian RMT, there are three main symmetry classes:

(i) Gaussian orthogonal ensemble (GOE).– It applies to systems that have time reversal invariance. It consists of matrices $\hat{H} = h_{ij}$ that are real and symmetric, whose elements h_{ij} with $i \geq j$ are statistically independent. The probability distribution $P(\hat{H})$ is invariant under orthogonal transformations of $\hat{H}$. The joint probability density distribution of its matrix elements reads

$$P(\{h_{ij}\}) = \left(\frac{A}{\pi}\right)^{N/2} \left(\frac{2A}{\pi}\right)^{N(N-1)/2} e^{-A\sum_{i,j} h_{ij}^2}, \tag{30}$$

where N is the matrix dimension and A is some constant.

(ii) Gaussian unitary ensemble (GUE).– This applies to systems without time reversal invariance (which can be broken, e.g., in the presence of a magnetic field). It consists of, in general, complex and Hermitian matrices, whose elements h_{ij} are

such that $\mathrm{Re}(h_{ij})$ and $\mathrm{Im}(h_{ij})$ for $i > j$ are statistically independent. The density distribution $P(\hat{H})$ is invariant under unitary transformations, and it reads

$$P(\{h_{ij}\}) = \left(\frac{A}{\pi}\right)^{N/2} \left(\frac{2A}{\pi}\right)^{N(N-1)/2} e^{-A\sum_{i,j}\mathrm{Re}(h_{ij})^2+\mathrm{Im}(h_{ij})^2}. \tag{31}$$

(iii) Gaussian symplectic ensemble (GSE).– It applies to systems with time reversal invariance but no rotational symmetry. It consists of Hermitian and selfdual matrices, whose elements h_{ij} are statistically independent quaternions. The density distribution $P(\hat{H})$ is invariant under symplectic transformations, and it takes the form

$$P(\{h_{ij}\}) = \left(\frac{A}{\pi}\right)^{N/2} \left(\frac{2A}{\pi}\right)^{N(N-1)/2} e^{-A\sum_{i,j}(h_0)_{ij}^2+(h_1)_{ij}^2+(h_2)_{ij}^2+(h_3)_{ij}^2}, \tag{32}$$

where $(h_n)_{ij}$ $(n = 0, 1, 2, 3)$ are the components of the quaternion h_{ij}.

Observe that the probability distributions (30), (31) and (32) depend on the matrix elements only through $\mathrm{Tr}(\hat{H}^2)$, which leads to the central limit theorem being satisfied. They are called Gaussian for this reason.

One crucial aspect of these RMT ensembles is that even though they are all generated from statistically independent random numbers, h_{ij}, their associated eigenvalues are strongly correlated. It can be shown [13] that the joint probability density function of the eigenvalues $\{\lambda_1, \ldots, \lambda_N\}$ is

$$P(\{\lambda_i\}) \propto e^{-A\sum_{k=1}^{N}\lambda_k^2} \prod_{n>m}^{N} |\lambda_n - \lambda_m|^\beta, \tag{33}$$

where β is the so-called Dyson symmetry index; it equals $\beta = 1, 2, 4$ for GOE, GUE and GSE. This formula is very clarifying from a phenomenological viewpoint: it tells us that in a Gaussian random ensemble, the eigenvalues behave as charged particles that repel one another. Two main paramount effects associated to quantum chaos can be discussed already from this expression. First, no two eigenvalues can assume the same value (there can be no degeneracies), as $P(\lambda_i, \lambda_j) \to 0$ when $\lambda_i \to \lambda_j$ (unless $\beta = 0$, which, incidentally, is used to denote integrable models, where level crossings are bound to happen; see next section). This defines one of the hallmark signatures of quantum chaotic spectra: *level repulsion*. In a quantum chaotic system, there can be no two overlapping eigenvalues, so they can be said to 'repel'. The intensity of such repulsion increases with β. But the effect of the term $\sum_{n>m}|\lambda_n - \lambda_m|^\beta$ is not only responsible for level repulsion. It is also the reason why eigenvalues are strongly correlated, in the probabilistic sense: it is due to this term that (33) does not factorize at all: $P(\{\lambda_i\}) \neq \prod_i P_i(\lambda_i)$. In fact, in a random matrix (and thus in a fully quantum chaotic system) there are long-range

correlations to *all* energy distances. Second, the exponential term $e^{-A\sum_{k=1}^{N}\lambda_k^2}$ heavily suppresses configurations of $\{\lambda_i\}$ with large values of $|\lambda_i|$; in other words, the eigenvalues cannot lie too far from the origin. In practice, this almost 'confines' eigenvalues, annihilating extreme events from the configuration. This metaphor is at the heart of another important property of chaotic systems: the *spectral rigidity*.

In essence, the RMT is a useful tool because it is mathematically tractable, and it allows us to obtain analytical results that we can then compare with experimental or numerical data extracted from realistic physical models. But beyond that, the ultimate reason why we care about the RMT at all is because the statistical features of quantum systems whose classical analogue is chaotic appear to be almost perfectly captured by its results. This is the object of study of *spectral statistics*. We will explain what we mean by this, but before that we need to take a small detour, which we hope will not be too technical.

Save the fluctuation: the unfolding procedure

It is often said that quantum chaos is concerned with the *universal fluctuations* of energy levels, and relates them to RMT. This may sound cryptic. What exactly is meant by the fluctuations of eigenvalues?

In classical mechanics, the possible values that the energy can assume define a continuous object, as these values belong to the real line. Looking through the prism of continuous probability theory, we may ask how many physical states exist with energy equal or less than E. The answer, of course, is given by the cumulative distribution function,

$$N_c(E) = \int\!\!\!\int \mathrm{d}^f\mathbf{q}\mathrm{d}^f\mathbf{p}\,\Theta[H(\mathbf{q},\mathbf{p}) - E], \tag{34}$$

where $\Theta(x)$ denotes the Heaviside distribution (or 'step function'). The subindex c reminds us that this applies to classical systems. Quantum spectra of bound systems, however, are discrete, so their level counting function is defined as

$$N(E) = \int_{-\infty}^{E} \mathrm{d}E'\,\rho(E') = \sum_n \Theta(E - E_n), \tag{35}$$

where

$$\rho(E) = \sum_n \delta(E - E_n) \tag{36}$$

is the density of states at energy E. The density of states contains complete information about the spectrum of a quantum system. It indicates the number of states per energy unit that exist in the system at energy E. For the moment, let us

consider a quantum system with a classical analogue. The classical (34) is an analytic function (with the exception of some particular systems where it may show discontinuities, as in excited-state quantum phase transitions, see below), but the quantum (35) is not differentiable, as it is a stair function. If the system is integrable, use of the SWI quantization rules [74]–[76], which we will not discuss in this thesis, shows that the slope of the quantum (35) is given by the classical (34). This means the number of states with energy less than E *fluctuates* and, on average, coincides with the corresponding classical counting. If the system is chaotic, the SWI rules do not apply (which was pointed out by Einstein in an early but largely ignored paper [77]) and we need to resort to a more general method developed by Gutzwiller in the 1970s [78] (which also applies to integrable systems, anyway). This is a semiclassical formalism, valid in the limit $\hbar \to 0$, that makes use of Feymann's path integral to calculate a propagator from which one can define a Green function. Integration of the Green function yields the density of states. A complete derivation of this result is quite mathematically heavy so we will content ourselves with the final result, which is [63]

$$\rho(E) = 2 \sum_{p} \sum_{r=1}^{\infty} A_{p,r}(E) \cos\left[\frac{r S_p(E)}{\hbar} + \nu_{p,r}\right]. \tag{37}$$

Here, p is the number of 'primitive' periodic orbits (those that cannot be decomposed into repetitions of simpler orbits), r is the number of primitive periodic orbits, $A_{p,r}$ is a quantity related to the orbit stability (this quantity is related to the Lyapunov exponent), S_r is the classical action, and $\nu_{p,r}$ is the Maslov index, related to the number of turning points of the dynamics. The semiclassical nature of this quantity is obvious as it makes use of classical periodic orbits. In practice, the calculation of (37) is quite complicated even in relatively simple models, and it can suffer from severe convergence issues. For our purposes, what is relevant about (37) is that it is the *full* density of states of the system, and all periodic orbits have been accounted for to arrive to this equation. Among these, there is one special, trivial kind of periodic orbits: those with period zero (i.e., when the particle remains immobile). The contribution of these orbits to (37) turns out to coincide with the classical density of states if it is properly normalized [79],

$$\overline{\rho}(E) = \frac{1}{(2\pi\hbar)^f} \int\!\!\int \mathrm{d}^f\mathbf{q}\mathrm{d}^f\mathbf{p}\, \delta[H(\mathbf{q},\mathbf{p}) - E], \tag{38}$$

where $2\pi\hbar = h$ is the phase space elementary cell size [this guarantees that $\int_{-\infty}^{\infty} \mathrm{d}E\, \overline{\rho}(E) = 1$]. This is called the *smooth* part of the density of states. When zero period orbits are excluded from the full density (37), we arrive at the so-called *fluctuating* part of the density of states, $\widetilde{\rho}(E)$.

Summarizing, for any quantum system with a classical analogue, a semiclassical calculation shows that the density of states can be separated into these two parts,

$$\rho(E) = \overline{\rho}(E) + \widetilde{\rho}(E). \tag{39}$$

Naturally, the same applies to the cumulative distribution function,

$$N(E) = \overline{N}(E) + \widetilde{N}(E). \tag{40}$$

The smooth part of the density of states contains system-dependent information related to the details of a particular model, but the fluctuating part is *universal*, as it merely depends on whether the classical analogue is chaotic or integrable. The universal correlations that quantum chaos analyzes with statistical tools and compares with the RMT are all contained in the fluctuating $\widetilde{\rho}(E)$. But what happens if our quantum system is not compatible with a semiclassical analogue? Think, for example, of one-dimensional $1/2$-spin models with nearest-neighbor interactions. These systems do not approach the semiclassical limit even as the number of spins grows to infinity, because the spin size is fixed to $1/2$. In that case, we must resign ourselves and assume that the semiclassical separations (39) and (40) remain valid, as is commonly accepted in the quantum chaos community, even if for lack of a better way to proceed.

Before one can begin the statistical analysis of energy levels, the fluctuating part of the density of states must be isolated from the smooth counterpart. This process is called *unfolding procedure*. Consider a sequence of energy levels $\{E_1 \leq \ldots \leq E_N\}$ coming from diagonalizing the Hamiltonian of a real physical system. From them, we can define the *unfolded energy level* as

$$\epsilon_n = \overline{N}(E_n) = \int_{-\infty}^{E} \mathrm{d}E' \, \overline{\rho}(E'). \tag{41}$$

This is the central object of the statistical analysis. By definition, $\epsilon_n \geq 0$. The unfolding procedure is an important aspect of quantum chaos because almost every spectral statistics depends on it being correctly performed (we will comment on a recent and notable exception below). Yet, it is also highly non-universal. The reason is that unless the form of the smooth density of states $\overline{\rho}(E)$ is known from first principles (which is almost never the case), there is not a unique way to do unfolding. In that case, it is very common to fit a smooth function to the computed density of states, for example a polynomial, and assume that this will play the role of $\overline{N}(E)$. In addition to this, the unfolding procedure can carry some subtle, undesired effects. Gómez *et al* [80] showed that certain forms of local unfolding methods (not discussed in this thesis) can spoil the relationship of the spectral analysis and the degree of chaoticity of the system and, recently, Corps and Relaño [81]

demonstrated that the unfolding procedure inevitably introduces spurious correlations in the unfolded eigenlevels, even if the original levels were uncorrelated (this may negatively impact the spectral statistics of quantum integrable systems, see below). This work belongs to the scientific production of the author of this thesis, although here we will not discuss it explicitly.

The quantum chaos conjecture

Wigner's original idea made it possible to understand the statistical properties of complex nuclei. At the time this was thought-provoking result, but the range of applicability of the RMT remained unclear for a long time. Should the predictive power of the RMT be restricted to very complex systems? This question was answered in 1984 by Bohigas, Giannoni and Schmit, leading to the conjecture that bears their name: the BGS conjecture (sometimes, even, 'the quantum chaos conjecture'). In their famous article [82], they studied the level statistics of a single particle placed in a Sinai billiard, which is a classically chaotic system. Approaching the semiclassical limit (i.e., at high enough energy), they found that the level statistics almost perfectly follow the predictions of the RMT. In particular, they studied the level spacing distribution, $P(s)$, where $s_n = \epsilon_{n+1} - \epsilon_n$ is the unfolded level spacing coming from a sequence of raw eigenvalues in ascending order, $\{E_1 \leq \ldots\ldots E_N\}$. By definition, the random variable s has unit average, $\langle s \rangle = 1$. Specifically, they found that in this system, $P(s)$ follows the Wigner-Dyson distribution,

$$P(s) = \frac{\pi}{2} s e^{-\pi s^2/4}, \tag{42}$$

in other words, the level spacing distribution expected in the RMT for the GOE ensemble. The (nearest-neighbor) spacing distribution is one of the most common spectral statistics. It clearly evidences the phenomenon of level repulsion, as $P(s) \sim s$ as $s \to 0$ (in general, for the Gaussian ensembles this is $P(s) \sim s^\beta$), as well as the exponential decay at $s \gg 1$ that can be argued to be a manifestation of chaotic spectral rigidity. The expression (42) is obtained from 2×2 GOE random matrices and is not exact in the $N \to \infty$ limit. However, it is remarkable that the $N \to \infty$ asymptotics are qualitatively and quantitatively close to the simple (42): this is popularly known as *Wigner's miracle*.

Guided by this result, Bohigas, Giannoni and Schmit formulated the following conjecture [82]:

*'Spectra of time reversal-invariant systems whose classical analogs are K systems show the **same fluctuation properties** as predicted by GOE (alternative stronger conjectures that cannot be excluded would apply to less chaotic systems, provided that they are ergodic).'*

The relevance of this short statement is hard to overemphasize. Effectively, it means that one can establish a bidirectional association between quantum chaos and the RMT, that one can say that a system is chaotic if it is describable by the RMT. Also, that the complexity of a quantum system is not necessary for it to be chaotic. Although the conjecture was formulated in the semiclassical limit, today we have come to collectively understand that it is permissible to say that even a quantum system without a classical analogue is chaotic if its level fluctuations are as in the RMT. In this case, it is still unclear what chaos may mean beyond some pragmatic compliance with the RMT. Recently, some advances in this question have been reported [83].

The RMT has been successfully applied to many systems well beyond its intended scope; some examples include supersymmetry [84], chiral symmetry [85], financial markets [86], and atmospheric correlations [87]. The spectral statistics of many quantum systems follow the Wigner-Dyson distribution. Some examples are heavy nuclei (i.e., the foundational Nuclear Data Ensemble but also recent analyses of ^{208}Pb [88]–[91]), Sinai billiards [82], or the hydrogen atom in a magnetic field [92]. Quantum systems with an accessible semiclassical limit have played an important role in the exploration of chaos, and in this category it is worth mentioning the Dicke model [93], an atom-field experimental system which has been in the center of much modern research [94]–[97]. Recently, strongly interacting many-particle models of condensed matter have become one of the best playgrounds to study quantum chaos and ergodicity. Some of these models include one-dimensional spin-1/2 or spin-polarized fermion lattices [17], [18], [98]–[102].

Is the BGS conjecture, then, universally valid, i.e., is it permissible to call it a theorem? Counterxamples have been found, but they normally are non-generic systems, such as arithmetic billiards [103] which have an exponentially large degeneracy of lengths of periodic orbits (see also [104]). In any case, the BGS conjecture has actually been mathematically proved at the semiclassical level. Based on previous works by Hannay *et al* [105]–[107], the universality of quantum chaos was demonstrated by Müller, Heusler, Haake and others in 2004 [108]. This was the germ of a series of papers [109]–[111], which constitute the foundations of a full periodic-orbit theory for quantum chaotic correlations.

Despite the usefulness of the RMT, there are certainly aspects of real systems that cannot be captured by its statistical description. For example, after a suitable scaling, the level density of the Gaussian random ensembles converge in the $N \to \infty$ limit to a semicircle distribution [13], which is quite unrealistic. From a conceptual viewpoint, in the RMT there is the implicit assumption of all-to-all couplings (the matrix is completely filled with random numbers), which is also unphysical.

In addition to determining the statistical behavior of eigenlevels, the RMT also provides predictions for the overall behavior of the corresponding eigenvectors. Through the matrix elements of observables, they play an important role in thermalization. Consider an arbitrary eigenvector written in some basis, $|\Phi\rangle = \sum_k \varphi_k |k\rangle$. For the GOE, invariance under orthogonal transformations implies that the joint probability distribution of the components φ_k [112] is

$$P(\{\varphi_k\}) \propto \delta \left(\sum_n \varphi_n^2 - 1 \right) \tag{43}$$

As a consequence, the eigenvectors of GOE random matrices, as we mentioned in Sec. 1.1.2, are basically random vectors with the only constraint that they must satisfy the normalization condition $\langle\Phi|\Phi\rangle = 1$. This was argued to be a sufficient condition for long-time averages to coincide with microcanonical phase space averages. Of course, the orthogonality of eigenvectors means that they cannot be completely independent, but the ensuing correlations are completely negligible for random matrices of moderate dimension. The end result is that, as implied also by the BGS conjecture, one can consider that the eigenvectors of strongly quantum chaotic systems in a typical basis (not fine-tuned) are indeed featureless random vectors [15], [16].

Related to the behavior of eigenvectors is the statistical theory for the matrix elements of arbitrary observables under the RMT [1]. Consider an Hermitian operator $\hat{O}$ written in its eigenbasis, $\hat{O} = \sum_k O_k |k\rangle \langle k|$, where $\hat{O}|k\rangle = O_k |k\rangle$, and a random matrix with eigenvectors $|\Phi_n\rangle$ and $|\Phi_m\rangle$. What does the RMT predict for the matrix elements $O_{mn} = \langle\Phi_m| \hat{O} |\Phi_n\rangle$? We can write

$$O_{mn} = \sum_k O_i \langle m|k\rangle \langle k|n\rangle \equiv \sum_k O_k (c_k^m)^* c_k^n, \tag{44}$$

where we have defined the expansion coefficients $c_k^m \equiv \langle k|m\rangle$. Taking into account that the eigenstates of random matrices are random vectors, we may perform an ensemble average, which we denote by $\langle\langle\bullet\rangle\rangle$: $\langle\langle (c_k^m)^* c_\ell^n \rangle\rangle = \frac{1}{D}\delta_{mn}\delta_{k\ell}$, where D is the matrix dimension. This yields

$$\langle\langle O_{nn}\rangle\rangle = \frac{1}{D}\sum_k O_k \equiv \overline{O}, \quad \langle\langle O_{mn}\rangle\rangle = 0 \ (m \neq n), \tag{45}$$

For the fluctuations around these values, using the properties of the Gaussian ensembles one can show [13] that

$$|\langle\langle O_{mn}^2\rangle\rangle| - |\langle\langle O_{mn}\rangle\rangle^2| = \left(\frac{1}{D} + \frac{2-\beta}{D}\delta_{mn} \right) \overline{O^2}, \tag{46}$$

with β the Dyson index. Equations (45) and (46) imply (14). One remark is convenient: In (45) and (46) we have considered an average over a large number of random matrices, and therefore (14) is valid only to leading order in $1/D$ (the eigenvectors of a random matrix are only orthogonal up to $1/D$ terms). However, because the fluctuations of operators are tiny for large D, one can safely assume that (14) is sufficiently accurate for most random Hamiltonians. It is also important to observe that in a strongly quantum chaotic system, (14) teaches us that the distribution of the fluctuations of the matrix elements O_{mn} around their mean value $\overline{O}$ is Gaussian ($O_{mn} - \overline{O}\delta_{mn}$ is a Gaussian random variable). In the next section we will briefly explain how this is related to the ETH ansatz.

1.2.3 Fitting the pieces: RMT $\subset$ ETH

We have already mentioned that, in its attempt to describe the statistical behavior of dynamical systems, the RMT can be too unrealistic. Aside from some unphysical features such as its prediction for the average level density (Wigner's semicircle), there are other issues that become troublesome if one wants to use the RMT to describe quantum thermalization. Realistic systems are clearly not random: (i) the expectation values of observables actually depend on temperature (or energy density), and (ii) not all observables approach relaxation at the same rate. In other words, the RMT prediction for O_{mn} given in (14) is lacking information that cannot be disregarded in real systems. This information, however, is contained in the ETH. In fact, one can say that the ETH is a generalization of the RMT; in other words, the RMT implies the ETH, but the converse is not true. The overall features of the ETH were provided in (11); however, the random term Δ_n therein hides some relevant information and for this reason we shall specify the ETH ansatz further. Equation (11) is a simplified version for the diagonal ETH. The most general form of the ETH, including off-diagonal matrix elements, reads [1]

$$O_{mn} = \langle \hat{O} \rangle_{\text{ME}}(\overline{E})\delta_{mn} + e^{-S(\overline{E})/2} f_O(\overline{E}, \omega) R_{mn}, \tag{47}$$

where $\overline{E} = (E_m + E_n)/2$ is the mean energy of the eigenstates $|E_n\rangle$ and $|E_m\rangle$ where the expectation value of $\hat{O}$ is taken, $\omega \equiv E_n - E_m$ is the energy difference of these eigenstates, $S(\overline{E})$ is the thermodynamic entropy evaluated at $\overline{E}$, and R_{mn} is a random real or complex variable with $\langle R_{mn} \rangle = 0$ and unit variance. The second term in the right-hand side of (47) is the random term Δ_n in (11). The structure of the eigenstates of realistic systems is encoded in the function f_O, which is a smooth function. The matrix elements O_{mn} can be real or complex depending on the symmetries of the Hamiltonian. For real matrix elements, it is necessary that

$R_{nm} = R_{mn}$ and $f_O(\overline{E}, -\omega) = f_O(\overline{E}, \omega)$, while for complex matrix elements we have $R^*_{nm} = R_{mn}$ and $f^*_O(\overline{E}, -\omega) = f_O(\overline{E}, \omega)$.

The ETH ansatz (47) bears much similarity with the RMT result (14), but (14) is more simplistic. Indeed, observe that in (47) the diagonal terms O_{nn} depend on the mean energy of the eigenstates, that is, they are not constant as in the RMT but a smooth function of energy. Also, in the off-diagonal elements the random fluctuations R_{mn} are modulated by the function $f_O(\overline{E}, \omega)$, which depends on both $\overline{E}$ and ω. Yet, all information of (14) is present in (47): *the ETH simplifies to the RMT within a very narrow energy window where $f_O(\overline{E}, \omega)$ is constant* (and, of course, one assumes that the microcanonical average does not vary in such small energy interval). The scale of this energy window is the so-called *Thouless energy* [35]. In single-particle systems, it equals [113]

$$E_{\text{Th}} = \frac{\hbar D}{L^2}, \tag{48}$$

where D is the diffusion constant, and L is the length of the system. If $\omega < E_{\text{Th}}$, then the Hamiltonian eigenstates behave as structureless random vectors, and the ETH and RMT coincide. Similarly, the Thouless energy gives the scale beyond which the universal description of the RMT breaks down. In practice, this irremediably limits the range of applicability of the RMT. It is clear from (48) that this characteristic scale vanishes in the thermodynamic limit as $E_{\text{Th}} \propto 1/L^2$, which could be interpreted as the total failure of the RMT for large systems. However, the mean level spacing decreases faster than algebraically in many models, which means that even a small energy window may contain, e.g., an exponentially large amount of states that can be described by the RMT.

In the case of interacting systems, such as disordered spin chains, the physical meaning of the Thouless energy is still not completely understood. However, there is some convincing evidence that it might be related to a complicated anomalous diffusion process [114]. The Thouless energy scale plays an important role in analyses of spectral statistics and relaxation towards equilibrium in many-body localizing systems, which we will review in Sec. 1.3.2.

1.3 EXCEPTIONS TO THERMAL BEHAVIOR

1.3.1 Integrability

A very common notion of integrable models is that they are relatively easy to deal with, as their motion is somehow more ordered and constrained than that of

chaotic models. Indeed, unlike chaos, which favors the thermalization process and can be seen as a catalyst for it, the integrability of a physical system can seriously hinder thermalization. In order to intuitively grasp why this is so, it is convenient to briefly recall the theoretical basis of integrability. Again, it will prove useful to separate the classical and quantum points of view.

Classical integrability

There are several definitions for integrability in the classical world, but here we will stick to the arguably most fruitful and common one: integrability in the sense of Liouville [3], [4].

Liouville classical integrability.– Consider a classical system described by a Hamiltonian, H, of n degrees of freedom, and a set of n dynamical functions, $\{f_i\}_{i=1}^n$ defined as $f_i : \mathcal{M} \times \mathbb{R} \to \mathbb{R}$, where $\mathcal{M}$ denotes the classical phase space. The system is said to be integrable by quadratures if the following conditions are satisfied:

- There exist n constants of motion[2] (or integrals of motion) in the form of dynamical functions, i.e., $\{f_i, H\} = \frac{\mathrm{d}}{\mathrm{d}t} f_i(\mathbf{q}(t), \mathbf{p}(t)) = 0$, $\forall i \in \{1, \ldots, n\}$.
- The constants of motion are mutually in involution, $\{f_i, f_j\} = 0$, $\forall i, j \in \{1, \ldots, n\}$.
- The constants of motion are functionally independent.

Under these circumstances, the corresponding differential equations of motion can be integrated explicitly. Through a canonical transformation, the canonical position and momentum can be mapped onto action-angle variables, and the dynamics becomes restricted to invariant tori, where the system exhibits periodic behavior. This is the content of the Arnold-Liouville theorem, which can be stated as follows:

Arnold-Liouville theorem.– Consider a set of n dynamical functions, $\{f_i\}_{i=1}^n$, and an integrable system of n degrees of freedom with Hamiltonian $H = H(\mathbf{q}, \mathbf{p}; t) \equiv E$. Consider also the n-dimensional surface of integrals of motion defined by

$$\mathcal{M}_f \equiv \{(\mathbf{q}, \mathbf{p}) \in \mathcal{M} \ / \ f_k(\mathbf{q}, \mathbf{p}) = F_k\}, \ k \in \{1, \ldots, n\}, \tag{49}$$

where F_k is a constant that can be taken to be system energy, E. Then, we have:

- If $\mathcal{M}_f$ is a compact and connected set, then it is diffeomorphic to an n-dimensional tori, $\mathbb{T} \equiv \mathbb{S}^1 \times \mathbb{S}^1 \times \ldots \times \mathbb{S}^1$, and in a neighborhood of $\mathbb{T} \subset \mathcal{M}$

2 We consider the Poisson bracket $\{f, g\} \equiv \sum_{i=1}^{n} [\frac{\partial f}{\partial q_i} \frac{\partial g}{\partial p_i} - \frac{\partial f}{\partial p_i} \frac{\partial g}{\partial q_i}]$, where f and g are dynamical functions.

one may introduce action-angle variables, $\{I_i\}_{i=1}^n$, $\{\phi_i\}_{i=1}^n$, $\phi_i \in [0, 2\pi)$, such that the angles ϕ_i form a basis of coordinates for $\mathcal{M}_f$, and the action variables $I_k = I_k(f_1, \ldots, f_n)$ are integrals of motion of the system.

- The canonical equations of the motion are

$$\dot{I}_k = 0, \ \dot{\phi}_k = \omega_k(I_1, \ldots, I_n), \ k \in \{1, \ldots, n\}. \tag{50}$$

Therefore, the system dynamics can be explicitly solved by quadratures, leading to

$$\phi_k(t) = \omega_k(t) + \phi_k(0), \ I_k(t) = I_k(0), \tag{51}$$

which corresponds to n circular motions with constant angular velocity ω_k, where, in general, $\omega_i \neq \omega_j$ if $i \neq j$.

From the Arnold-Liouville theorem it follows that the original Hamiltonian, $H = H(\{q_i\}_{i=1}^n, \{p_i\}_{i=1}^n)$, can be expressed in terms of the action-angle variables, $H = H(\{I_i\}_{i=1}^n, \{\phi_i\}_{i=1}^n)$. This basis of coordinates completely trivializes the integration of the differential equations of motion. Inverting the the canonical transformation from canonical position and momentum to action-angle variables, one discovers that in the original phase space the dynamics can be reduced to a set of n independent 2π-periodic trajectories. It is for this reason that the motion of a classically integrable system is said to be multiperiodic.

The previous theorem provides a solid mathematical definition for classical integrability. However, it is fair to say that as far as realistic physical systems are concerned, integrability is the exception rather than the norm. For example, in systems with interactions there are usually not as many integrals of motion as degrees of freedom. This applies particularly to many-body interacting systems, which may possess an extensive number of degrees of freedom.

Suppose that we add an integrability-breaking perturbation to a physical system that is integrable in the sense described in this section. How is classical chaos developed? Is it akin to a phase transition, in the sense that chaos appears in an abrupt way as the non-integrable perturbation is increased? Or is there a smooth crossover between integrability and chaos? In systems with a finite number of degrees of freedom, this question is answered by the celebrated Kolmogorov-Arnold-Moser (KAM) theorem [115]–[117]. In terms of its mathematical apparatus, a precise formulation of this theorem is beyond the scope of this work, but the interested reader may consult the classic book by Arnold [4]. The KAM theorem establishes the conditions under which the invariant tori of a deformed Hamiltonian, $H(I) = H_0(I) + \lambda H_1(I)$, where $H_0(I)$ is the original, integrable Hamiltonian,

and $H_1(I)$ is a non-integrable perturbation with a perturbation strength λ, get gradually deformed until they completely disappear. Phenomenologically, as the perturbation strength increases the trajectories leave the previously defined invariant tori, until they *densely* cover the entire available phase space. As a byproduct, this theorem may be used to define a hierarchy of chaos, which determines the degree of chaoticity of the system under consideration.

Intuitively, it is clear why, classically, thermalization is hampered by integrability. The constants of motion impose a set of conservation rules that are respected at all times during the evolution, which means that a lot of information about the initial state is preserved. In the simple case of a one-dimensional system whose dynamics is governed by a time-independent Hamiltonian, energy is an integral of motion and its conservation establishes a mathematical constraint between the position and momentum of the particle. As a consequence, no trajectory can cover the entire phase space and therefore the system is not chaotic.

Quantum integrability

Surprising as it may seem, the definition of quantum integrability has long been and continues to be the center of much debate in the scientific community (see, e.g., [118]–[123]). That many scientists cannot seem to agree on the very defining features of a quantum integrable system already suggests that this is not a trivial matter. Generally speaking, the marked differences between the classical and quantum worlds make it so that our notion of classical integrability is not properly suited to define quantum integrability. For the sake of completeness, and to illustrate the essence of the problem, below we will briefly summarize some typical definitions of quantum integrability. We also mention that one of the main difficulties of defining quantum integrability in a consistent way with classical integrability is that the counting of degrees of freedom varies significantly in both frameworks [123].

I1. Integrability *à la classique*.– The first notion of quantum integrability we will comment on comes from an attempt to translate directly the classical definition into quantum terms: A system is quantum integrable if we can find a maximal set of quantum operators $\hat{\mathcal{O}}_k$, $k = 1, \ldots, D$, where D stands for the Hilbert space dimension, which (i) commute with the quantum Hamiltonian, $[\hat{H}, \hat{\mathcal{O}}_k] = 0$; (ii) are mutually commuting, $[\hat{\mathcal{O}}_i, \hat{\mathcal{O}}_j] = 0$; and (iii) are independent.

This is one of the most common definitions for what a quantum integrable system is, probably because it reflects our classical intuition. However, it is also one definition that we should abandon as, mathematically speaking, it is just not useful. Indeed, we recall that the spectral theorem guarantees that any Hermitian

Hamiltonian with a finite Hilbert space dimension is diagonalizable; from such diagonalization, we may extract D Hamiltonian eigenstates, $|E_n\rangle$, that can then be used to construct the projectors $\hat{\mathcal{O}}_n = |E_n\rangle \langle E_n|$. The set of $\{\hat{\mathcal{O}}_n\}_n$ clearly satisfy all hypotheses in this definition of integrability; yet, it is hard to see how this could be useful, as it would immediately imply that all quantum systems are integrable. Admittedly, one may argue that this definition should remain useful if we were to explicitly exclude the eigenstate projectors as valid quantum operators. Even still, condition (iii) is mathematically impossible to satisfy as von Neumann pointed out in his work [124], where he proves that for any set of mutually commuting Hermitian operators, $\{\hat{\mathcal{O}}_i\}_{i=1}^n$, there exists an Hermitian operator, $\hat{O}$, such that each $\hat{\mathcal{O}}_i$ can be expressed as a function of $\hat{O}$: $\hat{\mathcal{O}}_i = f(\hat{O})$.

I2. Integrability as solvability.– Secondly, a system is quantum integrable if it can be solved exactly.

By this we usually mean that its complete set of eigenstates can be constructed explicitly (and, therefore, so can the corresponding eigenvalues). This definition is implicitly based on exploiting certain methods to diagonalize a Hamiltonian, such as the Bethe ansatz, in a way that we can obtain a closed expression for the eigenstates of the system.

I3. Integrability as harmonic oscillators.– Thirdly, a quantum system can be said to be integrable if it can be mapped to harmonic oscillators.

The problem with this definition is that such a mapping can be very hard to construct, which really defeats the purpose of it.

Lastly, we will emphasize the next two definitions of quantum integrability. Like the previous definitions, they also have some downsides; however, they will be particularly relevant in the context of this thesis. Instead of relying on certain mathematical methods that exactly diagonalize the system or focusing on its commutation properties, the next definitions are closely connected to the theory of quantum chaos regarding the statistical behavior of the Hamiltonian eigenlevels.

I4. Integrability in terms of level statistics.– A system is quantum integrable if its eigenlevels follow Poisson statistics.

This commonplace definition is backed up by the semiclassical theory developed in [125], certainly a foundational work in the study of level statistics of quantum systems whose classical analogue is regular. Let us consider that the spectrum of the quantum system has been previously desymmetrized, i.e., assuming that there is a unitary operator $\hat{R}$ such that $\hat{R}\hat{H}\hat{R}^\dagger = \hat{H}$, we suppose that the whole spectrum of $\hat{H}$ has been divided into sectors characterized by distinct eigenvalues of $\hat{R}$. In

that case, Berry and Tabor showed in 1977 [125] that for *generic* integrable systems, the unfolded level spacing distribution follows the simple expression

$$P(s) = e^{-s}, \;\; s \geq 0, \tag{52}$$

which is indicative of a Poissonian random process. In essence, this implies that in integrable systems the eigenlevels are uncorrelated. In the above expression, the level spacings are derived from unfolded eigenlevels. This phenomenology is in stark contrast with the strong correlation of eigenlevels in quantum chaotic systems. Clearly, according to this definition, integrability is defined in terms of statistical features of the quantum system, which does not rely on exact solutions at all. This method for detecting integrability is practical, as one merely needs to numerically diagonalize the system Hamiltonian and proceed with the standard statistical analysis of level fluctuations. Again, formally speaking, it is really not completely satisfactory, as there very well-known quantum systems, with a classical integrable counterpart, whose level statistics does not follow (52). For example, the eigenlevels of the one-dimensional harmonic oscillator are equiespaced and strongly correlated, as knowledge of a single energy level is enough to obtain the entire spectrum. For this definition to be consistent, one should at exclude from its range of applicability at least systems with a single degree of freedom. Superintegrable systems [126], [127], for which the number of integrals of motion is greater than the number of degrees of freedom, can also violate the Berry-Tabor result. Conversely, leaving these technical issues aside, can we really be sure that a system is quantum integrable if its level statistics is Poissonian? Strictly speaking, this must be answered in the negative: Relaño *et al* showed in [128] that for a class of Richardson-Gaudin models, which are integrable in the sense of definition I1, it is possible to adjust its internal parameters so that the level statistics follow the GOE predictions of quantum chaotic systems, contradicting I4. This violation of the above-mentioned Poissonian behavior may be argued to be an exception, as the Hamiltonian parameters were fine-tuned to precisely reproduce the predictions of the RMT; in fact, a very small interaction term was shown to be enough to quickly drive the system to the Poissonian regime. At this point it is also worth noting that the so-called Berry-Tabor result (52) stems from a semiclassical consideration that only takes into account physical systems with an infinite-dimensional Hilbert space (for example, dynamical billiards or harmonic oscillators). Nevertheless, it is striking that there is a whole body of literature strongly suggesting that the Berry-Tabor result should remain also valid for finite-dimensional quantum systems as well as for systems without a classical analogue [129], to the extent that the Poissonian behavior is today widely accepted as one of the main signatures of integrability in many-body quantum systems. In this thesis, we will associate a

Poissonian level spacing distribution with regularity and integrability, particularly in Chapter 2, where we consider the spectral statistics of many-body localizing disordered spin chains.

I5. Integrability and level crossings.– Consider a quantum system depending on a control parameter, $\hat{H}(\lambda)$. The quantum Hamiltonian $\hat{H}$ is integrable if it displays level crossings.

This is one aspect that strongly helps us tell integrable quantum systems from chaotic quantum systems, which show level repulsion instead of level crossings. From a phenomenological perspective, this is a relatively simple way to detect if a system is integrable, by representing its energy-level flow diagram (the $\lambda \times E$ plane). The level crossings associated to integrability occur between states characterized by the same quantum numbers afforded by a certain symmetry operator, i.e., they occur within a fixed symmetry sector[3]. Yet, it is sometimes hard to ascertain that such real crossings take place, as this must be distinguished from very small but non-zero energy gaps. This definition also has the shortcoming that it may be a bit too restrictive, as it only applies to quantum Hamiltonians with a control parameter.

The ETH has been shown to be invalid, in general, for quantum integrable systems [1]. A quite popular alternative to describe the asymptotic equilibrium values of observables in closed integrable systems was presented by Rigol *et al* in [130]. This is the so-called generalized Gibbs ensemble (GGE), which we briefly revisit below. For a detailed review, we recommend the review [131].

Generalized Gibbs ensemble.– In general, quantum integrable systems have an extensive number of conserved quantities, whose identification may not be trivial at all. The failure of the ETH in integrable systems is commonly attributed to the presence of these charges. Explicitly, when the population distribution $\{|c_n|^2\}$ after a quench is sufficiently narrow (which is normally the case in realistic many-body quantum systems), the long-time average of an observable $\hat{O}$, in the absence of degeneracies, can be approximated by the standard canonical ensemble, i.e.,

$$\overline{\langle \hat{O} \rangle} = \sum_n |c_n|^2 \langle E_n | \hat{O} | E_n \rangle \simeq \frac{1}{Z} \mathrm{Tr}\{\hat{O} e^{-\beta \hat{H}}\}, \tag{53}$$

where Z is the partition function $Z = \mathrm{Tr}\{e^{-\beta \hat{H}}\}$, and the inverse temperature β depends on the initial condition; for example, β may be such that the energy, $\langle \psi(0) | \hat{H} | \psi(0) \rangle$, is correctly reproduced. As we have mentioned, the canonical ensemble is generically incapable of describing the relaxation dynamics of integrable

3 Because the eigenlevels of different symmetry sectors are uncorrelated, level crossings between states with different quantum numbers can also occur in quantum chaotic systems. These level crossings, however, are not related to integrability.

systems. The GGE is a generalization of the canonical ensemble that accommodates the additional conservation rules imposed by the constants of motion present in integrable systems. Its density matrix can be cast in the form

$$\hat{\rho}_{\mathrm{GGE}} = \frac{1}{Z_{\mathrm{GGE}}} e^{-\sum_k \beta_k \hat{\mathcal{C}}_k}, \tag{54}$$

where $\hat{\mathcal{C}}_k$ denotes certain conserved charges, $\beta_k \in \mathbb{R}$ are the the corresponding Lagrange multipliers, and Z_{GGE} is its partition function. In this framework, the expectation value of an observable $\hat{O}$ is predicted to be $\langle \hat{O} \rangle = \mathrm{Tr}\left[\hat{O}\hat{\rho}_{\mathrm{GGE}}\right]$, and the kth Lagrange multiplier is implicitly defined through the condition

$$\langle \psi(0)| \hat{\mathcal{C}}_k |\psi(0)\rangle = \mathrm{Tr}\left[\hat{\mathcal{C}}_k \hat{\rho}_{\mathrm{GGE}}\right]. \tag{55}$$

For the GGE to properly describe equilibrium states, it is imperative, as suggested from its definition (54) itself, that the *right* constants of motion $\hat{\mathcal{C}}_k$ are taken into account. For example, in [130], [132] the GGE was shown to properly describe the equilibrium dynamics after a quantum quench of an integrable system of hard-core bosons. For the long-time averages of the studied observables to agree with the GGE prediction, the conserved quantities responsible for the integrability of the model were incorporated in (54). Say our quantum integrable system has a very large number of constants of motion $\hat{\mathcal{C}}_k$. How many of them should we include in the GGE description? On what basis should we discard the other constants of motion? Of course, if we were to use all projectors onto the Hamiltonian eigenstates as constants, $\hat{\mathcal{C}}_k = |E_k\rangle \langle E_k|$, then (54) exactly describes the equilibrium states of the system. This tautological result is not really useful, as we would have to deal with a huge number of constants as the system size of the model is increased. To solve this problem, in the GGE description one normally only includes constants $\hat{\mathcal{C}}_k$ with a small variance in the (narrow) distribution of populated states after the quench $|c_n|^2$. The GGE has been successfully employed to describe the equilibrium dynamics of a variety of integrable systems, such as the transverse-field Ising (TFIM) model [133]–[136], spin-1/2 XXZ chains [137]–[139], or bosons with contact interactions [140]–[142].

1.3.2 Localization

As previously mentioned, thermalization is associated to the loss of information about a system's initial state. The reason why some closed quantum systems can thermalize under their unitary dynamics is that part of the degrees of freedom of the whole system act as a reservoir. One of the most important exceptions to this behavior is found in localized systems. Here, we are interested in the localization

phenomenon that occurs in certain lattice systems with random disorder. In many of these models, one can take the amplitude of the disorder as a tunable parameter controlling a transition between a thermalizing phase and a localized phase; this makes them incredibly interesting systems on which to test fundamental predictions of quantum thermodynamics. The tools of quantum chaos, namely the statistical analysis of the energy spectrum and its associated RMT predictions, play a fundamental role in the determination of the dynamical nature in these systems: broadly speaking, in the localized regime the system behaves as an insulator with zero DC conductivity, and the fluctuations of energy levels are as in the Poisson ensemble for integrable systems; however, in the thermal regime the system displays ergodic behavior with metallic properties, the level statistics corresponding, e.g., to the GOE of quantum chaotic systems. This transition is traditionally called a metal-insulator transition. Such transitions can be found in non-interacting and single particle models as well as in strongly interacting systems. In what follows we will first review the basic notion of localization as put forward by Anderson, and then we will move on to the more modern phenomenon of many-body localization (MBL). Some results of this thesis are based on the latter.

Anderson localization

The original notion of localization was developed by Anderson and is sometimes referred to as single-particle or simply Anderson localization. In his seminal 1958 paper [143], he discovered that, under certain conditions, transport on 'random lattices' can be completely suppressed:

'In this simple model the essential ***randomness is introduced*** *by requiring the* ***energy to vary randomly from site to site****. It is shown that at low enough densities* ***no diffusion at all*** *can take place [...].'*

To illustrate the physics of Anderson localization, we may use the paradigmatic single-particle tight-binding Hamiltonian with linear dimension L,

$$\hat{H} = \sum_{n=1}^{L} \varepsilon_n \hat{c}_n^\dagger \hat{c}_n + t \sum_{\langle nm \rangle}^{L} \left(\hat{c}_n^\dagger \hat{c}_m + \hat{c}_m^\dagger \hat{c}_n \right), \tag{56}$$

where $\hat{c}_n^\dagger$ and $\hat{c}_n$ are the one-particle creation and annihilation operators acting on site n, $\langle nm \rangle$ indicates that the summation is restricted to nearest neighbors, t is the hopping amplitude. Randomness is introduced through the on-site energy ε_n, which can be taken as independent random numbers drawn from a uniform distribution, $\varepsilon_n \sim U[-W, W]$. The disorder strength is given by W and it can be taken as a control parameter driving the metal-insulator transition. In three or

more spatial dimensions, if W is small enough the eigenstates of (56) are extended with a probability amplitude for the eigenfunctions $|\psi_k(\mathbf{r})|^2 \sim L^{-d}$ with d the spatial dimension, and the dynamics is diffusive: the system is in the metallic regime. Yet, in one or two dimensions for all W or in three or more dimensions if W is large enough, all of the eigenstates become exponentially localized in the $L \to \infty$ limit, eigenfunctions following the asymptotic expression $|\psi_k(\mathbf{r})|^2 \sim e^{-|\mathbf{r}-\mathbf{R}_k|/\xi}$, where ξ is the *localization length* and $\mathbf{R}_k$ is the localization position of state k. Some important properties of Anderson localized systems is that they do not satisfy the ETH, their eigenstates exhibit area-law entanglement, there is no entanglement spreading, and they show no dephasing and no dissipation [144].

One point that is sometimes not sufficiently emphasized is that the inclusion of random disorder in the tight-binding model (56) means that it is possible to consider ensemble averages (actually, *disorder averages* coming from distinct disorder realizations of ε_n) of physical quantities, which catapults it into RMT territory. The level statistics of (56) have been thoroughly investigated in three-dimensional systems (because the problem is trivial for one and two dimensions: backscattering destructive interference means that there is no phase transition and Poisson level statistics is found irrespective of W in the limit $L \to \infty$). According to extensive analytical and numerical evidence [145]–[153], the general picture is as follows: in finite-L systems, the level statistics crosses over from chaotic Wigner-Dyson statistics for $W < W_c$ to Poisson statistics for $W > W_c$, where W_c is the critical disorder strength. In three-dimensional Anderson localized systems, therefore, one can properly speak of a metal-insulator phase transition which in the thermodynamic limit $L \to \infty$ takes place exactly at $W = W_c$. For the specific Hamiltonian (56), the critical disorder has been estimated to be $8 \lesssim W_c \lesssim 8.5$ [148], [149], although the precise value can vary slightly depending on the finite-size scaling assumptions. The theoretical value as obtained within the transfer matrix method is $W_c = 8.25$ [154], [155]. Note, however, that the numerical calculations in [156] indicate that W_c increases with spatial dimension, and for $d = 2 + \epsilon$, $\epsilon \ll 1$, diagrammatic techniques show that $W_c \propto \epsilon$ [157], [158]. The level statistics converge faster to the GOE and Poisson ensemble as L increases, but it becomes approximately L-independent near W_c, where a new universality class was found [145], [159]. Specifically, it was found that the level spacing distribution $P(s)$ at $W = W_c$ could not be well described by neither of the known RMT ensembles; $P(s)$ evidenced level repulsion but its asymptotic decay at $s \gg 1$ was slower than in (42) and closer to the Poissonian behavior (52). Besides, the level spacing distribution at W_c was numerically found to very approximately intersect the GOE (42) and Poisson (52) results around $s \approx 2$ for all L. The theoretical framework for this new universal statistics was later provided by Bogomolny *et al* in the series

of papers [160]–[162], which was dubbed as semi-Poisson because its behavior is intermediate between Wigner-Dyson and Poisson:

*'We propose a **plasma model** for spectral statistics displaying **level repulsion without long-range spectral rigidity**, i.e. statistics intermediate between random matrix and Poisson statistics similar to the ones found numerically at the **critical point of the Anderson metal-insulator transition** in disordered systems and in certain dynamical systems.'*

Semi-Poisson statistics follow from a short-range plasma model where the particles play the role of the eigenlevels and they interact only with their corresponding nearest neighbors [160], [162]–[165]. Technically speaking, in the plasma model the eigenvalues have a joint probability distribution identical to that of a one-dimensional Coulomb gas with $N+2$ particles with equilibrium positions $\{x_i\}_{i=0}^{N+1}$ in an interval of length I. The interaction between particles is mediated by a repulsive logarithmic potential restricted to a finite number of neighbors, $0 < j - i \leq h$. Restricting the interaction to first neighbors only, $h = 1$, this is $V(x_0, x_1, \ldots, x_{N+1}) = -\sum_i \log(x_i - x_{i-1})$ subject to the boundary condition $0 = x_0 < x_1 < \ldots < x_N < x_{N+1} = I$. In the large-$N$ limit, this affords the continuous family of level spacing distributions

$$P(s;\eta) = \frac{\eta^\eta s^{\eta-1} e^{-\eta s}}{\Gamma(\eta)}, \quad s \geq 0, \;\; \eta \in [1, +\infty), \tag{57}$$

where $\Gamma(\eta) = \int_0^\infty \mathrm{d}t\, t^{\eta-1} e^{-t}$. Observe that (57) reduces to the Poissonian result for $\eta = 1$, $P(s;\eta=1) = e^{-s}$. Strictly speaking, the semi-Poisson distribution is found for $\eta = 2$,

$$P(s;\eta=2) = 4se^{-2s}. \tag{58}$$

However, the term is sometimes used to refer to the complete family (57). If $\eta > 1$, the level spacing distribution exhibits level repulsion as $P(s) \propto s^{\eta-1} \to 0$ when $s \to 0$; however, its asymptotic decrease, $P(s) \sim e^{-\eta s}$ when $s \gg 1$, is much slower than in the case of quantum chaotic systems, which follow the Wigner surmise, $P(s) = a_\beta s^\beta e^{-b_\beta s^2} \sim e^{-b_\beta s^2}$ [63]. It is worth clarifying that the Gaussian RMT ensembles are *not* included in (57) for any value of η; indeed, in the RMT ensembles the level spacings are correlated random variables, but within the short-range plasma model they are statistically independent. For the curious reader, GOE, Poisson and semi-Poisson statistics are indeed very close at $s = 2$; their respective values are 0.136, 0.135 and 0.147.

An important aspect of Anderson localization is that it can be thought of as an eigenstate transition due to the existence of a *mobility edge* [166]–[168]. This is very relevant from the point of view of spectral statistics. As previously mentioned,

for values $W < W_c$ the system (56) is in a metallic phase characterized by Wigner-Dyson statistics. However, this is only the case if the states closer to the center of the spectrum are considered. At a fixed value of $W < W_c$, there is a certain *critical energy*, E_c, such that states with energy $|E| > E_c$ are, however, localized (the spectrum is very approximately symmetric and centered about zero energy). The transition to the localized phase occurs when the critical energy, viewed as a function of disorder $E_c = E_c(W)$, vanishes, $E_c(W \geq W_c) = 0$, which is an indication that all eigenstates are localized and no ergodic region can be found in the spectrum. The term 'mobility edge' is derived from the observation that electrons with exponentially localized wave functions do not contribute to transport [169]. We anticipate that a mobility edge is also present in the many-body analogue of the Anderson transition.

From an oversimplified perspective, it is not hard to understand why the random Hamiltonian (56) exhibits the above-mentioned behavior. If the disorder strength is excessive, $W \to \infty$, then (56) essentially behaves as a random diagonal matrix of the Gaussian diagonal ensemble, commonly used to model integrable systems, and Poisson statistics immediately emerge. From this insulating regime, decreasing the intensity of disorder is very close in spirit as perturbing the integrable system in a disorganized way, which then leads to Wigner-Dyson statistics. Of course, the Hamiltonian (56) does not display so simple a behavior, as in random matrices one expects that in the infinite-size limit a infinitesimally small perturbation is enough to bring the system to the chaotic regime, while in the metal-insulator transition there is a finite critical disorder in the $L \to \infty$ limit.

Aside from semi-Poisson universal statistics, on which we will focus later in this thesis, the metal-insulator transition is characterized by the fact that at the critical point $W = W_c$ the eigenstates are multifractal [170], [171], in other words, they are extended but nonergodic. It turns out that this phenomenology is also present in the many-body localization transition, so we will briefly explain what is meant by this. Consider a quantum state $|\Psi\rangle$ written in a certain basis with components ψ_n: $|\Psi\rangle = \sum_{n=1}^{N} \psi_n |n\rangle$. The generalized participation entropy is

$$S_q = \frac{1}{1-q} \ln \left(\sum_{n=1}^{N} \left(|\psi_n|^{2q} \right) \right) \tag{59}$$

Observe that S_q is a $q-$dependent quantity. For $q = 1$, it reduces to the Shannon entropy, $S_1 = -\sum_n |\psi_n|^2 \ln |\psi_n|^2$, while for $q = 2$ it is, up to sign, the well-known participation ratio, $S_2 = -\ln \left(\sum_{n=1}^{N} |\psi_n|^4 \right)$. In a completely *delocalized* (or ergodic) state as in random matrices, the components $\psi_n = 1/\sqrt{N}$, $\forall n$, and in this case $S_q = \ln N$. In a completely *localized* state, $\psi_{n'} = 1$ and $\psi_n = 0$ if $n \neq n'$. Therefore, $S_q = 0$. More generally, for a state that is equally localized on a finite set, i.e, $\psi_n = 1/\sqrt{M}$

if there are only M components $\psi_n \neq 0$, then $S_q = \ln M$ is constant. There exists an intermediate situation where eigenfunctions are extended, because they are not localized, but nonergodic, because not all components have the same probability. In this case, $S_q = D_q \ln N$, where $D_q \leq 1$ is called the fractal $q-$dimension, and we say that the state is *multifractal*. It is clear that for an ergodic or uniformly delocalized state, $D_q = 1$ for all q, while for a localized state it can only be $D_q \in \{0, 1\}$, also for all q. The defining aspect of multifractal states is that $D_q < 1$ does *not* coincide for all q. Intuitively, one can envision a multifractal state as one with relatively high probability of being found in certain regions of the Hilbert space and then with small but nonzero probability of being found in other regions. For $q \gg 1$ small components ψ_n are strongly suppressed in (59) while for $|q| \ll 1$ small ψ_n are relatively amplified.

There are many more interesting aspects about single-particle localization, but because they will play no role in this thesis we will omit them. The interested reader is referred to the review [144]. Anderson localization deserves a special place in the history of condensed matter physics; much of current research in disordered systems can be traced back to it. And even today, Anderson localization is studied in so-called random regular graphs, in which particles interact through neighbors located on some structures that locally look like a tree but have large loops, and there, too, a metal-insulator transition has been found [172]–[177]. The many-body localization transition, one of the main topics of interest in modern quantum dynamics, is the natural, almost innocent, extension of the ideas of Anderson.

Many-body localization

The exception to the ETH that MBL represents has attracted a lot of scientific attention inspired by fundamental questions as well as their technological applicability. Despite being at its infancy, there is a vast body of literature on the subject, and there interested reader can consult the reviews [178]–[181], which give a more detailed account than can allow ourselves here.

In a nutshell, MBL is localization with interactions, so the models of interest are now many-body systems on a static random potential, where the interplay between disorder and interactions gives rise to intricate phenomena. The MBL is a hard problem of quantum statistical mechanics to which a definite answer has not yet been provided. Some important limitations are associated to the small system sizes that can be accessed numerically as well as the ensuing finite-size effects, which in interacting many-body systems can be exceedingly strong.

The notion of MBL has many precursors, and the idea that even interacting electrons in random potentials can exhibit a metal-insulator transition at non-zero critical temperature had been present in the literature (see, e.g., [182]–[190]) before the recent explosion of interest. After the demonstration by Anderson that single-particle systems can show robust localization, that many-particle systems can host similar a similar phenomenon acquired the status of conjecture for a very long time. Some of the earliest steps in this direction include the work by Fleishman and Anderson [182], whose main finding was that in many-body systems localization can survive at least to lowest order in perturbation theory. In 1997, Altshuler *et al* [184] proved that MBL is a robust phenomenon to all orders in perturbation theory in the case of zero-dimensional systems, but the interactions effects remained unknown for higher dimensional models. Then, in 2006 Basko, Aleiner and Altshuler [191] used high order perturbation theory to show that high dimensional systems can have an insulating phase with zero DC conductivity even at finite temperature. Localization was often most naturally discussed in terms of electron (fermionic) systems but, in the context of spectral statistics, Santos showed in 2004 [188] that in a one-dimensional Heisenberg spin-1/2 chain, which is an integrable system, inclusion of a small disordered magnetic field (which plays the role of the random on-site energy in fermionic models) can give rise to an ergodic, quantum chaotic phase, and a localized, Poissonian phase for high enough disorder; further, that a single random defect in any chain position except for the edges can result in a similar effect. Recently, it was suggested that this may be quite generic and not unique to the Heisenberg chain [192]. Today, MBL is very commonly discussed in spin chains that are mathematically equivalent to spinless fermionic systems through the Jordan-Wigner transformation [193]; one such prototypical model is the XXZ Heisenberg with on-site random disorder [114], [194]–[203].

Perhaps one of the best well-known early numerical works on MBL is the 2007 paper by Oganesyan and Huse [204]. This work can be considered to be seminal in several aspects. First, the germ of very fundamental questions about the nature and even the very existence of the MBL phase transition were already clearly formulated:

'[...] the localization transition may be studied numerically through ***exact diagonalization*** *of small systems. [...] As expected, the spectral statistics of finite-size samples* ***cross over*** *from those of* ***orthogonal random matrices*** *in the diffusive regime at* ***weak random potential*** *to* ***Poisson statistics*** *in the localized regime at* ***strong randomness****. However, these data show deviations from simple one-parameter finite-size scaling: the apparent* ***mobility edge "drifts" as the system's size is increased****. Based on spectral statistics alone, we have thus been unable to make a strong numerical case for the* ***presence of a many-body localized phase*** *at nonzero T.'*

It is surprising that this extract from [204] remains to this day a succinct summary of some of the most important open questions in the field of MBL. Namely that, due to strong quantum correlations that are not present in single-particle systems and a strong dependence on the lattice number of sites, there is doubt as to whether the MBL phase is physically relevant. After a bit of rewording: Does the many-body localized phase exist? (i.e., is it not an unphysical artifact of our restricted numerical and analytical analyses?) And if it does exist, is the way in which it is accessed from the low disorder ergodic region a proper *phase transition*? In the thermodynamic limit when the number of particles $N \to \infty$, does the many-body localized phase appear abruptly at a critical disorder strength, W_c, as in Anderson localization? Or, is it rather a smooth dynamical crossover from ergodicity to localization, which then only strictly occurs in the $W \to \infty$ limit? The latter, of course, would lead to the conclusion that, unlike in single-particle systems, there is no many-body localized phase at all in infinite-size systems. It is important to emphasize that this riddle has precipitated into an intense scientific debate that has not yet been closed (see, e.g., [203], [205]–[208]). For example, Panda *et al* posit [206] that this question is impossible to answer because the system sizes and times that we can numerically and experimentally reach are insufficient to make a solid claim; we need new theoretical methods that go hand in hand with our computer simulations. Concurrently, Abanin *et al* [208] concluded that the transition indicators that are commonly used in numerical studies of the MBL are severely impacted by finite-size efects, which can limit the accuracy and credibility of their predictions in macroscopically large systems.

Before we delve into more technical aspects, let us return to the work [204]. A second reason for its fame is that it introduced a modern indicator of quantum chaos that has turned into a broadly used tool to analyze ergodicity breaking transitions through spectral statistics. In order to obtain solid results for their analysis of the level statistics across the MBL transition, the authors wished to eliminate the ambiguities inherent to the unfolding procedure, which is necessary to compute the level spacing distribution $P(s)$, or other long-range spectral indicators. Indeed, the spin-1/2 chains that so frequently serve as testbed for MBL do not have a classical analogue, and the unfolded level (41) is to be computed through some heuristic approximation of the smooth cumulative level density. It is clear that this process can be somewhat ill-defined, as there is not a unique way to do unfolding. For this reason, Oganesyan and Huse employed the dimensionless quantity that is today widely known as the *ratio of consecutive level spacings*,

$$r_n \equiv \frac{s_{n+1}}{s_n} = \frac{E_{n+1} - E_n}{E_n - E_{n-1}}, \tag{60}$$

where $\{E_n\}_{n=1}^{N}$ denote the eigenvalues of a given Hamiltonian in ascending order, $\{E_1 \leq \ldots \leq E_N\}$, and s_n is the nearest-neighbor level spacing. If the level density is sufficiently well behaved (i.e., it does not show peaks or singularities, for example), the ratio (60) does not require any unfolding. This is because in a very small energy window the system-specific contributions from the density of states cancel out, and thus one can perfectly work with the raw eigenvalues E_n instead of the unfolded ϵ_n. Although the ratio given in (60) is by far the most commonly used quantity, some variants have been proposed too [209]–[212]. The RMT description of (60) was derived from 3×3 random matrices by Atas *et al* [213], [214],

$$P(r) = \frac{1}{Z_\beta} \frac{(r + r^2)^\beta}{(1 + r + r^2)^{1+3\beta/2}}, \tag{61}$$

where Z_β is a trivial normalization constant and $\beta = 1, 2, 4$ is the Dyson index (for GOE, GUE and GSE). The Poisson result describing integrable systems and, in particular, the localized phase was given already in [204], $P(r) = 1/(1 + r)^2$. Several formulas for $P(r)$ that interpolate between integrability and chaos have been presented [215]–[218]. One of such formulas was provided by the author of this thesis [218].

The statistical behavior of the spectrum has been and continues to be one of the main approaches to MBL. Due to its simplicity, the ratio (60) is very frequently used in finite-size scaling analyses. As in the Anderson model (56), the level statistics in many many-body localizing systems depends on the region of the spectrum considered as they have a *many-body mobility edge*. This was suggested already in [204] and later further analyzed in, e.g., [200], [219]–[221], although the existence of many-body mobility edges has also been challenged by, e.g., [222]. For this reason, to keep the spectral analysis consistent usually a fraction of levels at the center of the band is selected and then used to compute (60). Although the particular details vary depending on the model studied, the general picture is that for small random disorder W the average level ratio (or, rather, its bounded variant $\widetilde{r}_n = \min\{r_n, 1/r_n\} \in [0, 1]$) is very close to the GOE result $\langle \widetilde{r} \rangle_{\text{GOE}} = 0.5307(1)$ [213], and as W is increased the quantity $\langle \widetilde{r} \rangle$ displays, in finite systems, a smooth transition to the localized phase, described by $\langle \widetilde{r} \rangle_{\text{P}} = 2 \ln 2 - 1 \approx 0.3863$ [204], [213]. This crossover has been observed in many works, e.g. [201], [223], [224], and one could argue that it is by now common knowledge in the field. As the linear size of the chain L is increased, the ergodic, chaotic region survives up to increasing values of W. In the $L \to \infty$ limit, is there a finite W_c at which the transition takes place? The results of the original [204] are inconclusive in this respect, as the authors discuss that their numerical analysis does not allow them to choose between these two alternatives: either that the drift they observe in the crossing points of the $\langle \widetilde{r} \rangle$

curves for different L as a function of W decelerates and converges to a finite W_c as $L \to \infty$, or that the drift continues indefinitely, which would imply $W_c \to \infty$ as $L \to \infty$ and thus no phase transition whatsoever. In fact, in very early works [186], [187] it was already argued that $W_c \sim L$, which again would be very bad news for the MBL phase. There are several ways to perform this finite-size scaling analysis. For example, one could consider that the critical disorder strength can be obtained from the scaling behavior of the W value such that the average level ratio departs from the GOE result, or one could say that such value should be determined by the crossing point of all $\langle \widetilde{r}(W) \rangle$ for different L. The latter is a common criterion, used for example in [219] for the spin-1/2 Heisenberg chain; the authors managed to make all of the ratios curves collapse into a single universal curve with scaling function $g[L^{1/\nu}(W - W_c)]$, obtaining a value $W_c = 3.72(6)$ for this model. Aside from the level ratios, other ergodicity breaking indicators as well as several scaling methods have been used to tackle this problem, see [114], [201], [203], [212], [219], [223], [225]–[229] for details. Very recent phenomenological renormalization group flow techniques suggest that the MBL transition exhibits certain features of the Berezinskii-Kosterlitz-Thouless class [207], [230]–[233]. The lower cost function approach to determine the critical disorder strength through level statistics and entanglement entropy in [203] provides an estimate $W_c \propto L$; the authors mention that this need not imply that the localized phase does not exist in the infinite-size limit as their scaling behavior is compatible with a function $W_c(L)$ that saturates at large L such as $W_c(L) = W_\infty \tanh(L/L_0)$, which reduces to a linear-L dependence when $L \ll L_0$. Generally speaking, certain rigorous results supporting the existence of the MBL transition in the $L \to \infty$ limit [234], [235] have served as a guide for consensus but, as we can see, there is an ongoing effort to determine, e.g., its class of universality.

Besides these generic points, there are many other intriguing aspects about the MBL transition. The ergodic, metallic region where the ETH is verified, hosts long-range deviations from RMT universal results; these can be evidenced through the Thouless energy scale as in [114], [236], [237]. This will be in our focus in one section of this thesis. Dynamically, this side of the transition is characterized by sub-diffusive processes and multifractal scalings [181], [238]–[240]. The intermediate region between full ergodicity and localization has been a common theme of many works. Some recent important discovery is that it may be influenced by so-called Griffiths effects, in which anomalously different disorder regions can control the dynamics [241]–[244]; nonetheless, some authors have also challenged this view [245]. The flow of level statistics observed in this intermediate region has also attracted a lot of attention and several phenomenological models have been devised to describe it. Here we mention mean-field plasma models with effective

power-law interactions between energy levels [201], [246], the Rosenzweig-Porter ensemble with multifractal eigenvectors [247], [248], the short-range plasma model [161] previously discussed for the Anderson localization and also some generalizations [212], [223]. Finally, in the localized phase the ETH is violated. This violation can be understood by the identification of a complete set of quasilocal integrals of motion, which were rigorously constructed by Imbrie [234], [235] for the disordered transverse-field Ising spin chain (see also the related works [249]–[254] on perturbative approaches that provide approximate constructions of these operators). These integrals of motion are the building blocks of the so-called emergent integrability of the many-body localized phase.

Because MBL violates the ETH due to the conservation of some local quantities, one may be led to believe that it is essentially similar to standard integrable systems. It is not. One fundamental reason is that the insulating, integrable-like behavior of the localized phase is due to the presence of a set of quasilocal integrals of motion that make this phase robust. This means that a weak integrability perturbation is not sufficient to take a system out of the MBL phase. Of course, this reminds us of the KAM theorem that explains the transition from integrability to chaos in classical mechanics. According to the KAM theorem, a weak integrability-breaking perturbation transforms the periodic orbits on the invariant tori into quasiperiodic orbits. For the KAM theorem to hold, the characteristic frequencies of the classical trajectories have to be incommensurable, because if this is the case then there are no resonant processes. In MBL systems, disorder can be seen as a natural mechanism for incommensurability, and therefore the fact that the MBL phase is stable under small perturbations can be understood as a quantum KAM theorem for many-body systems.

Before we end this discussion, let us mention that although the MBL was born as purely theoretical phenomenon, it is no longer so. Demonstrating that a given phase is thermal is usually very hard, as one needs to show that all physical local observables relax to the microcanonical average. However, showing that the phase is localized is much easier: a single physically relevant observable that fails to show ergodic evolution and does not relax is enough. MBL has been explored in platforms of ultracold atoms, like in the famous experiment [255], where the initial state of the system consists of particles that mainly occupy even sites. The authors observed that above a critical detuning strength, the imbalance saturates to a finite value, which is indicative of localization. Other experiments dealing with one-dimensional systems include [256] and [257]; the second provides experimental evidence of the logarithmic entanglement spreading theorized for the MBL phase [180]. The experiment [258] indicated that the MBL phase may exist also in two-dimensional systems subject to two-dimensional disorder. MBL is also explored

in ultracold ion platforms. Here we mention the experiment [259], where a disordered transverse-field Ising model developed a stationary magnetization above the critical disorder strength. MBL has also been observed with superconducting circuits: the authors of [260] used a modern spectroscopic technique that allowed them to measure the energy eigenlevels of the many-body system, and therefore they could actually compute the corresponding level spacing ratio statistics, their results agreeing with the theoretical expectation outlined in this section.

1.3.3 Symmetry-breaking and phase transitions

Phase transitions have captivated philosophers and physicists alike since ancient times. Simply put, the question is how a substance (matter) can adopt different forms (phases) depending on the value of certain parameters such as temperature or pressure, even though the nature of the constituents (atoms, particles) themselves remains unchanged. One paradigmatic example is found in the different phases of water, which can be summarized in a simple phase diagram. Reformulated in more technical terms, the question is how the macroscopic state of a system, usually composed of a huge number of particles, can be understood based on its microscopic properties. One of the first attempts to answer this fundamental riddle is found in the work of Greek philosopher Democritus, who is sometimes considered as the precursor of the atomic theory [261]. Democritus hypothesized that matter is composed of individual, indestructible units, which he called atoms, and depending on how these atomic units 'combine' and 'move in space' the resulting macroscopic object is different. Clearly, this idea is very rudimentary for the sophisticated understanding of nature of modern science. Of course, Democritus was mistaken in that atoms cannot be split into smaller units and also in the implicit idea that the macroscopic behavior of matter can be reduced to the sum of many individual behaviors, but it is fair to say that a very basic intuition of the notion of phase and how the same system can display different phases was already present in his theory. Anyway, as we know today, phase transitions are to be understood in the framework of statistical mechanics. The reason is that a phase transition is a form of emergent behavior exhibited by a physical system in the thermodynamic limit, i.e., in the limit when the number of particles and volume (or n-dimensional characteristic length) go to infinity, $N, V \to \infty$, while keeping the density constant, $N/V < \infty$. In this sense a phase transition is, roughly speaking, a cooperative phenomenon that cannot take place in systems with a very small number of constituents, much in the spirit of Anderson's famous *More is different* [262]. Phase transitions denote some forms of non-analytic behavior displayed

by certain physical systems as a tunable control parameter is varied. In classical phase transitions, these parameters are usually quantities that describe an overall, statistical aspect of the system, such as temperature in the case of thermal phase transitions (TPTs). The phase transition occurs at a special value of such a control parameter, which define a so-called *critical point*. Despite the inherent large-N character of phase transitions, their precursors can already be observed in systems with a finite but sufficiently large number of components. By studying these finite-size precursors, we can infer the characteristics of the phase transition in the thermodynamic limit through some scaling hypotheses. A crucial point is that this parameter-induced criticality generates different *phases* characterized by distinct thermodynamic and dynamical properties, usually encoded in the *order parameter*: a quantity that vanishes on one side of the transition and acquires a finite value on the other side (with some exceptions: there are some modern phase transitions for which an order parameter cannot be defined, or at least not in a trivial way; see below). The information contained in the order parameter is often a manifestation of *spontaneous symmetry-breaking*, which is responsible for many phase transitions. The basic idea of symmetry-breaking is that although the system Hamiltonian is invariant under a certain unitary transformation, equilibrium states do not obey this symmetry. This is connected to important structural changes that play an important role in the dynamical evolution of the system and, of course, in the thermalization process.

Although phase transitions were historically formulated in the framework of classical mechanics, the quantum paradigm has revealed that phase transitions can come in many surprising forms and shapes. In contrast with thermal phase transitions, which are controlled by thermal fluctuations, the quantum phase transition (QPT) [36], [263] is a phenomenon inherent to quantum mechanics and therefore mediated by quantum fluctuations; for this reason, it is sometimes called zero temperature phase transition. The excited-state quantum phase transition (ESQPT) [264], [265], discovered in the 2000s, extends the QPT to the high-lying excited states of a quantum system, with a non-analyticity defined by a *critical energy* rather than a critical value of the control parameter; essentially, it is a quantum phase transition deeply rooted in the classical limit of the system. Although all of these phase transitions imply dynamical consequences, they are really static, equilibrium phenomena, caused by some structural change of the system Hamiltonian. In very recent years some new forms of truly *dynamical* phase transitions (DPTs) [266]–[268] have been defined in which the non-analytic behavior appears in the time domain itself, displaying some *critical times*.

For a detailed analysis of broken ergodicity and its relations with symmetry-breaking, we recommend [269]. Adopting a classical viewpoint, let us highlight

some points of particular relevance. Some physical systems just happen to exhibit a phase space that is effectively divided into disconnected components, $\mathcal{M} = \cup_k \mathcal{M}_k$, with two main properties. First, each $\mathcal{M}_k$ has a confinement property whereby if an initial condition is prepared within $\mathcal{M}_k$ then the probability that it can be found in $\mathcal{M}_{k' \neq k}$ at a given observational time is very small. The confinement can be due to a number of structural reasons, such as energy barriers, or some dynamical reasons. Second, each $\mathcal{M}_k$ is characterized by ergodicity in relation to itself: phase and time averages coincide within $\mathcal{M}_k$, but not in the entire $\mathcal{M}$. Let $\hat{M}$ denote some order parameter. Typical statistical averages of $\hat{M}$ over the entire phase space $\mathcal{M}$ lead to $\langle \hat{M} \rangle = 0$, especially if the number of disconnected components is moderately large. However, if we restrict our averages to a single $\mathcal{M}_k$, we may very well have $\langle \hat{M} \rangle_k \neq 0$, which is the very definition of symmetry breaking. The phenomenology of QPTs, ESQPTs and DPTs is related to the emergence of such disconnected components that render the standard canonical and microcanonical ensembles incapable of describing the actual values of observables.

In the following we will review all of these phenomena. Although they will not play a central role in this thesis, we shall begin this trip with the thermal phase transitions.

Thermal phase transitions

Statistical mechanics meant a change of paradigm in the way we understand the physical reality. This theory provides a bridge between the macroscopic world, controlled by the collective interactions of many particles, and its microscopic description. It taught us that all thermodynamic quantities, which are global in the sense that they refer to macroscopic features that are to be understood 'on average', are derived from the partition function, which contains all information about the accessible microstates of a system [270].

Let us consider an equilibrium classical mechanical system whose dynamics is governed by a Hamiltonian H, and let us denote the set of all possible microconfigurations of the particles by $\{\mathbf{q}, \mathbf{p}\} \in \mathcal{M}$. Assuming that the system is coupled to an external bath at temperature T, all thermodynamic properties are fully describable by the partition function

$$Z(\beta) = \frac{1}{(2\pi\hbar)^f} \int_{\mathcal{M}} \mathrm{d}^f\mathbf{q}\mathrm{d}^f\mathbf{p} e^{-\beta H(\mathbf{q},\mathbf{p})} = \int_{-\infty}^{\infty} \mathrm{d}E\, \rho(E) e^{-\beta E}, \ \beta \in \mathbb{R}, \tag{62}$$

where $\beta \equiv 1/(k_B T)$ is the so-called inverse temperature (which, annoyingly, is not temperature but energy), and k_B is Boltzmann's constant.

In the context of quantum mechanics, the partition function (62) contains similar information. Assuming a canonical description for simplicity, it is formally rewritten as

$$Z(\beta) = \sum_n g_n e^{-\beta E_n}, \ \beta \in \mathbb{R}, \tag{63}$$

where E_n now denote the nth eigenvalue of the quantum Hamiltonian $\hat{H}$ and $g_n \in \mathbb{N}$ is its associated degeneracy factor, which plays a role similar to the level density $\rho(E)$ in the classical (62). The expectation value of an observable $\hat{O}$ in the system $\hat{H}$ at temperature β is identical to $\langle \hat{O} \rangle = \mathrm{Tr}\left[\hat{O}\hat{\rho}_{\mathrm{C}}\right]$ where

$$\hat{\rho}_{\mathrm{C}} = \frac{1}{Z(\beta)} e^{-\beta \hat{H}} \tag{64}$$

is the canonical density matrix (compare this quantity with the GGE (54), which is a canonical ensemble with generalized conserved quantities).

Thermodynamic quantities are then computed directly from the partition function through elementary mathematical operations. For example, the Helmholtz free energy reads

$$F = -\frac{1}{\beta} \ln Z. \tag{65}$$

Viewed as a function of temperature, the physically measurable $F(\beta)$ is a non-analytic function at the critical point $\beta = \beta_c$. Truthfully, such non-analyticity can be traced back to the more fundamental partition function. To the mathematical-oriented reader this may sound shocking. Take, for example, the quantum (64). How can a sum of analytic functions such as the exponential be a non-analytical function at any temperature? If this does not contradict the basic notions of mathematical analysis is because, as previously mentioned, phase transitions only occur in the thermodynamic limit, and the limit function of a sequence of analytical functions is not necessarily analytical [271].

Let us briefly introduce a more elaborate way to understand phase transitions that will be useful for subsequent parts of this thesis. Thermal phase transitions can be seen to originate from the zeros of a complexified partition function where the inverse temperature gets extended to the complex plane, $\beta \in \mathbb{R} \to \widetilde{\beta} \in \mathbb{C}$. If $Z(\widetilde{\beta}_0) = 0$ at a point $\beta_0 \in \mathbb{C}$ whose imaginary part $\mathrm{Im}(\widetilde{\beta}_0)$ vanishes in the thermodynamic limit, then the original partition function $Z(\beta)$ becomes non-analytic at $\beta = \mathrm{Re}(\widetilde{\beta}_0)$, signaling a thermal phase transition. This approach to phase transitions in a complex space of physical parameters was developed by Yang and Lee in 1952 [272], [273] (see also [274]–[278]), and recently they have been experimentally observed [279], [280]. The Yang-Lee zeros are at the heart of one kind of dynamical phase transition that we will discuss below.

Ground-state quantum phase transitions

The next type of phase transition is controlled by quantum fluctuations. They occur at zero temperature, which means that their main signatures are to be found in the ground-state of the system. In this thesis, the terms quantum phase transition and ground-state quantum phase transition will be used indistinctly, in order to differentiate these phenomena from ESQPTs.

To illustrate the relation of QPTs and symmetry-breaking, let us consider a quantum Hamiltonian depending on some control parameter, $\hat{H}(\lambda)$,

$$\hat{H}(\lambda) = \hat{H}_0 + \lambda \hat{H}_1, \ \lambda \in \mathbb{R}, \tag{66}$$

such that $[\hat{H}_0, \hat{H}_1] \neq 0$. In this setting, $\hat{H}_0$ and $\hat{H}_1$ may be characterized by different symmetries. Note, however, that more general Hamiltonians that (66) can be used to exemplify QPTs and its main phenomenology does not only apply to this particular form. QPTs emerge from the competition of the ground-states of $\hat{H}_0$ and $\hat{H}_1$ as a function of λ. Indeed, observe that at $\lambda = 0$ the properties of the full Hamiltonian $\hat{H}(\lambda)$ are simply those of $\hat{H}_0$. However, as the interaction λ is increased, so is the influence of $\hat{H}_1$. At the critical coupling $\lambda = \lambda_c$, where the QPT takes place, the ground-state of (66), $E_{\text{GS}}(\lambda)$, behaves as a non-analytic function of λ. For $\lambda > \lambda_c$, the Hamiltonian $\hat{H}_1$ wins over and features of $\hat{H}(\lambda)$ are in accordance with the symmetry properties of $\hat{H}_1$. If $\mathrm{d}E_{\text{GS}}(\lambda)/\mathrm{d}\lambda$ is discontinuous at λ_c, then the QPT is said to be of the first order; in general, if $E_{\text{GS}}(\lambda)$ is continuous but $\mathrm{d}^n E_{\text{GS}}(\lambda)/\mathrm{d}\lambda^n$ is discontinuous at λ_c, the transition is of the nth order (for $n = 2$, the term 'continuous', which dates all the way back to Ehrenfest's classification [281], is also used). Thus, we see that the order of the phase transition is assigned depending on the number of derivatives that one needs to perform to reach the discontinuity of the ground-state. Naturally, this means that high-order QPTs are harder to identify, but many important QPTs are of the first or second order. In first-order QPTs, at the critical point there is phase coexistence between the phases characterized by $\lambda < \lambda_c$ and $\lambda > \lambda_c$. A very important phenomenon associated to QPTs is the closing of the lowest-energy gap, that is, the ground-state and the first excited state become degenerate at $\lambda = \lambda_c$, even though they may be non-generate for any $\lambda \neq \lambda_c$. At the critical point some systems may develop symmetry-breaking: assuming that the Hamiltonian commutes with a unitary transformation $\hat{R}$, $\hat{R}\hat{H}(\lambda)\hat{R}^\dagger = \hat{H}(\lambda)$, for all λ, equilibrium states are not invariant under the action of $\hat{R}$, $\hat{R}|\psi_0\rangle \neq |\psi_0\rangle$, say, for $\lambda > \lambda_c$. Yet, we emphasize that not all QPTs are associated to symmetry-breaking. For example, in the Berezinskii-Kosterlitz-Thouless transition [282] observed in the two-dimensional XY model there is no symmetry-breaking whatsoever. The paradigmatic example

of a system with a symmetry-breaking QPT is found in the quantum Ising model of quantum magnetism [36], whose Hamiltonian is

$$\hat{H} = h \sum_{i=1}^{N} \hat{\sigma}_i^z - \lambda \sum_{\langle ij \rangle}^{N} \hat{\sigma}_i^x \hat{\sigma}_j^x, \tag{67}$$

where $h > 0$ is a dimensionless coupling and the constant $\lambda \in \mathbb{R}$ defines the type of magnetic interaction: if $\lambda > 0$, the interactions are ferromagnetic, if $\lambda < 0$ they are antiferromagnetic, and if $\lambda = 0$ then (67) reduces to a trivial many-body non-interacting system. Let us assume that $\lambda > 0$. The operators $\hat{\sigma}_i^\alpha$ are the well-known Pauli matrices, with commutation relations $[\hat{\sigma}_j^\alpha, \hat{\sigma}_j^\beta] = 2i\varepsilon_{\alpha\beta\gamma}\hat{\sigma}_j^\gamma$ ($\alpha, \beta, \gamma \in \{x, y, z\}$), where $\varepsilon_{\alpha\beta\gamma}$ is the Levi-Civita symbol. Clearly, the Hamiltonian (67) is of the form (66), as $[\hat{\sigma}_i^z, \hat{\sigma}_j^x] \neq 0$ if $i = j$. The model describes the interaction of $1/2$-spins placed in a regular lattice of with linear dimension N (the lattice can also be multidimensional, i.e, a hypercube). It is assumed that at each position of the lattice there is exactly one spin. The interactions between spins of different sites are restricted to nearest-neighbors only (hence the sum with $\langle ij \rangle$). Observe also that (67) is invariant under a 180 degree rotation around the z-axis, which means that it commutes with the parity operator

$$\hat{\Pi} = \prod_{i=1}^{N} \hat{\sigma}_i^z, \quad [\hat{H}, \hat{\Pi}] = 0, \tag{68}$$

for all h. Observe that $\hat{\Pi}$ is a $\mathbb{Z}_2$ symmetry of the kind discussed in Sec. 1.1.2, and thus its two eigenvalues, ± 1, can be used to label the system eigenstates. Physically, h can represent a uniform magnetic field in the z-direction, and it can be taken as a control parameter. The model (67) has a QPT at the critical field strength $h_c = \lambda$. How does the ground-state energy, $E_{\text{GS}}(h)$, vary as a function of h?

When $h = 0$, (67) is diagonal in the eigenbasis of $\hat{\sigma}_i^x$ and it reduces to the classical Ising model. In this classical model, without quantum fluctuations, the existence of a TPT at a critical temperature β_c in two dimensional lattices was established by Onsager in 1944 [283]; there is no TPT in one-dimensional chains, as Ising himself proved in his doctoral thesis a century ago, in 1924 (unbelievably enough, such thesis is unpublished and thus cannot be cited!) But here we are working at zero temperature. According to our choice of parameter signs, the system is ferromagnetic and the minimum energy corresponds the configuration where all spins are pointing upward *or* downward in the $x-$direction,

$$|\text{GS}(h=0)\rangle = \prod_{i=1}^{N} |\uparrow\rangle_i, \quad \text{or} \quad |\text{GS}(h=0)\rangle = \prod_{i=1}^{N} |\downarrow\rangle_i, \tag{69}$$

where $|\uparrow\rangle_i$ and $|\downarrow\rangle_i$ are the eigenstates of $\hat{\sigma}_i^x$ with eigenvalue 1 and -1, respectively. This ground-state is degenerate because both configurations have the same energy. This is the *ferromagnetic* or *ordered phase* of the model, which is defined by a non-zero value of the average magnetization along the $x-$direction,

$$\hat{M} = \frac{1}{N}\sum_{i=1}^{N} \hat{\sigma}_i^x. \tag{70}$$

In the ferromagnetic phase and in the thermodynamic limit, the ground-state has $\langle \hat{M} \rangle = \pm 1$ (depending on which of the two ground-states are considered as well as the parity of the number of particles). Before we move on, let us have a word about the degeneracy of the ground-state in this phase. Strictly speaking, at finite N such degeneracy is only exact when no magnetic field is applied, $h = 0$. Turning on the magnetic field, even if it is maintained below its critical value, $0 < h < h_c$, will inevitably break this degeneracy, so the ground-state will become unique. Nevertheless, it can be rigorously shown that in the infinite-size limit $N \to \infty$ this ground-state degeneracy survives to any finite order in perturbation theory in $h < h_c$ [36]. This is a consequence of the conservation of the parity (68): in the infinite-size limit $N \to \infty$, there is no tunneling between the majority of up and down spin sectors for any small non-zero h. Despite this, if an infinitesimally small *external* perturbation is applied to (67), the system will automatically choose one of the two ground-states, and this is what is meant by symmetry-breaking in this context. As mentioned, not all QPTs need to be accompanied by symmetry-breaking; it is a system-dependent feature intimately related to its conserved quantities, such as parity.

If $h \neq 0$ the Hamiltonian is influenced by the terms $\hat{\sigma}_i^z$, whose effect is to flip the Ising spins. As a consequence of this term, the Hamiltonian (67) is no longer diagonal in the eigenbasis of $\hat{\sigma}_i^x$, but it is also not diagonal in the eigenbasis of $\hat{\sigma}_i^z$: the magnetic field along the perpendicular direction to the alignment of spins is the source of *quantum fluctuations*. It is clear that in the limit $h \gg 1$ the magnetic field term dominates and, up to corrections of order $1/h$, the ground-state is given by

$$|\mathrm{GS}(h \to \infty)\rangle = \prod_{i=1}^{N} \left(\frac{|\uparrow\rangle_i + |\downarrow\rangle_i}{\sqrt{2}} \right), \tag{71}$$

In contrast to the case of $h = 0$, this ground-state is unique, and the corresponding average magnetization vanishes: $\langle \hat{M} \rangle = 0$. For this reason, this is called the *paramagnetic* or *disordered phase*. As we can see, the magnetization (70) acts as an order parameter of the QPT.

Let us mention that in some cases the Ising Hamiltonian (67) is rewritten so that the spins are aligned along the $z-$direction rather than $x-$direction, i.e., $\hat{\sigma}_i^z$ is replaced by $\hat{\sigma}_i^x$ and viceversa. Naturally, the results here reviewed do not change qualitatively as such transformation is a trivial rotation. In passing we note that, even though it is not the most commonly used model for this purpose, the Ising chain (67) can display MBL if the magnetic field is made site-dependent (not global) and random, which goes on to show the versatility of the model [178]–[181].

There are some other aspects of QPTs that we will not treat in this thesis, such as the universality of critical exponents in second-order phase transitions or the theory of the renormalization group, because they will play no role in our results. If the reader is interested in these related subjects, we invite them to take a look at the review by Fisher [284] or the well-known book by Stanley [285].

One should suspect that the phases originated in a QPT of the type of the Ising model should behave quite differently. This is already suggested by the behavior of the average magnetization (70), but what about thermalization? In the Ising model, we have seen that the ground-state of the ordered phase is symmetry-broken, because in the thermodynamic limit two states of opposite parity attain the minimal energy value allowed by the Hamiltonian. However, in the disordered phase this degeneracy is lifted, i.e., the $\mathbb{Z}_2$ symmetry is restored. Yet, one may argue that this effect should not be exceedingly problematic for thermalization: for example, one normally prepares an initial state with the ground-state of an initial Hamiltonian, and then takes it out of equilibrium through a quantum quench. The quench takes the system out of equilibrium because it almost always populates a very large number of states of the final Hamiltonian. But if only the ground-state is degenerate then, statistically, thermalization may be controlled by the other non-degenerate states which heavily outnumber the isolated ground-state. While we make little to no objection to this argument, we pose the following question: what if we were to extend the degeneracy to high-lying excited states of the system at a fixed h within the symmetry-broken phase? Clearly, if an extensive energy region is composed of degenerate eigenlevels, then there is no doubt that thermalization can be severely impacted. This hypothetical structure of states may look fine-tuned or unrealistic, but it is definitely not wishful thinking: many systems which exhibit ESQPTs, discussed in the next section, display this precise behavior.

Excited-state quantum phase transitions

Despite its incredible amount of literature and the many physical effects that have been shown to connect to ESQPTs, its study is definitely a very young discipline which has only barely surpassed adolescence. Some precursors of the ESQPT con-

cept were studied already in the 1990s by Caru and Rusu [286], [287], who focused on the consequences of a phase-space separatrix in systems with a single effective degree of freedom, and then by subsequent studies in the content of many-body quantum physics [288]–[290]. In the mid 2000s, new form of non-analytic behavior was observed in the spectrum of certain nuclear collective models by Cejnar, Heinze, Macek *et al* [291]–[293]. These singular quantal spectra were the germ of the foundation of ESQPTs, later formalized by Caprio, Cejnar and Iachello in their 2008 seminal paper [264]. In the abstract of this work we find many keywords in the field of ESQPTs:

'Phenomena analogous to ground-state quantum phase transitions have recently been noted to occur among states throughout the ***excitation spectra*** *of certain many-body models. These excited state phase transitions are manifested as simultaneous* ***singularities in the eigenvalue spectrum*** *(including the* ***gap*** *or* ***level density****),* ***order parameters****, and* ***wave function*** *properties.'*

Indeed, today the term ESQPT is normally used to refer to several kinds of non-analytic behavior in the excited spectrum of certain infinite-size isolated quantum systems. This is in contrast with the QPT that typically mainly affects the ground-state of the model, showing non-smooth behavior as a function of a control parameter λ. In the ESQPTs, the non-analyticity appears at a given excitation energy, yielding a critical energy E_c of the ESQPT. The defining signatures of the ESQPT are discontinuities in the level density $\rho(E)$ or in some of its derivatives, $\mathrm{d}^f\rho(E)/\mathrm{d}E^f$, where f denotes the number of 'collective' degrees of freedom of the system. If the system has f degrees of freedom, then the singularity appears in the $(f-1)$th derivative of $\rho(E)$, while lower order derivatives are perfectly continuous [264], [294]. In particular, this means that $f = 1$ systems exhibit the strongest signatures of ESQPTs, already in the level density itself. It also suggests that searching for ESQPT-like behavior in systems with large f can be increasingly difficult. Normally, the level density as obtained from Gutzwiller's trace formula (38) is enough to observe the precursors of an ESQPT at a finite system size, but the behavior of the oscillatory component of the density of states has been analyzed also for $f = 2$ systems by Stránský *et al* [295]. In its current mathematical framework, ESQPTs are rooted in instabilities of the classical Hamiltonian flow, i.e., they are a quantum manifestation of the unstable stationary points of the classical equations of motion. Depending on the kind of stationary point, the singularity appearing in the density of states can be, for example, logarithmic or an abrupt discontinuity similar to a step function; a classification of the nature of ESQPTs for arbitrary degrees of freedom was constructed by Stránský and Cejnar [296].

The above discussion helps to understand why the vast majority of systems where ESQPTs have been observed are so-called *collective* or *fully-connected* systems

for which the quantum degrees of freedom can be described through a collective or global algebra that encompasses all the individual algebras associated with each constituent. A paradigmatic example is the fully-connected transverse-field Ising model, where the nearest-neighbors interactions (see (67)) are discarded in favor of collective interactions where each spin interacts with every other in the chain. This effectively decouples the number of degrees of freedom, f, from the number of particles of the system, N, in such a way that even in the infinite-size limit $N \to \infty$, f remains fixed. The collective description of these systems has important consequences: it is often said that in these models the infinite-size limit $N \to \infty$ leads to the classical limit, $\hbar \to 0$, and therefore the properties of large quantum collective systems can be explored through some sort of mean-field limit affording a classical Hamiltonian. It should be noted, however, that there are certain properties of quantum collective systems that cannot be captured by classical limits (notably, effects related to entanglement or quantum coherence, which have no classical analogue whatsoever, and also purely quantum finite-size effects); nevertheless, many important aspects, such as the level density or the dynamics of observables, can certainly be explored classically, which turns the classical limit into a powerful tool to describe the quantum system in the infinite-size limit. Another consequence of the 'collectivization' of these quantum models is that they do not obey standard thermodynamics in many ways. The reason is that their Hilbert space dimension grows much slower than exponentially with the number of particles, 2^N, and the microcanonical and canonical ensembles do not agree in the limit $N \to \infty$. Even the equipartition theorem is violated as the average energy per degree of freedom diverges when $N \to \infty$. Thermodynamic analyses in these collective systems have been reported in, e.g., [297]–[300].

Viewed as a function of a control parameter, one may define a critical line $E_c(\lambda)$ where the ESQPT occurs at each value of λ. In this regard, the effects of ESQPTs also prominently appear in the so-called *level-flow diagram*, i.e., a two-dimensional graph where all or many eigenvalues are represented as a function of λ, as illustrated by Cejnar and Stránský in [301]. This way to detect instabilities in the level dynamics nicely connects with previous ideas of Peres and his test for chaotic dynamics, in which diagonal expectation values of observables, O_{nn}, are represented as a function of energy [302]: the Peres lattices. A common signature of ESQPTs in the level dynamics of low-f systems is the clustering of eigenlevels around a certain excitation energy well above the ground-state energy. The critical line $E_c(\lambda)$ quite frequently (but not always) demarcates the limits of two spectral regions where the eigenlevels behave qualitatively differently: 'below' the ESQPT, $E < E_c(\lambda)$, and 'above' the ESQPT, $E > E_c(\lambda)$ (although this distinction is arbitrary and for the sake of concreteness). As a consequence, in many systems the

ESQPT is also responsible for the generation of phases with well differentiated dynamical features, which we will briefly discuss below. In many systems, the level-flow diagram reveals that the critical energy can only be defined for values of the control parameter larger than a specific one, i.e., that ESQPTs are not found throughout the entire plane $\lambda \times E$. Very commonly, the critical line $E_c(\lambda)$ converges to the ground-state at at value of λ that exactly coincides with the QPT critical coupling, $E_c(\lambda = \lambda_c) = E_{\rm GS}(\lambda_c)$, and for $\lambda > \lambda_c$ the curve $E_c(\lambda)$ departs from the ground-state, its functional form being system-dependent. In these cases, the QPT is an open door to the ESQPT domain. In this sense, we like to say in the community that, loosely speaking, an ESQPT is an extension of the QPT singularity to excited states. But strictly speaking this picture does not generically hold: ESQPTs and QPTs are independent phenomena, stemming from fundamentally different mechanisms, and ESQPTs can occur even if the Hamiltonian does not undergo a QPT at all. Some explicit examples were studied by Relaño *et al* [29], [303] and Stránský *et al* [304].

In the early days, ESQPTs had been mainly identified in certain collective systems describing nuclear behavior (see, e.g., [291]–[293]). These models were all integrable. Soon it was revealed that ESQPTs are not unique to integrable models but they can perfectly well show up in non-integrable or even chaotic systems. The connections between ESQPTs and chaotic dynamics were explicitly considered for the first time in 2011 by Pérez-Fernández *et al* [94] using the Dicke model, an atom-field collective system where the spin degrees of freedom are coupled to a classical electromagnetic field, and then further explored by Bastarrachea-Magnani *et al* in the sequence of papers [95], [305]–[307] dealing with the same model. Previous attempts to connect chaoticity with some form of phase transition, in particular with the ground-state QPT, had been presented by Emary and Brandes [96], [308]. Despite the apparent relationship between the instability associated to chaos and ESQPTs, it seems that they can occur independently and whether or not there is a fundamental reason to believe that they should be linked is still unknown. Broadly speaking, the sharp signatures of ESQPTs can become blurred precisely due to chaos [309], [310].

ESQPTs can be understood as spectral phase transitions whose effects directly manifest in the energy levels of a quantum system. However, the ensuing spectral non-analytic behavior is directly transferred to the expectation value of observables in the Hamiltonian energy basis: these, too, can develop 'peaks' in the infinite-size limit (for $f = 1$ systems), which is another static signature of ESQPTs [265]. This has been very frequently observed in a variety of different collective systems and effectively constitutes an alternative method to search for low-f ESQPTs [94], [309], [311]–[319].

The above contains a discussion of the basic features of ESQPTs, but so far they have been purely static, either concerning the energy values or the expectation values of observables in the Hamiltonian eigenbasis. In recent years, so many *dynamical* consequences of ESQPTs have been reported that we do not intend to review them in detail. The anomalous quantum decoherence at the ESQPT was studied by Relaño, Pérez-Fernández *et al* [320], [321] and then by Kloc *et al* [322], with the conclusion that, depending on the out-of-equilibrium protocol, the ESQPT can either stabilize or speed up its decay to equilibrium. General implications of ESQPTs for system dynamics, localization and the structure of eigenstates close to the transition have been presented by Santos, Pérez-Bernal *et al* in [317], [323]. Symmetry-breaking equilibrium states reside in some collective models where one of the phases induced by the ESQPT is composed by degenerate pairs of eigenlevels, originally observed by Puebla *et al* [313], [324]; recently, thorough investigations and formalization of the nature of such symmetry-breaking states and their equilibration properties have been put forward in the series of papers by Corps *et al* [29], [325]–[331], which constitute part of the results of this thesis. ESQPTs can give rise to irreversibility without dissipation [332] and reversible quantum information spreading [333]. They have been investigated in terms of their classical and semi-classical phase space dynamics by Wang and Pérez-Bernal [334], [335] and by Kloc *et al* [336].

We should emphasize that although ESQPTs play an important role in collective systems with a small number of degrees of freedom, it is a relatively widespread transition that has been found in many different models from quite diverse areas of physics. These include molecular physics with, e.g., the vibron model describing the bending dynamics of certain atomic systems [337]–[345], quantum optical physics with the Dicke, Tavis-Cummings and related algebraic atom-field systems [95], [297], [304]–[307], [312], [314], [315], [322], [324], [332], [346]–[351] and, in general, condensed matter physics with, e.g., the fully connected transverse-field Ising model or the two-site Bose-Hubbard model [303], [321], [352]–[360]. Only recently, Cejnar, Stránský *et al* have provided extensions of the ESQPT concept to resonant states in the continuum [265], [361], almost concurrently with the observation of ESQPT-like behavior in open systems weakly coupled to an environment whose dynamics is described by a quantum Liouvillian by Rubio-García *et al* [362], with a contribution of the author of this thesis. On the experimental side, common signatures of ESQPTs have been observed in some of the above systems [337], [345], [363]–[365], and the formation of a degenerate phase and associated dynamics on a Kerr resonator has been reported in the experimental simulation by Chávez-Carlos *et al* [366].

We will end this section with an example illustrating a simple but versatile collective system where ESQPTs have been studied. But before that, let us give some final considerations about ESQPTs. The first issue we want to address is how ESQPTs and QPTs can have very different phenomenology, even though they are certainly intertwined in many systems. One important difference is that it is not possible to speak of first order or continuous ESQPTs, as we do with QPTs. This is motivated by the level crossings and clustering that often demarcate the ESQPT critical line and which can be observed in the level-flow diagram. In some systems such crossings are sharper than in others (normally as a consequence of the number of degrees of freedom or the presence of quantum chaos), so perhaps this could be used as a guide for classification. Unfortunately, this is an ill-defined approach because the only guaranteed signature of ESQPTs is a non-analyticity in the level density, which may occur even if no such crossings of levels appear in the level-flow diagram. A second question is whether ESQPTs have an associated order parameter. The answer is again negative, as order parameters are usually connected to symmetry-breaking, but ESQPTs stem from certain classical instabilities in the Hamiltonian flow, which is a fundamentally different origin. In fact, there are many models where ESQPTs do not break any symmetry, such as in the Tavis-Cummings model. Nevertheless, there are also systems where ESQPTs do break a global Hamiltonian symmetry, and in those cases it is usually possible to define an order parameter (one example will be given below). Yet it is important to note that order parameters are not in general applicable to ESQPTs.

In ending this section, let us momentarily go back to the nearest-neighbor transverse-field Ising model (67). This is a many-body system with *finite-range* interactions as the spin couplings in the interacting term are of the two-body type, but it can be turned into a *collective* many-body system if we allow all-to-all couplings in the spin interaction terms. The Hamiltonian is then

$$\hat{H} = \frac{h}{2}\sum_{i=1}^{N}\hat{\sigma}_i^z - \frac{\lambda}{4N}\sum_{i,j=1}^{N}\hat{\sigma}_i^x\hat{\sigma}_j^x. \tag{72}$$

Observe that the nearest-neighbors sum $\sum_{\langle ij\rangle}$ has been removed from the second term, and it is now global instead: $\sum_{ij}$. The normalization factor $1/N$ has been added to this term in order to ensure that the Hamiltonian (72) is an extensive operator of N, i.e., that the energy per particle E/N is an intensive quantity. The remaining factors of $1/2$ and $1/4$ have been introduced for notational convenience that will now become clear. The Hamiltonian (72) is already a fully-connected system, but it is written in terms of the individual spin operators $\hat{\sigma}_i^\alpha$. Introducing

the so-called collective spin operators, $\hat{J}_\alpha \equiv \frac{1}{2}\sum_i \hat{\sigma}_i^\alpha$ ($\alpha = x, y, z$) allows us to rewrite it in the more familiar form

$$\hat{H} = h\hat{J}_z - \frac{\lambda}{N}\hat{J}_x^2. \tag{73}$$

This Hamiltonian is a particular case of the Lipkin-Meshkov-Glick (LMG) model [367]–[369]. Although it was originally formulated in the fermionic language as a schematic example of the nuclear shell model, it has been revealed as a powerful testbed for a range of different physical phenomena outside of nuclear physics, including quantum phase transitions (see, e.g., [320], [356], [370]–[373]), and it has recently been experimentally realized with cold atoms [374]. Observe that the Hamiltonian (73) conserves the total spin operator $\hat{\mathbf{J}}^2 \equiv \hat{J}_x^2 + \hat{J}_y^2 + \hat{J}_z^2$, $[\hat{H}, \hat{\mathbf{J}}^2] = 0$, for any values of its parameters. This conservation rule allows us to separate the Hamiltonian matrix in symmetry sectors according to the eigenvalues of $\hat{\mathbf{J}}^2$, $\hbar^2 j(j+1)$, with $j = 0, \ldots, N/2$. We normally focus on the maximally symmetric sector, defined by the condition $j = N/2$, which contains the ground-state of the full Hamiltonian; the dimension of this sector is $D = 2j + 1 = N + 1$. This is to be compared with the total Hilbert space dimension, which is $D_T = 2^N$. Due to this heavy Hilbert space dimension reduction, it is possible to exactly diagonalize very large system sizes, sometimes effectively very close to infinite-size limit $N \to \infty$ or $j \to \infty$ (these two quantities are indistinctly used in the literature as infinite-size limit parameters). Similarly to its finite-range counterpart (67), the LMG model is invariant under a parity transformation, which in this case takes the form

$$\hat{\Pi} = e^{i\pi(j+\hat{J}_z)}. \tag{74}$$

Clearly, it is a $\mathbb{Z}_2$ operator whose two eigenvalues ± 1 are used as quantum numbers to assign to the eigenvalues of $\hat{H}$ according to $\hat{\Pi}\,|E_{n\pm}\rangle = \pm\,|E_{n\pm}\rangle$. The LMG model has a QPT at the critical coupling strength $\lambda_c = h$. For $\lambda > \lambda_c$, it also exhibits an ESQPT at the critical energy $E_c = -hj$. In order to keep discussion brief, the classical limit of the LMG model will be included for completeness in the corresponding results section of this thesis, but for now let us simply mention that it has a single classical degree of freedom and, thus, its level density $\rho(E)$ shows a singularity, in this case logarithmic, at $E = E_c$. We will make extensive use of the LMG model in many parts of this thesis because the spectral phases generated by the ESQPT are of the type that we are interested in. Specifically, in the infinite-size limit, for $\lambda > \lambda_c$ and $E < E_c$ the LMG model exhibits a full symmetry-broken phase where the eigenvalues of opposite parity are degenerate, $E_{n+} = E_{n-}$, while for $\lambda < \lambda_c$ or $\lambda > \lambda_c$ and $E > E_c$ the degeneracy is lifted and it shows a symmetry-restored phase, $E_{n+} \neq E_{n-}$. The origin of such degeneracies can be interpreted

through the geometry of the classical phase, which is of the double-well potential kind.

Dynamical phase transitions

The previous forms of non-analytic behavior that a closed quantum system can exhibit, as we have mentioned, are really equilibrium phase transitions caused by some sudden structural changes of the Hamiltonian eigenstates and eigenvalues. Of course, because these are crucial ingredients of the Schrödinger equation, which control the dynamics, these static changes have dynamical consequences. In recent years, two other kinds of phase transitions have received a great deal of attention. These are called, in general, dynamical phase transitions, although the term is quite broad. There are two especially relevant DPTs, sometimes referred to as DPT-I and DPT-II, which we discuss in this thesis. DPTs-I and DPTs-II have in common that they are both usually revealed by the non-equilibrium dynamics of a closed quantum system. Although some physical models can display both DPTs, such as the fully connected transverse-field Ising model [326], [327], [375], [376] or the Rabi model [377], a fundamental mechanism that offers some simultaneous explanation for them is still lacking. Nevertheless, some connections between DPTs-I and DPTs-II have been proposed [370], [372], [375], [376], [378]–[381].

(i) Type I dynamical phase transitions: order parameters.- Consider a Hamiltonian depending on a control parameter, $\hat{H}(\lambda)$, and suppose that an initial state is prepared at an initial λ_i. Frequently, this initial state is simply the ground-state of $\hat{H}(\lambda_i)$. Then, we perform a quench, $\lambda_i \to \lambda_f$, and measure the dynamical evolution of a suitably chosen physical observable, $\langle \hat{O}(t) \rangle$, in the time-evolving wavefunction at $\hat{H}(\lambda_f)$. After a transient time of non-universal behavior, the system will enter the so-called pre-thermalization regime [382], [383], when observables approach a long-lived steady state. We may then measure the value of this steady state, and repeat the same experiment, for example, with the only modification of the final value of the quench parameter, λ_f. We will then have obtained a curve $\overline{\langle \hat{O} \rangle}(\lambda_f)$ of the steady state of $\hat{O}$ as a function of λ_f. In a DPT-I, $\overline{\langle \hat{O} \rangle}(\lambda_f)$ becomes non-analytic, in the infinite-size limit, at a certain critical point, $\lambda_{f,c}$. Note, however, that other non-equilibrium protocols are possible, e.g., one may change λ_i rather than λ_f. In this sense, DPTs-I are characterized by a non-analytic point of a non-equilibrium order parameter, and the critical point separates two *dynamical* phases [365], [374], [384]–[392]. In many realizations of DPTs-I, these dynamical phases can be termed ordered and disordered, similarly to the phases often generated by a QPT. Yet, we emphasize that DPTs-I are fundamentally different from QPTs in that the critical point for DPTs-I in general does not coincide with the QPT critical point [387]. In

fact, for DPTs-I such critical point depends on the initial state that is taken out of equilibrium itself, as different initial states give rise to different population probabilities in the post-quench Hamiltonian, which leads to a different average energy.

A particular class of systems where DPTs-I have been abundantly studied is that of models with short- or infinite-range interactions and that undergo a QPT; for other kinds of models that can support DPTs-I, the reader is referred to the recent review by Marino *et al* [266]. In our chosen class of systems, two ground-state phases are generated as a consequence of the QPT: in one phase, a discrete $\mathbb{Z}_2$ symmetry is broken, and in the other it is restored. A quench from the symmetry-broken ground-state (the ordered phase) can induce two completely different dynamical patterns. If the final state ends up in the symmetry-breaking phase of the final Hamiltonian, then the instantaneous order parameter displays oscillations around a broken-symmetry effective state, i.e., the corresponding steady state is, in general, different from zero (although it can also assume such value). However, if the final state ends up in the symmetry-restored phase, the oscillations of the order parameter occur around a symmetric state, which means that its steady value is zero. Models of quantum magnetism are very often employed to study DPTs-I, and in this case the order parameter is the total magnetization along the direction where the spins are aligned.

In this thesis, we will also work with this class of models, and we will analyze the role played by ESQPTS and the ensuing degenerate spectral phases in the dynamical evolution of the non-equilibrium order parameter. This nicely connects with the notion of equilibration in models with an extensive number of degeneracies which, in our models, appear on one side of the ESQPT. For such highly degenerate systems, the long-time average cannot be described through the microcanonical ensemble, and thus one cannot properly speak of 'thermalization'. However, the dynamics may still reach long-lived steady states that are similar, at least in spirit, to thermalized states. Motivated by the phenomenology of DPTs-I, we will develop a framework to describe such states through general symmetry arguments.

Type II dynamical phase transitions: singularities in return probabilities.- The second kind of DPT, termed DPT-II, is a different from of non-analytic behavior appearing in closed systems that evolve under coherent, unitary dynamics [267], [268]. It is defined by singularities certain return probabilities, associated with an instantaneous loss of memory about the initial preparation of the system. DPTs-II have been observed in numerous systems, such as [268], [280], [371], [393]–[405]. A DPT-II is a purely dynamical effect that has no equilibrium counterpart [403], [406], [407], and therefore it may be interpreted as a phase *transition in time*. Like

DPTs-I, DPTs-II show a strong dependence on the initial conditions [371], [372], [396].

The notion of DPT-II dates back to the 2013 seminal work by Heyl *et al* [393], whose achievement was to formally extend the thermal phase transition, driven, of course, by temperature, to the quantum dynamical regime:

'A phase transition indicates a sudden change in the properties of a large system. For temperature-driven phase transitions this is related to nonanalytic behavior of the free energy density at the critical temperature [...] We show that a close analogue of this behavior can occur in the ***real time evolution*** *of quantum systems, namely* ***nonanalytic behavior*** *at a* ***critical time****. We denote such behavior a* ***dynamical phase transition*** *[...]'*

Let us again consider an initial state that is taken out of equilibrium by a quench, $\lambda_i \to \lambda_f$. Then one may consider the overlap amplitude

$$G(t) = \langle \Psi_0(\lambda_i)| \, e^{-i\hat{H}(\lambda_f)t} \, |\Psi_0(\lambda_i)\rangle \tag{75}$$

of a given initial state, $|\Psi_{t=0}(\lambda_i)\rangle$, with itself after unitary evolution following a quench, $\Psi_t(\lambda_f) \; = e^{-i\hat{H}(\lambda_f)t} \, |\Psi_0(\lambda_i)\rangle$. DPT-II are defined by non-analytical times, t_c, of $G(t)$ or, equivalently, of its corresponding return probability:

$$\mathrm{SP}(t) = |G(t)|^2. \tag{76}$$

The quantity in (76) is also called *survival probability*, as it measures the probability that the time-evolved state 'recalls' its initial value at a given time t. It is worth mentioning that the survival probability plays an important role in many areas of non-equilibrium many-body quantum physics, including quantum chaos and its relation to thermalization (see, e.g., the series of papers by Santos *et al* [408]–[412]), although in this thesis we will not treat these other aspects. In fact, DPTs-II frequently appear in the short-time dynamics, i.e., before the system has equilibrated.

The key idea of [393] is that if the return amplitude (75) is seen as a function in the complex plane through the identification $G(t) \to G(z \equiv it)$, then it is formally reminiscent of the partition function in equilibrium statistical mechanics, $Z_\beta = \mathrm{Tr}\, e^{-\beta\hat{H}}$, which is responsible for the free energy per particle, $F/N = -(1/\beta N) \ln Z_\beta$, becoming non-analytic at a critical temperature β_c. Extending further this analogy, Heyl *et al* proposed a dynamical quantum quantity that may play the role of the equilibrium free energy. This is known as the *rate function*, and it can be written

$$\widetilde{r}_N(t) = -\frac{1}{N} \ln \mathrm{SP}(t), \tag{77}$$

where N is the number of particles of the system. The rate function (77) is by far the most common indicator of DPTs-II. In the infinite-size limit of many one-dimensional systems, in a neighborhood of $t = t_c$ the rate function behaves as

$r(t) \equiv \lim_{N\to\infty} r_N(t) \sim |(t-t_c)/t_c|$ which, graphically speaking, is a 'kink'. We note that these kinks are local maxima of $r_N(t)$, which in turn correspond to minima of the survival probability (76). This phenomenon was exemplified in [393] with the transverse-field Ising model, as its exact solvability allowed the authors to compute the exact values of the critical times. Most systems cannot be solved exactly, and therefore exact diagonalization is used to numerically study the singularities in the rate function.

In the case of systems that have a symmetry-broken phase with degenerate eigenvalues, the study of DPTs-II is undertaken with a slightly different quantity, as proposed by Heyl in [394] for the XXZ chain. For concreteness, let us assume that a $\mathbb{Z}_2$ parity symmetry is broken in a certain phase of a system (such as one of the phases induced by an ESQPT), although the argument can be trivially generalized for a $\mathbb{Z}_n$ symmetry. The initial state $|\Psi_0(\lambda_i)\rangle$ can be chosen to be a general superposition of the two symmetry-broken lowest-energy eigenstates of $\hat{H}(\lambda_i)$, $|E_{0,\pm}(\lambda_i)\rangle$. After a quench, DPTs-II manifest in the critical times of the parity-projected return probability (PPRP),

$$\begin{aligned}\mathcal{L}(t) = &\ \left\langle E_{0,+}(\lambda_i)\right| e^{-i\hat{H}(\lambda_f)t} \left|\Psi_0(\lambda_i)\right\rangle \Big|^2 \\ &+ \left\langle E_{0,-}(\lambda_i)\right| e^{-i\hat{H}(\lambda_f)t} \left|\Psi_0(\lambda_i)\right\rangle \Big|^2 .\end{aligned} \tag{78}$$

Let us redefine

$$\mathcal{L}_{\pm}(t) = \left\langle E_{0,\pm}(\lambda_i)\right| e^{-i\hat{H}(\lambda_f)t} \left|\Psi_0(\lambda_i)\right\rangle \Big|^2 \tag{79}$$

so that $\mathcal{L}(t) = \mathcal{L}_+(t) + \mathcal{L}_-(t)$. Here, $\mathcal{L}_{\pm}(t)$ are the return probabilities to the positive-parity and negative-parity projections of the initial state. Analogously to (77), the corresponding rate function is

$$r_N(t) = -\frac{1}{N} \ln \mathcal{L}(t). \tag{80}$$

To understand the meaning of DPTs-II in symmetry-breaking models, it is convenient to note that each of the terms in the PPRP, $\mathcal{L}_{\pm}(t)$, follows a law [394], [413]

$$\mathcal{L}_{\pm}(t) = e^{-N\Omega_{\pm}(t)}, \tag{81}$$

where $\Omega_{\pm}(t)$ is an intensive ($N-$independent) quantity. The argument put forward by Heyl in [394] is that DPTs-II occur whenever the functions $\Omega_{\pm}(t)$ intersect, i.e., that the critical times satisfy $\Omega_+(t_c) = \Omega_-(t_c)$. One of the results of this thesis is that in spectral phases with exact degeneracies, such crossings are impossible [326], [327], so this mechanism does not explain the kinks observed in the rate

functions of certain collective models. As we will see, in this case the origin of the kinks is to be found in the full survival probability (76) extended to the complex plane, an idea that was already present in [393].

Part II

RESULTS

2 BREAKING ERGODICITY VIA DISORDER

As discussed in 1.3.2, many-body localization constitutes a robust mechanism for ergodicity breaking, leading to the loss of thermal behavior in disordered many-body quantum systems. There is an on-going debate dealing with the existence and stability of the many-body localized phase in the infinite-size limit and whether the numerical and experimental tools presently available are well suited to investigate this phenomenon. Although in this preliminary Chapter we do not aim to provide a definite answer to this question, we propose a mechanism to distinguish ergodic from non-ergodic phases in disordered many-body systems with an ergodicity-breaking phase transition. This Chapter will help us connect with the results from subsequent parts of this thesis, where our focus is on systems where the dynamics in non-ergodic phases depends on a set of emergent constants of motion rooted in various forms of symmetry-breaking.

This Chapter contains two sections. In Sec. 2.1 we review the $J_1 - J_2$ spin model, a Hamiltonian displaying many-body localization and frequently employed in its analysis. Then, in Sec. 2.2 we provide an integrated picture for the transition from ergodicity to localization. The contents of this Chapter are based on [237].

2.1 PRELIMINARIES

2.1.1 Hamiltonian model

For illustration purposes, in this Chapter we consider the $J_1 - J_2$ spin$-1/2$ chain. This model is essentially a generalization of the Heisenberg chain prototypical in studies of ergodicity-breaking in many-body quantum systems [114], [188], [194], [196]–[201], [203], [410], [414]. Contrarily to the Heisenberg chain, the $J_1 - J_2$ model is not Bethe integrable in the absence of disorder [193]. The Hamiltonian

incorporates the coupling parameters J_1 and J_2 quantifying the intensity of next to nearest-neighbors interactions, and it reads (in a system of units where $\hbar = 1$)

$$\begin{aligned}\hat{H} = &\sum_{\ell=1}^{L} \omega_\ell \hat{S}_\ell^z + J_1 \sum_{\ell=1}^{L} \left(\hat{S}_\ell^x \hat{S}_{\ell+1}^x + \hat{S}_\ell^y \hat{S}_{\ell+1}^y + \lambda_1 \hat{S}_\ell^z \hat{S}_{\ell+1}^z\right) \\ &+ J_2 \sum_{\ell=1}^{L} \left(\hat{S}_\ell^x \hat{S}_{\ell+2}^x + \hat{S}_\ell^y \hat{S}_{\ell+2}^y + \lambda_2 \hat{S}_\ell^z \hat{S}_{\ell+2}^z\right)\end{aligned} \tag{82}$$

where $\hat{S}_\ell^{x,y,z}$ are the total spin operators at site $\ell \in \{1, \ldots, L\}$. Periodic boundary conditions are employed in our numerical simulations. We set the coupling constants to $J_1 = J_2 = 1$, corresponding to the anti-ferromagnetic version of the system. We fix $\lambda_1 = \lambda_2 = 0.55$ (the authors of [203] also considered these parameter values). This system is disordered due to the presence of the uniformly and independently randomly distributed $\omega_\ell \sim \mathcal{U}(-\omega, \omega)$, where ω denotes the disorder strength. The Jordan-Wigner transformation [193] makes it possible to map the Hamiltonian (82) to a spinless fermionic chain. The operator $\hat{S}^z := \sum_i \hat{S}_i^z$ is a conserved quantity for all values of λ and ω, $[\hat{H}, \hat{S}^z] = 0$, so for simplicity we restrict ourselves to the symmetry sector $S^z = 0$, where S^z is the eigenvalue of the operator $\hat{S}^z$. The dimension of such subspace is $d = \binom{L}{L/2}$, which grows as $d \sim 2^L/\sqrt{\pi L/2}$ when $L \to \infty$; therefore, full exact diagonalization can normally be performed up to chain lengths $16 \lesssim L \lesssim 18$. For our spectral analyses, we only work with the $N = d/4$ central energy states $\{|E_n\rangle\}_{n=1}^N$. This number ranges from $N = 63$ for $L = 10$ to $N = 3217$ for $L = 16$.

2.1.2 Long-range spectral statistics: the power spectrum of the unfolded level spacings

As mentioned in Sec. 1.2.2, the trademark feature of quantum chaotic system is the presence of level correlations in the spectrum. Long-range spectral statistics refer to the statistical analysis of eigenlevels separated by large energy index distances (i.e., levels $E_i, E_j \in \{E_n\}_{n=1}^N$ with $|i - j| \lesssim N$), as opposed to short level index distances, $|i - j| \ll N$, whose statistical features are analyzed through short-range spectral statistics. Long-range spectral analysis allows us to obtain the so-called Thouless energy scale, E_{Th}: basically, beyond this energy scale the universal RMT description breaks down [35], [145]. For level index distances larger than E_{Th}, long-range deviations from the chaotic RMT results can be found even in systems where short-range measures such as the level spacing distribution, $P(s)$, closely resembles the Wigner-Dyson distribution (42). In the context of disordered many-

body quantum systems, several long-range indicators of chaos have been used, such as the level number variance [114] or the spectral form factor [212].

In our treatment of long-range spectral correlations, we will use the δ_n spectral statistic [320], [415]–[419], which is defined as the difference between the nth unfolded level and the corresponding energy value in a perfectly equiespaced spectrum with $\langle \varepsilon_n \rangle = n$:

$$\delta_n = \varepsilon_n - n, \quad n \in \{1, \ldots, N\}. \tag{83}$$

Here, ϵ_n is obtained through the unfolding procedure as specified in (41). Because δ_n can be understood as a discrete time series where the discrete time is represented by the level index n, one can consider its Fourier transform and then its square modulus yields the power spectrum:

$$\langle P_k^{\delta} \rangle = \langle |\mathcal{F}(\delta_n)|^2 \rangle = \left\langle \left(\frac{1}{\sqrt{N}} \sum_{n=1}^{N} \delta_n \exp\left(\frac{-2\pi i k n}{N} \right) \right)^2 \right\rangle, \tag{84}$$

with $k \in \{1, 2, \ldots, k_{\mathrm{Ny}}\}$, and where $k_{\mathrm{Ny}} = N/2$ is the Nyquist frequency. The angular brackets $\langle \cdot \rangle$ denote average over random realizations (in our case, these will be due to disorder). As shown by Relaño *et al* in [415], when $k/N \ll 1$ and $N \gg 1$, the power spectrum in quantum integrable systems behaves as $\langle P_k^{\delta} \rangle \simeq 1/k^2$, while in chaotic systems $\langle P_k^{\delta} \rangle \simeq 1/k$. This power-law feature is universal for chaotic and integrable systems, regardless of the symmetry class of the model under consideration (GOE, GUE, GSE).

2.2 ANALYSIS IN THE $J_1 - J_2$ RANDOM MODEL

2.2.1 Looking at the tails: extreme events as a function of disorder

Diagonal fluctuations around the microcanonical average

If we compare the definition of the δ_n statistic (83) and the diagonal expectation values of observables according to the ETH in (11), we observe that they are formally similar, with the exception that the Δ_n term in (11) is not dimensionless, unlike δ_n. To conveniently compare these two quantities, we normalize Δ_n by its standard deviation $\sigma_{\Delta_n} = \langle \Delta_n^2 \rangle$,

$$\widetilde{\Delta}_n = \frac{\Delta_n}{\sigma_{\Delta_n}} = \frac{O_{nn}}{\sigma_{\Delta_n}} - \frac{\langle \hat{O} \rangle_{\mathrm{ME}}}{\sigma_{\Delta_n}}, \ n \in \{1, \ldots, N\}. \tag{85}$$

Here, we consider the diagonal fluctuations (85) across the MBL transition. The observable $\hat{O}$ under study will be the one-dimensional momentum distribution,

$$\hat{n}_q = \frac{1}{L}\sum_{m,n=1}^{L} e^{2\pi i(m-n)q/L}\hat{s}_m^+\hat{s}_n^-, \;\; q \in \{0,\ldots,L-1\}, \tag{86}$$

where $\hat{S}^{\pm} = \hat{S}_x \pm i\hat{S}_y$ are the usual ladder spin operators. The diagonal matrix elements O_{nn} of this observable give us access to its fluctuations $\widetilde{\Delta}_n$. Also, to compute the corresponding microcanonical average $\langle\hat{O}\rangle_{\text{ME}}$ we fit a polynomial of degree 4 to the O_{nn}. This fitting procedure eliminates the spurious effects caused by averages over finite energy windows [80].

To clarify the spectral region considered in our analyses, in Table 1 we summarize the number of states $N = d/4$ in the center of the energy band and the number of disorder realizations performed for each value of the system size L. Due to computational limitations, we have not been able to increase L beyond 16 sites. Also, we do not consider systems with $L < 10$ because these sizes are too small to be representative of the system's dynamics.

L	Levels in the central region	Realizations
10	63	5000
12	231	1400
14	858	375
16	3217	100

Table 1: Number of levels in the central region of the spectrum that is considered in the calculations $N = d/4$ and number of realizations for each value of the number of sites L in the J_1-J_2 model (82). The corresponding eigenvalues $\{E_n\}_{n=1}^{N}$ and eigenstates $\{|E_n\rangle\}_n$ have been obtained by exact diagonalization.

Given a random variable X, the kurtosis excess $\gamma_2(X)$ is defined as

$$\gamma_2(X) \equiv \text{Kurt}[X] - 3 = \left\langle \left(\frac{X-\mu}{\sigma}\right)^4 \right\rangle - 3. \tag{87}$$

Here, $\mu = \langle X\rangle$ denotes the average value of X while $\sigma^2 = \langle X^2\rangle - \langle X\rangle^2$ is its variance. For a Gaussian distribution, $\gamma_2 = 0$. The kurtosis excess is then revealed as a useful tool to analyze whether the extreme events are more or less important than in a Gaussian distribution. If $\gamma_2 > 0$, the distribution $P(X)$ has heavier tails than a Gaussian while the opposite is true if $\gamma_2 < 0$. Of course, we will focus on the

kurtosis excess of the random variable $\widetilde{\Delta}_n$. We note that in Ref. [420] the kurtosis excess of the diagonal elements O_{nn} themselves was employed to study the onset of thermal behavior.

In Fig. 1 we have represented the kurtosis excess as a function of the disorder strength for $L = 10, 12, 14, 16$. For small ω, in the ergodic phase of the system, we essentially find Gaussian behavior, $\gamma_2(\widetilde{\Delta}_n) \approx \gamma_2(\mathcal{G}) = 0$; finite-size effects mean that for larger L this behavior is reproduced better. This suggests that in this disorder region the ETH is fulfilled and thermalization should occur. For larger ω, we observe an increase in the probability of extreme events, but this is not monotonic; rather, $\gamma_2(\widetilde{\Delta}_n)$ exhibits a maximum at a certain value of the disorder which depends on L, say $\omega_c(L)$. After reaching this peak, γ_2 decreases with ω. For very large ω, $\gamma_2 < 0$. In summary, it seems that $\omega_c(L)$ is a singular point in the transition from the ergodic to the MBL phase, characterized by a maximum probability of extreme events for the diagonal fluctuations.

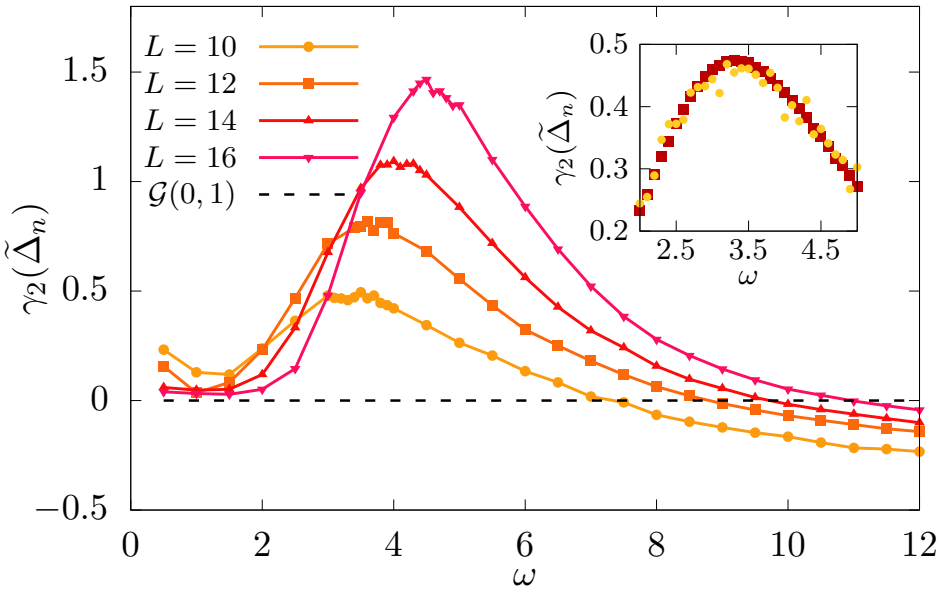

Figure 1: Kurtosis excess, (87), as a function of the disorder strength ω for different values of the number of sites, $L \in \{10, 12, 14, 16\}$. The kurtosis excess for a Gaussian distribution $\mathcal{G}(0, 1)$ is represented by a black, dashed line. The inset shows the kurtosis excess for $L = 10$, calculated from 10^5 disorder realizations (red squares) and 10^3 realizations (yellow circles). All results correspond to averages over all values of q.

These results illustrate how the ergodicity-breaking transition to the MBL phase is initiated by an increase of the probability of extreme events of the fluctuations

$\widetilde{\Delta}_n$. This is connected with the abundance of non-thermalizing initial conditions in this transient region [236]. Yet, according to Fig. 1, the MBL phase is not defined by a large γ_2, but by large σ_{Δ_n} but less heavy tails than a Gaussian, as we show below.

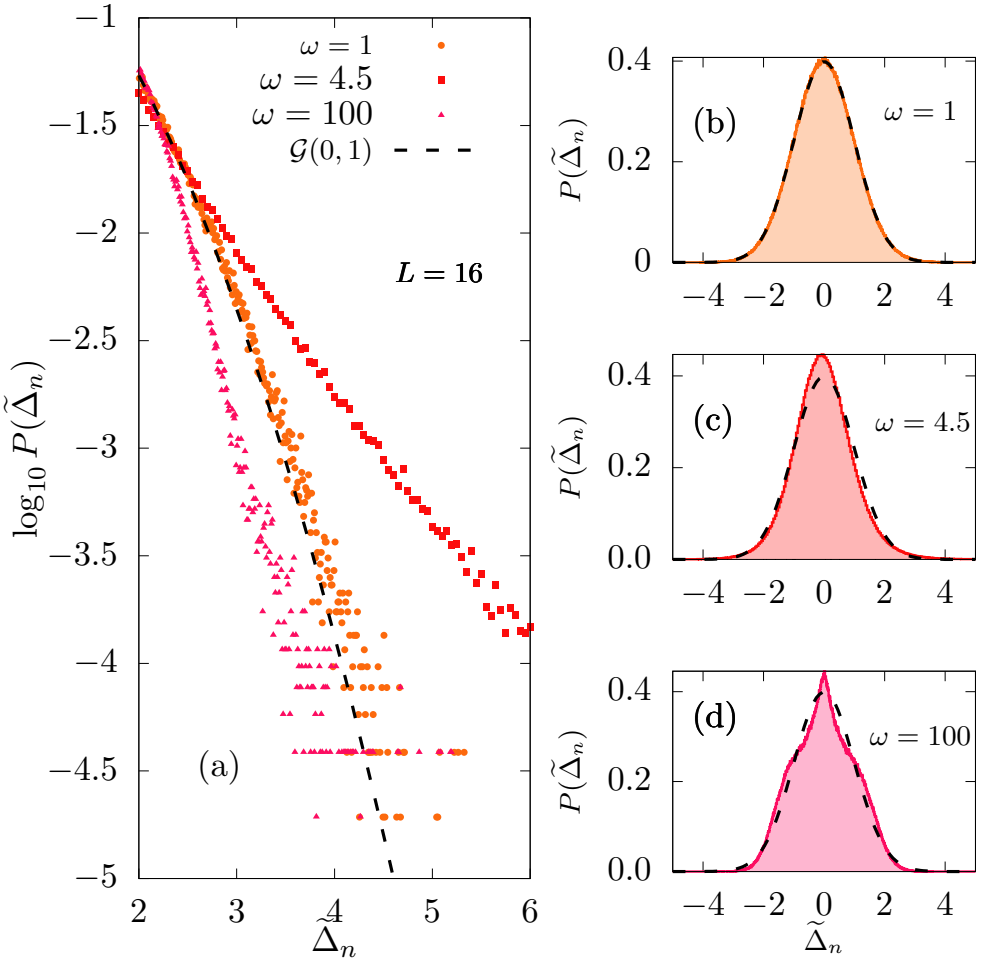

Figure 2: (a): Tails of the distribution of $\widetilde{\Delta}_n$ defined in (85) for $L = 16$ and different values of disorder, $\omega \in \{1, 4.5, 100\}$. (b)-(d): Probability distribution $P(\widetilde{\Delta}_n)$ for, from top to bottom, $\omega \in \{1, 4.5, 100\}$. The probability density function of a Gaussian $\mathcal{G}(0,1)$ has been represented by black, dashed lines.

The distribution of the diagonal fluctuations, $P(\widetilde{\Delta}_n)$, for $L = 16$ is represented in Fig. 2. On the right-hand side we show $P(\widetilde{\Delta}_n)$ for three values of disorder. For $\omega = 1$, $P(\widetilde{\Delta}_n)$ resembles a Gaussian distribution very closely. For $\omega = 4.5$, near the singular point $\omega_c(L = 16)$ (see below), this Gaussian behavior is not so good, and the tails of $P(\widetilde{\Delta}_n)$ decay more slowly, which is in agreement with the positive $\gamma_2(\widetilde{\Delta}_n)$ in Fig. 1 for this value of ω. In the MBL transition, the breakdown of the ETH has been previously associated with long tailed distributions of this type (see, e.g., [229], [236], [243], [244]). For $\omega = 100$, deep in the MBL phase, the previous

behavior has been completely destroyed, with the tails of the distribution decaying faster than in a Gaussian. In the left column of Fig. 2 we zoom on the tails of these three distributions, confirming the interpretation that we have presented.

Estimating the transition critical point

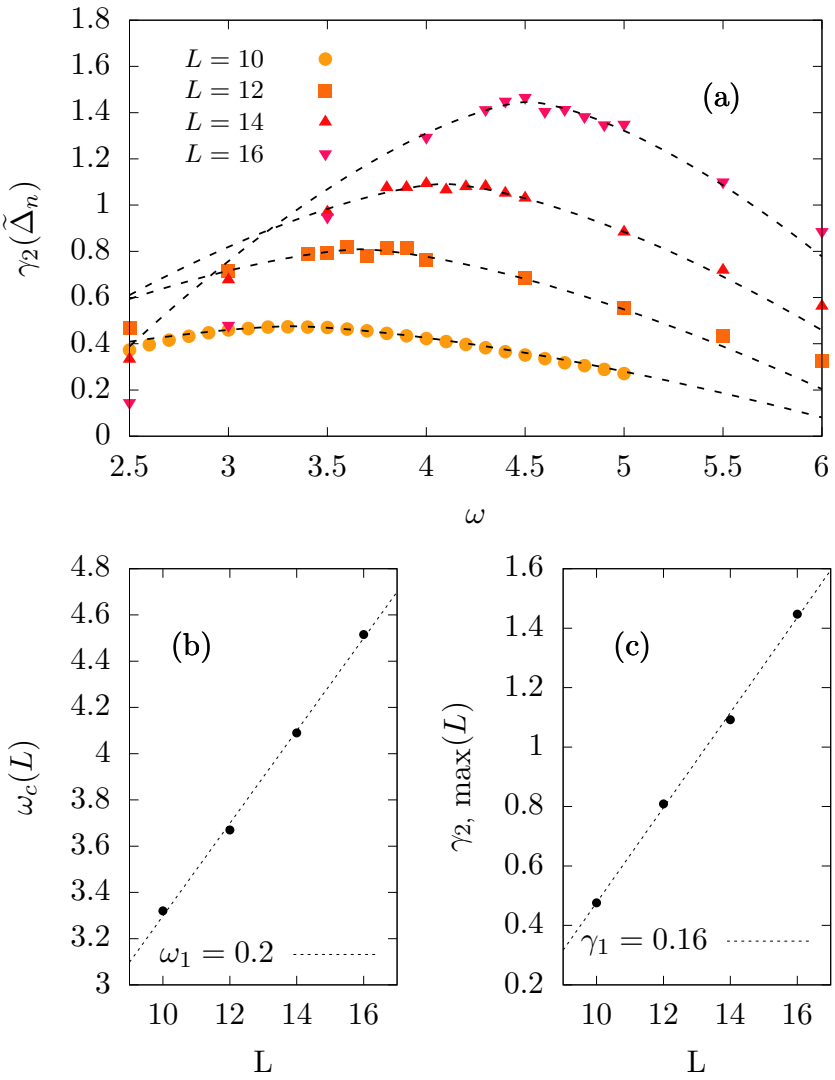

Figure 3: (a) Kurtosis excess, $\gamma_2(\widetilde{\Delta}_n)$, defined in (87), as a function of ω for several number of chain sites, $L \in \{10, 12, 14, 16\}$. The dashed line shows the fit to Eq. 88. (b) Critical value, $\omega_c(L)$, as a function of the system size, L. The dotted line displays the best linear fit, $\omega_c(L) = \omega_0 + \omega_1 L$. (c) Maximum of the kurtosis excess, $\gamma_{2,\max}(L)$, as a function of L. The dotted line shows the best linear fit to the points, $\gamma_{2,\max}(L) = \gamma_0 + \gamma_1 L$.

We would like to start by emphasizing that a precise numerical estimation of the critical point $\omega_c(L)$ can be quite computationally expensive. The inset of Fig.

1 we represent the kurtosis excess near its maximum for $L = 10$, computed with 10^3 (yellow) and 10^5 (red) realizations. While the red curve affords a reliable value for $\omega_c(L = 10)$, the fluctuations in the yellow curve make this task more complicated. Because disorder realizations take increasingly longer times as L increases, to estimate the position of the critical point for larger L we consider the ansatz

$$\gamma_2(\omega) = a\,|\omega - \omega_c(L)|^{3/2} + \gamma_{2,\max}(L), \tag{88}$$

and fit the curves for the kurtosis excess for different L. In Fig. 3(a) we observe that the kurtosis excess is very well described by Eq. (88). Yet, we emphasize that this ansatz is not related to actual critical exponents, as it depends explicitly on L (in other words, its shape lacks universality). Fig. 3(b) indicates that the precursor of the MBL critical point is quite well described by the linear scaling $\omega_c(L) = \omega_0 + \omega_1 L$, with $\omega_0 = 1.3$ and $\omega_1 = 0.2$. In passing we note that these results are in good agreement with those in Refs. [203], [207], although the authors of these works considered the critical point as obtained from the entanglement entropy and spectral statistics. This linear behavior of $\omega_c(L)$ at low L does not immediately imply $\omega_c(L) \to \infty$ as $L \to \infty$; indeed, the linear behavior could be only valid for such small values of L, with a more general expression of $\omega_c(L)$ saturating its value in the large-L limit (Refs. [421], [422] present arguments in this direction based on phenomenological renormalization group flows). Interestingly, also the maximum value of the kurtosis excess seems to be quite well described by a linear law of the form $\gamma_{2,\max}(L) = \gamma_0 + \gamma_1 L$, with $\gamma_0 = -1.12$ and $\gamma_1 = 0.16$, as shown in Fig. 3(c).

These results strongly suggest that if a critical point exits in the thermodynamic limit, $\omega_c(\infty)$, this value of disorder must be such that $\gamma_2(\widetilde{\Delta}_n)$ is maximized. As we show below, the behavior of spectral statistics across the MBL transition is also fully compatible with this hypothesis.

2.2.2 Spectral statistics across the transition

In this section we show that the probability of extreme events previously analyzed can also be taken as an indicator of the disorder strength beyond which the chaotic, ergodic phase is abandoned. Indeed, as we show below, the spectral statistics are qualitatively different for values larger and smaller than $\omega_c(L)$: for $\omega \lesssim \omega_c(L)$, the system is quantum chaotic with a Thouless energy larger than the Heisenberg energy, the mean energy distance between levels, while for $\omega \gtrsim \omega_c(L)$ the eigenlevels behave as independently distributed random numbers but with some degree of level repulsion.

As mentioned before, here we employ two chaos indicators: the nearest-neighbor spacing distribution (NNSD), $P(s)$ (short-range statistic), and the δ_n defined in (83) (long-range statistic). We work on the unfolded energy scale for both of these statistics; the smooth part of the cumulative density function is calculated by fitting a polynomial of degree 10 to the actual Hamiltonian eigenvalues $\{E_n\}_{n=1}^{N}$, which allows us to obtain the unfolded levels $\{\epsilon_n\}_{n=1}^{N}$.

Semi-Poisson behavior at the transition

Quantum chaotic systems are characterized by level correlations, while in quantum integrable systems the eigenlevels have a behavior close to independent random numbers. In the Anderson model, a prototypical system for single-particle localization, the metallic and insulating phases exhibit Wigner-Dyson and Poisson statistics, respectively [14]. Right at the critical point of the metal-insulator transition, level statistics are universal and quite closely described by the the semi-Poisson distribution (57). What can be said about many-body systems?

For the family of distributions in Eq. (57), the power spectrum of δ_n was computed analytically by Corps and Relaño in [81],

$$\langle P_k^{\delta}\rangle(\eta) := \left(\frac{N}{\eta N+1}\right)\left(\frac{1}{4\sin^2(\omega_k/2)}, \quad \omega_k := \frac{2\pi k}{N+1}, \right. \tag{89}$$

where N is the number of uncorrelated level spacings in the spectrum (normalized by the mean), $k \in \{1, 2, \ldots, N+1\}$. In (89), $\eta \in [1, +\infty)$ is a continuous parameter. Poissonian statistics correspond to $\eta = 1$, and $\eta = 2$ gives rise to semi-Poisson statistics. As η varies, the power spectrum is essentially unchanged with the exception of a vertical translation. For the single-particle Anderson model, η changes from 2 to 1 as the dimensionality increases [156].

In this section, we show that, for $\omega \gtrsim \omega_c(L)$, the level statistics of our Hamiltonian (82) are very well described, at least phenomenologically, by the semi-Poisson model. To compute $P(s)$, we consider the $d/3$ at the center of the energy band, and then we remove the $2\lfloor d/48 \rfloor$ levels closest to the edges before and after unfolding, producing a final number of levels $N = \lfloor d/4 \rfloor$, as in Table 1. Finally, we fit (57) to our numerical histograms of $P(s)$ to estimate the value of η. The corresponding results are plotted in Fig. 4. Below $\omega = 4.7$ in Fig. 4(a), the semi-Poisson model does not provide such a good description of the numerical histograms. We note that this disorder value is very close to the critical disorder calculated in Fig. 3, $\omega_c(16) = 4.52$.

Fig. 4 clearly shows that the semi-Poisson model (57) provides a very good description of level statistics for $\omega > \omega_c(16)$. It is interesting to note that for $\omega = 5.0$ we find almost completely semi-Poissonian level spacings, $\eta \approx 2.079$. For

$\omega = 4.7$, the fit yields $\eta \approx 2.274$, i.e., a level repulsion stronger than in GOE random matrices. Yet, this could be a finite-size effect or a consequence of the proximity to the critical point $\omega_c(L = 16)$. The general picture is that η decreases with ω into the MBL phase; for $\omega = 12$, level statistics are essentially Poissonian, $\eta \approx 1.058$. We expect the family of distributions (57) not to describe $P(s)$ for $\omega < 4.7$. The reason is that in that case the system is headed towards the chaotic phase, with correlated spacings, but (57) is derived assuming statistically independent spacings.

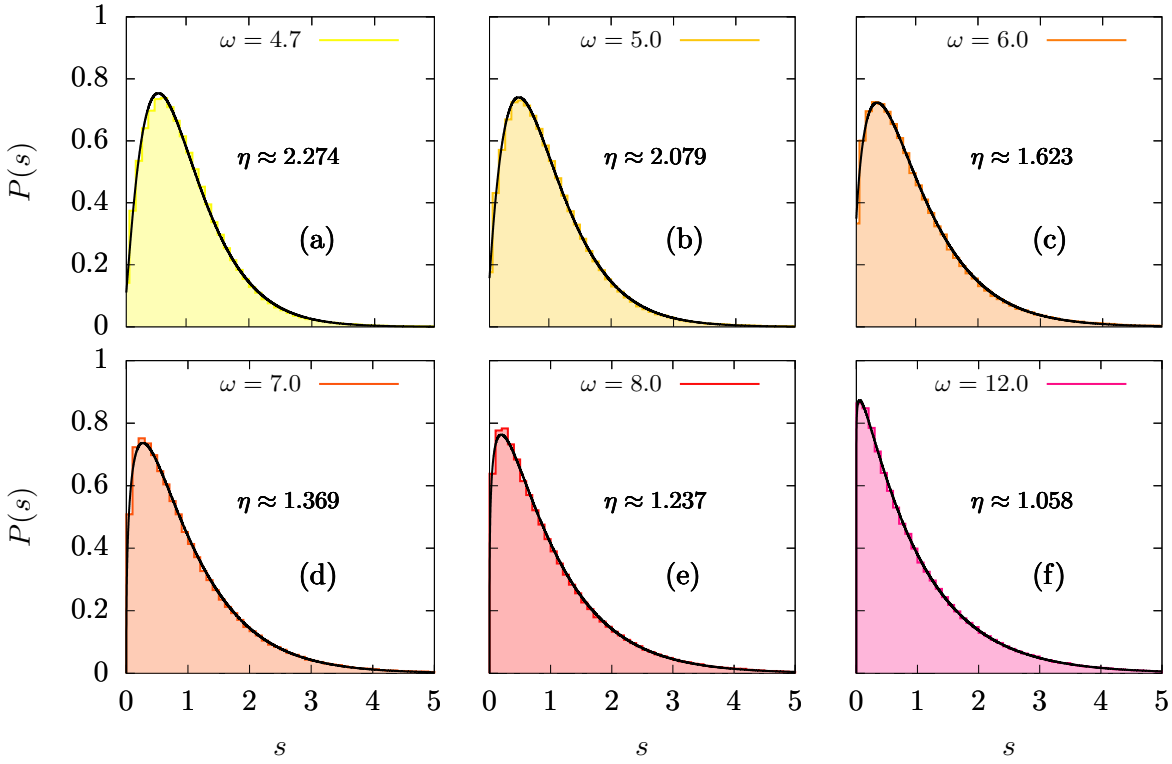

Figure 4: Level spacing distribution for different values of disorder, $\omega \in \{4.7, 5.0, 6.0, 7.0, 8.0, 12.0\}$. Solid, black lines represent the best nonlinear fit of (57) to the histograms of $P(s)$. System size is $L = 16$.

Long-range measures of level statistics corroborate this picture. In Fig. 5 we present the power spectrum $\langle P_k^\delta \rangle$ together with (89) for the values of η extracted from $P(s)$ for the same values of ω. The Poisson ($\eta = 1$) and GOE (see [416] for mathematical expressions) results are also shown for reference. For $\omega \gtrsim 5.0$, the numerical and semi-Poisson curves show almost perfect agreement. It is insightful to observe that for $\omega = 4.7$ the power spectrum intercepts the GOE curve for frequencies $k \approx 10^3$, supporting our hypothesis that this value of disorder (or, rather, a value of disorder close enough to this value) separates two regimes of qualitatively different spectral statistics. As ω is increased, η decreases towards the Poisson result, and the power spectrum undergoes a smooth crossover, approaching the

theoretical Poisson curve vertically. In all cases shown here, the first frequencies of the power spectrum show a strange behavior, but this is an expected consequence of the unfolding procedure [80], [81].

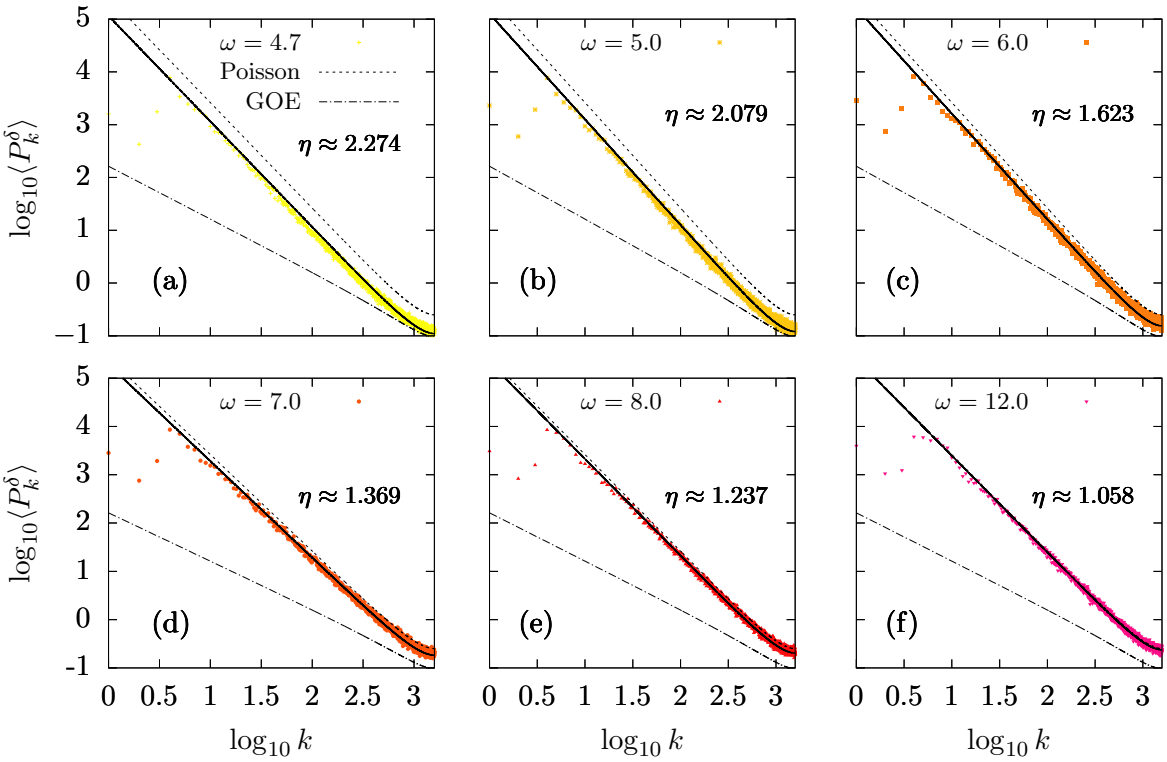

Figure 5: Power spectrum $\langle P_k^\delta \rangle$, defined in (84), for different values of disorder, $\omega \in \{4.7, 5.0, 6.0, 7.0, 8.0, 12.0\}$ (color points). Solid, black lines represent (89) for the values of η obtained from the nearest-neighbor spacing distribution in Fig. 4. Top and bottom dashed lines are the Poisson [Eq. (89) with $\eta = 1$] and GOE (see Ref. [416] for explicit formulae) results, respectively. System size is $L = 16$.

Ergodicity-breaking and Thouless energy

The power spectrum of the chaotic phase of the model is represented in Fig. 6 for several values of disorder. For very small disorder, $\omega = 0.5$ and $\omega = 1.0$, the numerics almost perfectly agrees with the GOE predictions. Yet, we observe pronounced deviations towards the Poisson curve as ω is increased but still in the chaotic phase. These deviations occur at low frequencies (i.e., large eigenlevel index distances) and they are connected to the Thouless energy E_{Th}. Strictly speaking, though, the power spectrum only gives us access to the Thouless frequency, k_{Th}. This frequency makes it possible to define a characteristic length of the problem, $\ell_{\text{Th}} = N/k_{\text{Th}}$: two energy levels, E_n and E_m exhibit RMT correlations if their

level index distance is such that $|n-m| < \ell_{\text{Th}}$. In this sense, a completely chaotic spectrum, say the spectrum of GOE random matrices, has the maximum value of ℓ_{Th} (or the lowest value of k_{Th}), because in that spectrum long-range RMT correlations are shared between *all* eigenlevels. In other words, an increasing value of k_{Th} means that the spectrum loses long-range correlations and thus becomes less chaotic. We can estimate the Thouless frequency k_{Th} as the lowest possible frequency such that $\langle P_k^\delta \rangle$ fluctuates *below* the GOE curve, which gives us a good approximation $k_{\min} \approx k_{\text{Th}}$. In Fig. 6, we have identified the estimated value $k_{\min}$ with vertical arrows. It is clearly observed that $k_{\min}$ increases with the disorder strength ω. Near the critical point $\omega_c(L = 16) \approx 4.7$, $k_{\min}$ reaches its maximal value.

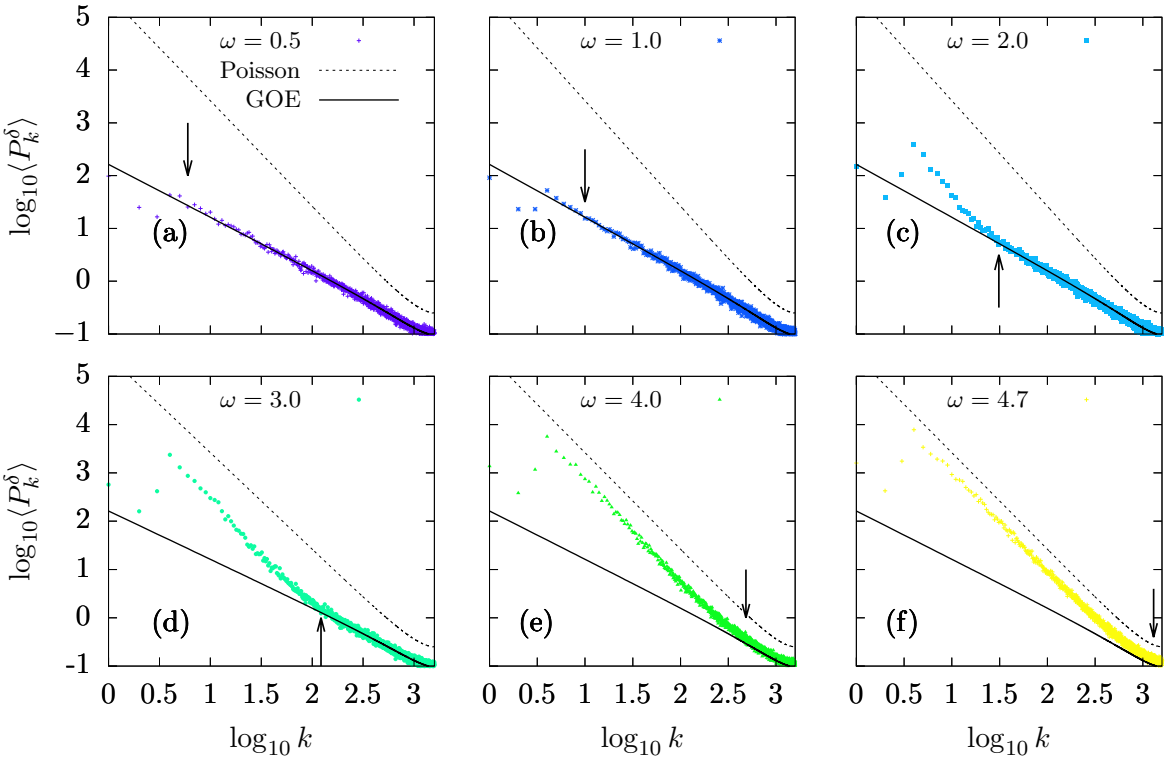

Figure 6: Power spectrum $\langle P_k^\delta \rangle$, defined in (84), for different values of disorder, $\omega \in \{0.5, 1.0, 2.0, 3.0, 4.0, 4.7\}$ (color points). Top and bottom black lines are the Poisson [Eq. (89) with $\eta = 1$] and GOE (see Ref. [416] for explicit formulae) results, respectively. The value of $k_{\min}$ for a fixed value of ω is represented by arrows in all panels. System size is $L = 16$.

Integrating the transition

Let us summarize the transition landscape that we have presented in this Chapter. In Fig. 7 we focus on the indicators of the MBL transition obtained from level statistics. In particular, Fig. 7(a) shows $k_{\rm min}$ as a function of disorder. Because the value of $k_{\rm min}$ for $\omega \ll \omega_c(L)$ is very small, $k_{\rm min}/N \ll 1$, the resulting Thouless energy is large. And since the power spectrum separates from the GOE curve as ω increases in the ergodic phase, the value of $k_{\rm min}$ grows steadily with ω. When the power spectrum completely departs from the GOE curve, $k_{\rm min}$ reaches the Nyquist frequency, $k_{\rm min} = k_{\rm Ny} = N/2$, which has been represented with a gray horizontal line as a guide for the eye. When this happens, quantum correlations of RMT are destroyed to all energy distances (on the unfolded scale). We note that $k_{\rm min}$ jumps quite abruptly to $k_{\rm Ny}$ at $\omega \approx 4.7$, which is consistent with our numerical observation that the MBL critical point for $L = 16$ should be close to this disorder value. This means that $\langle P_k^\delta \rangle$ ceases to follow the RMT predictions at a disorder strength compatible with $\omega_c(L)$, the singular point computed from the fluctuations in the diagonal matrix elements.

On the other side of the transition, for $\omega \gtrsim \omega_c(L)$, the power spectrum very approximately follows (89) as a consequence of the destruction of chaotic level correlations. In Fig. 7(b), we display the variation of the η parameter with disorder strength, revealing a smooth decreasing function of ω.

Thus, the finite-L MBL transition as measured from spectral statistics seems to display the following three stages:

(i) Full or moderate level correlations in the spectrum in a chaotic region, $0.5 \lesssim \omega \lesssim \omega_c(L)$;

(ii) No level correlations but still level repulsion in a 'semi-Poisson region', $\omega_c(L) \lesssim \omega < \infty$;

(iii) No level correlations and no level repulsion in the Poisson limit, $\omega \to \infty$ (at least for finite systems).

Finally, we connect our analyses of spectral statistics with the extreme events across the transition computed from the kurtosis excess of the diagonal fluctuations of observables. This is presented in Fig. 8. Figure 8(a) depicts the kurtosis excess $\gamma_2(L)/\gamma_{2,\rm max} = \gamma_2(L)/\left(\gamma_0 + \gamma_1 L\right)$, as a function of $\omega - \omega_c(L) = \omega - \omega_0 - \omega_1 L$, for several L. The curves appear to collapse around $\omega = \omega_c(L)$, which is indeed indicative of a phase transition. Figure 8(b) offers a similar finite-size scaling but for spectral statistics. In particular, we have calculated the distance between the

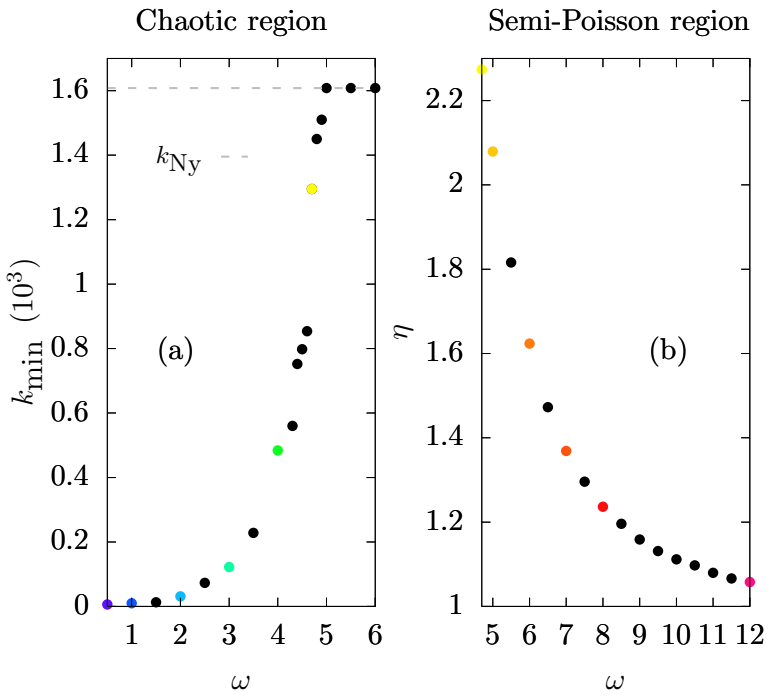

Figure 7: General landscape of long-range spectral statistics across the MBL transition. (a): For small values of disorder, $\omega \lesssim \omega_c(L=16)$, we represent the characteristic frequency $k_{\rm min}$ as a function of ω and compare it to the Nyquist frequency $k_{\rm Ny} = N/2$ (gray, dashed line). A small $k_{\rm min}$ corresponds to a large Thouless energy and vice versa. (b): For large values of disorder, $\omega \gtrsim \omega_c(L=16)$, we plot η obtained from a single-parameter fit of the generalized semi-Poisson distribution (57) to the numerically obtained NNSD ($\eta = 1$ corresponds to the full Poisson limit). For convenience of the reader, colored points represent the values of $k_{\rm min}$ and η for the same values of disorder and color code as in Figs. 4, 5, and 6.

numerics in $P(s)$ and the intermediate statistics (57) with η fixed after fitting it to the numerical $P(s)$,

$$\Delta_{\rm SP} = \frac{1}{N_b}\sum_{i=1}^{N_b}\Big|P_H(s_i) - P(s_i;\eta)\Big|^2 . \tag{90}$$

Here, $P_H(s)$ represents the numerical histograms, $P(s;\eta)$ is (57), and N_b is the total number of histogram bins. We plot $\Delta_{\rm SP}(L)$ versus, again[1], $\omega - \omega_c(L) = \omega - \omega_0 - \omega_1 L$. Around $\omega = \omega_c(L)$, the curves abruptly approach a zero value. Differently put, the transition indicators obtained from the ETH and RMT seem to agree excellently.

1 We emphasize that $\omega_c(L)$ here has been obtained from the kurtosis excess, not from spectral statistics.

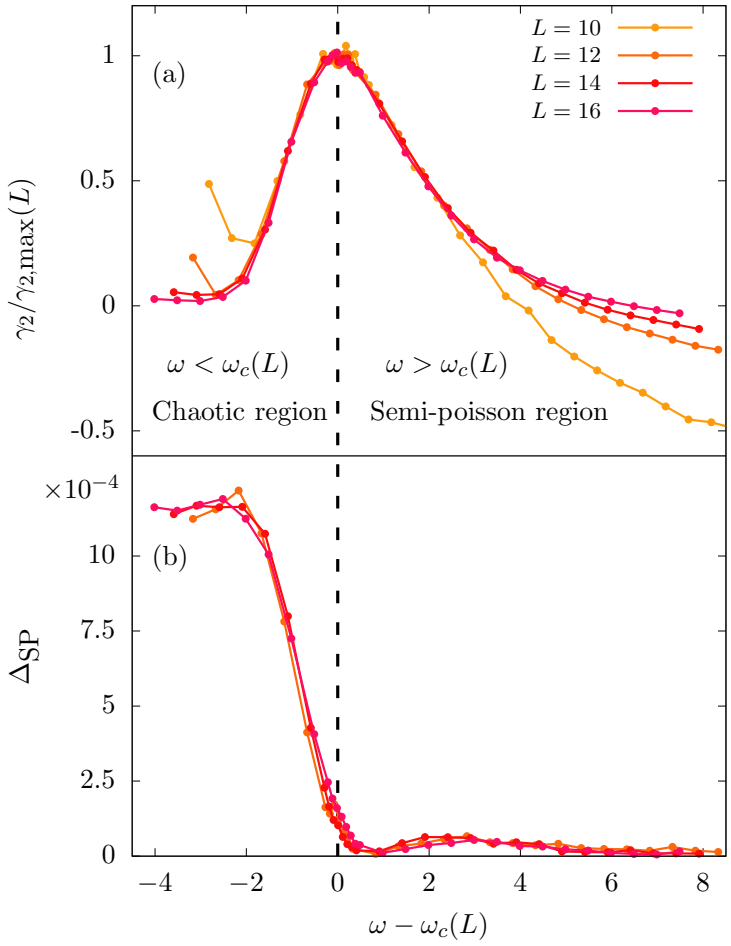

Figure 8: (a): Kurtosis excess of the distribution of $\widetilde{\Delta}_n$, re-scaled with its maximum value for each system size, $\gamma_{2,\max}$, as a function of $\omega - \omega_c(L)$, for $L = 10$, 12, 14, and 16. The black, dashed line shows the singular point, $\omega = \omega_c(L)$. (b): Distance between the numerical NNSD and the family of intermediate statistics (57), Δ_{SP}, as a function of $\omega - \omega_c(L)$, for $L = 12$, 14, and 16.

2.3 CONCLUSIONS

In this Chapter we have analyzed the ergodicity-breaking phase transition brought about by disorder in many-body systems, the so-called many-body localization transition. Through the study of the extreme events in the diagonal expectation values with respect to the expectations of the microcanonical ensemble we define a critical value of the disorder, $\omega_c(L)$, such that the probability of extreme events reaches a maximum. This critical disorder value is also tightly connected with non-smooth variations in the spectral statistics, indicating a clear change in the dynamical regime of the system. Summarizing, the critical point $\omega_c(L)$ separates two different dynamical phases:

A chaotic phase, corresponding to small disorder values, $\omega < \omega_c(L)$. On the unfolded scale, eigenlevels separated by distances smaller than a certain characteristic length, ℓ_{max}, follow RMT results; however, for unfolded distances larger than ℓ_{max} RMT-like correlations are lost [236]. For small ω values, the ETH is fulfilled. We observe an increase of the kurtosis excess $\gamma_2(\widetilde{\Delta}_\eta)$ with ω, deviating from the Gaussian expectation. This means that although generic initial conditions will thermalize to the microcanonical average for these disorder strengths, it is also a lot more probable to find anomalous initial conditions that fail to do so. The increasing values of the probability of extreme events are thus connected to the gradual loss of chaos in the spectrum. For disorder values close to $\omega \approx \omega_c(L)$, the Thouless energy approaches the Heisenberg energy, which marks the depart of the system from its ergodic phase.

A semi-Poisson phase, corresponding to $\omega > \omega_c(L)$. At this point the probability of extreme events of Fig. 1 starts diminishing (for $L = 16$). In this disorder regime, Eqs. (57) and (89) account for both short and long-range spectral statistics, suggesting that the eigenlevels approximately behave as identically distributed random numbers that still show level repulsion, in an intermediate situation between GOE and Poisson. For $L < \infty$, the Poisson limit is only strictly reached when $\omega \to \infty$.

In summary, in the many-body localization we observe a disorder-driven change from ergodicity to ergodicity-breaking. In a sense, this transition shares some features with a phase transition (in particular, a spectral phase transition). The results presented in this Chapter are correlated with the existence of certain operators that behave as conserved quantities in the non-ergodic phase. Yet, it is hard to extrapolate our analyses to the infinite-size limit, partly due to the system sizes accessible to numerical exact diagonalization. This pushes us to reverse the order of this question: can we find constants of motion characterizing non-ergodic phases due to symmetry-breaking? This will be in our focus in the next Chapter, where we explore the description of equilibrium states in symmetry-breaking phases in detail.

3 CONSTANTS OF MOTION AND $\mathbb{Z}_2$ SYMMETRY-BREAKING

The eigenstate thermalization hypothesis can be argued to play a central role in the foundations of quantum statistical mechanics in closed quantum systems. This is a robust theory expected to hold in a vast number of systems subjected only to the condition that their behavior is 'close enough' to random matrices, which constitute a prototypical theoretical framework for quantum ergodicity. However, as advanced in Sec. 1.1, the standard thermal ensembles can tremendously fail to describe the long-time equilibration values of observables in quantum systems with symmetry-breaking. Specifically, symmetry-breaking can lead to broken ergodicity. In [269] a two-level approach to statistical mechanics in symmetry-breaking systems was proposed. The main idea is that standard statistical mechanics does not work when the dynamics is constrained to disjoint portions of the phase space, so thermal averages need to be computed separately over various *components* or regions. Together with existing theoretical proofs on the nature of the MBL phase, our analyses of Sec. 2 suggest that a traditional phase transition is not necessary for an ergodicity-breaking transition to occur, and the non-ergodicity is related to the conservation of a set of operators. In this Chapter we study ergodicity breaking phase transitions in systems without disorder, our results being applicable to both finite-range interacting systems and their fully-connected counterparts. Non-ergodicity, and thus the breakdown of the ETH in these systems, is due to symmetry-breaking. We will focus on discrete $\mathbb{Z}_2$ symmetry-breaking, although our results can be generalized to systems with $\mathbb{Z}_n$ or even in some cases continuous symmetries (see our work [423], published after this the writing of this thesis was completed). We discuss the impact of our theory on the excited-state and dynamical phase transitions introduced in Sec. 1.3.3, which are currently the focus of much research in quantum many-body dynamics, as well as their connection to a form of spectral Schrödinger cat states.

This Chapter is organized as follows. The foundation of our theory of equilibration in quantum systems with $\mathbb{Z}_2$ symmetry-breaking phases is presented in Sec. 3.2, which is based on our original article [330], a generalization of our previous work [325]. An extensive application of our theory to dynamical phase transitions can be found in Sec. 3.3, which is based on our works [326], [327], [329]. Finally,

the description of equilibration in the presence of so-called energy cat states is presented in Sec. 3.4, and it is based on [29].

3.1 MOTIVATION: DISCRETE SYMMETRY-BREAKING IN FULLY-CONNECTED MODELS

Our theory for the constants of motion constraining the dynamical evolution in quantum systems with $\mathbb{Z}_2$ symmetry-breaking is developed in the general framework of Sec. 3.2. For illustration purposes, in this section we resort to the case of a fully-connected systems where ESQPTs are prominent.

As advanced in Sec. 1.3.3, ESQPTs and symmetry-breaking are fundamentally unrelated phenomena. However, a large group of systems displaying ESQPTs are also deeply impacted by symmetry-breaking. For this reason, this class of fully-connected models constitute an extremely versatile platform to test our ideas. We show that this type of ESQPT splits the spectrum into two different excited-state quantum phases. These phases can be identified by an operator which is a constant of motion (in the sense that its dynamical evolution does not change over time) in just one of them, while it is no longer constant in the other phase. A graphically convenient way to understand the meaning of this constant of motion is through the classical phase space of the quantum Hamiltonian; however, we note that the model does not need to have a well-defined classical limit for this operator to be constant. In essence, this operator signals to which part of phase space (or, more generally, to which 'disjoint component' of the system, in the sense of [269]) a given quantum state is attached to, and assigns it a conserved quantum number, with important thermodynamic consequences.

For the moment, we will restrict ourselves to a system where the classical limit is accessible. Consider a quantum system governed by a Hamiltonian $\hat{H}$, and assume that in the $\hbar \to 0$ limit it can be described by the classical energy functional $H(\mathbf{x})$, where $\mathbf{x} \equiv (\{\mathbf{q}_i\}_{i=1}^{f}, \{\mathbf{p}_i\}_{i=1}^{f}) \in \mathbb{R}^{2f}$ accounts for all relevant canonical coordinates, and $f \in \mathbb{N}$ is the number of classical degrees of freedom. As previously mentioned, ESQPTs are caused by certain unstable fixed points, $\mathbf{x}_c$, of the Hamiltonian flow, $\nabla H(\mathbf{x}_c) = 0$, producing a critical energy $E_c \equiv H(\mathbf{x_c})$ where the non-analytic behavior takes place [265]. Assume that there exists a dynamical function, $f(\mathbf{x})$, such that:

(i) $f(\mathbf{x})$ is nullified at the ESQPT unstable fixed point, $f(\mathbf{x_c}) = 0$, and

(ii) On one of the spectral phases induced by the ESQPT (e.g., for $E < E_c$), every classical trajectory is such that $f(t) \equiv f(\mathbf{x}[t]) < 0$ or $f(t) > 0$, $\forall t$, depending on

the initial condition, i.e., the sign of $f(t)$ remains constant in time. However, on the other spectral phase of the ESQPT (e.g., for $E > E_c$), the sign of $f(t)$ is not conserved anymore.

Then, there exists a quantum operator,

$$\hat{\mathcal{C}} \equiv \text{sign}\,[\hat{f}(\hat{\mathbf{x}})] \tag{91}$$

which is a constant of motion only in the first of these two phases, $E < E_c$.

In the definition (91), the sign of an operator $\hat{f}$ is defined

$$\text{sign}\,(\hat{f}) \equiv F\,\text{sign}\,(D)\,F^{-1} = F\,\text{diag}\,[\text{sign}\,(\{d_i\})]F^{-1}, \tag{92}$$

where D is a diagonal matrix whose elements $\{d_i\}_i$ are the eigenvalues of $\hat{f}$, and F is a matrix whose columns are the eigenvectors of $\hat{f}$. Integral representations of the sign operator have been studied, e.g., in [424], [425]. Therefore, it is clear that the operator $\hat{\mathcal{C}}$ has only two eigenvalues, ± 1, and thus it represents a $\mathbb{Z}_2$ symmetry in the phase where it is constant. It should be emphasized, however, that the existence of this constant of motion, in principle, is unrelated to the exact discrete symmetry of the model under consideration, and thus it is not necessarily a consequence of spontaneous symmetry-breaking as observed in certain physical models. In other words, such an operator can also be a constant in systems without spontaneous symmetry-breaking.

Fully-connected systems constitute one class of models where the above conditions, and thus the existence of $\hat{\mathcal{C}}$ as a conserved quantity, are satisfied. These models are also usually very convenient because the ESQPT signatures are prominent already for quite small system sizes. Examples are the Lipkin-Meshkov-Glick model, the Rabi and Dicke models, spinor Bose-Einstein condensates and Bose mixtures in a double-well potential, the coupled top, and the two-fluid Lipkin model [264], [297], [305], [312]–[314], [320], [321], [324], [334]–[336], [352], [357], [426], [427], to name a few. In all these systems, an ESQPT occurs at $E = E_c$ below which the classical phase space is split into disconnected wells. The operator $\hat{\mathcal{C}}$ identifies to which classical well a quantum state belongs.

To be more specific, let us write the quantum Hamiltonian $\hat{H} = \sum_n E_n \hat{P}_n$, where $\hat{P}_n$ is the projector onto the eigenspace with energy E_n. Then, $\left[\hat{\mathcal{C}}, \hat{P}_n\right] = 0$, $\forall n \,/\, E_n < E_c$, and $\left[\hat{\mathcal{C}}, \hat{P}_n\right] \neq 0$, $\forall n \,/\, E_n > E_c$. In other words, $\langle \hat{\mathcal{C}} \rangle$ is conserved by any time evolution, $|\psi(t)\rangle$, such that[1] $\langle \psi(t)| \hat{H} |\psi(t)\rangle = \langle E \rangle < E_c$, however, this conservation rule no longer holds if $E > E_c$. For this reason, there exists at least one phase where equilibrium [428] and non-equilibrium [429] thermodynamics cannot

1 Of course, here we are implicitly assuming that the distribution of populated eigenstates is sufficiently narrow so that the part of the wavefunction populating $E > E_c$ can be neglected.

be properly described without this operator. However, the phase where $\hat{\mathcal{C}}$ is no longer constant can be described with the standard tools of statistical mechanics.

Later in this thesis we will discuss many examples of systems where this constant of motion can be defined, as well as its relation to symmetry-breaking. To keep it short, here we simply propose to take a look at the classical phase space of the LMG model (73) introduced in Sec. 1.3.3. The mathematical details of this classical limit are gathered in Sec. 3.3.1. As our goal in this section is to illustrate the meaning of $\hat{\mathcal{C}}$, we will leave the technical details to the corresponding section.

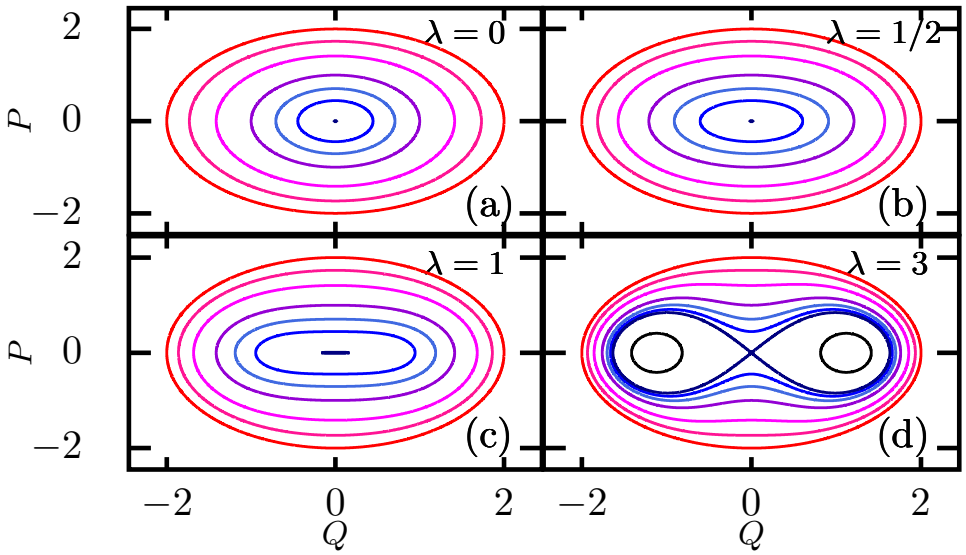

Figure 9: Classical phase space of the LMG model (141) with $h = 1$ and several values of λ. Different classical orbits at different energies are represented by lines of different colors. Magenta-red lines show higher energies, while purple-blue lines show lower energies.

In Figure 9 we represent the classical orbits of the energy functional $H(Q, P)$ obtained from the quantum Hamiltonian $\hat{H}$ in (73). For $\lambda > \lambda_c = h$, an ESQPT takes place at $E_c = -hj$. This is the case of panel (d) of this figure [the rest of the panels will be discussed elsewhere, see Sec. 3.3.1]. We can clearly observe that for $E < E_c$, the phase space is disconnected and classical orbits are trapped either at $Q > 0$ or $Q < 0$. However, for $E > E_c$, the phase space becomes topologically compact, and every trajectory has access to the geometrical regions with $Q > 0$ and $Q < 0$. In addition to this, at the ESQPT critical point (where orbits 'intersect'), we exactly have $Q = 0$. Thus, one may indeed define a function $f(Q)$ verifying the properties (i) and (ii) specified above. From this discussion, it is clear that f should be such that $f(Q) \propto Q$, its precise form being to some extent arbitrary. In terms of physically meaningful quantities, it can be shown [see (143) in Sec. 3.3.1] that the collective magnetization along the $x-$axis, $\hat{J}_x = \frac{1}{2}\sum_i \hat{\sigma}_i^x$, has a classical counterpart

given by $j_x = Q\sqrt{4-Q^2-P^2}/2$ with $Q^2+P^2 \leq 4$. Therefore, classical function $\mathcal{C} = \text{sign}(j_x)$ is trivially a conserved quantity for $E < E_c$. We posit that the quantum operator $\hat{\mathcal{C}} = \text{sign}(\hat{J}_x)$ is also a *quantum* conserved quantity in the same spectral phase. The mathematical foundation of this observation is presented in the following section.

3.2 GENERAL FRAMEWORK

We have already discussed in Sec. 1.1.2 that, strictly speaking, the unitary time evolution of quantum mechanics is incompatible with equilibrium states. Shifting our focus away from this rigid understanding of equilibration, it has been shown that the time-evolved wave function of an isolated quantum system, for sufficiently long times, almost always ends up fluctuating around an effective equilibrium state,

$$\hat{\rho}_{\text{eq}} = \lim_{\tau\to\infty} \frac{1}{\tau} \int_0^\tau |\Psi(t)\rangle \langle\Psi(t)| \, \mathrm{d}t, \tag{93}$$

which provides the same results in experimentally realistic situations, see [12], [25], [430]–[434]. In other words, even though the time evolution does not lead an initial wave function to an equilibrium state itself, its dynamical expectation value for almost any observable can be effectively described by a certain $\hat{\rho}_{\text{eq}}$. In this section, our goal is to provide a characterization of such equilibrium states when spontaneous symmetry-breaking (SSB) occurs. We should emphasize that our results generally apply to systems with $\mathbb{Z}_2$ symmetry-breaking phases or states, and for this reason they can and will be employed later in this thesis dealing with certain dynamical aspects of many-body quantum systems.

Consider a time-evolving wave function

$$|\Psi(t)\rangle = \sum_n \sum_{k=\pm} c_{n,k} e^{-iE_{n,k}t} \; |E_{n,k}\rangle \;, \tag{94}$$

where k labels the symmetry sectors of some discrete $\mathbb{Z}_2$ symmetry. Let us consider the typical scenario in this thesis of systems with a spectral phase transition: for $E < E_c$, we have a symmetry-breaking phase with pairwise level degeneracies, $E_{n,+} = E_{n,-}$, while for $E > E_c$ we have a symmetric phase such that $E_{n,+} \neq E_{n,-}$.

Within the symmetric phase, where the spectrum does not show level degeneracies, the time-averaged density matrix in (93) is diagonal in the Hamiltonian

eigenbasis. This is because the off-diagonal contributions have been destroyed by the infinite-time average,

$$\hat{\rho}_{\text{eq}}(E > E_c) = \sum_{n,k} \Big(|c_{n,k}|^2 \; E_{n,k} \quad E_{n,k} \; . \tag{95}$$

This is simply the standard result of the diagonal ensemble, typical of non-degenerate systems where the ETH is trivially valid [1], [21].

Yet, as advanced in the Introduction, in the symmetry-breaking phase, say $E < E_c$, level degeneracies imply that off-diagonal terms also survive the infinite-time average. Explicitly,

$$\begin{aligned} \hat{\rho}_{\text{eq}}(E < E_c) = \sum_{n,k} \Big(& |c_{n,k}|^2 \; E_{n,k} \quad E_{n,k} \\ + \sum_n \Big(& c^*_{n,+} c_{n,-} \, |E_{n,-}\rangle \langle E_{n,+}| + \sum_n \Big(c_{n,+} c^*_{n,-} \, |E_{n,+}\rangle \langle E_{n,-}| \, . \end{aligned} \tag{96}$$

Therefore, in a symmetry-breaking phase we need to take into account these off-diagonal terms if we hope to describe equilibrium values of observables. Note that in the above equation some complex-valued elements are present: therefore, in general, equilibrium values are not described by real operations only.

In this section, we derive a set of constants of motion in symmetry-broken phases, necessary to build statistical ensembles describing the equilibrium process of many-body quantum systems. For illustration purposes, we consider the paradigmatic one-dimensional transverse-field Ising model,

$$\hat{H}_{\text{TFIM}} = -\sum_{i<j} V_{ij} \hat{\sigma}^x_i \hat{\sigma}^x_j + h \sum_i \Big(\hat{\sigma}^z_i . \tag{97}$$

Here, V_{ij} models the reach and geometry of the interaction. In our numerical experiments, we consider long range ferromagnetic interactions, $V_{ij} = J|i-j|^{-\alpha} > 0$, $J > 0$, displaying a symmetry-breaking phase for $h < h_c = J$ and $T < T_c$ when $\alpha < 2$ [435] characterized by ferromagnetic order. Here, the power-law exponent $\alpha \in [0, \infty)$ controls the range of interactions: for $\alpha = 0$, the system becomes fully-connected, and it is formally analogous to the LMG model in (73); the limit $\alpha \to \infty$ leads the system to the nearest-neighbor TFIM. J is a coupling constant. The Hamiltonian (97) is invariant under the $\mathbb{Z}_2$ parity transformation

$$\hat{\Pi} = \prod_{i=1}^{N} \Big(\hat{\sigma}^z_i , \tag{98}$$

whose two eigenvalues, $+1$ and -1, allow us to classify the system eigenstates in symmetry sectors.

The TFIM (97) is also invariant under the inversion operator $\hat{\mathcal{I}}$, which essentially implements a reflection along the center of the spin chain. Considering the computational site basis, whose elements can be taken as the tensor product of the orientation of the ith spin ($i = 1, 2, \ldots, N$) along the z-axis, $|\phi\rangle = \bigotimes_{i=1}^{N} |\phi_i\rangle_z$, $\phi_i \in \{\uparrow, \downarrow\}$, we have that

$$\hat{\mathcal{I}} \, |\phi_1 \, \phi_2 \, \ldots \, \phi_N\rangle_z = |\phi_N \, \ldots \, \phi_2 \, \phi_1\rangle_z \tag{99}$$

In our numerical results, we will only work with states in the positive inversion sector, i.e., those verifying $\hat{\mathcal{I}} \, |\phi\rangle = |\phi\rangle$.

In order to reduce the computational burden and reach larger system sizes, in our numerical calculations we consider periodic boundary conditions (PBCs). As a result, the translation operator,

$$\hat{\mathcal{T}} \, |\phi_1 \, \phi_2 \, \cdots, \phi_N\rangle_z = |\phi_N \, \phi_1 \, \cdots, \phi_{N-1}\rangle_z \, , \tag{100}$$

is also a symmetry of (97). We again only work with states in the positive translation sector such that $\hat{\mathcal{T}} \, |\phi\rangle = |\phi\rangle$, i.e., the zero-momentum basis. Although the operators $\hat{\mathcal{I}}$ and $\hat{\mathcal{T}}$ are not commuting, every eigenvector of $\hat{\mathcal{T}}$ with eigenvalue 1 is also an eigenvector of $\hat{\mathcal{I}}$ with eigenvalue 1. Because the parity (98) commutes with both $\hat{\mathcal{I}}$ and $\hat{\mathcal{T}}$, we are able to work with the two parity sectors simultaneously.

A consequence of the use of PBCs is that the potential V_{ij} in (97) can be written $V_{ij} = \frac{J}{\mathcal{N}(\alpha)} D_{ij}^{-\alpha}$, where $D_{ij} = \frac{1}{\min\{|i-j|, N-|i-j|\}}$ and $\mathcal{N}(\alpha) = \frac{1}{N-1} \sum_{i \neq j} D_{ij}^{-\alpha}$ is the so-called Kac factor [436]; it is necessary to enforce Hamiltonian intensiveness when $\alpha < 1$, however it can be omitted if $\alpha \geq 1$.

Thus, we pose the following question: if a finite system is isolated from any environment, how does it become magnetized upon entering the SB phase?

3.2.1 Assumptions

Our theory applies to quantum systems satisfying the hypotheses presented below. We first establish what structural properties we ask of the quantum system.

H1.– There exists a unitary $\mathbb{Z}_2$ symmetry, $\hat{\Pi}$, verifying $\hat{\Pi}\hat{H}\hat{\Pi}^\dagger = \hat{H}$. The operator $\hat{\Pi}$ has only two eigenvalues, $\mathrm{Spec}(\hat{\Pi}) = \{+1, -1\}$. Usually, this operator is called *parity*.

In the case of the TFIM (97), $\hat{H}$ is invariant under a 180 degrees rotation around the z-axis, and therefore it commutes with the operator $\hat{\Pi} = \prod_j \hat{\sigma}_j^z$.

H2.– Below a certain *critical* temperature, $T < T_c$, there exist two symmetry-breaking equilibrium states, $\hat{\rho}_{\mathrm{eq}}^{(i)}$ and $\hat{\rho}_{\mathrm{eq}}^{(ii)}$, with orthogonal supports and fulfilling $\hat{\Pi}\hat{\rho}_{\mathrm{eq}}^{(i)}\hat{\Pi}^\dagger = \hat{\rho}_{\mathrm{eq}}^{(ii)}$. However, for $T > T_c$ equilibrium states are symmetric, so they are invariant under $\hat{\Pi}$: $\hat{\Pi}\hat{\rho}_{\mathrm{eq}}\hat{\Pi}^\dagger = \hat{\rho}_{\mathrm{eq}}$.

This last hypothesis is expected to hold only in the TL. In finite-N systems, however, $\hat{\rho}_{\text{eq}}^{(i)}$ and $\hat{\rho}_{\text{eq}}^{(ii)}$ are actually prethermal states in which the system stays for a very long time before eventually reaching a final symmetric thermal state (see below for a discussion of the typical timescales when this happens). As shown in Sec. 3.2.6, these states can be stabilized even away from the TL.

It is important to note that a consequence of these hypotheses is that below the critical energy defined through the critical temperature, $E_c = E(T_c)$, in the infinite-size limit the spectrum is composed of pairs of degenerate states that belong to different parity sectors, i.e., $E_{n,+} = E_{n,-}$ for all n such that $E_n < E_c$. In finite-size systems such degeneracy is only approximately realized, but the energy gap $|E_{n,+} - E_{n,-}|$ closes *exponentially* with system size, meaning that even for relatively small systems these pairs of levels are essentially already degenerate.

The physical consequences of (H2) are usually identified by an *order parameter*, $\hat{M}$. On $\hat{M}$, we impose the following conditions:

M1.– The eigenvectors of $\hat{M}$, $\hat{M}\,|m_n\rangle = m_n\,|m_n\rangle$, are rotated by $\hat{\Pi}$ as $\hat{\Pi}\,|m_n\rangle = |-m_n\rangle$.

M2.– Let $\hat{P}_{m_n}$ be the projector onto the m_n eigenspace. If $m_n < 0$, the expectation value of $\hat{P}_{m_n}$ in the equilibrium state $\hat{\rho}_{\text{eq}}^{(i)}$ vanishes: $\langle \hat{P}_{m_n} \rangle_{(i)} = \text{Tr}[\hat{\rho}_{\text{eq}}^{(i)} \hat{P}_{m_n}] = 0$. Together with (H2), this implies that if $m_n > 0$, then $\langle \hat{P}_{m_n} \rangle_{(ii)} = 0$.

These two properties imply that $\text{Tr}[\hat{\rho}_{\text{eq}} \hat{M}] = 0$ for any symmetric equilibrium state.

(M1) and (M2), together with (H2), describe the typical behavior in SB phase transitions: if the system is cooled to $T < T_c$, SSB makes it choose between an equilibrium state in which only positive values of $\hat{M}$ can be observed, and another equilibrium state in which $\hat{M}$ can have only negative values. Phenomenologically speaking, this leads to a kind of *dynamical barrier* splitting the phase space into two disjoint or disconnected regions (even if there is no actual classical phase space), preventing the system from going from one part to the other [437]–[439]. For (97), the order parameter is given by the total ferromagnetic magnetization, $\hat{M}_x = \sum_i \hat{\sigma}_i^x$ (sometimes we will use subscripts x, y, z to emphasize what kind of magnetization we are referring to, although the order parameter will generically be $\hat{M} = \hat{M}_x$). Thus, for $\hat{\rho}_{\text{eq}}^{(i)}$ we have $\langle \hat{M}_x \rangle > 0$, and likewise for $\hat{\rho}_{\text{eq}}^{(ii)}$ we must have $\langle \hat{M}_x \rangle < 0$.

3.2.2 First result

The previous mathematical hypotheses allow us to formulate the following:

Theorem 1.– *(H1) and (H2), together with (M1) and (M2), hold if and only if*

$$\hat{\mathcal{C}} \equiv \text{sign}\,(\hat{M}) \;\; and \;\; \hat{\mathcal{K}} \equiv \frac{i}{2}[\hat{\mathcal{C}}, \hat{\Pi}] \tag{101}$$

are constants of the motion below the critical energy, and the set $\{\hat{\mathcal{C}}, \hat{\mathcal{K}}, \hat{\Pi}\}$ *verify the SU(2) commutation algebra.*

Below we provide a proof for this theorem.

Proof 1.– We start by showing that there exist two equilibrium states with orthogonal supports, $\rho_{\text{eq}}^{(i)}$ and $\rho_{\text{eq}}^{(ii)}$, in a given subspace spanned by a number of Hamiltonian eigenstates if and only if $\hat{\mathcal{C}} = \text{sign}(\hat{M})$ is a constant of motion, provided that $\hat{M}$ fulfills (M2). We note that in this part of the proof the existence of the discrete symmetry $\hat{\Pi}$ is not necessary.

Forward implication.- Because $\hat{\rho}_{\text{eq}}^{(i)}$ and $\hat{\rho}_{\text{eq}}^{(ii)}$ are equilibrium states, they commute with the Hamiltonian of the system, $[\hat{H}, \hat{\rho}_{\text{eq}}^{(i)}] = [\hat{H}, \hat{\rho}_{\text{eq}}^{(ii)}] = 0$. Furthermore, as these two equilibrium states have orthogonal supports, there exists a common diagonal basis for $\hat{H}$, $\rho_{\text{eq}}^{(i)}$ and $\rho_{\text{eq}}^{(ii)}$. Therefore, the complete Hilbert space can be broken into at least two subspaces: the first subspace, $\mathcal{H}_i$, is spanned by the Hamiltonian eigenstates that generate the support of $\hat{\rho}_{\text{eq}}^{(i)}$, say $\mathcal{B}_i = \left\{ \left| E_1^{(i)} \right\rangle \left(\ldots, \left| E_N^{(i)} \right\rangle \right\}$; the second subspace, $\mathcal{H}_{ii}$, is spanned by the Hamiltonian eigenstates that generate the support of $\hat{\rho}_{\text{eq}}^{(ii)}$, $\mathcal{B}_{ii} = \left\{ \left| E_1^{(ii)} \right\rangle \left(\ldots, \left| E_M^{(ii)} \right\rangle \right\}$. Due to the orthogonality of $\hat{\rho}_{\text{eq}}^{(i)}$ and $\hat{\rho}_{\text{eq}}^{(ii)}$, these two Hilbert spaces are disjoint, so $\left| E_k^{(i)} \right\rangle \left(\notin \mathcal{B}_{ii}$ and viceversa. This does not exclude the possibility that there may exist a third Hilbert subspace, $\mathcal{H}_{iii}$, where neither of the $\hat{\rho}_{\text{eq}}^{(k)}$ is supported, so that $\mathcal{H} = \bigoplus_{k=i,ii,iii} \mathcal{H}_k$. Hypothesis (H2) establishes that the eigenstates $\left| E_n^{(k)} \right\rangle$, $k \in \{i, ii\}$, have energies below the critical energy E_c, and that the third subspace, $\mathcal{H}_{iii}$, is spanned by eigenstates with energies above the critical energy, where every equilibrium state is symmetric. Note, however, that Theorem 1 could be formulated without this requirement, but the second main result, Theorem 2, would not hold without it.

In order to analyze the dynamics below the critical energy, we consider an arbitrary initial state spanned by $\mathcal{B}_i \cup \mathcal{B}_{ii}$, say

$$|\Psi(0)\rangle = \sum_{n=1}^{N} c_n^{(i)}(0) \;\; \left| E_n^{(i)} \right\rangle \left(+ \sum_{n=1}^{M} c_n^{(ii)}(0) \;\; \left| E_n^{(ii)} \right\rangle \right., \tag{102}$$

with $\sum_{n=1}^{N} \; c_n^{(i)}(0) \;^2 + \sum_{n=1}^{M} \; c_n^{(ii)}(0) \;^2 = 1$. Then, the time-evolving wave function, $|\Psi(t)\rangle = e^{-i\hat{H}t} |\Psi(0)\rangle$ ($\hbar = 1$), reads

$$|\Psi(t)\rangle = \sum_{n=1}^{N} c_n^{(i)}(0)\, e^{-iE_n^{(i)}t} \;\; \left| E_n^{(i)} \right\rangle \left(+ \sum_{n=1}^{M} c_n^{(ii)}(0)\, e^{-iE_n^{(ii)}t} \;\; \left| E_n^{(ii)} \right\rangle \right. . \tag{103}$$

According to (M2), below the critical energy the Hamiltonian eigenstates spanning $\mathcal{H}_i$ and $\mathcal{H}_{ii}$ can be expanded in the eigenbasis of the order parameter, $\hat{M}\,|M_n\rangle = m_n\,|M_n\rangle$, with a suitable sign of the eigenvalues M_n. Therefore, eigenvectors belonging to $\mathcal{B}_i$ can be written as linear combinations of eigenstates of $\hat{M}$ with positive eigenvalues,

$$E_n^{(i)}\rangle = \sum_{m,M_m>0} \alpha_m^{(n)}\,|M_m\rangle\,, \tag{104}$$

and eigenvectors belonging to $\mathcal{B}_{ii}$ can be written as linear combinations of eigenstates of $\hat{M}$ with negative eigenvalues,

$$E_n^{(ii)}\rangle = \sum_{m,M_m<0} \beta_m^{(n)}\,|M_m\rangle\,. \tag{105}$$

Normalization of $E_n^{(k)}\rangle$ imposes $\sum_n |\alpha_m^{(n)}|^2 = \sum_n |\beta_m^{(n)}|^2 = 1$. Then, the first term in Eq. (103) is the projection of $|\Psi(t)\rangle$ over the subspace spanned by the eigenstates of $\hat{M}$ with positive eigenvalues, and, as $\hat{\mathcal{C}} = \text{sign}(\hat{M})$, it is also the projection of $|\Psi(t)\rangle$ over the subspace spanned by the eigenstates of $\hat{\mathcal{C}}$ with eigenvalue $c = 1$. The same reasoning shows that the second term in Eq. (103) is the projection of $|\Psi(t)\rangle$ over the subspace spanned by the eigenstates of $\hat{\mathcal{C}}$ with eigenvalue $c = -1$. Therefore, the probability of obtaining $c = 1$ in a measurement of $\hat{\mathcal{C}}$ is

$$p(c=1) = \sum_{i=1}^{N} c_n^{(i)}(t)^{\,2} = p\sum_{i=1}^{N} c_n^{(i)}(0)^{\,2} \tag{106}$$

which remains constant throughout the whole time evolution. The exact same reasoning shows that $p(c=-1)$ also remains constant, and therefore $\hat{\mathcal{C}}$ is a constant of motion below the critical energy.

Backward implication.- This implication is straightforward. If there exists a constant of motion, $\hat{\mathcal{C}}$, with two eigenvalues, $c = \pm 1$, then there exist two orthogonal equilibrium states, the first one spanned by the eigenstates of $\hat{\mathcal{C}}$ with $c = 1$, and the second one spanned by the eigenstates of $\hat{\mathcal{C}}$ with $c = -1$.

Now, we consider the case in which both hypothesis (H1) and (H2) hold.

Forward implication.- (H1) establishes the existence of a parity operator, $\hat{\Pi}$, commuting with the system Hamiltonian, $[\hat{H}, \hat{\Pi}] = 0$. Since $\hat{\mathcal{K}}$ is a function of $\hat{\mathcal{C}}$ and $\hat{\Pi}$, both of which are constant in the SB phase ($\hat{\Pi}$ is constant also outside of the SB phase), then it is clear that the quantity $\hat{\mathcal{K}}$ is constant in the SB phase. The point is to show that $\{\hat{\mathcal{C}}, \hat{\mathcal{K}}, \hat{\Pi}$ fulfill the SU(2) commutation rules.

To prove this, let us consider the parity transformation of an eigenstate belonging to $\mathcal{H}_i$ (the same argument can be applied to an eigenstate belonging to $\mathcal{H}_{ii}$). As $\mathcal{H} = \bigoplus_{k=i,ii,iii} \mathcal{H}_k$, we can write

$$\hat{\Pi} \ E_n^{(i)}\rangle = \sum_j \alpha_j^{(n)} \ E_j^{(i)}\rangle + \sum_k \beta_k^{(n)} \ E_k^{(ii)}\rangle + \sum_l \gamma_l^{(n)} \ E_l^{(iii)}\rangle . \tag{107}$$

As (H2) applies to any equilibrium state within $\mathcal{B}_i$, we have that

$$\hat{\Pi} \ E_n^{(i)}\rangle\langle E_n^{(i)} \ \hat{\Pi}^\dagger \in \mathcal{B}_{ii}, \ \forall n, \tag{108}$$

so $\alpha_j^{(n)} = \gamma_l^{(n)} = 0, \forall j, \ l, \ n$, and therefore

$$\hat{\Pi} \ E_n^{(i)}\rangle = \sum_k \beta_k^{(n)} \ E_k^{(ii)}\rangle , \tag{109}$$

with $\beta_k^{(n)} \in \mathbb{C}$. Then, the equilibrium state $\hat{\rho}_{\text{eq}}^{(i)} = \ E_n^{(i)}\rangle\langle E_n^{(i)} \ $ transforms as

$$\hat{\Pi}\hat{\rho}_{\text{eq}}^{(i)}\hat{\Pi}^\dagger = \sum_k |\beta_k^{(n)}|^2 \ E_k^{(ii)}\rangle\langle E_k^{(ii)} \ + \sum_{k\neq l} \beta_k^{(n)}(\beta_l^{(n)})^* \ E_k^{(ii)}\rangle\langle E_l^{(ii)} \ . \tag{110}$$

Due to (H2), the previous equation equals $\hat{\rho}_{\text{eq}}^{(ii)}$, i.e., an equilibrium state, which is diagonal in the Hamiltonian eigenbasis as $[\hat{H}, \hat{\rho}_{\text{eq}}^{(ii)}] = 0$. But this is only possible if there is just one coefficient $\beta_k^{(n)}$ different from zero in Eq. (109), that is, if

$$\hat{\Pi} \ E_n^{(i)}\rangle = \beta_n \ E_n^{(ii)}\rangle \tag{111}$$

And, because $\text{Tr}\left[\hat{\rho}_{\text{eq}}^{(ii)}\right] = 1$, we further conclude that $|\beta_n|^2 = 1$. Because we can multiply any vector by an arbitrary phase without changing the expectation value of any operator, we may choose, without loss of generality, $\beta_n = 1, \forall n$.

As a consequence of this result, $E_n^{(i)} = E_n^{(ii)}, \forall n$ in the SB phase (if this were not the case, $\hat{\Pi}$ would not be a constant of motion). Then, as $E_n^{(i)}\rangle$ can be always written as a linear combination of eigenstates of $\hat{M}$ with positive eigenvalues and the opposite holds for $E_n^{(ii)}\rangle$, we obtain

$$\hat{\mathcal{C}} \ E_n^{(i)}\rangle = E_n^{(i)}\rangle \tag{112}$$

$$\hat{\mathcal{C}} \ E_n^{(ii)}\rangle = - E_n^{(ii)}\rangle \tag{113}$$

$\forall n$. Hence, all the eigenspaces giving rise to the SB phase share the same properties for $\hat{\mathcal{C}}$ and $\hat{\Pi}$, and therefore we can calculate the properties of $\hat{\mathcal{K}}$ in a single

eigenspace without loss of generality. The action of this operator on $\left| E_n^{(i)} \right\rangle$ and $\left| E_n^{(ii)} \right\rangle$ is.

$$\begin{aligned} \hat{\mathcal{K}} \left| E_n^{(i)} \right\rangle &= \frac{i}{2}\hat{\mathcal{C}}\hat{\Pi} \left| E_n^{(i)} \right\rangle - \frac{i}{2}\hat{\Pi}\hat{\mathcal{C}} \left| E_n^{(i)} \right\rangle \\ &= \frac{i}{2}\hat{\mathcal{C}} \left| E_n^{(ii)} \right\rangle - \frac{i}{2}\hat{\Pi} \left| E_n^{(i)} \right\rangle = -i \left| E_n^{(ii)} \right\rangle \end{aligned} \tag{114}$$

$$\begin{aligned} \hat{\mathcal{K}} \left| E_n^{(ii)} \right\rangle &= \frac{i}{2}\hat{\mathcal{C}}\hat{\Pi} \left| E_n^{(ii)} \right\rangle - \frac{i}{2}\hat{\Pi}\hat{\mathcal{C}} \left| E_n^{(ii)} \right\rangle \\ &= \frac{i}{2}\hat{\mathcal{C}} \left| E_n^{(i)} \right\rangle + \frac{i}{2}\hat{\Pi} \left| E_n^{(ii)} \right\rangle = i \left| E_n^{(i)} \right\rangle \end{aligned} \tag{115}$$

Thus, in the eigenbasis $\left\{ \left| E_n^{(i)} \right\rangle, \left| E_n^{(ii)} \right\rangle \right\}$, we get

$$\hat{\mathcal{C}} = \begin{pmatrix} 1 & 0 \\ 0 & -1 \end{pmatrix}, \; \hat{\mathcal{K}} = \begin{pmatrix} 0 & i \\ -i & 0 \end{pmatrix}, \; \hat{\Pi} = \begin{pmatrix} 0 & 1 \\ 1 & 0 \end{pmatrix} \tag{116}$$

Therefore $\{\hat{\mathcal{C}}, \hat{\mathcal{K}}, \hat{\Pi}$ satisfy the SU(2) commutation rules. If we demote $\hat{\mathcal{C}} \equiv \hat{X}_1$, $\hat{\mathcal{K}} \equiv \hat{X}_2$, and $\hat{\Pi} \equiv \hat{X}_3$, then $\left[\hat{X}_i, \hat{X}_j\right] = i\varepsilon_{ijk}\hat{\sigma}_k$, where ε_{ijk} is the Levi-Civita symbol.

Backward implication.- This is again trivial. If $\{\hat{\mathcal{C}}, \hat{\mathcal{K}}, \hat{\Pi}$ are constants of motion and satisfy the SU(2) commutation rules in a given eigenspace, then there exist two orthogonal equilibrium states (one spanned by $\left| E_n^{(i)} \right\rangle$ and the other one spanned by $\left| E_n^{(ii)} \right\rangle$) which are transformed by $\hat{\Pi}$ according to (H2). And this is immediately generalized for a larger SB phase composed by several eigenspaces. ■

An important remark is in order. In this proof, we have not considered the possibility that the order parameter $\hat{M}$ may have a zero eigenvalue. The reason is that (H2) together with (M1) and (M2) imply that the projection of all the eigenstates in $\mathcal{B}_i$ and $\mathcal{B}_{ii}$ over the subspace spanned by the eigenstates of $\hat{M}$ with zero eigenvalue must be equal to zero. Indeed, were this not the case, observe that (M1) establishes that $\hat{\Pi} \left| m_n = 0 \right\rangle = \left| m_n = 0 \right\rangle$, so the support of $\hat{\Pi}\hat{\rho}_{\text{eq}}^{(i)}\hat{\Pi}^\dagger$ could not be orthogonal to the support of $\hat{\rho}_{\text{eq}}^{(i)}$.

In practical terms, if the order parameter $\hat{M}$ has at least a zero eigenvalue, we can redefine $\hat{\mathcal{C}} = \text{sign}^*(\hat{M})$, with the modified signum function given by

$$\text{sign}^*(x) = \begin{cases} 1 & \text{if } x > 0, \\ -1 & \text{if } x < 0, \\ 0 & \text{if } x = 0. \end{cases} \tag{117}$$

This modification has no impact on the Theorems proved in this section, so we will write $\hat{\mathcal{C}}$ irrespective of whether $\hat{M}$ possesses a zero eigenvalue or not.

A direct consequence of Theorem 1, which we will not prove explicitly as it follows trivially from Proof 1, is the following:

Corollary 1.– $\langle\hat{\mathcal{C}}\rangle = 1$ if and only if the state equilibrates at $\hat{\rho}_{\text{eq}}^{(i)}$ (and similarly for $\langle\hat{\mathcal{C}}\rangle = -1$ and $\hat{\rho}_{\text{eq}}^{(ii)}$).

Theorem 1 provides a solid link between $\hat{\mathcal{C}}$ and the two different equilibrium states characterizing a SB phase. Yet, the consequences of Theorem 1 go far beyond this seemingly strictly mathematical result, as demonstrated by the second main result of this section.

3.2.3 Second result

Let us consider the following hypothesis:

H3.– Let $\hat{\rho} = \frac{1}{Z}e^{-\beta\hat{H}}$ denote a canonical density matrix. Then, the quantum fluctuations, σ_E, around the average energy, $\langle E\rangle_\rho = \text{Tr}[\hat{\rho}\hat{H}]$, vanish in the thermodynamic limit, $\left(\frac{\sigma_E}{\langle E\rangle}\right)_\rho \to 0$ as $N \to \infty$ (as typically fulfilled in realistic systems).

In conjunction with our previous result, this hypothesis allows us to prove the second main result of this section:

Theorem 2.– *If a physical system satisfies (H1)-(H3), then the density matrix*

$$\hat{\rho}_{\text{NATS}} = \frac{1}{Z}e^{-\beta\hat{H}-\lambda_c\hat{\mathcal{C}}-\lambda_k\hat{\mathcal{K}}-\lambda_\pi\hat{\Pi}\hat{\Pi}}, \tag{118}$$

where Z ensures that $\text{Tr}[\hat{\rho}_{\text{NATS}}] = 1$, $\beta = (kT)^{-1}$, and k is the Boltzmann constant, is an equilibrium state for $T < T_c$.

This theorem can be proved as follows:

Proof 2.– Within each subspace of the symmetry-breaking phase, $\mathcal{H}_{SB} = \mathcal{H}_i \oplus \mathcal{H}_{ii}$, spanned by the eigenvectors $\left\{ E_n^{(i)}\right\rangle \left(E_n^{(ii)}\right\rangle\}$ (with $E_n^{(i)} = E_n^{(ii)} = E_n$, the operators $\hat{\mathcal{C}}$, $\hat{\mathcal{K}}$ and $\hat{\Pi}\hat{\Pi}$ take the matrix forms given in Eq. (116). Therefore, in the Hamiltonian subspace with support in the above basis, the combination $\hat{R} = \beta\hat{H} + \beta_c\hat{\mathcal{C}} + \beta_k\hat{\mathcal{K}} + \beta_\pi\hat{\Pi}\hat{\Pi}$ is a block diagonal matrix of 2×2 matrices. For an n-dimensional SB phase, this is

$$\hat{R}_{SB} = \text{diag}\{\hat{R}_n\}_n, \quad \hat{R}_n = \begin{pmatrix} \beta E_n + \beta_c & \beta_\pi + i\beta_k \\ \beta_\pi - i\beta_k & \beta E_n - \beta_c \end{pmatrix}. \tag{119}$$

In the symmetry-restored or disordered phase, $\mathcal{H}_D = \mathcal{H}_{iii}$, above the critical temperature, the precise form of $\hat{R}_D$ is unknown. In the total Hilbert space $\mathcal{H}$,

$$\hat{R} = \begin{pmatrix} \hat{R}_{SB} & 0 \\ 0 & \hat{R}_D \end{pmatrix}, \tag{120}$$

where $\hat{R}_{SB}$ is a matrix of order $\dim(\mathcal{H}_{SB})$ and $\hat{R}_D$ is a matrix of order $\dim(\mathcal{H}_D)$. The exponential matrix of $\hat{R}$ must necessarily have the same structure. Therefore, we can build the following matrix

$$\hat{D} = \frac{e^{\hat{R}}}{Z} \equiv \frac{1}{Z} \begin{pmatrix} \hat{T}_{SB} & 0 \\ 0 & \hat{T}_D \end{pmatrix}, \tag{121}$$

where $Z = \mathrm{Tr}[e^{\hat{R}}]$ is a normalization constant. As $\hat{R}$ is Hermitian, $\hat{D}$ is a positive-definite matrix with $\mathrm{Tr}[\hat{D}] = 1$, due to the normalization constant Z. Therefore, it is a density matrix, and all its eigenvalues are $d_n > 0$.

Let us assume now that the canonical and microcanonical ensemble are equivalent, so that $\sigma_E/E \to 0$ in the TL, as stated in hypothesis (H3). This means that if $\beta > \beta_c$ ($T < T_c$), the probability of populating a state beyond E_c becomes zero in the TL, and therefore, $\mathrm{Tr}\ \hat{T}_D \to 0$ in the TL. Furthermore since $\hat{D}$ is definite positive, all eigenvalues of $\hat{T}_D$ must remain positive for any finite system size, becoming zero in the TL. And, because $\hat{D} = \hat{D}^\dagger$, this further implies that $\hat{T}_D \to 0$, and that $\mathrm{Tr}\ \hat{T}_{SB} \to 1$ in the TL. Finally, as $\hat{T}_{SB}$ is a block diagonal matrix composed of 2×2 matrices, and for $E < E_c$ the eigenvalues of opposite parity become degenerate in the TL, this means that $[\hat{H}, \hat{D}] \to 0$ in the TL. ■

As a technical note, for the last part of the proof to hold, the symmetry-breaking subspace $\mathcal{H}_{SB}$ needs to be spanned by all the eigenstates below the critical energy. Otherwise, there is the possibility that some eigenstates that belong to the symmetric subspace may be populated at particular values of $T < T_c$, and thus it is not possible to guarantee that $\hat{T}_D \to 0$ in the TL. For this reason, this requirement has been included in (H2).

The density matrix in (118) is formally a non-Abelian thermal state (NATS) [440], composed by a set of non-commuting charges [428], [441]–[443]. Yet, these charges are substantially different from those typically employed in the construction of a GGE [130]–[132] or a NATS; in particular, because they are not locally additive quantities. Despite this, they are necessary to describe the behavior of usual locally additive quantities, as we illustrate below. In (118), β stands for the temperature, and λ_c, λ_k and λ_π denote the values of $\langle\hat{\mathcal{C}}\rangle$, $\langle\hat{\mathcal{K}}\rangle$ and $\langle\hat{\Pi}\rangle$. On the one hand, $\hat{\mathcal{C}}$ measures the probability of observing positive and negative values of the order parameter, and therefore its value can be determined through the measurement of $\hat{M}$. On the other hand, $\hat{\Pi}$ and $\hat{\mathcal{K}}$ do not have a tangible classical interpretation; rather, these operators are linked to quantum coherence between the two eigenspaces of $\hat{\mathcal{C}}$. In the case of the TFIM, the parity $\hat{\Pi}$ is related to an interference pattern in the transverse field, $\hat{J}_z$: if $\langle\hat{\Pi}\rangle = 1$, the population of the eigenstates of $\hat{J}_z$ with odd eigenvalues is zero, while the opposite happens if $\langle\hat{\Pi}\rangle = -1$. Lastly, the operator $\hat{\mathcal{K}}$

is also linked to quantum interference effects on the magnetization along different directions, though we have not been able to find a simple interpretation for it.

From Theorem 2 it follows that *a quantum system displays discrete $\mathbb{Z}_2$ SSB if and only if it can equilibrate at any of the possibilities given by* (118). Further, it allows us to formulate a complete classification of symmetry-breaking equilibrium states in the ordered phase:

ES1.– *Regular symmetry-breaking states.* Given the properties of the order parameter and the operators $\hat{\mathcal{C}}$, $\hat{\mathcal{K}}$ and $\hat{\Pi}$, the usual symmetry-breaking states, giving rise to $\hat{\rho}_{\rm eq}^{(i)}$ and $\hat{\rho}_{\rm eq}^{(ii)}$ in hypothesis (H2), are characterized by $\langle\hat{\mathcal{C}}\rangle = \pm 1$, and $\langle\hat{\mathcal{K}}\rangle = \langle\hat{\Pi}\rangle = 0$. Therefore, they are recovered if $\lambda_k = \lambda_\pi = 0$ and $\lambda_c \to \pm\infty$.

ES2.– *Mixture of standard symmetry-breaking states.* If $\lambda_k = \lambda_\pi = 0$ but $|\lambda_c| < \infty$, Eq. (118) allows for a statistical mixture of the two types of regular symmetry-breaking equilibrium states from ES1. The relative weights of $\hat{\rho}_{\rm eq}^{(i)}$ and $\hat{\rho}_{\rm eq}^{(ii)}$ in the mixture are determined by the value of the λ_c multiplier. In this case there is no quantum coherence between these branches.

ES3.– *Superpositions of regular symmetry-breaking states.* Finally, if $\lambda_k \neq 0$ and/or $\lambda_\pi \neq 0$, then the equilibrium state in (118) is a superposition of states with $\langle\hat{\mathcal{C}}\rangle = 1$ and $\langle\hat{\mathcal{C}}\rangle = -1$. Because $\hat{\mathcal{K}}$ and $\hat{\Pi}$ are conserved in the ordered phase, so is the quantum coherence between the states building up this superposition. In particular, if $\langle\hat{\mathcal{C}} + \hat{\mathcal{K}} + \hat{\Pi}\rangle = 1$, then the NATS (118) consist in a mixture of states with the same relative phase between the $\langle\hat{\mathcal{C}}\rangle = 1$ and the $\langle\hat{\mathcal{C}}\rangle = -1$ sectors.

For $T > T_c$, neither $\hat{\mathcal{C}}$ nor $\hat{\mathcal{K}}$ are conserved operators. Therefore, equilibrium states are described by (118) only if $\lambda_c = \lambda_k = 0$. Another possibility is that a symmetry-breaking term is added to the Hamiltonian. As a consequence, $\hat{\Pi}$ is not conserved, and the only relevant constant of motion is $\hat{\mathcal{C}}$. This last case is considered in detail in Sec. 3.2.6 below.

From the discussion above it follows that in order to determine the equilibrium state that the system will reach, the initial values of the operators $\hat{\Pi}$, $\hat{\mathcal{C}}$ and $\hat{\mathcal{K}}$ are necessary (see below for an explicit numerical example). To be specific, if the system is prepared in an initial state $|\Psi(0)\rangle$ in the symmetry-broken phase ($E < E_c$), the final equilibrium state, described by the density matrix $\hat{\rho}_{\rm eq}$, fulfills the relations

$$\mathrm{Tr}[\hat{\rho}_{\rm eq}\hat{H}] = \langle\Psi(0)|\,\hat{H}\,|\Psi(0)\rangle\,, \tag{122a}$$

$$\mathrm{Tr}[\hat{\rho}_{\rm eq}\hat{\mathcal{C}}] = \langle\Psi(0)|\,\hat{\mathcal{C}}\,|\Psi(0)\rangle\,, \tag{122b}$$

$$\mathrm{Tr}[\hat{\rho}_{\rm eq}\hat{\mathcal{K}}] = \langle\Psi(0)|\,\hat{\mathcal{K}}\,|\Psi(0)\rangle\,, \tag{122c}$$

$$\mathrm{Tr}[\hat{\rho}_{\rm eq}\hat{\Pi}] = \langle\Psi(0)|\,\hat{\Pi}\,|\Psi(0)\rangle\,, \tag{122d}$$

reflecting the fact that the probabilities of observing any of the possible values of these four observables are conserved throughout the entire time evolution. Therefore, the inverse temperature, β, and the multipliers λ_c, λ_k, and λ_π depend *only* on the initial configuration of the system. The NATS (118) can thus be interpreted as the equilibrium state maximizing the entropy $S(\hat{\rho}) = -\text{Tr}[\hat{\rho}\log\hat{\rho}]$ conditioned by the restrictions in (122): this equilibrium state only contains the information encapsulated in this set of equations (this idea was originally devised by Jaynes [444]). We emphasize that the multipliers $\{\lambda_c, \lambda_k, \lambda_\pi\}$ are therefore not obtained through any kind of fitting method.

To fix ideas, the main highlights of our theory can be summarized in the following three points:

(A) Within a single two-dimensional subspace of degenerate states it possible to define three operators that act as constants of motion. Within a single subspace, they take the SU(2) structure presented in (116). Importantly, these operators are the same for all eigenspaces of degenerate states. This makes it possible to find macroscopic superpositions without any kind of fine tuning.

(B) In every $\mathbb{Z}_2$ symmetry-breaking phase, these SU(2) operators can be constructed from (i) the order parameter, $\hat{M}$, and (ii) the global $\mathbb{Z}_2$ symmetry of the Hamiltonian. Therefore,

(C) The NATS equilibrium state (118) is a *universal* equilibrium ensemble.

The existence of *coherent superpositions* of branches of the order parameter ($\langle\hat{M}\rangle > 0$ and $\langle\hat{M}\rangle < 0$) is an important physical byproduct of our results.

What about finite-size systems, where (H2) is not exactly fulfilled? As mentioned before, this form of emergent symmetry-breaking, of which the eigenlevel degeneracy is a consequence, is only strictly realized in the $N \to \infty$ limit. What are the typical times of constancy of $\hat{\rho}_{\text{NATS}}$, i.e., up to what times can we consider it to be an stationary state? This form of $\mathbb{Z}_2$ symmetry-breaking entails exponential closure of the gap of quasi-degenerate levels of opposite parity. This is not the case for systems with continuous symmetry-breaking, where the gap typically closes as a power-law instead [423], [445]. Let us assume that $|E_{n,+} - E_{n,-}| \propto e^{-\nu N}$, where $\nu \equiv \nu(E/N)$ is a coefficient that depends on the energy per particle of the pair of eigenlevels involved. We can assume that ν does not vary significantly in a small window around the macroscopic energy E/N. Now, let us evaluate the expectation value of the $\hat{\mathcal{C}}$ operator in the eigenspace $\{|E_{n,+}\rangle, |E_{n,-}\rangle\}$. Consider the state $|\varphi\rangle = (|E_{n,+}\rangle + |E_{n,-}\rangle)/\sqrt{2}$. Then,

$$\langle\varphi(t)|\,\hat{\mathcal{C}}\,|\varphi(t)\rangle = \cos(\Delta E t), \tag{123}$$

where $\Delta E = E_{n,+} - E_{n,-}$ [note that the diagonal elements of $\hat{\mathcal{C}}$ vanish in states of the same parity]. The period of this oscillatory term is clearly $\tau = 2\pi/\Delta E$, which

is exponentially large in N, $\tau \propto e^{\nu N}$. To be more specific, let us calculate the time such that $\langle \hat{\mathcal{C}}(t) \rangle$ deviates only slightly from its initial value, $\langle \hat{\mathcal{C}}(t) \rangle < \langle \hat{\mathcal{C}}(t = 0) \rangle - \varepsilon = 1 - \varepsilon$, where $\varepsilon > 0$ can be infinitesimally small. Upon Taylor expansion of (123), we get $1 - \frac{\Delta E^2 t^2}{2} < 1 - \varepsilon$, i.e.,

$$t > \frac{\sqrt{2\varepsilon}}{|\Delta E|} \propto \sqrt{\varepsilon} e^{\nu N}, \tag{124}$$

which is, too, exponentially large in N. As a consequence, the time of constancy of the NATS state (118) is so long even in finite-size systems that we can safely assume that for most experimentally (and also numerically!) accessible times the state is stationary. A numerical evaluation of this prethermalization time scaling with N is presented later on, in Fig. 12(d) of Sec. 3.2.6. We do not intend to anticipate the results of that section, but let us briefly mention that for the TFIM (97) with only $N = 28$ particles, the prethermalization time for $\varepsilon = 10^{-3}$ is $t \approx 10^{17}$ s, which is already basically the age of the Universe! In passing that we have performed this analysis in a single energy subspace for simplicity; yet, since the exponent $\nu(E/N)$ varies smoothly with the macroscopic energy, any state sufficiently narrow in energy, such as the NATS (118), can be characterized by approximately the same ν. Therefore, these results essentially remain unchanged if one considers more than a single energy subspace.

Let us end this discussion with a technical note. In order to prove Theorem 2, which establishes that the NATS density matrix (118) is an equilibrium state for $T < T_c$, we have made use of hypothesis (H3). Therefore, for the NATS to be an equilibrium state in the infinite-size limit, it is imperative that the energy fluctuations vanish as $N \to \infty$. This requirement can be fulfilled only in systems whose level density increases fast enough with energy. For this reason, in the case of fully-connected systems, we expect (118) not to behave as an equilibrium state even for very large system sizes. Another serious drawback to using (118) to describe the equilibrium values of observables in fully-connected systems is that in these models the microcanonical and canonical descriptions do *not* coincide (see, e.g., [297]–[300] for explicit illustrations in systems with ESQPTs). Since in this thesis we are interested in closed quantum systems, a microcanonical version of (118), particularly useful in the context of collective systems, will be developed later on, in Sec. 3.3.2.

A note on equilibration

We find it interesting to provide a simple example illustrating the extent to which the operators in (101) of Theorem 1 play a role in the determination of the possible equilibrium states of a system. For this numerical illustration we prefer to make

use of the LMG model, defined in (73), because it allows us to perform a large system-size calculation. We recall that this model can be seen as a special case of the TFIM in (97) when $\alpha \to 0$ (infinite-range interactions), which we will consider in the next parts of this section. For the LMG model (73), the total collective magnetization along the x-axis plays the role of the order parameter, $\hat{M} = \hat{J}_x = \frac{1}{2}\sum_i \hat{\sigma}_i^x$.

We have prepared three different initial states as superpositions of the nearly exactly degenerate finite-N LMG model with $\lambda = 1$ and certain h_i. These initial states are taken out of equilibrium through a quantum quench $h_i \to h_f$. The three procedures are as follows:

Procedure 1.– At $h_i = 0$, we prepare the initial state

$$|\Psi_1(0)\rangle = \frac{1}{\sqrt{2}}[|E_{0+}(h=0)\rangle + |E_{0-}(h=0)\rangle], \tag{125}$$

and perform a quench $h_i = 0 \to h_f = 0.4$.

Procedure 2.– At $h_i = 0.8$, we prepare the initial state

$$|\Psi_1(0)\rangle = \frac{1}{\sqrt{2}}[|E_{0+}(h=0.8)\rangle + |E_{0-}(h=0.8)\rangle], \tag{126}$$

and perform a quench $h_i = 0.8 \to h_f = 0.4$.

Procedure 3.– At $h_i = 0$, we prepare the initial state

$$|\Psi_1(0)\rangle = \sqrt{p}\,|E_{0+}(h=0)\rangle + \sqrt{1-p}\,|E_{0-}(h=0)\rangle\,, \tag{127}$$

with $p = 0.902$, and perform a quench $h_i = 0 \to h_f = 0.4$.

We have measured the average energy of these initial states in the corresponding final Hamiltonian, the expectation value of $\langle\hat{\mathcal{C}}\rangle$, and the initial and the equilibrium expectation values of the order parameter. These results are summarized in Table 2. The system size is $N = 3200$, and $j = N/2$.

First of all, we can clearly observe that for all procedures the quench essentially populates final Hamiltonian eigenstates with the same energy, $\langle E\rangle/j = -0.5$. Since in all cases $h_f = 0.4$ and in the LMG model the symmetry-breaking phase is located for energy values $E/j < -h$ when $h < \lambda$ [see discussion around (73)], it is clear that all of these states end up in the $\mathbb{Z}_2$ symmetry-breaking phase, below the ESQPT. In fact, all of them are also prepared in an initial symmetry-breaking phase, for the same arguments. Therefore, we can expect the results of our theory of conserved charges to be applicable to all of these non-equilibrium processes. The expectation value of the $\hat{\mathcal{C}}$ operator, calculated as $\hat{\mathcal{C}} = \text{sign}(\hat{J}_x)$ (see Sec. 3.1), is equal to 1 for procedures 1 and 2 and 0.6 for procedure 3. This value remains constant in the initial and final Hamiltonian. We have computed the value of the

Procedure	$\langle E\rangle/j$	$\langle\hat{\mathcal{C}}\rangle$	$\langle\hat{M}(0)\rangle$	$\langle\hat{M}\rangle_{\rm eq}$
1	-0.5	1	1600	1258.92
2	-0.5	1	959	1258.92
3	-0.5	0.6	959	754.56

Table 2: Expectation values of several quantities for procedures 1-3, with initial states defined in Eqs. (125,127,126). Average energy of the initial state in the final Hamiltonian, $\langle E\rangle/j$, value of $\hat{\mathcal{C}}$, value of $\hat{M}$ in the initial state and its equilibrium value in the final Hamiltonian.

order parameter in the initial states, $\langle\hat{M}(0)\rangle$, as well as its equilibrium value in the final Hamiltonian, computed according to Eq. (96).

These results allow us to conclude that the initial value of the order parameter does *not* determine the final equilibrium value of the initial state after a quench. In other words, that the equilibrium state is *not* a function of $\langle\hat{M}(0)\rangle$. Indeed, even though procedures 2 and 3 have the same initial $\langle\hat{M}(0)\rangle$, the value of the magnetization in their equilibrium states is different. Thus, $\hat{M}$ alone is insufficient to predict what the final equilibrium value will be. However, initial states characterized by the same value of $\hat{\mathcal{C}}$ do evolve towards the same equilibrium state, even if their initial magnetization values are different! This is exemplified by the results of procedures 1 and 2. In summary, the value of $\hat{\mathcal{C}}$ is necessary to determine the final equilibrium value.

3.2.4 Numerical realization of equilibrium states

According to our general theory and, in particular, the results of the NATS in Sec. 3.2.3, in a $\mathbb{Z}_2$ symmetry-breaking phase it is possible to find three kinds of qualitatively different equilibrium states, dubbed ES1, ES2 and ES3. In this section, we again make use to the fully-connected LMG model (73) to numerically build these states and consider finite-size scaling analyses. As before, we work with the maximally symmetric sector, with $j = N/2$.

In order to construct the corresponding equilibrium states, here we propose three quantum protocols taking an initial wave function to the symmetry-broken phase of the model (i.e., below the ESQPT critical energy, $E < E_c$). In all of these processes, $\lambda = 1$ and h is varied as indicated below. To identify the class of symmetry-breaking equilibrium state resulting from each process, we monitor the behavior of the distribution of the collective magnetization along the x- and

$z-$axes. The former is related to the information contained in $\hat{\mathcal{C}}$, while the latter is useful to measure the quantum correlations between magnetization branches, thus allowing us to determine whether we are dealing with a quantum superposition with coherence (ES3) or just a mixture of regular symmetry-breaking states (ES2).

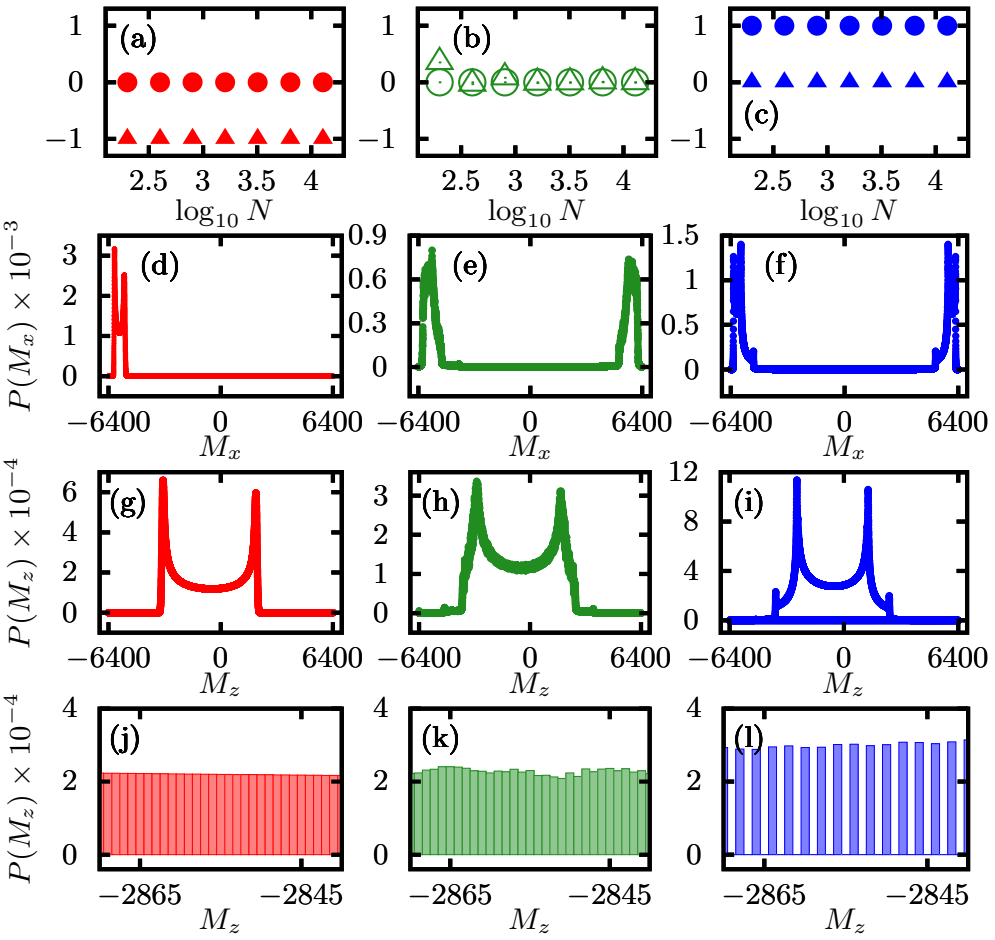

Figure 10: Signatures of the symmetry-breaking equilibrium states ES1, ES2 and ES3. Results for ES1 are shown in the left column, those for ES2 are shown in the middle column, and those for ES3 in the right column. For all three protocols (see main text), we compute the distribution of the eigenvalues of the collective magnetization along the x-axis, $\hat{M}_x = \hat{J}_x$, and z-axis, $\hat{M}_z = \hat{J}_z$. The time evolution takes place in the LMG model (73) with $j = N/2$. System size is $j = 6400$ except in panels where the finite-size scaling behavior is considered. In (a),(b),(c), triangles correspond to the expectation value of $\hat{\mathcal{C}}$, while circles correspond to $\hat{\Pi}$.

Protocol 1.– We start with a fully polarized initial state in the x-direction, $|\Psi(0)\rangle = |\downarrow\downarrow\cdots\downarrow\rangle_x$, with an initial transverse magnetic field $h = 0.4$ that is linearly decreased as $h = 0.4 - 0.3t/\tau$, with $t \in [0, \tau]$ and $\tau = 40$ ms (to make contact with experiments, our timescales coincide with those in [446]).

In this protocol, the time-evolving state is always in the symmetry-breaking phase ($E < E_c$). Because our chosen initial condition has $\langle \hat{\mathcal{C}} \rangle = -1$, the final equilibrium state belongs to class ES1. This is clearly shown in the left column of Fig. 10. The distribution $P(M_x)$ of the eigenvalues of the operator $\hat{M}_x = \sum_i \hat{\sigma}_i^x$, with $j = 6400$, shown in Fig. 10(d), is clearly peaked close to its minimal value, $M_x \approx -j$, indicating a high degree of polarization in the x-direction (note also that the probability $P(M_x > 0) = 0$). The distribution of the eigenvalues of $\hat{m}_z = \sum_i \hat{\sigma}_i^z$ is depicted in Fig. 10(g),(j). Although in this case it does not offer any significant information as only one of the magnetization branches is populated, we will see below that in general it does contain the signatures of the quantum coherence between magnetization branches. Finally, a finite-size scaling of the value of $\hat{\mathcal{C}}$ (triangles) and $\hat{\Pi}$ (circles) is shown in Fig. 10(a). It is worth noting that these values remain constant for all values of the number of particles N considered, suggesting that the ES1 states are robust and that the situation should not change in the TL.

Protocol 2.– We start with the same initial condition as in Protocol 1, with the same initial value of the transverse field, $h = 0.4$. Then, we linearly increase its value as $h = 0.4 + 0.8t/\tau$, with $t \in [0, \tau]$ and $\tau = 40$ ms. We let the system relax at the Hamiltonian with $h = 1.2$ during $\tau = 500$ ms. Lastly, we linearly decrease the transverse field until it reaches a value $h = 0.1$ through the ramp $h = 1.2 - 1.1t/\tau$, with $t \in [0, \tau]$ and $\tau = 40$ ms.

In this protocol, the system spends a significant amount of time normal phase of the LMG model and ends up in the symmetry-breaking phase. For this reason, the initial value of $\hat{\mathcal{C}}$ is expected to be erased by dephasing (see [29], [332] and Sec. 3.3.2 below for a detailed explanation of this mechanism). Thus, the final equilibrium state is expected to belong to class ES2, with $\langle \hat{\mathcal{C}} \rangle$, $\langle \hat{\mathcal{K}} \rangle$ and $\langle \hat{\Pi} \rangle$ roughly equal to zero as we are dealing with a regular mixture of symmetry-breaking equilibrium states. This picture is corroborated by the results shown in the middle column of Fig. 10. The distribution of $\hat{M}_x$ in Fig. 10(e) illustrates a clear bimodal distribution peaked at its edges, $M_x \approx -j$ and $+j$. This state exhibits no quantum coherence between magnetization branches as depicted in Fig. 10(h),(k) for the $\hat{M}_z$ operator [this result is similar to that in Fig. 10(g),(j)]. For this reason, this is not an ES3 state, but ES2. Finally, the scaling of the value of $\hat{\mathcal{C}}$ and $\hat{\Pi}$ in Fig. 10(b) show a clear constant behavior with N.

Protocol 3.– We start with a fully polarized initial state in the z-direction, $|\Psi(0)\rangle = |\uparrow\uparrow\cdots\uparrow\rangle_z$, with $h = 1.2$, and then linearly decrease the transverse field, $h = 1.2 - 1.1t/\tau$, with $t \in [0, \tau]$ and $\tau = 40$ ms.

In this last protocol, the initial state lays within the normal phase, has $\langle \hat{\Pi} \rangle = 1$ and coincides very approximately with the ground-state of the LMG Hamiltonian

with $h = 1.1$. Then, the time-dependent protocol makes it enter the symmetry-breaking phase of the LMG model. The state then undergoes a number of non-adiabatic transitions as a consequence of the crossing of the QPT at $h = 1$. Finally, as $\hat{\Pi}$ is an exact constant of motion for all values of h, the system ends in the symmetry-breaking phase with some energy excess, $\langle\hat{\Pi}\rangle = 1$ and $\langle\hat{\mathcal{C}}\rangle = \langle\hat{\mathcal{K}}\rangle = 0$. The result is an ES3 symmetry-breaking equilibrium state. The corresponding numerical results are shown in the right column of Fig. 10. The distribution of $\hat{M}_x$, in Fig. 10(f), is similar to that in Fig. 10(e) of Protocol 2, but the distribution of $\hat{M}_z$, in Fig. 10(i),(l), is completely different: in this case, it evidences the existence of quantum coherence between the magnetization branches: there are 'gaps' in the distribution $P(M_z)$ for certain M_z, ensuing from the interference pattern. In particular, we find that $P(M_z) = 0$ for odd values of M_z. Finally, the scaling of $\hat{\mathcal{C}}$ in Fig. 10(c) shows constant behavior for all N considered. This suggests that it is possible to construct equilibrium macroscopic superpositions, as the scaling to the TL seems completely stable.

3.2.5 Implementation in cold atom platforms

Here we propose an experimental protocol to prepare equilibrium states falling into the category ES3, i.e., equilibrium states with coherent superpositions of different branches of the order parameter. The special feature of this protocol, and its difference with those presented in Sec. 3.2.4, is that it will allow us to select the relative between the $\hat{\mathcal{C}}$ sectors. Our proposal is based on quantum technologies state-of-the-art techniques. The choice of the model Hamiltonian (97) is based precisely on its experimental versatility and accessibility. The protocol consists of the following steps:

S1.- Start from a fully polarized state in the x-direction, $|\uparrow\uparrow\cdots\uparrow\uparrow\rangle_x$ or $|\downarrow\downarrow\cdots\downarrow\downarrow\rangle_x$ with $h = 0$.

S2.- Activate an adiabatic ramp to slowly increase the transverse field from $h = 0$ to $h = h_1 = 1.2$ kHz $> h_c$.

S3.- Let the system relax at h_1 during a controlled time, τ_R.

S4.- Activate a second adiabatic ramp to slowly decrease the transverse field from $h = h_1$ to $h = h_2 = 0.5$ kHz $< h_c$.

S5.- Quench the system from $h = h_2$ to $h = h_3 = 0.1$ kHz $< h_2$.

The initial state is a symmetry-breaking ground-state of (97) with $h = 0$ and $\langle\hat{\Pi}\rangle = 0$; thus, the unitary time evolution only introduces an irrelevant global phase until $h = h_c$, provided that step S2 is basically adiabatic, i.e., it is performed slowly enough. Then, as parity remains conserved when crossing h_c, both the

ground-state ($\langle\hat{\Pi}\rangle = 1$), $|E_{0,+}\rangle$, and the first excited state ($\langle\hat{\Pi}\rangle = -1$), $|E_{0,-}\rangle$, become equally populated. Hence, as S4 induces basically the same changes that S2 in the time-evolved wave function, the system is in a superposition of the lowest-energy eigenstates of $\hat{H}(h_2)$,

$$|\Psi\rangle = \sqrt{p}\,|E_{0,+}\rangle + e^{i\phi}\sqrt{1-p}\,|E_{0,-}\rangle\,, \tag{128}$$

with $p = 1/2$ and an uncontrolled phase $\phi = \phi_q$ just before S5, if S3 is not performed. In the TL, (148) is stationary when $h < h_c$, because $E_{0,+} = E_{0,-}$.

As a consequence of step S3, an extra *controlled* phase, ϕ_R, is introduced in the state after S4. In terms of the gap $\Delta E_0 = |E_{0,+} - E_{0,-}|$, at $\hat{H}(h_1)$, this phase reads $\phi_R = \Delta E_0\,\tau_R$, so *a complete 2π-period in the final phase $\phi = \phi_q + \phi_R$ can be explored by considering $0 \leq \tau_R < 2\pi/\Delta E_0$*. Finally, the effect of S5 is to heat up the system. If the final temperature is $T < T_c$, then $\langle\hat{\mathcal{C}}\rangle_\Psi = 2\sqrt{p(1-p)}\cos\phi$, and $\langle\hat{\mathcal{K}}\rangle_\Psi = 2\sqrt{p(1-p)}\sin\phi$ remain constant and only depend on the controllable phase. Therefore, by tuning τ_R appropriately, this protocol allows us to prepare initial states with controlled values of $\langle\hat{\mathcal{C}}\rangle$ and $\langle\hat{\mathcal{K}}\rangle$. As for the parity operator, $\langle\hat{\Pi}\rangle_\Psi = 2p - 1$, and thus $\langle\hat{\Pi}\rangle = 0$.

Our proposed protocol has one main drawback, though: the state evolving in time crosses a QPT critical point twice. The uncontrolled excitations that this process may induce have been studied, e.g., in [447]–[449]; among other things, these excitations can destabilize the dynamics. In order to assess their importance for our protocol in practical terms, we recall that the QPT of the TFIM is in the universality class of its fully-connected counterpart when $\alpha < 5/3$ [450]. Compared to the finite-range TFIM (97), the fully-connected model has the advantage that it allows for exact diagonalization of very large spin chains, which is convenient to estimate the relevance of the QPT-induced excitations.

In Fig. 11(a) we represent $\langle\hat{\mathcal{C}}\rangle$ and $\langle\hat{\mathcal{K}}\rangle$ for two values of the driving time after the step S4, following an adiabatic ramp given by $h(t) = t/\tau_q$. These observables are represented as a function of the relaxation time, τ_R, that the state spends in the intermediate Hamiltonian, $\hat{H}(h_1)$. If the driving is slow enough, $\tau_q = 40.96$ ms (following the timescales of the experimental realization in [446]), periodic oscillations are found in both observables; here, the theoretical behavior for a 2π-period in the relative phase ϕ is represented by solid curves. However, if the driving is fast, $\tau_q = 0.9$ ms, the oscillatory pattern is lost. We note that in order to recover the 2π-periodic behavior in larger systems we need longer times [451]; a similar protocol, crossing the QPT once through an exponential ramp, has been reported in [446], [452]–[454].

Having considered these preliminary results, now let us imagine that we have successfully performed this preparation procedure with the long-range (finite-

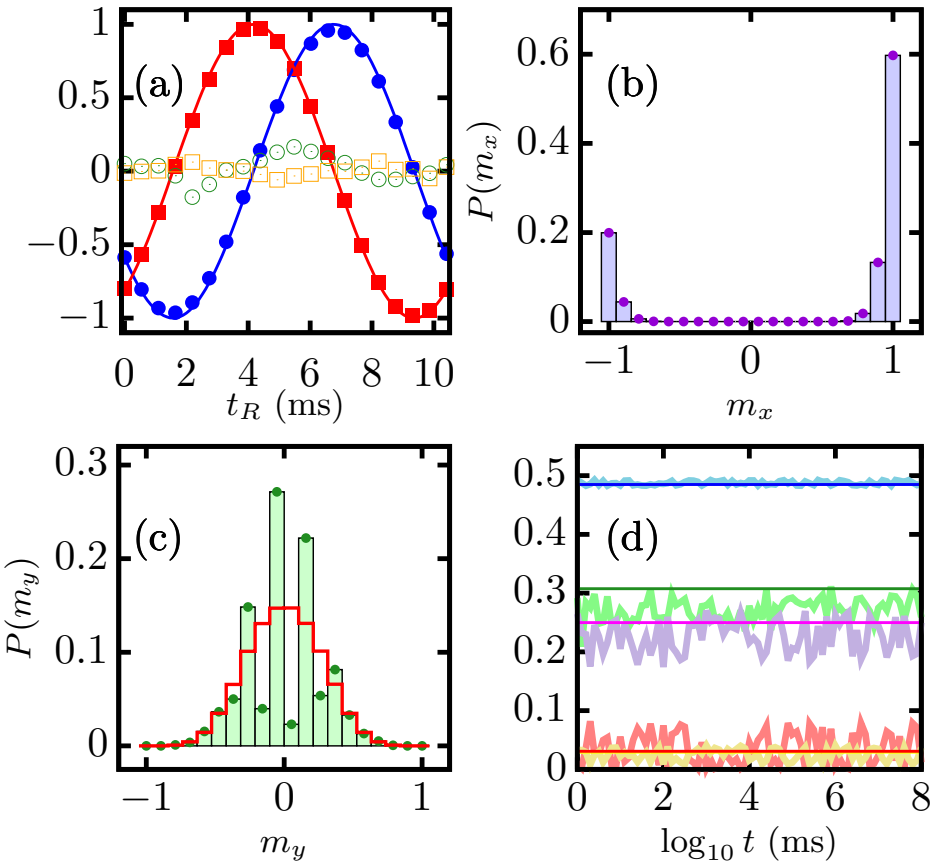

Figure 11: (a) Values of $\hat{\mathcal{C}}$ (circles) and $\hat{\mathcal{K}}$ (squares) after step S4, as a function of the relaxation time t_R, for $\tau_q = 40.96$ ms (filled) and $\tau_q = 0.9$ ms (empty). The perfectly periodic result expected for an adiabatic protocol is represented with solid lines in all cases. System size is $N = 20$. (b) Distribution of the scaled magnetization, $m_x = M_x/N$, corresponding to a quench $h_2 = 0.5$ kHz $\rightarrow$ $h_3 = 0.1$ kHz in the TFIM (97) with $\alpha = 1.1$, $J = 2$ kHz, and $N = 19$. The initial state (148) has $p = 1/2$ and $\phi = \pi/3$. (c) Distribution of $m_y = M_y/N$ (filled, green) for the same quench, and distribution resulting from an initial state with $\phi = 0$ (red steps). (d) Instantaneous evolution of $\hat{m}_x$ (blue) and the probability $P(m_y, t)$ of measuring m_y at time t; $my = -2/N, -1/N, 1/N, 2/N$ (red, green, yellow, purple). NATS predictions (118) are shown with solid horizontal lines.

range interacting) TFIM (97). After step S4, we obtain state of the form (148) with $p = 1/2$ and $\phi = \pi/3$. We recall that ϕ here is a tunable phase, and its value $\phi = \pi/3$ has been chosen for this numerical example. Our next step is to numerically study the consequences of S5. We work with power-law interactions, $V_{ij} \propto J\,|i-j|^{-\alpha}$, with $\alpha = 1.1$ and $J = 2$ kHz, and do the final quench: $h = 0.5$ kHz $\rightarrow$ $h = 0.1$ kHz. We note that because $\alpha > d$, where d is the spatial dimension of the chain, we avoid spurious effects typical of systems with long-range interactions [455].

The resulting time-averaged probability of measuring a value $m_x \in [-1, 1]$ of the scaled magnetization, $\hat{m}_x = (1/N)\sum_i \hat{\sigma}_i^x$, is shown in Fig. 11(b). We clearly observe an asymmetric $P(m_x)$ distribution: it is not invariant under a 180 degree rotation around the z-axis, which is indicative of SB. These results are complemented with the time evolution $\langle \hat{m}_x(t)\rangle$, and the predictions of (118), $\mathrm{Tr}\left[\hat{m}_x\hat{\rho}_{\mathrm{NATS}}\right]$, with $\beta = 0.78219$, $\lambda_c = -3.39076$, $\lambda_k = -5.87297$ and $\lambda_\pi = 0$, shown in Fig. 11(d). These results clearly evidence the fluctuations of $\langle \hat{m}_x(t)\rangle$ around the effective equilibrium state $\hat{\rho}_{\mathrm{NATS}}$, and confirm that the SSB, identified by the condition $\langle \hat{m}_x\rangle \neq 0$, is stable. It is worth noting that although this is a SB state, it is not a regular one where there is only non-zero probability of observing either positive or negative values of $\hat{M}_x$.

The main conclusion of these results is that that we can induce SSB by following our proposed driving protocol, and they clearly show that in order to predict the expectation value of the order parameter the information of the operator $\hat{\mathcal{C}}$ is required. Yet, so far we have not analyzed the role played by the $\hat{\mathcal{K}}$ operator. A related question is whether the resulting equilibrium state is a superposition of the two SB branches. To answer this, we consider $\hat{m}_y = (1/N)\sum_i \hat{\sigma}_i^y$, whose time-averaged probability distribution, $P(m_y)$, is represented in Fig. 11(c). The large $P(m_y = -1/N, 2/N)$ and small $P(m_y = -2/N, 1/N)$ values evidence an interference pattern whose shape critically depends on $\langle\hat{\mathcal{K}}\rangle$. The results for case with $\langle\hat{\mathcal{K}}\rangle = 0$ is also shown in this figure. In this case, the probability distribution is indicative of system equilibrated at either $\rho_{\mathrm{eq}}^{(i)}$, $\rho_{\mathrm{eq}}^{(ii)}$ or a statistical mixture of both. Additionally, the time evolving probabilities of measuring the eigenvalues $m_y = -2/N, -1/N, 1/N, 2/N$ are shown in Fig.11(d). We observe that this interference pattern is stable as the probabilities do not significantly change over time. Thus, the experimental techniques presented in [446] can be used to discriminate between $\langle\mathcal{K}\rangle = 0$ and $\langle\mathcal{K}\rangle \neq 0$; in the last case, an equilibrium state with a coherent superposition of the two SB branches emerges. Finally, the effective equilibrium values of these probabilities are very well described by the NATS, $\mathrm{Tr}\left[\hat{P}_{m_y}\hat{\rho}_{\mathrm{NATS}}\right]$. The small discrepancies between numerical long-time averages and ensemble computed values are due to the system size considered, which is $N = 19$ only.

3.2.6 Symmetry-breaking perturbation and stabilization

So far, we have considered the exact Hamiltonian (97). However, real systems are usually affected by small perturbations; these perturbations can be of an intrinsic nature or due to imperfections in the structure of the model. Such perturbations are often considered to be the main mechanism of SSB. Thus, here we study the

effect of a symmetry-breaking perturbation, ϵ, added to the clean Hamiltonian. Our perturbed Hamiltonian is

$$\hat{H}_\epsilon = \hat{H}_{\text{TFIM}} + \frac{\epsilon}{2}\sum_i \hat{\sigma}_i^x, \tag{129}$$

where, typically, $|\epsilon| \ll 1$.

One may ask what the equilibrium value of the order parameter is when the perturbation is added, in the infinite-size limit. In the absence of conserved quantities aside from energy, the canonical ensemble $\hat{\rho}_C = e^{-\beta\hat{H}_\epsilon}/Z$, see (64), should be enough to predict such value, $\text{Tr}[\hat{\rho}_C\hat{M}]$. In the standard theory of SSB, the term proportional to ϵ breaks the symmetry and therefore the order parameter acquires a non-zero value, $\langle\hat{M}\rangle \neq 0$. In order to illustrate the usual understanding of SSB, we propose the following toy model. We assume that:

- The system has a Gaussian density of states, $\varrho(E)$. This is typically fulfilled by realistic many-body quantum systems.
- The energy E is an extensive quantity. As a consequence, the total spectral width scales with the number of particles, $|E_{\max} - E_{\min}| \propto N$.
- The total number of states of the system is proportional to 2^N.

A simple realization of these assumptions is to consider that the density of states takes the form

$$\varrho(E) = \frac{2^N}{\sqrt{2\pi N^2}} e^{-\frac{E^2}{2N^2}}, \tag{130}$$

which is a Gaussian distribution with mean $\mu = 0$ and standard deviation $\sigma = N$. The corresponding partition function is then $Z = \sum_n e^{-\beta E_n} = \int_{-\infty}^{\infty} \mathrm{d}E\, \varrho(E) e^{-\beta E}$.

Due to the ϵ-induced symmetry-breaking, this level density can be split into two terms. This is because the whole spectrum $\{E_n\}$ can be separated into two subsets: first, we have the eigenlevels $\{E_n^+\}$, corresponding to eigenstates such that the order parameter $\langle\hat{M}\rangle > 0$; second, the eigenlevels $\{E_n^-\}$ are associated to $\langle\hat{M}\rangle < 0$. Note that this separation is unrelated to the parity operator, which is not a symmetry of the Hamiltonian as soon as $\epsilon \neq 0$. Thus,

$$\varrho(E) = \varrho_+(E) + \varrho_-(E), \tag{131}$$

with

$$\varrho_+(E) = \frac{2^{N-1}}{\sqrt{2\pi N^2}} e^{-\frac{(E-\epsilon N)^2}{2N^2}} \tag{132}$$

and

$$\varrho_-(E) = \frac{2^{N-1}}{\sqrt{2\pi N^2}} e^{-\frac{(E+\epsilon N)^2}{2N^2}}. \tag{133}$$

Observe that the mean value of $\varrho_+(E)$ is $\mu_+ = \epsilon N$, while for $\varrho_-(E)$ this is $\mu_- = -\epsilon N$. The partition function can be computed exactly and reads

$$Z \equiv Z(\beta, \epsilon, N) = 2^{N-1} e^{\frac{1}{2}\beta N(-2\epsilon+\beta N)}(1 + e^{2\beta\epsilon N}). \tag{134}$$

What is the value of the $\hat{\mathcal{C}}$ operator under the canonical ensemble, $\hat{\rho}_C$? We have

$$\begin{aligned} \langle\hat{\mathcal{C}}\rangle &= \mathrm{Tr}[\hat{\mathcal{C}}\hat{\rho}_C] \\ &= \frac{1}{Z(\beta,\epsilon,N)} \iint_{-\infty}^{\infty} \mathrm{d}E\,[\varrho_+(E) - \varrho_-(E)] e^{-\beta E} \\ &= -\mathrm{Tanh}(\beta\epsilon N). \end{aligned} \tag{135}$$

The result is a function of three parameters, $\langle\hat{\mathcal{C}}\rangle \equiv \langle\hat{\mathcal{C}}\rangle(\beta, \epsilon, N)$. Here, $N > 0$ and we will assume $\beta > 0$. However, $\epsilon \in \mathbb{R}$ can take any sign. Thus, within the framework of the standard canonical ensemble, the following conclusions ensue:

- The sign of the value of $\hat{\mathcal{C}}$ entirely depends on the sign of ϵ. In particular, $\langle\hat{\mathcal{C}}\rangle \propto -\mathrm{sign}(\epsilon)$. Therefore, if the sign of the perturbation changes with time, the polarization of the equilibrium state should change accordingly.

- The value of $\hat{\mathcal{C}}$ depends on the number of particles N and the temperature β. For a larger value of β (smaller value of T), a smaller value of N is necessary to have $\langle\hat{\mathcal{C}}\rangle \approx \pm 1$, i.e., to obtain a fully polarized state along the x-axis. For this reason, according to the canonical ensemble, the ground-state ($\beta = \infty$, $T = 0$) becomes fully polarized even for a relatively small number of particles. However, higher energy eigenstates, corresponding to smaller β, should require a larger N.

- If $\epsilon > 0$, then $\lim_{N\to\infty}\langle\hat{\mathcal{C}}\rangle(\beta, \epsilon, N) = -1$, and therefore the double limit

  $$\lim_{\epsilon\to 0^+} \lim_{N\to\infty} \langle\hat{\mathcal{C}}\rangle(\beta, \epsilon, N) = -1. \tag{136}$$

  If $\epsilon < 0$, we have instead

  $$\lim_{\epsilon\to 0^-} \lim_{N\to\infty} \langle\hat{\mathcal{C}}\rangle(\beta, \epsilon, N) = 1. \tag{137}$$

  However, the double limit

  $$\lim_{N\to\infty} \lim_{\epsilon\to 0} \langle\hat{\mathcal{C}}\rangle(\beta, \epsilon, N) = 0, \tag{138}$$

  and therefore these limits do not commute.

- According to the previous point, when $\epsilon \neq 0$ the only possible equilibrium states in the $N \to \infty$ limit in the standard theory of SSB are those with $\langle \hat{\mathcal{C}} \rangle = \pm 1$ (depending on the sign of the perturbation ϵ), i.e., fully polarized states along the direction of the magnetization. These are states of the type ES1. No other states are allowed.

Do these predictions, coming from the standard canonical ensemble, really describe the equilibrium states of the perturbed TFIM (129)? As we will show below, the canonical ensemble in general gives wrong predictions for the equilibrium values in systems to which our theory of symmetry-breaking equilibrium states applies. The reason is that $\hat{\rho}_C$ does not take into account the information contained in the $\hat{\mathcal{C}}$ operator. Because $\hat{\mathcal{C}}$ is conserved in the time evolution, this information about the initial state is preserved. In particular, according to our theory:

- If the perturbation, ϵ, fluctuates and changes its sign, the value of $\hat{\mathcal{C}}$ remains constant, and therefore the system is not taken out of equilibrium. In other words, the final equilibrium state is controlled by the initial value of $\hat{\mathcal{C}}$.

- In the standard theory, large values of N are required to obtain fully-polarized states as β decreases (i.e., at increasingly higher T). However, in our description of SSB the TL is reached even for small values of N, regardless of the value of β. This is because when $\epsilon \neq 0$, the eigenlevel degeneracies in the ordered phase are destroyed; since the gap of levels of opposite parity when $\epsilon = 0$ closes exponentially with N, even a small value of ϵ is sufficient to break the degeneracies at an exponential rate with N. Then, the $\hat{\mathcal{C}}$ operator selects the population of states in the NATS (118) (according to the multiplier λ_c).

- In our framework for SSB the non-commutation of the limits $\lim_{N\to\infty}$ and $\lim_{\epsilon\to 0}$ play no role.

- Contrary to the results of the canonical ensemble, the NATS (118) (with $\lambda_\pi = \lambda_k = 0$ when $\epsilon \neq 0$) allows for the existence of ES2 equilibrium states.

As mentioned before, we should note that $\hat{\Pi}$ is not a conserved quantity if $\epsilon \neq 0$. However, as shown in Theorem 1, the invariance of the Hamiltonian under $\hat{\Pi}$ is actually not necessary to define a critical temperature below which $\hat{\mathcal{C}} = \text{sign}(\hat{M})$ (maybe with a different definition for the order parameter $\hat{M}$) is still conserved by the time evolution. Also, if $|\epsilon| \ll 1$, we can expect the order parameter $\hat{M}$ to very approximately coincide with the order parameter of the unperturbed $\epsilon = 0$ case. We then suspect that when $\epsilon \neq 0$ the system may support equilibrium states

described by (118) with $\lambda_c \neq 0$ and $\lambda_\pi = \lambda_k = 0$ for $T < T_c$ that does not change much with respect to its $\epsilon = 0$ value.

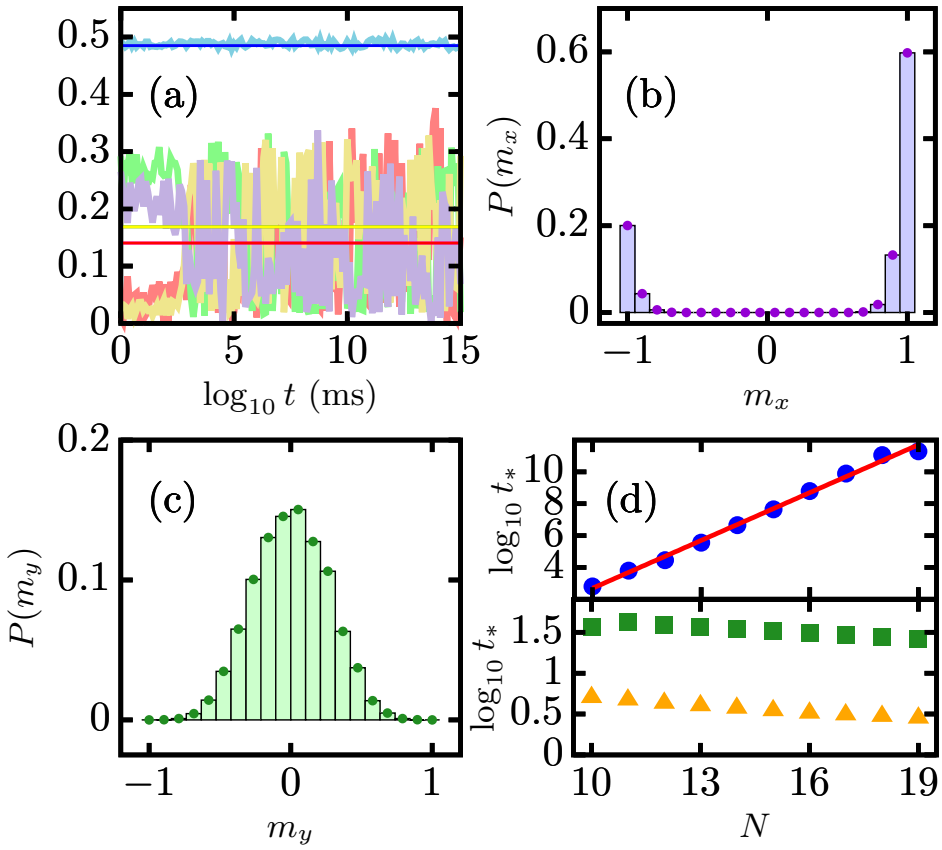

Figure 12: (a) Same as in Fig. 11(d) but in the symmetry-broken Hamiltonian (129) with $\epsilon = 10^{-4}$. The NATS predictions (118), with $\lambda_k = \lambda_c = 0$ and $\beta = 0.7822, \lambda_c = -0.55005$, are plotted as horizontal lines with the same color code as before. (b) Distribution of the scaled magnetization m_x for $\epsilon = 10^{-4}$ after the quench $h_2 = 0.5$ kHz ($\epsilon = 0$) $\to$ $h_3 = 0.1$ kHz ($\epsilon = 10^{-4}$). (c) Distribution of m_y. (d) (Top) Scaling of the time of constancy, t_*, of $\hat{\mathcal{C}}$ with N at $\epsilon = 0$ (points). Red line depicts the best fit $t_* \sim 10^{\nu N}$ with $\nu \approx 1.0015$. t_* is obtained as the first value of t such that $|\hat{\mathcal{C}}(t_*) - \hat{\mathcal{C}}(t = 0)| > 10^{-3}$. (Bottom) Scaling of the constancy time t_* of $\hat{\mathcal{K}}$ in (129) with $\epsilon = 10^{-4}$ (squares) and $\epsilon = -10^{-3}$ (triangles). All results correspond to a quench from an initial state (148) with $p = 1/2$, $\phi = \pi/3$ at $\epsilon = 0$, evolving under (129).

In order to test our theory in a setting easily accessible to experiments, we consider again step S4 of our protocol and we perform a final quench from $h = 0.5$ kHz and $\epsilon = 0$ to $h = 0.1$ kHz and different values of ϵ.

Let us momentarily focus on the time evolution over very long times. Figure 12(a) illustrates how the value of $\langle \hat{m}_x(t) \rangle \neq 0$ remains constant for huge times. Its associated time-averaged probability distribution, basically indistinguishable

from that of the case $\epsilon = 0$, is shown in Fig. 12(b). A remark is convenient: the expectation value of $\hat{m}_x$ in the ground-state of the perturbed system is $\langle \hat{m}_x \rangle < 0$ (because $\epsilon > 0$); however, we observe that the SSB is stabilized with $\langle \hat{m}_x \rangle > 0$. The explanation for this apparent inconsistency is that because $\hat{\mathcal{C}}$ is conserved the probabilities of positive and negative magnetization are constant, even if the sign of ϵ changes with time (see below for an explicit demonstration of this fact). This result is impossible under the standard theory of SSB illustrated above with our proposed toy model. The canonical ensemble would yield $\langle \hat{m}_x \rangle < 0$ for the time-evolving SSB state, which is clearly incorrect. The upper panel of Fig. 12(d) presents a finite-size scaling of the survival time of the SSB state for the case $\epsilon = 0$. The plot reveals an exponential growth of this time with N, which is a consequence of the exponential closure of energy gaps between eigenstates with different parity values within the SB phase $T < T_c$. Interestingly, in the perturbed case, $\epsilon \neq 0$, the SSB actually survives for arbitrarily long times, regardless of $|\epsilon| \neq 0$ and N.

In Fig. 12(a) we also represent the time evolution of the probability of measuring the eigenvalues $m_y = -2/N, -1/N, 1/N, 2/N$ for $\epsilon = 10^{-4}$. The results of the $\epsilon = 0$ and $\epsilon = 10^{-4}$ show qualitative differences. Namely, in the perturbed case we find a pre-thermal state at long times, which survives up to $t \sim 10^3$ ms. The behavior of these probabilities is compatible with a superposition of different SB branches. Yet, the evolution at even longer times reveals that this pattern is not robust: the associated time-averaged probability distribution of $\hat{m}_y$ is shown in Fig. 12(c). The Gaussian shape of this distribution is compatible with the system being equilibrated at $\hat{\rho}_{\text{eq}}^{(i)}$, $\hat{\rho}_{\text{eq}}^{(ii)}$ or a statistical mixture of both. Finally, the lower panel of Fig. 12(d) depicts a finite-size scaling of the survival time of the interference pattern. We estimate the survival time, the time during which $\hat{\mathcal{K}}$ remains approximately constant, with two values of the perturbation, $\epsilon = 10^{-4}$ and $\epsilon = -10^{-3}$. The behavior of the survival time with N suggests that the superposition of different SB branches is destroyed by infinitesimal perturbations in the thermodynamic limit. In other words, equilibrium states of the type ES3 are not possible when $\epsilon \neq 0$. Despite this, our results show that the SSB itself is however stabilized by such perturbations.

To end this section, we will explicitly illustrate one of the failures of the standard theory of SSB mentioned above. According to, e.g., the canonical ensemble, the sign of the $\hat{\mathcal{C}}$ operator (and thus the sign of the order parameter itself) should depend on the sign of the perturbation ϵ. Thus, if the system is exposed to random variations of the perturbation, the value of these operators should change abruptly according to the sign of ϵ. We show here that real physical systems do not exhibit this behavior, meaning that the standard SSB theory fails to describe the dynamics in this scenario.

Let us prepare an initial state $|\Psi(0)\rangle$ in the clean TFIM (97) with $h_i = 0.5$ kHz, $J = 2$ kHz, $\alpha = 1.1$. The initial state is taken to be of the form (148) with $p = 1/2$ and $\phi = \pi/3$, with $|E_{0,\pm}\rangle$ being the opposite-parity lowest-energy eigenstates of the TFIM with these parameter values. We then perform a quench to $h = 0.1$, leaving the remaining parameters unchanged. In this Hamiltonian, we compute the time evolution $|\Psi(t)\rangle$ up to $t = 500$ ms. After this step, we perform twenty consecutive quantum quenches to the perturbed TFIM (129) with the same parameters as in the last Hamiltonian but with values of the perturbation ϵ drawn from a Gaussian distribution of zero mean and deviation 10^{-2}, $\epsilon \sim \mathcal{G}(0, 10^{-2})$. This is to say that in each of these consecutive quenches, the final wave function is taken as the initial wave function in the next Hamiltonian, and each of these Hamiltonians where the dynamics takes place has a random value of the perturbation, which can obviously also change sign. In each of these quenches, we let the wave function evolve during $t = 1000$ ms.

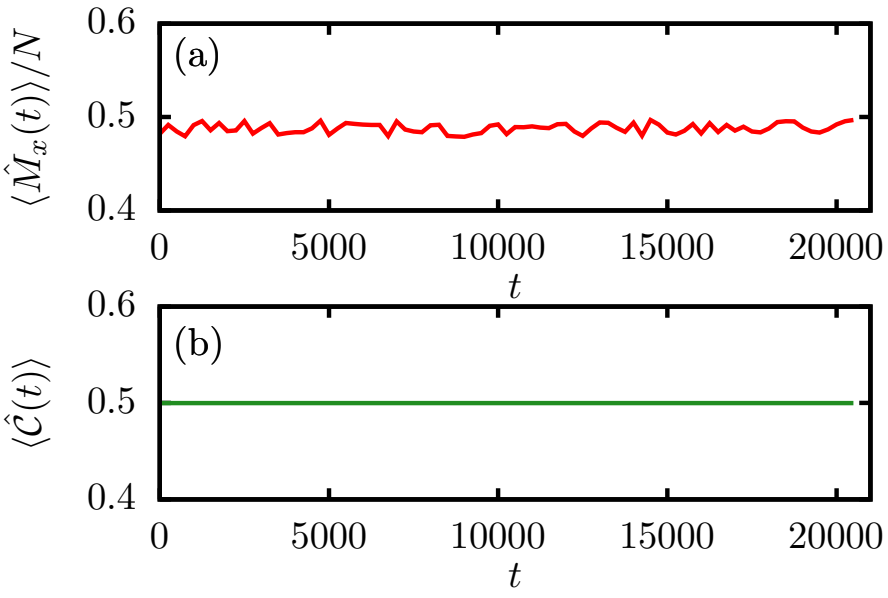

Figure 13: (a) Time expectation value of the order parameter (magnetization along the x-axis), $\langle \hat{M}_x(t) \rangle$ and (b) of its sign operator, $\langle \hat{\mathcal{C}}(t) \rangle$, for the random quench procedure explained in the main text. System size of the TFIM (97) and deformed TFIM (129) is $N = 19$.

We have measured the value of the order parameter $\hat{M}_x$ and the $\hat{\mathcal{C}}$ operator in the protocol described above. The results are presented in Fig. 13. It is clearly observed that although the sign of the perturbation ϵ changes randomly in certain Hamiltonians of the consecutive quenches, the sign of the order parameter $\hat{M}_x$ does not change, and the same is true for the $\hat{\mathcal{C}}$ operator, which remains constant. These results are in complete contradiction with the expectations from the standard

theory of SSB. Rather, the formalism devised in this section of this thesis is necessary to properly describe the values of observables both in $\mathbb{Z}_2$ symmetry-broken phases and in Hamiltonians where SSB takes place. These results also provide solid support to our hypothesis that the $\hat{\mathcal{C}}$ operator should still be constant despite the presence of the perturbation ϵ.

3.3 APPLICATION TO DYNAMICAL PHASE TRANSITIONS

In this section we explicitly discuss a connection of the two kinds of DPTs and ESQPTs [265] in collective quantum systems. To illustrate this connection, we focus on the fully-connected transverse-field Ising model. Both kinds of DPTs are explained by the behavior of the operator $\hat{\mathcal{C}}$, which is a constant of motion only in one of the two phases separated by the critical energy of the ESQPT. According to our theory, below this critical energy, in the symmetry-broken phase, $\hat{\mathcal{C}}$ commutes with the energy projectors in the TL, the dynamical order parameter characteristic of DPTs-I can be different from zero, and the main mechanism leading to non-analytical points in the return probability is precluded. Contrarily, above the ESQPT critical energy, the symmetry-restored phase, the dynamical order parameter always vanishes, and the main mechanism for non-analytic points in the return probability is allowed. The classical interpretation of this theory is discussed as well as some of its consequences, including the suppression of classical behavior for critical quenches leading to ESQPT spectral region, the information erasure ensuing from adiabatically crossing the critical line, and the distinction between 'anomalous' and 'normal' DPT-II dynamical phases (see also [371], [456]).

For concreteness, the numerical results in this section are performed with the fully-connected transverse-field Ising model (the LMG model) [290], [320], [354]–[357], [367], [457], [458], but it should be noted that our results are valid for a broad class of collective quantum systems, encompassing the Rabi and Dicke quantum optical models [94], [305], [309], [312], [314], [322], [347]–[350], [459], the coupled top [335], spinor Bose-Einstein condensates [427], or the two-site Bose-Hubbard Hamiltonian [352].

The general arguments of our physical theory have been laid out in the previous section. To make this Chapter self-contained, here we present a brief summary of the typical structure of fully-connected systems exhibiting an ESQPT to which our results apply. Let us consider a Hamiltonian $\hat{H}(\lambda)$, depending on some control parameter, λ, with the following properties:

(i) It is invariant under a $\mathbb{Z}_2$ symmetry, $\hat{\Pi}$, the parity operator, such that $[\hat{H}(\lambda), \hat{\Pi}] = 0$, $\forall\lambda$, allowing to classify the eigenstates of $\hat{H}(\lambda)$, $E_{n,k}$, according to $\hat{\Pi}\ E_{n,k} = k\ E_{n,k}$ with $k = \pm 1$ and $n = 0, 1, 2, ...$ A typical example of this transformation is the inversion of the transverse magnetic field in the LMG model, $\hat{J}_x \to -\hat{J}_x$.

(ii) A QPT [36] occurs at a critical value of the control parameter, λ_c. This critical point separates two dynamically different ground-state phases. In one phase, say $\lambda > \lambda_c$, the ground-state is two-fold degenerate in the TL (there are pairs of eigenvalues of opposite parity which coincide, $E_{n,+} = E_{n,-}$), leading to a symmetry-broken ground-state. Examples include the ferromagnetic ordered phase in the fully connected transverse-field Ising model, or the superradiant phase of the Dicke and Rabi models. In the other phase, say $\lambda < \lambda_c$, the ground-state is unique, and it has a well-defined value of the parity symmetry. For example, one may think of the disordered paramagnetic phase in the fully-connected transverse-field Ising model, or the normal phase in the Dicke and Rabi models.

(iii) In the ordered phase, $\lambda > \lambda_c$, certain properties of the ground-state get transferred up to an excited critical energy, e.g. $E_{\rm gs} < E < E_c$, where an ESQPT occurs. Quite commonly, the spectral phase $E < E_c$ harbors pairs of eigenlevels of opposite parity that become exactly degenerate in the TL [265], [325]; for this reason, broken-symmetry equilibrium or steady states can be found here [313], [332]. However, for $E > E_c$ the symmetry is restored, the previous level degeneracies get broken, and broken-symmetry equilibrium states can no longer be found. The limits between these two phases are demarcated by a singularity in the density of states at $E = E_c$, the defining feature of the ESQPT.

According to our theory, in the symmetry-breaking phase, $\lambda > \lambda_c$ and $E < E_c$, it is possible to define an operator, $\hat{\mathcal{C}}$, that becomes a constant of motion in the TL. Furthermore, this operator does not commute with the parity symmetry, $[\hat{\mathcal{C}}, \hat{\Pi}] \neq 0$. As previously discussed, a mathematical consequence of this structure is the existence of a third constant of motion in this phase, $\hat{\mathcal{K}} = \frac{i}{2}[\hat{\mathcal{C}}, \hat{\Pi}]$.

In Fig. 14 we provide a schematic representation of the phase diagram of systems with the above structural properties. Two distinct dynamical phases emerge, (I) and (II). Regarding DPTs-I, starting from an initial broken-symmetry state in (II) and quenching it to (I), there exist dynamical order parameters which always vanish, $\overline{m} = 0$; this is a consequence of the operators $\hat{\mathcal{C}}$ and $\hat{\mathcal{K}}$ not being constant in this phase. However, a quench leading the initial state from (II) to (II) also will produce dynamical order parameters that may be non-zero, $\overline{m} \neq 0$ as a consequence of the conservation of $\hat{\mathcal{C}}$ and $\hat{\mathcal{K}}$ (for specific initial states it may also be that $\overline{m} = 0$, but this is not the general case in this phase). Regarding DPTs-II, the same quench protocol will reveal a regular phase in (I) and an anomalous phase in (II). These two phases are separated by the ESQPT critical energy, E_c. The maximum

energy of the system, $E_{\max}$, can be finite (LMG model) or infinite (Dicke and Rabi models).

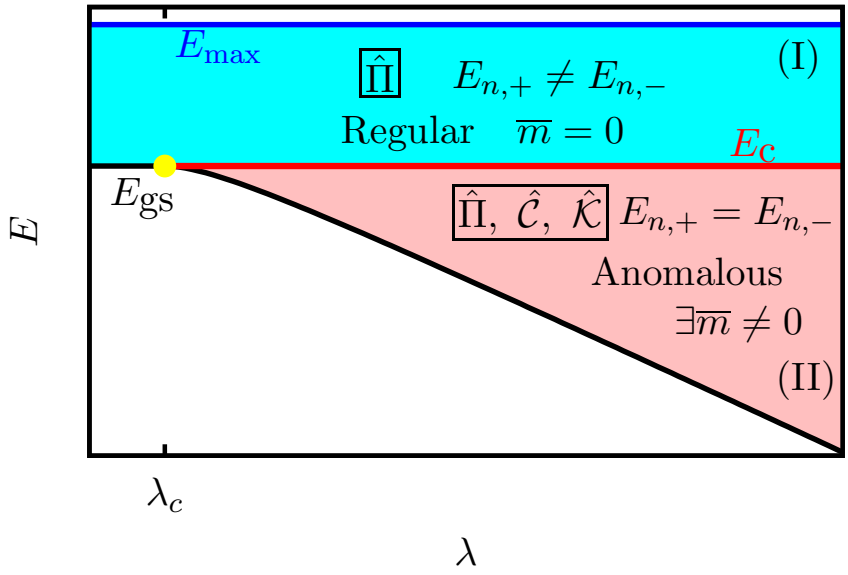

Figure 14: Schematic representation of the phase diagram of the class of systems with structural properties as in the LMG model. Energy is represented as a function of some control parameter, λ. The ground-state $E_{\rm gs}$ is represented gby a black solid line. A QPT takes place at $\lambda = \lambda_c$ (yellow circle). When $\lambda > \lambda_c$, the critical energy E_c (thick red line) marks the ESQPT. Two dynamically distinct phases are denoted I and II. In each of them, certain operators are constant in the infinite-size limit. In (I) levels belonging to different parity sectors are different, $E_{n,+} \neq E_{n,-}$, while in (I) we find pairwise degeneracies, $E_{n,+} = E_{n,-}$, with the parity symmetry being broken. Phase (I) is characterized by a zero order parameter $\overline{m} = 0$, while in (II) this order parameter can take a non-zero value, $\overline{m} \neq 0$. A quantum quench starting from a symmetry-breaking state in (II) to (I) causes regular cusps in the return probability, while quenching the system to (II) will reveal an anomalous phase (see main text and discussions).

3.3.1 Classical limit of the fully-connected transverse field Ising model

The basic properties of the LMG model have been specified already around Eq. (73). As noted, this Hamiltonian represents a collective system, an all-to-all system where each individual spin feels the interaction with every other spin in the chain and with the same intensity. In this class of models, the number of degrees of freedom remains finite when the collective spin length increases boundlessly, and thus the infinite-size limit, $j \to \infty$, coincides with the classical limit, $\hbar \to 0$ [265]. The

SU(2) Bloch coherent state allows us to obtain a mean-field classical Hamiltonian. Consider

$$|\omega\rangle = \left(\frac{1}{1+|\omega|^2}\right)^j e^{\omega \hat{J}_+} |j,-j\rangle\,, \tag{139}$$

where $|j,-j\rangle$ is the state with spin j and $\langle \hat{J}_z\rangle = -j$, and

$$\omega = \frac{Q+iP}{\sqrt{4-P^2-Q^2}} \in \mathbb{C} \tag{140}$$

with Q and P real variables. We then obtain the intensive energy functional

$$H(Q,P;\lambda) \equiv \frac{\langle\omega|\,\hat{H}\,|\omega\rangle}{j} = -h + \frac{h}{2}(Q^2+P^2) - \frac{\lambda}{8}Q^2(4-P^2-Q^2). \tag{141}$$

Here, (Q,P) are canonical variables belonging to a 2-dimensional ball of radius 2, which leads to a classical phase space of the form $\mathcal{M} = \{(Q,P) \in \mathbb{R}^2 \;:\; 0 \leq Q^2+P^2 \leq 4\}$. It is clear that the classical model (141) has a single degree of freedom, $f=1$. In order to make our comparisons with the quantum Hamiltonian more convenient, we define the intensive energy scale associated with the classical Hamiltonian $\epsilon \equiv E/j$, where E denotes the actual eigenvalues of the quantum Hamiltonian (73).

The Bloch coherent states make it possible to obtain a classical representation of any dynamical function. The classical limit of the collective magnetization is

$$j_z = \frac{\langle\omega|\,\hat{J}_z\,|\omega\rangle}{j} = \frac{Q^2+P^2}{2} - 1, \tag{142}$$

while for the parity-breaking spin operator j_x we have

$$j_x = \frac{\langle\omega|\,\hat{J}_x\,|\omega\rangle}{j} = \frac{Q}{2}\sqrt{4-P^2-Q^2}. \tag{143}$$

The structure and phase transitions of the classical model can be analyzed through the fixed points of (141) [265], $\nabla H\,_{(Q*,P*)} = 0$,

$$\frac{\partial H}{\partial P} = P\left(h + \frac{\lambda}{4}Q^2\right) = \frac{\mathrm{d}Q}{\mathrm{d}t}, \tag{144}$$

$$\frac{\partial H}{\partial Q} = -Q\left[(\lambda - h) + \frac{\lambda}{4}\left(-P^2-2Q^2\right)\right] = -\frac{\mathrm{d}P}{\mathrm{d}t}. \tag{145}$$

By equating Eqs. (144,145) to zero, we can calculate different real solutions depending on the value of $\lambda \geq 0$. All critical points are of the type $(Q,P) = (Q,0)$. If $\lambda < h$, the only critical point has $Q=0$, corresponding to $\epsilon = -h$. This is the

ground-state energy when $\lambda < h$. However, if $\lambda \geq h$, there exist two additional critical points, $Q = \pm\sqrt{2(\lambda - h)/\lambda}$. A second order QPT occurs at the critical value of the control parameter $\lambda_c = h$. By virtue of the Hamiltonian symmetry $H(Q, 0) = H(-Q, 0)$, these two critical points give rise to the same energy value, $\epsilon = -(h^2 + \lambda^2)/2\lambda$, which is the ground-state energy if $\lambda \geq h$. The previous critical point with $Q = 0$ corresponds to an unstable fixed point if $\lambda \geq h$, defining an ESQPT at $\epsilon_c = -h, \forall \lambda > \lambda_c$. In our numerical calculations, $h = 1$ will be kept fixed, and λ will be taken as the only controllable parameter.

Portraits of the classical phase space have been represented in Fig. 9, where each line corresponds to a classical orbit with fixed energy, i.e., the set of points (Q, P) such that $H(Q, P) = \epsilon$. For $\lambda = 0$ the LMG model reduces to $\hat{H} = -h\hat{J}_z$, which is essentially an harmonic oscillator with classical dynamics governed by $H = -h + h(Q^2 + P^2)/2$, composed of concentric circumferences. Here, the ground-state is unique. A value $\lambda \neq 0$ but $\lambda < \lambda_c$ disrupts the perfect harmonic behavior, but the ground-state remains unique as shown in Fig. 9(b-c). However, the classical phase space changes drastically when $\lambda > \lambda_c$, see Fig. 9(d) for $\lambda = 3$. We highlight three main aspects: (i) the ground-state becomes two-fold degenerate, leading to a double-well potential with minima at a given Q and also at its mirrored image, $-Q$; (ii) $(0, 0)$ becomes an unstable fixed point, corresponding to energy $\epsilon_c = -1$ (for $h = 1$); and (iii) for $\epsilon < \epsilon_c$ trajectories are trapped within either the right or left classical wells, depending on the initial condition, but if $\epsilon > \epsilon_c$ the whole phase space becomes available.

The 'singular' behavior occurring at energy $\epsilon_c = -1$ is due to an ESQPT. To see why, let us calculate the classical level density [264], [294] which, according to Gutzwiller's trace formula [61], can be approximated as ($\hbar = 1$)

$$\varrho(\epsilon) = \frac{1}{2\pi} \iint_{\mathcal{M}} \mathrm{d}Q\mathrm{d}P\, \delta[\epsilon - H(Q, P)]. \tag{146}$$

This level density is shown in Fig. 15 for the same values of λ as in Fig. 9. When $\lambda = 0$ the spectrum is equiespaced and, thus, $\varrho(\epsilon)$ is a uniform distribution. A value $\lambda \neq 0$ creates a ramp-shaped distribution with a peak at its border, $\epsilon = -1$. But the ESQPT signatures are best exemplified by the case $\lambda > \lambda_c$, where a *logarithmic singularity* is clearly visible, e.g. for $\lambda = 3$.

As explained in Sec. 3.1, where the model we are interested in was used to illustrate the geometrical meaning of our general theory in Sec. 3.2, in the symmetry-broken phase $\lambda > \lambda_c$ and $E < E_c$, the operator

$$\hat{\mathcal{C}} = \mathrm{sign}\,(\hat{J}_x). \tag{147}$$

is an emergent conserved quantum quantity in the infinite-size limit. According to our general theory, (147) defines a discrete $\mathbb{Z}_2$ symmetry with two eigenvalues,

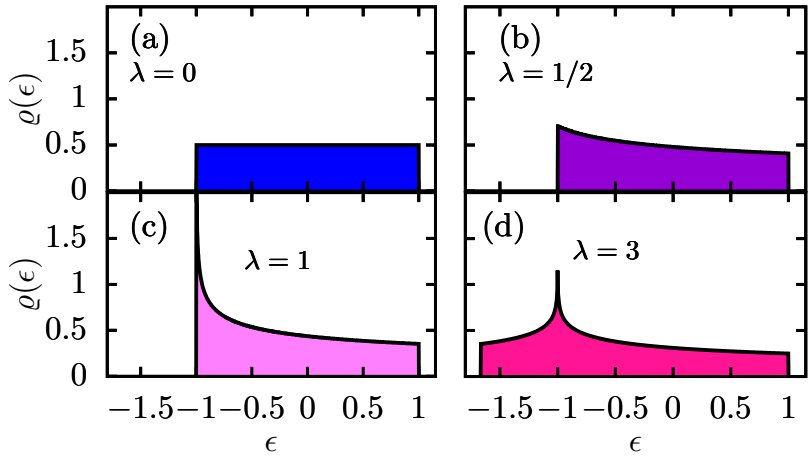

Figure 15: Representation of the level density of the LMG model with $h = 1$ and for different values of λ. The numerical density of states obtained from the quantum Hamiltonian, Eq. (73), with $j = 10000$, are presented with color histograms, and the classical approximation to the level density, Eq. (146), is shown with black lines in all cases.

Spec $(\hat{\mathcal{C}}) = \{\pm 1\}$ [325]. But this operator is a *partial* symmetry as it does not commute with the whole Hamiltonian, only with the projectors onto the Hamiltonian eigenspaces with associated energies below the ESQPT critical line. As shown in [325], if $|E_{n,\pm}\rangle$ denote the Hamiltonian eigenstates with energy below E_c the eigenvectors of $\hat{\mathcal{C}}$ are $(|E_{n,+}\rangle \pm |E_{n,-}\rangle)/\sqrt{2}$, and $\langle E_{n,\pm}|\,\hat{\mathcal{C}}\,|E_{n,\mp}\rangle = \pm 1$. We note that the sign in ± 1 here is not related to parity; rather, it is an arbitrary global phase pertaining to each of the eigenstates $|E_{n,\pm}\rangle$. Thus, it can be simply fixed to $+1$ without loss of generality [325]. The operator (147) can be used to establish a quantum-classical correspondence; specifically, given an arbitrary state $|\varphi(t)\rangle$, the expectation value $\langle\hat{\mathcal{C}}(t)\rangle = \langle\varphi(t)|\,\hat{\mathcal{C}}\,|\varphi(t)\rangle \in [-1, 1]$ indicates whether $|\varphi(t)\rangle$ is attached to the left (-1) or right (+1) classical energy well, or if it is a superposition (between -1 and +1).

3.3.2 Dynamical order parameters: dynamical phase transition of type I

As explained in Sec. 1.3.3, DPTs-I are mainly signaled by non-analytic points in the non-equilibrium order parameter after a quantum quench protocol [365], [374], [384]–[391]. Our goal in this section is to show how in a large class of collective quantum systems these phase transitions stem from a symmetry restoration brought about by the ESQPT. One of our main results is the proposal of an extension of the standard microcanonical ensemble [1] to describe the long-time average of order parameters in symmetry-broken phases, where the order parameter

acquires a finite value. To this end, we will make use of the three noncommuting charges of Sec. 3.2.

Taking an initial state out of equilibrium: quantum quenches

In order to emphasize in what Hamiltonian (initial or final) the time evolution takes place, let us slightly change the notation: instead of $|\Psi(t)\rangle$, which can be ambiguous, $|\Psi_t(\lambda)\rangle$ will refer to the time evolution occurring in the Hamiltonian with control parameter λ and at time t. Similar notation will refer to the eigenstates of the Hamiltonian, so $|E_n(\lambda)\rangle$ refers to the nth eigenstate of the Hamiltonian $\hat{H}(\lambda)$.

To generate non-equilibrium dynamics, we start from a superposition of the symmetry-broken ground-state at an initial value of the control parameter $\lambda_i > \lambda_c$,

$$|\Psi_0(\lambda_i)\rangle = \sqrt{\alpha}\,|E_{0,+}(\lambda_i)\rangle + e^{i\phi}\sqrt{1-\alpha}\,|E_{0,-}(\lambda_i)\rangle\,, \tag{148}$$

where $\alpha \in [0,1]$, $\phi \in [0, 2\pi)$. It should be emphasized that this choice of initial state is experimentally relevant as it has been considered in recent realizations [374], [388], [395] with $\alpha = 1/2$ and $\phi = 0$. To make contact with experiments, in this section we also adopt the scale where $h \sim$ MHz, so $t \sim \mu$s. We perform a quench $\lambda_i \to \lambda_f$, and let the state evolve in time under the final Hamiltonian ($\hbar = 1$),

$$\begin{aligned} \Psi_t(\lambda_f) \;&= e^{-i\hat{H}(\lambda_f)t}\,|\Psi_0(\lambda_i)\rangle \\ &= \sum_n \sum_{k=\pm} \Big(E_{n,k}(\lambda_f)\;\Psi_0(\lambda_i)\;\; e^{-iE_{n,k}(\lambda_f)t}\;\; E_{n,k}(\lambda_f)\;\Big) \;. \end{aligned} \tag{149}$$

After the quench, the distribution of populated states, also called the local density of states (LDOS), can be written

$$P(E) = \sum_n \sum_{k=\pm} \Big(|c_{n,k}|^2 \delta(E - E_{n,k}), \tag{150}$$

where the coefficients $c_{n,k} \equiv \;E_{n,k}(\lambda_f)\;\Psi_0(\lambda_i)\;$. Figure 16 shows this distribution for several values of the collective spin-length, j (the system size parameter, as we are working with the sector $j = N/2$ of the LMG model), starting from different values of $\lambda_i > \lambda_c$, $\alpha = 1/2$ and $\phi = 0$, and all finishing at $\lambda_f = 1.75$. The average energy of the quenched state, $\sum_n \sum_{k=\pm} |c_{n,k}|^2 \epsilon_{n,k}(\lambda_f)$, strongly depends on λ_i, so it can be driven from one side of the ESQPT, $E < E_c$, to the other, $E > E_c$. A technical detail is that, for visualization purposes, this distribution of populated states is scaled by the mean level spacing, $\langle s \rangle$, $s_n = \epsilon_{n+1} - \epsilon_n$, because the rescaled energy spectrum $\{\epsilon_n\}$ gets denser j increases. It is clear that as j increases the

width of the distribution decreases, becoming more peaked precisely around the infinite-j average given by the classical limit (dashed vertical lines). In (a) and (c), the distributions are non-negligible essentially on only one side of the ESQPT: in (a) $P(\epsilon)$ shows significant population for $\epsilon < \epsilon_c = -1$, while in (c) the opposite is true. However, in (b) the average energy very approximately coincides with $\epsilon_c = -1$. In the last case, we observe a clear dip of the distribution exactly at the critical energy, as previously noticed, e.g., in [317], [460]. The dynamical implications of this feature will be discussed later.

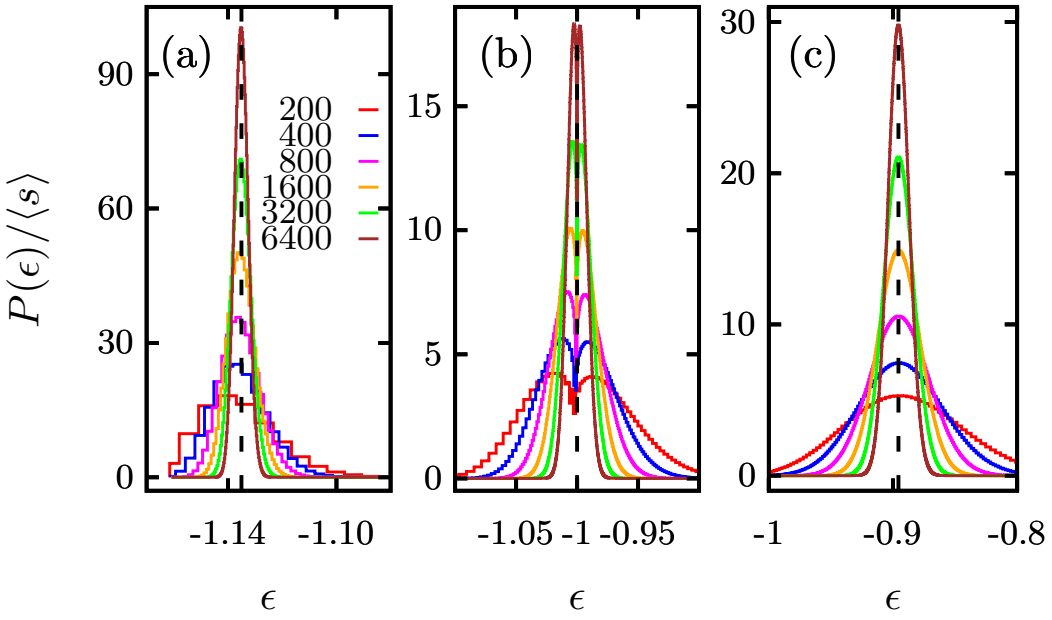

Figure 16: Probability of populated states (LDOS), defined in (150), after a quench $\lambda_i \to \lambda_f = 1.75$ from the initial state Eq. (148) with $\alpha = 1/2$ and $\phi = 0$ in the LMG model (73). The values of the initial control parameter and the average energy of the quenched state in the final Hamiltonian are (a) $\lambda_i = 2.5$, $\epsilon(\lambda_f) = -1.135$ (b) $\lambda_i = 7$, $\epsilon(\lambda_f) = -1$, and (c) $\lambda_i = 27.5$, $\epsilon(\lambda_f) = -0.89567$. The system size j ranges from 200 to 6400 as indicated in (a). The black dashed lines represent the classical value of the final average energy of the quenched state.

Post-quench relaxation dynamics

Here we analyze the relaxation dynamics for each of the quenches considered in Fig. 16. Figure 17 represents the quantum dynamics of the parity-breaking operator $\hat{J}_x$. Its expectation value at a given time t is

$$\langle \hat{J}_x(t) \rangle = \Psi_t(\lambda_f) \ \hat{J}_x \ \Psi_t(\lambda_f) \ . \tag{151}$$

In the broad class of systems sharing physical properties with the LMG model, this operator is commonly used as an order parameter [266] [i.e., $m(t) = \langle \hat{J}_x(t) \rangle$ in Fig. 14]. The dynamical evolution of its classical counterpart, Eq. (143), is determined by the Hamilton equations Eqs. (144,145). Because we are dealing with a fully-connected model, quantum and classical dynamics coincide in the limit $j \to \infty$. In Fig. 17(a-c) an oscillatory pattern can be observed. For small j, quantum and classical dynamics only agree for relatively short times, and for longer times we observe damping combined with dephasing deviating from the perfect $j \to \infty$ classical oscillation. The time when the different quantum results deviate from the classical evolution increases with j, but it shows some peculiarities depending on the region of the spectrum where the initial state ends after the quench. For example, in Fig. 17(a) the quenched state only significantly populates states below the ESQPT and $\langle \hat{\mathcal{C}} \rangle = +1$ is conserved; as a consequence, the quenched state is trapped within the right classical well. Indeed, in this case $\langle \hat{J}_x(t) \rangle$ remains positive for all t. Likewise, classically, $j_x(t) \propto Q(t)$, which is positive in the right energy well [cf. Fig. 9(d)]. A completely different case is represented in Fig. 17(c), where the quench only populates final Hamiltonian eigenstates with energy above E_c. Here, $\langle \hat{\mathcal{C}} \rangle$ is not conserved and therefore both classical energy wells are accessible. Therefore, the time evolution of the order parameter features both positive and negative values. The situation considered in Fig. 17(b) is intermediate: the average quench energy coincides with the ESQPT critical energy, but both sides of the spectrum are populated. Classically, $j_x(t)$ exhibits a decay at short times, and for $t \gtrsim 10$ it plateaus at zero, which is the corresponding value of the classical ESQPT critical point, $j_x \propto Q = 0$. We note that a classical trajectory exactly traversing the critical line of the phase space [e.g., the black line in Fig. 9(d), which seems to cross itself] has access to the other side; however, leaving the fixed point requires a infinite time. In any case, at the ESQPT critical energy the quantum dynamics shows drastic deviations from the expected classical evolution.

In Fig. 17(d-f) we have plotted the same dynamical evolution as before but for longer timescales. Generally, after the dynamics has completely deviated from the classical predictions, it enters a new regime characterized by oscillations around a steady-state value, and then a series of dynamical revivals echo its short-time behavior [461]. For very long times, the dynamics eventually becomes very noisy with no clear pattern, as shown in Fig. 17(d,f). In these two cases, the time of first revival and the time interval between two consecutive revivals increase as j increases. Yet, in Fig. 17(e), corresponding to the critical quench, the dynamics simply fluctuates around some steady value with no revivals at all.

From this discussion, two particularly relevant timescales can be defined: the time when the quantum dynamics deviates from its large-j classical result, t_{SC}, and

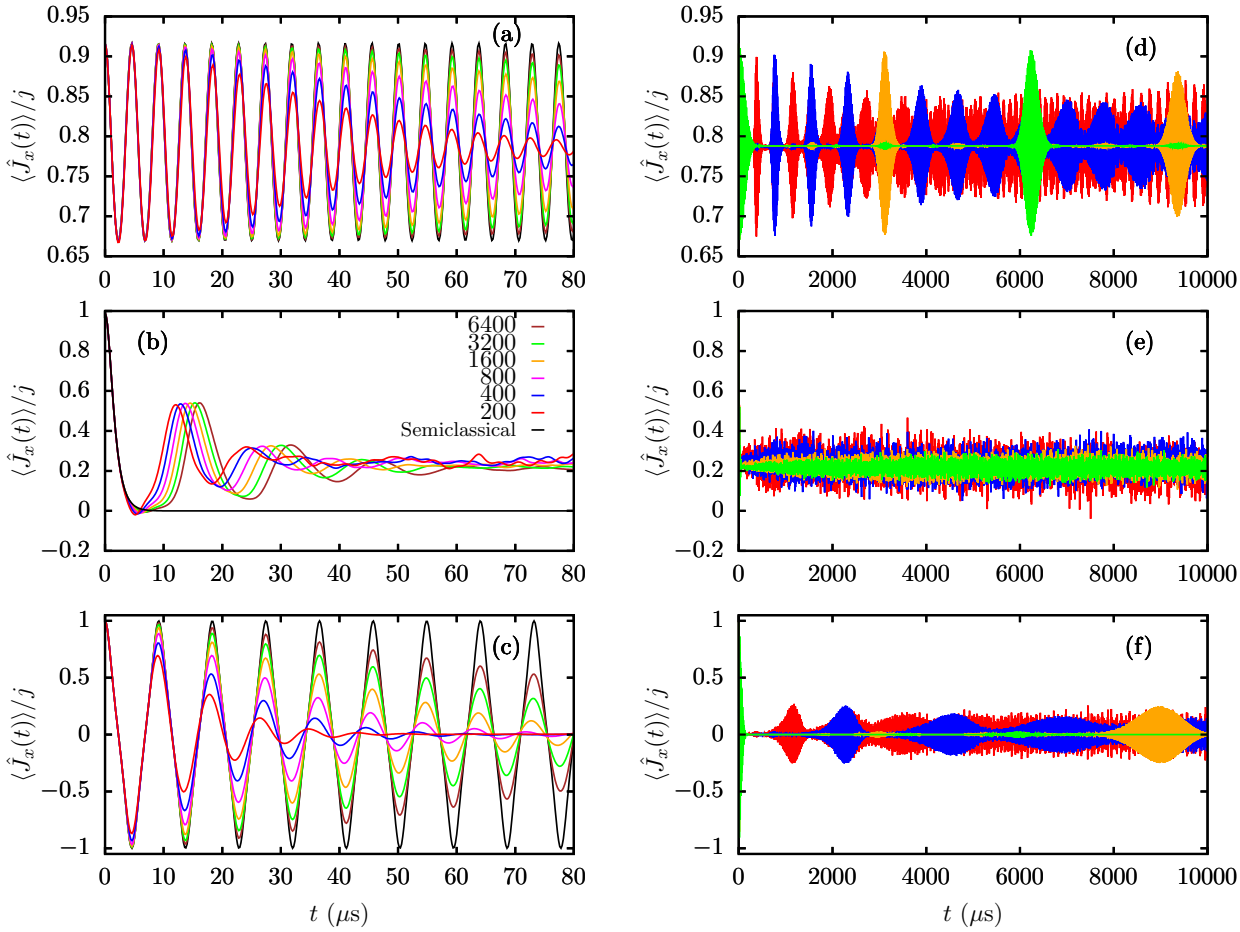

Figure 17: Numerical analysis of DPTs-I in the LMG model (73). We represent the time-expectation value of $\hat{J}_x$ after a quench $\lambda_i \to \lambda_f = 1.75$. We perform quenches with initial states of the form in (148) with $\alpha = 1/2$ and $\phi = 0$. Because $\langle \hat{\mathcal{C}} \rangle = 1$, the wave function is always initially localized in the right energy well. The initial values of the control parameter and the final average energies of the quenched states are (a,d) $\lambda_i = 2.5$, $\epsilon(\lambda_f) = -1.135$ (b,e) $\lambda_i = 7$, $\epsilon(\lambda_f) = -1$, and (c,f) $\lambda_i = 27.5$, $\epsilon(\lambda_f) = -0.89567$. The color code is indicated in (b) and followed in all panels. In (a,b,c), the classical dynamical evolution following the Hamilton equations is shown with black lines.

the time when the first revival occurs, t_{R}, which we briefly analyze here. We may estimate t_{SC} by computing the difference between quantum and classical results, looking for the first value of time such that this quantum-classical discrepancy is greater than a given arbitrary but suitably chosen bound. For t_{SC} this bound is 0.1. Similarly, to estimate t_{R}, we compute the first time when the absolute value of the time evolution exceeds an arbitrary bound, only after the classical expectation has been completely lost. This bound is 0.85 for Fig. 17(d) and 0.15 for Fig. 17(e). In Fig. 18 we represent the behavior with system size, j, of these two timescales. For

dynamics taking place at a definite side of the ESQPT, i.e. $E > E_c$ and $E < E_c$, t_{SC} grows algebraically as $t_{\mathrm{SC}} \sim \sqrt{j}$ [266], [381]; however, for the quench ending at the ESQPT criticality, this time is a lot smaller, and it only scales logarithmically with j as $t_{\mathrm{SC}} \sim \log_{10} j$. Assuming a macroscopic system with $N = 10^{24}$ atoms, this logarithmic law leads to $t \approx \log_{10} 10^{24} = 24$ μs, which is negligible compared to $t \approx \sqrt{10^{24}} = 10^{12}$ μs for quenches above or below E_c. In fact, one may argue that a DPT takes place for these macroscopic system sizes: below or above the ESQPT, the dynamics consists of persistent oscillations, while at the ESQPT the dynamics simply fluctuates around a certain stationary value as in Fig. 17(b,e) after a extremely short time has elapsed. Finally, for quenches ending above or below E_c the time where the first revival takes place follows the linear scaling $t_{\mathrm{R}} \sim j$, while for quenches ending right at the ESQPT no revivals occur.

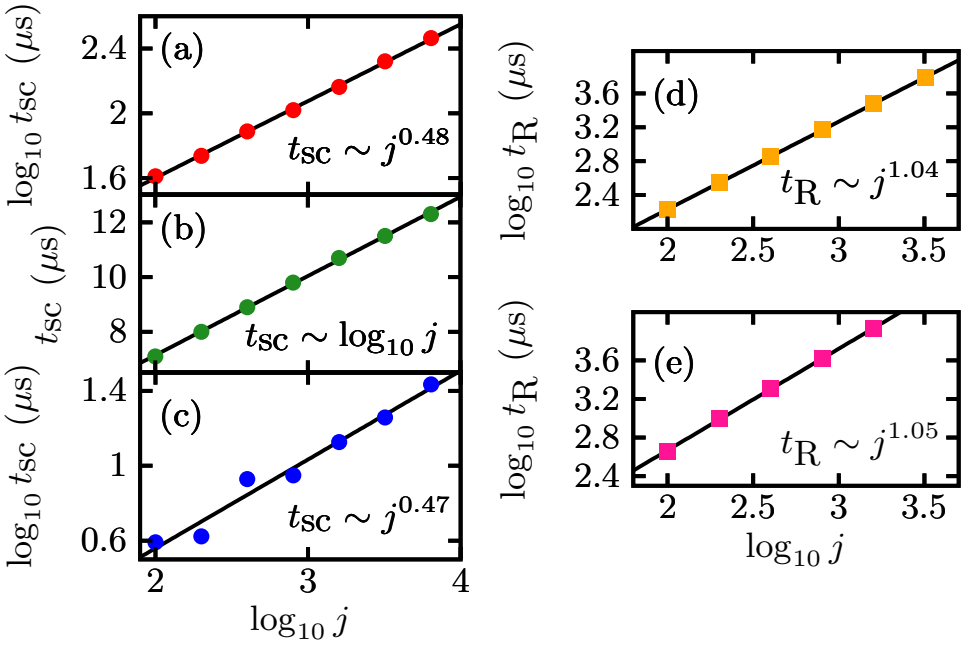

Figure 18: Scaling of the classical time t_{sc} and the revival time t_{R} as a function of system size j, extracted from the time evolution of $\hat{J}_x$ in Fig. 17. (a-c) correspond to Fig. 17(a-c), respectively, while (d-e) correspond to Fig. 17(d) and Fig. 17(f), respectively.

Describing equilibration dynamics: the generalized microcanonical ensemble

We have already discussed in Sec. 3.2.1 that the NATS (118) is an equilibrium state, in the infinite-size limit, in the symmetry-breaking phase ($T < T_c$). In the case of collective systems with a similar structure to the LMG, this symmetry-breaking phase is found for $\lambda > \lambda_c$ and $E < E_c$. The ESQPT demarcates the limits of

the symmetry-breaking and symmetry-restored phases. Because in collective systems the microcanonical and canonical descriptions do not coincide [265], in order to properly describe these symmetry-breaking equilibrium states we need to construct a microcanonical version from the NATS . According to our general theory of Sec. 3.2, for $E < E_c$ the operators $\{\hat{\Pi}, \hat{\mathcal{C}}, \hat{\mathcal{K}}\}$ are conserved in the infinite-size limit, while for $E > E_c$ only $\hat{\Pi}$ (which is not an emergent constant of motion but an exact one) is conserved. It would therefore seem that two separate equilibrium ensembles are necessary to describe our generic system, with an ill-defined transient region between $E < E_c$ and $E > E_c$ (the ESQPT at $E = E_c$). Luckily, this issue can be circumvented by employing the following variation of the operators $\hat{\mathcal{C}}$ and $\hat{\mathcal{K}}$,

$$\widetilde{C} = \mathbb{I}_{E<E_c} \hat{\mathcal{C}} \mathbb{I}_{E<E_c}, \tag{152}$$

$$\widetilde{K} = \mathbb{I}_{E<E_c} \hat{\mathcal{K}} \mathbb{I}_{E<E_c}, \tag{153}$$

where $\mathbb{I}_{E<E_c} \equiv \sum_n \theta_n \hat{P}_n$, $\hat{P}_n$ is the projector to the eigenspace with energy E_n, and $\theta_n = 1$ if $E_n < E_c$ and $\theta_n = 0$ if $E_n > E_c$. Observe that $\langle \widetilde{C} \rangle$ and $\langle \widetilde{K} \rangle$ are the exact same as $\langle \hat{\mathcal{C}} \rangle$ and $\langle \hat{\mathcal{K}} \rangle$ for $E < E_c$, but are equal to zero for $E > E_c$. As a consequence, $\widetilde{C}$ and $\widetilde{K}$ do commute with the full Hamiltonian in the TL. Furthermore, these two operators, together with $\hat{\Pi}$ and with the identity, close a SU(2) algebra in every subspace of degenerate energy levels. In a single eigenspace of the eigenbasis common to $\hat{H}$ and $\hat{\Pi}$, $\{|E_{n,+}\rangle, |E_{n,-}\rangle\}$, they can be written [note the difference with (116), where the eigenbasis of $\hat{M}$ was used instead of that of $\hat{\Pi}$]

$$\hat{\mathcal{C}} = \begin{pmatrix} 0 & 1 \\ 1 & 0 \end{pmatrix}, \; \hat{\mathcal{K}} = \begin{pmatrix} 0 & -i \\ i & 0 \end{pmatrix}, \; \hat{\Pi} = \begin{pmatrix} 1 & 0 \\ 0 & -1 \end{pmatrix} \tag{154}$$

The set of noncommuting [428], [440], [462] charges $\{\hat{\Pi}, \widetilde{C}, \widetilde{K}\}$ can be used to build any 2×2 Hermitian matrix accounting for all quantum coherences between parity sectors in a single energy eigenspace. The NATS (118) can then be adapted to the microcanonical description as $\hat{\rho}_{\text{GME}} = \hat{\rho}_{\text{ME}} e^{-\lambda_\pi \hat{\Pi} - \lambda_c \widetilde{C} - \lambda_k \widetilde{K}}$, which for convenience can be simplified further to

$$\hat{\rho}_{\text{GME}}(E, p, c, k) = \hat{\rho}_{\text{ME}}(E) \left(\mathbb{I} + p\, \hat{\Pi} + c\, \widetilde{C} + k\, \widetilde{K} \right) \tag{155}$$

where

$$\hat{\rho}_{\text{ME}}(E) = \frac{1}{2(N_+ + N_-)} \sum_n \left(|E_{n,+}\rangle \langle E_{n,+}| + |E_{n,-}\rangle \langle E_{n,-}| \right) \tag{156}$$

denotes the standard microcanonical ensemble [1], defined by the condition that all parity doublets, $|E_{n,+}\rangle$ and $|E_{n,-}\rangle$, within a small energy window around the average energy value, $\langle E \rangle = \text{Tr}[\hat{\rho}\hat{H}]$, are equally populated (irrespective of whether

these parity doublets are degenerate). This ensemble is properly normalized, $\mathrm{Tr}\hat{\rho}_{\mathrm{GME}}(E) = 1$. $N_{\pm}$ denotes the number of parity doublets above (N_+)/below (N_-) E_c populated (e.g., by a quantum quench). We dub the density matrix $\hat{\rho}_{\mathrm{GME}}(E, p, c, k)$ as *generalized microcanonical ensemble* (GME). Unlike the standard microcanonical ensemble, in addition to the average energy it also depends on the parameters $p, c, k \in \mathbb{R}$ which, similarly to the multipliers in the NATS (118), are determined solely by the initial condition: $\mathrm{Tr}[\hat{\rho}_{\mathrm{GME}}\hat{\Pi}] = \langle\hat{\Pi}\rangle$, $\mathrm{Tr}[\hat{\rho}_{\mathrm{GME}}\widetilde{C}] = \langle\widetilde{C}\rangle$, and $\mathrm{Tr}[\hat{\rho}_{\mathrm{GME}}\widetilde{K}] = \langle\widetilde{K}\rangle$. Explicitly, in the large-N limit these values read

$$\langle\hat{\Pi}\rangle = p, \tag{157}$$

$$\langle\widetilde{C}\rangle = c\frac{N_-}{N_+ + N_-}, \tag{158}$$

and

$$\langle\widetilde{K}\rangle = k\frac{N_-}{N_+ + N_-}, \tag{159}$$

whence one may calculate the parameters p, c, k.

The main features of this statistical ensemble are:

(A) It reproduces the quantum coherence between parity sectors if and only if $E < E_c$ as (155) has off-diagonal elements in the parity eigenbasis if $c \neq 0$ and/or $k \neq 0$. For this reason, the equilibrium value of the order parameter (or of any other parity-breaking observable), $\mathrm{Tr}\left[\hat{\rho}_{\mathrm{GME}}(E, p, c, k)\hat{J}_x\right]$, can be non-zero only if $E < E_c$. Note, however, that not very initial condition leads to a symmetry-breaking equilibrium state even if $E < E_c$; these can occur if an only if $c \neq 0$ and/or $k \neq 0$. In other words, the ensemble reproduces the physically observed fact that in the symmetry-broken phase the order parameter of DPTs-I can acquire a finite value, $\overline{m} \neq 0$ [cf. Fig. 14].

(B) For $E > E_c$, (155) becomes diagonal in the Hamiltonian eigenbasis. Hence, if $E > E_c$, $\mathrm{Tr}\left[\hat{\rho}_{\mathrm{GME}}(E, p, c, k)\hat{J}_x\right] = 0$ invariably, for any initial condition. This is to say that the GME also reproduces the observation that order parameters of DPTs-I are always $\overline{m} = 0$ in a symmetry-restored phase [cf. Fig. 14].

In other words, according to (155), it is the ESQPT non-analyticity that causes DPTs-I. If an initial state prepared in the symmetry-broken phase is quenched onto the symmetry-restored phase, then the information pertaining to quantum coherence between parity sectors is completely destroyed.

Now, let us numerically test the applicability of (155). Similarly to the standard microcanonical ensemble [1], also in the GME we will assume that all states within a certain energy window ΔE centered at the average energy, $[\langle E\rangle - \Delta E, \langle E\rangle + \Delta E]$,

are equally populated. Here, $\langle E\rangle = \sum_n \sum_{k,=\pm} |c_{n,k}|^2 E_{n,k}(\lambda_f)$ is the average energy of the quenched state in the final Hamiltonian. The microcanonical energy window ΔE is composed of the $2N+1$ levels of positive parity around the target energy $\langle E\rangle$ and the $2N+1$ levels of negative parity. Our energy window is chosen as $\Delta E = 2\sigma$ where $\sigma^2 = \sum_n \sum_{k,=\pm} |c_{n,k}|^2 (E_{n,k}(\lambda_f) - \langle E\rangle)^2$. Essentially, we compute the number of parity doublets (regardless of whether or not the corresponding energies $E_{n,\pm}$ are degenerate) below and above E_c in the corresponding energy window, N_- and N_+, and through Eqs. (157, 158, 159), we calculate the parameters p, c, k.

Consider a state with eigenvalue $E_{n,k} \leq E_c$ within the microcanonical window. Then, in the subspace $\{|E_{n,+}\rangle, |E_{n,-}\rangle\}$ the GME takes the matrix form

$$\hat{\rho}_n(E_{n,k} \leq E_c) = \frac{1}{2} \begin{pmatrix} 1+p & c-ik \\ c+ik & 1-p \end{pmatrix}. \tag{160}$$

Because $\mathrm{Tr}\,[\hat{\rho}_n^2(E_{n,k} \leq E_c)] = (1+p^2+c^2+k^2)/2$, not all conceivable states make physical sense, only those such that $p^2+c^2+k^2 \leq 1$ do.

On the other hand, for a state $E_{n,k} > E_c$ falling within the GME energy window, we have

$$\hat{\rho}_n(E_{n,k} > E_c) = \frac{1}{2} \begin{pmatrix} 1+p & 0 \\ 0 & 1-p \end{pmatrix}. \tag{161}$$

Observe that Eq. (161) is a diagonal matrix in the parity eigenbasis $\{|E_{n,+}\rangle, |E_{n,-}\rangle\}$.

Finally, for states lying outside the GME energy window, say $E_{n,k} \notin [\langle E\rangle - \Delta E, \langle E\rangle + \Delta E]$, the associated block is simply the null matrix, $\hat{\rho}_n = 0 \times \mathbb{I}_2$.

If, instead of just one eigenspace, we consider the entire Hamiltonian-parity eigenbasis, $\{|E_{1,+}\rangle, |E_{1,+}\rangle, \ldots, E_{N,+}, E_{N,-}\}$, the full GME is represented by a block-diagonal matrix where the blocks (160) and (161) are located in the diagonal: $\hat{\rho}_{\mathrm{GME}} = \mathrm{diag}\,(\{\hat{\rho}_n\}_n)/Z$, where the normalization constant is $Z = N_+ + N_-$. If the energy of the quenched state overlaps the ESQPT, the GME is built from the contribution of states both above and below $E = E_c$.

After the GME has been built, we are ready to compare the long-time average of physically relevant observables, $\hat{O}$, with its equilibrium predictions,

$$\langle \hat{O}\rangle_{\mathrm{GME}} = \mathrm{Tr}\,[\hat{\rho}_{\mathrm{GME}}\hat{O}]. \tag{162}$$

We have computed the infinite-time average of observables in states taken out of equilibrium by a quantum quench. After the quench, we let the wave function relax during 10^3 μs in the final Hamiltonian. For convenience, in our protocols the equilibrium state is always of the type Eq. (148) with $\alpha = 1/2$ and $\phi = 0$. To access

different spectral regions of the final Hamiltonian, we vary the initial λ_i, and the final control parameter is always $\lambda_f = 1.75$. If the interested reader would like to see a case with $\phi \neq 0$, this can be found in our paper [327].

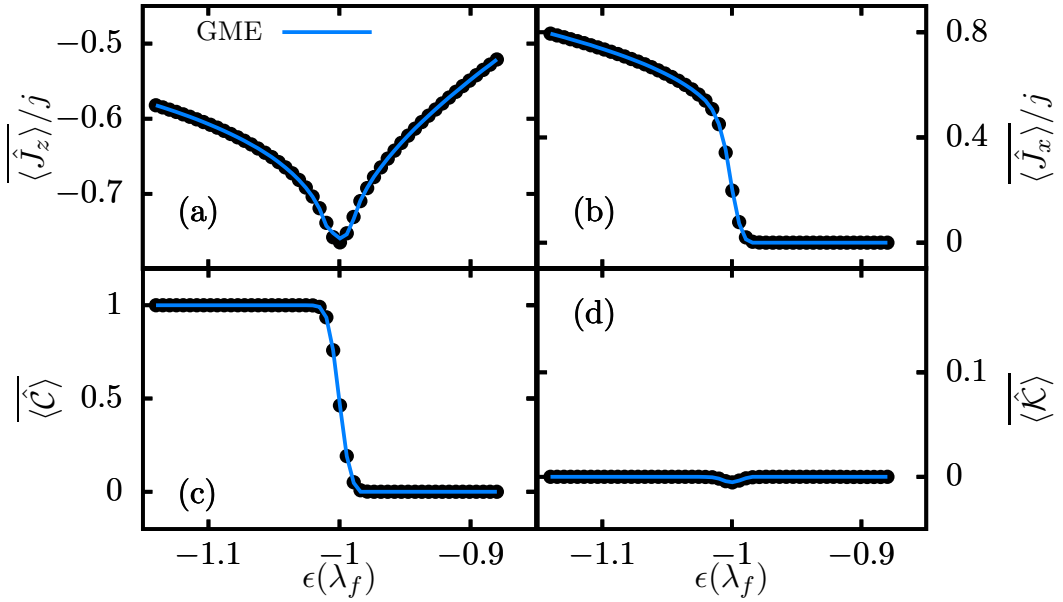

Figure 19: Equilibrium values (long-time averages) of representative observables after a quantum quench $\lambda_i \to \lambda_f = 1.75$ as a function of the average energy in the final Hamiltonian, $\epsilon(\lambda_f)$, for the LMG model (73). System size fixed to $j = 6400$. The initial state is always of the form (148) with $\alpha = 1/2$ and $\phi = 0$. Black points represent the exact averages while the GME prediction, (162), is shown with blue lines.

The long-time averages are shown with black circles in Fig. 19 for $\hat{J}_z$, $\hat{J}_x$, $\hat{\mathcal{C}}$ and $\hat{\mathcal{K}}$ as a function of the final energy within the range $-1.1 \lesssim \epsilon(\lambda_f) \lesssim -0.9$, crossing the ESQPT at $\epsilon_c = -1$. Precursors of non-analytic behavior the ESQPT at ϵ_c can be seen in all observables. This non-analytic point is transferred directly from the level density to the expectation values of observables in systems with a single classical degree of freedom [265], although in systems with higher f they may not appear so clearly. So, for example, in Fig. 19(a) there is quite a marked minimum in the long-time average of $\hat{J}_z$. The behavior of the order parameter is shown in Fig. 19(b): $\hat{J}_x$ acquires a finite value in the symmetry-breaking phase, and then it goes to zero after crossing the ESQPT. As j increases, these precursors become more sharp towards actual non-analytic behavior [cf. Fig. 20]. It is therefore clear why $\hat{J}_x$ can be taken as the order parameter of DPTs-I, $\overline{m} = \overline{\langle \hat{J}_x \rangle}$, occurring at the ESQPT in the infinite-size limit. Finally, the behavior of the operators $\hat{\mathcal{C}}$ and $\hat{\mathcal{K}}$ is shown in Fig. 19(c,d). Due to the choice of initial state with $\alpha = 1/2$ and $\phi = 0$, the equilibrium values of these operators for $E < E_c$ are $\langle \hat{\mathcal{C}} \rangle = 1$ and

$\langle \hat{\mathcal{K}} \rangle = 0$. These values remain constant if the quench is such that $E \lesssim E_c$. For $E > E_c$, these operators are no longer constant, but their infinite-time averages vanish completely, which explains why there is also no variation in these long-time averages when $E > E_c$. Close to $E = E_c$, the precursors of a phase transition between these two values can be seen in the figure. If reader is interested in a case where $\overline{\langle \hat{\mathcal{K}} \rangle} \neq 0$ in the symmetry-breaking phase $E < E_c$, we refer them to our paper [327]. The equilibrium predictions of the GME are shown with a solid line. Anyhow, the long-time averages and the GME agree excellently.

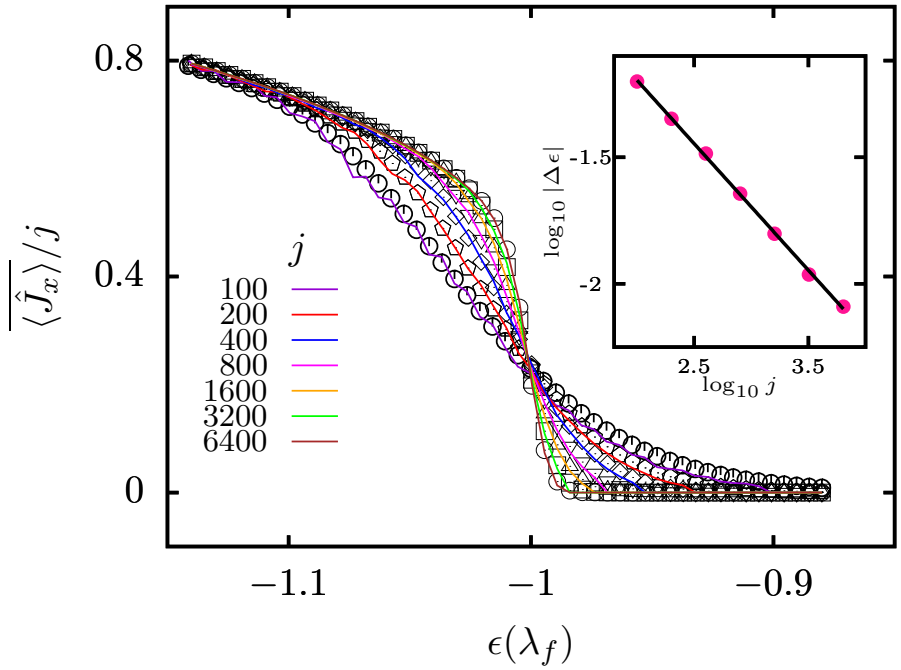

Figure 20: Long-time average of $\hat{J}_x$ after a quench $\lambda_i \to \lambda_f = 1.75$ represented as a function of the average final energy of the quenched state, $\epsilon(\lambda_f)$, for different system sizes. In all cases, the initial state is of the form (148) with $\alpha = 1/2$ and $\phi = 0$. The exact numerical averages are represented with points of different shapes depending on system size, while color lines show the GME prediction in (155). The finite-size scaling of $\Delta\epsilon = \epsilon_c(j) - \epsilon_c(\infty)$, with a bound $\gamma = 1/20$, is shown in the inset, which reveals a power-law behavior $|\Delta\epsilon| \sim 1/\sqrt{j}$.

To end this section, we shall specially treat the order parameter of the DPT-I, $\overline{\langle \hat{J}_x \rangle}$. In Fig. 20 we present our finite-size scaling analysis of its equilibration value across the transition. This figure clearly depicts how the smooth precursors of the transition acquire an abrupt character as j increases. Let us mention that although the agreement with the GME is generally good for all j, it does improve as j increases because the GME depends on operators that become strictly constant only in the TL. All finite-j curves intersect around $\epsilon \approx \epsilon_c = -1$, suggesting DPT-

I criticality in the TL. The finite-j precursor of the critical energy characterizing the DPT-I, $\epsilon_c(j)$, can be computed by calculating the last value of $\epsilon(\lambda_f)$ such that $\overline{\langle \hat{J}_x \rangle} > \gamma$, where γ is some arbitrary bound[2]. Here, we choose $\gamma = 1/20$. In the inset of Fig. 20 the difference between this precursor and the ESQPT critical energy in the TL, $\epsilon_c(\infty) = -1$, $|\Delta\epsilon| = |\epsilon_c(j) - \epsilon_c(\infty)|$, is represented as a function of j. We find a neat power-law behavior $|\Delta\epsilon| \sim 1/\sqrt{j}$; precisely, this is $|\Delta\epsilon| \sim 10^a j^b$ with $a = -0.195664$ and $b = -0.500194$. These results provide solid support for the DPT-I occurring *exactly* at $E = E_c$ in the TL.

Information erasure upon crossing an ESQPT

Contrary to the previous section, where an initial state was quenched to a final, *fixed* λ_f, here we are interested in the dynamics of an initial state undergoing an actual time-dependent slow process after a quench, where $\lambda_f = \lambda_f(t)$ varies smoothly. The process consists of the following steps:

(i) Our initial state is of the type in Eq. (148) with an initial control parameter $\lambda_i > \lambda_c$.

(ii) We suddenly quench the state, $\lambda_i \to \lambda_f$.

(iii) After the quench, the dynamics is governed by the time-dependent Schrödinger equation, $i\frac{\mathrm{d}|\Psi(\lambda(t))\rangle}{\mathrm{d}t} = \hat{H}(\lambda(t))\,|\Psi(\lambda(t))\rangle$, with $\lambda(t=0) = \lambda_f$, where $\lambda(t)$ is a slowly-varying function[3].

Using the $\hat{J}_z$ eigenbasis $\{|m\rangle\}_{m=-j}^{j}$, the instantaneous wave function can be formally written as $|\Psi_t(\lambda(t))\rangle = \sum_{m=-j}^{j} \varphi_m(t)\,|m\rangle$. In this basis, we can numerically solve the following system of $2j+1$ coupled differential equations:

$$
\begin{aligned}
i\frac{\mathrm{d}}{\mathrm{d}t}\varphi_m(t) = \varphi_m(t)\left[hm - \frac{\lambda(t)}{2N}(j(j+1)-m^2)\right]\Bigg(\\
- \frac{\lambda(t)}{4N}\left[\varphi_{m+2}(t)\sqrt{j(j+1)-m(m+1)}\sqrt{j(j+1)-(m+2)(m+1)}\right] \\
- \frac{\lambda(t)}{4N}\left[\varphi_{m-2}(t)\sqrt{j(j+1)-m(m-1)}\sqrt{j(j+1)-(m-2)(m-1)}\right],
\end{aligned}
\tag{163}
$$

for all $m = -j, ..., j$, and where $N = 2j$ is the number of spin-1/2 particles. The solution of this system of equations at time t is then $\{\varphi_m(t)\}_{m=-j}^{j}$. Our goal is to simulate a two-stage forward-backward process between $\lambda(t=0) = \lambda_0$ and

2 The point is that it does not matter what γ is as long as it is sufficiently small.

3 The goal of step (ii) is to excite the initial state so that the subsequent slow evolution of step (iii) drives it through the ESQPT. If step (ii) is skipped, then at most one may be able to drive the initial wave function through the QPT, which is not our focus.

$\lambda(t=\tau)=\lambda_1$, with τ denoting the time duration of each stage of the protocol. For the control parameter $\lambda(t)$, we choose the linear function

$$\lambda(t)=\begin{cases}\lambda_0+\Delta\lambda\frac{t}{\tau}, & 0\leq t\leq\tau\\ 2\lambda_1-\lambda_0-\Delta\lambda\frac{t}{\tau}, & \tau\leq t\leq 2\tau\end{cases} \tag{164}$$

where $\Delta\lambda=\lambda_1-\lambda_0$. In the case of a perfectly adiabatic process, the rapidity is $\tau\to\infty$; however, finite values of τ that are sufficiently high can already get close enough to adiabaticity. We fix $\tau=500$ μs, which we find suitable for our purposes.

Our initial states, all of the form Eq. (148), have $\lambda_i=3$ and $\alpha=3/4$, while we allow ϕ to take different values. These initial parity-broken states can be fully localized within one of the classical wells or in a quantum superposition of them depending on ϕ. The quench is $\lambda_0\equiv\lambda_f=1.75$, and the time-dependent Schrödinger equation is solved from λ_0 to $\lambda_1=0.5$, and then from λ_1 back to λ_0.

In Fig. 21 we represent the average energy of the wave function along the forward-backward process. The protocol drives the state across the ESQPT twice; first during the forward stage, and then during the backward stage (horizontal dashed line at $\epsilon_c=-1$). Because τ is sufficiently high, the evolution is close to adiabatic and for this reason the energy is a symmetric function of time. Another consequence of this is that the average energy of the initial and final states coincide: $\langle\Psi(0)|\,\hat{H}(\lambda(0))\,|\Psi(0)\rangle=\langle\Psi(2\tau)|\,\hat{H}(\lambda(2\tau))\,|\Psi(2\tau)\rangle$, meaning that basically no excitations occur. The predictions of the GME at each time instant are represented with a blue line, showing excellent agreement with the real time evolution (black).

We have monitored the evolution of relevant observables as the wave function follows this protocol, which are shown in Fig. 22(a-d) for different initial conditions (the only change is in ϕ). For $\langle\hat{J}_z(t)\rangle$ we only consider one initial state with $\phi=0$, because the time evolution of this observable does not show any dependence on ϕ. The time evolution of $\hat{J}_z$ would apparently be compatible with a reversible process: oscillations aside, its mean values at the beginning and at the end of the protocol are basically the same. However, panels (b-d), which depict the dynamics of $\hat{J}_x$, $\hat{\mathcal{C}}$, and $\hat{\mathcal{K}}$, show this is not the case. All of these observables either become zero ($\hat{J}_x$) or fluctuate around zero ($\hat{\mathcal{C}}$, $\hat{\mathcal{K}}$) after some time, and this coincides with the times when the wave function is crossing the ESQPT [see Fig. 21]. This is a manifestation of the DPT-I. The forward protocol ends at $t=\tau$, and then the backward protocol drives the system until $t=2\tau$. Remarkably, although the initial and final average energies are the same [cf. Fig. 21], the initial and final values of $\hat{J}_x$, $\hat{\mathcal{C}}$, and $\hat{\mathcal{K}}$ are nothing alike. This is telling us that the process is really *irreversible*: we have lost information contained in the initial state

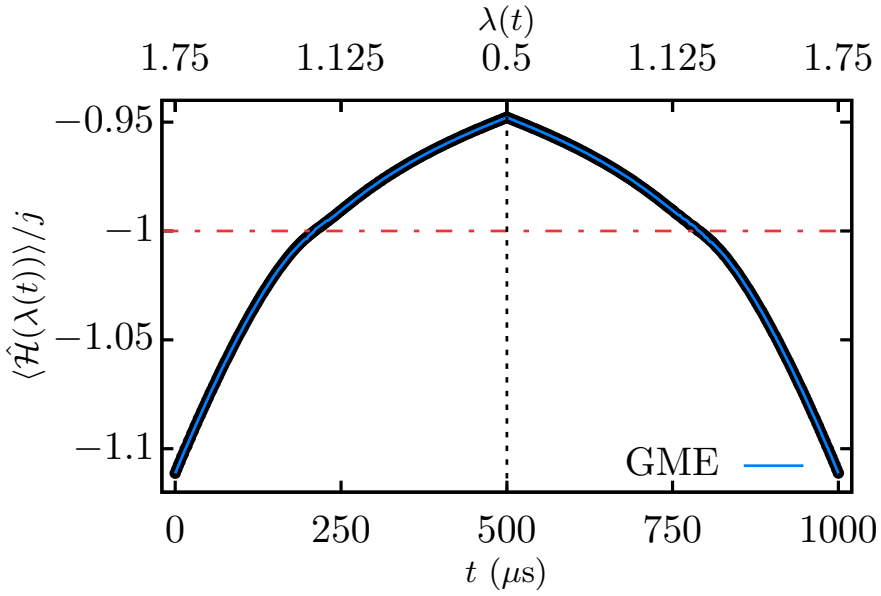

Figure 21: Average energy of the initial state evolving in time according to the Schrödinger equation, (163). For visual clarity, the forward and backward processes are separated by a dashed vertical line. The GME expectation for the average energy, (155), is marked by the blue line. The ESQPT critical energy is represented with a horizontal red dotted-dashed line. The driving parameter $\lambda(t)$ follows (164) with $\tau = 500$. System size is $j = 1000$.

upon crossing the ESQPT criticality. In order to interpret this result, let us recall that crossing the ESQPT means reaching the symmetry-restored phase of the LMG model, and in that case the equilibrium density matrix $\hat{\rho}_{\text{eq}} = \lim_{t\to\infty} \frac{1}{t}\int_0^t \mathrm{d}t'\, \hat{\rho}(t')$, with $\hat{\rho}(t) = |\Psi(t)\rangle\langle\Psi(t)|$, becomes diagonal and the off-diagonal coherence is destroyed. Because the driving time τ is larger than the classical time t_{SC}, in essence related to the typical time where diffusion of the wave packet occurs, the real $\hat{\rho}(t)$ remains very close to the effective $\hat{\rho}_{\text{eq}}$. The information of the initial state cannot be recovered simply by crossing the ESQPT again in the backward process. We should note that because $[\hat{\Pi}, \hat{H}(\lambda)] = 0$, $\forall\lambda$, the expectation values of operators such as $\hat{\Pi}$ are not affected by this mechanism; however, it does affect $\langle\hat{\mathcal{C}}\rangle$, $\langle\hat{\mathcal{K}}\rangle$ and, in general, all physical magnitudes whose equilibrium values depend on $\hat{\mathcal{C}}$ and $\hat{\mathcal{K}}$, such as $\hat{J}_x$ [325]. To quantify this further, in Table 3 we have gathered the values of the GME parameters p, c, k at the beginning and the end of the entire protocol. Even though p, which comes from $\hat{\Pi}$, remains constant, the parameters $c \propto \langle\hat{\mathcal{C}}\rangle$ and $k \propto \langle\hat{\mathcal{K}}\rangle$ change completely, confirming the irreversible nature of the protocol. In this table we also report the value of the von Neumann entropy $S = -\operatorname{Tr}[\hat{\rho}_n \log \hat{\rho}_n]$ of each of the 2×2 blocks of the GME. As we can see, the entropy grows from the

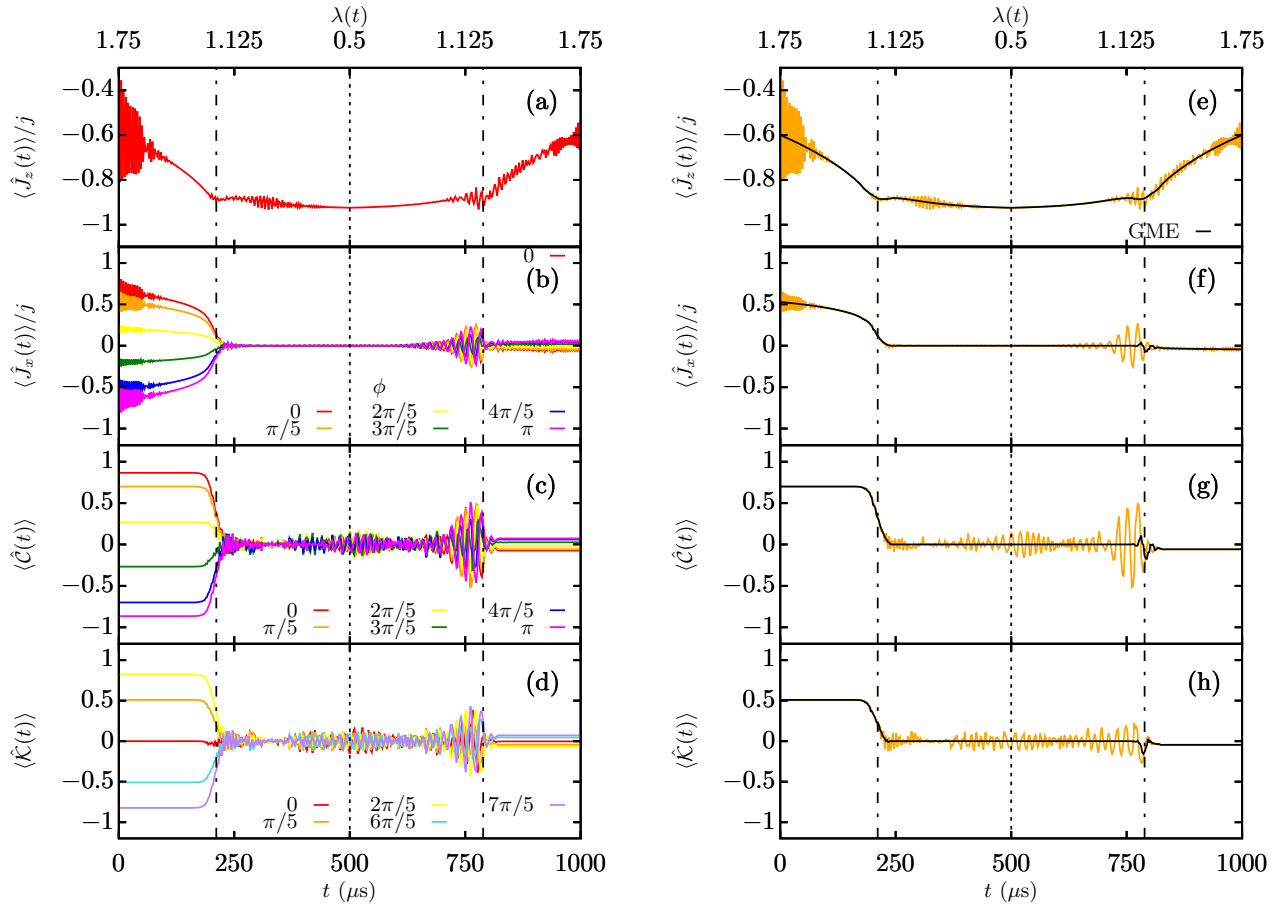

Figure 22: Time expectation value of relevant observables after a quantum quench $\lambda_i = 3 \to \lambda_f = 1.75$, with an initial state of the type in (148) with $\alpha = 3/4$ and different values of ϕ (color lines). System size is $j = 1000$. The wave function evolves according to the time-dependent Schrödinger equation (163) with a driving parameter $\lambda(t)$ defined in (164). The duration of the forward and backward processes is $\tau = 500$ each. For clarity, the forward and backward protocols are separated by a vertical dashed line at $\tau = 500$ in all panels. The time where the time-evolving wave function crosses the ESQPT are marked by dotted-dashed lines (two in each panel). In (e-h) the parameters of the initial state are $\alpha = 3/4$ and $\phi = \pi/5$, with the GME prediction (155) being shown with a black solid line.

initial time to the final time of the protocol. This is a clear manifestation of the loss of information.

Summarizing, the DPT-I is connected with a mechanism whereby some of the information contained in the initial condition is destroyed. A detailed discussion on the origin of this mechanism in a similar model can be found in Ref. [332].

Time	p	c	k	S
$t=0$	0.5	0.7006	0.5090	2.3×10^{-4}
$t=2\tau$	0.5	-0.0576	-0.0458	0.5594

Table 3: Values of p, c, k and the von Neumann entropy S at the beginning ($t=0$) and end ($t=2\tau$) of the adiabatic process in Fig. 22(e-h).

Before we end this section, we would like to briefly comment on the suitability of the GME to describe this kind of time-dependent protocols. Along this protocol we take the expectation value of the time-evolving wave function, but this state is never really allowed to relax during long times. For this reason, in our results we can clearly observe the effects of short-time dynamics, which is highly non-universal. Although an effective equilibrium state may not be actually reached for these short times, we have seen that the GME still does a good job at estimating the *average value* around which the wave function fluctuates. Obviously, the exact form of these fluctuations cannot be described by an equilibrium ensemble such as the GME. In Fig. 22(e-h) we pick an initial state with $\alpha=3/4$ and $\phi=\pi/5$, and represent analogous results to those in Fig. 22(a-d). On top of the numerical results, the GME expectation is represented with a black line. As we have discussed, the average values of the dynamics are still excellently described by the GME.

3.3.3 Cusps in return probabilities: dynamical phase transitions of the type II

This section is devoted to the analysis of DPTs-II in collective systems exhibiting an ESQPT. We provide analytical results, valid in the TL, showing that the main mechanism for DPTs-II previously proposed in [394] is only allowed when the energy of the quenched state is above the critical energy of the ESQPT, $E>E_c$ (symmetric phase), while it is forbidden if $E<E_c$ (symmetry-broken phase). Our analytical calculations are accompanied by numerical results on the LMG model.

Analytical restrictions for DPTs-II

As advanced in Sec. 1.3.3, to analyze DPTs-II one usually considers as an initial state $|\Psi_0(\lambda_i)\rangle$ a general superposition of the degenerate ground-state in the degenerate phase (where the $\mathbb{Z}_2$ symmetry may be broken), in our case $E<E_c$. Then, a quench $\lambda_i>\lambda_c\to\lambda_f$ is performed, and the state is allowed to evolve in time under the new Hamiltonian, $\Psi_t(\lambda_f)$. In the case of broken-symmetry models, DPTs-II are defined through the non-analytic times in the PPRP [394] given in (78).

We recall that the corresponding rate function is given by (80). According to [394], [413], each of the terms in the PPRP, $\mathcal{L}_{\pm}(t)$, follows the law in (81). Therefore, we can write

$$r_N(t) = \Omega_+(t) - \frac{1}{N}\ln\left[1 + e^{-N(\Omega_-(t)-\Omega_+(t))}\right] \tag{165}$$

Let us consider the second term on the right-hand side of this equation. (i) if $\Omega_-(t) > \Omega_+(t)$, then $\lim_{N\to\infty} -\frac{1}{N}\ln[1 + e^{-N(\Omega_-(t)-\Omega_+(t))}] = 0$, while (ii) if $\Omega_+(t) > \Omega_-(t)$, then $\lim_{N\to\infty} -\frac{1}{N}\ln[1 + e^{-N(\Omega_-(t)-\Omega_+(t))}] = \Omega_-(t) - \Omega_+(t)$. In other words, in the TL one has

$$r(t) \equiv \lim_{N\to\infty} r_N(t) = \begin{cases} \Omega_+(t), & \Omega_-(t) > \Omega_+(t) \\ \Omega_-(t), & \Omega_-(t) < \Omega_+(t). \end{cases} \tag{166}$$

The value of time, t_*, such that the functions $\Omega_{\pm}(t)$ intersect define a singular point through the condition $\Omega_+(t_*) = \Omega_-(t_*)$. We expect $r_N(t)$ to remain an analytic function analytic at $t = t_*$ in finite-N systems, only fully realizing a non-analyticity in the large-N limit. From Eq. (166) it is obvious that the nth derivative of $r(t)$ is $\mathrm{d}^n r(t)/\mathrm{d}t^n = \mathrm{d}^n\Omega_{\min}(t)/\mathrm{d}t^n$ where $\Omega_{\min}(t) \equiv \min\{\Omega_+(t), \Omega_-(t)\}$. This way, one may be temped to define the *order* of a DPT-II through the value of n for which $\mathrm{d}^n r(t)/\mathrm{d}t^n$ becomes discontinuous.

In this section we provide analytical restrictions regarding the kind of spectral phases where the above mechanism can be said to be responsible for DPTs-II. Let us consider an initial state of the form Eq. (148) at λ_i, and quench it to λ_f. Because $\hat{\Pi}$ is an exact symmetry of the Hamiltonian, we can expand the initial eigenvectors of $\hat{H}(\lambda_i)$ as a combination of the final eigenvectors of $\hat{H}(\lambda_f)$ *of the same parity*. Thus, for example, the broken-symmetry ground-state at λ_i can be rewritten as

$$|E_{0,\pm}(\lambda_i)\rangle = \sum_n c_{n,\pm}\ E_{n,\pm}(\lambda_f)\ . \tag{167}$$

The same strategy can be used to rewrite the quenched state as a combination of eigenstates of the final Hamiltonian:

$$\begin{aligned} \Psi_t(\lambda_f) \ &= \sqrt{\alpha}\sum_n c_{n,+}e^{-iE_{n,+}(\lambda_f)t}\ E_{n,+}(\lambda_f) \\ &+ e^{i\phi}\sqrt{1-\alpha}\sum_n c_{n,-}e^{-iE_{n,-}(\lambda_f)t}\ E_{n,-}(\lambda_f)\ . \end{aligned} \tag{168}$$

By virtue of parity conservation, the different terms of the PPRP are

$$\begin{aligned}\mathcal{L}_+(t) = &\quad E_{0,+}(\lambda_i)\ \Psi_t(\lambda_f)\ \ ^2 \\ &= \sqrt{\alpha}\sum_n c_{n,+}e^{-iE_{n,+}(\lambda_f)t}\ \ E_{0,+}(\lambda_i)\ E_{n,+}(\lambda_f)\ \ ^2 \\ &= \alpha\ \sum_n \Big(c_{n,+}|^2 e^{-iE_{n,+}(\lambda_f)t}\ \ ^2 ,\end{aligned} \tag{169}$$

and

$$\mathcal{L}_-(t) = (1-\alpha)\ \sum_n \Big(c_{n,-}|^2 e^{-iE_{n,-}(\lambda_f)t}\ \ ^2 . \tag{170}$$

For convenience, let us define

$$f_\pm(t) \equiv \sum_n \Big(c_{n,\pm}|^2 e^{-iE_{n,\pm}(\lambda_f)t}. \tag{171}$$

In that case, the PPRP components are

$$\mathcal{L}_+(t) = \alpha|f_+(t)|^2, \quad \mathcal{L}_-(t) = (1-\alpha)|f_-(t)|^2. \tag{172}$$

The main result of this section is the following. Its consequences will be discussed later on.

Result.– If $E < E_c$ (in a symmetry-breaking phase), then $f_+(t) = f_-(t)$, $\forall t$.

Let us prove this result. First, in the symmetry-breaking phase pairs of levels of opposite parity are exactly degenerate in the $N \to \infty$ limit, $E_{n,+}(\lambda_f) = E_{n,-}(\lambda_f)$ for all n such that $E_{n,\pm} < E_c$ [325]. Therefore, oscillatory parts in $f_\pm(t)$ are the same. Thus, we only need to focus on the $c_{n,\pm}$.

Because $\hat{\Pi}$ is an exact conserved quantity, $E_{n,+}(\lambda_f)\ E_{0,-}(\lambda_i)\ = 0$ for all n, as these eigenstates belong to different parity sectors. Therefore,

$$c_{n,+} = \ E_{n,+}(\lambda_f)\ E_{0,+}(\lambda_i)\ \ . \tag{173}$$

For $E < E_c$ (in the $N \to \infty$ limit), we know that $\hat{\mathcal{C}}$ becomes a conserved quantity. Yet it cannot be diagonalized in the same basis as parity as $\hat{\mathcal{C}}$ inverts the parity of any Fock state [325],

$$\hat{\mathcal{C}}\,|E_{0,\pm}(\lambda_i)\rangle = |E_{0,\mp}(\lambda_i)\rangle\,. \tag{174}$$

Also, because $\hat{\mathcal{C}}$ is a unitary operator, $\hat{\mathcal{C}}^\dagger\hat{\mathcal{C}} = 1$. Then,

$$\begin{aligned}|c_{n,+}| = &\quad E_{n,+}(\lambda_f)\ E_{0,+}(\lambda_i) \\ &= \quad E_{n,-}(\lambda_f)\ \hat{\mathcal{C}}^\dagger\hat{\mathcal{C}}\,|E_{0,-}(\lambda_i)\rangle \\ &= \quad E_{n,-}(\lambda_f)\ E_{0,-}(\lambda_i)\quad = |c_{n,-}|\,.\end{aligned} \tag{175}$$

It follows that $f_+(t) = f_-(t)$ in the TL, if the population coefficients are only non-zero in the spectral phase defined by $E < E_c$.

Two physically relevant consequences follow from this formal result.

Consequence 1.– The constancy of $\hat{\mathcal{C}}$ if $E < E_c$ implies $\Omega_+(t)$ and $\Omega_-(t)$ cannot intersect. Therefore *the mechanism for DPTs-II proposed in [394] is forbidden for quenches below the critical energy*, $E < E_c$. It is only allowed if the quench leads the state to the symmetry-restored phase, $E > E_c$.

The proof follows trivially. Indeed, let us assume that $f_+(t) = f_-(t)$ for all t; then, if $\alpha \in (0, 1)$, Eq. (172) implies

$$\frac{\mathcal{L}_+(t)}{\mathcal{L}_-(t)} = \frac{\alpha}{1-\alpha}, \quad \forall t. \tag{176}$$

Then, depending on α, we have:

- If $\alpha = 1/2$, then $\mathcal{L}_+(t) = \mathcal{L}_-(t)$ for all t, which implies that $\Omega_+(t) = \Omega_-(t)$ for all t.
- If $0 < \alpha < 1/2$, Eq. (176) implies $\mathcal{L}_+(t) < \mathcal{L}_-(t)$ for all t, and from Eq. (81) this implies that $\Omega_+(t) > \Omega_-(t)$ for all t.
- If $1/2 < \alpha < 1$, then $\Omega_-(t) > \Omega_+(t)$.
- In the limit cases where $\alpha = 1$ or $\alpha = 0$, we have that either $\mathcal{L}_+(t) = |f(t)|^2 \geq 0 = \mathcal{L}_-(t)$ or $\mathcal{L}_-(t) = |f(t)|^2 \geq 0 = \mathcal{L}_+(t)$.

This list exhausts all possibilities, and in none of them a crossing can take place in the functions $\Omega_\pm(t)$. In summary, in a symmetry-breaking phase $E < E_c$ the physically observed cusps in the rate function of the PPRP is necessarily due to a different mechanism than that proposed in [394].

Up to this point, our focus has been on DPTs-II appearing on the PPRP of Ref. [394]. What is about the standard survival probability, SP(t)? We recall that it is given by (76).This quantity is also a measure of the degree of 'memory' that the time-evolved state $\Psi_t(\lambda_f)$ keeps about its initial self, $|\Psi_0(\lambda_i)\rangle$, but here there are no projections onto individual parity subspaces. In principle, SP(t) [Eq. (76)] should be different from $\mathcal{L}(t)$ [Eq. (78)], because $\mathcal{L}(t)$ does not keep track of the quantum interference between eigenstates of opposite parity. Is this true? When is it true?

We again start with an initial state Eq. (148) with $\lambda_i > \lambda_c$, and do a quench, $\lambda_i \to \lambda_f$. The survival probability Eq. (76) is then

$$\begin{aligned} \mathrm{SP}(t) = \; & \alpha \sum_n \Big(c_{n,+} e^{-iE_{n,+}(\lambda_f)t} \;\; E_{0,+}(\lambda_i) \;\; E_{n,+}(\lambda_f) \\ & + (1-\alpha) \sum_n \Big(c_{n,-} e^{-iE_{n,-}(\lambda_f)t} \;\; E_{0,-}(\lambda_i) \;\; E_{n,-}(\lambda_f) \Big)^2 . \end{aligned} \tag{177}$$

Using Eq. (167) and the definition of $f_{\pm}(t)$ in Eq. (171), this is

$$\mathrm{SP}(t) = |\alpha f_+(t) + (1-\alpha) f_-(t)|^2 . \tag{178}$$

From this expression, two kinds of behaviors emerge:

(i) If $E < E_c$ (symmetry-breaking phase), then, $f_+(t) = f_-(t) \equiv f(t)$ for all t, implying

$$\mathrm{SP}(t) = |f(t)|^2 = \mathcal{L}_+(t) + \mathcal{L}_-(t) = \mathcal{L}(t). \tag{179}$$

So it turns out that Eq. (78) and Eq. (76) coincide *exactly* if $E < E_c$ and *in the TL*.

(ii) If $E > E_c$ (symmetry-restored phase), then, in general, $f_-(t) \neq f_+(t)$. This implies that

$$\begin{aligned} \mathrm{SP}(t) &= \alpha^2 |f_+(t)|^2 + (1-\alpha)^2 |f_-(t)|^2 \\ &\quad + \alpha(1-\alpha)\left[f_+(t) f_-^*(t) + f_+^*(t) f_-(t)\right] \\ &\neq \alpha |f_+(t)|^2 + (1-\alpha)|f_-(t)|^2 = \mathcal{L}(t). \end{aligned} \tag{180}$$

So in the general case, Eq. (78) and Eq. (76) are different functions in this case. But there are some exceptions: if $\alpha = 0$ or $\alpha = 1$, then obviously $\mathrm{SP}(t) = \mathcal{L}(t)$, as in this case the initial state Eq. (148) has either positive or negative parity, and thus no parity sector interference is possible to begin with.

Thus we have arrived at the second main consequence of the analytical results in this section:

Consequence 2.– If $E < E_c$, the PPRP, $\mathcal{L}(t)$ [Eq. (78)], and the survival probability, $\mathrm{SP}(t)$ [Eq. (76)], coincide in the TL. If $E > E_c$, these quantities are, in general, different.

Numerical analysis of the rate functions

Having presented our analytical results concerning DPTs-II, here we numerically study the rate function of the PPRP, $\mathcal{L}(t)$ [Eq. (78)], that of the survival probability, $\mathrm{SP}(t)$ [Eq. (76)]. We consider an initial state such as Eq. (148) with $\alpha = 1/2$ and $\phi = 0$, at an initial Hamiltonian defined by $\lambda_i > \lambda_c$. This state is taken out of equilibrium through a quantum quench $\lambda_i \to \lambda_f$ where $\lambda_f = 1.6$. Therefore, the average energy of the quenched state simply depends on λ_i. In order to observe better the non-analytic nature of the rate function $r_N(t)$, we also calculate its first derivative, $\mathrm{d}r_N(t)/\mathrm{d}t$. We numerically work with 500 significant figures; this is because $r_N(t)$ drops below the standard precision limit for a relatively small number of particles. In Fig. 23(a-c) we report our results for $r_N(t)$, while Fig. 23(d-f) shows the first time derivative of this quantity. The system size parameter, $j = N/2$, is

indicated in all panels. Similarly to the PPRP, whose rate function is given by Eq. (80), the rate function of the survival probability is (77) and our numerical results are in Fig. 24. In both figures, the rows are arranged according to the final energy of the quenched state: $\epsilon = -1.07 < \epsilon_c$ (first row), $\epsilon_c = -1$ (second row), and $\epsilon = -0.92 > \epsilon_c$ (third row). This corresponds to different spectral phases of the model: symmetry-breaking phase (first row), right at the ESQPT (second row), and symmetry-restored phase (third row).

Firstly, let us focus on Fig. 23(a-b) and Fig. 24(a-b), for $\epsilon < \epsilon_c$. The rate function of the PPRP and the survival probability essentially coincide, in agreement with our analytical arguments. Basically, this is due to the conservation of $\hat{\mathcal{C}}$ in the TL in this spectral region. The small differences between these rate functions for small system sizes are to be expected: the conservation of the $\hat{\mathcal{C}}$ operator is only fully realized in the TL [325]. The functions $r_N(t)$ and $\widetilde{r}_N(t)$ show a set of maxima, but these maxima seem to be of different nature. Indeed, the first maximum, occurring at $t \approx 3$, seems to be quite smooth with no apparent non-analytic behavior. Despite this, the remaining maxima appear to feature kinks which become sharper with j. Although these kinks seem to suggest non-analytic points in the TL, we have analytically shown that DPTs-II cannot happen in the symmetry-breaking phase. Accordingly, the corresponding time derivatives, in Figs. 23(d) and 24(d), do not exhibit any clear finite-size scaling to the TL (black arrows emphasize these apparent kinks and their derivatives in the figures). It should be noted that this DPT-II phase has been dubbed 'anomalous' (see [371] for the origin of this term) because all kinks in $r_N(t)$ and $\widetilde{r}_N(t)$ only occur after the first minimum of these functions. The results in [371] seem to suggest that number of smooth local maxima before the kinks appear depends on the average energy of the quenched state; dynamics away from the critical energy of the ESQPT appears to produce a greater number of smooth maxima.

Secondly, let us consider the opposite spectral region, the symmetry-restored phase with $\epsilon > \epsilon_c$. The rate functions in Figs. 23(c) and 24(c) are completely different. According to our analytical results, the PPRP and the survival probability are different mathematical functions in this region. In the case of the kinks of $r_N(t)$, the time derivatives in Fig. 23(f) reveal a clear finite-size scaling to the TL, which would suggest the presence of a DPT-II in the infinite-size limit: the first time derivative of $r_N(t)$, $\lim_{N\to\infty} \mathrm{d}r_N/\mathrm{d}t$, seems to be discontinuous at a given critical time, $t = t_*$, in the TL. Yet, the time derivatives of the kinks of $\widetilde{r}_N(t)$ in Fig. 24(c,f) are very similar to those of the case $\epsilon < \epsilon_c$ [Fig. 24(a,d)]: $\mathrm{d}\widetilde{r}_N(t)/\mathrm{d}t$ does not show a clean scaling pattern when j increases. This DPT-II phase has been dubbed 'regular' in [371] and its defining feature is that the kinks appear before the first minimum in $r_N(t)$ or $\widetilde{r}_N(t)$.

Finally, we have also considered the special case where the quench leads the initial state right to the ESQPT criticality, $\epsilon = \epsilon_c$. Figures 23(b) and 24(b) illustrate how $r_N(t)$ and $\widetilde{r}_N(t)$ are also different functions here. We emphasize the most striking difference between $r_N(t)$ and $\widetilde{r}_N(t)$: $\mathrm{d}r_N/\mathrm{d}t$ seems to show a discontinuity when $j \to \infty$ around $t_* \approx 3.75$ [Fig. 23(e)], yet in $\mathrm{d}\widetilde{r}_N(t)/\mathrm{d}t$ [Fig. 24(e)] no such discontinuity seems to exist at all.

To end this section, we analyze whether the critical times of DPTs-II and the zeros of the order parameter of DPTs-I are connected. It has been proposed in [371], [396] that, at least for the first-neighbors transverse-field Ising model, they are related; to be more specific, a zero of the order parameter seems to be correlated with a critical time in the rate functions. Figure 25(a) shows $r_N(t)$ and $\widetilde{r}_N(t)$ for $\lambda_i = 7.437$ and $j = 1600$, while Fig. 25(b) depicts the time evolution of the order parameter, $\langle \hat{J}_x(t) \rangle$, and $\langle \hat{\mathcal{C}}(t) \rangle$ for the same quench. The quench leads the initial state to the symmetry-restored phase, $\epsilon > \epsilon_c$, starting from the symmetry-breaking phase, $\epsilon < \epsilon_c$. The times when $r_N(t)$ shows precursors of non-analytic behavior are quite close to the times when the order parameter is nullified, $\langle \hat{J}_x(t) \rangle = 0$ and also $\langle \hat{\mathcal{C}}(t) \rangle = 0$. However, the correspondence is not exact. For this reason, it may seem that we are unable to guarantee if this correlation is rooted in a common DPT-I and DPT-II mechanism. It is interesting to observe that the non-analytical points in $r_N(t)$ take place when the functions $r_N(t)$ and $\widetilde{r}_N(t)$ separate and also at times when they coincide again. Considering $f_\pm(t)$ [Eq. (171)], this suggests that the first non-analytical point in $r_N(t)$ occurs when $f_+(t)$ and $f_-(t)$ separate; the second non-analyticity occurs when $f_+(t)$ and $f_-(t)$ coincide again; and this creates a pattern that repeats itself over time. However, the kinks observed in $\widetilde{r}_N(t)$ do not appear to be connected to the times when $\langle \hat{J}_x(t) \rangle$ and $\langle \hat{\mathcal{C}}(t) \rangle$ vanish.

3.3.4 Watching the seeds of DPTs-II: the complex-time survival amplitude

Complexifying the survival amplitude

In the general setting adopted in this Chapter, the survival amplitude of the initial state in the evolving state reads, according to (75),

$$G(t) = \langle \Psi_0(\lambda_i) | \Psi_t(\lambda_f) \rangle = \sum_n |c_n|^2 e^{-itE_n(\lambda_f)}. \tag{181}$$

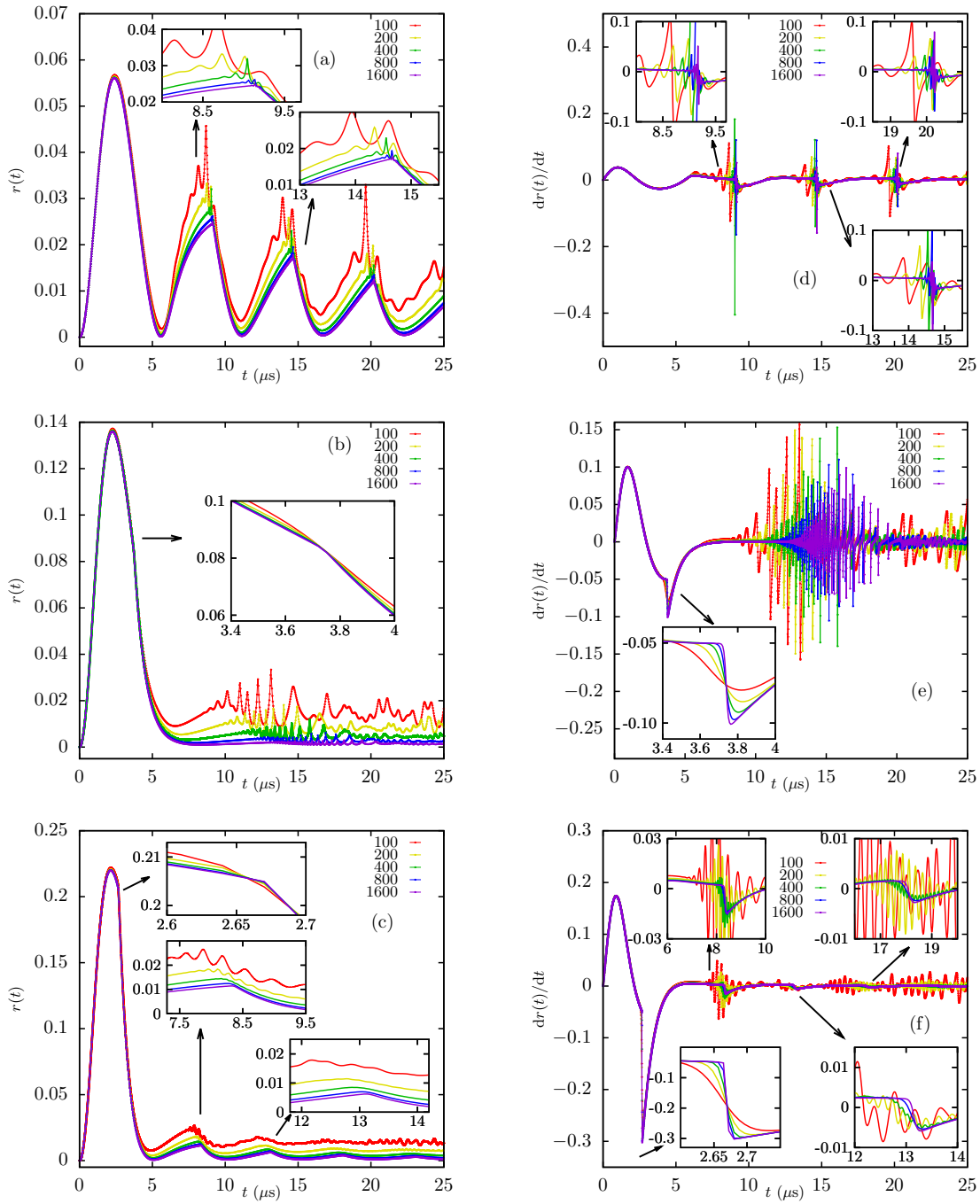

Figure 23: (a-c) Rate function $r_N(t)$ of the PPRP $\mathcal{L}(t)$, defined in (80), for quenches $\lambda_i \to \lambda_f = 1.6$ and (a) $\lambda_i = 2.535$, (b) $\lambda_i = 4$ and (c) $\lambda_i = 7.437$. (d-f) Time derivatives $r'_N(t)$ associated with the rate function $r_N(t)$ in (a-c), respectively. The final average energy after the quench is (a,d) $\epsilon = -1.07 < \epsilon_c$, (b,e) $\epsilon = \epsilon_c = -1$ and (c,f) $\epsilon = -0.92 > \epsilon_c$. Different values of system size are indicated. Insets show magnifications. The initial state (148) has $\alpha = 1/2$ and $\phi = 0$.

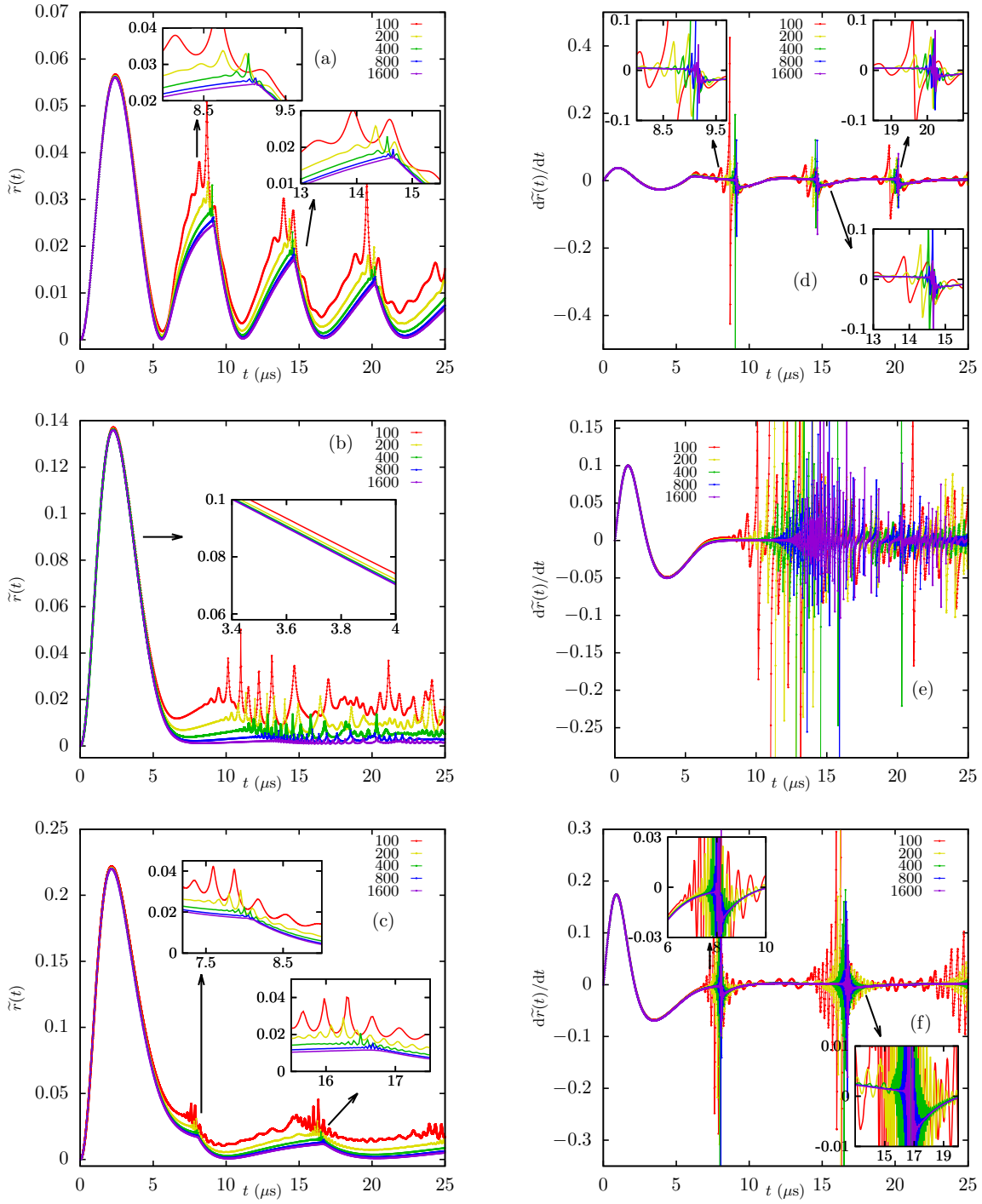

Figure 24: Results analogous to those in Fig. 23 but for the survival probability rate function, $\widetilde{r}(t)$, as defined in (77).

This quantity is completely determined by the final Hamiltonian eigenvalues $E_n(\lambda_f)$ and the corresponding population probabilities $|c_n|^2$. The survival *probability* of the initial state after time t is then trivially $\mathrm{SP}(t) = |G(t)|^2$, as defined in (76). As advanced in the Introduction, the zeros of the survival amplitude can be seen as a

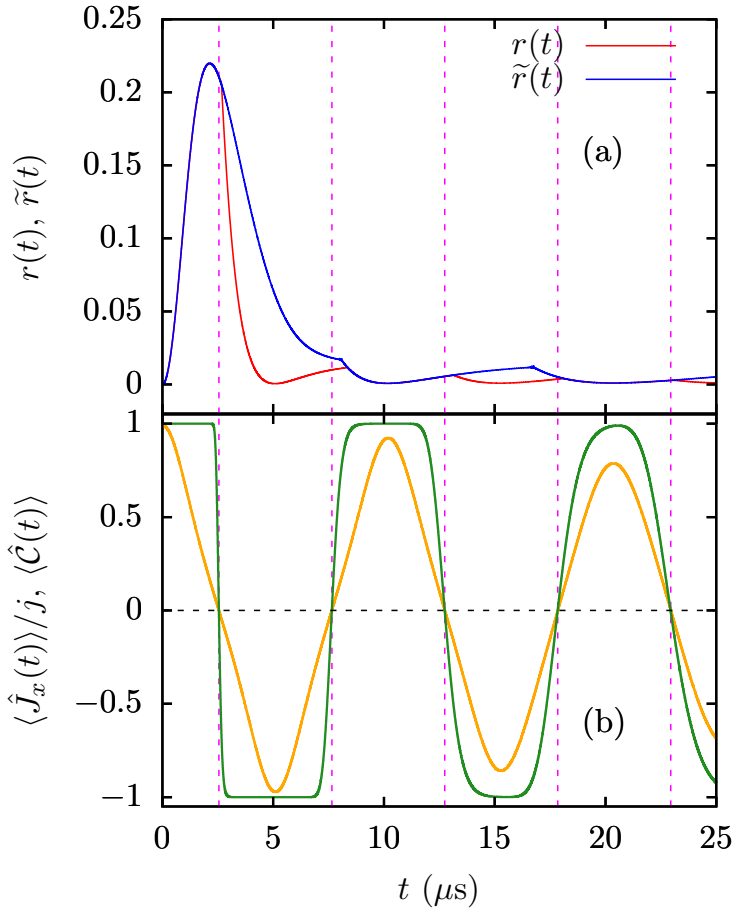

Figure 25: Comparing the DPT-I and DPT-II indicators after a quench $\lambda_i = 7.347 \to \lambda_f = 1.6$ from an initial state of the form (148) with $\alpha = 1/2$ and $\alpha = 0$. The average final energy is $\epsilon = -0.92 > \epsilon_c$. System size is $j = 1600$. (a) $r_N(t)$ and $\widetilde{r}_N(t)$; (b) dynamics of $\hat{J}_x$ (orange) and $\hat{\mathcal{C}}$ (green). The times of zero value of the order parameter, $\langle \hat{J}_x(t)\rangle = 0$, are signaled with dashed vertical lines.

form of critical effect due to their similarity to zeros of the partition function (63), which constitute a well established description of the TPTs. By definition, $Z(\beta)$ in any finite system cannot vanish if β is a real number, but it can take values arbitrarily close to zero. Therefore, these values can imply singular behavior in certain thermodynamic observables. TPTs can be understood through true zeros of a complexified partition function

$$Z(z) = \sum_n g_n e^{-zE_n}, \tag{182}$$

where the inverse temperature is extended to the complex plane: $z = \mathrm{Re}(z) + i\,\mathrm{Im}(z) \in \mathbb{C}$. If $Z(z_0) = 0$ at a point $z_0 \in \mathbb{C}$ whose imaginary part $\mathrm{Im}(z_0)$ drops to zero as the system size increases, the real partition function $Z(\beta)$ in the infinite-

size limit generates a TPT exactly at $\beta = \mathrm{Re}(z_0)$, as analyzed for the first time in Ref. [272], [273] and then further studied in Refs. [274]–[278]. The key point is that this approach makes it possible to trace the finite-size precursors of the critical behavior.

The survival amplitude (181) is mathematically similar to the partition function (182) at $z = -it$. Erasing the dependence of energies on λ_f, we define

$$\mathcal{Z}(z) = \sum_n |c_n|^2 e^{-zE_n} = \sum_n |c_n|^2 e^{-\beta E_n} e^{-itE_n}, \tag{183}$$

where $z = \beta + it \in \mathbb{C}$. The physical interpretation of this quantity is twofold. First, it can be understood as a partition function of a fictitious system with $g_n \propto |c_n|^2$ in complexified inverse temperature. Zeros of $\mathcal{Z}(z)$ near the β axis would imply precursors of a TPT in that system. Secondly, we may interpret (183) in terms of $G(t)$, Eq. (181), in a complexified time. Zeros of this function near the t axis (imaginary axis of z) generate precursors of critical behavior in the time domain. In particular, if $\mathcal{Z}(z_0) = 0$ at a point $z_0 \in \mathbb{C}$ whose real part $\mathrm{Re}(z_0)$ drops to zero with increasing system size, the real survival amplitude $A(t)$ in the infinite-size limit generates a DPT at time $t = \mathrm{Im}(z_0) \equiv t_0$.

The quantity (183) with any value of β is proportional to the survival amplitude of a system with modified population coefficients. Defining normalized population probabilities $\widetilde{p}_n(\beta) \equiv |c_n|^2 e^{-\beta E_n} / \sum_k |c_k|^2 e^{-\beta E_k}$, the survival amplitude of the corresponding state is given by

$$\mathcal{G}(\beta, t) = \sum_n \widetilde{p}_n(\beta) e^{-itE_n} = \frac{\mathcal{Z}(\beta + it)}{\mathcal{Z}(\beta + i0)}. \tag{184}$$

The original survival amplitude (181) is then recovered for $\beta = 0$, while if $\beta \neq 0$ this formula yields survival amplitudes of quantum states with enhanced populations of low-energy ($\beta > 0$) or high-energy ($\beta < 0$) parts of the spectrum. Therefore, a zero of $\mathcal{Z}(z)$ at any $z_0 = \beta_0 + it_0$ represents an actual time singularity at $t = t_0$ of a system with occupation probabilities $\widetilde{p}_n(\beta_0)$.

We note that zeros of $\mathcal{Z}(z)$ are determined by two independent conditions on the vanishing real and imaginary parts, and therefore they form in general infinitely many isolated points in the complex plane. Because the function (183) is differentiable in both real variables β and t, regular Taylor expansion in a vicinity of points $\mathcal{Z}(z_0) = 0$ is allowed. A direct way to locate these points makes use of the nodal lines of $\mathcal{Z}(z)$, that is, the contour lines obtained by imposing separately the conditions $\mathrm{Re}\,\mathcal{Z}(z) = 0$ and $\mathrm{Im}\,\mathcal{Z}(z) = 0$. Zeros of $\mathcal{Z}(z)$ then appear at intersections of these lines.

Numerical results on the LMG model, (73), will be shown below.

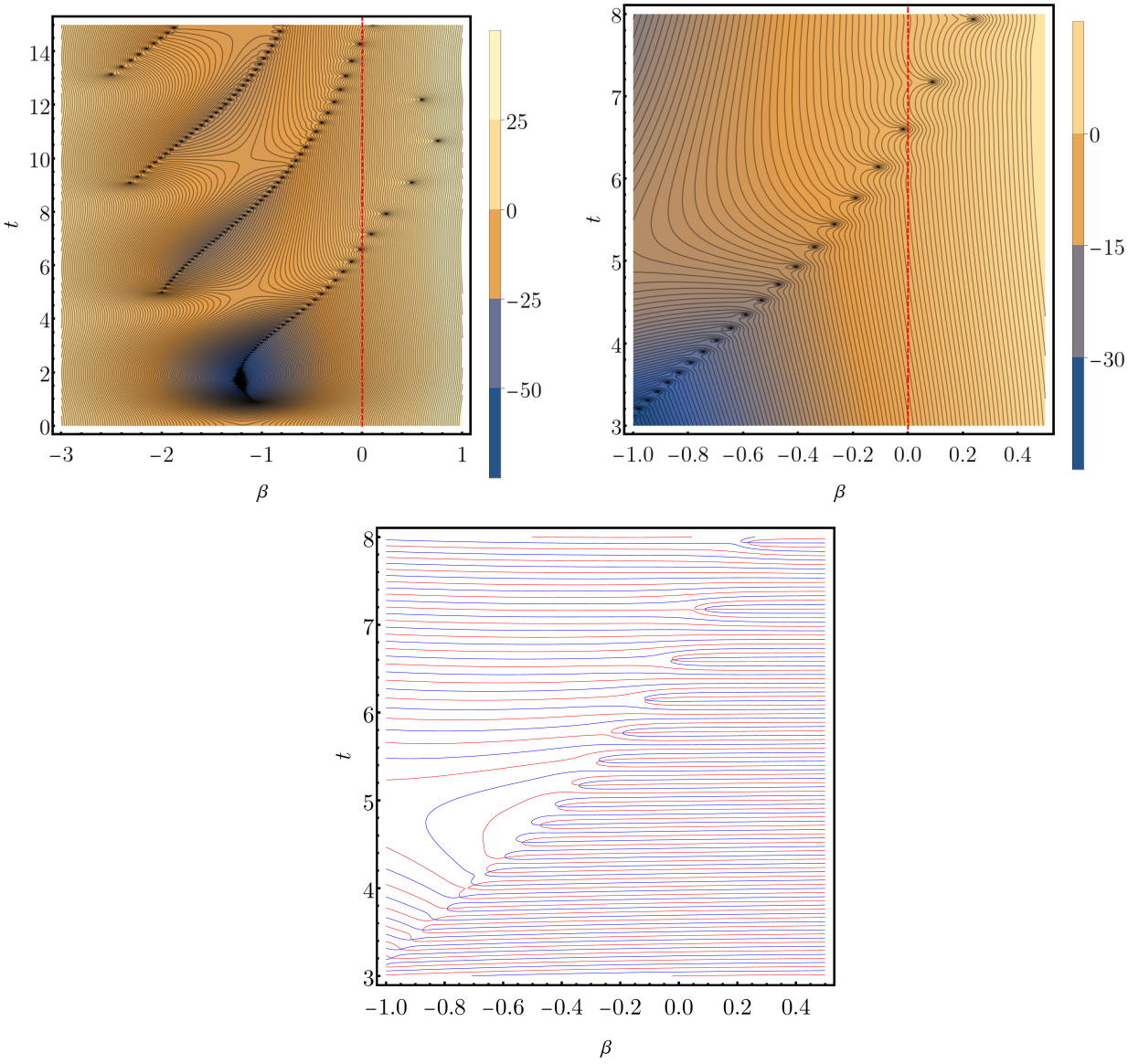

Figure 26: Contour maps of $\log_{10}|\mathcal{Z}(\beta+it)|^2$, defined in (183), in the plane $\beta \times t$ (top row). The t-axis ($\beta = 0$ line) is represented by red, vertical lines. A contour map within a smaller (β, t) window is shown in the top, right panel. The bottom row shows the nodal lines of this last plot, with red (blue) lines corresponding to the real (imaginary) part of (183). We perform a quantum quench $\lambda_i = 7 \to \lambda_f = 1.5$ departing from an initial state of the form (148) with $\alpha = 1/2$ and $\phi = 0$. System size is $j = 30$, and the magnetic field is $h = 1$.

First, let us focus on the quenches that do not cross the ESQPT critical line. In Fig. 26 we consider a backward quench $\lambda_i = 7 \to \lambda_f = 1.5$ for an initial state (148) consisting of equally weighted symmetry-broken eigenstates $\alpha = 1/2$ and $\phi = 0$. The probability associated to the resulting complexified partition function,

$|\mathcal{Z}(\beta+it)|^2$, is represented in the $\beta \times t$ plane (upper left); we represent the contours for several fixed values of such probability. A pattern of zeros of $\mathcal{Z}(z)$ is clearly observed. The complexification of the time variable means that only zeros close to $\beta = 0$ have a sensible impact on the survival probability, the defining feature of DPTs-II. Despite this, the curvature of the contours close to $\beta = 0$ suggest that the survival probability may still be affected even if no zero falls exactly on the $\beta = 0$ line. These pictures provide useful information on the general behavior of the survival probability which can be harder to identify through the associated rate function. In the bottom panel of Fig. 26 we represent the nodal lines of Eq. (183). Red and blue curves are for the real and imaginary part of $\mathcal{Z}(\beta+it)$, respectively. As previously explained, the zeros observed in the upper right panel neatly correspond to *crossing points* of such nodal lines, where the real and imaginary parts of $\mathcal{Z}(\beta+it)$ vanish simultaneously.

Figure 27 shows the zeros of the complex $\mathcal{Z}(\beta+it)$ after a relatively short backward quench with both $\lambda_i, \lambda_f > \lambda_c$. We find a very good correspondence between the times when the rate function exhibits a kink and the times where a zero is close to the $\beta = 0$ line in the complex-time partition function, namely, around $t \approx 8$ and $t \approx 14$. The first maximum of the rate function, around $t \approx 2$, does not correspond to a DPT-II because there is no zero around $\beta = 0$ at $t \approx 2$ in $\mathcal{Z}(\beta+it)$; therefore, this maximum is due to a different mechanism (see below).

It is interesting to observe that the zeros of $\mathcal{Z}(\beta+it)$ appear to form ordered structures similar to lines. As the system size increases, the structures seem to approach a continuum. To corroborate this impression, we perform a finite-size scaling of the number of zeros of $\mathcal{Z}(\beta+it)$ within a fixed region of the $\beta \times t$ plane, and to count such number of zeros, $N_0 = N_0(j)$, we proceed as follows. The key point is to make use of the residue theorem of complex analysis, according to which the integral of a complex function $f(z)$ around a closed path γ is equal to the sum of the residues of $f(z)$ at its poles. Because the complexified partition function is an analytic function, in a neighborhood of its zeros z_0 it can be expanded as

$$\mathcal{Z}(z) \approx a_1(z-z_0) + a_2(z-z_0)^2 + \mathcal{O}((z-z_0)^3), \tag{185}$$

while its derivative reads

$$\frac{d\mathcal{Z}(z)}{dz} \approx a_1 + 2a_2(z-z_0) + \mathcal{O}((z-z_0)^2), \tag{186}$$

with certain $a_k \in \mathbb{C}$. Let us introduce the function

$$f(z) = \frac{d}{dz} \ln \mathcal{Z}(z). \tag{187}$$

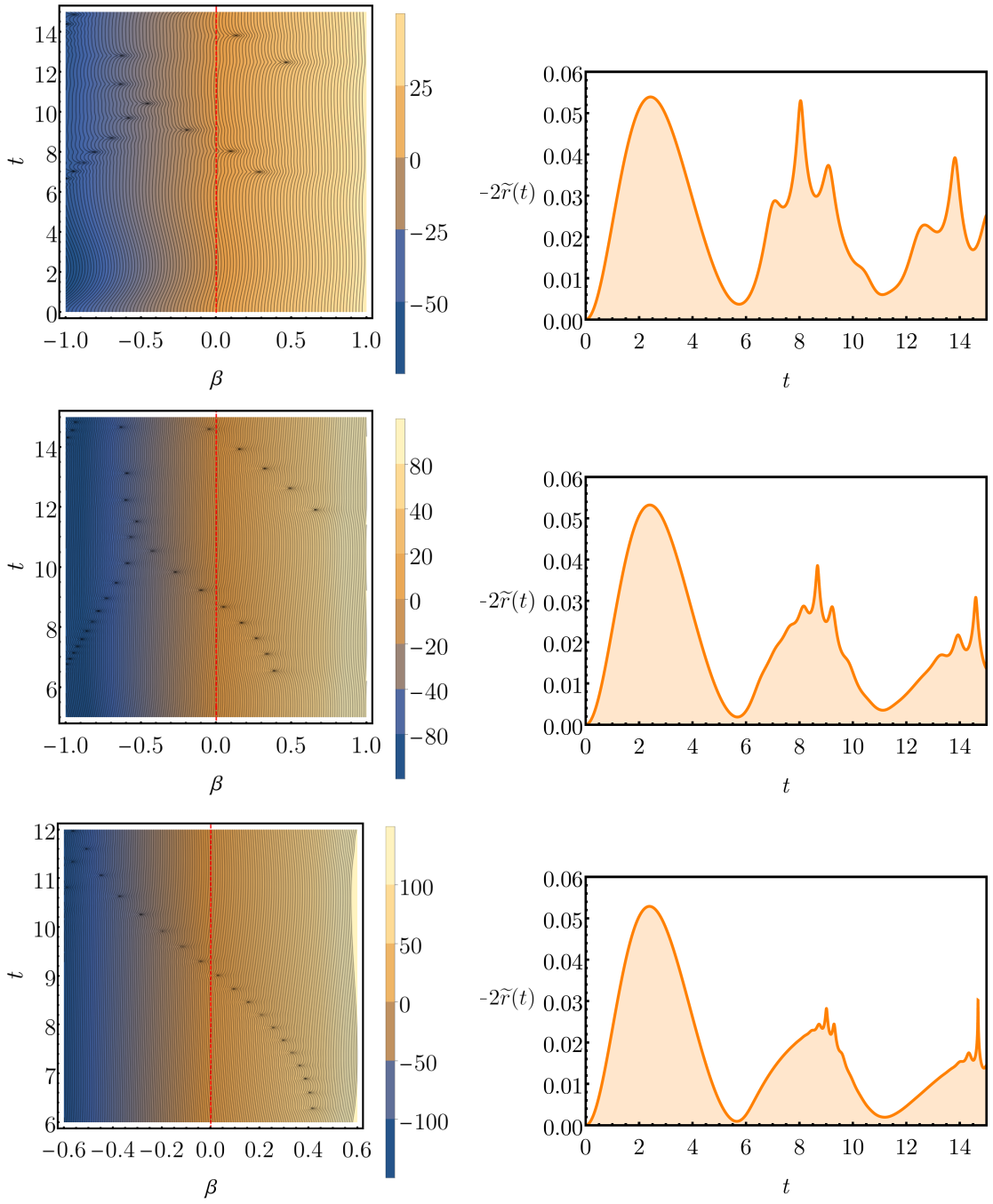

Figure 27: Contour maps of $\log_{10}|\mathcal{Z}(\beta+it)|^2$, defined in (183) (left column), and associated rate functions of the survival probability, $\mathrm{SP}(t) = |\mathcal{Z}(it)|^2$ (right column). We have performed a quench $\lambda_i = 2.6 \to \lambda_f = 1.6$, departing from an initial state (148) with $\alpha = 1/2$ and $\phi = 0$. The average final energy is $\langle \epsilon_f \rangle = -1.07 < \epsilon_c$. The t-axis ($\beta = 0$) is marked by vertical dashed lines (left column). System size is $j = 50, 100, 200$ (for upper, middle and lower rows). We have decided to zoom in the contour plots as system size increases in order to facilitate the observation of zeros.

The zeros of $\mathcal{Z}(z)$ correspond to poles of $f(z)$. Indeed, if $a_1 \neq 0$, then, close to a zero of $\mathcal{Z}(z)$,

$$f(z) \approx \frac{a'_{-1}}{z - z_0} + a'_0 + a'_1(z - z_0) + \mathcal{O}((z - z_0)^2), \tag{188}$$

for some $a'_k \in \mathbb{C}$, in general $a'_k \neq a_k$. Importantly, $a'_{-1} = 1$, so the residue of $f(z)$ at the pole is $\text{Res}_{z=z_0} f(z) = 1$. If the root at $z = z_0$ happens to be of a higher order, i.e., if $a_1 = a_2 = \cdots = a_{k-1} = 0, a_k \neq 0$, then the first k terms in (186) vanish and the pole in $f(z)$ has $\text{Res}_{z=z_0} f(z) = k$. This is a consequence of the multiplicity of such root. Thus, the number N_0 of roots of $\mathcal{Z}(z)$ for a fixed system size j can be computed as

$$\oint_\gamma f(z)dz = 2\pi i N_0. \tag{189}$$

We have calculated N_0 for several system sizes j in a small rectangular region of the complex plane containing the $\beta = 0$ line, similar to the region depicted in the top, rightmost panel of Fig. 27. The result is shown in Fig. 28, which reveals a strongly linear behavior $N_0 \sim j$. This suggests that in the infinite-size limit, the density of zeros in the chains crossing the t axis becomes infinite and the survival probability is nullified in this part of the complex $\beta \times t$ parameter space.

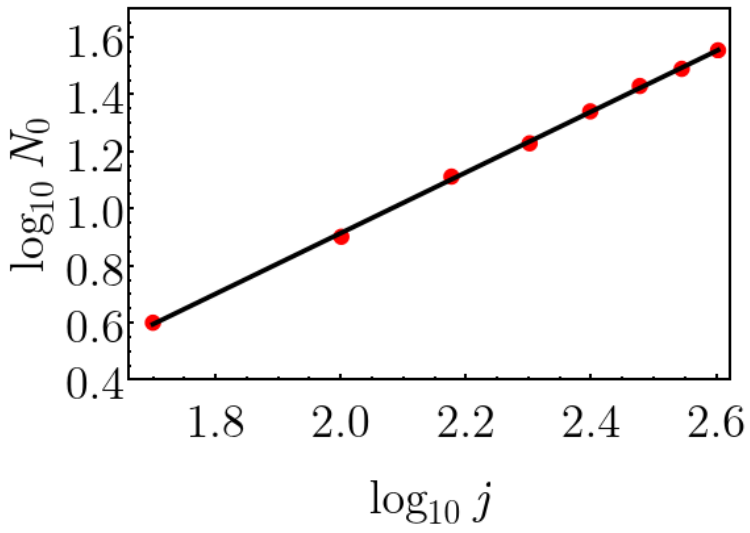

Figure 28: Scaling of the number of zeros of $\mathcal{Z}(\beta + it)$, see (183), within a rectangular region in the $\beta \times t$ plane with $\beta \in (-0.5, 0.5), t \in (6, 12)$. Through a least-squares fit, we obtain a linear law $N_0(j) \sim j^{1.06335}$. We have performed a quench $\lambda_i = 2.6 \to \lambda_f = 1.6$, with an initial state (148) with $\alpha = 1/2$ and $\phi = 0$ (similarly to Fig. 27).

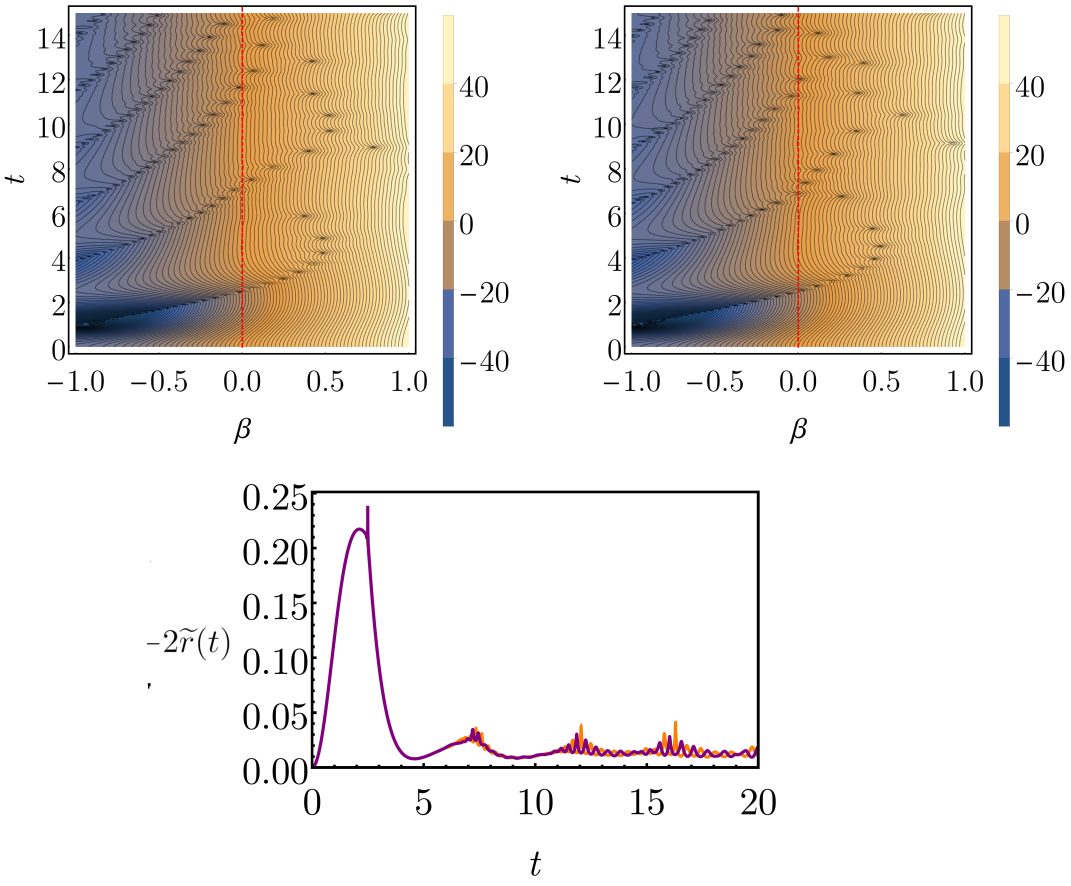

Figure 29: Contour maps of $\log_{10}|\mathcal{Z}(\beta+it)|^2$, defined in (183), in the $\beta \times t$ plane (top row). Vertical red dashed lines signal the t-axis ($\beta = 0$). We have performed a quench $\lambda_i = 10 \to \lambda_f = 1.6$ from an initial state (148) with $\phi = 0$, and $\alpha = 0.1$ (top, left), $\alpha = 0.9$ (top, right). The average final energy is $\langle \epsilon_f \rangle = -0.89 > \epsilon_c$, and system size is $j = 50$. The bottom panel depicts the rate functions of SP(t) for the same quench processes (the orange line is for $\alpha = 0.1$, while the purple line is for $\alpha = 0.9$). In this panel, $j = 100$.

Varying the initial condition

DPTs-II do not depend on the relative phase ϕ in a symmetry-broken initial state of the form (148). Indeed, the complexified survival amplitude can be split into positive and negative parity contributions,

$$\mathcal{Z}(z) = \alpha \sum_n |c_{n,+}|^2 e^{-zE_{n,+}(\lambda_f)} + (1-\alpha) \sum_n |c_{n,-}|^2 e^{-zE_{n,-}(\lambda_f)} \tag{190}$$

where $c_{n,\pm} \equiv E_{n,\pm}(\lambda_f)\ E_{0,\pm}(\lambda_i)$. Therefore, the survival probability SP$(t) = |\mathcal{Z}(it)|^2$ does not depend on ϕ either. However, the location of such initial state in classical phase space does show a dependence on the phase ϕ because $\langle \hat{\mathcal{C}} \rangle =$

$2\sqrt{\alpha(1-\alpha)}\cos\phi$. In any case, the behavior of the non-analytical times in the rate functions does in general depend on α. We have two different cases depending on the average energy of the state undergoing a quench.

If the quench only populates the eigenstates of the final Hamiltonian in the symmetry-broken phase, $E < E_c$, according to the results in Sec. 3.3.3, the populations of positive and negative states coincide up to a phase $|c_{n,+}| = |c_{n,-}| \equiv |c_n|$ in the infinite-size limit. Thus, it follows from Eq. (190) that $\mathcal{Z}(z)$ is also independent of α as these contributions cancel out in the infinite-size limit. Hence we obtain $\mathcal{Z}(z) = \sum_n |c_n|^2 e^{-zE_n}$ as in Eq. (183). For finite-size systems, this equality only holds approximately; however, the exponentially close energy doublets and the constancy of $\hat{\mathcal{C}}$ as j increases [325] guarantee that finite-size effects are negligible even far away from the $j \to \infty$ limit.

If, however, the quench only populates eigenstates of the final Hamiltonian in a symmetric phase, $E > E_c$, $\mathcal{Z}(z)$ depends on α even in the large-j limit. Since the negative-parity eigenlevels are systematically larger than the positive-parity ones, $E_{n,-} > E_{n,+}$, the positive and negative parity contributions to Eq. (190) are not equivalent; this implies that $\mathcal{Z}(z)$ is not symmetric under the transformation $\alpha \to 1-\alpha$. This can be observed in Fig. 29, where we represent $|\mathcal{Z}(z)|^2$ for a quench departing from two initial states with $\alpha = 0.1$ or $\alpha = 0.9$. The zeros occur at different coordinates in the complex plane, as expected. However, the zeros at the $\beta = 0$ line occur at roughly equivalent times, as illustrated in the bottom panel of Fig. 29. It is clear that the rate functions for $\alpha = 0.1$ and $\alpha = 0.9$ are not mathematically the same, but they are still influenced by the exceptional points of $\mathcal{Z}(\beta + it)$ at similar times.

Impact of the average energy of the quenched state

Information of the quench protocol is directly encoded in the complex-time survival amplitude (183). For arbitrary quenches $\lambda_i \to \lambda_f$ the final Hamiltonian population is non-universal and strongly depends on the fine details of the quench parameters. For the LMG model, the parity symmetry means that the full LDOS, $P(E)$, can be separated into positive and negative contributions:

$$\begin{aligned} P(E) &= P_+(E) + P_-(E) \\ &= \sum_n |c_{n,+}|^2 \delta(E - E_{n,+}) + \sum_n |c_{n,-}|^2 \delta(E - E_{n,-}), \end{aligned} \tag{191}$$

where $c_{n,\pm} \equiv E_{n,\pm}(\lambda_f)\ \Psi_0(\lambda_i)$, with $P_\pm(E)$ denoting the population of positive/negative final eigenstates. The critical times and the shape of the survival probability itself depend on to which part of the energy spectrum the initial state

is led by the quench [322], [326]. In fact, phase diagrams of DPTs have been constructed precisely based on those changes. Thus, analyzing the effect of the alteration of the final average energy on the complex-time survival amplitude is important.

In Fig. 30 we focus on three quenches $\lambda_i \to \lambda_f = 1.6$ with the only modification that the initial states Eq. (148) are built with different λ_i, but with a fixed value of $\alpha = 0.5$. As expected, the LDOS is clearly different for $\lambda_i = 2.3, 4, 20$: the average energy increases for larger quench amplitudes. For $\lambda_i = 2.3$ as $\Delta\lambda = |\lambda_i - \lambda_f|$ is small, the after-quench average energy is $\langle \epsilon_f \rangle = -1.08 < \epsilon_c$, so the state populates the ground-state of the final Hamiltonian most significantly. For $\lambda_i = 4$, $\langle \epsilon_f \rangle = -1 = \epsilon_c$, eigenstates are populated on both sides of the ESQPT at ϵ_c; as a consequence, $P_+(E)$ and $P_-(E)$ are almost equal only for eigenstates with energy below ϵ_c. Finally, for $\lambda_i = 20$, $\langle \epsilon_f \rangle = -0.85$ and the quench mainly populates eigenstates above the ESQPT. The after-quench energy distribution has an impact on the location of the zeros of $\mathcal{Z}(\beta + it)$, and in particular it affects which chain of zeros intersects the $\beta = 0$ line and at what times. The overall pattern of zeros shifts towards higher β as the average energy increases, as shown in the contour plots of $|\mathcal{Z}(\beta + it)|^2$. The times when the survival probability rate function shows sharp peaks and whether or not these peaks occur in a quasiperiodic fashion is thus tightly connected with the LDOS.

Exceptional points in the neighborhood of an ESQPT

As mentioned in the Introduction, many dynamical consequences of ESQPT have been thoroughly studied [317], [322], [326], [335], [336], [460]. In particular, critical quenches where the final state has the highest population right at the ESQPT spectral region can produce a variety of stabilizing or destabilizing effects. One common consequence is that the survival probability ceases to show the characteristic succession of revivals up to saturation to a stable infinite-time value [320], [322], [336], [347].

In Fig. 31 we represent the contour plots of $|\mathcal{Z}(\beta + it)|^2$ together with the corresponding rate function for the same quench presented in previous Fig. 30 (middle column), although the system size parameter j has been increased in this case. In other words, this is a so-called critical quench. The rate function is clearly destabilized, with an overall pattern that is qualitatively different from that obtained for quenches that do not overlap the ESQPT criticality (see Fig. 27). An extensive number of zeros cluster together around the $\beta = 0$ line in a disorganized way, in stark contrast with the behavior of Fig. 27, where the zeros close to the $\beta = 0$ line occur in a quasiperiodic way. Interestingly, the zeros appearing away from the $\beta = 0$ line

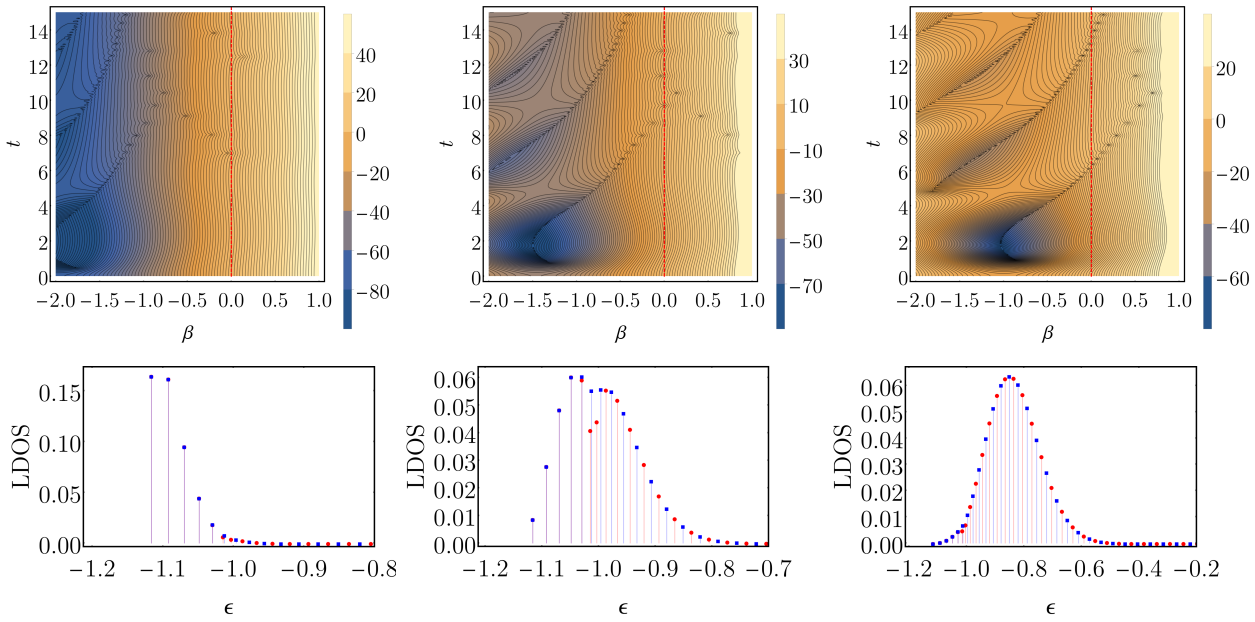

Figure 30: Contour maps of $\log_{10}|\mathcal{Z}(\beta+it)|^2$, defined in (183), in the $\beta \times t$ plane (top). The t-axis ($\beta = 0$) is marked by dashed, vertical line (red). The bottom panels depict the LDOS for the panels on top; here, circles correspond to the population coefficients of positive-parity states in the final Hamiltonian, $|c_{n,+}|^2$, while blue squares denote the same for negative-parity states, $|c_{n,-}|^2$. We have performed three quenches $\lambda_i \to \lambda_f = 1.6$, departing from an initial state (148) with parameters $\alpha = 1/2$ and $\phi = 0$. The values of λ_i are $\lambda_i = 2.3$ in the left column (under the ESQPT), $\lambda_i = 4$ in the middle column (onto the ESQPT), and $\lambda_i = 20$ in the right column (above the ESQPT). System size is $j = 50$.

do not form this erratic pattern. In other words, quenches away from the ESQPT produce the rate function behavior expected in fully connected models [326], [327], [371], [372], [377].

According to our results in Sec. 3.3.2 (see [326], [327] for details), there exists a mathematical restriction on the non-analytical points of the PPRP, $\mathcal{L}(t)$, originally proposed in [394] for systems with symmetry-broken phases. In particular, we showed that (i) *no crossings* of the $\Omega_{\pm}(t)$ functions occur in the symmetry-broken phase and, therefore, this mechanism [394] does not properly explain the appearance of kinks in its rate function in this spectral region and that (ii) in the symmetry-broken phase, both kinds of return probabilities are exactly the same in the infinite-size limit, $\mathcal{L}(t) = \mathrm{SP}(t)$, while in the symmetry-restored phase these functions differ, $\mathcal{L}(t) \neq \mathrm{SP}(t)$. In the symmetry-broken phase, the non-analytical kinks in $\mathcal{L}(t)$ can be traced back to the zeros of $\mathrm{SP}(t)$.

Here, we further investigate DPTs-II in connection with ESQPTs. Our main finding is that the regular or anomalous nature of DPTs-II is not linked to presence

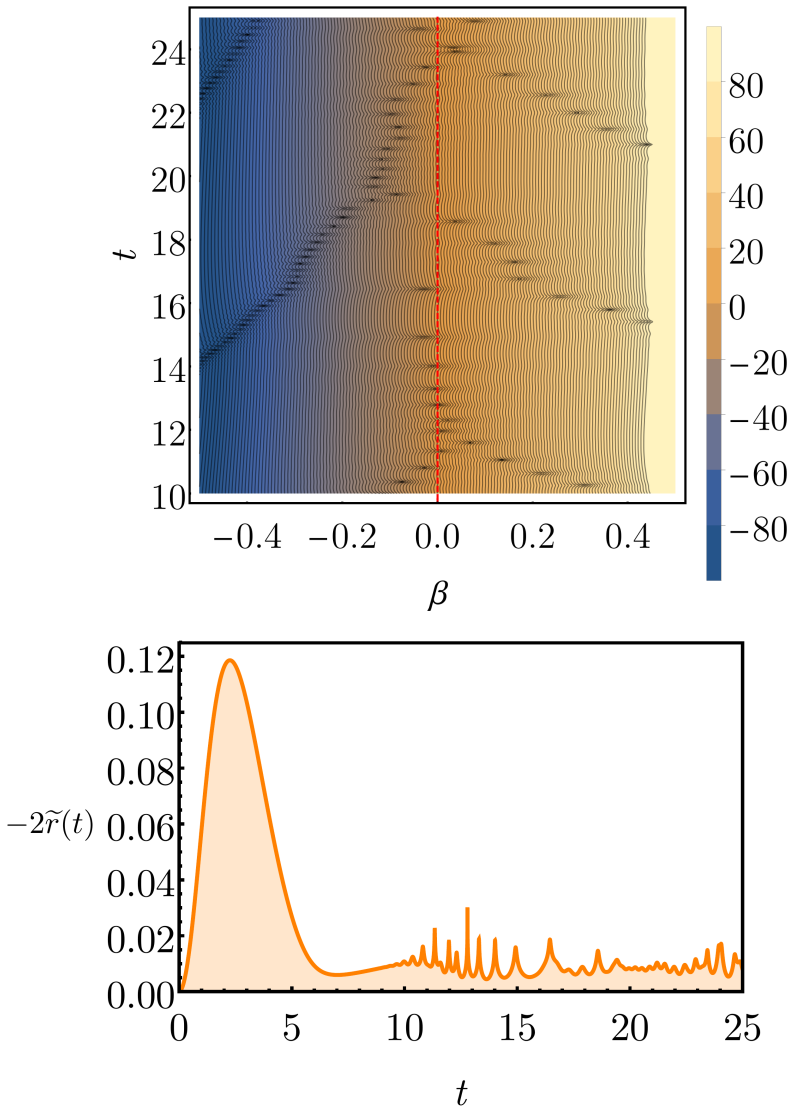

Figure 31: Contour map of $\log_{10}|\mathcal{Z}(\beta+it)|^2$, defined in (183), in the $\beta \times t$ plane (top), with system size $j = 200$. The t-axis ($\beta = 0$) is marked by a red, vertical line. The associated survival probability rate function (bottom). We have performed a quantum quench onto the ESQPT critical point, $\lambda_i = 4 \to \lambda_f = 1.6$ with $h = 1$, departing from an initial state (148) with $\alpha = 1/2$ and $\phi = 0$.

of the ESQPT if the initial state is prepared in a symmetric phase (note that these results are not in contradiction with those of 3.3.3, where the initial state was chosen in the symmetry-broken phase). In Fig. 32 we display the complex-time survival amplitude and the rate function of the survival probability for a quench in the magnetic field, $h_i = 0.8 \to h_f = 0$, with $\lambda = 1$ fixed. The spectrum of the final Hamiltonian is completely degenerate in parity doublets because the ESQPT at $\epsilon_c = -h$ coincides with the upper boundary of the spectrum $\epsilon_{\max} = h$ at $h_f = 0$. In Fig. 32, three lines of zeros of $\mathcal{Z}(\beta+it)$ cross the $\beta = 0$ line around $t \approx 1, 6, 16$,

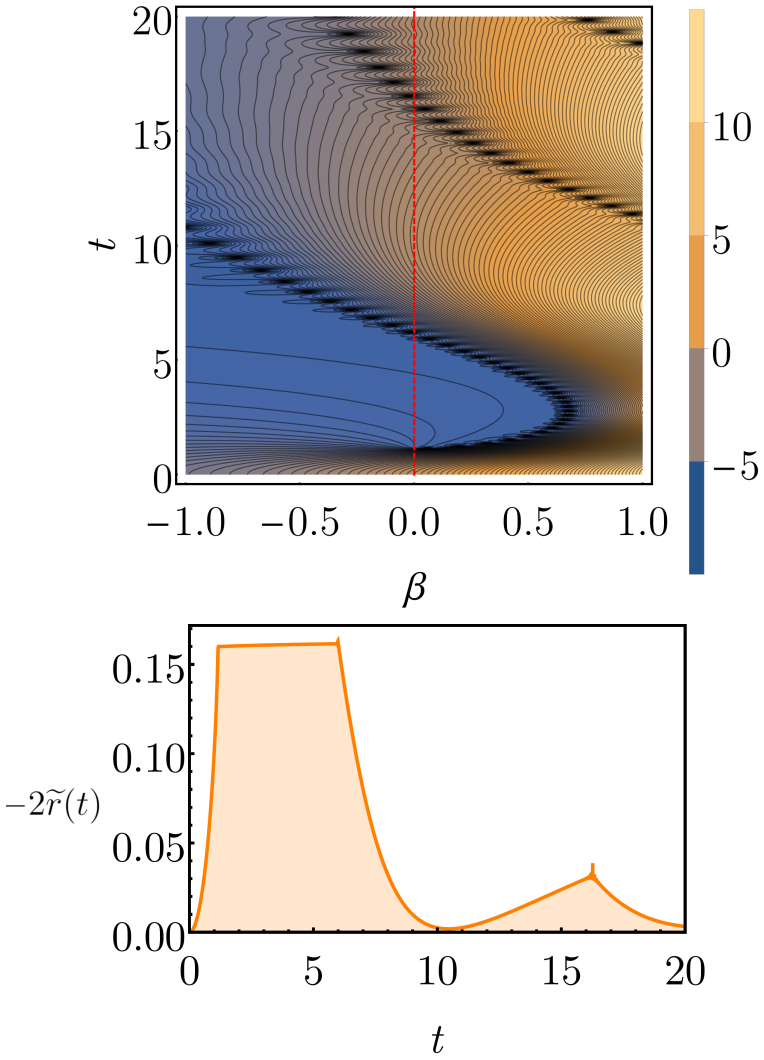

Figure 32: Contour maps of $\log_{10}|\mathcal{Z}(\beta+it)|^2$, defined in (183), in the $\beta \times t$ plane (top); with the system size being $j = 50$. The t-axis ($\beta = 0$) is marked by a red vertical line. The resulting survival probability rate function (bottom), for $j = 400$. We have performed a quantum quench $h_i = 0.8 \to h_f = 0$ with $\lambda = 1$ departing from an initial state of the form (148) with $\alpha = 1/2$ and $\phi = 0$.

with the corresponding non-analytic points showing up in the rate function. The first non-analyticity at $t \approx 1$ occurs even before the second revival of $\mathrm{SP}(t)$, which means that this is a regular DPT. We emphasize that no ESQPT has been crossed in this non-equilibrium protocol. The rate function in the interval $1 \lesssim t \lesssim 6$ is very much flat, which can be understood from the weakly varying contour lines of $\mathcal{Z}(z)$ in this time interval. Note also that the first two non-analytic points in the rate function are of a different nature as those previously analyzed in this section: there are no 'peaks' but 'breaks' instead. Shapes likes this have been observed before, e.g., in [372].

3.4 THERMODYNAMICS OF ENERGY CAT STATES INDUCED BY ESQPT CRITICALITIES

Proposed by E. Schrödinger [28], the existence of so-called cat states is one of the most intriguing aspects of the quantum world. Cat states are commonly understood as macroscopic quantum superpositions of classical states, nonexistent under classical mechanics. The main shortcoming of these states is that they can be hard to control and are very sensitive to quantum decoherence [463], which can be caused from anything from the dissipation in thermal fluctuations to the measuring procedure itself. For these reasons, cat states are not usually observed in the wild [464], [465]. Yet, quantum optical techniques [466] or superconducting cavities [467] have made it possible to engineer them in the laboratory.

Theoretically, the generation of robust cat states has been explored in many ways [468], [469]. This includes, for example, preparing a normal ground-state, and then changing the control parameter of the Hamiltonian in such a way that the initial state ends up in such a superposition of the lowest energy manifold of the new Hamiltonian [470]–[473]. Interestingly, the origin of these two qualitatively different ground-states is very often rooted in a quantum phase transition [36], which causes a non-analytic change of the ground-state properties of the system. Thus, in a bosonic Josephson junction the ground-state changes from separable Fock states to cat states at a quantum critical point [352], [474]. The technique proposed to generate cat states in [471] is also based on the effects of such a phase transition.

Our goal here is to show that the non-equilibrium dynamics ensuing from a quantum quench can be used to create macroscopic quantum superpositions. The special feature of our technique is that these cat states occur both in the spatial and the spectral domain (the state is excited and not restricted to the ground-state manifold only). As we shall see, the main ingredient is the presence of a number of ESQPTs through which we drive our initial state. Our numerical simulations are performed with a modified version of the quantum optical Rabi model. Its ESQPTs can be successfully identified by the constant of motion that we have previously presented in Sec. 3.2. At the end of this section, we focus on the thermodynamics of these energy cat states and propose an equilibrium ensemble capable of describing the equilibration dynamics in these situations.

3.4.1 Deformed Rabi Hamiltonian

The Rabi model [475], [476] is a paradigmatic fully-connected system in studies of phase transitions. Physically, it describes the interaction between a single bosonic field with frequency ω and a two-level atom with constant level splitting ω_0. Here we consider a modification of this model, which reads

$$\hat{H}_\alpha = \omega \hat{a}^\dagger \hat{a} + \omega_0 \hat{J}_z + \sqrt{\omega\omega_0} g(\hat{a}^\dagger + \hat{a})\hat{J}_x + \sqrt{\frac{\omega_0}{2}}\alpha(\hat{a}^\dagger + \hat{a}), \tag{192}$$

where $\hat{a}$ and $\hat{a}^\dagger$ are the bosonic annihilation and creation operators, g is the atom-field coupling parameter, and $\hat{\mathbf{J}}$ is the angular momentum for a $j = 1/2$ particle. For $\alpha = 0$, (192) reduces to the standard Rabi model. The term proportional to α is a symmetry-breaking deformation which implies important qualitative modifications in the critical behavior of the system. Also, for $\alpha = 0$ the Rabi Hamiltonian is invariant under the parity transformation $\hat{\Pi} = e^{i\pi(j+\hat{J}_z)}$, while it is clear that for $\alpha \neq 0$ this conservation is destroyed, $[\hat{H}_{\alpha\neq 0}, \hat{\Pi}] \neq 0$. This is therefore an example of a system without $\mathbb{Z}_2$ symmetries to which our general theory of equilibrium states still applies. Indeed, it was shown in Sec. 3.2 that the existence of a $\mathbb{Z}_2$ symmetry is not necessary for the $\hat{\mathcal{C}}$ operator to behave as a constant of motion under certain circumstances. As we will show, $\hat{\mathcal{C}}$ is still required to properly describe the equilibrium values of observables in spatially separated *components* (in the sense of [269]) of the model. Other symmetry-breaking deformations include a term proportional to $\hat{J}_x$ [477], [478] or to $(a^\dagger + a)\hat{J}_z$ [304]. In our analyses, we fix $\alpha = 1/2$. It has been shown [314], [348] that in the Rabi model the limit $\omega_0/\omega \to \infty$ is formally equivalent to the thermodynamic limit: the reason is that this limit is equivalent to an infinite effective number of photons. Because the system is a fully-connected model, this limit also coincides with the classical limit. In our numerical simulations we fix $\omega = 1$, so the thermodynamic limit is reached by simply increasing ω_0. The photonic part of the Hilbert space dimension is unbounded, so we truncate the number of photons to a finite value n_{ph}. The effective total Hilbert space dimension reads $D = 2(n_{\text{ph}} + 1)$, where the value of n_{ph} has been optimized in order to reach convergence for sufficiently large ω_0/ω.

Classical limit

The classical limit of Eq. (192) is obtained by substituting the photonic operators by the position and momentum operators of the harmonic oscillator, $\hat{p} = i(\hat{a}^\dagger - \hat{a})/\sqrt{2}$ and $\hat{q} = (\hat{a}^\dagger + \hat{a})/\sqrt{2}$, and then diagonalizing the resulting Hamiltonian matrix

[314]. Considering the intensive energy scale $\epsilon \equiv E/(\omega_0 j) = 2E/\omega_0$ (with E denoting the actual extensive eigenvalues of the model), we obtain

$$H_\alpha(p,q) = \frac{\omega}{\omega_0}\left(p^2+q^2\right)\left(\sqrt{1+\frac{2\omega g^2 q^2}{\omega_0}}+\frac{2\alpha q}{\sqrt{\omega_0}}\right), \tag{193}$$

where $(p,q) \in \mathbb{R}^2$. The classical phase space is unbounded, $\mathcal{M} = \mathbb{R}^2$, and there is $f = 1$ effective classical degree of freedom. Many physically relevant properties of the quantum model such as the photonic and atomic population of the ground-state converge to the classically expected results as $\omega_0/\omega \to \infty$.

Non-analytic features of the classical phase space and level density

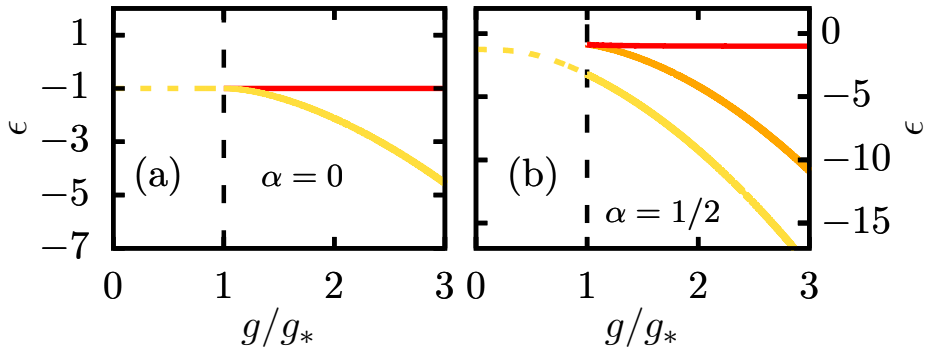

Figure 33: Energies associated to the critical points of the Rabi classical Hamiltonian (193) as a function of the control parameter g/g_* for (a) the standard Rabi model, $\alpha = 0$ and (b) the deformed Rabi model with $\alpha = 1/2$. The ground-state energy is represented in yellow, while ESQPTs critical energies are represented with orange and red lines.

The ground-state energy, $\epsilon_{\rm GS}$, and the ESQPTs energies $\epsilon_{c1,c2}$ of the system can be obtained as the energies $\epsilon = H_\alpha(p_*, q_*)$ corresponding to particular critical points of Eq. (193) satisfying $\nabla H_{\alpha\ (p_*,q_*)} = 0$. For the standard Rabi model, $\alpha = 0$, the critical coupling strength $g_*(\alpha = 0) = 1$ marks a ground-state QPT where these values change abruptly. The ground-state energy can be calculated analytically: for $g \leq g_*(\alpha = 0)$, it is $\epsilon_{\rm GS} = -1$, whereas for $g \geq g_*(\alpha = 0)$, we have $\epsilon_{\rm GS} = -(1 + g^4)/2g^2$. Besides, for $g \geq g_*(\alpha = 0)$ a second critical point, associated with an ESQPT, appears at energy $\epsilon_c = -1$ [314]. These results are illustrated in Fig. 33(a). The structure of the model changes qualitatively when the deformation strength is switched on, $\alpha \neq 0$. For $\alpha \neq 0$, critical points can be calculated analytically but they cannot be expressed in terms of elementary functions. Figure 33(b) shows the critical energies for our case of interest, $\alpha = 1/2$. Two regimes are separated by the

critical coupling $g_*(\alpha = 1/2) \approx 1.7872$. For $g < g_*(\alpha = 1/2)$, we observe a single line corresponding to $\epsilon_{\rm GS}$. However, at $g = g_*(\alpha = 1/2)$ this scenario changes and for $g \geq g_*(\alpha = 1/2)$ we find two more critical energies, different from $\epsilon_{\rm GS}$. These energies grow apart with g.

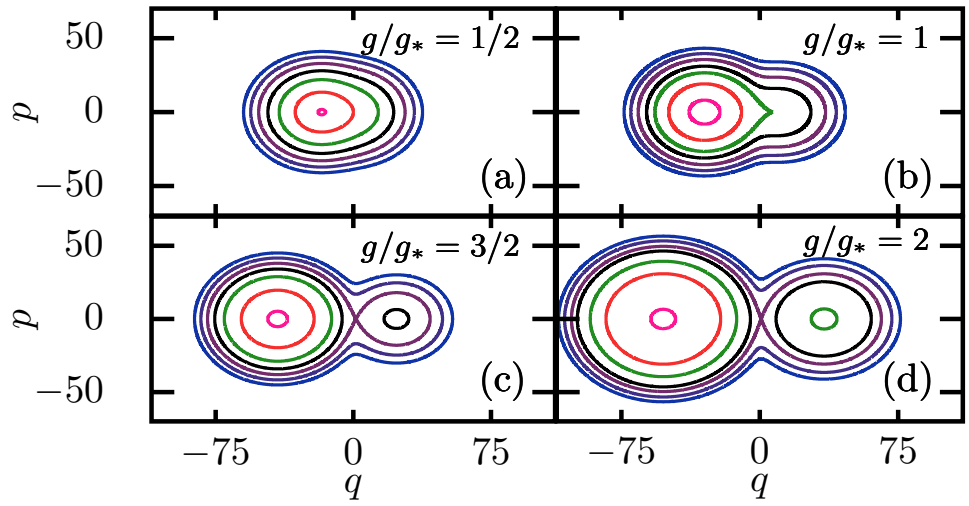

Figure 34: Portraits of the classical phase space of the deformed Rabi Hamiltonian, (193), for $\alpha = 1/2, \omega = 1, \omega_0 = 300$, for different fixed values of the control parameter g. For $g < g_*(\alpha = 1/2) \approx 1.7872$ the phase space is compact at all energies, while for $g > g_*$ the two previously disconnected classical wells merge at a given critical energy.

These critical points can be understood via the structure of the classical phase space. In Fig. 34 we show several classical orbits of Eq. (193) with $\alpha = 1/2$, with different lines corresponding to different constant energies.

In Fig. 34(a), we observe that for $g = g_*/2 < g_*$ the classical potential allows for a single, global minimum, corresponding to the ground-state energy. The deformation brought about by $\alpha \neq 0$ is apparent: the the contour curves do not conform a circumference, as they do for $\alpha = 0$ (not shown). Similar phase space portraits are found for $g < g_*$. However, at $g = g_*$ the general picture changes: in Fig. 34(b) there appears a critical energy with non-smooth behavior, evidenced by a sort of cusp. As we will corroborate though the calculation of the level density (see below), this energy is associated with an ESQPT. The case $g > g_*$ is analyzed in Fig. 34(c)-(d). These plots show a completely different phase space portrait, two minima (instead of one) and a maximum. We also note that such minima are asymmetric, although the maximum is still close to $q = 0$. The first minimum is the ground-state energy, $\epsilon_{\rm GS}$, while the second minimum, at ϵ_{c1}, and the single maximum, at ϵ_{c2}, are critical points associated to ESQPTs of different kinds. For

our subsequent analysis, it is important to observe that for $\epsilon_{c1} \leq \epsilon \leq \epsilon_{c2}$ the classical phase space is topologically disconnected, while above ϵ_{c2} it is compact. The transition from a single-well to a double-well classical potential is marked by the critical coupling g_*.

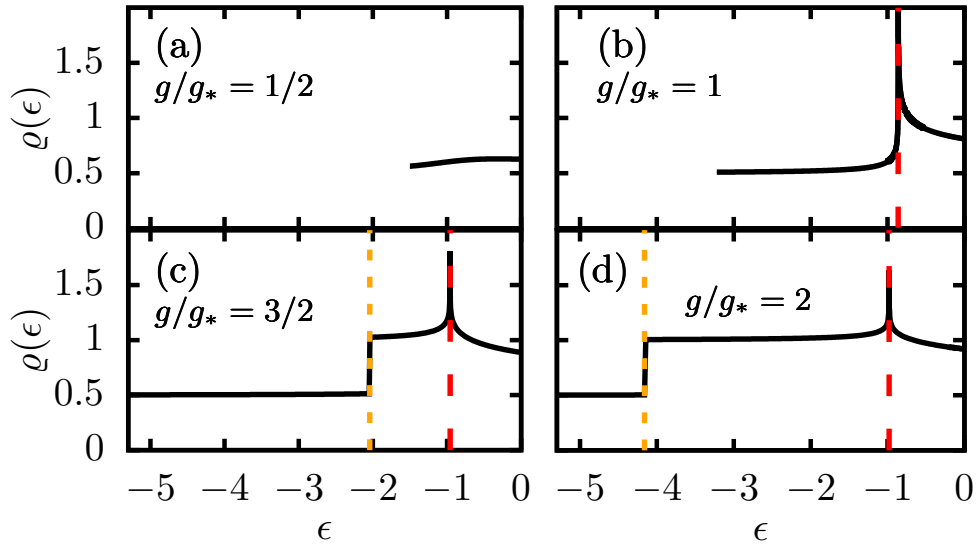

Figure 35: Classical level density $\varrho(\epsilon)$, computed from (194), of the deformed Rabi Hamiltonian (193), with $\alpha = 1/2$ and for different values of the control parameter g. The values of energy at which a finite jump takes place are denoted as ϵ_{c1} and signaled by dotted orange lines, while the logarithmic singularities, ϵ_{c2}, are represented by dashed red lines. For the values of g considered, these critical energies are: (b) $\epsilon_{c1} = -0.8620$; (c) $\epsilon_{c1} = -2.0426$, $\epsilon_{c2} = -0.9584$; (d) $\epsilon_{c1} = -4.1596$, $\epsilon_{c2} = -0.9784$.

In order to certify the different types of ESQPTs present in the system, we compute the classical level density. Due to the peculiar infinite-size limit of the Rabi model, we use the following normalization:

$$\varrho(\epsilon) \equiv \frac{\omega}{\omega_0}\frac{1}{2\pi\hbar}\int \mathrm{d}p \iint \mathrm{d}q\, \delta[\epsilon - H_\alpha(p,q)]. \tag{194}$$

Aside from the ground-state critical points, the second local minimum produces jumps in $\varrho(\epsilon)$, while the local maxima is connected with a logarithmic singularity in $\varrho(\epsilon)$ at the ESQPTs critical energies. Figure 35 displays $\varrho(\epsilon)$ for the same parameters as in Fig. 34. We find a smooth level density in Fig. 35(a), as for $g < g_*$ there are no ESQPTs. In Fig. 35(b) we focus on the critical coupling $g = g_*$, with a single, logarithmic singularity in $\varrho(\epsilon)$. As exemplified in Fig. 35(c)-(d), the difference $|\epsilon_{c1} - \epsilon_{c2}|$ increases with $g > g_*$. Indeed, the first critical energy, ϵ_{c1}, corresponds to the second local minima appearing in Fig. 34(c)-(d), and it produces a finite

jump in $\varrho(\epsilon)$. By contrast, the second critical energy, ϵ_{c2}, corresponds to the local maxima in Fig. 34(c)-(d), yielding a logarithmic divergence in $\varrho(\epsilon)$.

ESQPTs without QPTs

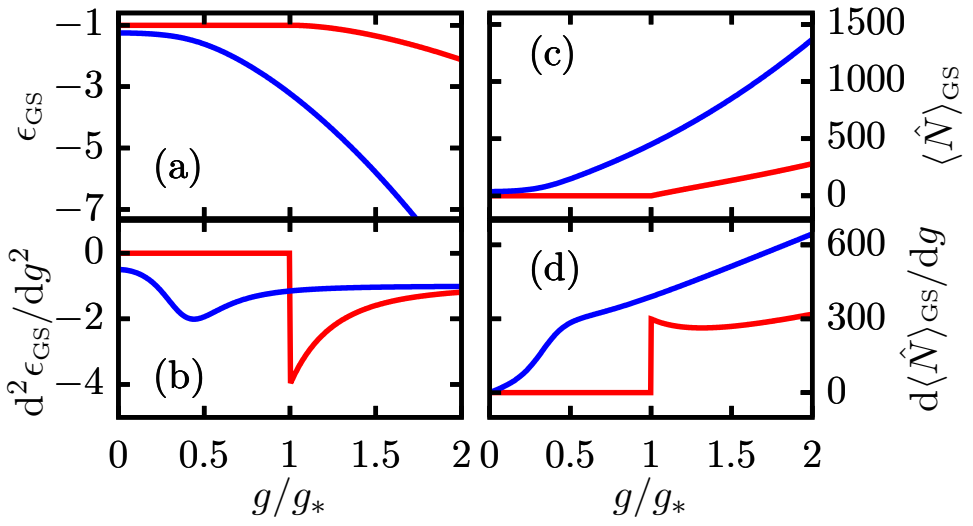

Figure 36: Common signatures of ground-state quantum phase transitions. (a)-(b): The ground-state energy $\epsilon_{\rm GS}$ and its second derivative with respect to the coupling parameter g. (c)-(d): Population of photos in the ground-state, $\langle\hat{N}\rangle_{\rm GS}$, and its first derivative with respect to g. Results for the standard Rabi model ($\alpha = 0$) are represented with red lines, while those for the deformed Rabi model ($\alpha = 1/2$) are shown with blue lines.

Although our system supports several types of ESQPTs, they are not connected with any QPT in the ground-state. To prove this, we take a closer look at the physical quantities that do become non-analytic in the case $\alpha = 0$ and compare them with the case $\alpha = 1/2$.

In Fig. 36(a)-(b) we represent the second derivative of the ground-state energy, $\mathrm{d}^2\epsilon_{\rm GS}/\mathrm{d}g^2$; clearly, it becomes discontinuous for $g = g_*(\alpha = 0)$. Indeed, $\mathrm{d}^2\epsilon_{\rm GS}/\mathrm{d}g^2 = 0$ for $g < g_*(\alpha = 0)$ while $\mathrm{d}^2\epsilon_{\rm GS}/\mathrm{d}g^2 = 2 + 3(-1 - g^4)/g^4$ for $g > g_*(\alpha = 0)$. However, in the deformed Hamiltonian $\alpha = 1/2$ this non-analiticity is completely smoothed out, as observed in Fig. 36(b).

The normal-superradiant transition is perhaps one of the most well-known features of the Rabi model ($\alpha = 0$). This transition is simply a manifestation of its second-order QPT. When $\alpha = 0$, for $g < g_*(\alpha = 0) = 1$, we find a so-called normal phase transition, characterized by a vanishing number of photons in the ground-state, $\langle\hat{N}\rangle_{\rm GS} \equiv 0$. However, for $g > g_*(\alpha = 0)$ there is a non-zero population

$\langle \hat{N} \rangle_{\mathrm{GS}} > 0$. In other words, $\langle \hat{N} \rangle_{\mathrm{GS}}$ can be taken as an order parameter of the transition, although it is not linked to the $\mathbb{Z}_2$ symmetry of the model. In Fig. 36(c)-(d) we represent these quantities for $\alpha = 0$ and $\alpha = 1/2$. For $\alpha = 0$, we clearly observe that $\langle \hat{N} \rangle_{\mathrm{GS}}$ is non-analytic, especially in its derivative in Fig. 36(d), where a finite jump in $\mathrm{d}\langle \hat{N} \rangle_{\mathrm{GS}}/\mathrm{d}g$ is observed. However, when $\alpha = 1/2$, $\langle \hat{N} \rangle_{\mathrm{GS}} > 0$ for all values of g, i.e., implying that the normal-superradiant phase transition is destroyed. As a result, $\mathrm{d}\langle \hat{N} \rangle_{\mathrm{GS}}/\mathrm{d}g$ is smooth for $\alpha = 1/2$ for all g.

In closing this section, we believe it its worth mentioning that although the QPT in the $\alpha = 0$ case is linked to symmetry-breaking, ESQPTs are not related to this mechanism. Therefore, a system may exhibit ESQPTs in the total absence of an underlying QPT.

3.4.2 Quantum manifestations of classically asymmetric energy wells

Identifying wells through diagonal elements of observables

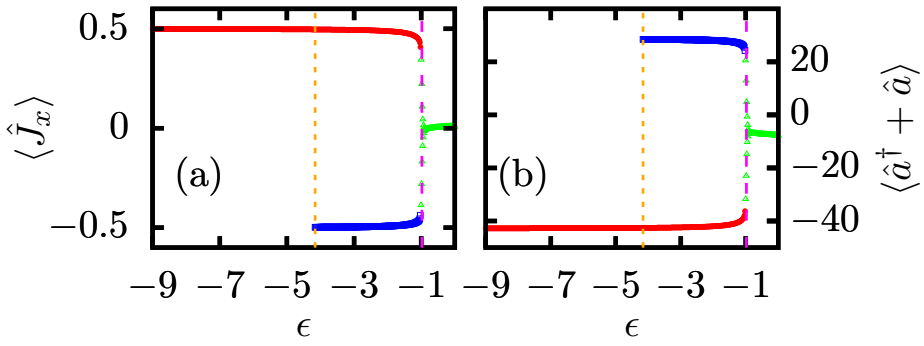

Figure 37: Diagonal expectation values of physical observables, in the Hamiltonian energy eigenbasis of the deformed Rabi model, (192), with system parameters $\omega = 1$ $\omega_0 = 100$, $\alpha = 1/2$ and $g/g_* = 2$. (a) $\hat{J}_x$ and (b) $\hat{a}^\dagger + \hat{a}$, as a function of the energy of the corresponding eigenstate. The ESQPTs critical energies $\epsilon_{c1} \approx -4.1596$ and $\epsilon_{c2} \approx -0.9785$ are represented by orange and magenta vertical lines. Green triangles represent the diagonal expectation values corresponding to eigenstates in the spectral region where the operator $\hat{\mathcal{C}}$ does behave as a constant of motion, while eigenstates for which $\langle \epsilon | \hat{\mathcal{C}} | \epsilon \rangle \leq -0.95$ and $\langle \epsilon | \hat{\mathcal{C}} | \epsilon \rangle \geq 0.95$ are represented with red and blue points, respectively. The cutoff photon number is 2000.

The asymmetric double well structure of the deformed model has important physical consequences. In order to illustrate them, we start by analyzing the diagonal expectation values of physically relevant observables in the Hamiltonian eigenbasis, $\langle \hat{O}_n \rangle \equiv \langle \epsilon_n | \hat{O} | \epsilon_n \rangle$. We fix $g/g_* = 2$ and $\omega_0 = 100$, and we consider the

operators $\hat{J}_x$ and $\hat{a}^\dagger + \hat{a}$. Our results are in Fig. 37. This figure reveals a double-branch structure appearing for energies $\epsilon_{c1} \leq \epsilon \leq \epsilon_{c2}$. The main conclusion of these results is that there should be a direct connection between the topology of classical phase space and the properties of quantum eigenstates: indeed, contour plots in Fig. 34(d) show that for $\epsilon_{c1} \leq \epsilon \leq \epsilon_{c2}$, classical trajectories are trapped either on the left ($q < q_c$) or the right ($q > q_c$) part of the phase space, while for $\epsilon \leq \epsilon_{c1}$ all trajectories belong to the left part. This is mimicked in the quantum case, since the operator $\hat{a}^\dagger + \hat{a}$ is essentially equivalent to $\hat{q}$. Also, these results suggest that the ETH is invalid in this system, as it requires the diagonal matrix elements to behave as a smooth function of energy. However, in our case, Fig. 37 shows abrupt variations in the diagonal matrix elements when $\epsilon_{c1} \leq \epsilon \leq \epsilon_{c2}$. Therefore, neither the microcanonical, nor the standard Gibbs ensemble are expected to hold for this system. This discussion suggests that hypothesis (H2) of our theory in Sec. 3.2.1 applies to this model, even though there is no $\hat{\Pi}$ symmetry and hypothesis (H1) plays no role here. Thus, a certain operator $\hat{\mathcal{C}}$ acts as a constant of motion in an appropriate spectral region of the model. Motivated by our previous analyses, in particular by properties of the classical trajectories, it is natural to conclude that the operator

$$\hat{\mathcal{C}} \equiv \text{sign}(\hat{q} - q_c \mathbb{I}) \tag{195}$$

is an emergent constant of motion only in the region ϵ_{c2} in the infinite-size limit. Here, q_c denotes the classical position corresponding to the critical energy ϵ_{c2} and $\mathbb{I}$ is the identity matrix. Because $\hat{\mathcal{C}}$ is a $\mathbb{Z}_2$ discrete operator, $\text{Spec}\,(\hat{\mathcal{C}}) = \pm 1$, we have that $\langle \epsilon_n | \hat{\mathcal{C}} | \epsilon_n \rangle = -1$ if the eigenstate $|\epsilon_n\rangle$ is attached to the left part of the classical phase space ($q < q_c$), and $\langle \epsilon_n | \hat{\mathcal{C}} | \epsilon_n \rangle = 1$ if it is attached to the right part ($q > q_c$). In Fig. 37, red points are chosen for eigenstates such that $\langle \epsilon_n | \hat{\mathcal{C}} | \epsilon_n \rangle = -1$, while for blue points $\langle \epsilon_n | \hat{\mathcal{C}} | \epsilon_n \rangle = 1$. For $\epsilon \geq \epsilon_{c2}$, $\hat{\mathcal{C}}$ is not constant, these eigenstates being represented by green triangles. We conclude that *below* ϵ_{c2}, *it is possible to classify the eigenstates in two types: they either fulfill* $\langle \epsilon_n | \hat{\mathcal{C}} | \epsilon_n \rangle - 1$ *or* $\langle \epsilon_n | \hat{\mathcal{C}} | \epsilon_n \rangle = 1$. This classification according to the quantum number provided by the $\hat{\mathcal{C}}$ operator has important effects in the dynamics, as we will show below. Also, since in this model the parity symmetry is broken, there exists no $\hat{\mathcal{K}}$ operator, even though $\hat{\mathcal{C}}$ is still constant for a given range of energies in the infinite-size limit.

Follow the eigenlevel

The level-flow diagram of the quantum model Eq. (192) is represented in Fig. 38. This diagram allows to visualize the structure of quantum levels as a function of the control parameter, g, in a convenient way. We observe that the structure of the

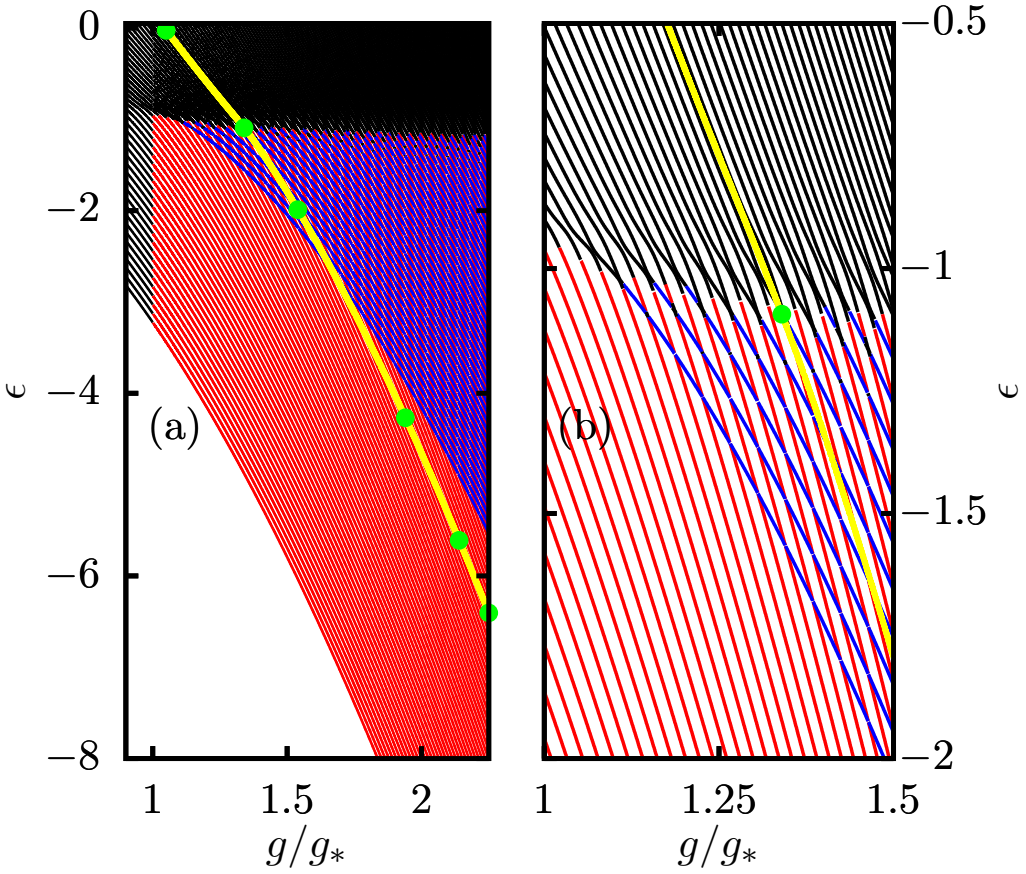

Figure 38: (a) Level-flow diagram ($g \times E$ plane) of the deformed Rabi Hamiltonian (192) with parameters $\omega = 1$, $\omega_0 = 20$, and $\alpha = 1/2$. The lowest energy line represents the ground-state, while upper lines represent the excited states. Black lines show energy levels in the spectral region where the operator $\hat{\mathcal{C}}$ does not behave as a constant of motion; eigenlevels for which $\langle\epsilon|\,\hat{\mathcal{C}}\,|\epsilon\rangle \leq -0.95$ and $\langle\epsilon|\,\hat{\mathcal{C}}\,|\epsilon\rangle \geq 0.95$ are represented with red and blue lines, respectively. The yellow thick line represents the energy of the sequentially quenched state of Sec. 3.4.3, i.e., $\epsilon_g = \langle\Psi(g)|\,\hat{\mathcal{H}}(g)\,|\Psi(g)\rangle$. The special special cases of $(g/g_*, \epsilon_g)$ whose energy distribution is shown in Fig. 43 are represented with green points. (b) Zoom of the flow diagram. The cutoff number of photons is 570.

level flow closely resembles the classical picture in Fig. 33(b). The signatures of the logarithmic divergence of the level density near $\epsilon_{c2} \approx -1$ is apparent: eigenlevels tend to collapse onto a single line around this energy value. Figure 38(b) shows a magnification of the level-flow diagram. Level crossings seemingly take place for $\epsilon_{c1} \leq \epsilon \leq \epsilon_{c2}$. However, for $\epsilon \leq \epsilon_{c1}$ no level crossings occur. In these plots, the eigenlevels have been characterized through the operator $\hat{\mathcal{C}}$. Eigenlevels whose eigenstates belong to the left classical well, $\langle\hat{\mathcal{C}}\rangle = -1$, have been plotted in red, while states in the right classical well, $\langle\hat{\mathcal{C}}\rangle = +1$, are plotted in blue. Finally, black

lines are used to represent the eigenlevels of states such that $\hat{\mathcal{C}}$ is not constant, namely for $g < g_*$ at all energies and for $g > g_*$ only at energies $\epsilon > \epsilon_{c2}$. In any case, the level diagram clearly shows that blue and red eigenlevels appear to cross for $\epsilon_{c1} \leq \epsilon \leq \epsilon_{c2}$.

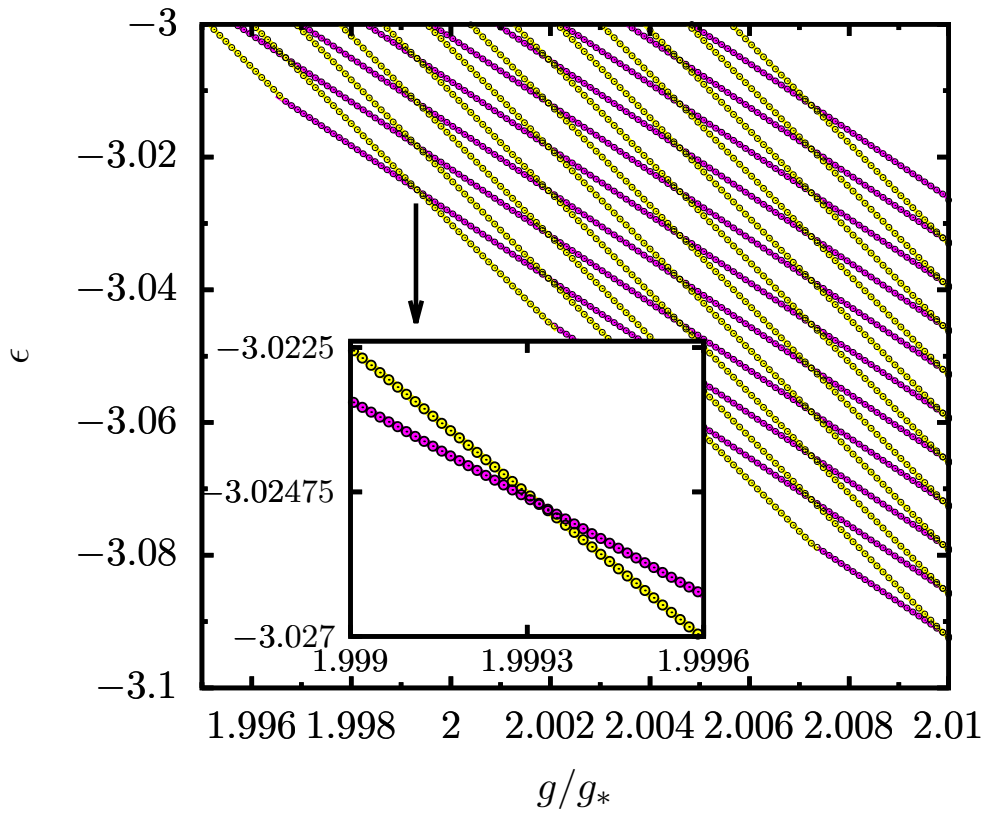

Figure 39: Magnification of the level-flow diagram of the deformed Rabi Hamiltonian (192) for $1.995 \leq g \leq 2.01$ and parameters $\omega = 1$, $\omega_0 = 300$, and $\alpha = 1/2$. Empty circles represent the numerically computed energy levels of the quantum model, while color lines depict the classical (infinite-size limit) energy levels calculated from the quantization (196); levels with $\langle \hat{\mathcal{C}} \rangle = -1$ are shown with yellow lines, while if $\langle \hat{\mathcal{C}} \rangle = +1$ magenta lines are used. In the inset we focus on a single level crossing. The cutoff photon number is 5000.

As the Neumann-Wigner theorem [479] states that exact (real) level crossings are allowed only if there exists an exact quantum number labeling the corresponding eigenstates unambiguously, we expect the crossings visible in Fig. 38 to be avoided crossings. This is because according to our theory of conserved charges, presented in Sec. 3.2, $\hat{\mathcal{C}}$ becomes an exact constant of motion only in the infinite-size limit, while the level-flow diagram has obviously been computed for a finite $\omega_0 = 20$, very far away from $\omega_0/\omega \to \infty$. To obtain a definite answer to this question, we go back to the classical limit. It was shown in [315], [349] that the Einstein-Brillouin-

Keller (EBK) action quantization rules [77], [480], [481] can be used to determine the eigenlevels of Eq. (192) in the thermodynamic limit. This requires solving the integral equation

$$\oint\!\!\!\!\!\!\int_{\Gamma_\pm} p(\epsilon, q)\mathrm{d}q = 2\pi(n + a_n), \tag{196}$$

where $p(\epsilon, q)$ follows from inversion of Eq. (193) for a fixed value of ϵ. This is a closed loop integral over $\Gamma_\pm$ which covers the left $(-)$ and the right $(+)$ part of the phase space separately. The quantities a_n are related to the Maslov index of the corresponding trajectory; they are equal to $1/4$ for each turning point, i.e., $a_n = 1/2$. Finally, it should be noted that in the Rabi model the vacuum energy of the harmonic oscillator, $E = \omega/2$, is removed. Therefore, the eigenlevels computed from (196) need to be shifted for them to coincide with the actual eigenlevels of the Rabi model.

Figure 39 provides a comparison of the theoretical prediction afforded by Eq. (196) for $\omega_0 = 300$ and $1.995 \leq g/g_* \leq 2.010$, with the eigenvalues coming from diagonalization of the quantum model Eq. (192). The classical, theoretical curves go through several exact crossings, and the quantum, numerical eigenlevels cannot be easily distinguished from the corresponding theoretical predictions. The single level crossing presented in the inset, with $1.9990 \leq g/g_* \leq 1.9996$, confirms that the discrepancies between the EBK and the exact energy levels are basically negligible.

We expect this result to have important consequences in the dynamical properties of the system. Indeed, according to Fig. 38, the rapidity at which the value of every energy level changes with g, $\epsilon_n(g)$, depends on $\langle\epsilon_n|\hat{\mathcal{C}}\,|\epsilon_n\rangle$; to be more precise, the 'speed' $|\mathrm{d}\epsilon_{n,-}/\mathrm{d}g| > |\mathrm{d}\epsilon_{n,+}/\mathrm{d}g|$, where the subindex $-$ identifies the energy levels with $\langle\epsilon_n|\hat{\mathcal{C}}\,|\epsilon_n\rangle = -1$, and the subindex $+$, the energy levels with $\langle\epsilon_n|\hat{\mathcal{C}}\,|\epsilon_n\rangle = +1$. This pushes us to formulate the following conjecture:

In an adiabatic evolution where the initial wave function is a superposition of states with $\langle\hat{\mathcal{C}}\rangle = \pm 1$, the energy of states with $\langle\hat{\mathcal{C}}\rangle = -1$ will show a faster variation with the control parameter g and, as a consequence, crossing the spectral region $\epsilon_{c1} \leq \epsilon \leq \epsilon_{c2}$ adiabatically can lead to a superposition of different macroscopic energies. This effect should be relevant even in finite-size systems, where level crossings are not exact but avoided.

Below we provide evidence in favor of this intuition, including a finite-size scaling analysis.

Non-adiabatic transitions in finite-size systems

Let us first investigate the variation of the diagonal expectation values of $\hat{\mathcal{C}}$ as the control parameter g is gradually changed. We focus on the control parameter

window $g/g_*(\alpha) \in [1.6, 1.7]$. For each value of ω_0, which basically controls how close we are to the infinite-size limit, we determine the eigenlevel ϵ_p closest to $\epsilon = -0.8$ at $g/g_*(\alpha) = 1.6$; this eigenlevel is denoted as ϵ_p. Then, we monitor the diagonal expectation values of $\hat{\mathcal{C}}$ in $|\epsilon_p\rangle$ and $|\epsilon_{p-1}\rangle$ as g varies, $\langle\epsilon_p(g)|\,\hat{\mathcal{C}}\,|\epsilon_p(g)\rangle \equiv \langle\hat{\mathcal{C}}\rangle_{p,g}$. We expect that as g is varied the eigenlevels ϵ_p and ϵ_{p-1} will at some point cross the ESQPT at ϵ_{c2}, as implied by the curvature of the level-flow diagram in Fig. 38. We note that since we start at $g/g_* = 1.6$, the eigenlevels ϵ_p and ϵ_{p-1} are initially above ϵ_{c2}, i.e., in the spectral region where $\hat{\mathcal{C}}$ is not constant. As the ESQPT at ϵ_{c2} is crossed, $\hat{\mathcal{C}}$ acts as an approximate constant of motion and the diagonal expectation values of $\hat{\mathcal{C}}$ in these eigenstates can only be $+1$ or -1. This picture is confirmed by the results shown in Fig. 40(a)-(b) for $\omega_0 = 55$ (a) and $\omega_0 = 603$ (b). For sufficiently large g, $\langle\hat{\mathcal{C}}\rangle_{p,g}$ shows abrupt changes between -1 and $+1$ at specific values of g; the same is observed for $\langle\hat{\mathcal{C}}\rangle_{p-1,g}$. The reason is that at these values of g the system exhibits finite-size precursors of level crossings, entailing a swap of the conserved quantities. On the other hand, for sufficiently small values of g the expectation values considered are not ± 1, which is to be expected since for those g the operator $\hat{\mathcal{C}}$ is not a constant of motion in the high-lying part of the spectrum where ϵ_p and ϵ_{p-1} belong. Finally, these figures also reveal a transient region between these the two scenarios explained above. This transient region is a finite-size effect and should disappear in the infinite-size limit, where the ESQPT singularity is fully realized. In order to confirm this, we define the g-width $\Delta g_T \equiv g_{0.05} - g_{0.95}$, where $g_{0.05}$ stands for the last value of the coupling g such that $1 - \langle\hat{\mathcal{C}}\rangle^2_{p,g} \geq 0.05$, and $g_{0.95}$ represents the first value of g such that $1 - \langle\hat{\mathcal{C}}\rangle^2_{p,g} \leq 0.95$. Figure 40(c) displays $\Delta g_{\rm T}$ as a function of ω_0. We obtain a clear power-law behavior $\Delta g_{\rm T} \sim 1/\omega_0^z$ with $z \approx 1$, which suggests that $\Delta g_{\rm T} \to 0$ as $\omega_0 \to \infty$. In other words, as the limit $\omega_0 \to \infty$ is approached, there is an abrupt change between a parameter region with change from a region in which $\langle\hat{\mathcal{C}}\rangle^2 - \langle\hat{\mathcal{C}}^2\rangle = 1 - \langle\hat{\mathcal{C}}^2\rangle \sim 1$ to a region where $\langle\hat{\mathcal{C}}\rangle^2 - \langle\hat{\mathcal{C}}^2\rangle = 1 - \langle\hat{\mathcal{C}}^2\rangle \sim 0$. These plots also show that the number of level crossings is an increasing function of ω_0.

Let us now assume that we perform a time-dependent protocol, $g(t)$, crossing the ESQPT at energy ϵ_{c2}, from an initial state prepared from an eigenstate of the Hamiltonian at a given g. The time-dependent wave function can be written as $|\Psi(t)\rangle = \sum_n c_n(t)\,|\epsilon_n(t)\rangle$, where $|\epsilon_n(t)\rangle$ are the instantaneous eigenstates for Eq. (192) with $g(t)$. Here, the time-dependent population coefficients $c_n(t)$ evolve according to the differential equation ($\hbar = 1$)

$$\dot{c}_m(t) + \left[i\epsilon_m(t) + \langle\epsilon_m(t)|\,\dot{\epsilon_m}(t)\rangle\right] c_m(t) = \sum_{n\neq m} \frac{\langle\epsilon_m(t)|\,\dot{\mathcal{H}}\,|\epsilon_n(t)\rangle}{\epsilon_m(t) - \epsilon_n(t)} c_n(t), \qquad (197)$$

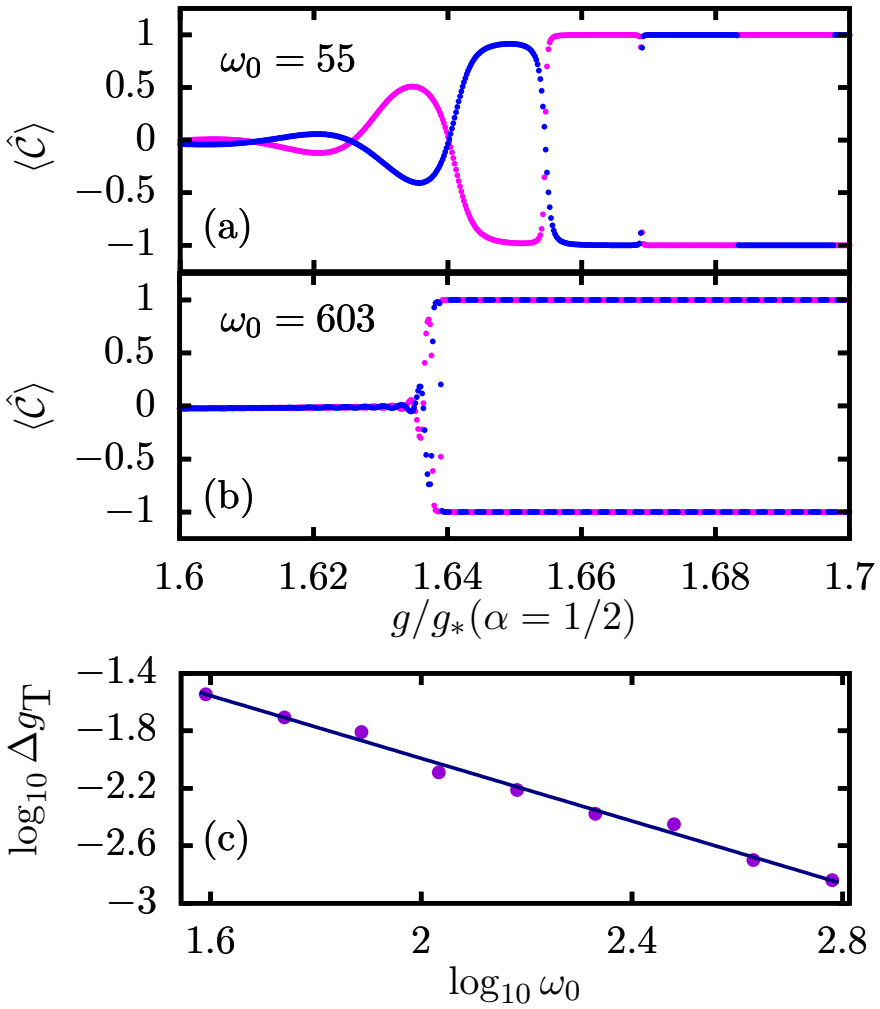

Figure 40: (a-b) Diagonal expectation values (in the Hamiltonian energy basis) of $\hat{\mathcal{C}}$ in the eigenstate $|\epsilon_p(g)\rangle$ (blue) such that $\epsilon_p(g/g_* = 1.6) \approx -0.8$ and in the eigenstate with lower energy closest to the previous level, $|\epsilon_{p-1}(g)\rangle$ (magenta), as a function of g. For (a), $\omega_0 = 55$, and for (b), $\omega_0 = 603$. (c) Finite-size scaling of the size of the parameter space region, Δg_{T}, displaying transient behavior (see text for discussions), revealing the power-law $\Delta g_{\mathrm{T}} \sim 1/\omega_0^z$ with $z \approx 1$. The cutoff photon number is $n_{ph} \in [812, 8977]$, which has been optimized according to the value of ω_0.

where $\dot{\bullet}$ indicates a time derivative. The left-hand side of Eq. (197) accounts for the phase acquired by any coefficient $c_n(t)$ as a result of the time evolution, whereas the right-hand side depends on non-adiabatic transitions between the instantaneous eigenstates. In order to estimate the relevance of such transitions in finite-size systems, we consider the quantity

$$\hat{\mathcal{H}}_{\mathrm{int}}^{n,n+1} \equiv \frac{\langle E_{n+1}(g)| \hat{\mathcal{H}}_{\mathrm{int}} |E_n(g)\rangle}{E_n(g) - E_{n+1}(g)}. \tag{198}$$

with

$$\hat{\mathcal{H}}_{\text{int}} = \sqrt{\omega\omega_0}(\hat{a}^\dagger + \hat{a})\hat{J}_x. \tag{199}$$

This quantity encapsulates the contribution of neighboring energy states to non-adiabatic transitions following a time-dependent protocol $g(t)$. Figure 41(a-b) depicts our results for $\omega_0 = 55$ and 603, and $g/g_* = 1.65$ fixed. Moreover, in Fig. 41(c-d) we represent the product of the diagonal expectation values $C_{nn} = \langle E_n|\,\hat{\mathcal{C}}\,|E_n\rangle$ in adjacent eigenstates. For $\epsilon_{\text{GS}} \leq \epsilon \leq \epsilon_{c1}$ these expectation values are non-vanishing, meaning that transitions between states E_n and E_{n+1} are allowed. The reason is that the states E_n and E_{n+1} are characterized by the same value of $\hat{\mathcal{C}}$, and therefore transitions between them are allowed. However, for $\epsilon_{c1} \leq \epsilon \leq \epsilon_{c2}$, the spectral region between both ESQPTs, the transition amplitudes vanish, which is indicative of transitions being forbidden here. The reason is that between the two ESQPTs adjacent eigenstates effectively belong to different symmetry subspaces, characterized by the $\hat{\mathcal{C}}$ operator. This is clearly observed in Fig. 41(c-d), which show that for adjacent eigenstates $C_{nn} \times C_{n+1\,n+1} = -1$. For $\epsilon \geq \epsilon_{c2}$, $\hat{\mathcal{C}}$ no longer acts as a constant of motion and therefore the classification of eigenstates in symmetry sectors no longer holds. As a consequence, for $\epsilon \geq \epsilon_{c2}$ transitions between adjacent eigenstates are again possible.

We end this section with a more stringent analysis of the behavior of level crossings in finite-ω_0 systems. Now, our focus will be on a single level crossing. Assuming that a Landau-Zener transition [482] consecutively mixes states with different quantum numbers, around a typical crossing the probability of non-adiabatic transitions roughly equals $P_{\text{ND}} \sim e^{-2\pi\Gamma}$ where $\Gamma = (\Delta E)^2/4(\mathrm{d}\Delta E/\mathrm{d}t)$ and ΔE is the gap of the two levels involved in the crossing. This estimation provides a relation between the rate of variation of the coupling parameter in a protocol, $\mathrm{d}g/\mathrm{d}t$, and a definite value of the probability P_{ND}, namely

$$\frac{\mathrm{d}g}{\mathrm{d}t} = -\frac{\pi(\Delta E)^2}{2\ln P_{\text{ND}}}\left(\frac{\mathrm{d}\Delta E}{\mathrm{d}g}\right)^{-1}. \tag{200}$$

In case of an diabatic evolution with an abrupt change of $\langle\hat{\mathcal{C}}\rangle$ at each crossing, $P_{\text{ND}} \ll 1$. For our model, the gap of eigenlevels near a crossing scales as $\Delta E(g) \sim \omega_0 g$ [cf. Fig. 39] and thus for a fixed value of P_{ND}, Eq. (200) implies $\mathrm{d}g/\mathrm{d}t \sim (\Delta E)^2/\omega_0$. For this reason, in order to estimate the protocol rapidity $|\mathrm{d}g/\mathrm{d}t|$ necessary to keep P_{ND} below a certain threshold we need to perform an analysis of how the gap ΔE at an avoided crossing varies with ω_0.

To perform these calculations, standard precision algorithms (double precision arithmetic) may be insufficient because the distance of the levels at the avoided crossing can be below their precision limit; as a consequence, higher precision

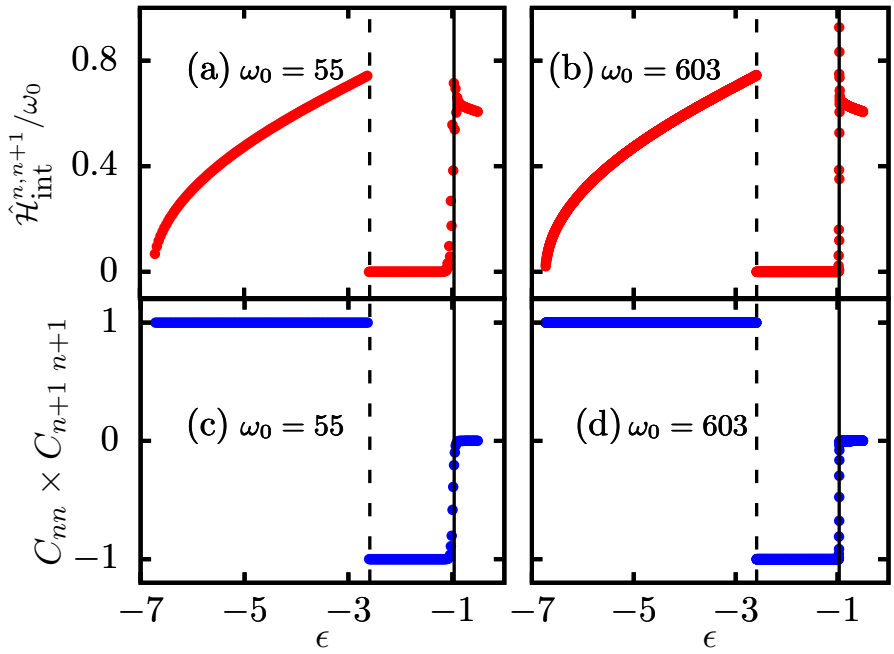

Figure 41: (a-b) Expectation values of $\hat{\mathcal{H}}_{\rm int}$, defined in (198), in consecutive Hamiltonian eigenstates as a function of energy (mean energy of states E_n and E_{n+1}) for (a) $\omega_0 = 55$ and $\omega_0 = 603$. (c-d) Product of the diagonal values of $\hat{\mathcal{C}}$ in consecutive eigenstates, C_{nn} and $C_{n+1\,n+1}$, as a function of the (mean) energy for (c) $\omega_0 = 55$ and (d) $\omega_0 = 603$. System parameters are $\omega = 1$, $\alpha = 1/2$, and $g/g_* = 1.65$. The first ESQPT critical energy, $\epsilon_{c1} = -2.5886$, is marked with black dashed lines, while the second ESQPT, $\epsilon_{c2} = -0.9668$, is marked with full black lines. The photon number cutoff $n_{\rm ph} \in [752, 8135]$ has been optimized according to the value of ω_0.

computations are used, which are considerably time-consuming. We consider two pairs of energy levels close to a given energy at some initial value of the control parameter, $g_i \approx 1.9 g_*$, $\epsilon_n(g_i)$ and $\epsilon_{n+1}(g_i)$, before the avoided crossing occurs, up to some final value, $g_f \approx 2.0 g_*$, after the crossing has taken place (the precise values depend on ω_0). Then, we divide the total span in g into 20 equal parts, and calculate the distance of the two eigenlevels, $|\epsilon_n(g_k) - \epsilon_{n+1}(g_k)|$, at each of these points. We keep only the smallest of these distances in absolute value, ΔE, and the corresponding value of g, g_m. Then, we consider a narrower g-span between g_{m-1} and g_{m+1}, and divide it again into 20 equal parts, to repeat the exact same procedure. This is looped for several iterations, and in each iteration we zoom in on the region where the avoided crossing is expected to occur. For an avoided crossing, the distance between eigenlevels ΔE must saturate to a finite value, as the two levels do not exactly overlap. The results for ΔE, as a function of the resolution $\Delta g = g_{k+1} - g_{k-1}$, are shown in Fig. 42(a,c) for different values of ω_0; in

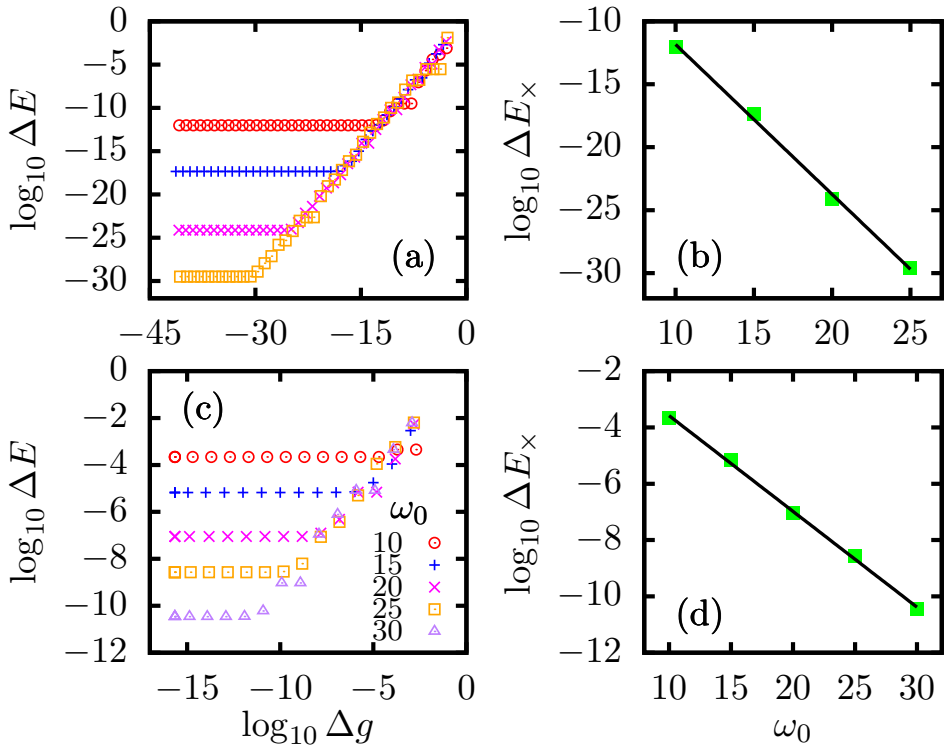

Figure 42: (a,c) Estimation of the minimum separation of eigenlevels around an avoided crossing, ΔE, as a function of the control parameter width, Δg for the deformed Rabi model (192) with $\alpha = 1/2$. Different symbols are used to represent the case of different value of ω_0 [see legend in (c)]. In (a), the studied crossings take place at $\epsilon \approx -4$, whereas in (c) they occur for $\epsilon \approx -2$. (b,d) Finite-size scaling, as a function of the thermodynamic limit parameter ω_0, of the saturation of the minimum distance at an avoided crossing for the same crossings in (a,c). We find exponential decays of the form $\Delta E_\times(\omega_0) \sim 10^{-\delta\omega_0}$ with $\delta \approx 1.19$ in (b), and $\delta \approx 0.34$ in (d).

(a), the pair of levels studied are close to $\epsilon = -4$ for all ω_0, while in (c) they are close to $\epsilon = -2$. The extremely small values where the saturation of ΔE occurs in (a) are remarkable; for $\omega_0 = 10$, the distance of the pair of levels at the crossing is $\Delta E \sim 10^{-13}$, which further decreases as ω_0 is increased, and to resolve this avoided crossing one needs to consider the evolution of the levels within a width of $\Delta g \sim 10^{-14}$, which is already a very small variation of the coupling parameter. We emphasize that for $\omega_0 = 15$, which is relatively far away from the thermodynamic limit, the saturation distance is already below the standard numerical precision limit, $\Delta E \sim 10^{-17}$. In (c), ΔE shows the same qualitative behavior as in (a), but the gap between levels is larger. The value at which ΔE saturates will be now denoted $\Delta E_\times$; this value estimates the gap of the pair of levels at the avoided crossing. This is represented in Fig. 42(b,d) as a function of ω_0, directly obtained

from panels (a,c), respectively. In both cases, this level gap exhibits an exponential decay of the form $\Delta E_\times \sim 10^{-\delta\omega_0}$, $\delta > 0$, indicating that the *avoided crossings are transformed exponentially into real crossings* as ω_0 increases, $\Delta E_x \to 0$. The value of δ depends on the energy around which the avoided crossing takes place; δ decreases as the logarithmic ESQPT around $\epsilon \approx -1$ is approached, as the ESQPT is only fully realized in the limit $\omega_0 \to \infty$.

This analysis allows us to estimate the rate of variation of g such that the time evolution is effectively adiabatic and the two wave functions near a level crossing do not swap. From Eq. (200), we have $\mathrm{d}g/\mathrm{d}t \sim (\Delta E)^2/\omega_0 \sim 10^{-2\delta\omega_0}/\omega_0$, which is exponentially small in ω_0. We emphasize that these values are below standard numerical precision already for quite small values of ω_0. Therefore, for numerically and experimentally relevant processes, $P_{\mathrm{ND}} \sim 1$ at each avoided crossing, meaning that the conservation of $\langle\hat{\mathcal{C}}\rangle$ is essentially perfect, even though this operator is strictly constant only in the $\omega_0 \to \infty$ limit.

Summarizing, even in finite-size systems, non-adiabatic transitions between levels with different values of $\langle\hat{\mathcal{C}}\rangle$ are very much suppressed. In the next section, we will take advantage of this effect to engineer an energy cat state through unitary time evolution of an initial wave function.

3.4.3 Engineering cat states in the spectral domain

Our protocol has the following steps. We prepare an initial state as the ground-state of the Hamiltonian Eq. (192), i.e., $|\Psi(g_{\mathrm{ini}})\rangle = |\epsilon_{\mathrm{GS}}(g_{\mathrm{ini}})\rangle$ with $g_{\mathrm{ini}} = 2.5g_*$. This initial state is then quenched, $g_{\mathrm{ini}} \to g_{\mathrm{fin}} = 1.05g_*(\alpha)$, leading the wave function to a spectral region above ϵ_{c2}. Immediately after this initial quench, the state will be well located around the corresponding value of $\langle\hat{q}\rangle$. A slow driving $g(t)$ is then simulated by sequentially quenching $g_i \to g_{i+1}$, $i = 1, 2, ...$, such that $g_1 \equiv g_{\mathrm{fin}}$, according to $g_{i+1} = g_i + \Delta_g$ with a step $\Delta_g = 2 \times 10^{-5}$ sufficiently small to suppress non-adiabatic transitions. After each quench, the non-equilibrium state is allowed to relax during a time $\tau = 10^6$ (arbitrary units). According to the time-independent Schrödinger equation, this state reads

$$|\Psi(g)\rangle = \sum_n c_n(g) e^{-iE_n(g)\tau} |E_n(g)\rangle\,, \tag{201}$$

where all energies and eigenstates are now those corresponding to a Hamiltonian with a given g, $\hat{\mathcal{H}}(g)\,|E(g)\rangle = E(g)\,|E(g)\rangle$, and $c_n(g_i) \equiv \langle E_n(g_i)|\Psi(g_{i-1})\rangle$. This process of small quenches comes close to a real time-dependent protocol where $g(t)$ varies continuously, and it is also less computationally demanding.

At each value of g, the LDOS reads

$$P(\epsilon(g)) \equiv \sum_n |\langle \epsilon_n(g)|\Psi(g)\rangle|^2 \delta(\epsilon - \epsilon_n) = \sum_n |c_n(g)|^2 \delta(\epsilon - \epsilon_n). \tag{202}$$

Clearly, since the initial state is the ground-state of the initial Hamiltonian, $P(\epsilon(g = g_{\rm ini})) = \delta(\epsilon - \epsilon_{\rm GS}(g_{\rm ini}))$ with $\epsilon_{\rm GS}(g_{\rm ini}) = -13.4128$ (not shown). Quenching this initial state to $g_{\rm fin}$ has the effect of widening this peak distribution. For visual convenience, in Fig. 38 we have represented the trajectory followed by the wave function with a full yellow line. As expected, the average energy of the wave function decreases with g.

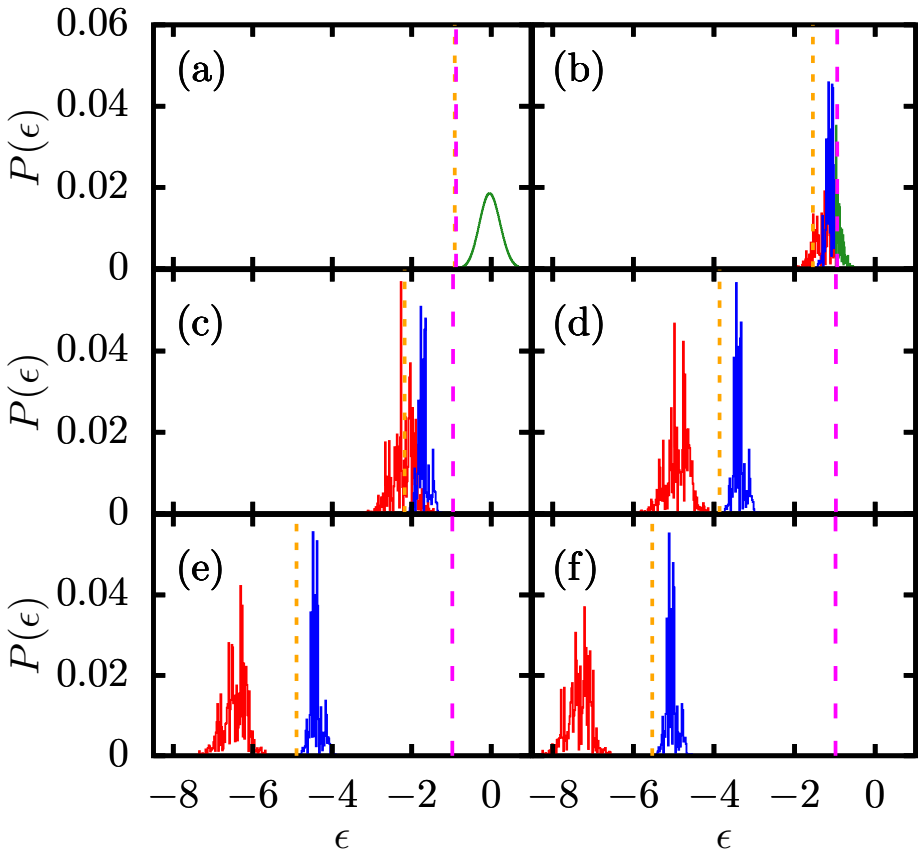

Figure 43: Distribution of populated states (LDOS) [see (202)] of the Rabi Hamiltonian at several values of the coupling parameter g. System parameters are $\omega = 1$, $\omega_0 = 100$, and $\alpha = 1/2$. The value of g/g_* changes in each panel as (a) 1.05, (b) 1.34, (c) 1.54, (d) 1.94, (e) 2.14, and (f) 2.25. The ESQPTs critical energies ϵ_{c1} and ϵ_{c2} are represented with dotted orange and dashed magenta vertical lines in each case, respectively. The cutoff in the number of photons is $n_{\rm ph} = 1900$.

In Fig. 43 we show six cases of the full distribution. These cases correspond to the green points in Fig. 38. The ESQPTs critical energies ϵ_{c1} (orange) and ϵ_{c2} (magenta) have been represented with dashed vertical lines. A green distribution

indicates that the populated eigenstates do not have $\hat{\mathcal{C}}$ assigned quantum number as this operator is not a constant of motion for those values of energy; red and blue distributions indicate that the corresponding eigenstates have $\langle\hat{\mathcal{C}}\rangle \leq -0.95$ and $\langle\hat{\mathcal{C}}\rangle \geq 0.95$, respectively. Figure 43(a) shows $P(\epsilon)$ after the first quench $g_{\text{ini}} \to g_{\text{fin}}$. The LDOS is close to a Gaussian distribution with mean $\langle\epsilon\rangle \approx 0$. The form of the distribution is a consequence of the initial state at g_{ini} being the ground-state of the system, which closely resembles a coherent state. The LDOS has significantly widened in Fig. 43(b) as a consequence of non-adiabatic transitions, and it has almost completely crossed the logarithmic ESQPT at ϵ_{c2}. For $\epsilon \leq \epsilon_{c2}$ the classical phase space already features disconnected trajectories to which $\hat{\mathcal{C}}$ assigns quantum numbers of opposite sign. This is the reason why two different modes start to show up in the distribution $P(\epsilon)$ (in red vs. blue). In Fig. 43(c) the wave function has completely crossed the logarithmic ESQPT at ϵ_{c2}. Importantly, the part of $P(\epsilon)$ associated to $\langle\hat{\mathcal{C}}\rangle = -1$ has a lower average energy than the part with $\langle\hat{\mathcal{C}}\rangle = +1$. As previously explained, this is expected from the level-flow diagram Fig. 38: eigenstates with different $\hat{\mathcal{C}}$ quantum numbers have different level curvatures, which gives rise to essentially independent dynamical evolutions. The separation between the two modes in the LDOS then increases with g. Thus, Fig. 38(d) shows a now completely clear bimodal structure in the LDOS. This panel also shows how the mode of $P(\epsilon)$ with $\langle\hat{\mathcal{C}}\rangle = -1$ has *crossed* the first critical line at ϵ_{c1}, while the part of $P(\epsilon)$ with $\langle\hat{\mathcal{C}}\rangle = +1$ gets trapped before this barrier. The reason for this is that when the quantum package approaches the ESQPT at ϵ_{c1}, only the mode of the LDOS with $\langle\hat{\mathcal{C}}\rangle = -1$ will be able to pass through, and the mode with $\langle\hat{\mathcal{C}}\rangle = +1$ will be inevitably restrained above this critical energy: indeed, states with $\langle\hat{\mathcal{C}}\rangle = +1$ are simply not allowed below ϵ_{c1} [cf. Fig. 38]. Consequently, as time goes by the two modes of a new bimodal distribution $P(\epsilon) = P(\epsilon_+) + P(\epsilon_-)$ will be increasingly further apart in energy. This picture is confirmed in Fig. 43(d)-(f), which illustrate the inevitable emergence of energy cat states.

Before we end this section, we interpret the formation of energy cat states in terms of the classical limit of the model. We solve the eigensystem $\hat{q}\,|q_n\rangle = q_n\,|q_n\rangle$ of the bosonic quadrature $\hat{q} = (\hat{a}^\dagger + \hat{a})/\sqrt{2}$. The eigenvalues of $\hat{q}$, q_n, are related to the position of the wave function in the classical two-dimensional phase space. Following the quench protocol explained above, we compute the time-averaged probability that the quenched wave function $|\Psi(g)\rangle$ be found at q_n, i.e.,

$$P(q_n) = \sum_m \overline{P(\epsilon_m)}\,|\,\langle q_n|\epsilon_m\rangle\,|^2. \tag{203}$$

Figure 44 shows the probability $P(q_n)$ for several values of g. Figure 44(a) clearly shows that the wave function can explore both regions of the classical phase space.

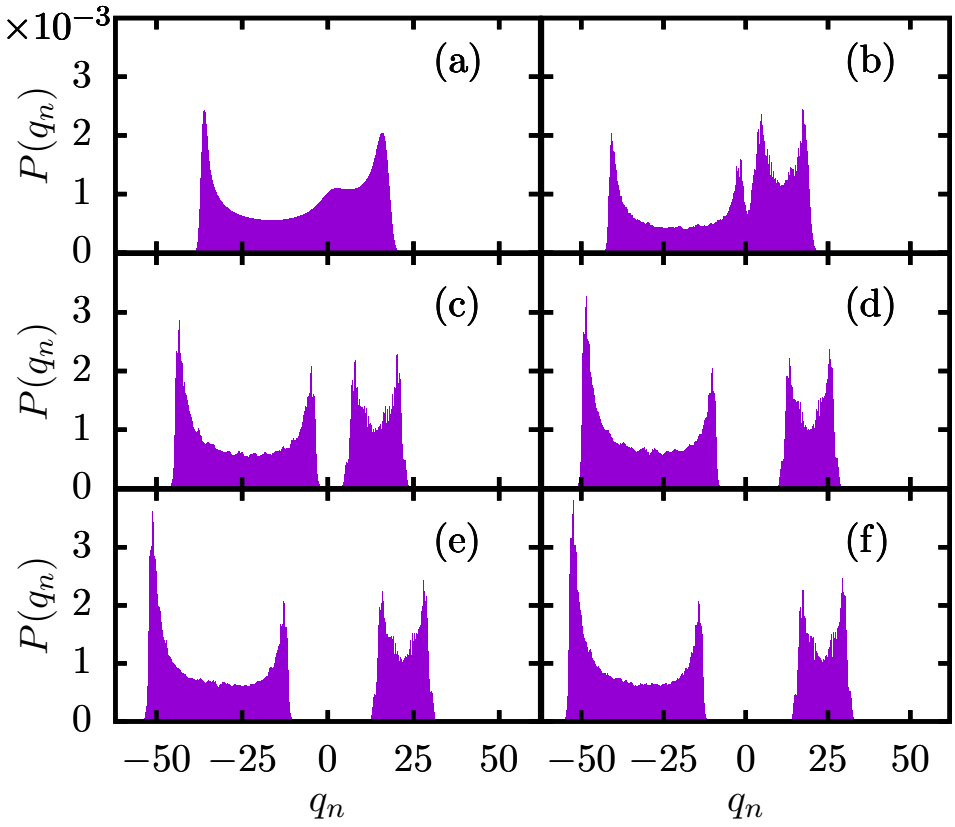

Figure 44: Probability of measuring the quenched state $|\Psi(g)\rangle$ at the generalized position q_n, defined in (203). The parameters of the deformed Rabi model (192) are $\omega = 1$, $\omega_0 = 100$, and $\alpha = 1/2$. Following our previous result in Fig. 43, the value of the control parameter g/g_* is: (a) 1.05, (b) 1.34, (c) 1.54, (d) 1.94, (e) 2.14, and (f) 2.25. The cutoff in the number of photons is $n_{\rm ph} = 1900$.

This is due to the wave function average energy being above the second ESQPT at ϵ_{c2}, where the classical phase space is connected [cf. Fig. 34]. In Fig. 44(b) we observe that the wave function is only now starting to separate into two disconnected packets, with a small dip in probability near $q_n = 0$. Finally, Fig. 44(c-f) illustrates how the separation of the modes increases with g. We note that the deformed Hamiltonian, with $\alpha \neq 0$, features an asymmetric double-well structure and, as a consequence, the probabilities $P(q_n)$ are different at each side of the classical phase space: $P(q_n)$ is wider for $q_n < q_{c2}$. Summarizing, the energy cat states induced by the parity-breaking ESQPT also imply the formation of *spatial* cat states, leading to a coherent superposition of two macroscopically distinct states.

3.4.4 Equilibrium dynamics in energy cat states

Having established the formation of energy cat states in the deformed Rabi model, we pose the following question: is it possible to describe the long-time effective equilibrium values under these circumstances?

As explained in Sec. 1.1.2, quantum thermalization refers to the process by which the expectation value of a physical observable attains a stable equilibrium value around which it simply oscillates for sufficiently long times [1]; this equilibrium value coincides with its long-time average. However, an equilibrated state is only called thermal if it can be described by a thermal ensemble of statistical mechanics. It follows from (9) that, in the absence of degeneracies, the long-time average of an observable $\hat{O}$ can be written

$$\overline{\langle \hat{O} \rangle} = \sum_n P(E_n) \langle E_n | \hat{O} | E_n \rangle \tag{204}$$

with $P(E_n) \equiv |c_n|^2$ being the LDOS, and $c_n = \langle E_n | \Psi(0) \rangle$. From this expression it is clear that $\overline{\langle \hat{O} \rangle}$ strongly depends on the diagonal expectation values $O_{nn} = \langle E_n | \hat{O} | E_n \rangle$ such that the population distribution $P(E_n)$ attains high values, whereas the full average is less sensitive to expectation values for eigenstates with small $P(E_n)$.

In order to analyze the equilibration dynamics under energy cat states, we monitor the expectation value of physically relevant observables as the quench protocol described in the previous section is carried out. In each iteration of the protocol, the initial state is the final state of the previous iteration, and this is used to calculate the LDOS at each step of the protocol. Equations (204) and (10) allow us to compute the long-time averages and corresponding microcanonical values. In Fig. 45 we represent the exact long-time averages and the predictions of the standard microcanonical ensemble and compare them with a generalization of the microcanonical ensemble that we develop below. Figure 45(a) depicts $\hat{\mathcal{C}}$ as a function of $g/g_*(\alpha = 1/2)$. This figure clearly shows how $\langle \hat{\mathcal{C}} \rangle$ gets stuck at $\langle \hat{\mathcal{C}} \rangle \sim -0.2$ below ϵ_{c2} (black points), which is a consequence of the conservation of $\hat{\mathcal{C}}$. The standard microcanonical average is shown with empty triangles. This thermal average fails to describe the real long-time averages due to the pathological form of the LDOS under cat states. For $g/g_* \gtrsim 2.1$, the microcanonical average reaches its minimum possible value, $\langle \hat{\mathcal{C}} \rangle = -1$. This is because all eigenstates within a small window around the global average energy $\langle E \rangle$ have $\langle \epsilon_n | \hat{\mathcal{C}} | \epsilon_n \rangle = -1$. As a consequence, in order to properly describe the real long-time average of the $\hat{\mathcal{C}}$ operator, simply weighting the population of each state in a small energy window around the average energy will not be enough for energy cat states. This method will always

yield $\langle\hat{\mathcal{C}}\rangle = -1$, which is certainly not the real value attained by this operator. This remark is important because this weighting method has been used to build a generalized microcanonical ensemble in [483], and the generalized Gibbs ensemble is also rooted in this[4].

As previously mentioned, this anomalous behavior is a consequence of the bimodal structure of the LDOS in an energy cat state. Let us consider that the LDOS can be split into two parts, $P(E_n) = P(E_{n,+}) + P(E_{n,-})$, where $E_{n,\pm}$ denotes the states with $\langle\hat{\mathcal{C}}\rangle = \pm 1$, respectively. Therefore, $\mathcal{P}(E_{n,\pm}) \equiv P(E_{n,\pm})/\sum_n P(E_{n,\pm})$ are the corresponding probability distributions. Unlike $P(E_n)$, each $\mathcal{P}(E_{n,\pm})$ is a unimodal distribution, so it is well centered about its average value and they are closer to a Gaussian distribution, as visible in Fig. 43(d)-(f). Thus, one may compute the mean energy of the states with definite a charge $\langle\hat{\mathcal{C}}\rangle = \pm$, $\langle E_\pm\rangle = \sum_n E_{n,\pm}\mathcal{P}(E_{n,\pm})$. In essence, this is equivalent to two simultaneous microcanonical averages, where each average is performed around the mean energy of states with a definite $\hat{\mathcal{C}}$ quantum charge, $\langle E_{n,+}\rangle$ and $\langle E_{n,-}\rangle$. Therefore, we propose the following variation of the microcanonical ensemble:

$$\begin{aligned}\overline{\langle\hat{O}\rangle}_{\text{ME2}} = \frac{p_+}{N_+} \sum_{E_{n,+}\in[E_+-\Delta E_+,E_++\Delta E_+]} \langle E_{n,+}|\,\hat{O}\,|E_{n,+}\rangle + \\ + \frac{p_-}{N_-} \sum_{E_{n,-}\in[E_--\Delta E_-,E_-+\Delta E_-]} \langle E_{n,-}|\,\hat{O}\,|E_{n,-}\rangle\,,\end{aligned} \tag{205}$$

with

$$p_\pm \equiv \frac{1 \pm \overline{\langle\hat{\mathcal{C}}\rangle}}{2}. \tag{206}$$

Here, $p_\pm$ denote the probability that a wave function be fully localized within the left (-1) or right $(+1)$ classical energy well. For a general superposition, we have $0 \leq p_\pm \leq 1$ and $p_+ + p_- = 1$. The rest of Eq. (205) has the same interpretation as in the standard microcanonical ensemble Eq. (10), with the exception that now two averages are performed instead of just one, within two different energy windows that can potentially contain a different number of states. It is worth noting that Eq. (205) is built taking into consideration the separation in energy subspaces allowed by $\hat{\mathcal{C}}$, so the ensemble is undefined in spectral regions where $\hat{\mathcal{C}}$ is not a constant of motion. Also, by definition $\overline{\langle\hat{\mathcal{C}}\rangle}_{\text{ME2}} = p_+ - p_- = \overline{\langle\hat{\mathcal{C}}\rangle}$.

Let us reconsider the results in Fig. 45. In addition to $\langle\hat{\mathcal{C}}\rangle$, in Fig. 45(b) we show our results for $\langle\hat{a}^\dagger\hat{a}\rangle$ and Fig. 45(c) shows those of $\langle\hat{a}^\dagger + \hat{a}\rangle$. In these figures,

4 At least under the conditions where microcanonical and canonical ensemble become equivalent, the generalized Gibbs ensemble gives rise to a distribution which is only significantly populated within a small energy window around the expected value for the energy, with an irregular shape determined by the expected values of other constants of motion.

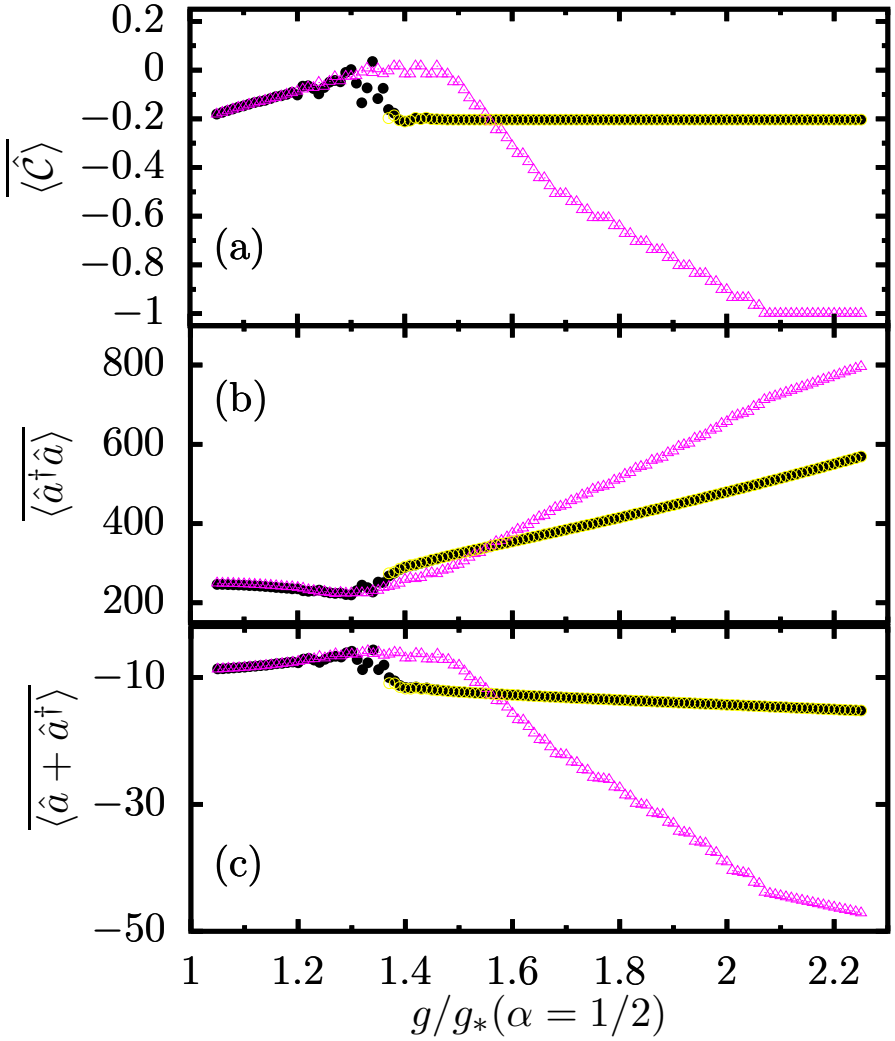

Figure 45: Analysis of equilibrium values of physical observables in the energy cat states. Exact long-time averages (204) are represented with black points; the predictions of the standard microcanonical ensemble (10) are represented with empty triangles, and those of the modified microcanonical ensemble (205) are shown with empty circles. The parameters of the deformed Rabi model (192) are $\omega = 1$, $\omega_0 = 100$, and $\alpha = 1/2$. For the standard microcanonical ensemble, we have considered a window consisting of 30 states on both sides of the average energy (a total of $N = 61$ states), whereas for the modified microcanonical ensemble each of the energy windows has 15 levels on each side of the average energy ($N_+ = N_- = 31$). In (205), $p_+ = 0.3984$ and $p_- = 0.6016$. The cutoff in the number of photons is $n_{\rm ph} = 1900$.

empty yellow circles represent the predictions of the generalized microcanonical ensemble in Eq. (205), is represented by empty yellow circles. It has only been computed for g such that $\hat{\mathcal{C}}$ acts a constant of motion. Although for small values

of g close to $g_{\text{fin}} = 1.05 g_*(\alpha = 1/2)$ the exact long-time averages and the standard microcanonical values agree very well, further increasing g brings about significant discrepancies and already for $g/g_*(\alpha = 1/2) \gtrsim 1.3$ they do not agree at all. However, the predictions of the generalized microcanonical ensemble, Eq. (205), provide a perfect description for all three observables and for the values of g where $\hat{\mathcal{C}}$ is constant.

We conclude that in order to properly describe the long-time effective values of physical observables in energy cat states our generalized version of the microcanonical ensemble, Eq. (205), has to be used instead of the standard Eq. (10). A byproduct of our results is that energy cat states are characterized by two different internal energies, leading to different temperatures. For an generic isolated quantum system, the microcanonical temperature [270] can be defined as $1/T = \partial S(E)/\partial E$, where $S(E)$ is the system's entropy (we have set $k_B = 1$). In the case of our energy cat states, characterized by average energies E_+ and E_-, the entropy can be written as a bivariate function, $S(E_+, E_-) = \ln\left[\varrho_+(E_+) + \varrho_-(E_-)\right]$, where $\varrho_\pm(E_\pm)$ denotes the part of the level density pertaining to states with opposite quantum charges, $\langle \hat{\mathcal{C}} \rangle = \pm 1$. Therefore, we can define two different microcanonical temperatures, $1/T_\pm = \partial S(E_+, E_-)/\partial E_\pm$, each one evaluated at the corresponding value of the average energy of the bimodal distribution of the cat state.

3.5 CONCLUSIONS

In this Chapter we have presented a theory for constants of motion in systems with $\mathbb{Z}_2$ symmetry-breaking phase transitions. These constants of motion are revealed as operators whose time evolution becomes frozen at its initial value in the infinite-size limit of the system. They are, therefore, emergent constants of motion that restrict the dynamical behavior of the system in a significant way. Our general framework relies on the concept of symmetry-breaking and symmetric phases, where equilibrium states of different nature can be found depending on whether they break or remain invariant under some global symmetry of the system. In particular, in symmetry-broken phases it is possible to build a constant of motion, $\hat{\mathcal{C}}$, directly from the order parameter of the phase transition. A second emergent constant of motion, $\hat{\mathcal{K}}$, then immediately emerges from $\hat{\mathcal{C}}$ and some global symmetry of the system, $\hat{\Pi}$, closing a SU(2) algebra in the symmetry-broken phase. Our theory applies to a wide range of quantum many-body systems exhibiting $\mathbb{Z}_2$ symmetry-breaking phase transitions; in this Chapter, we have presented numer-

ical illustrations in power-law interacting spin chains and also in fully-connected systems such as the LMG model. The advantage of the latter is that in our collective models it is possible to really approach the infinite-size limit due to the conservation of total angular momentum, which reduces the Hilbert space dimension from exponential to linear. Additionally, these models undergo an ESQPT which splits the spectrum into symmetry-breaking and symmetric phases, which makes them extremely useful for our purposes. We should note that our results on the deformed Rabi model exemplify how our general theory in Sec. 3.2 still applies to systems where no $\mathbb{Z}_2$ symmetry is present as long as the model displays disconnected components where the dynamics is restricted. These components can take the form of quantum wells, and these can be equivalent or asymmetric.

After presenting the theory itself, we have analyzed how it can be employed to understand several physical mechanisms. Currently, dynamical phase transitions I and II are the focus of much theoretical and experimental research. Our study of DPTs has been carried out in the LMG model, which can be understood as the fully-connected version of the transverse-field Ising model, a prototypical system to study DPTs. We have shown that in the symmetry-broken phase, where the DPT-I order parameter is non-zero, the effective long-time equilibrium states can be described by a generalization of the ETH that incorporates the information contained in the set of constants of motion $\{\hat{\mathcal{C}}, \hat{\mathcal{K}}, \hat{\Pi}\}$. However, in the symmetric phase, where the DPT-I order parameter vanishes, the only relevant constant of motion is the global symmetry $\hat{\Pi}$, and the standard ETH arguments are valid again. We expect our results to be generically valid for any phase transition giving rise to spectral phases with the mathematical properties presented in our theory. Regarding DPTs-II, characterized by non-analytical values of some return amplitudes at so-called critical times, we have provided both analytical and numerical results. We have proved that the previously accepted mechanism for the appearance of critical times can only take place in the symmetric phase, while it is forbidden in the symmetry-broken phase. The presence of degenerate eigenlevels of opposite parity plays an important part in the mathematical proof, as well as the constancy of the $\hat{\mathcal{C}}$ operator. We have also shown that in the symmetry-broken phase the parity-projected return probability and the usual survival probability exactly coincide in the infinite-size limit, whereas they are different functions in the symmetric phase. Our numerical results corroborate this picture. Importantly, the final average energy of state initially prepared in the symmetry-broken phase and then taken out of equilibrium through a quantum quench plays an important role in the phase diagram of DPTs-II. If the final energy is such that the state ends up in the symmetry-broken phase, one will observe an anomalous DPT-II phase, whereas if the state ends up in the symmetric spectral phase one will find the

so-called regular DPT-II phase. In the case of $\mathbb{Z}_2$ fully-connected models sharing structural properties with the LMG model, the change of phase type is triggered by the ESQPT non-analiticity. In this Chapter we have also defined a complexified survival amplitude and we have analyzed its versatility in unveiling the presence of non-analytical times in the survival probability. In the future, it will be interesting to establish a robust connection between the DPTs and the thermal phase transitions present in many systems that also exhibit ESQPTs. We have already taken important steps in this direction [484].

In the last section of this Chapter we have studied the equilibration process in the presence of cat states. Our model Hamiltonian is a deformed version of the famous Rabi model, a quantum optical system modeling the interaction between light and a single two-level atom. The system exhibits two ESQPTs of different nature, stemming from the modification of the classical phase space induced by the addition of a deformation term in the Hamiltonian, which breaks the parity symmetry that the usual Rabi model usually has. The first ESQPT is of the jump type, and above its defining critical energy one may find two disconnected classical wells, whereas below this critical energy there is a single classical well. The second ESQPT, of the logarithmic type, marks the critical energy above which these two wells merge into a single one. We have proposed a protocol to create an energy cat state –a Schrödinger cat state involving a quantum superposition of both different positions and energies– by slowly crossing these two different ESQPTs. In practice, this is accomplished by sequentially quenching a state in such a way that a periodic driving in the control parameter is simulated. We have studied the time evolution of typical observables in these energy cat states. The fact that the local density of states resembles a bimodal distribution means that the ETH is invalid. We have shown that the effective long-time equilibrium states of observables can be described by a generalization of the microcanonical ensemble once the information of the $\hat{\mathcal{C}}$ operator is properly accommodated. In short, this last part of the Chapter exemplifies an application of $\hat{\mathcal{C}}$ to a system with no parity $\mathbb{Z}_2$ symmetry.

4 CHAOS IN A DEFORMED DICKE MODEL

In the previous parts of this thesis we have provided abundant evidence on the effect that symmetry-breaking can have on quantum dynamics, namely the loss of quantum ergodicity as a consequence of the appearance of a set of quantum conserved quantities. If thermalization is impacted by this phenomenon, it is natural to suspect that its main triggering mechanism, chaos, will also exhibit some peculiar behavior. Most of the systems considered in Sec. 3 are fully-connected systems with a single classical effective degree of freedom and, therefore, they do not support chaotic dynamics in any way. For this reason, in this Chapter we will focus on a system with two degrees of freedom. Its key feature is that for certain values of the control parameters its dynamics is constrained to disconnected regions, which means not all configurations can be simultaneously accessed from any given point of the phase space. Can such a system be chaotic? If this question is to be answered affirmatively, what is the effect of disconnected wells on its onset? Although the results of this thesis are mostly theoretical, in this Chapter we also directly connect with experimental results confirming our predictions.

This Chapter contains three sections. In Sec. 4.1 we provide an overview of the deformed version of the Dicke model that we employ in subsequent sections. Sec. 4.2 is devoted to our theoretical analysis of chaos in the deformed Dicke model, and it is based on our article [328]. Finally, Sec. 4.3 focuses on an experimental realization of the model as well as a verification of the main physical points discussed in our theoretical study, this section being based on our article [485].

4.1 PRELIMINARIES

4.1.1 Deformed Dicke model

We consider a deformation of the Dicke Hamiltonian, formally analogous to the deformation of the Rabi Hamiltonian analyzed in Sec. 3.4, where we include a direct coupling to an external bosonic reservoir,

$$\hat{H} = \omega \hat{a}^\dagger \hat{a} + \omega_0 \hat{J}_z + \frac{2\lambda}{\sqrt{N}} \hat{J}_x (\hat{a}^\dagger + \hat{a}) + \sqrt{\frac{N\omega_0}{2}} \alpha (\hat{a}^\dagger + \hat{a}), \tag{207}$$

where we have set $\hbar = 1$. As in the standard Dicke model, the parameter ω is the frequency of the bosonic field, while ω_0 represents a constant splitting of the atom eigenlevels (energy difference). For our analyses, we fix $\omega = \omega_0 = 1$ throughout. Here, $\hat{a}^\dagger$ and $\hat{a}$ are the usual bosonic creation and annihilation operators, and $\hat{\mathbf{J}} = (\hat{J}_x, \hat{J}_y, \hat{J}_x)$ are collective pseudo-spin operators acting on the N two-level atoms. The Hamiltonian (207) conserves the total spin operator, $[\hat{H}, \hat{\mathbf{J}}^2] = 0$. Therefore, the Hamiltonian can be split into symmetry sectors according to the eigenvalues of $\hat{\mathbf{J}}^2$, denoted $j(j+1)$. The dynamics of each of these symmetry sectors is independent from the others. We consider the maximally symmetric sector, defined by $j = N/2$, which is more relevant for experimental realizations [486] as the ground-state of the system is contained in this sector. In order to compare quantum and classical results, we define the rescaled energy $\epsilon \equiv E/(\omega_0 j)$, which is intensive and thus does not depend on system size. Finally, the constant α is the deformation strength. The standard Dicke Hamiltonian is recovered for $\alpha = 0$. A value $\alpha \neq 0$ gives rise to important qualitative changes in the structure of the model. One of the most relevant changes is that the Dicke Hamiltonian with $\alpha = 0$ is invariant under a $\mathbb{Z}_2$ parity transformation; in particular, it commutes with the operator $\hat{\Pi} \equiv \exp[i\pi(j + \hat{J}_z + \hat{a}^\dagger \hat{a})]$. However, if $\alpha \neq 0$ commutation relation is broken, $[\hat{H}, \hat{\Pi}] \neq 0$. When $\alpha = 0$, the Dicke model undergoes a second-order QPT at the critical coupling $\lambda_c(\alpha = 0) \equiv \sqrt{\omega\omega_0}/2$, and for $\lambda > \lambda_c(\alpha = 0)$ its level density exhibits a logarithmic singularity at $\epsilon_c = -1$ in its first derivative [94], [305]. If $\alpha \neq 0$, the model becomes less mathematically tractable, and most of these special values cannot be written in terms of elementary functions (see [81]).

As mentioned in the Introduction, the Dicke model has played an important role in the field of quantum statistical mechanics and in particular in analyses of chaos and thermalization (see, e.g., [95], [300], [305], [309]). Indeed, the model is in general non-integrable for all values of α. However, certain adiabatic constants of motion have been identified in the low-lying region of the spectrum close the ground-state; in this spectral region, the system does approximately behave as an integrable model [349]. More details on these features will be given later on.

In order to diagonalize the Hamiltonian (207) numerically, we employ the Dicke-Fock basis $\{|m, n\rangle\}$ where $|m, n\rangle = |m\rangle \otimes |n\rangle$ is the tensor product of the atomic and bosonic constituents. The atomic quantum number m can only vary in the range $m = -j, -j+1, \ldots, j-1, j$, while the quantum number associated to the photonic part of the Hilbert space $n = 0, 1, 2, ...$ can take any non-negative value and is thus unbounded. For this reason, we note that the total Hilbert space is infinite-dimensional for any value of the infinite-size limit parameter j (or N). As in the Rabi model of Sec. 3.4, computing numerical results necessarily means that some sort of cut-off must be implemented in the photonic part of the Hilbert space.

By truncating the number of photons $n = 0, 1, \ldots, n_{\rm ph} < \infty$, the dimension of the truncated Hilbert space reads $D = (2j+1)(n_{\rm ph}+1)$. In this Chapter, all of our numerical simulations have been carried out with $N = 60$ atoms and $n_{\rm ph} = 720$. Our numerical results are properly converged up to energies $\epsilon \approx 1.83$ (higher energy states are not reliable due to the truncation of the Hilbert space). In any case, we will only consider energies $\epsilon \leq 1$. Convergence of results is imposed by requiring that the relative difference between eigenvalues calculated with $n_{\rm ph}$ and $\lfloor 1.1 n_{\rm ph} \rfloor$ photons be smaller than 10^{-3}; states for which this difference is larger than 10^{-3} are discarded.

4.1.2 The classical deformed Dicke Hamiltonian

In the infinite-size limit $N \to \infty$ ($j \to \infty$), many properties of the quantum Hamiltonian (207) converge to the behavior expected from its classical limit. This mean-field solution can be computed by taking the expectation value of the quantum model $\hat{H}$ in Glauber-Bloch coherent states, defined through the tensor product $|\text{GB}\rangle \equiv |q,p\rangle \otimes |Q,P\rangle$. On the one hand, the bosonic part is described by the Glauber coherent state $|q,p\rangle$, which can be written

$$|q,p\rangle = \exp\left\{-\frac{j}{4}(q^2+p^2)\right\}\exp\left\{\sqrt{\frac{j}{2}}(q+ip)\hat{a}^\dagger\right\}|0\rangle\,, \tag{208}$$

where $|0\rangle$ is the radiation vacuum. On the other hand, the atomic part is described by the Bloch coherent state $|Q,P\rangle$, which reads

$$|Q,P\rangle = \left(1-\frac{Q^2+P^2}{4}\right)^j \exp\left\{\frac{Q+iP}{\sqrt{4-P^2-Q^2}}\hat{J}_+\right\}|j,-j\rangle\,, \tag{209}$$

with $|j,-j\rangle$ representing the state with all atoms in the ground-state. A mathematical expression for the classical Hamiltonian can be completely worked out by making use of the standard techniques of Glauber-Bloch states [487]. We arrive at the following intensive energy functional:

$$\begin{aligned} H \equiv \frac{\langle \text{GB}|\,\hat{H}\,|\text{GB}\rangle}{\omega_0 j} &= \frac{\omega}{2\omega_0}(q^2+p^2) + \frac{1}{2}(Q^2+P^2) \\ &+ \frac{2\lambda q Q}{\omega_0}\sqrt{1-\frac{1}{4}(Q^2+P^2)} - 1 + \sqrt{\frac{2}{\omega_0}}\alpha q. \end{aligned} \tag{210}$$

Here, the variables $\mathbf{x} \equiv (q,p,Q,P) \in \mathcal{M}$ are classical canonical coordinates. While the photonic variables (q,p) are unbounded, $q,p \in \mathbb{R}$, the atomic part of the classical space is restricted to a 2-dimensional ball of radius 2, $\mathbb{S}^2 \equiv \{(Q,P) \in \mathbb{R}^2 \;:\; 0 \leq Q^2+P^2 \leq 4\}$. In other words, the total phase space is $\mathcal{M} = \mathbb{R}^2 \times \mathbb{S}^2 \subset \mathbb{R}^4$. Because

the model is fully-connected, the effective Planck constant $\hbar_{\text{eff}} = 1/j$ vanishes in the infinite-size limit [488].

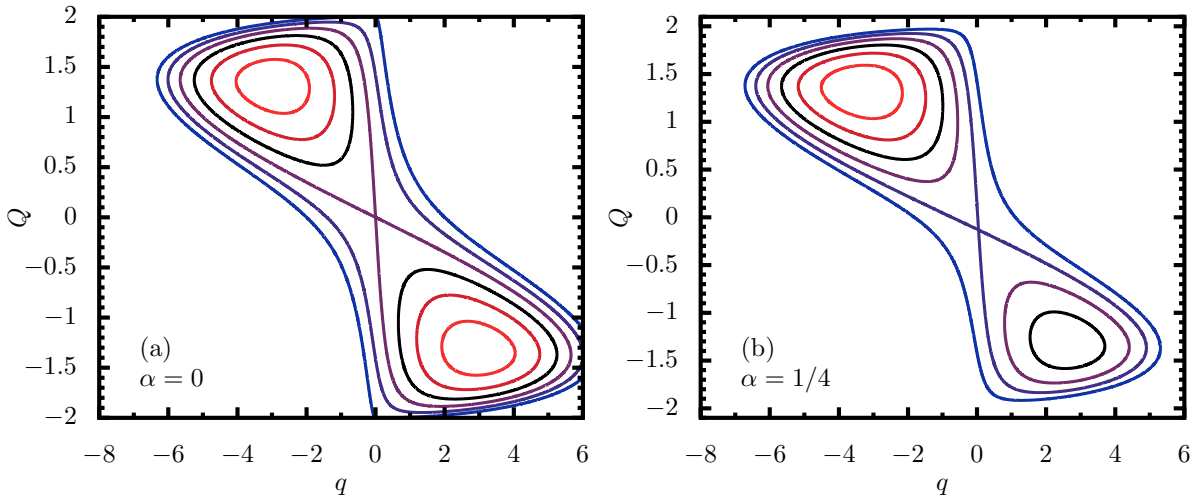

Figure 46: Analysis of the classical phase space of the Dicke Hamiltonian. We represent the projection on the (q, Q) plane of the constant energy surfaces of the classical limit derived in (210). System parameters are $\omega_0 = \omega = 1$ and $\lambda = 3/2$, and we consider two values of the deformation α and several values of the reduced energy: for (a), $\alpha = 0$, $\epsilon = -4, -3, -2, -1, 0, 1$, and for (b), $\alpha = 1/4$ and $\epsilon = -4.99, -3.99, -2.99, -1.99, -0.99, 0.01$ (from red to blue).

The above classical energy functional (210) allows us to obtain several special energy values in the infinite-size limit, such as the ground-state or ESQPTs. As already demonstrated in this thesis, the classical coordinates associated to these energies can be computed as critical points $\mathbf{x}^*$ of the Hamiltonian flow, $\nabla H_{\mathbf{x}=\mathbf{x}^*} = \mathbf{0}$, with associated energy values $\epsilon^* = H(\mathbf{x}^*)$. In the case of the traditional Dicke model, $\alpha = 0$, analytical expressions for these extremal points can be explicitly obtained. In the interacting phase, $\lambda > \lambda_c(\alpha = 0)$, these critical points are of the form $\mathbf{x}^* = (q^*, 0, Q^*, 0)$ with

$$(q^*, Q^*) = (0,0), \quad -\sqrt{\frac{4\lambda^2}{\omega^2} - \frac{\omega_0^2}{4\lambda^2}}, \sqrt{2 - \frac{\omega\omega_0}{2\lambda^2}}\Bigg)\Bigg(\sqrt{\frac{4\lambda^2}{\omega^2} - \frac{\omega_0^2}{4\lambda^2}}, -\sqrt{2 - \frac{\omega\omega_0}{2\lambda^2}}\Bigg)\Bigg(\tag{211}$$

We would like to draw the reader's attention to the fact that when $\alpha = 0$ the classical Hamiltonian remains invariant under the transformation $q \to -q$ and $Q \to -Q$. Therefore, for each critical point (q, p, Q, P), $(-q, p, -Q, P)$ is also a

critical point, and both have the same energy. Thus, the second and third critical points in (211) are associated to the same energy, the ground-state energy, which is degenerate in the infinite-size limit. The first critical point is of a completely different nature; it is associated with a logarithmic ESQPT taking place at $\epsilon_c = -1$. In Fig. 46(a) we represent the phase space for $\alpha = 0$. Since the full phase space is four-dimensional, we have chosen to plot the surface projections on the (q, Q) plane. Different energies correspond to different line colors. This figure clearly shows the presence of two symmetric global minima for $\alpha = 0$. For $\epsilon \leq \epsilon_c$ these classical wells are disconnected, while the ESQPT at $\epsilon = \epsilon_c$ (purple line) marks the transition to a connected phase space.

It is clear from (210) that the symmetry $H(q, p, Q, P) \to H(-q, p, -Q, P)$ is broken as soon as $\alpha \neq 0$, and as a consequence the previous structure is distorted. As we mentioned before, in this case we cannot provide simple mathematical expressions for the Hamiltonian critical points but need to evaluate them numerically. In our theoretical analysis of chaos, we will set $\alpha = 1/4$ for definiteness, but in our experimental realization α will vary. Together with the choice $\omega_0 = \omega = 1$ (in resonance), there are two ESQPTs which appear for atom-field couplings $\lambda > \lambda_c(\alpha = 1/4) = \frac{1}{8}\sqrt{13 + 5\sqrt{17}} \approx 0.725$. For the special case $\lambda = 3/2 > \lambda_c(\alpha = 1/4)$, we find the critical points $\mathbf{x}^*_{GS} = (-3.339, 0, 1.342, 0)$, $\mathbf{x}^*_1 = (2.623, 0, -1.322, 0)$, and $\mathbf{x}^*_2 = (0.045, 0, -0.133, 0)$. These are associated to the ground-state energy, $\epsilon_{GS} = H(\mathbf{x}^*_{GS}) = -5.673$ and the ESQPTs critical energies $\epsilon_{c1} = H(\mathbf{x}^*_1) = -3.565$ and $\epsilon_{c2} = H(\mathbf{x}^*_2) = -0.992$. Figure 46(b) for the case $\alpha = 1/4$ helps us to physically interpret these critical points. Due to the non-vanishing deformation strength $\alpha \neq 0$, the ground-state is no longer degenerate; instead, we find two asymmetric, non-equivalent minima at different energies, similar to the behavior of the deformed Rabi model in Sec. 3.4. The second minimum corresponds to $\mathbf{x}^*_1$, defining a critical energy $\epsilon_{c1} > \epsilon_{GS}$. This is the energy beyond which the second classical well appears. Finally, the critical point $\mathbf{x}^*_2$ associated with ϵ_{c2} merges the two classical wells in the (q, Q) plane, giving rise to a logarithmic ESQPT (because the system has $f = 2$ classical degrees of freedom, the singularity is to be found in the first derivative of the level density).

4.2 THEORETICAL ANALYSIS OF CHAOS AND CONSERVED QUANTITIES

4.2.1 The traces of classical chaos

Intersecting the trajectory: Poincaré sections

The onset of chaotic dynamics in classical physics is very frequently analyzed with two main tools which we employ below. The Poincaré sections [489] are one such tool. Their advantage is that they provide a pictorial and convenient representation of the development of chaos. To compute these sections, we proceed as follows. We first need to choose an initial condition $\mathbf{x}(t=0) = (q(0), p(0), Q(0), P(0))$ with a fixed energy, $\epsilon = H(\mathbf{x}(t=0))$. This initial condition is then allowed to evolve in time according to the Hamilton equations,

$$\frac{\mathrm{d}q}{\mathrm{d}t} = \frac{\partial H}{\partial p} = \frac{\omega}{\omega_0} p, \tag{212}$$

$$\frac{\mathrm{d}p}{\mathrm{d}t} = -\frac{\partial H}{\partial q} = -\frac{\omega}{\omega_0} q - \frac{2\lambda Q}{\omega_0}\sqrt{1 - \frac{1}{4}(Q^2+P^2)} - \sqrt{\frac{2}{\omega_0}}\alpha, \tag{213}$$

$$\frac{\mathrm{d}Q}{\mathrm{d}t} = \frac{\partial H}{\partial P} = P - \frac{\lambda q Q P}{2\omega_0\sqrt{1 - \frac{1}{4}(Q^2+P^2)}}, \tag{214}$$

$$\frac{\mathrm{d}P}{\mathrm{d}t} = -\frac{\partial H}{\partial Q} = -Q + \frac{\lambda q Q^2}{2\omega_0\sqrt{1 - \frac{1}{4}(Q^2+P^2)}} - \frac{2\lambda q\sqrt{1 - \frac{1}{4}(Q^2+P^2)}}{\omega_0}, \tag{215}$$

with a set of initial conditions $q(t=0) = q_0$, $p(t=0) = p_0$, $Q(t=0) = Q_0$, and $P(t=0) = P_0$. By solving this system of differential equations we can obtain the classical trajectory at any time, $\mathbf{x}(t)$. Its energy, $H(\mathbf{x}(t))$, is conserved throughout the entire time evolution, $H(\mathbf{x}(t)) = H(\mathbf{x}(0))$ for all t. We then need to consider the intersection of the trajectory with a given hyperplane at each time t. We have decided to compute the intersections with $P = 0$. When $\mathbf{x}(t)$ is such that $P(t) = 0$, we collect the value of the rest of coordinates at that time. Finally, we plot them in the (q, p) plane.

Regular (integrable) and chaotic dynamics produce completely different phase space portraits. For regular trajectories, intersections with the chosen hyperplane

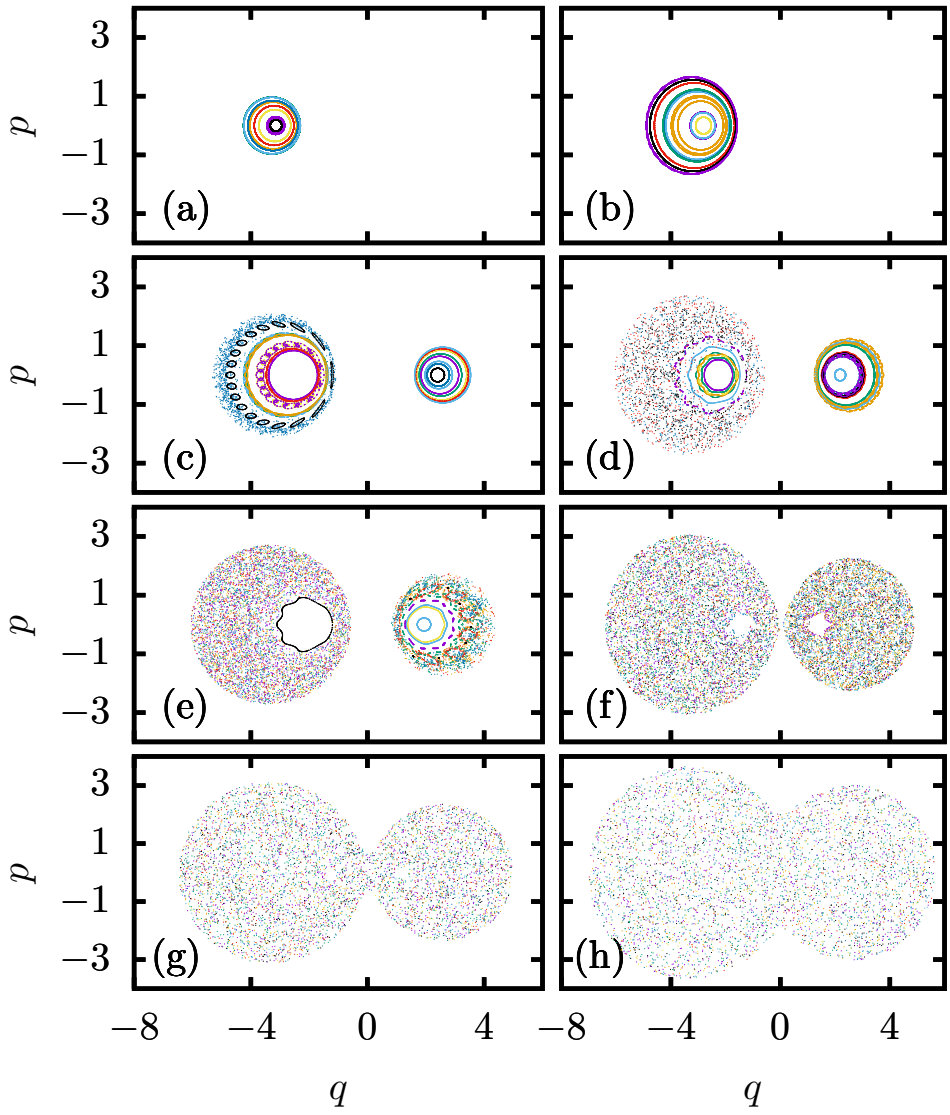

Figure 47: Analysis of classical chaos with Poincaré sections, computed through the classical analogue (210) in the (p, q) plane by intersecting the trajectories with the $P = 0$ hyperplane. The energy of the classical trajectories is different in each of the panels: (a) $\epsilon = -5$, (b) $\epsilon = -4$, (c) $\epsilon = -3$, (d) $\epsilon = -2.5$, (e) $\epsilon = -2$, (f) $\epsilon = -1$, (g) $\epsilon = -0.8$, and (h) $\epsilon = 1$. In all panels, each trajectory is associated to a single point color.

usually give rise to one-dimensional, ordered structures with the form of ovals (these are called toroidal structures). However, chaotic trajectories can explore all available phase space in a seemingly disordered way. As explained by the Kolmogorov-Arnold-Moser theorem [4], in the transition from regularity to chaos the regular parts of phase space get distorted.

Figure 47 shows our results for the Poincaré sections. In each panel the energy of the initial condition is different. In Figure 47(a)-(b) we represent the Poincaré sec-

tions for low energy trajectories. We observe that these trajectories are organized in ordered toroidal structures, reflecting the fact that close to the ground-state the system is approximately integrable. We also note that in these panels we observe a single structure located on the left hand-side of the phase space. This is because the energy of these trajectories is below ϵ_{c1}, and thus the second classical well does not exist yet. In 47(c) the energy is greater than the ESQPT critical energy ϵ_{c1}, and thus the right well is already present in the phase portrait. We highlight that the left well already shows some signatures of chaos; in comparison, the right well is completely regular at this value of energy. A clearer example has been represented in Fig. 47(d); in this case, the left well is almost completely chaotic even though the right well is still basically regular. Figure 47(e)-(h), exemplify how further increasing the energy leads to more chaos, and in particular we observe how regularity is also lost in the right well as energy increases. Finally, when the energy is high enough, the regular behavior is completely destroyed and we observe an irregular mesh of points throughout all available phase space, as shown in 47(g)-(h).

Exponentially diverging: characteristic Lyapunov exponents

Poincaré sections are useful to gain a general qualitative understanding of the degree of chaos in the system, but they do not really provide a quantitative estimate of this chaoticity. To this end, we now compute the characteristic Lyapunov exponents associated with the classical trajectories at fixed energies. As discussed in Sec. 1.2.1, classical chaos is commonly characterized by an exponential divergence of infinitesimally nearby trajectories. By contrast, in the case of regular trajectories such a separation can be algebraic at most.

An efficient algorithm to compute the Lyapunov exponents was presented in Sec. 1.2.1 (see also [45], [306] for details). This method basically involves solving a system of ordinary differential equations. The system comprises to main parts: the so-called dynamical problem (24) and the variational problem (25). In our case, the deformed Dicke model has $f = 2$ classical degrees of freedom, so we need to solve a system of twenty coupled differential equations. The technical details of our calculations are as follows. For each energy and each of the two wells, we randomly choose 100 different initial conditions $\mathbf{x}(0) \in \mathcal{M}$; we then time-evolve them, which affords $\mathbf{x}(t)$. The computing time span is at most $t = 2500$, but we only consider the trajectories until a time cutoff $t_{\max} \leq 2500$ obtained as the last time value such that the numerical error is $|\epsilon - H(\mathbf{x}(t_{\max}))| \leq 10^{-5}$. We would like to emphasize that numerically evaluating a system of twenty ordinary differential equations up to these time values can be computationally expensive. For each trajectory, we select 5000 different perturbations $\delta\mathbf{x}(0)$ randomly, all of them with

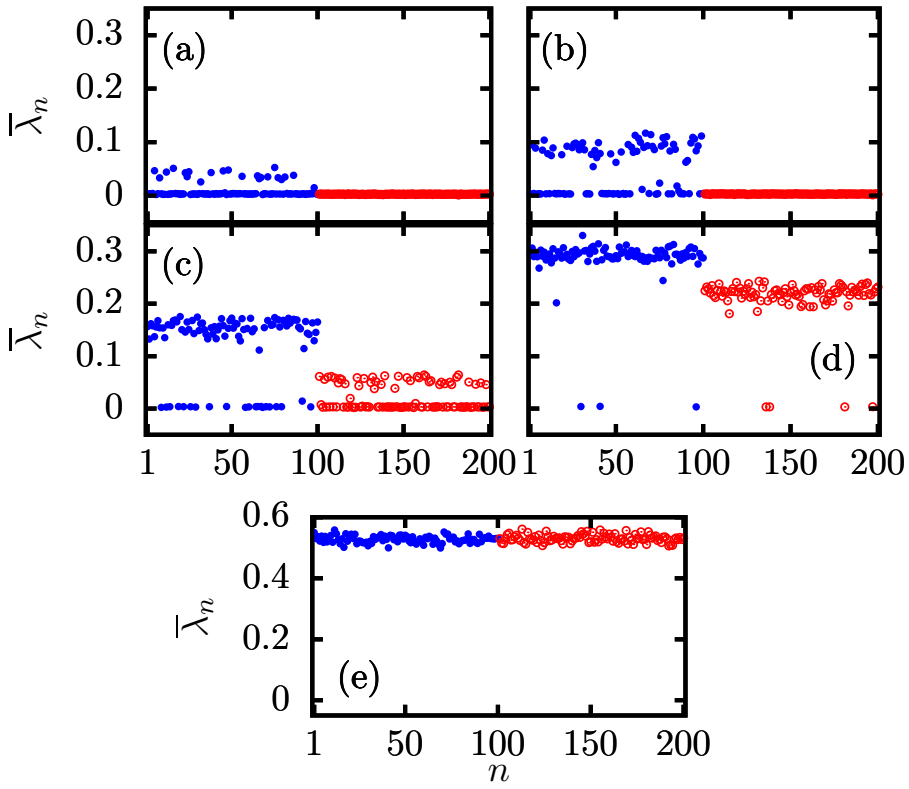

Figure 48: Analysis of classical chaos via mean Lyapunov exponents, $\overline{\lambda}_n$, averaged over 5000 randomly chosen perturbations for different values of energy. The energy of the trajectories considered in each of the panels is (a) $\epsilon = -3$, (b) $\epsilon = -2.5$, (c) $\epsilon = -2$, (d) $\epsilon = -1$ and (e) $\epsilon = 0$. The Lyapunov exponents associated to initial conditions belonging to the left energy well are represented in blue (left), while for initial conditions in the right well the Lyapunov exponents are shown in red (right).

size $\|\delta\mathbf{x}(0)\| = 10^{-6}$, and then compute the Lyapunov exponent $\lambda_{n,k}$ associated to the nth trajectory and the kth perturbation. Next, the perturbation-averaged Lyapunov exponent for each trajectory is computed as $\overline{\lambda}_n = (1/5000)\sum_{k=1}^{5000}\lambda_{n,k}$. We gather our results in Fig. 48. In all panels, the first 100 blue points correspond to trajectories departing from initial conditions in the left energy well, while the following 100 red points are associated to trajectories in the right well. We observe a clear transition from regularity to chaos, and the qualitative agreement with the Poincaré sections of Fig. 47 is very good. Figure 48(a) illustrates how in the right energy all of our sampled initial conditions have vanishing Lyapunov exponents, meaning that at $\epsilon = -3$ the right well is indeed regular. However, in the left energy well there is a non-negligible number of initial conditions giving rise to positive Lyapunov exponents; these trajectories diverge exponentially following a very small perturbation. But in the left well there are also some vanishing Lya-

punov exponents, i.e., some trajectories are still regular. This tells us that at this value of energy the left classical well exhibits a mixed phase space, where regular and chaotic trajectories coexist. Increasing the energy to $\epsilon = -2.5$ produces the results in Fig. 48(b). In this case, all sampled trajectories in the right well are still regular, but there are more chaotic trajectories in the left well than in the previous panel, as this well becomes increasingly chaotic. Figure 48(c) focuses on $\epsilon = -2$. The main qualitative difference with the previous panels is that the right well already supports a number of chaotic trajectories, with many trajectories remaining regular. Fig. 48(d) shows the case of $\epsilon = -1$: here, most trajectories are chaotic in both the left and right wells, so the rare stability islands that can survive even in chaotic systems are highly suppressed. It should be noted that the mean Lyapunov exponent is significantly higher in the left well than in the right well. This indicates that upon a slight perturbation of a chaotic initial condition, the separation occurs faster in the left well than in the right well. Finally, 48(e) shows the case of $\epsilon = 0$. Since in this case $\epsilon > \epsilon_{c2}$, both classical wells have merged into a single one, and chaos becomes very similar irrespective of the region of the phase space where the initial condition was chosen.

The ratio of the number of trajectories with positive Lyapunov exponents to the total number of trajectories gives an estimate of the volume of the classical phase space where stability islands have been destroyed and chaos dominates the dynamics. This quantity is represented in Table 4 for the Lyapunov exponents in Fig. 48, for the same energy values and for both classical wells. These results are very good agreement with the general scenario discussed above.

Energy	Left well	Right well
$\epsilon = -3$	0.22	0
$\epsilon = -2.5$	0.57	0
$\epsilon = -2$	0.8	0.4
$\epsilon = -1$	0.97	0.96
$\epsilon = 0$	1	1

Table 4: Ratio of the number of chaotic trajectories to the total number of trajectories calculated from the Lyapunov exponents of Fig. 48, considering the same energy values and both classical energy wells. A Lyapunov exponent is considered to be numerically positive if it is greater than 10^{-2}.

These results constitute strong support for the fact that switching on the perturbation parameter α has an important impact on the development of chaos, at least in the classical limit. This is in contrast with the behavior of the standard Dicke model ($\alpha = 0$) [94], [95], for which chaos merely depends on the energy of the trajectory but not on the region of phase space where the initial condition is prepared. Summarizing, the development of chaos completely decouples in the deformed Dicke model.

4.2.2 Signatures of quantum chaos

Let us now examine the quantum version of the model, given by Eq. (207). Our previous results indicate that the onset of classical chaos cannot be described with the energy of the trajectories as the only parameter. It seems that chaos is not blind to the asymmetry brought about by the deformation strength α. Therefore, a natural question is: does chaos depend on additional conserved quantities, besides energy, also in the quantum world?

Ratio of consecutive level spacings

As explained in 1.2.2, a traditional way to identify quantum chaos is through the statistical analysis of the Hamiltonian eigenlevels. The spectral statistics of quantum chaotic systems follow the universal results of the RMT. In this case, the deformed Dicke model (207) has time reversal invariance, and thus the GOE theoretical results should describe its chaotic behavior. We have already shown in 4.2.1 that, classically, there is an important distinction in the development of chaos in the left and right wells. It is therefore natural to inspect the level statistics of the quantum model corresponding to each of the two energy wells.

In order to achieve this, we classify the quantum eigenstates in relation to the properties of the asymmetric classical energy wells. The structure of the classical phase space of this model is quite similar to that of the deformed Rabi model, previously discussed in Sec. 3.4, and therefore we refer the reader to that section for details. Although the deformed Dicke model is not invariant under the parity $\mathbb{Z}_2$ transformation, it is still possible to employ the constant of motion presented in Sec. 3.2 [see Theorem 1 and (101)], as its existence does not depend on the parity operator. However, in this case the additional $\hat{\mathcal{K}}$ operator does not exist. According to the classical phase space depicted in Fig. 46, for $\epsilon \leq \epsilon_{c2}$ the function sign $(q - q_{c2})$, where $q_{c2} = q_2^*$ is the classical coordinate corresponding to the second ESQPT

critical energy ϵ_{c2} (i.e., the q for which the curves appear to cross) is conserved. Therefore, the operator

$$\hat{\mathcal{C}} \equiv \text{sign}\,(\hat{q} - q_{c2}\mathbb{I}) \tag{216}$$

acts as a discrete $\mathbb{Z}_2$ constant of motion for energies $\epsilon \leq \epsilon_{c2}$, in the infinite-size limit. For $\epsilon_{c1} \leq \epsilon \leq \epsilon_{c2}$, the operator $\hat{\mathcal{C}}$ assigns quantum numbers to the Hamiltonian eigenstates. If a quantum eigenstate belongs to the left well, then $\langle E_n|\,\hat{\mathcal{C}}\,|E_n\rangle = -1$, and $\langle E_n|\,\hat{\mathcal{C}}\,|E_n\rangle = +1$ if it belongs to the right well. Observe the similarity of (216) for this model and (195) for the deformed Rabi model.

In Fig. 49 we present the distribution of consecutive level spacings, $P(\widetilde{r})$, in the energy range $\epsilon_{c1} \leq \epsilon \leq -2$ for several cases. For details on the origin of this distribution, see (60) in Sec. 1.3.2. In Fig. 49(a) we represent $P(\widetilde{r})$ computed from the entire set of (ordered) eigenlevels in the specified energy range, without classifying them according to the value of $\hat{\mathcal{C}}$ in the corresponding eigenstates. In other words, we mix states belonging to the left and right classical wells. The numerical histograms are approximately described by the Poisson theoretical curve, although significant deviations are also obvious. The emergence of Poissonian behavior is not surprising: eigenlevels belonging to different symmetry sectors of $\hat{\mathcal{C}}$ are uncorrelated, and therefore in mixing these states level correlations, the main characteristic of quantum chaotic spectra, is destroyed. Let us now consider $P(\widetilde{r})$ built from states with a definite value of $\hat{\mathcal{C}}$. The results of the previous section, in particular those in Fig. 48, suggest that if the quantum-classical correspondence is not violated, in the energy range $\epsilon_{c1} \leq \epsilon \leq -2$ we should have more chaos in the left well than in the right well. In Fig. 49(b) we focus on states classically placed in the left well, while Fig. 49(c) shows $P(\widetilde{r})$ for states in the right well. Although finite-size effects and the impossibility to perform ensemble averages to improve the statistical significance of these histograms mean that we cannot make strong, definite statements, we can clearly observe that these distributions are completely different than that in Fig. 49(a). In fact, $P(\widetilde{r})$ in Fig. 49(b) is relatively similar to the GOE result, while in Fig. 49(c) it seems to deviate more.

Obtaining clearer ratio distributions would mean numerically diagonalizing larger system sizes, which unfortunately we cannot do due to limitations of our machines. But this does not mean that all hope is lost. Below, we will use the so-called Peres lattices, which focus on individual eigenstates rather than on the statistical description of eigenlevels, to provide a clearer response to our questions.

Peres lattices

This method to detect quantum chaos was presented by Peres in the 1980s [58], basically around the same time when the BGS conjecture of quantum chaos was

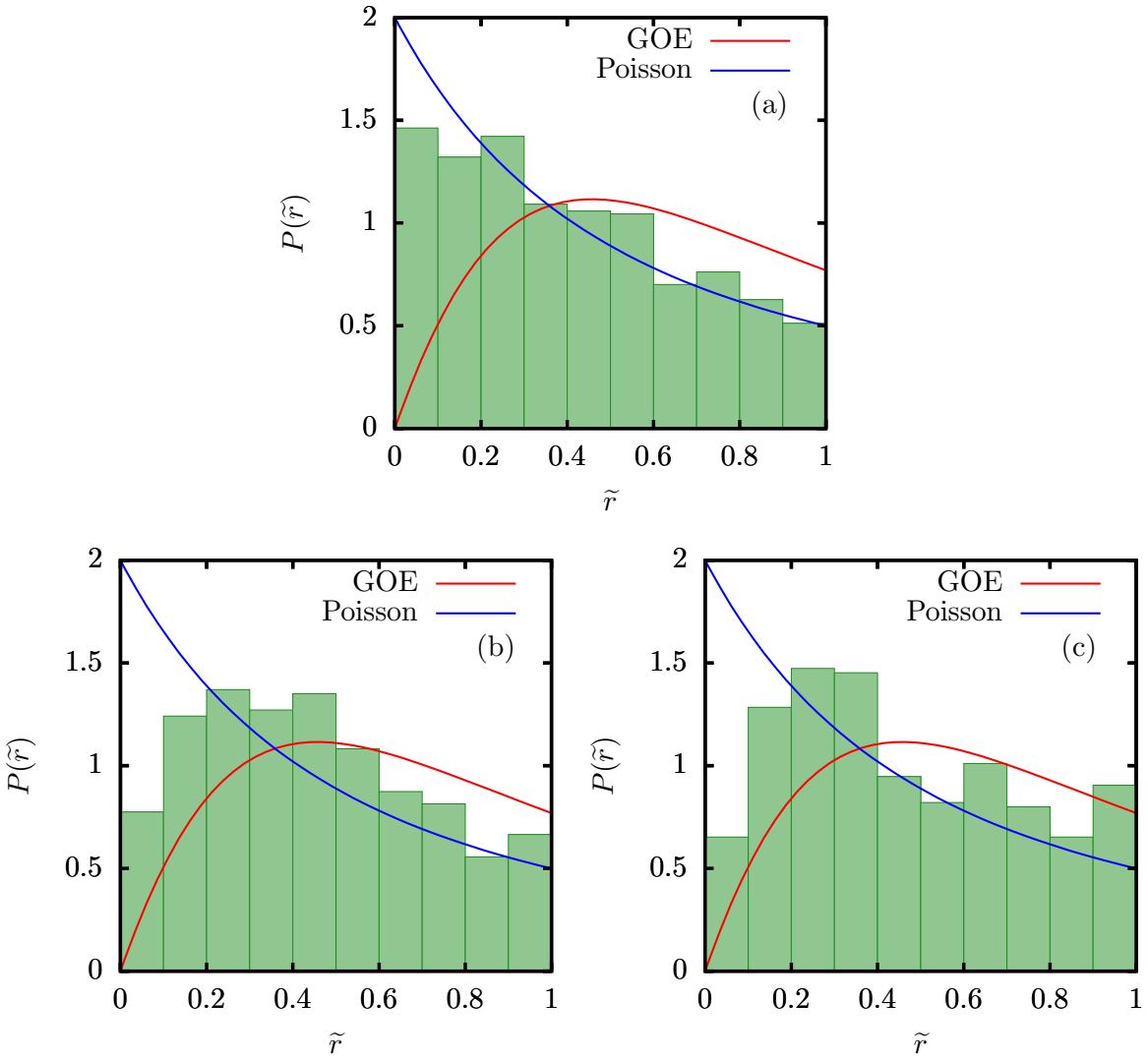

Figure 49: Distribution of the ratio of consecutive level spacings, $\widetilde{r}_n = \min\{r_n, 1/r_n\}$, with r_n in Eq. (60), for the eigenlevels of the deformed Dicke model (207) in the energy range $\epsilon_{c1} \leq \epsilon \leq -2$. (a) $P(\widetilde{r})$ constructed from all energy levels in this range, mixing states with $\langle \hat{\mathcal{C}} \rangle = +1$ and $\langle \hat{\mathcal{C}} \rangle = -1$. (b) $P(\widetilde{r})$ of states with $\langle \hat{\mathcal{C}} \rangle = -1$ (left classical well). (c) $P(\widetilde{r})$ of states with $\langle \hat{\mathcal{C}} \rangle = +1$ (right classical well). Model parameters are $N = 60$, $\alpha = 1/4$, $\lambda = 3/2$, $n_{\rm ph} = 720$. The corresponding GOE (chaos) and Poisson (regularity) theoretical curves are also plotted for reference.

established. Peres' approach can be succinctly summarized as follows [490]. The method deals with generic, few-body observables, say $\hat{O}$, whose diagonal expectation values in the eigenbasis of a given Hamiltonian, $O_{nn} = \langle E_n | \hat{O} | E_n \rangle$, are computed. Viewed as a function of the eigenenergies, the values $O_{nn}(E_n)$ produce two types of very different structures. In the case of regular dynamics, we obtain

an ordered set of points in the (E_n, O_{nn}) plane (hence the name 'lattice'); however, chaotic dynamics is associated with a disordered set of points. Between these two limiting behaviors, integrability breaking terms can give rise to perturbations of the regular lattices, full chaos only appearing when the whole regular structure has been destroyed. Therefore, Peres lattices provide an alternative method to unveil quantum chaos and integrability, and they complement the traditional level statistics analysis. Yet, Peres lattices are less frequently used in the study of quantum chaos than spectral statistics. One of the reasons may be that there are no universal, theoretical descriptions of what a Peres lattice should look like if a system is chaotic, unlike the universal RMT results for spectral statistics. Peres lattices are similar in spirit to Poincaré sections, although we should emphasize that they are in no way formal analogues of Poincaré sections. Finally, we should stress that Peres lattices are also very insightful in the analysis of thermalization and the ETH. Indeed, according to, e.g., (47), for the ETH to hold the diagonal expectation values of few-body observables in the Hamiltonian eigenbasis need to behave a smooth function of energy. Non-smooth structures in the plane (E_n, O_{nn}) can hint at a failure of the system to thermalize, at least for certain observables.

In Fig. 50 we represent the Peres lattices for some observables of our choice. First, in 50(a) we show the diagonal expectation values of the $\hat{\mathcal{C}}$ operator defined in Eq. (216). For energies between the first and second ESQPT critical energies, ϵ_{c1} and ϵ_{c2} (marked by vertical dashed lines), only two values are possible: $+1$ and -1. And for $\epsilon \leq \epsilon_{c1}$, the only possible value is -1. This is because for $\epsilon \leq \epsilon_{c1}$ the right classical well does not yet exist, and therefore eigenstates can only belong to the left well. Throughout this figure, blue points represent eigenstates with $\langle \hat{\mathcal{C}} \rangle = -1$, while red points represent the expectation values for eigenstates with $\langle \hat{\mathcal{C}} \rangle = +1$. This clearly shows that our general theory of constants of motion, presented in Sec. 3.2, is indeed valid even though there is no $\mathbb{Z}_2$ symmetry in this model. Above a certain energy, the expectation values of $\hat{\mathcal{C}}$ can be different from ± 1, and they are arranged in a seemingly disorganized pattern. Although the energy that marks the appearance of chaos seems to be connected with the ESQPT at energy ϵ_{c2}, it is really unrelated: we should note that chaos appears well below ϵ_{c2} even in the Poincaré sections presented in Fig. 47.

Regarding quantum thermalization and the ETH, Fig. 50(a) already tells us that the standard microcanonical ensemble will be incapable of describing the long-time averages of observables, as the diagonal expectation values of the $\hat{\mathcal{C}}$ operator do not behave as a smooth function of energy, with clear jumps between adjacent eigenstates. In other words, the conservation law established by $\hat{\mathcal{C}}$ has a vital impact the dynamics of non-equilibrium states.

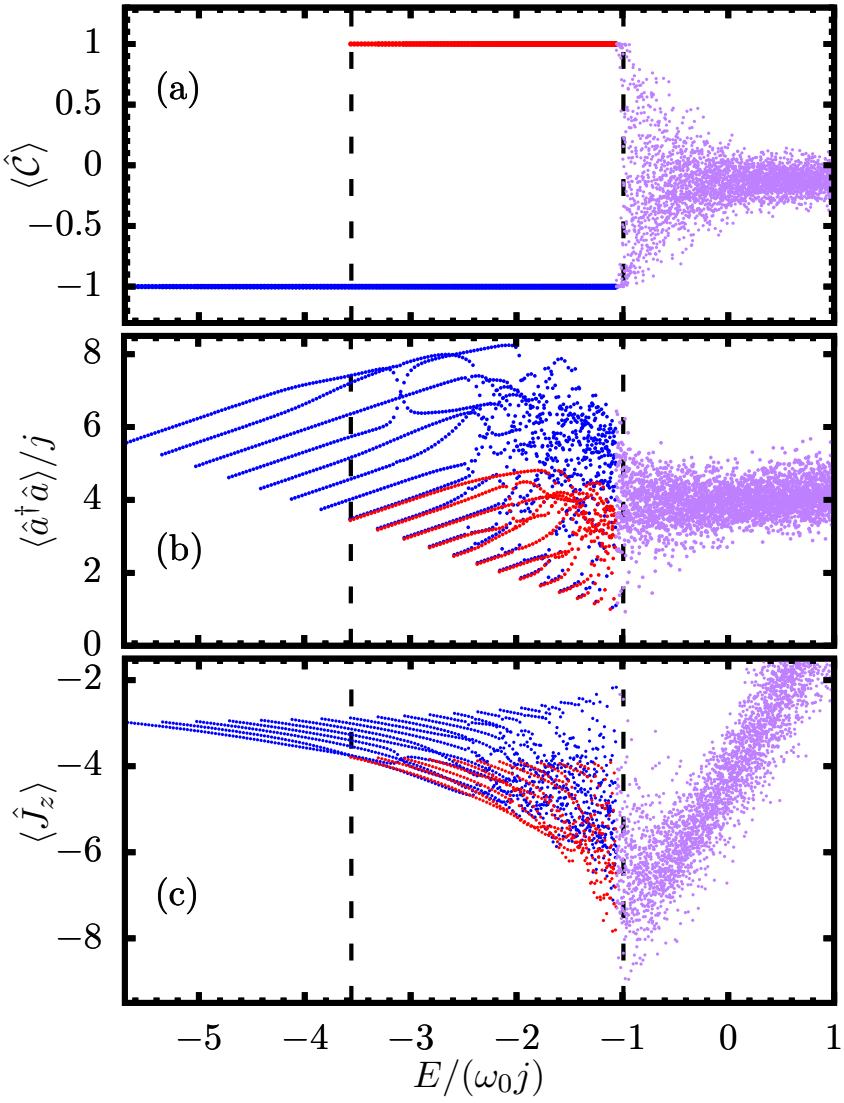

Figure 50: Analysis of quantum chaos via Peres lattices, calculated for representative observables in the Hamiltonian eigenstates of (207). Our chosen observables are: (a) the constant of motion operator (216); (b) the number of photons operator $\hat{a}^\dagger \hat{a}$; and (c) the atomic collective spin observable $\hat{J}_z$. The expectation values in Hamiltonian eigenstates such that $\langle E_n | \hat{\mathcal{C}} | E_n \rangle = -1$ (which belong to the left classical well) are represented as blue points, while if $\langle E_n | \hat{\mathcal{C}} | E_n \rangle = +1$ (right classical well) such expectation values are represented with red points. The expectation value in eigenstates such that $\hat{\mathcal{C}}$ is not a constant of motion are plotted with purple points. The ESQPT critical energies $\epsilon_{c1} = -3.565$ and $\epsilon_{c2} = -0.992$ are depicted with two dashed vertical lines. The number of atoms is $N = 2j = 60$ and the photonic cutoff number is $n_{\rm ph} = 720$.

To end this section, let us analyze the results presented in Fig. 50(b),(c). In Fig. 50(b) we focus on the number of photons, $\langle \hat{a}^\dagger \hat{a} \rangle$. For sufficiently low energies

we observe a completely regular lattice of blue points. We can even establish a qualitative correspondence between the results of the Peres lattices and those of the Poincaré sections: if we focus on energy $\epsilon = -5$, i.e., just slightly above the ground-state energy, we observe a regular behavior that is also apparent in Fig. 47(a), where the classical trajectories are also regular. The same reasoning applies to energy $\epsilon = -4$, see Fig. 47(b) for comparisons with Poincaré sections. The case of $\epsilon = -3$ is more interesting: here the right energy well is already accessible, and the red diagonal expectation values are arranged in an organized fashion, which reminds us of the behavior of the right well close to its own minimum energy. Despite this, we can observe some deviations from perfect regularity in the eigenstates associated to the left well, and this is in agreement with the results in Fig. 47(c), where we observe that chaos has already started to appear, although some remnants of regularity manage to survive. At energy $\epsilon = -2.5$, the red expectation values are still basically regular, but in the blue ones the perturbation is now strong. It is interesting to compare this picture with Fig. 47(d), whose left well now shows a very small regular portion, surrounded by a chaotic sea; meanwhile, the right well continues to show strong signatures of regularity. For $\epsilon = -2$, the blue expectation values are even more perturbed, and some integrability breaking is also visible in the red points too. Classically, this scenario is also present, as Fig. 47(e) indicates. Increasing the energy beyond $\epsilon = -2$ we observe a gradual evolution of chaos until the regular portions are completely destroyed. This description of the onset of chaos is not unique to the photonic number; for example, the atomic inversion, $\hat{J}_z$, shows analogous results, which can be found in Fig. 50(c).

These results confirm that we can establish a meaningful quantum-classical correspondence in the onset of chaos: in order to ascertain the degree of chaos in the system, the trajectories or eigenstates energies is not sufficient, and we need the information provided by the $\hat{C}$ operator.

Onset of chaos: when integrability breaks down

One of the features in the Peres lattices of Fig. 50(b),(c) is the appearance of a set of ordered points at low energies, within an energy interval from the ground-state up to some intermediate spectral region. In this section we focus on this band structure, as it will allow us to present a more quantitative description of the development of chaos than that gained from the analysis of the Peres lattices.

As we have mentioned before, the Dicke model is in general a non-integrable model. Despite this, its low-energy region can be considered as approximately integrable, as shown in [315], [349]. This quasi-integrability stems from the conservation of an additional operator, $\hat{J}_{z'}$, which makes it possible to divide the

full spectrum into a set of $2j+1$ independent bands according to its eigenvalues. Assuming that the motion of the atoms in the Dicke model is much faster than that of the bosons, one may employ the Born-Oppenheimer approximation [491] and solve for the bosonic coordinates. In order to accomplish this, one replaces the boson creation and annihilation operators by the classical approximation $\hat{a} = (1/\sqrt{2})(\hat{q} + i\hat{p})$, $\hat{q} = (\hat{a}^\dagger + \hat{a})/\sqrt{2}$. According to [349], this yields a set of $2j+1$ effective classical Hamiltonians with the form

$$E_{m'} = \frac{\omega}{2}(p^2+q^2) + \omega_0\sqrt{\left(1+\frac{\lambda^2}{\lambda_c^2}\frac{\omega q^2}{\omega_0 j}\right)m' + \sqrt{N\omega_0}\alpha q}, \tag{217}$$

with $m' = -j, -j+1, \ldots, j-1, j$ being the eigenvalues of the operator

$$\hat{J}_{z'} \equiv \frac{\hat{J}_z + \sqrt{\frac{\lambda^2}{\lambda_c^2}\frac{\omega}{\omega_0}\frac{1}{2j}}(\hat{a}+\hat{a}^\dagger)\hat{J}_x}{\sqrt{\left(1+\frac{\lambda^2}{\lambda_c^2}\frac{\omega}{\omega_0}\frac{1}{2j}(\hat{a}+\hat{a}^\dagger)^2\right)}}, \tag{218}$$

an adiabatic invariant that acts as a constant of motion up to moderate energies [349]. In this equation, $\lambda_c = \lambda_c(\alpha = 0) = \sqrt{\omega\omega_0}/2$. Equation (217) tells us that at sufficiently low energies the Dicke model, which has two classical effective degrees of freedom, can be approximately described as a set of $2j+1$ independent integrable models with a single degree of freedom. The classical energy surfaces are then given by $E_{m'}$ in Eq. (217). The ground-state of the model is to be found in the $m' = -j$ surface. Therefore, at these low energies the quantum eigenlevels depend on two different numbers, encapsulated in $E_{m',n}$: the band where a level is found is indicated by m', and the position of that level relative to the minimum energy of the band where it is located is indicated by n. Therefore, one may use the diagonal expectation values $\langle E_n | \hat{J}_{z'} | E_n \rangle \in \{-j, -j+1, \ldots, j-1, j\}$ to classify the system's eigenstates in bands.

It would seem that the adiabatic invariant $\hat{J}_{z'}$ (218) and the operator $\hat{\mathcal{C}}$ (216) may have some sort of connection; however, they do not. Their physical origins are completely unrelated: while $\hat{J}_{z'}$ labels the band to which a given low-energy eigenstate belongs, the operator $\hat{\mathcal{C}}$ indicates in which classical energy well that eigenstate is trapped. These details are independent: for example, two states with different values of $\hat{\mathcal{C}}$ can still be found in the same band of $\hat{J}_{z'}$. Besides this, there is a certain spectral region where these two operators act as constants of motion simultaneously: $\hat{\mathcal{C}}$ is constant for energies below ϵ_{c2}, i.e., as long as the classical wells are disconnected, while $\hat{J}_{z'}$ is valid up to some energy value that depends on the particular values of the parameters of the model (see [349] for details). At intermediate energies below the second ESQPT and at low energies near the ground-state, both operators act simultaneously as constants of motion, providing

two independent quantum numbers, $\langle \hat{J}_{z'} \rangle$ and $\langle \hat{\mathcal{C}} \rangle$, labeling the system states. Since both operators can be diagonalized in the eigenbasis of $\hat{a} + \hat{a}^\dagger$, they are commuting observables, $[\hat{J}_{z'}, \hat{\mathcal{C}}] = 0$.

In [315], [349] the adiabatic invariant $\hat{J}_{z'}$ was proposed as a tool to detect the onset of quantum chaos. In particular, quantum chaos should emerge when $\hat{J}_{z'}$ ceases to be a constant of motion. As a quantitative measure of quantum chaos, we consider the dispersion of $\hat{J}_{z'}$ in the Dicke Hamiltonian eigenstates,

$$(\Delta \hat{J}_{z'})^2 = \langle E_n | \hat{J}_{z'}^2 | E_n \rangle - (\langle E_n | \hat{J}_{z'} | E_n \rangle)^2 \geq 0. \tag{219}$$

The operator $\hat{J}_{z'}$ is a good conserved quantity when this dispersion is zero. A non-zero value of $(\Delta \hat{J}_{z'})^2$ is indicative of the spectrum bands being destroyed and of chaos entering the system.

In Fig. 51 we represent the dispersion (219) as a function of energy. This dispersion vanishes near the minimum energy of each of the two classical wells, so for those energies $\hat{J}_{z'}$ is essentially constant and the corresponding eigenstates can be split into independent bands. For the eigenstates with $\langle \hat{\mathcal{C}} \rangle = -1$ (left classical well), a vanishing dispersion is maintained roughly up to $\epsilon \approx -3.5$. After this point, the dispersion continues to grow with energy. Qualitatively similar results are found for the eigenstates with $\langle \hat{\mathcal{C}} \rangle = +1$ (right classical well), except that in this case we find a vanishing dispersion up to higher energies, $\epsilon \approx -2.5$.

These results confirm that the onset of chaos takes place at markedly different energies. In this sense, for $\epsilon \leq \epsilon_{c2}$, the system effectively behaves as two independent models whose analyses need to be carried out independently.

4.3 EXPERIMENTAL REALIZATION OF THE DEFORMED DICKE MODEL

4.3.1 Experimental platform

Let us now move on to our experimental realization of the deformed Dicke model. This part of the thesis contains both experimental and theoretical results. The experimental results were performed by our collaborators at the Universidad Nacional Autónoma de México, while the author of this thesis was in charge of the theoretical calculations as well as the theoretical parametrization of the experiment. State-of-the-art techniques in quatum technologies, such as superconducting circuits [492] and cold atom platforms [493], [494] have been used to explore the standard Dicke model. In addition, atom-cavity systems [495], [496] have also made

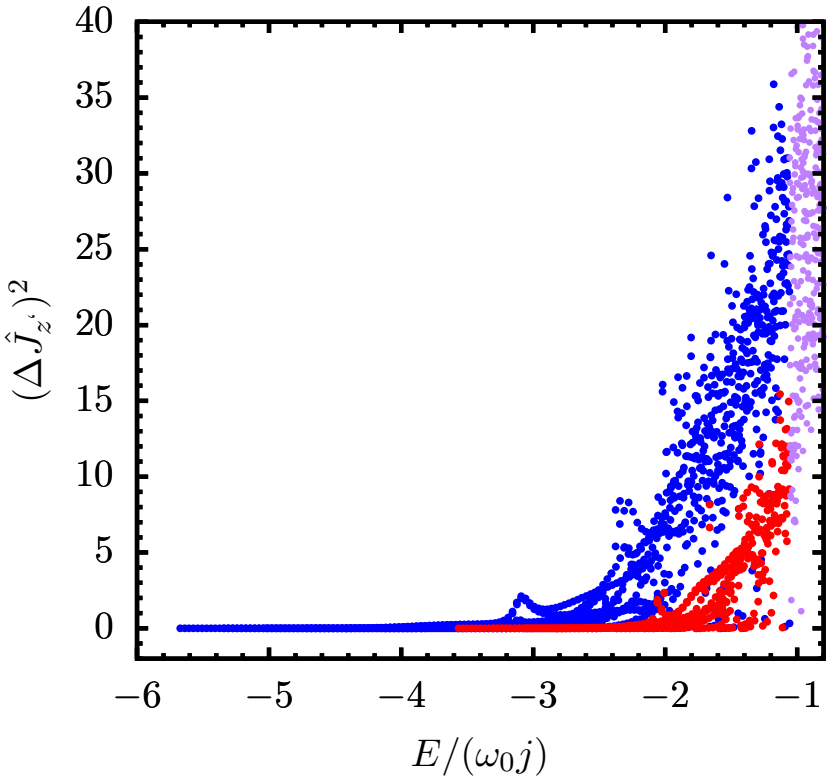

Figure 51: Analysis of the onset of quantum chaos through the adiabatic invariant in (218). We plot the dispersion (219) of the adiabatic invariant $\hat{J}_{z'}$ in the deformed Dicke Hamiltonian eigenbasis. We follow the color code in previous Fig. 50. We observe that for Hamiltonian eigenstates whose eigenvalues are close to the minimum energy of each of the two classical wells, $(\Delta \hat{J}_{z'})^2 = 0$, which is a signature of the Hamiltonian behaving a set of independent integrable systems. The condition for the onset of chaos is $(\Delta \hat{J}_{z'})^2 \neq 0$, which takes place at different energies depending on the particular well. The number of atoms is $N = 60$ and the photonic cutoff is $n_{\text{ph}} = 720$.

it possible to analyze several extensions of the model without deformation. Surprisingly, experimental realizations of the classical dynamics of the model do not particularly abound. The development of platforms that can properly implement these dynamical features remains a promising venue of research as they would make it possible to easily verify the main predictions of the model as well as provide new insights into its properties. A experimental realization of the classical non-deformed Dicke model was presented in [497]. The experimental platform consists of two non-linearly coupled synthetic LC circuits, and it relies on electrical networks of resistors, capacitors, operational amplifiers and analog multipliers [498]. The key point of these electronic platforms is that their voltage transfer-functions can be controlled through linear and non-linear operations and, as a

consequence, it is possible to experimentally solve a set of differential equations. Thus, the temporal evolution of the voltages of the electronic device is controlled precisely by the same equations as the original system that one wants to simulate [499], [500].

Through the prism of these electronic platforms, the classical functional of energy in (210) can be seen as a set of two non-linearly coupled harmonic oscillators subject to some external stimulus in the field section. For this reason, it can be mapped to electrical variables of LC oscillators, where L and C denote the inductance and capacitance. This transformation gives rise to a system of two non-autonomous LC oscillators connected through a non-linear coupling, essentially mapping the classical canonical variables (q, p, Q, P) to normalized electrical variables $(I_{L_1}, V_{C_1}, I_{L_2}, V_{C_2})$, where I_L stands for the induction current while the capacitor voltage is represented by V_C. The classical Hamiltonian (210) can be rewritten as

$$H = \frac{\omega}{2\omega_0}(\tilde{I}_{L_1}^2 + \tilde{V}_{C_1}^2) + \frac{1}{2}(\tilde{I}_{L_2}^2 + \tilde{V}_{C_2}^2) + \frac{\lambda \tilde{I}_{L_1}\tilde{I}_{L_2}}{\omega_0}\sqrt{4 - \tilde{V}_{C_2}^2 + \tilde{I}_{L_2}^2} - 1 + \sqrt{\frac{2}{\omega_0}}\alpha \tilde{I}_{L_1}, \tag{220}$$

with $\omega^2 = 1/L_1C_1$ and $\omega_0^2 = 1/L_2C_2$ being the natural frequencies of the oscillator-1 and oscillator-2, respectively. The non-linear interaction between the LC oscillators is controlled by the coupling strength λ, while in this setting the deformation strength α is accounts for the intensity of the external stimulus. In the results of this section, we fix $\omega = 1$ and $\omega_0 = 1$ while the values of λ and α are allowed to vary in order to access the different physical regimes of the model.

The classical equations of motion of the non-deformed $(\alpha = 0)$ and deformed $(\alpha \neq 0)$ Dicke models are very similar; basically, the only difference is found in the equation for $\mathrm{d}p/\mathrm{d}t$, which contains an additional term $-\sqrt{2/\omega_0}\alpha$. Although this term is exogenous to the circuit, it can be experimentally controlled by including a direct voltage signal in the integrator for the differential equation describing the voltage of the capacitor in $\tilde{V}_{C_1}$. Technically, this voltage is supplied by a digital-analog converted (DAC) with an MCP4921 series. Experimentally, our platforms allows values of α such that $\sqrt{2}\alpha \in (-2.5, 2.5)$ and $\lambda \in (-2.5, 2.5)$. In summary, we are able to experimentally control the free parameters λ and α via software. A schematic representation of the electronics for the deformed Dicke model is shown in Fig. 52(a). The parts of the circuit corresponding to the standard Dicke model $(\alpha = 0)$ have been represented with black lines, while the circuitry of the exogenous deforming term $\alpha \neq 0$ is shown with blue lines. For more details on the experimental setup, we refer the interested reader to [485].

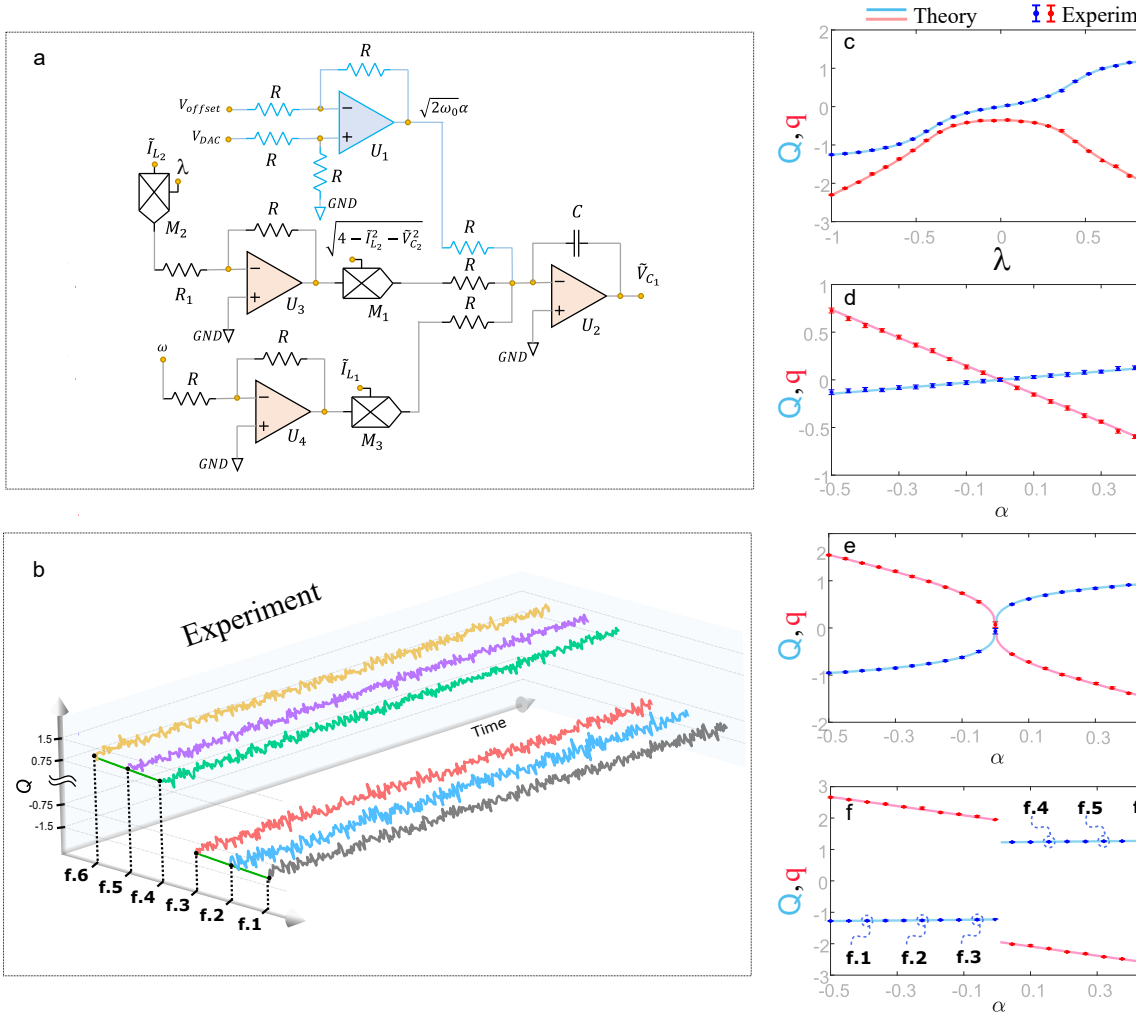

Figure 52: (a) Electric circuit describing the voltage differential equation in the capacitor-1. Here, U_j and M_j denote general-purpose operational amplifiers and analog multipliers. The resistor and capacitor values are R =10 $K\Omega$, R_1 =1 $K\Omega$, and C =10 μF. V_{offset} is a direct voltage of 2.5 volts and V_{DAC} is the α-dependent voltage signal. (b) Time evolution of Q in the ground-state for $\lambda = 1$ and several values of α: (f.1) $\alpha = -0.39$, (f.2) $\alpha = -0.225$, (f.3) $\alpha = -0.06$, (f.4) $\alpha = 0.155$, (f.5) $\alpha = 0.32$, and (f.6) $\alpha = 0.485$.

4.3.2 Exploring the ground-state features

The ground-state of the system is a particular case of equilibrium points of the classical Hamiltonian (210) with the minimum possible energy. For the non-deformed model, $\alpha = 0$, the closed-form expressions for this energy are $E_0(\lambda) = -\omega_0 j$ for $\lambda \leq \lambda_c$, in the normal phase, and $E_0(\lambda)/j = -\omega_0/2(\lambda_c^2/\lambda^2 + \lambda^2/\lambda_c^2)$ for $\lambda > \lambda_c$, in the superradiant phase. The transition between these ground-state phases is demarcated by the critical coupling $\lambda_c = \sqrt{\omega\omega_0}/2$. However, similarly to the deformed Rabi model of Sec. 3.4, when $\alpha \neq 0$ there is no normal-superradiant phase

transition in the ground-state and, as we have seen in the theoretical analysis of Sec. 4.2, two asymmetric wells may emerge for appropriate values of λ and α.

In order to proceed with our experimental analysis of the ground-state in the deformed Dicke model, we fix one of the two free parameters and allow the remaining parameter to vary. In Fig. 53(a)-(d) report our results on the ground-state coordinates q and Q for the following values of the the control parameters: (a) $\alpha = 0.25$, (b) $\lambda = 0.1 < \lambda_c$, (c) $\lambda = 0.5 = \lambda_c(\alpha = 0)$, and (d) $\lambda = 1 > \lambda_c$. The theoretical predictions for the q and Q coordinates are represented by blue and red solid lines, respectively, respectively, while points of the same color are associated to the experimental measurements. Because the ground-state is a stationary point of the dynamics, our bi-parametric electronic platform exhibits constant voltage signal along time as visible in Fig. 52(b). We note that inevitable electronic noise means that the voltage signal associated to ground-state points cannot be perfectly flat, but it is still very close to constancy. The presence of electronic noise can also be observed in the rest of the panels. For this reason, in Fig. 53(a)-(d) the errorbars represent the standard deviations of the time series for each of the (q, Q) coordinates, while the points represent their respective average values.

We have also studied the variation with λ and α of the atomic inversion and mean photon number in the ground-state, for the same cases considered in Fig. 53(a)-(d). The classical counterpart of these observables can be computed through Glauber-Bloch coherent states, $|\mathrm{GB}\rangle$. For the atomic inversion, we obtain

$$j_z = \frac{\langle \mathrm{GB}| \hat{J}_z |\mathrm{GB}\rangle}{j} = \frac{P^2 + Q^2}{2} - 1, \tag{221}$$

while the classical counterpart of the mean photon number reads

$$\langle n \rangle = \frac{\langle \mathrm{GB}| \hat{n} |\mathrm{GB}\rangle}{j} = \frac{p^2 + q^2}{2}. \tag{222}$$

These classical quantities are represented as a function of λ and α in Fig. 53(e)-(l). In Fig. 53(e)-(f), we fix $\alpha = 0.25$; in (g)-(h), $\lambda = 0.1$; in (i)-(j), $\lambda = 0.5$; and in (k)-(l), $\lambda = 1$.

When α is fixed, the q and Q coordinates vary smoothly with λ; this is clearly visible in 53(a). A similarly smooth evolution for the atomic inversion and the mean photon number can be observed in Fig. 53(e) and Fig. 53(f), respectively. The observed increase of Q with λ is due to the fact that as λ grows from $\lambda = 0$, when there are no interactions and the ground-state is located right at the center of the phase space ($Q = 0$), the system will enter a double-well region at some value of α, and because in this case $\alpha > 0$, the ground-state will be shifted to the right part of the phase space ($Q > 0$). If λ is decreased from $\lambda = 0$, analogous results are obtained, although in this case the ground-state shifts to $Q < 0$. If we

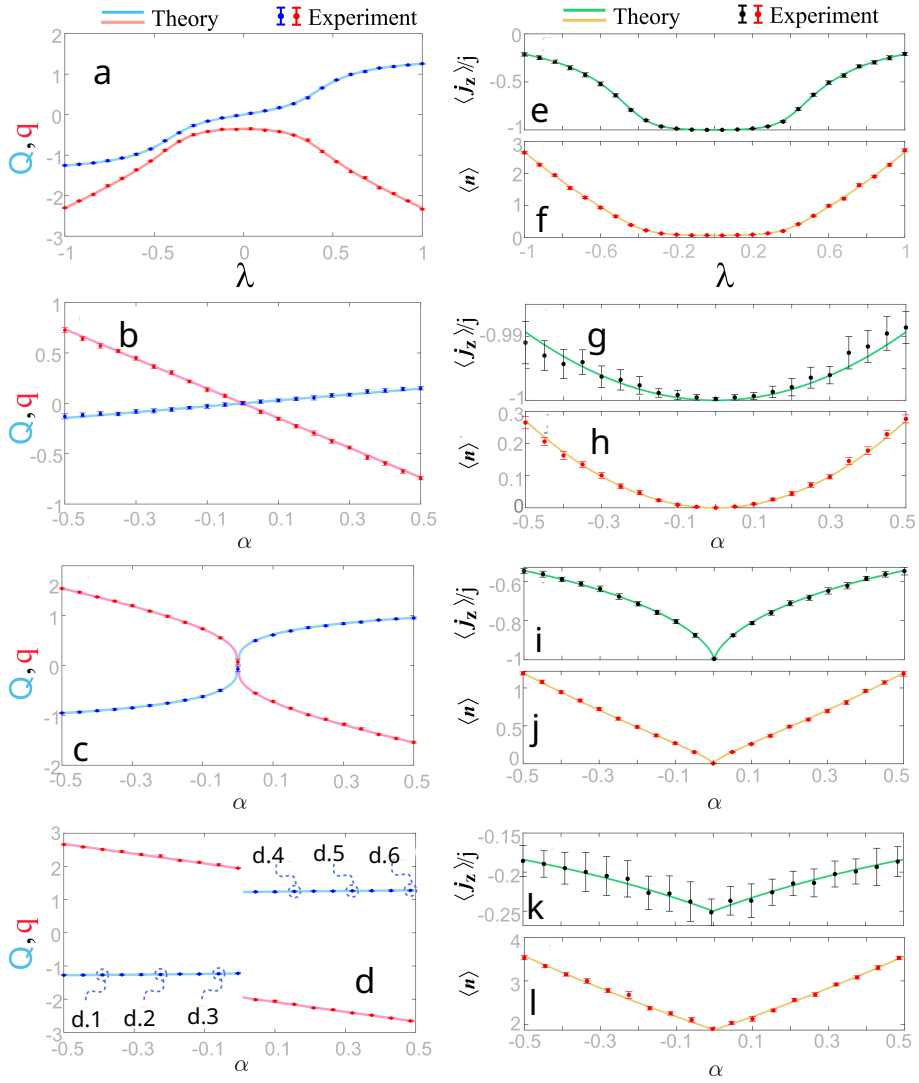

Figure 53: Experimental vs. theoretical analysis of the ground-state properties. (a-d) Ground-state q and Q of the classical version of the deformed Dicke model with $\omega = \omega_0 = 1$, as a function of λ and α. In each case, the free parameter values are: (a) $\alpha = 0.25$, (b) $\lambda = 0.1 < \lambda_c$, (c) $\lambda = \lambda_c = 0.5$ and (d) $\lambda = 1 > \lambda_c$. Panels (e)-(g)-(i)-(k) show the atomic inversion, $\langle j_z \rangle / j$, and (f)-(h)-(j)-(l) the mean photon number $\langle n \rangle$ as a function of λ and α. (e)-(f) correspond to the case $\alpha = 0.25$, (g)-(h) to $\lambda = 0.1$, (i)-(j) to $\lambda = 0.5$, and (k)-(l) to $\lambda = 1$. Solid lines denote theoretical predictions obtained via numerical simulations and points represent experimental measurements. Error bars correspond to the standard deviation of the experimental results.

fix $\lambda = 0.1 < \lambda_c$ and allow α to vary, the behavior of the ground-state is montonic as Fig. 53(b) clearly illustrates; the associated atomic inversion and mean photon number are in Fig. 53(g)-(h). The interpretation for this case is that the condition $\lambda < \lambda_c$ only allows for one classical well, but it is shifted to the left ($Q < 0$) or right

($Q > 0$) depending on the sign of α. The ground-state is found at the center of phase space ($Q = 0$) only if there is no deformation, $\alpha = 0$. In Fig. 53(c) we focus on $\lambda = 0.5 = \lambda_c$ and allow α to vary. At $\alpha = 0$, the q and Q coordinates undergo a second-order quantum phase transition; this is the well-known QPT of the non-deformed Dicke model. The atomic inversion and mean photon number also show clear signatures of the QPT in Fig. 53(i) and Fig. 53(j), with j_z approaching -1 and $\langle n \rangle$ vanishing as $\alpha \to 0$. For $\alpha \neq 0$, the deformation forces the classical phase space to become asymmetric, which explains the evolution of the coordinates towards negative or positive values, depending on $|\alpha|$. Finally, if $\lambda = 1 > \lambda_c$, the signatures of a first-order QPT are clearly visible in 53(d), where the canonical q, Q variables exhibit a finite discontinuity at $\alpha = 0$. Note, however, that there is no such discontinuity in j_z and $\langle n \rangle$, as shown in Fig. 53(k) and Fig. 53(l).

In all cases, the numerically computed predictions agree very well with the experimental values. The canonical variables q, Q can be successfully used to mark the different phase transitions of the model.

4.3.3 Measuring chaos and phase transitions

Our next step is to characterize the different dynamical regimes of the deformed Dicke model. To this end, in Fig. 54 we present a two-dimensional phase diagram of the model, where the different phases are driven by the values of the λ and α parameters. This diagram describes the phases of the system in the infinite-size limit, $N \to \infty$, and thus it is relevant for finite-size scaling considerations. The diagram is mainly divided into two zones, the limits of which are demarcated by orange solid lines. We note that these lines originate at the quantum critical point $\lambda_c(\alpha = 0)$. In the gray-shaded portions of the diagram the classical trajectories are confined in a single energy well, while in the orange-shaded regions a double-well structure emerges. Since the phase space is four-dimensional, projections of the classical trajectories in the (q, p) and (Q, P) planes give rise to spatially separated lobes. For each value of λ, the transition from the single to the double-well structure takes place at a critical value of the deformation strength, $\alpha_c = \alpha_c(\lambda)$. These critical values have been numerically evaluated since a closed-form expression for the critical curve $\alpha_c(\lambda)$ is out of reach, and they are represented by the orange line. In accordance with our theoretical analysis presented in Sec. 4.1.2, for $\alpha = 0$ and $\lambda \geq \lambda_c$ the Hamiltonian supports two symmetric global energy minima (in other words, the ground-state is degenerate), while for $\alpha \neq 0$ the parity symmetry is broken and, as a consequence, two asymmetric energy wells may emerge depending on the values of λ. For $\alpha > 0$, the global ground-state

has $Q > 0$, while if $\alpha < 0$, it has $Q < 0$. The second classical well then appears on the opposite side of phase space and at a higher energy value. The model also supports a logarithmic ESQPT merging the previously disconnected classical wells, but it can only occur in the region of parameter space defined by the conditions $\alpha \leq \alpha_c(\lambda)$ and $\lambda \geq \lambda_c$ (i.e., in the orange-shaded region of the diagram).

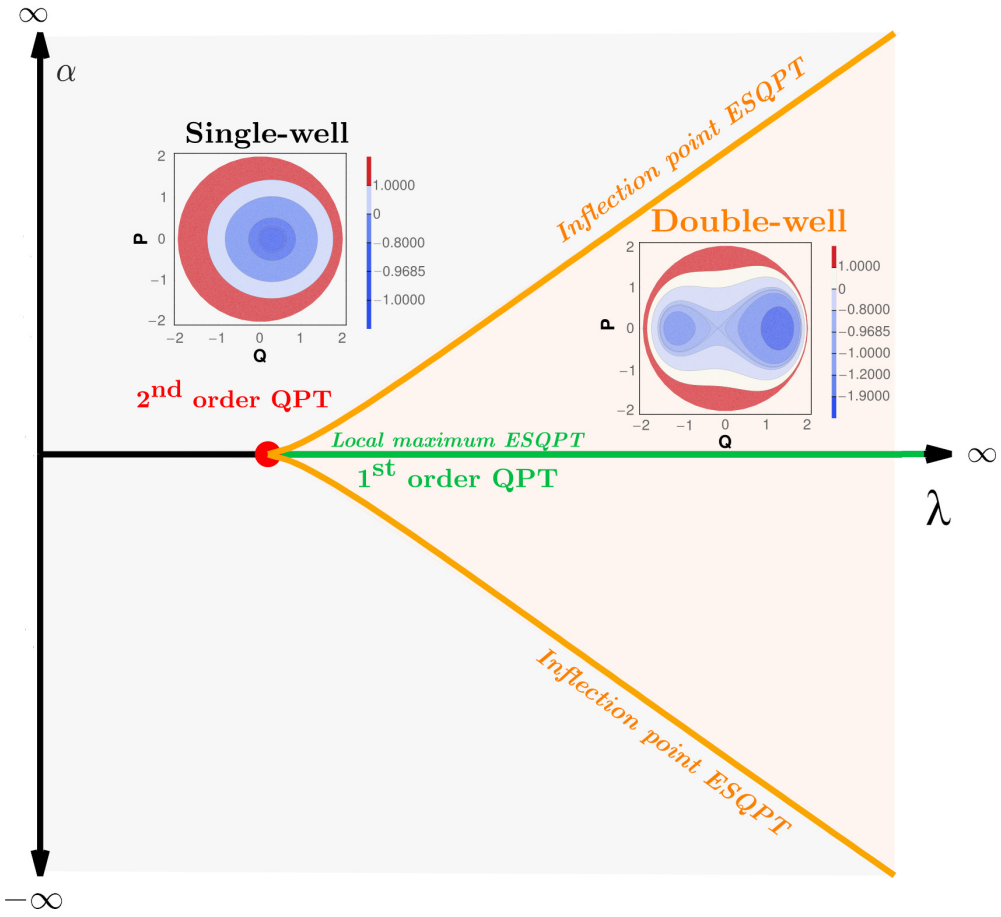

Figure 54: Schematic representation of the phase diagram of the deformed Dicke model, taking λ and α as control parameters. There is a second-order QPT at $\alpha = 0$, $\lambda_c = \sqrt{\omega\omega_0}/2$. When $\lambda > \lambda_c$, we identify a critical value α_c such that if $\alpha > \alpha_c$ the classical system can only support a single energy well, while if $\alpha < \alpha_c$ the system may exhibit up to two classical wells; in this case, the wells become connected at a certain ESQPT critical energy. Orange lines show the numerically obtained function $\alpha_c(\lambda)$. The green horizontal line represents a first-order QPT taking place at $\alpha = 0$ when $\lambda > \lambda_c(\alpha = 0)$. For illustration purposes, the single- and double-well scenarios are exemplified by two classical space portraits, obtained as the projection on the (Q, P) plane of the four-dimensional contour surfaces of the classical Hamiltonian (210) for fixed energy values (see colorbars).

In Fig. 55 we present our results dealing with the development of chaos and compare numerical and experimental results. We focus on different energies and deformation strengths, (a) $\epsilon = -1.9993$ and $\alpha = 0.5$, (b) $\epsilon = -2.0007$ and $\alpha = 0.5$, (c) $\epsilon = -1.4997$ and $\alpha = 0.7$, (d) $\epsilon = -1.4984$ and $\alpha = 0.7$, (e) $\epsilon = -0.9998$ and $\alpha = 1.1$, (f) $\epsilon = -0.6830$ and $\alpha = 1.41$, (g) $\epsilon = -0.6657$ and $\alpha = 1.43$, (h) $\epsilon = -2.0001$ and $\alpha = 1.5$ and, (i) $\epsilon = -12.0001$ and $\alpha = 1.5$. In all cases, the atom-field coupling is fixed at $\lambda = 1.5$. The theoretical predictions of the trajectories in the (q, p) and (Q, P) planes and the overall time evolution $(q(t), p(t), Q(t), P(t))$ are shown on the left-hand side of Fig. 55, whereas the corresponding electrical coordinates (I_{L_1}, V_{C_1}, I_{L_2}, V_{C_2}) and their projections in the planes (I_{L_1}, V_{C_1}) and (I_{L_2}, V_{C_2}) are located on the right-hand side of the figure. For $\lambda = 1.5$, the critical value of the deformation strength is $\alpha_c \approx 1.43019$. Figure 55(a)-(e) focuses on deformation strengths $\alpha \leq \alpha_c$, when the system exhibits two disconnected energy wells. In order to explore the dynamics of each well, we choose two different initial conditions. The trajectory in the right well, in Fig. 55(a), is periodic and thus it is indicative of regular dynamics, even though the trajectory in the left well, and at the same energy, densely covers all the available phase space, meaning that this well is chaotic. Also, note that the phase space volume in the left well is considerably larger than that of the right well, which is a consequence of the asymmetry created by the deformation strength α. These results are in good qualitative agreement with our previous theoretical analysis in Sec. 4.2, with our main conclusion being that the parity-breaking perturbation forces the chaotic domain to develop separately within each of the wells. Similarly to the previous case, when $\epsilon \approx -1.5$ and $\alpha = 0.7$ we observe two disconnected wells; the left well exhibits chaos and the right well displays regular dynamics, see Figs. 55(c)-(d). Fig. 55(e) depicts a regular trajectory with a toroidal structure evolving in the right well, with $\epsilon \approx -1$ and $\alpha = 1.1$.

We have examined the behavior of the system close to the critical value of the deformation strength: Fig. 55(f) shows the case of $\alpha = 1.41$, while Fig. 55(g) deals with $\alpha = 1.43$. When $\alpha = 1.41 < \alpha_c$, the system still supports two disconnected wells, but the potential barrier between them is small due to the proximity to the critical point. For this reason, we have prepared an initial condition in the right well to ascertain if the experimental electronic noise is enough to force the trajectory to move towards the left well. Our results indicate that stochastic fluctuations are not strong enough to induce this well shift, as Fig. 55(f) shows. As depicted in Fig. 55(g), for $\alpha = 1.43 \approx \alpha_c$, the trajectory ends in the left well exhibiting regular behavior.

Finally, we have considered two values of the deformation strength $\alpha > \alpha_c$, where the system exhibits only one classical well. For $\alpha = 1.5$ and at sufficiently

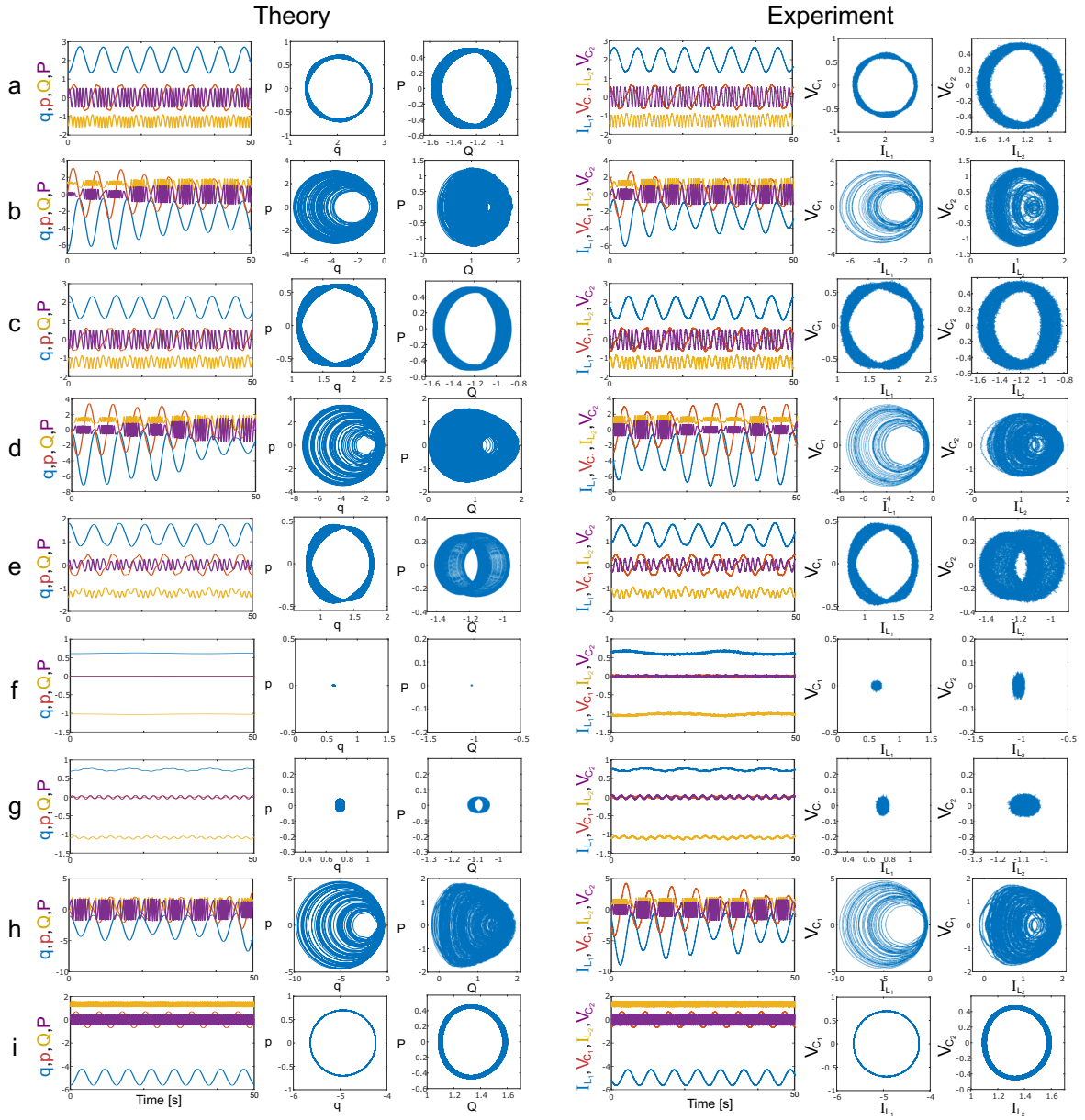

Figure 55: Comparison of theoretical and experimental measurements of chaos. We represent the temporal evolution of the coordinates (q, p, Q, P) and the projections of the trajectories in the planes (q, p) and (Q, P) for numerical simulations and experimental measurements. The energy of the trajectories and the parameters are: (a) $\epsilon = -1.9993$ and $\alpha = 0.5$, (b) $\epsilon = -2.0007$ and $\alpha = 0.5$, (c) $\epsilon = -1.4997$ and $\alpha = 0.7$, (d) $\epsilon = -1.4984$ and $\alpha = 0.7$, (e) $\epsilon = -0.9998$ and $\alpha = 1.1$, (f) $\epsilon = -0.6830$ and $\alpha = 1.41$, (g) $\epsilon = -0.6657$ and $\alpha = 1.43$, (h) $\epsilon = -2.0001$ and $\alpha = 1.5$ and, (i) $\epsilon = -12.0001$ and $\alpha = 1.5$. In each case, the initial conditions (q, p, Q, P) are set to: (a) $(1.32, 0, -1.5, 0)$, (b) $(-6.736, 0, 1.5, 0)$, (c) $(2.374, 0, -1, 0)$, (d) $(-0.29, 0, 1, 0)$, (e) $(1.797, 0, -1.4, 0)$, (f) $(0.694, 0, -1.1, 0)$, (g) $(0.608, 0, -1.019, 0)$, (h) $(-1, 0, -0.201, 0)$ and (i) $(-5.638, 0, 1.1, 0)$. We set $\lambda = 1.5$, $\omega = 1\ \mathrm{s}^{-1}$ and $\omega_0 = 1\ \mathrm{s}^{-1}$ in all cases.

high energy, $\epsilon \approx -2$, Fig. 55(h) clearly shows that the dynamics is chaotic. However, close to the ground-state, $\epsilon \approx -12.0001$, regularity is found as in Fig. 55(i). As explained in Sec. 4.2.2, the deformed Dicke model can be described by a set of adiabatic invariants near the ground-state energy, and for this reason the dynamics is very approximately integrable [315], [349].

4.4 CONCLUSIONS

In this Chapter we have presented an analysis of the onset of chaos and the phase transitions of a deformed version of the Dicke model.

The most relevant features of the classical limit of the model have been presented in the first part of this Chapter. Because the deformed Dicke model is a fully connected system, the classical limit provides a powerful framework to analyze the behavior of the infinite-size limit of the corresponding quantum system which can only be approached numerically otherwise. The system exhibits two ESQPTs, rooted in different non-analytical changes of the phase space volume. For the system parameters in our focus, only one classical well can be found below a certain critical energy, and between this first critical energy and a second critical energy there appears a new classical well which, however, is disconnected form the ground-state energy well. Above the second critical energy, these wells become connected. The first critical energy is associated with a jump discontinuity in the level density, while the second one manifests through a logarithmic singularity in the infinite-size limit.

In the second part of this Chapter we have presented a theoretical study of classical and quantum chaos in the model. Our main result is that chaos can develop independently, and at different rates, in both wells as long as these remain disconnected; above the second critical energy, we observe that the degree of chaos becomes homogeneous in both wells. This quantum-classical correspondence is very well exemplified by Poincaré sections and classical Lyapunov exponents, as well as Peres lattices for the quantum case. In our analyses of the quantum model, the use of the $\hat{\mathcal{C}}$ operator plays a fundamental role in establishing a separation of the system's eigenvalues according to what classical well they are attached to.

Finally, the third part of this Chapter deals with an experimental realization of the deformed Dicke model and a study of its phase transitions and chaos. The model is simulated experimentally through a bi-parametric electronic platform. By appropriately tuning the electrical current and the capacitor voltage one is able to reproduce the Hamilton equations governing the classical dynamics of the system.

Depending on the values of its two control parameters, the system exhibits first- and second-order phase transitions in its ground-state manifold, which we be monitored through the electronic variables having a direct correspondence with the canonical coordinates in phase space. The agreement of numerical and experimental results is very good in all cases. We also compare numerical and experimental results for the development of chaos, validating our previous theoretical studies.

Part III

CONCLUSIONS AND BIBLIOGRAPHY

5 GENERAL CONCLUSIONS

CONCLUSIONS

The research activity summarized in this thesis has a common goal: to push the frontiers of our understanding of many-body quantum systems, whose natural complexity makes the questions of chaos and thermalization very relevant. In particular, we have payed closed attention to the interconnections between these two physical phenomena in systems where some sort of exception to thermal behavior is present. Chaos is generally understood as the main catalyst for thermalization both in the classical and quantum regimes, and it is usually expected in sufficiently complicated systems. Contrarily, integrability, many-body localization and some forms of symmetry-breaking phase transitions can seriously hamper the system's ability to reach thermal equilibrium. It is important to emphasize that all of these can occur even in complex quantum systems. Although the study of quantum chaos emerged in the context of nuclear physics, modern research has found a powerful testbed in models native to condensed matter physics, some of which can be realized experimentally through recent quantum technology platforms.

The main achievements of this thesis can be summarized as follows:

Presenting a coherent landscape for the many-body localization transition. This has been the goal of Chapter 2, partially based on [237]. Disorder plays an important role in many fields of condensed matter physics and can enable a plethora of technological applications. In the context of complex spin chains, mathematically equivalent to spinless fermion systems, disorder drives the transition from a metallic thermal regime, where the dynamics is chaotic, to an insulating localized phase, characterized by a special form of emergent integrability. We have analyzed the transition by exploiting the tools of random matrix theory and the eigenstate thermalization hypothesis. To be more specific, in our integrated scenario the transition to many-body localization roughly starts at the disorder strength, $\omega_c(L)$, such that the probability of extreme events reaches a maximum value, as evidenced by the kurtosis excess of the diagonal fluctuations with respect to the microcanonical value. For disorder strengths $\omega < \omega_c(L)$, the system is in the chaotic regime, where it exhibits a $\omega-$depedent Thouless energy scale. As ω increases below $\omega_c(L)$, chaotic long-range level correlations are increasingly reduced, and at $\omega = \omega_c(L)$

the Thouless energy is minimal. As a consequence, the model departs from the chaotic phase. For $\omega > \omega_c(L)$, the transition to the fully Poissonian regime can be surprisingly well described by a family of semi-Poisson statistics, whose main feature is that level spacings behave as independent random variables even though some degree of level repulsion still persists. Our results are compatible with many-body localization being a robust phase in the thermodynamic limit.

Describing equilibrium states in symmetry-broken phases. This is the overarching theme of Chapter 3, based on our publications [29], [325]–[327], [330]. Phase transitions are ubiquitous in many-body systems, and they are often caused by symmetry-breaking. In this Chapter we have made use of both fully-connected and finite-range interacting systems. In the context of fully-connected systems with an excited-state quantum phase transition, such as the Lipkin-Meshkov-Glick model, the critical line splits the spectrum into two phases with markedly different thermodynamic properties. In the infinite-size limit, it is separated into a symmetry-breaking phase, with parity doublets, and a symmetric phase, with no degeneracies. Although the ESQPT non-analiticity is not clearly observable in systems with many degrees of freedom, some of these dynamical properties can still be found in sufficiently long-range spin chains. As a consequence of symmetry-breaking, the standard arguments of the eigenstate thermalization hypothesis become invalid, and effective long-time equilibrium values cannot be described through the microcanonical ensemble. In this chapter, we have developed a theoretical framework precisely to describe these equilibrium states in systems with $\mathbb{Z}_2$ symmetry-breaking. Our arguments are general and apply to a wide range of physical systems. The main point of the theory consists in the identification of a set of emerging conserved quantities in $\mathbb{Z}_2$ symmetry-breaking phases, these operators being directly connected with the order parameter of the underlying phase transition. We provide extensions of the standard canonical and microcanonical ensembles describing the long-time average of relevant observables in symmetry-broken phases. Further, we illustrate the relevance of our framework in the understading of dynamical phase transitions of the two types (DPT-I and DPT-II). In the case of collective systems, DPTs-I are rooted in non-smooth variations of the geometry of the associated classical space, and the order parameter takes a non-zero value when our defined operators act as constants of motion. As for DPTs-II, we address one of the foundational explanations for the non-analytical times in the parity-projected return probabilities and invalidate it, showing that the believed mechanism for this phenomenon is not possible in symmetry-broken phases. For initial states in symmetric phases that are later taken out of equilibrium, we show that the standard classification of regular and anomalous cusps can be related to the spectral phase where the state ends up after the quench: whether

the final state is in a symmetry-breaking or symmetric phase deeply impacts its short-time behavior so characteristic of DPTs-II. In this Chapter we also define and analyze a complex-time survival probability. The zeroes (exceptional points) of this magnitude across the $\beta = 0$ line give rise to DPTs-II. Our complex-time extension allows us to watch the origin and gradual development of dynamical critical structures. Finally, we provide a generalization of the microcanonical ensemble that is suitable to describe equilibrium states under energy cat states where the local density of states is a highly bimodal distribution.

Exploring chaos in systems with asymmetic wells theoretically and experimentally. This is the topic of our last Chapter 4, based on original publications [328] and [485]. In this Chapter we study a deformed version of the quantum optical Dicke model. The deformation is responsible for the appearance of an additional jump excited-state quantum phase transition. For the range of energies for which two asymmetric energy wells exist, we study the development of chaos both at the classical and quantum level. Classically, we employ Poincaré sections and the largest Lyapunov exponents while for the quantum case we make use of Peres lattices representing the diagonal values of convenient observables. Our main conclusion is that the deformation added to the Hamiltonian is capable of completely decoupling the onset of chaos in the two wells, which develops in an independent way and at different energies. The second part of this Chapter contains an experimental realization of the deformed Dicke model through a biparametric electronic platform mimicking the classical Hamilton equations of motion, which govern the dynamics of the model in the infinite-size limit. Several phase transitions are explored as well as the onset of chaos, yielding excellent agreement of theoretical and experimental results.

CONCLUSIONES

La actividad científica resumida en esta tesis tiene un objetivo común: ampliar las fronteras de nuestro entendimiento de los sistemas cuánticos de muchos cuerpos, cuya inherente complejidad hace que el caos y la termalización adquieran gran relevancia. En particular, nos hemos centrado en las interrelaciones entre estos dos fenómenos físicos en sistemas en los que está presente alguna forma de excepción al comportamiento térmico. Normalmente se entiende que el caos es el principal catalizador de la termalización tanto en el mundo clásico como en el cuántico, y se espera encontrarlo en sistemas que sea lo suficientemente complicados. Por el contrario, la integrabilidad, la localización de muchos cuerpos y algunos tipos de transiciones de fase que rompen simetrías pueden dificultar seriamente que el sistema alcance el equilibrio térmico. Es importante enfatizar que todos estos fenómenos pueden ocurrir incluso en complejos sistemas cuánticos. Aunque el estudio del caos cuántico nace en el seno de la física nuclear, la investigación moderna en este ámbito ha encontrado en modelos propios de la materia condensada un *testbed* formidable. Además, algunos de estos sistemas pueden ser realizados experimentalmente a través de las recientes plataformas de tecnologías cuánticas.

Los principales logros de esta tesis se pueden resumir como sigue:

Presentar un paisaje coherente para la transición de localización de muchos cuerpos. Este ha sido el objetivo del Capítulo 2, basado parcialmente en [237]. El desorden tiene un papel fundamental en muchas áreas de la física de la materia condensada y puede habilitar una gran grantidad de aplicaciones tecnológicas. En el contexto de complejas cadenas de espín, que son matemáticamente equivalentes a sistemas de fermiones sin espín, el desorden es el responsable de la transición de un régimen metálico y térmico, donde la dinámica es caótica, a una fase aislante y localizada, caracterizada por una forma especial de integrabilidad emergente. Hemos analizado la transición haciendo uso de herramientas de teoría de matrices aleatorias y de la hipótesis de termalización de autoestados. Para ser más específicos, en nuestro escenario integrado la transición a la localización de muchos cuerpos empieza, aproximadamente, en el valor del desorden, $\omega_c(L)$, tal que la probabilidad de eventos extremos alcanza un valor máximo, como evidencia el exceso de kurtosis de las fluctuaciones diagonales con respecto a su valor microcanónico. Para valores del desorden $\omega < \omega_c(L)$, el sistema está en el régimen cáotico, donde muestra una energía de Thouless que depende de ω. A medida que ω aumenta por debajo de $\omega_c(L)$, las correlaciones de largo alcance entre los niveles de energía, características del caos cuántico, se reducen cada vez más, hasta que para $\omega = \omega_c(L)$ la energía de Thouless es mínima. Como consecuencia, el modelo

abandona la fase caótica. Para $\omega > \omega_c(L)$, la transición al régimen totalmente Poissoniano se puede describir sorprendentemente bien por una familia de estadística de semi-Poisson. Su principal característica es que los espaciamientos de niveles de energía se comportan como variables aleatorias independientes aunque presentan cierto grado de repulsión. Nuestros resultados son compatibles con la existencia de una fase de localización de muchos cuerpos robusta en el límite termodinámico.

Describir los estados de equilibrio en fases con ruptura de simetría. Este es el tema general del Capítulo 3, basado en nuestras publicaciones [29], [325]–[327], [330]. Las transiciones de fase son ubicuas en los sistemas de muchos cuerpos, y frecuentemente están causadas por alguna ruptura de simetría. En este Capítulo nos hemos servido tanto de sistemas colectivos como de sistemas con interacción de largo alcance. En el contexto de los sistemas colectivos con una transición de fase de estados excitados, como el módelo de Lipkin-Meshkov-Glick, la línea crítica divide el espectro en dos fases con propiedades termodinámicas completamente diferentes. En el límite de tamaño infinito, resulta dividido en una fase de ruptura de simetría, con dobletes de paridad, y una fase simétrica, sin degeneraciones. Aunque la ESQPT no se observa claramente en sistemas con muchos grados de libertad, algunas de estas propiedades dinámicas se pueden encontrar en sistemas no colectivos con alcance de interacción suficientemente largo. Como consecuencia de la ruptura de simetría, los argumentos estándar de la hipótesis de termalización de autoestados resultan inválidos, y los valores de equilibrio efectivo a largo tiempo no se pueden describir a través de la colectividad microcanónica. En este Capítulo, hemos desarrollado un marco teórico precisamente para describir estos estados de equilibrio en sistemas con ruptura de simetría $\mathbb{Z}_2$. Nuestros argumentos son generales y aplican a una gran variedad de sistemas físicos. El punto principal de la teoría consiste en la identificación de un conjunto de cantidades conservadas en fases con ruptura de simetría $\mathbb{Z}_2$. Estos operadores están directamente conectados con el parámetro de orden de la transición de fase. Proporcionamos extensiones de las colectividades canónica y microcanónica para describir el promedio a largo tiempo de observables relevantes en las fases con ruptura de simetría. Además, ilustramos la utilidad de nuestra teoría para entender las transiciones de fase dinámicas de ambos tipos (DPT-I y DPT-II). En el caso de sistemas colectivos, mostramos que las DPT-I se deben a variaciones bruscas en la geometría del espacio de fases clásico asociado, y el parámetro de orden toma un valor distinto de cero cuando los operadores que definimos actúan como constantes del movimiento. Con respecto a las DPT-II, abordamos una de las explicaciones fundacionales sobre el origen de puntos no analíticos en la probabilidad de supervivencia proyectada en paridad e invalidamos esta explicación, mostrando que el mecanismo propuesto anteriormente en la literatura para este fenómeno no

puede tener lugar en fases con ruptura de simetría. Para estados iniciales en fases simétricas que son sacados del equilibrio, mostramos que la clasificación estándar en puntos no analíticos regulares y anómalos puede relacionarse con la fase espectral en la que termina un estado como consecuencia de un *quench*: el hecho de que el estado final esté en una fase con ruptura de simetría o una fase simétrica tiene un gran impacto en su evolución a corto plazo, que es la principal característica de las DPT-II. En este Capítulo también definimos y analizamos una función de probabilidad de supervivencia con tiempo complejo. Los ceros (puntos excepcionales) de esta magnitud a lo largo de la línea $\beta = 0$ dan lugar a DPTs-II. Nuestra extensión al plano complejo nos permite observar el origen y el desarrollo gradual de las diversas estructuras dinámicas. Finalmente, proponemos una generalización de la colectividad microcanónica para describir estados de equilibrio en estados energéticos de tipo gato, donde la densidad local de estados es una distribución fuertemente bimodal.

Explorar el caos en sistemas con pozos asimétricos teórica y experimentalmente. Este es el tema de nuestro último Capítulo 4, basado en nuestras publicaciones originales [328] y [485]. En este Capítulo estudiamos una versión deformada del modelo de Dicke, importante en óptica cuántica. La deformación es la responsable de que aparezca una nueva transición de fase de estados excitados de tipo salto. En el rango de energías para el que existen dos pozos de energía asimétricos, estudiamos el desarrollo del caos tanto a nivel clásico como cuántico. Clásicamente, empleamos el las secciones de Poincaré y el mayor exponente de Lyapunov mientras que para el caso cuántico utilizamos redes de Peres, que representan los valores diagonales de observables convenientes. Nuestra principal conclusión es que la deformación añadida al sistema completamente desacopla la aparición del caos en los dos pozos, de manera que se desarrolla de forma independiente y a energías distintas. La segunda parte de este Capítulo contiene una realización experimental del modelo deformado de Dicke a través de una plataforma electrónica biparamétrica, la cuál es capaz de simular las ecuaciones clásicas del movimiento de Hamilton; estas gobiernan la dinámica del sistema en el límite de tamaño infinito. Hemos explorado distintas transiciones de fase y el desarrollo del caos, obteniendo un acuerdo excelente entre valores teóricos y experimentales.

BIBLIOGRAPHY

[1] L. D'Alessio, Y. Kafri, A. Polkovnikov, and M. Rigol, "From quantum chaos and eigenstate thermalization to statistical mechanics and thermodynamics," *Advances in Physics*, vol. 65, pp. 239–362, 3 May 2016, ISSN: 0001-8732. DOI: 10.1080/00018732.2016.1198134.

[2] J. M. Deutsch, "Eigenstate thermalization hypothesis," *Reports on Progress in Physics*, vol. 81, p. 082 001, 8 Aug. 2018, ISSN: 0034-4885. DOI: 10.1088/1361-6633/aac9f1.

[3] J. V. José and E. J. Saletan, *Classical Dynamics*. Cambridge University Press, Aug. 1998, ISBN: 9780521631761. DOI: 10.1017/CBO9780511803772.

[4] V. I. Arnold, *Mathematical Methods of Classical Mechanics*. New York: Springer, 1989.

[5] S.-K. Ma, *Statistical Mechanics*. Wspc; Illustrated edition, May 1985, ISBN: 978-9971966072.

[6] Y. G. Sinai, "Dinamicheskie sistemy s uprugimi otrazheniyami. ergodicheskie svoistva rasseivayushchikh bil'yardov," *Usp. Mat. Nauk*, vol. 25, p. 141, 1970.

[7] N. Simányi, "Conditional proof of the boltzmann-sinai ergodic hypothesis," *Inventiones mathematicae*, vol. 177, pp. 381–413, 2 Aug. 2009, ISSN: 0020-9910. DOI: 10.1007/s00222-009-0182-x.

[8] ——, "Proof of the ergodic hypothesis for typical hard ball systems," *Annales Henri Poincaré*, vol. 5, pp. 203–233, 2 Apr. 2004, ISSN: 1424-0637. DOI: 10.1007/s00023-004-0166-8.

[9] L. A. Bunimovich, "On the ergodic properties of nowhere dispersing billiards," *Communications in Mathematical Physics*, vol. 65, pp. 295–312, 3 Oct. 1979, ISSN: 0010-3616. DOI: 10.1007/BF01197884.

[10] L. Boltzmann, *Vorlesungen über Gastheorie. II: Theorie van der Waals; Gase mit Zusammengesetzten Molekülen; Gasdissociation; Schlussbemerkungen*. Leizpig, Verlag von Johann Ambrosius Barth, 1898.

[11] E. Fermi, J. Pasta, and S. Ulam, "Studies of nonlinear problems," *Technical report. Los Alamos National Laboratory*, 1955.

[12] P. Reimann, "Foundation of statistical mechanics under experimentally realistic conditions," *Phys. Rev. Lett.*, vol. 101, p. 190 403, 19 Nov. 2008, ISSN: 0031-9007. DOI: 10.1103/PhysRevLett.101.190403.

[13] M. L. Mehta, *Random Matrices*. Amsterdam: Elsevier, 1990.

[14] T. Guhr, A. Müller–Groeling, and H. A. Weidenmüller, "Random-matrix theories in quantum physics: Common concepts," *Physics Reports*, vol. 299, pp. 189–425, 4-6 Jun. 1998, ISSN: 03701573. DOI: 10.1016/S0370-1573(97)00088-4.

[15] J. M. Deutsch, "Quantum statistical mechanics in a closed system," *Phys. Rev. A*, vol. 43, pp. 2046–2049, 4 Feb. 1991, ISSN: 1050-2947. DOI: 10.1103/PhysRevA.43.2046.

[16] M. V. Berry, "Regular and irregular semiclassical wavefunctions," *Journal of Physics A: Mathematical and General*, vol. 10, pp. 2083–2091, 12 Dec. 1977, ISSN: 0305-4470. DOI: 10.1088/0305-4470/10/12/016.

[17] L. F. Santos and M. Rigol, "Onset of quantum chaos in one-dimensional bosonic and fermionic systems and its relation to thermalization," *Phys. Rev. E*, vol. 81, p. 036 206, 3 Mar. 2010, ISSN: 1539-3755. DOI: 10.1103/PhysRevE.81.036206.

[18] ——, "Localization and the effects of symmetries in the thermalization properties of one-dimensional quantum systems," *Phys. Rev. E*, vol. 82, p. 031 130, 3 Sep. 2010, ISSN: 1539-3755. DOI: 10.1103/PhysRevE.82.031130.

[19] M. Srednicki, "Chaos and quantum thermalization," *Phys. Rev. E*, vol. 50, pp. 888–901, 2 Aug. 1994, ISSN: 1063-651X. DOI: 10.1103/PhysRevE.50.888.

[20] ——, "Thermal fluctuations in quantized chaotic systems," *Journal of Physics A: Mathematical and General*, vol. 29, pp. L75–L79, 4 Feb. 1996, ISSN: 0305-4470. DOI: 10.1088/0305-4470/29/4/003.

[21] ——, "The approach to thermal equilibrium in quantized chaotic systems," *Journal of Physics A: Mathematical and General*, vol. 32, pp. 1163–1175, 7 Feb. 1999, ISSN: 0305-4470. DOI: 10.1088/0305-4470/32/7/007.

[22] J. R. Garrison and T. Grover, "Does a single eigenstate encode the full hamiltonian?" *Phys. Rev. X*, vol. 8, p. 021 026, 2 Apr. 2018, ISSN: 2160-3308. DOI: 10.1103/PhysRevX.8.021026.

[23] G. Biroli, C. Kollath, and A. M. Läuchli, "Effect of rare fluctuations on the thermalization of isolated quantum systems," *Phys. Rev. Letters*, vol. 105, p. 250 401, 25 Dec. 2010, ISSN: 0031-9007. DOI: 10.1103/PhysRevLett.105.250401.

[24] H. Tasaki, "From quantum dynamics to the canonical distribution: General picture and a rigorous example," *Phys. Rev. Lett.*, vol. 80, pp. 1373–1376, 7 Feb. 1998, ISSN: 0031-9007. DOI: 10.1103/PhysRevLett.80.1373.

[25] N. Linden, S. Popescu, A. J. Short, and A. Winter, "Quantum mechanical evolution towards thermal equilibrium," *Phys. Rev. E*, vol. 79, p. 061 103, 6 Jun. 2009, ISSN: 1539-3755. DOI: 10.1103/PhysRevE.79.061103.

[26] S. Goldstein, J. L. Lebowitz, R. Tumulka, and N. Zanghì, "Canonical typicality," *Phys. Rev. Letters*, vol. 96, p. 050 403, 5 Feb. 2006, ISSN: 0031-9007. DOI: 10.1103/PhysRevLett.96.050403.

[27] J. Gemmer and G. Mahler, "Distribution of local entropy in the hilbert space of bi-partite quantum systems: Origin of jaynes' principle," *The European Physical Journal B - Condensed Matter*, vol. 31, pp. 249–257, 2 Jan. 2003, ISSN: 1434-6028. DOI: 10.1140/epjb/e2003-00029-3.

[28] E. Schrodinger, "Die gegenwertige situation in der quantenmechanik," *Die Naturwissenschaften*, vol. 23, pp. 823–828, 49 Dec. 1935, ISSN: 0028-1042. DOI: 10.1007/BF01491914.

[29] Á. L. Corps and A. Relaño, "Energy cat states induced by a parity-breaking excited-state quantum phase transition," *Phys. Rev. A*, vol. 105, p. 052 204, 5 May 2022, ISSN: 2469-9926. DOI: 10.1103/PhysRevA.105.052204.

[30] M. P. Müller, E. Adlam, L. Masanes, and N. Wiebe, "Thermalization and canonical typicality in translation-invariant quantum lattice systems," *Communications in Mathematical Physics*, vol. 340, pp. 499–561, 2 Dec. 2015, ISSN: 0010-3616. DOI: 10.1007/s00220-015-2473-y.

[31] T. Mori and N. Shiraishi, "Thermalization without eigenstate thermalization hypothesis after a quantum quench," *Phys. Rev. E*, vol. 96, p. 022 153, 2 Aug. 2017, ISSN: 2470-0045. DOI: 10.1103/PhysRevE.96.022153.

[32] J. H. Eberly, N. B. Narozhny, and J. J. Sanchez-Mondragon, "Periodic spontaneous collapse and revival in a simple quantum model," *Phys. Rev. Letters*, vol. 44, pp. 1323–1326, 20 May 1980, ISSN: 0031-9007. DOI: 10.1103/PhysRevLett.44.1323.

[33] Z. D. Gaeta and C. R. Stroud, "Classical and quantum-mechanical dynamics of a quasiclassical state of the hydrogen atom," *Phys. Rev. A*, vol. 42, pp. 6308–6313, 11 Dec. 1990, ISSN: 1050-2947. DOI: 10.1103/PhysRevA.42.6308.

[34] H. Poincaré, "Sur le problème des trois corps et les équations de la dynamique," *Acta Math.*, vol. 13, p. 1, 1890.

[35] J. T. Edwards and D. J. Thouless, "Numerical studies of localization in disordered systems," *Journal of Physics C: Solid State Physics*, vol. 5, pp. 807–820, 8 Apr. 1972, ISSN: 0022-3719. DOI: 10.1088/0022-3719/5/8/007.

[36] S. Sachdev, *Quantum Phase Transitions*. Cambridge University Press, 1999.

[37] Merriam-Webster Dictionary. (2024). "Definition of 'chaos'," [Online]. Available: https://www.merriam-webster.com/dictionary/chaos.

[38] Cambridge Dictionary. (2024). "Definition of 'chaos'," [Online]. Available: https://dictionary.cambridge.org/dictionary/english/chaos.

[39] E. N. Lorenz, "Deterministic nonperiodic flow," *Journal of the Atmospheric Sciences*, vol. 20, pp. 130–141, 2 Mar. 1963, ISSN: 0022-4928. DOI: 10.1175/1520-0469(1963)020<0130:DNF>2.0.CO;2.

[40] E. N. Lorenz, *The Essence of Chaos*. University of Washington Press, 1995, ISBN: 9780295975146.

[41] H. Poincaré, *Science et méthode*. Editions Ducourt, 2020, ISBN: 979-8654041081.

[42] H. G. Schuster, *Deterministic chaos*. Wiley-VCH Verlag GmbH, 1995, ISBN: 978-3527290888.

[43] S. H. Strogatz, *Nonlinear Dynamics and Chaos: With Applications to Physics, Biology, Chemistry, and Engineering*. CRC Press, 2015, ISBN: 978-0813349107.

[44] P. Cvitanovich, *Universality in chaos*. CRC Press, 1989, ISBN: 9780852742600.

[45] C. L. O. P. T. S, *Practical Numerical Algorithms for Chaotic Systems*. New York: Springer, 1989.

[46] F. C. M. Cencini and A. Vulpiani, *Chaos from simple models to complex systems*. Singapore: World Scientific, 2015.

[47] V. I. Osledec, "A multiplicative ergodic theorem: Lyapunov characteristic numbers for dynamical systems," *Trans. Moscow Math. Soc.*, vol. 19, 197 1968.

[48] S. Pilatowsky-Cameo, J. Chávez-Carlos, M. A. Bastarrachea-Magnani, P. Stránský, S. Lerma-Hernández, L. F. Santos, and J. G. Hirsch, "Positive quantum lyapunov exponents in experimental systems with a regular classical limit," *Phys. Rev. E*, vol. 101, p. 010 202, 1 Jan. 2020, ISSN: 2470-0045. DOI: 10.1103/PhysRevE.101.010202.

[49] J. v. Neumann, "Zur operatorenmethode in der klassischen mechanik," *The Annals of Mathematics*, vol. 33, p. 587, 3 Jul. 1932, ISSN: 0003486X. DOI: 10.2307/1968537.

[50] E. Hopf, "On causality, statistics and probability," *Journal of Mathematics and Physics*, vol. 13, pp. 51–102, 1-4 Apr. 1934, ISSN: 00971421. DOI: 10.1002/sapm193413151.

[51] ——, *Ergodentheorie*. Springer Berlin Heidelberg, 1937, ISBN: 978-3-540-04881-7. DOI: 10.1007/978-3-642-86630-2.

[52] J. W. Gibbs, *Elementary Principles in Statistical Mechanics*. Charles Scribner's Sons, Mar. 1902.

[53] Y. G. Sinai, "K obosnovaniyu ergodicheskoi gipotezy dlya odnoi dinamicheskoi sistemy statisticheskoi mekhaniki," *Dokl. Akad. nauk SSSR*, vol. 6, p. 1261, 153 1963.

[54] Y. G. Sinai, "Dynamical systems with elastic reflections," *Russian Mathematical Surveys*, vol. 25, pp. 137–189, 2 Apr. 1970, ISSN: 0036-0279. DOI: 10.1070/RM1970v025n02ABEH003794.

[55] A. N. Kolmogorov, "Entropy per unit time as a metric invariant of automorphism," *Doklady of Russian Academy of Sciences*, vol. 124, p. 754, 1959.

[56] Y. G. Sinai, "On the notion of entropy of a dynamical system," *Doklady of Russian Academy of Sciences*, vol. 124, p. 768, 1959.

[57] M. Hillery, R. O'Connell, M. Scully, and E. Wigner, "Distribution functions in physics: Fundamentals," *Physics Reports*, vol. 106, pp. 121–167, 3 Apr. 1984, ISSN: 03701573. DOI: 10.1016/0370-1573(84)90160-1.

[58] A. Peres, "Stability of quantum motion in chaotic and regular systems," *Phys. Rev. A*, vol. 30, pp. 1610–1615, 4 Oct. 1984, ISSN: 0556-2791. DOI: 10.1103/PhysRevA.30.1610.

[59] A. Peres, Ed., *Quantum Theory: Concepts and Methods*. Springer Netherlands, 2002, ISBN: 978-0-7923-3632-7. DOI: 10.1007/0-306-47120-5.

[60] Z. Rudnick, "Quantum chaos?" *Notices of the American Mathematical Society*, vol. 55, p. 32, 2008.

[61] M. C. Guztwiller, *Chaos in Classical and Quantum Mechanics*, 1st. New York: Springer, 1990.

[62] F. Haake, *Quantum Signatures of Chaos*. Berlin: Springer, 2010.

[63] H.-J. Stöckmann, *Quantum chaos: an introduction*. Cambridge University Press, 2008, ISBN: 978-0521027151.

[64] J. Gómez, K. Kar, V. Kota, R. Molina, A. Relaño, and J. Retamosa, "Many-body quantum chaos: Recent developments and applications to nuclei," *Physics Reports*, vol. 499, pp. 103–226, 4-5 Mar. 2011, ISSN: 03701573. DOI: 10.1016/j.physrep.2010.11.003.

[65] F. Borgonovi, F. Izrailev, L. Santos, and V. Zelevinsky, "Quantum chaos and thermalization in isolated systems of interacting particles," *Physics Reports*, vol. 626, pp. 1–58, Apr. 2016, ISSN: 03701573. DOI: 10.1016/j.physrep.2016.02.005.

[66] M. V. Berry, "The bakerian lecture, 1987. quantum chaology," *Proceedings of the Royal Society of London. A. Mathematical and Physical Sciences*, vol. 413, pp. 183–198, 1844 Sep. 1987, ISSN: 0080-4630. DOI: 10.1098/rspa.1987.0109.

[67] E. P. Wigner, "Characteristic vectors of bordered matrices with infinite dimensions," *The Annals of Mathematics*, vol. 62, p. 548, 3 Nov. 1955, ISSN: 0003486X. DOI: 10.2307/1970079.

[68] ——, "Characteristics vectors of bordered matrices with infinite dimensions ii," *The Annals of Mathematics*, vol. 65, p. 203, 2 Mar. 1957, ISSN: 0003486X. DOI: 10.2307/1969956.

[69] ——, "On the distribution of the roots of certain symmetric matrices," *The Annals of Mathematics*, vol. 67, p. 325, 2 Mar. 1958, ISSN: 0003486X. DOI: 10.2307/1970008.

[70] F. J. Dyson, "Statistical theory of the energy levels of complex systems. i," *Journal of Mathematical Physics*, vol. 3, pp. 140–156, 1 Jan. 1962, ISSN: 0022-2488. DOI: 10.1063/1.1703773.

[71] ——, "Statistical theory of the energy levels of complex systems. ii," *Journal of Mathematical Physics*, vol. 3, pp. 157–165, 1 Jan. 1962, ISSN: 0022-2488. DOI: 10.1063/1.1703774.

[72] ——, "Statistical theory of the energy levels of complex systems. iii," *Journal of Mathematical Physics*, vol. 3, pp. 166–175, 1 Jan. 1962, ISSN: 0022-2488. DOI: 10.1063/1.1703775.

[73] C. W. J. Beenakker, "Random-matrix theory of quantum transport," *Reviews of Modern Physics*, vol. 69, pp. 731–808, 3 Jul. 1997, ISSN: 0034-6861. DOI: 10.1103/RevModPhys.69.731.

[74] A. Sommerfeld, "Zur quantentheorie der spektrallinien," *Annalen der Physik*, vol. 356, pp. 125–167, 18 1916, ISSN: 00033804. DOI: 10.1002/andp.19163561802.

[75] W. Wilson, *Phil. Mag.*, vol. 29, p. 795, 1915.

[76] J. Ishiwara, *Tokyo Sugako Buturigakkawi Kizi*, vol. 8, p. 106, 1915.

[77] A. Einstein, "Zum quantensatz von sommerfeld und epstein," *Verh. Dtsch. Phys. Ges.*, vol. 19, 1917.

[78] M. C. Gutzwiller, "Periodic orbits and classical quantization conditions," *Journal of Mathematical Physics*, vol. 12, pp. 343–358, 3 Mar. 1971, ISSN: 0022-2488. DOI: 10.1063/1.1665596.

[79] M. Brack and R. Bhaduri, *Semiclassical physics*. CRC Press, May 2019, ISBN: 978-0367314156.

[80] J. M. G. Gómez, R. A. Molina, A. Relaño, and J. Retamosa, "Misleading signatures of quantum chaos," *Phys. Rev. E*, vol. 66, p. 036 209, 3 Sep. 2002, ISSN: 1063-651X. DOI: 10.1103/PhysRevE.66.036209.

[81] Á. L. Corps and A. Relaño, "Long-range level correlations in quantum systems with finite hilbert space dimension," *Phys. Rev. E*, vol. 103, p. 012 208, 1 Jan. 2021, ISSN: 2470-0045. DOI: 10.1103/PhysRevE.103.012208.

[82] O. Bohigas, M. J. Giannoni, and C. Schmit, "Characterization of chaotic quantum spectra and universality of level fluctuation laws," *Phys. Rev. Lett.*, vol. 52, pp. 1–4, 1 Jan. 1984, ISSN: 0031-9007. DOI: 10.1103/PhysRevLett.52.1.

[83] P. Kos, M. Ljubotina, and T. Prosen, "Many-body quantum chaos: Analytic connection to random matrix theory," *Phys. Rev. X*, vol. 8, p. 021 062, 2 Jun. 2018, ISSN: 2160-3308. DOI: 10.1103/PhysRevX.8.021062.

[84] K. Efetov, *Supersymmetry in Disorder and Chaos*. Cambridge University Press, Oct. 1996, ISBN: 9780521470971. DOI: 10.1017/CBO9780511573057.

[85] J. Verbaarschot, "Random matrix model approach to chiral symmetry," *Nuclear Physics B - Proceedings Supplements*, vol. 53, pp. 88–94, 1-3 Feb. 1997, ISSN: 09205632. DOI: 10.1016/S0920-5632(96)00602-0.

[86] L. Laloux, P. Cizeau, J.-P. Bouchaud, and M. Potters, "Noise dressing of financial correlation matrices," *Phys. Rev. Lett.*, vol. 83, pp. 1467–1470, 7 Aug. 1999, ISSN: 0031-9007. DOI: 10.1103/PhysRevLett.83.1467.

[87] M. S. Santhanam and P. K. Patra, "Statistics of atmospheric correlations," *Phys. Rev. E*, vol. 64, p. 016 102, 1 Jun. 2001, ISSN: 1063-651X. DOI: 10.1103/PhysRevE.64.016102.

[88] O. Bohigas, R. U. Haq, and A. Pandey, "Fluctuation properties of nuclear energy levels and widths : Comparison of theory with experiment," in. Springer Netherlands, 1983, pp. 809–813. DOI: 10.1007/978-94-009-7099-1_179.

[89] R. U. Haq, A. Pandey, and O. Bohigas, "Fluctuation properties of nuclear energy levels: Do theory and experiment agree?" *Phys. Rev. Lett.*, vol. 48, pp. 1086–1089, 16 Apr. 1982, ISSN: 0031-9007. DOI: 10.1103/PhysRevLett.48.1086.

[90] B. Dietz, A. Heusler, K. H. Maier, A. Richter, and B. A. Brown, "Chaos and regularity in the doubly magic nucleus ^{208}Pb," *Phys. Rev. Lett.*, vol. 118, p. 012 501, 1 Jan. 2017, ISSN: 0031-9007. DOI: 10.1103/PhysRevLett.118.012501.

[91] L. Muñoz, R. A. Molina, J. M. G. Gómez, and A. Heusler, "Examination of experimental evidence of chaos in the bound states of ^{208}Pb," *Phys. Rev. C*, vol. 95, p. 014 317, 1 Jan. 2017, ISSN: 2469-9985. DOI: 10.1103/PhysRevC.95.014317.

[92] D. Wintgen and H. Friedrich, "Classical and quantum-mechanical transition between regularity and irregularity in a hamiltonian system," *Phys. Rev. A*, vol. 35, pp. 1464–1466, 3 Feb. 1987, ISSN: 0556-2791. DOI: 10.1103/PhysRevA.35.1464.

[93] R. H. Dicke, "Coherence in spontaneous radiation processes," *Phys. Rev.*, vol. 93, pp. 99–110, 1 Jan. 1954, ISSN: 0031-899X. DOI: 10.1103/PhysRev.93.99.

[94] P. Pérez-Fernández, A. Relaño, J. M. Arias, P. Cejnar, J. Dukelsky, and J. E. García-Ramos, "Excited-state phase transition and onset of chaos in quantum optical models," *Phys. Rev. E*, vol. 83, p. 046 208, 4 Apr. 2011, ISSN: 1539-3755. DOI: 10.1103/PhysRevE.83.046208.

[95] M. A. Bastarrachea-Magnani, S. Lerma-Hernández, and J. G. Hirsch, "Comparative quantum and semiclassical analysis of atom-field systems. ii. chaos and regularity," *Phys. Rev. A*, vol. 89, p. 032 102, 3 Mar. 2014, ISSN: 1050-2947. DOI: 10.1103/PhysRevA.89.032102.

[96] C. Emary and T. Brandes, "Chaos and the quantum phase transition in the dicke model," *Phys. Rev. E*, vol. 67, p. 066 203, 6 Jun. 2003, ISSN: 1063-651X. DOI: 10.1103/PhysRevE.67.066203.

[97] A. Altland and F. Haake, "Equilibration and macroscopic quantum fluctuations in the dicke model," *New Journal of Physics*, vol. 14, p. 073 011, 7 Jul. 2012, ISSN: 1367-2630. DOI: 10.1088/1367-2630/14/7/073011.

[98] L. F. Santos, F. Borgonovi, and F. M. Izrailev, "Onset of chaos and relaxation in isolated systems of interacting spins: Energy shell approach," *Phys. Rev. E*, vol. 85, p. 036 209, 3 Mar. 2012, ISSN: 1539-3755. DOI: 10.1103/PhysRevE.85.036209.

[99] C. Kollath, G. Roux, G. Biroli, and A. M. Läuchli, "Statistical properties of the spectrum of the extended bose–hubbard model," *Journal of Statistical Mechanics: Theory and Experiment*, vol. 2010, P08011, 08 Aug. 2010, ISSN: 1742-5468. DOI: 10.1088/1742-5468/2010/08/P08011.

[100] L. Pausch, E. G. Carnio, A. Rodríguez, and A. Buchleitner, "Chaos and ergodicity across the energy spectrum of interacting bosons," *Phys. Rev. Lett.*, vol. 126, p. 150 601, 15 Apr. 2021, ISSN: 0031-9007. DOI: 10.1103/PhysRevLett.126.150601.

[101] G. Montambaux, D. Poilblanc, J. Bellissard, and C. Sire, "Quantum chaos in spin-fermion models," *Phys. Rev. Lett.*, vol. 70, pp. 497–500, 4 Jan. 1993, ISSN: 0031-9007. DOI: 10.1103/PhysRevLett.70.497.

[102] A. Relaño, "Thermalization in an interacting spin system in the transition from integrability to chaos," *Journal of Statistical Mechanics: Theory and Experiment*, vol. 2010, P07016, 07 Jul. 2010, ISSN: 1742-5468. DOI: 10.1088/1742-5468/2010/07/P07016.

[103] E. B. Bogomolny, B. Georgeot, M.-J. Giannoni, and C. Schmit, "Chaotic billiards generated by arithmetic groups," *Phys. Rev. Lett.*, vol. 69, pp. 1477–1480, 10 Sep. 1992, ISSN: 0031-9007. DOI: 10.1103/PhysRevLett.69.1477.

[104] L. Benet, F. Leyvraz, and T. H. Seligman, "Wigner-dyson statistics for a class of integrable models," *Phys. Rev. E*, vol. 68, p. 045 201, 4 Oct. 2003, ISSN: 1063-651X. DOI: 10.1103/PhysRevE.68.045201.

[105] J. H. Hannay and A. M. O. D. Almeida, "Periodic orbits and a correlation function for the semiclassical density of states," *Journal of Physics A: Mathematical and General*, vol. 17, pp. 3429–3440, 18 Dec. 1984, ISSN: 0305-4470. DOI: 10.1088/0305-4470/17/18/013.

[106] M. Sieber and K. Richter, "Correlations between periodic orbits and their role in spectral statistics," *Physica Scripta*, vol. T90, p. 128, 1 2001, ISSN: 0031-8949. DOI: 10.1238/Physica.Topical.090a00128.

[107] M. Sieber, "Leading off-diagonal approximation for the spectral form factor for uniformly hyperbolic systems," *Journal of Physics A: Mathematical and General*, vol. 35, pp. L613–L619, 42 Oct. 2002, ISSN: 0305-4470. DOI: 10.1088/0305-4470/35/42/104.

[108] S. Müller, S. Heusler, P. Braun, F. Haake, and A. Altland, "Semiclassical foundation of universality in quantum chaos," *Phys. Rev. Lett.*, vol. 93, p. 014 103, 1 Jul. 2004, ISSN: 0031-9007. DOI: 10.1103/PhysRevLett.93.014103.

[109] ——, "Periodic-orbit theory of universality in quantum chaos," *Phys. Rev. E*, vol. 72, p. 046 207, 4 Oct. 2005, ISSN: 1539-3755. DOI: 10.1103/PhysRevE.72.046207.

[110] S. Heusler, S. Müller, A. Altland, P. Braun, and F. Haake, "Periodic-orbit theory of level correlations," *Phys. Rev. Lett.*, vol. 98, p. 044 103, 4 Jan. 2007, ISSN: 0031-9007. DOI: 10.1103/PhysRevLett.98.044103.

[111] S. Müller, S. Heusler, A. Altland, P. Braun, and F. Haake, "Periodic-orbit theory of universal level correlations in quantum chaos," *New Journal of Physics*, vol. 11, p. 103 025, 10 Oct. 2009, ISSN: 1367-2630. DOI: 10.1088/1367-2630/11/10/103025.

[112] T. A. Brody, J. Flores, J. B. French, P. A. Mello, A. Pandey, and S. S. M. Wong, "Random-matrix physics: Spectrum and strength fluctuations," *Reviews of Modern Physics*, vol. 53, pp. 385–479, 3 Jul. 1981, ISSN: 0034-6861. DOI: 10.1103/RevModPhys.53.385.

[113] E. Akkermans and G. Montambaux, *Mesoscopic Physics of Electrons and Photons*. Cambridge University Press, May 2007, ISBN: 9780521855129. DOI: 10.1017/CBO9780511618833.

[114] C. L. Bertrand and A. M. García-García, "Anomalous thouless energy and critical statistics on the metallic side of the many-body localization transition," *Phys. Rev. B*, vol. 94, p. 144 201, 14 Oct. 2016, ISSN: 2469-9950. DOI: 10.1103/PhysRevB.94.144201.

[115] A. N. Kolmogorov, "On conservation of conditionally periodic motions for a small change in hamilton's function," *Dokl. Akad. Nauk SSSR*, vol. 98, p. 527, 1954.

[116] V. I. Arnold, "Proof of a theorem of a. n. kolmogorov on the preservation of conditionally periodic motions under a small perturbation of the hamiltonian," *Usp. Mat. Nauk*, vol. 18, p. 13, 1963.

[117] J. K. Moser, "On invariant curves of area-preserving mappings of an annulus," *Nachr. Akad. Wiss. Göttingen II*, vol. 1, p. 1, 1962.

[118] J.-S. Caux and J. Mossel, "Remarks on the notion of quantum integrability," *Journal of Statistical Mechanics: Theory and Experiment*, vol. 2011, no. 02, P02023, Feb. 2011. DOI: 10.1088/1742-5468/2011/02/P02023. [Online]. Available: https://dx.doi.org/10.1088/1742-5468/2011/02/P02023.

[119] S. Weigert, "The problem of quantum integrability," *Physica D: Nonlinear Phenomena*, vol. 56, pp. 107–119, 1 Apr. 1992, ISSN: 01672789. DOI: 10.1016/0167-2789(92)90053-P.

[120] J. Clemente-Gallardo and G. Marmo, "Towards a definition of quantum integrability," *International Journal of Geometric Methods in Modern Physics*, vol. 06, pp. 129–172, 01 Feb. 2009, ISSN: 0219-8878. DOI: 10.1142/S0219887809003448.

[121] L. D. Faddeev, "What is complete integrability in quantum mechanics," in. Apr. 2007, pp. 83–90. DOI: 10.1090/trans2/220/04.

[122] J. Hietarinta, "Classical versus quantum integrability," *Journal of Mathematical Physics*, vol. 25, pp. 1833–1840, 6 Jun. 1984, ISSN: 0022-2488. DOI: 10.1063/1.526373.

[123] W. Zhang, "Quantum nonintegrability in finite systems," *Physics Reports*, vol. 252, pp. 1–100, 1-2 Feb. 1995, ISSN: 03701573. DOI: 10.1016/0370-1573(94)00081-D.

[124] J. v. Neumann, "Uber funktionen von funktionaloperatoren," *Annals of Mathematics*, vol. 32, no. 2, pp. 191–226, 1931, ISSN: 0003486X. DOI: 10.2307/1968185.

[125] M. V. Berry and M. Tabor, "Level clustering in the regular spectrum," *Proceedings of the Royal Society of London. A. Mathematical and Physical Sciences*, vol. 356, pp. 375–394, 1686 Sep. 1977, ISSN: 0080-4630. DOI: 10.1098/rspa.1977.0140.

[126] J. C. Barba, F. Finkel, A. González-López, and M. A. Rodríguez, "The berry-tabor conjecture for spin chains of haldane-shastry type," *EPL (Europhysics Letters)*, vol. 83, p. 27005, 2 Jul. 2008, ISSN: 0295-5075. DOI: 10.1209/0295-5075/83/27005.

[127] ——, "Polychronakos-frahm spin chain of BC_N type and the berry-tabor conjecture," *Phys. Rev. B*, vol. 77, p. 214422, 21 Jun. 2008, ISSN: 1098-0121. DOI: 10.1103/PhysRevB.77.214422.

[128] A. Relaño, J. Dukelsky, J. M. G. Gómez, and J. Retamosa, "Stringent numerical test of the poisson distribution for finite quantum integrable hamiltonians," *Phys. Rev. E*, vol. 70, p. 026208, 2 Aug. 2004. DOI: 10.1103/PhysRevE.70.026208.

[129] A. Enciso and D. Peralta-Salas, "Classical and quantum integrability of hamiltonians without scattering states," *Theoretical and Mathematical Physics*, vol. 148, pp. 1086–1099, 2 Aug. 2006, ISSN: 0040-5779. DOI: 10.1007/s11232-006-0103-8.

[130] M. Rigol, V. Dunjko, V. Yurovsky, and M. Olshanii, "Relaxation in a completely integrable many-body quantum system: An ab initio study of the dynamics of the highly excited states of 1d lattice hard-core bosons," *Phys. Rev. Lett.*, vol. 98, p. 050 405, 5 Feb. 2007, ISSN: 0031-9007. DOI: 10.1103/PhysRevLett.98.050405.

[131] L. Vidmar and M. Rigol, "Generalized gibbs ensemble in integrable lattice models," *Journal of Statistical Mechanics: Theory and Experiment*, vol. 2016, p. 064 007, 6 Jun. 2016, ISSN: 1742-5468. DOI: 10.1088/1742-5468/2016/06/064007.

[132] M. Rigol, A. Muramatsu, and M. Olshanii, "Hard-core bosons on optical superlattices: Dynamics and relaxation in the superfluid and insulating regimes," *Phys. Rev. A*, vol. 74, p. 053 616, 5 Nov. 2006. DOI: 10.1103/PhysRevA.74.053616.

[133] P. Calabrese, F. H. L. Essler, and M. Fagotti, "Quantum quench in the transverse-field ising chain," *Phys. Rev. Lett.*, vol. 106, p. 227 203, 22 Jun. 2011, ISSN: 0031-9007. DOI: 10.1103/PhysRevLett.106.227203.

[134] ——, "Quantum quenches in the transverse field ising chain: Ii. stationary state properties," *Journal of Statistical Mechanics: Theory and Experiment*, vol. 2012, P07022, 07 Jul. 2012, ISSN: 1742-5468. DOI: 10.1088/1742-5468/2012/07/P07022.

[135] ——, "Quantum quench in the transverse field ising chain: I. time evolution of order parameter correlators," *Journal of Statistical Mechanics: Theory and Experiment*, vol. 2012, P07016, 07 Jul. 2012, ISSN: 1742-5468. DOI: 10.1088/1742-5468/2012/07/P07016.

[136] L. Bucciantini, M. Kormos, and P. Calabrese, "Quantum quenches from excited states in the ising chain," *Journal of Physics A: Mathematical and Theoretical*, vol. 47, p. 175 002, 17 May 2014, ISSN: 1751-8113. DOI: 10.1088/1751-8113/47/17/175002.

[137] B. Wouters, J. D. Nardis, M. Brockmann, D. Fioretto, M. Rigol, and J.-S. Caux, "Quenching the anisotropic heisenberg chain: Exact solution and generalized gibbs ensemble predictions," *Phys. Rev. Lett.*, vol. 113, p. 117 202, 11 Sep. 2014, ISSN: 0031-9007. DOI: 10.1103/PhysRevLett.113.117202.

[138] E. Ilievski, J. D. Nardis, B. Wouters, J.-S. Caux, F. H. L. Essler, and T. Prosen, "Complete generalized gibbs ensembles in an interacting theory," *Phys. Rev. Lett.*, vol. 115, p. 157 201, 15 Oct. 2015, ISSN: 0031-9007. DOI: 10.1103/PhysRevLett.115.157201.

[139] B. Pozsgay, "The generalized gibbs ensemble for heisenberg spin chains," *Journal of Statistical Mechanics: Theory and Experiment*, vol. 2013, P07003, 07 Jul. 2013, ISSN: 1742-5468. DOI: 10.1088/1742-5468/2013/07/P07003.

[140] J.-S. Caux and R. M. Konik, "Constructing the generalized gibbs ensemble after a quantum quench," *Phys. Rev. Lett.*, vol. 109, p. 175 301, 17 Oct. 2012, ISSN: 0031-9007. DOI: 10.1103/PhysRevLett.109.175301.

[141] J. Mossel and J.-S. Caux, "Exact time evolution of space- and time-dependent correlation functions after an interaction quench in the one-dimensional bose gas," *New Journal of Physics*, vol. 14, p. 075 006, 7 Jul. 2012, ISSN: 1367-2630. DOI: 10.1088/1367-2630/14/7/075006.

[142] M. Collura, S. Sotiriadis, and P. Calabrese, "Equilibration of a tonks-girardeau gas following a trap release," *Phys. Rev. Lett.*, vol. 110, p. 245 301, 24 Jun. 2013, ISSN: 0031-9007. DOI: 10.1103/PhysRevLett.110.245301.

[143] P. W. Anderson, "Absence of diffusion in certain random lattices," *Phys. Rev.*, vol. 109, pp. 1492–1505, 5 Mar. 1958, ISSN: 0031-899X. DOI: 10.1103/PhysRev.109.1492.

[144] F. Evers and A. D. Mirlin, "Anderson transitions," *Reviews of Modern Physics*, vol. 80, pp. 1355–1417, 4 Oct. 2008, ISSN: 0034-6861. DOI: 10.1103/RevModPhys.80.1355.

[145] B. I. Shklovskii, B. Shapiro, B. R. Sears, P. Lambrianides, and H. B. Shore, "Statistics of spectra of disordered systems near the metal-insulator transition," *Phys. Rev. B*, vol. 47, pp. 11 487–11 490, 17 May 1993, ISSN: 0163-1829. DOI: 10.1103/PhysRevB.47.11487.

[146] S. A. K. B. L. Altshuler I. Kh. Zharekeshev and B. I. Shklovskii, *Sov. Phys. Solid State*, vol. 31, p. 65, 1989.

[147] ——, "Repulsion between energy levels and the metal-insulator transition," *Sov. Phys. JETP*, vol. 67, p. 625, 1988.

[148] I. K. Zharekeshev and B. Kramer, "Scaling of level statistics at the disorder-induced metal-insulator transition," *Phys. Rev. B*, vol. 51, pp. 17 239–17 242, 23 Jun. 1995, ISSN: 0163-1829. DOI: 10.1103/PhysRevB.51.17239.

[149] E. Hofstetter and M. Schreiber, "Statistical properties of the eigenvalue spectrum of the three-dimensional anderson hamiltonian," *Phys. Rev. B*, vol. 48, pp. 16 979–16 985, 23 Dec. 1993, ISSN: 0163-1829. DOI: 10.1103/PhysRevB.48.16979.

[150] U. Sivan and Y. Imry, "Energy-level correlation function and ac conductivity of a finite disordered system," *Phys. Rev. B*, vol. 35, pp. 6074–6083, 12 Apr. 1987, ISSN: 0163-1829. DOI: 10.1103/PhysRevB.35.6074.

[151] S. N. Evangelou and E. N. Economou, "Spectral density singularities, level statistics, and localization in a sparse random matrix ensemble," *Phys. Rev. Lett.*, vol. 68, pp. 361–364, 3 Jan. 1992, ISSN: 0031-9007. DOI: 10.1103/PhysRevLett.68.361.

[152] S. N. Evangelou, "Level-spacing function p (s) at the mobility edge," *Phys. Rev. B*, vol. 49, pp. 16 805–16 808, 23 Jun. 1994, ISSN: 0163-1829. DOI: 10.1103/PhysRevB.49.16805.

[153] E. Hofstetter and M. Schreiber, "Relation between energy-level statistics and phase transition and its application to the anderson model," *Phys. Rev. B*, vol. 49, pp. 14 726–14 729, 20 May 1994, ISSN: 0163-1829. DOI: 10.1103/PhysRevB.49.14726.

[154] B. Kramer and A. MacKinnon, "Localization: Theory and experiment," *Reports on Progress in Physics*, vol. 56, pp. 1469–1564, 12 Dec. 1993, ISSN: 0034-4885. DOI: 10.1088/0034-4885/56/12/001.

[155] A. MacKinnon and B. Kramer, "The scaling theory of electrons in disordered solids: Additional numerical results," *Zeitschrift für Physik B Condensed Matter*, vol. 53, pp. 1–13, 1 Mar. 1983, ISSN: 0722-3277. DOI: 10.1007/BF01578242.

[156] A. M. García-García and E. Cuevas, "Dimensional dependence of the metal-insulator transition," *Phys. Rev. B*, vol. 75, p. 174 203, 17 May 2007, ISSN: 1098-0121. DOI: 10.1103/PhysRevB.75.174203.

[157] D. Vollhardt and P. Wölfle, "Scaling equations from a self-consistent theory of anderson localization," *Phys. Rev. Lett.*, vol. 48, pp. 699–702, 10 Mar. 1982, ISSN: 0031-9007. DOI: 10.1103/PhysRevLett.48.699.

[158] ——, "Anderson localization in $d <\sim$ 2dimensions: A self-consistent diagrammatic theory," *Phys. Rev. Lett.*, vol. 45, pp. 842–846, 10 Sep. 1980, ISSN: 0031-9007. DOI: 10.1103/PhysRevLett.45.842.

[159] I. K. Zharekeshev and B. Kramer, "Asymptotics of universal probability of neighboring level spacings at the anderson transition," *Phys. Rev. Lett.*, vol. 79, pp. 717–720, 4 Jul. 1997, ISSN: 0031-9007. DOI: 10.1103/PhysRevLett.79.717.

[160] E. B. Bogomolny, U. Gerland, and C. Schmit, "Models of intermediate spectral statistics," *Phys. Rev. E*, vol. 59, R1315–R1318, 2 Feb. 1999, ISSN: 1063-651X. DOI: 10.1103/PhysRevE.59.R1315.

[161] E. Bogomolny, U. Gerland, and C. Schmit, "Short-range plasma model for intermediate spectral statistics," *The European Physical Journal B*, vol. 19, pp. 121–132, 1 Jan. 2001, ISSN: 1434-6028. DOI: 10.1007/s100510170357.

[162] E. Bogomolny and C. Schmit, "Spectral statistics of a quantum interval-exchange map," *Phys. Rev. Lett.*, vol. 93, p. 254 102, 25 Dec. 2004, ISSN: 0031-9007. DOI: 10.1103/PhysRevLett.93.254102.

[163] H. Hernández-Saldaña, J. Flores, and T. H. Seligman, "Semi-poisson statistics and beyond," *Phys. Rev. E*, vol. 60, pp. 449–452, 1 Jul. 1999, ISSN: 1063-651X. DOI: 10.1103/PhysRevE.60.449.

[164] O. Giraud, J. Marklof, and S. O'Keefe, "Intermediate statistics in quantum maps," *Journal of Physics A: Mathematical and General*, vol. 37, pp. L303–L311, 28 Jul. 2004, ISSN: 0305-4470. DOI: 10.1088/0305-4470/37/28/L01.

[165] D. Wintgen and H. Marxer, "Level statistics of a quantized cantori system," *Phys. Rev. Lett.*, vol. 60, pp. 971–974, 11 Mar. 1988, ISSN: 0031-9007. DOI: 10.1103/PhysRevLett.60.971.

[166] R. Abou-Chacra, D. J. Thouless, and P. W. Anderson, "A selfconsistent theory of localization," *Journal of Physics C: Solid State Physics*, vol. 6, pp. 1734–1752, 10 May 1973, ISSN: 0022-3719. DOI: 10.1088/0022-3719/6/10/009.

[167] S. M. Girvin and M. Jonson, "Dynamical electron-phonon interaction and conductivity in strongly disordered metal alloys," *Phys. Rev. B*, vol. 22, pp. 3583–3597, 8 Oct. 1980, ISSN: 0163-1829. DOI: 10.1103/PhysRevB.22.3583.

[168] R. Abou-Chacra and D. J. Thouless, "Self-consistent theory of localization. ii. localization near the band edges," *Journal of Physics C: Solid State Physics*, vol. 7, pp. 65–75, 1 Jan. 1974, ISSN: 0022-3719. DOI: 10.1088/0022-3719/7/1/015.

[169] J. Fröhlich, F. Martinelli, E. Scoppola, and T. Spencer, "Constructive proof of localization in the anderson tight binding model," *Communications in Mathematical Physics*, vol. 101, pp. 21–46, 1 Mar. 1985, ISSN: 0010-3616. DOI: 10.1007/BF01212355.

[170] A. D. Mirlin and F. Evers, "Multifractality and critical fluctuations at the anderson transition," *Phys. Rev. B*, vol. 62, pp. 7920–7933, 12 Sep. 2000, ISSN: 0163-1829. DOI: 10.1103/PhysRevB.62.7920.

[171] M. Schreiber and H. Grussbach, "Multifractal wave functions at the anderson transition," *Phys. Rev. Lett.*, vol. 67, pp. 607–610, 5 Jul. 1991, ISSN: 0031-9007. DOI: 10.1103/PhysRevLett.67.607.

[172] K. S. Tikhonov, A. D. Mirlin, and M. A. Skvortsov, "Anderson localization and ergodicity on random regular graphs," *Phys. Rev. B*, vol. 94, p. 220 203, 22 Dec. 2016, ISSN: 2469-9950. DOI: 10.1103/PhysRevB.94.220203.

[173] M. Sade and R. Berkovits, "Localization transition on a cayley tree via spectral statistics," *Phys. Rev. B*, vol. 68, p. 193 102, 19 Nov. 2003, ISSN: 0163-1829. DOI: 10.1103/PhysRevB.68.193102.

[174] I. García-Mata, O. Giraud, B. Georgeot, J. Martin, R. Dubertrand, and G. Lemarié, "Scaling theory of the anderson transition in random graphs: Ergodicity and universality," *Phys. Rev. Lett.*, vol. 118, p. 166 801, 16 Apr. 2017, ISSN: 0031-9007. DOI: 10.1103/PhysRevLett.118.166801.

[175] M. Pino, "Scaling up the anderson transition in random-regular graphs," *Phys. Rev. Research*, vol. 2, p. 042 031, 4 Nov. 2020, ISSN: 2643-1564. DOI: 10.1103/PhysRevResearch.2.042031.

[176] K. S. Tikhonov and A. D. Mirlin, "Critical behavior at the localization transition on random regular graphs," *Phys. Rev. B*, vol. 99, p. 214 202, 21 Jun. 2019, ISSN: 2469-9950. DOI: 10.1103/PhysRevB.99.214202.

[177] M. Sade, T. Kalisky, S. Havlin, and R. Berkovits, "Localization transition on complex networks via spectral statistics," *Phys. Rev. E*, vol. 72, p. 066 123, 6 Dec. 2005, ISSN: 1539-3755. DOI: 10.1103/PhysRevE.72.066123.

[178] R. Nandkishore and D. A. Huse, "Many-body localization and thermalization in quantum statistical mechanics," *Annual Review of Condensed Matter Physics*, vol. 6, pp. 15–38, 1 Mar. 2015, ISSN: 1947-5454. DOI: 10.1146/annurev-conmatphys-031214-014726.

[179] F. Alet and N. Laflorencie, "Many-body localization: An introduction and selected topics," *Comptes Rendus Physique*, vol. 19, pp. 498–525, 6 Sep. 2018, ISSN: 16310705. DOI: 10.1016/j.crhy.2018.03.003.

[180] D. A. Abanin, E. Altman, I. Bloch, and M. Serbyn, "Colloquium: Many-body localization, thermalization, and entanglement," *Reviews of Modern Physics*, vol. 91, p. 021 001, 2 May 2019, ISSN: 0034-6861. DOI: 10.1103/RevModPhys.91.021001.

[181] D. J. Luitz and Y. B. Lev, "The ergodic side of the many-body localization transition," *Annalen der Physik*, vol. 529, p. 1 600 350, 7 Jul. 2017, ISSN: 0003-3804. DOI: 10.1002/andp.201600350.

[182] L. Fleishman and P. W. Anderson, "Interactions and the anderson transition," *Phys. Rev. B*, vol. 21, pp. 2366–2377, 6 Mar. 1980, ISSN: 0163-1829. DOI: 10.1103/PhysRevB.21.2366.

[183] L. Fleishman, D. C. Licciardello, and P. W. Anderson, "Elementary excitations in the fermi glass," *Phys. Rev. Lett.*, vol. 40, pp. 1340–1343, 20 May 1978, ISSN: 0031-9007. DOI: 10.1103/PhysRevLett.40.1340.

[184] B. L. Altshuler, Y. Gefen, A. Kamenev, and L. S. Levitov, "Quasiparticle lifetime in a finite system: A nonperturbative approach," *Phys. Rev. Lett.*, vol. 78, pp. 2803–2806, 14 Apr. 1997, ISSN: 0031-9007. DOI: 10.1103/PhysRevLett.78.2803.

[185] R. Berkovits and B. I. Shklovskii, "Statistics of energy spectra of a strongly disordered system of interacting electrons," *Journal of Physics: Condensed Matter*, vol. 11, pp. 779–786, 3 Jan. 1999, ISSN: 0953-8984. DOI: 10.1088/0953-8984/11/3/017.

[186] P. H. Song and D. L. Shepelyansky, "Low-energy transition in spectral statistics of two-dimensional interacting fermions," *Phys. Rev. B*, vol. 61, pp. 15 546–15 549, 23 Jun. 2000, ISSN: 0163-1829. DOI: 10.1103/PhysRevB.61.15546.

[187] B. Georgeot and D. L. Shepelyansky, "Quantum chaos border for quantum computing," *Phys. Rev. E*, vol. 62, pp. 3504–3507, 3 Sep. 2000, ISSN: 1063-651X. DOI: 10.1103/PhysRevE.62.3504.

[188] L. F. Santos, "Integrability of a disordered heisenberg spin-1/2 chain," *Journal of Physics A: Mathematical and General*, vol. 37, pp. 4723–4729, 17 Apr. 2004, ISSN: 0305-4470. DOI: 10.1088/0305-4470/37/17/004.

[189] L. F. Santos, G. Rigolin, and C. O. Escobar, "Entanglement versus chaos in disordered spin chains," *Phys. Rev. A*, vol. 69, p. 042 304, 4 Apr. 2004, ISSN: 1050-2947. DOI: 10.1103/PhysRevA.69.042304.

[190] L. F. Santos, M. I. Dykman, M. Shapiro, and F. M. Izrailev, "Strong many-particle localization and quantum computing with perpetually coupled qubits," *Phys. Rev. A*, vol. 71, p. 012 317, 1 Jan. 2005, ISSN: 1050-2947. DOI: 10.1103/PhysRevA.71.012317.

[191] D. Basko, I. Aleiner, and B. Altshuler, "Metal–insulator transition in a weakly interacting many-electron system with localized single-particle states," *Annals of Physics*, vol. 321, pp. 1126–1205, 5 May 2006, ISSN: 00034916. DOI: 10.1016/j.aop.2005.11.014.

[192] L. F. Santos, F. Pérez-Bernal, and E. J. Torres-Herrera, "Speck of chaos," *Phys. Rev. Research*, vol. 2, p. 043 034, 4 Oct. 2020, ISSN: 2643-1564. DOI: 10.1103/PhysRevResearch.2.043034.

[193] M. Takahashi, *Thermodynamics of One-Dimensional Solvable Models*, 1st. Cambridge University Press, 1999, ISBN: 978-0521551434.

[194] T. C. Berkelbach and D. R. Reichman, "Conductivity of disordered quantum lattice models at infinite temperature: Many-body localization," *Phys. Rev. B*, vol. 81, p. 224 429, 22 Jun. 2010, ISSN: 1098-0121. DOI: 10.1103/PhysRevB.81.224429.

[195] N. Y. Halpern, C. D. White, S. Gopalakrishnan, and G. Refael, "Quantum engine based on many-body localization," *Phys. Rev. B*, vol. 99, p. 024 203, 2 Jan. 2019, ISSN: 2469-9950. DOI: 10.1103/PhysRevB.99.024203.

[196] A. Maksymov, P. Sierant, and J. Zakrzewski, "Energy level dynamics across the many-body localization transition," *Phys. Rev. B*, vol. 99, p. 224 202, 22 Jun. 2019, ISSN: 2469-9950. DOI: 10.1103/PhysRevB.99.224202.

[197] S. Bera, H. Schomerus, F. Heidrich-Meisner, and J. H. Bardarson, "Many-body localization characterized from a one-particle perspective," *Phys. Rev. Lett.*, vol. 115, p. 046 603, 4 Jul. 2015, ISSN: 0031-9007. DOI: 10.1103/PhysRevLett.115.046603.

[198] T. Enss, F. Andraschko, and J. Sirker, "Many-body localization in infinite chains," *Phys. Rev. B*, vol. 95, p. 045 121, 4 Jan. 2017, ISSN: 2469-9950. DOI: 10.1103/PhysRevB.95.045121.

[199] L. Herviou, S. Bera, and J. H. Bardarson, "Multiscale entanglement clusters at the many-body localization phase transition," *Phys. Rev. B*, vol. 99, p. 134 205, 13 Apr. 2019, ISSN: 2469-9950. DOI: 10.1103/PhysRevB.99.134205.

[200] T. Chanda, P. Sierant, and J. Zakrzewski, "Many-body localization transition in large quantum spin chains: The mobility edge," *Phys. Rev. Research*, vol. 2, p. 032 045, 3 Aug. 2020, ISSN: 2643-1564. DOI: 10.1103/PhysRevResearch.2.032045.

[201] M. Serbyn and J. E. Moore, "Spectral statistics across the many-body localization transition," *Phys. Rev. B*, vol. 93, p. 041 424, 4 Jan. 2016, ISSN: 2469-9950. DOI: 10.1103/PhysRevB.93.041424.

[202] E. J. Torres-Herrera and L. F. Santos, "Extended nonergodic states in disordered many-body quantum systems," *Annalen der Physik*, vol. 529, p. 1 600 284, 7 Jul. 2017, ISSN: 0003-3804. DOI: 10.1002/andp.201600284.

[203] J. Šuntajs, J. Bonča, T. Prosen, and L. Vidmar, "Ergodicity breaking transition in finite disordered spin chains," *Phys. Rev. B*, vol. 102, p. 064 207, 6 Aug. 2020, ISSN: 2469-9950. DOI: 10.1103/PhysRevB.102.064207.

[204] V. Oganesyan and D. A. Huse, "Localization of interacting fermions at high temperature," *Phys. Rev. B*, vol. 75, p. 155 111, 15 Apr. 2007, ISSN: 1098-0121. DOI: 10.1103/PhysRevB.75.155111.

[205] P. Sierant, D. Delande, and J. Zakrzewski, "Thouless time analysis of anderson and many-body localization transitions," *Phys. Rev. Lett.*, vol. 124, p. 186 601, 18 May 2020, ISSN: 0031-9007. DOI: 10.1103/PhysRevLett.124.186601.

[206] R. K. Panda, A. Scardicchio, M. Schulz, S. R. Taylor, and M. Žnidarič, "Can we study the many-body localisation transition?" *EPL (Europhysics Letters)*, vol. 128, p. 67 003, 6 Feb. 2020, ISSN: 1286-4854. DOI: 10.1209/0295-5075/128/67003.

[207] J. Šuntajs, J. Bonča, T. Prosen, and L. Vidmar, "Quantum chaos challenges many-body localization," *Phys. Rev. E*, vol. 102, p. 062 144, 6 Dec. 2020, ISSN: 2470-0045. DOI: 10.1103/PhysRevE.102.062144.

[208] D. Abanin, J. Bardarson, G. D. Tomasi, S. Gopalakrishnan, V. Khemani, S. Parameswaran, F. Pollmann, A. Potter, M. Serbyn, and R. Vasseur, "Distinguishing localization from chaos: Challenges in finite-size systems," *Annals of Physics*, vol. 427, p. 168 415, Apr. 2021, ISSN: 00034916. DOI: 10.1016/j.aop.2021.168415.

[209] V. K. B. Kota and N. D. Chavda, "Embedded random matrix ensembles from nuclear structure and their recent applications," *International Journal of Modern Physics E*, vol. 27, p. 1 830 001, 01 Jan. 2018, ISSN: 0218-3013. DOI: 10.1142/S0218301318300011.

[210] U. T. Bhosale, S. H. Tekur, and M. S. Santhanam, "Scaling in the eigenvalue fluctuations of correlation matrices," *Phys. Rev. E*, vol. 98, p. 052 133, 5 Nov. 2018, ISSN: 2470-0045. DOI: 10.1103/PhysRevE.98.052133.

[211] S. H. Tekur, U. T. Bhosale, and M. S. Santhanam, "Higher-order spacing ratios in random matrix theory and complex quantum systems," *Phys. Rev. B*, vol. 98, p. 104 305, 10 Sep. 2018, ISSN: 2469-9950. DOI: 10.1103/PhysRevB.98.104305.

[212] P. Sierant and J. Zakrzewski, "Model of level statistics for disordered interacting quantum many-body systems," *Phys. Rev. B*, vol. 101, p. 104 201, 10 Mar. 2020, ISSN: 2469-9950. DOI: 10.1103/PhysRevB.101.104201.

[213] Y. Y. Atas, E. Bogomolny, O. Giraud, and G. Roux, "Distribution of the ratio of consecutive level spacings in random matrix ensembles," *Phys. Rev. Lett.*, vol. 110, p. 084 101, 8 Feb. 2013, ISSN: 0031-9007. DOI: 10.1103/PhysRevLett.110.084101.

[214] Y. Y. Atas, E. Bogomolny, O. Giraud, P. Vivo, and E. Vivo, "Joint probability densities of level spacing ratios in random matrices," *Journal of Physics A: Mathematical and Theoretical*, vol. 46, p. 355 204, 35 Sep. 2013, ISSN: 1751-8113. DOI: 10.1088/1751-8113/46/35/355204.

[215] A. Sarkar, M. Kothiyal, and S. Kumar, "Distribution of the ratio of two consecutive level spacings in orthogonal to unitary crossover ensembles," *Phys. Rev. E*, vol. 101, p. 012 216, 1 Jan. 2020, ISSN: 2470-0045. DOI: 10.1103/PhysRevE.101.012216.

[216] N. Chavda, H. Deota, and V. Kota, "Poisson to goe transition in the distribution of the ratio of consecutive level spacings," *Physics Letters A*, vol. 378, pp. 3012–3017, 41 Aug. 2014, ISSN: 03759601. DOI: 10.1016/j.physleta.2014.08.021.

[217] N. Chavda and V. Kota, "Probability distribution of the ratio of consecutive level spacings in interacting particle systems," *Physics Letters A*, vol. 377, pp. 3009–3015, 42 Dec. 2013, ISSN: 03759601. DOI: 10.1016/j.physleta.2013.09.013.

[218] Á. L. Corps and A. Relaño, "Distribution of the ratio of consecutive level spacings for different symmetries and degrees of chaos," *Phys. Rev. E*, vol. 101, p. 022 222, 2 Feb. 2020, ISSN: 2470-0045. DOI: 10.1103/PhysRevE.101.022222.

[219] D. J. Luitz, N. Laflorencie, and F. Alet, "Many-body localization edge in the random-field heisenberg chain," *Phys. Rev. B*, vol. 91, p. 081 103, 8 Feb. 2015, ISSN: 1098-0121. DOI: 10.1103/PhysRevB.91.081103.

[220] I. Mondragon-Shem, A. Pal, T. L. Hughes, and C. R. Laumann, "Many-body mobility edge due to symmetry-constrained dynamics and strong interactions," *Phys. Rev. B*, vol. 92, p. 064 203, 6 Aug. 2015, ISSN: 1098-0121. DOI: 10.1103/PhysRevB.92.064203.

[221] J. A. Kjäll, J. H. Bardarson, and F. Pollmann, "Many-body localization in a disordered quantum ising chain," *Phys. Rev. Lett.*, vol. 113, p. 107 204, 10 Sep. 2014, ISSN: 0031-9007. DOI: 10.1103/PhysRevLett.113.107204.

[222] W. D. Roeck, F. Huveneers, M. Müller, and M. Schiulaz, "Absence of many-body mobility edges," *Phys. Rev. B*, vol. 93, p. 014 203, 1 Jan. 2016, ISSN: 2469-9950. DOI: 10.1103/PhysRevB.93.014203.

[223] P. Sierant and J. Zakrzewski, "Level statistics across the many-body localization transition," *Phys. Rev. B*, vol. 99, p. 104 205, 10 Mar. 2019, ISSN: 2469-9950. DOI: 10.1103/PhysRevB.99.104205.

[224] W. Buijsman, V. Cheianov, and V. Gritsev, "Random matrix ensemble for the level statistics of many-body localization," *Phys. Rev. Lett.*, vol. 122, p. 180 601, 18 May 2019, ISSN: 0031-9007. DOI: 10.1103/PhysRevLett.122.180601.

[225] B. Bauer and C. Nayak, "Area laws in a many-body localized state and its implications for topological order," *Journal of Statistical Mechanics: Theory and Experiment*, vol. 2013, P09005, 09 Sep. 2013, ISSN: 1742-5468. DOI: 10.1088/1742-5468/2013/09/P09005.

[226] J. A. Kjäll, J. H. Bardarson, and F. Pollmann, "Many-body localization in a disordered quantum ising chain," *Phys. Rev. Lett.*, vol. 113, p. 107 204, 10 Sep. 2014, ISSN: 0031-9007. DOI: 10.1103/PhysRevLett.113.107204.

[227] T. Devakul and R. R. P. Singh, "Early breakdown of area-law entanglement at the many-body delocalization transition," *Phys. Rev. Lett.*, vol. 115, p. 187 201, 18 Oct. 2015, ISSN: 0031-9007. DOI: 10.1103/PhysRevLett.115.187201.

[228] S. Ghosh, A. Acharya, S. Sahu, and S. Mukerjee, "Many-body localization due to correlated disorder in fock space," *Phys. Rev. B*, vol. 99, p. 165 131, 16 Apr. 2019, ISSN: 2469-9950. DOI: 10.1103/PhysRevB.99.165131.

[229] D. J. Luitz, "Long tail distributions near the many-body localization transition," *Phys. Rev. B*, vol. 93, p. 134 201, 13 Apr. 2016, ISSN: 2469-9950. DOI: 10.1103/PhysRevB.93.134201.

[230] A. Morningstar, D. A. Huse, and J. Z. Imbrie, "Many-body localization near the critical point," *Phys. Rev. B*, vol. 102, p. 125 134, 12 Sep. 2020, ISSN: 2469-9950. DOI: 10.1103/PhysRevB.102.125134.

[231] A. Morningstar and D. A. Huse, "Renormalization-group study of the many-body localization transition in one dimension," *Phys. Rev. B*, vol. 99, p. 224 205, 22 Jun. 2019, ISSN: 2469-9950. DOI: 10.1103/PhysRevB.99.224205.

[232] A. Goremykina, R. Vasseur, and M. Serbyn, "Analytically solvable renormalization group for the many-body localization transition," *Phys. Rev. Lett.*, vol. 122, p. 040 601, 4 Jan. 2019, ISSN: 0031-9007. DOI: 10.1103/PhysRevLett.122.040601.

[233] P. T. Dumitrescu, A. Goremykina, S. A. Parameswaran, M. Serbyn, and R. Vasseur, "Kosterlitz-thouless scaling at many-body localization phase transitions," *Phys. Rev. B*, vol. 99, p. 094 205, 9 Mar. 2019, ISSN: 2469-9950. DOI: 10.1103/PhysRevB.99.094205.

[234] J. Z. Imbrie, "On many-body localization for quantum spin chains," *Journal of Statistical Physics*, vol. 163, pp. 998–1048, 5 Jun. 2016, ISSN: 0022-4715. DOI: 10.1007/s10955-016-1508-x.

[235] ——, "Diagonalization and many-body localization for a disordered quantum spin chain," *Phys. Rev. Lett.*, vol. 117, p. 027 201, 2 Jul. 2016, ISSN: 0031-9007. DOI: 10.1103/PhysRevLett.117.027201.

[236] Á. L. Corps, R. A. Molina, and A. Relaño, "Thouless energy challenges thermalization on the ergodic side of the many-body localization transition," *Phys. Rev. B*, vol. 102, p. 014 201, 1 Jul. 2020, ISSN: 2469-9950. DOI: 10.1103/PhysRevB.102.014201.

[237] Á. L. Corps, R. Molina, and A. Relaño, "Signatures of a critical point in the many-body localization transition," *SciPost Physics*, vol. 10, p. 107, 5 May 2021, ISSN: 2542-4653. DOI: 10.21468/SciPostPhys.10.5.107.

[238] N. Macé, F. Alet, and N. Laflorencie, "Multifractal scalings across the many-body localization transition," *Phys. Rev. Lett.*, vol. 123, p. 180 601, 18 Oct. 2019, ISSN: 0031-9007. DOI: 10.1103/PhysRevLett.123.180601.

[239] M. Filippone, P. W. Brouwer, J. Eisert, and F. von Oppen, "Drude weight fluctuations in many-body localized systems," *Phys. Rev. B*, vol. 94, p. 201 112, 20 Nov. 2016, ISSN: 2469-9950. DOI: 10.1103/PhysRevB.94.201112.

[240] D. J. Luitz, I. Khaymovich, and Y. B. Lev, "Multifractality and its role in anomalous transport in the disordered xxz spin-chain," *SciPost Physics Core*, vol. 2, p. 006, 2 Apr. 2020, ISSN: 2666-9366. DOI: 10.21468/SciPostPhysCore.2.2.006.

[241] R. B. Griffiths, "Nonanalytic behavior above the critical point in a random ising ferromagnet," *Phys. Rev. Lett.*, vol. 23, pp. 17–19, 1 Jul. 1969, ISSN: 0031-9007. DOI: 10.1103/PhysRevLett.23.17.

[242] H. P. Lüschen, P. Bordia, S. Scherg, F. Alet, E. Altman, U. Schneider, and I. Bloch, "Observation of slow dynamics near the many-body localization transition in one-dimensional quasiperiodic systems," *Phys. Rev. Lett.*, vol. 119, p. 260 401, 26 Dec. 2017, ISSN: 0031-9007. DOI: 10.1103/PhysRevLett.119.260401.

[243] K. Agarwal, S. Gopalakrishnan, M. Knap, M. Müller, and E. Demler, "Anomalous diffusion and griffiths effects near the many-body localization transition," *Phys. Rev. Lett.*, vol. 114, p. 160 401, 16 Apr. 2015, ISSN: 0031-9007. DOI: 10.1103/PhysRevLett.114.160401.

[244] S. Gopalakrishnan, K. Agarwal, E. A. Demler, D. A. Huse, and M. Knap, "Griffiths effects and slow dynamics in nearly many-body localized systems," *Phys. Rev. B*, vol. 93, p. 134 206, 13 Apr. 2016, ISSN: 2469-9950. DOI: 10.1103/PhysRevB.93.134206.

[245] F. Weiner, F. Evers, and S. Bera, "Slow dynamics and strong finite-size effects in many-body localization with random and quasiperiodic potentials," *Phys. Rev. B*, vol. 100, p. 104 204, 10 Sep. 2019, ISSN: 2469-9950. DOI: 10.1103/PhysRevB.100.104204.

[246] V. E. Kravtsov, I. V. Lerner, B. L. Altshuler, and A. G. Aronov, "Universal spectral correlations at the mobility edge," *Phys. Rev. Lett.*, vol. 72, pp. 888–891, 6 Feb. 1994, ISSN: 0031-9007. DOI: 10.1103/PhysRevLett.72.888.

[247] P. Shukla, "Localization to ergodic transitions: Is rosenzweig–porter ensemble the hidden skeleton?" *New Journal of Physics*, vol. 18, p. 021 004, 2 Feb. 2016, ISSN: 1367-2630. DOI: 10.1088/1367-2630/18/2/021004.

[248] V. E. Kravtsov, I. M. Khaymovich, E. Cuevas, and M. Amini, "A random matrix model with localization and ergodic transitions," *New Journal of Physics*, vol. 17, p. 122 002, 12 Dec. 2015, ISSN: 1367-2630. DOI: 10.1088/1367-2630/17/12/122002.

[249] V. Ros, M. Müller, and A. Scardicchio, "Integrals of motion in the many-body localized phase," *Nuclear Physics B*, vol. 891, pp. 420–465, Feb. 2015, ISSN: 05503213. DOI: 10.1016/j.nuclphysb.2014.12.014.

[250] S. J. Thomson and M. Schiró, "Time evolution of many-body localized systems with the flow equation approach," *Phys. Rev. B*, vol. 97, p. 060 201, 6 Feb. 2018, ISSN: 2469-9950. DOI: 10.1103/PhysRevB.97.060201.

[251] D. Pekker, B. K. Clark, V. Oganesyan, and G. Refael, "Fixed points of wegner-wilson flows and many-body localization," *Phys. Rev. Lett.*, vol. 119, p. 075 701, 7 Aug. 2017, ISSN: 0031-9007. DOI: 10.1103/PhysRevLett.119.075701.

[252] L. Rademaker and M. Ortuño, "Explicit local integrals of motion for the many-body localized state," *Phys. Rev. Lett.*, vol. 116, p. 010 404, 1 Jan. 2016, ISSN: 0031-9007. DOI: 10.1103/PhysRevLett.116.010404.

[253] A. Chandran, I. H. Kim, G. Vidal, and D. A. Abanin, "Constructing local integrals of motion in the many-body localized phase," *Phys. Rev. B*, vol. 91, p. 085 425, 8 Feb. 2015, ISSN: 1098-0121. DOI: 10.1103/PhysRevB.91.085425.

[254] T. E. O'Brien, D. A. Abanin, G. Vidal, and Z. Papić, "Explicit construction of local conserved operators in disordered many-body systems," *Phys. Rev. B*, vol. 94, p. 144 208, 14 Oct. 2016, ISSN: 2469-9950. DOI: 10.1103/PhysRevB.94.144208.

[255] M. Schreiber, S. S. Hodgman, P. Bordia, H. P. Lüschen, M. H. Fischer, R. Vosk, E. Altman, U. Schneider, and I. Bloch, "Observation of many-body localization of interacting fermions in a quasirandom optical lattice," *Science*, vol. 349, pp. 842–845, 6250 Aug. 2015, ISSN: 0036-8075. DOI: 10.1126/science.aaa7432.

[256] P. Bordia, H. P. Lüschen, S. S. Hodgman, M. Schreiber, I. Bloch, and U. Schneider, "Coupling identical one-dimensional many-body localized systems," *Phys. Rev. Lett.*, vol. 116, p. 140 401, 14 Apr. 2016, ISSN: 0031-9007. DOI: 10.1103/PhysRevLett.116.140401.

[257] A. Lukin, M. Rispoli, R. Schittko, M. E. Tai, A. M. Kaufman, S. Choi, V. Khemani, J. Léonard, and M. Greiner, "Probing entanglement in a many-body–localized system," *Science*, vol. 364, pp. 256–260, 6437 Apr. 2019, ISSN: 0036-8075. DOI: 10.1126/science.aau0818.

[258] J.-y. Choi, S. Hild, J. Zeiher, P. Schauß, A. Rubio-Abadal, T. Yefsah, V. Khemani, D. A. Huse, I. Bloch, and C. Gross, "Exploring the many-body localization transition in two dimensions," *Science*, vol. 352, pp. 1547–1552, 6293 Jun. 2016, ISSN: 0036-8075. DOI: 10.1126/science.aaf8834.

[259] J. Smith, A. Lee, P. Richerme, B. Neyenhuis, P. W. Hess, P. Hauke, M. Heyl, D. A. Huse, and C. Monroe, "Many-body localization in a quantum simulator with programmable random disorder," *Nature Physics*, vol. 12, pp. 907–911, 10 Oct. 2016, ISSN: 1745-2473. DOI: 10.1038/nphys3783.

[260] P. Roushan, C. Neill, J. Tangpanitanon, V. M. Bastidas, A. Megrant, R. Barends, Y. Chen, Z. Chen, B. Chiaro, A. Dunsworth, A. Fowler, B. Foxen, M. Giustina, E. Jeffrey, J. Kelly, E. Lucero, J. Mutus, M. Neeley, C. Quintana, D. Sank, A. Vainsencher, J. Wenner, T. White, H. Neven, D. G. Angelakis, and J. Martinis, "Spectroscopic signatures of localization with interacting photons in superconducting qubits," *Science*, vol. 358, pp. 1175–1179, 6367 Dec. 2017, ISSN: 0036-8075. DOI: 10.1126/science.aao1401.

[261] M. F. L'Annunziata, "Radioactivity hall of fame-part i," in. Elsevier, 2007, pp. 47–70. DOI: 10.1016/B978-0-444-52715-8.50031-1.

[262] P. W. Anderson, "More is different," *Science*, vol. 177, pp. 393–396, 4047 Aug. 1972, ISSN: 0036-8075. DOI: 10.1126/science.177.4047.393.

[263] M. Vojta, "Quantum phase transitions," *Reports on Progress in Physics*, vol. 66, pp. 2069–2110, 12 Dec. 2003, ISSN: 0034-4885. DOI: 10.1088/0034-4885/66/12/R01.

[264] M. Caprio, P. Cejnar, and F. Iachello, "Excited state quantum phase transitions in many-body systems," *Annals of Physics*, vol. 323, pp. 1106–1135, 5 May 2008, ISSN: 00034916. DOI: 10.1016/j.aop.2007.06.011.

[265] P. Cejnar, P. Stránský, M. Macek, and M. Kloc, "Excited-state quantum phase transitions," *Journal of Physics A: Mathematical and Theoretical*, vol. 54, p. 133 001, 13 Apr. 2021, ISSN: 1751-8113. DOI: 10.1088/1751-8121/abdfe8.

[266] J. Marino, M. Eckstein, M. S. Foster, and A. M. Rey, "Dynamical phase transitions in the collisionless pre-thermal states of isolated quantum systems: Theory and experiments," *Reports on Progress in Physics*, vol. 85, p. 116 001, 11 Nov. 2022, ISSN: 0034-4885. DOI: 10.1088/1361-6633/ac906c.

[267] M. Heyl, "Dynamical quantum phase transitions: A review," *Reports on Progress in Physics*, vol. 81, p. 054 001, 5 May 2018, ISSN: 0034-4885. DOI: 10.1088/1361-6633/aaaf9a.

[268] ——, "Dynamical quantum phase transitions: A brief survey," *EPL (Europhysics Letters)*, vol. 125, p. 26 001, 2 Feb. 2019, ISSN: 1286-4854. DOI: 10.1209/0295-5075/125/26001.

[269] R. Palmer, "Broken ergodicity," *Advances in Physics*, vol. 31, no. 6, pp. 669–735, 1982. DOI: 10.1080/00018738200101438.

[270] R. K. Pathria and P. D. Beale, *Statistical Mechanics*, 3rd. Elsevier, 2011.

[271] R. G. Bartle and D. R. Sherbert, *Introduction to real analysis*. Wiley, 2011, ISBN: 978-0471433316.

[272] C. N. Yang and T. D. Lee, "Statistical theory of equations of state and phase transitions. i. theory of condensation," *Phys. Rev.*, vol. 87, pp. 404–409, 3 Aug. 1952, ISSN: 0031-899X. DOI: 10.1103/PhysRev.87.404.

[273] T. D. Lee and C. N. Yang, "Statistical theory of equations of state and phase transitions. ii. lattice gas and ising model," *Phys. Rev.*, vol. 87, pp. 410–419, 3 Aug. 1952, ISSN: 0031-899X. DOI: 10.1103/PhysRev.87.410.

[274] S. Grossmann and W. Rosenhauer, "Phase transitions and the distribution of temperature zeros of the partition function," *Zeitschrift für Physik A Hadrons and nuclei*, vol. 218, pp. 437–448, 5 Oct. 1969, ISSN: 0939-7922. DOI: 10.1007/BF01392423.

[275] C. Itzykson, R. Pearson, and J. Zuber, "Distribution of zeros in ising and gauge models," *Nuclear Physics B*, vol. 220, pp. 415–433, 4 Sep. 1983, ISSN: 05503213. DOI: 10.1016/0550-3213(83)90499-6.

[276] B. Derrida, "The zeroes of the partition function of the random energy model," *Physica A: Statistical Mechanics and its Applications*, vol. 177, pp. 31–37, 1-3 Sep. 1991, ISSN: 03784371. DOI: 10.1016/0378-4371(91)90130-5.

[277] P. Borrmann, O. Mülken, and J. Harting, "Classification of phase transitions in small systems," *Phys. Rev. Lett.*, vol. 84, pp. 3511–3514, 16 Apr. 2000, ISSN: 0031-9007. DOI: 10.1103/PhysRevLett.84.3511.

[278] B.-B. Wei, S.-W. Chen, H.-C. Po, and R.-B. Liu, "Phase transitions in the complex plane of physical parameters," *Scientific Reports*, vol. 4, p. 5202, 1 Jun. 2014, ISSN: 2045-2322. DOI: 10.1038/srep05202.

[279] K. Brandner, V. F. Maisi, J. P. Pekola, J. P. Garrahan, and C. Flindt, "Experimental determination of dynamical lee-yang zeros," *Phys. Rev. Lett.*, vol. 118, p. 180 601, 18 May 2017, ISSN: 0031-9007. DOI: 10.1103/PhysRevLett.118.180601.

[280] X. Peng, H. Zhou, B.-B. Wei, J. Cui, J. Du, and R.-B. Liu, "Experimental observation of lee-yang zeros," *Phys. Rev. Lett.*, vol. 114, p. 010 601, 1 Jan. 2015, ISSN: 0031-9007. DOI: 10.1103/PhysRevLett.114.010601.

[281] G. Jaeger, "The ehrenfest classification of phase transitions: Introduction and evolution," *Archive for History of Exact Sciences*, vol. 53, pp. 51–81, 1 May 1998, ISSN: 0003-9519. DOI: 10.1007/s004070050021.

[282] J. M. Kosterlitz and D. J. Thouless, "Ordering, metastability and phase transitions in two-dimensional systems," *Journal of Physics C: Solid State Physics*, vol. 6, pp. 1181–1203, 7 Apr. 1973, ISSN: 0022-3719. DOI: 10.1088/0022-3719/6/7/010.

[283] L. Onsager, "Crystal statistics. i. a two-dimensional model with an order-disorder transition," *Phys. Rev.*, vol. 65, pp. 117–149, 3-4 Feb. 1944, ISSN: 0031-899X. DOI: 10.1103/PhysRev.65.117.

[284] M. E. Fisher, "The renormalization group in the theory of critical behavior," *Reviews of Modern Physics*, vol. 46, pp. 597–616, 4 Oct. 1974, ISSN: 0034-6861. DOI: 10.1103/RevModPhys.46.597.

[285] E. Stanley, *Introduction to Phase Transitions and Critical Phenomena*. Oxford University Press, 1993, ISBN: 978-0195014587.

[286] J. R. Cary and P. Rusu, "Separatrix eigenfunctions," *Phys. Rev. A*, vol. 45, pp. 8501–8512, 12 Jun. 1992, ISSN: 1050-2947. DOI: 10.1103/PhysRevA.45.8501.

[287] ——, "Quantum dynamics near a classical separatrix," *Phys. Rev. A*, vol. 47, pp. 2496–2505, 4 Apr. 1993, ISSN: 1050-2947. DOI: 10.1103/PhysRevA.47.2496.

[288] M. Reis, M. T. Cunha, A. C. Oliveira, and M. Nemes, "Relation between quantum phase transitions and classical instability points in the pairing model," *Physics Letters A*, vol. 344, pp. 164–169, 2-4 Sep. 2005, ISSN: 03759601. DOI: 10.1016/j.physleta.2005.06.064.

[289] W. Zhang, D. L. Zhou, M.-S. Chang, M. S. Chapman, and L. You, "Coherent spin mixing dynamics in a spin-1 atomic condensate," *Phys. Rev. A*, vol. 72, p. 013 602, 1 Jul. 2005, ISSN: 1050-2947. DOI: 10.1103/PhysRevA.72.013602.

[290] F. Leyvraz and W. D. Heiss, "Large-N scaling behavior of the Lipkin-Meshkov-Glick model," *Phys. Rev. Lett.*, vol. 95, p. 050 402, 5 Jul. 2005, ISSN: 0031-9007. DOI: 10.1103/PhysRevLett.95.050402.

[291] P. Cejnar, M. Macek, S. Heinze, J. Jolie, and J. Dobeš, "Monodromy and excited-state quantum phase transitions in integrable systems: Collective vibrations of nuclei," *Journal of Physics A: Mathematical and General*, vol. 39, pp. L515–L521, 31 Aug. 2006, ISSN: 0305-4470. DOI: 10.1088/0305-4470/39/31/L01.

[292] S. Heinze, P. Cejnar, J. Jolie, and M. Macek, "Evolution of spectral properties along the o(6)-u(5) transition in the interacting boson model. i. level dynamics," *Phys. Rev. C*, vol. 73, p. 014 306, 1 Jan. 2006, ISSN: 0556-2813. DOI: 10.1103/PhysRevC.73.014306.

[293] M. Macek, P. Cejnar, J. Jolie, and S. Heinze, "Evolution of spectral properties along the o(6)-u(5) transition in the interacting boson model. ii. classical trajectories," *Phys. Rev. C*, vol. 73, p. 014 307, 1 Jan. 2006, ISSN: 0556-2813. DOI: 10.1103/PhysRevC.73.014307.

[294] P. Stránský, M. Macek, and P. Cejnar, "Excited-state quantum phase transitions in systems with two degrees of freedom: Level density, level dynamics, thermal properties," *Annals of Physics*, vol. 345, pp. 73–97, Jun. 2014, ISSN: 00034916. DOI: 10.1016/j.aop.2014.03.006.

[295] P. Stránský, M. Macek, A. Leviatan, and P. Cejnar, "Excited-state quantum phase transitions in systems with two degrees of freedom: II. finite-size effects," *Annals of Physics*, vol. 356, pp. 57–82, May 2015, ISSN: 00034916. DOI: 10.1016/j.aop.2015.02.025.

[296] P. Stránský and P. Cejnar, "Classification of excited-state quantum phase transitions for arbitrary number of degrees of freedom," *Physics Letters A*, vol. 380, pp. 2637–2643, 34 Aug. 2016, ISSN: 03759601. DOI: 10.1016/j.physleta.2016.06.031.

[297] P. Pérez-Fernández and A. Relaño, "From thermal to excited-state quantum phase transition: The dicke model," *Phys. Rev. E*, vol. 96, p. 012 121, 1 Jul. 2017, ISSN: 2470-0045. DOI: 10.1103/PhysRevE.96.012121.

[298] M. A. Bastarrachea-Magnani, S. Lerma-Hernández, and J. G. Hirsch, "Thermal and quantum phase transitions in atom-field systems: A microcanonical analysis," *Journal of Statistical Mechanics: Theory and Experiment*, vol. 2016, p. 093 105, 9 Sep. 2016, ISSN: 1742-5468. DOI: 10.1088/1742-5468/2016/09/093105.

[299] P. Cejnar and P. Stránský, "Heat capacity for systems with excited-state quantum phase transitions," *Physics Letters A*, vol. 381, pp. 984–990, 11 Mar. 2017, ISSN: 03759601. DOI: 10.1016/j.physleta.2017.01.022.

[300] A. Relaño, "Anomalous thermalization in quantum collective models," *Phys. Rev. Lett.*, vol. 121, p. 030 602, 3 Jul. 2018, ISSN: 0031-9007. DOI: 10.1103/PhysRevLett.121.030602.

[301] P. Cejnar and P. Stránský, "Impact of quantum phase transitions on excited-level dynamics," *Phys. Rev. E*, vol. 78, p. 031 130, 3 Sep. 2008, ISSN: 1539-3755. DOI: 10.1103/PhysRevE.78.031130.

[302] A. Peres, "New conserved quantities and test for regular spectra," *Phys. Rev. Lett.*, vol. 53, pp. 1711–1713, 18 Oct. 1984, ISSN: 0031-9007. DOI: 10.1103/PhysRevLett.53.1711.

[303] A. Relaño, C. Esebbag, and J. Dukelsky, "Excited-state quantum phase transitions in the two-spin elliptic gaudin model," *Phys. Rev. E*, vol. 94, p. 052 110, 5 Nov. 2016, ISSN: 2470-0045. DOI: 10.1103/PhysRevE.94.052110.

[304] P. Stránský, P. Cejnar, and R. Filip, "Stabilization of product states and excited-state quantum phase transitions in a coupled qubit-field system," *Phys. Rev. A*, vol. 104, p. 053 722, 5 Nov. 2021, ISSN: 2469-9926. DOI: 10.1103/PhysRevA.104.053722.

[305] M. A. Bastarrachea-Magnani, S. Lerma-Hernández, and J. G. Hirsch, "Comparative quantum and semiclassical analysis of atom-field systems. i. density of states and excited-state quantum phase transitions," *Phys. Rev. A*, vol. 89, p. 032 101, 3 Mar. 2014, ISSN: 1050-2947. DOI: 10.1103/PhysRevA.89.032101.

[306] J. Chávez-Carlos, M. A. Bastarrachea-Magnani, S. Lerma-Hernández, and J. G. Hirsch, "Classical chaos in atom-field systems," *Phys. Rev. E*, vol. 94, p. 022 209, 2 Aug. 2016, ISSN: 2470-0045. DOI: 10.1103/PhysRevE.94.022209.

[307] M. A. Bastarrachea-Magnani, B. López-del-Carpio, J. Chávez-Carlos, S. Lerma-Hernández, and J. G. Hirsch, "Regularity and chaos in cavity qed," *Physica Scripta*, vol. 92, p. 054 003, 5 May 2017, ISSN: 0031-8949. DOI: 10.1088/1402-4896/aa6640.

[308] C. Emary and T. Brandes, "Quantum chaos triggered by precursors of a quantum phase transition: The dicke model," *Phys. Rev. Lett.*, vol. 90, p. 044 101, 4 Jan. 2003, ISSN: 0031-9007. DOI: 10.1103/PhysRevLett.90.044101.

[309] C. M. Lóbez and A. Relaño, "Entropy, chaos, and excited-state quantum phase transitions in the dicke model," *Phys. Rev. E*, vol. 94, p. 012 140, 1 Jul. 2016, ISSN: 2470-0045. DOI: 10.1103/PhysRevE.94.012140.

[310] I. García-Mata, E. Vergini, and D. A. Wisniacki, "Impact of chaos on precursors of quantum criticality," *Phys. Rev. E*, vol. 104, p. L062202, 6 Dec. 2021, ISSN: 2470-0045. DOI: 10.1103/PhysRevE.104.L062202.

[311] D. Larese and F. Iachello, "A study of quantum phase transitions and quantum monodromy in the bending motion of non-rigid molecules," *Journal of Molecular Structure*, vol. 1006, pp. 611–628, 1-3 Dec. 2011, ISSN: 00222860. DOI: 10.1016/j.molstruc.2011.10.016.

[312] T. Brandes, "Excited-state quantum phase transitions in dicke superradiance models," *Phys. Rev. E*, vol. 88, p. 032 133, 3 Sep. 2013, ISSN: 1539-3755. DOI: 10.1103/PhysRevE.88.032133.

[313] R. Puebla and A. Relaño, "Non-thermal excited-state quantum phase transitions," *EPL (Europhysics Letters)*, vol. 104, p. 50 007, 5 Dec. 2013, ISSN: 0295-5075. DOI: 10.1209/0295-5075/104/50007.

[314] R. Puebla, M.-J. Hwang, and M. B. Plenio, "Excited-state quantum phase transition in the rabi model," *Phys. Rev. A*, vol. 94, p. 023 835, 2 Aug. 2016, ISSN: 2469-9926. DOI: 10.1103/PhysRevA.94.023835.

[315] M. A. Bastarrachea-Magnani, A. Relaño, S. Lerma-Hernández, B. López-del-Carpio, J. Chávez-Carlos, and J. G. Hirsch, "Adiabatic invariants for the regular region of the dicke model," *Journal of Physics A: Mathematical and Theoretical*, vol. 50, p. 144 002, 14 Apr. 2017, ISSN: 1751-8113. DOI: 10.1088/1751-8121/aa6162.

[316] M. Kloc, P. Stránský, and P. Cejnar, "Monodromy in dicke superradiance," *Journal of Physics A: Mathematical and Theoretical*, vol. 50, p. 315 205, 31 Aug. 2017, ISSN: 1751-8113. DOI: 10.1088/1751-8121/aa7a95.

[317] L. F. Santos, M. Távora, and F. Pérez-Bernal, "Excited-state quantum phase transitions in many-body systems with infinite-range interaction: Localization, dynamics, and bifurcation," *Phys. Rev. A*, vol. 94, p. 012 113, 1 Jul. 2016, ISSN: 2469-9926. DOI: 10.1103/PhysRevA.94.012113.

[318] M. Macek and A. Leviatan, "First-order quantum phase transitions: Test ground for emergent chaoticity, regularity and persisting symmetries," *Annals of Physics*, vol. 351, pp. 302–362, Dec. 2014, ISSN: 00034916. DOI: 10.1016/j.aop.2014.08.019.

[319] G. Engelhardt, V. M. Bastidas, W. Kopylov, and T. Brandes, "Excited-state quantum phase transitions and periodic dynamics," *Phys. Rev. A*, vol. 91, p. 013 631, 1 Jan. 2015, ISSN: 1050-2947. DOI: 10.1103/PhysRevA.91.013631.

[320] A. Relaño, "Chaos-assisted tunneling and $1/f^{\alpha}$ spectral fluctuations in the order-chaos transition," *Phys. Rev. Lett.*, vol. 100, p. 224 101, 22 Jun. 2008, ISSN: 0031-9007. DOI: 10.1103/PhysRevLett.100.224101.

[321] P. Pérez-Fernández, A. Relaño, J. M. Arias, J. Dukelsky, and J. E. García-Ramos, "Decoherence due to an excited-state quantum phase transition in a two-level boson model," *Phys. Rev. A*, vol. 80, p. 032 111, 3 Sep. 2009, ISSN: 1050-2947. DOI: 10.1103/PhysRevA.80.032111.

[322] M. Kloc, P. Stránský, and P. Cejnar, "Quantum quench dynamics in dicke superradiance models," *Phys. Rev. A*, vol. 98, p. 013 836, 1 Jul. 2018, ISSN: 2469-9926. DOI: 10.1103/PhysRevA.98.013836.

[323] F. Pérez-Bernal and L. F. Santos, "Effects of excited state quantum phase transitions on system dynamics," *Fortschritte der Physik*, vol. 65, p. 1 600 035, 6-8 Jun. 2017, ISSN: 0015-8208. DOI: 10.1002/prop.201600035.

[324] R. Puebla, A. Relaño, and J. Retamosa, "Excited-state phase transition leading to symmetry-breaking steady states in the dicke model," *Phys. Rev. A*, vol. 87, p. 023 819, 2 Feb. 2013, ISSN: 1050-2947. DOI: 10.1103/PhysRevA.87.023819.

[325] Á. L. Corps and A. Relaño, "Constant of motion identifying excited-state quantum phases," *Phys. Rev. Lett.*, vol. 127, p. 130 602, 13 Sep. 2021, ISSN: 0031-9007. DOI: 10.1103/PhysRevLett.127.130602.

[326] ——, "Dynamical and excited-state quantum phase transitions in collective systems," *Phys. Rev. B*, vol. 106, p. 024 311, 2 Jul. 2022, ISSN: 2469-9950. DOI: 10.1103/PhysRevB.106.024311.

[327] ——, "Theory of dynamical phase transitions in quantum systems with symmetry-breaking eigenstates," *Phys. Rev. Lett.*, vol. 130, p. 100 402, 10 Mar. 2023, ISSN: 0031-9007. DOI: 10.1103/PhysRevLett.130.100402.

[328] Á. L. Corps, R. A. Molina, and A. Relaño, "Chaos in a deformed dicke model," *Journal of Physics A: Mathematical and Theoretical*, vol. 55, p. 084 001, 8 Feb. 2022, ISSN: 1751-8113. DOI: 10.1088/1751-8121/ac4b16.

[329] Á. L. Corps, P. Stránský, and P. Cejnar, "Mechanism of dynamical phase transitions: The complex-time survival amplitude," *Phys. Rev. B*, vol. 107, p. 094 307, 9 Mar. 2023, ISSN: 2469-9950. DOI: 10.1103/PhysRevB.107.094307.

[330] Á. L. Corps and A. Relaño, "General theory for discrete symmetry-breaking equilibrium states," 2023. arXiv: 2303.18020 [quant-ph].

[331] Á. L. Corps, P. Pérez-Fernández, and A. Relaño, "Relaxation time as a control parameter for exploring dynamical phase diagrams," *Phys. Rev. B*, vol. 108, p. 174 305, 17 Nov. 2023. DOI: 10.1103/PhysRevB.108.174305.

[332] R. Puebla and A. Relaño, "Irreversible processes without energy dissipation in an isolated Lipkin-Meshkov-Glick model," *Phys. Rev. E*, vol. 92, p. 012 101, 1 Jul. 2015, ISSN: 1539-3755. DOI: 10.1103/PhysRevE.92.012101.

[333] Q. Hummel, B. Geiger, J. D. Urbina, and K. Richter, "Reversible quantum information spreading in many-body systems near criticality," *Phys. Rev. Lett.*, vol. 123, p. 160 401, 16 Oct. 2019, ISSN: 0031-9007. DOI: 10.1103/PhysRevLett.123.160401.

[334] Q. Wang and F. Pérez-Bernal, "Signatures of excited-state quantum phase transitions in quantum many-body systems: Phase space analysis," *Phys. Rev. E*, vol. 104, p. 034 119, 3 Sep. 2021, ISSN: 2470-0045. DOI: 10.1103/PhysRevE.104.034119.

[335] ——, "Characterizing the Lipkin-Meshkov-Glick model excited-state quantum phase transition using dynamical and statistical properties of the diagonal entropy," *Phys. Rev. E*, vol. 103, p. 032 109, 3 Mar. 2021, ISSN: 2470-0045. DOI: 10.1103/PhysRevE.103.032109.

[336] M. Kloc, D. Šimsa, F. Hanák, P. R. Kaprálová-Žďánská, P. Stránský, and P. Cejnar, "Quasiclassical approach to quantum quench dynamics in the presence of an excited-state quantum phase transition," *Phys. Rev. A*, vol. 103, p. 032 213, 3 Mar. 2021, ISSN: 2469-9926. DOI: 10.1103/PhysRevA.103.032213.

[337] D. Larese, F. Pérez-Bernal, and F. Iachello, "Signatures of quantum phase transitions and excited state quantum phase transitions in the vibrational bending dynamics of triatomic molecules," *Journal of Molecular Structure*, vol. 1051, pp. 310–327, Nov. 2013, ISSN: 00222860. DOI: 10.1016/j.molstruc.2013.08.020.

[338] F. Iachello and S. Oss, "Algebraic approach to molecular spectra: Two-dimensional problems," *The Journal of Chemical Physics*, vol. 104, pp. 6956–6963, 18 May 1996, ISSN: 0021-9606. DOI: 10.1063/1.471412.

[339] F. Iachello, F. Pérez-Bernal, and P. Vaccaro, "A novel algebraic scheme for describing nonrigid molecules," *Chemical Physics Letters*, vol. 375, pp. 309–320, 3-4 Jul. 2003, ISSN: 00092614. DOI: 10.1016/S0009-2614(03)00851-0.

[340] F. Pérez-Bernal, L. Santos, P. Vaccaro, and F. Iachello, "Spectroscopic signatures of nonrigidity: Algebraic analyses of infrared and raman transitions in nonrigid species," *Chemical Physics Letters*, vol. 414, pp. 398–404, 4-6 Oct. 2005, ISSN: 00092614. DOI: 10.1016/j.cplett.2005.07.119.

[341] F. Pérez-Bernal and F. Iachello, "Algebraic approach to two-dimensional systems: Shape phase transitions, monodromy, and thermodynamic quantities," *Phys. Rev. A*, vol. 77, p. 032 115, 3 Mar. 2008, ISSN: 1050-2947. DOI: 10.1103/PhysRevA.77.032115.

[342] F. Pérez-Bernal and O. Álvarez-Bajo, "Anharmonicity effects in the bosonic u(2)-so(3) excited-state quantum phase transition," *Phys. Rev. A*, vol. 81, p. 050 101, 5 May 2010, ISSN: 1050-2947. DOI: 10.1103/PhysRevA.81.050101.

[343] J. Khalouf-Rivera, F. Pérez-Bernal, and M. Carvajal, "Anharmonicity-induced excited-state quantum phase transition in the symmetric phase of the two-dimensional limit of the vibron model," *Phys. Rev. A*, vol. 105, p. 032 215, 3 Mar. 2022, ISSN: 2469-9926. DOI: 10.1103/PhysRevA.105.032215.

[344] J. Khalouf-Rivera, M. Carvajal, and F. Perez-Bernal, "Quantum fidelity susceptibility in excited state quantum phase transitions: Application to the bending spectra of nonrigid molecules," *SciPost Physics*, vol. 12, p. 002, 1 Jan. 2022, ISSN: 2542-4653. DOI: 10.21468/SciPostPhys.12.1.002.

[345] J. Khalouf-Rivera, F. Pérez-Bernal, and M. Carvajal, "Excited state quantum phase transitions in the bending spectra of molecules," *Journal of Quantitative Spectroscopy and Radiative Transfer*, vol. 261, p. 107 436, Mar. 2021, ISSN: 00224073. DOI: 10.1016/j.jqsrt.2020.107436.

[346] A. Relaño, J. M. Arias, J. Dukelsky, J. E. García-Ramos, and P. Pérez-Fernández, "Decoherence as a signature of an excited-state quantum phase transition," *Phys. Rev. A*, vol. 78, p. 060 102, 6 Dec. 2008, ISSN: 1050-2947. DOI: 10.1103/PhysRevA.78.060102.

[347] P. Pérez-Fernández, P. Cejnar, J. M. Arias, J. Dukelsky, J. E. García-Ramos, and A. Relaño, "Quantum quench influenced by an excited-state phase transition," *Phys. Rev. A*, vol. 83, p. 033 802, 3 Mar. 2011, ISSN: 1050-2947. DOI: 10.1103/PhysRevA.83.033802.

[348] M.-J. Hwang, R. Puebla, and M. B. Plenio, "Quantum phase transition and universal dynamics in the rabi model," *Phys. Rev. Lett.*, vol. 115, p. 180 404, 18 Oct. 2015, ISSN: 0031-9007. DOI: 10.1103/PhysRevLett.115.180404.

[349] A. Relaño, M. A. Bastarrachea-Magnani, and S. Lerma-Hernández, "Approximated integrability of the dicke model," *EPL (Europhysics Letters)*, vol. -116, p. 50 005, 5 Dec. 2016, ISSN: 0295-5075. DOI: 10.1209/0295-5075/116/50005.

[350] M. Kloc, P. Stránský, and P. Cejnar, "Quantum phases and entanglement properties of an extended dicke model," *Annals of Physics*, vol. 382, pp. 85–111, Jul. 2017, ISSN: 00034916. DOI: 10.1016/j.aop.2017.04.005.

[351] C. M. Lóbez and A. Relaño, "Can we retrieve information from quantum thermalized states?" *Journal of Statistical Mechanics: Theory and Experiment*, vol. 2021, p. 083 104, 8 Aug. 2021, ISSN: 1742-5468. DOI: 10.1088/1742-5468/ac0ede.

[352] A. Relaño, J. Dukelsky, P. Pérez-Fernández, and J. M. Arias, "Quantum phase transitions of atom-molecule bose mixtures in a double-well potential," *Phys. Rev. E*, vol. 90, p. 042 139, 4 Oct. 2014, ISSN: 1539-3755. DOI: 10.1103/PhysRevE.90.042139.

[353] J. Gamito, J. Khalouf-Rivera, J. M. Arias, P. Pérez-Fernández, and F. Pérez-Bernal, "Excited-state quantum phase transitions in the anharmonic Lipkin-Meshkov-Glick model: Static aspects," *Phys. Rev. E*, vol. 106, p. 044 125, 4 Oct. 2022, ISSN: 2470-0045. DOI: 10.1103/PhysRevE.106.044125.

[354] P. Ribeiro, J. Vidal, and R. Mosseri, "Exact spectrum of the Lipkin-Meshkov-Glick model in the thermodynamic limit and finite-size corrections," *Phys. Rev. E*, vol. 78, p. 021 106, 2 Aug. 2008, ISSN: 1539-3755. DOI: 10.1103/PhysRevE.78.021106.

[355] ——, "Thermodynamical limit of the Lipkin-Meshkov-Glick model," *Phys. Rev. Lett.*, vol. 99, p. 050 402, 5 Aug. 2007, ISSN: 0031-9007. DOI: 10.1103/PhysRevLett.99.050402.

[356] O. Castaños, R. López-Peña, J. G. Hirsch, and E. López-Moreno, "Classical and quantum phase transitions in the Lipkin-Meshkov-Glick model," *Phys. Rev. B*, vol. 74, p. 104 118, 10 Sep. 2006, ISSN: 1098-0121. DOI: 10.1103/PhysRevB.74.104118.

[357] J. E. García-Ramos, P. Pérez-Fernández, and J. M. Arias, "Excited-state quantum phase transitions in a two-fluid lipkin model," *Phys. Rev. C*, vol. 95, p. 054 326, 5 May 2017, ISSN: 2469-9985. DOI: 10.1103/PhysRevC.95.054326.

[358] D. J. Nader, C. A. González-Rodríguez, and S. Lerma-Hernández, "Avoided crossings and dynamical tunneling close to excited-state quantum phase transitions," *Phys. Rev. E*, vol. 104, p. 064 116, 6 Dec. 2021, ISSN: 2470-0045. DOI: 10.1103/PhysRevE.104.064116.

[359] J. Cabedo and A. Celi, "Excited-state quantum phase transitions in spin-orbit-coupled bose gases," *Phys. Rev. Research*, vol. 3, p. 043 215, 4 Dec. 2021, ISSN: 2643-1564. DOI: 10.1103/PhysRevResearch.3.043215.

[360] J. Cabedo, J. Claramunt, and A. Celi, "Dynamical preparation of stripe states in spin-orbit-coupled gases," *Phys. Rev. A*, vol. 104, p. L031305, 3 Sep. 2021, ISSN: 2469-9926. DOI: 10.1103/PhysRevA.104.L031305.

[361] P. Stránský, M. Šindelka, M. Kloc, and P. Cejnar, "Complex density of continuum states in resonant quantum tunneling," *Phys. Rev. Lett.*, vol. 125, p. 020 401, 2 Jul. 2020, ISSN: 0031-9007. DOI: 10.1103/PhysRevLett.125.020401.

[362] Á. Rubio-García, Á. L. Corps, A. Relaño, R. A. Molina, F. Pérez-Bernal, J. E. García-Ramos, and J. Dukelsky, "Exceptional spectral phase in a dissipative collective spin model," *Phys. Rev. A*, vol. 106, p. L010201, 1 Jul. 2022, ISSN: 2469-9926. DOI: 10.1103/PhysRevA.106.L010201.

[363] N. F. Zobov, S. V. Shirin, O. L. Polyansky, J. Tennyson, P.-F. Coheur, P. F. Bernath, M. Carleer, and R. Colin, "Monodromy in the water molecule," *Chemical Physics Letters*, vol. 414, pp. 193–197, 1-3 Oct. 2005, ISSN: 00092614. DOI: 10.1016/j.cplett.2005.08.028.

[364] B. Dietz, F. Iachello, M. Miski-Oglu, N. Pietralla, A. Richter, L. von Smekal, and J. Wambach, "Lifshitz and excited-state quantum phase transitions in microwave dirac billiards," *Phys. Rev. B*, vol. 88, p. 104 101, 10 Sep. 2013, ISSN: 1098-0121. DOI: 10.1103/PhysRevB.88.104101.

[365] T. Tian, H.-X. Yang, L.-Y. Qiu, H.-Y. Liang, Y.-B. Yang, Y. Xu, and L.-M. Duan, "Observation of dynamical quantum phase transitions with correspondence in an excited state phase diagram," *Phys. Rev. Lett.*, vol. 124, p. 043 001, 4 Jan. 2020, ISSN: 0031-9007. DOI: 10.1103/PhysRevLett.124.043001.

[366] J. Chávez-Carlos, T. L. M. Lezama, R. G. Cortiñas, J. Venkatraman, M. H. Devoret, V. S. Batista, F. Pérez-Bernal, and L. F. Santos, "Spectral kissing and its dynamical consequences in the squeeze-driven kerr oscillator," *npj Quantum Information*, vol. 9, p. 76, 1 Jul. 2023, ISSN: 2056-6387. DOI: 10.1038/s41534-023-00745-1.

[367] H. Lipkin, N. Meshkov, and A. Glick, "Validity of many-body approximation methods for a solvable model: (i). exact solutions and perturbation theory," *Nuclear Physics*, vol. 62, pp. 188–198, 2 Feb. 1965, ISSN: 00295582. DOI: 10.1016/0029-5582(65)90862-X.

[368] N. Meshkov, A. Glick, and H. Lipkin, "Validity of many-body approximation methods for a solvable model: (ii). linearization procedures," *Nuclear Physics*, vol. 62, pp. 199–210, 2 Feb. 1965, ISSN: 00295582. DOI: 10.1016/0029-5582(65)90863-1.

[369] A. Glick, H. Lipkin, and N. Meshkov, "Validity of many-body approximation methods for a solvable model: (iii). diagram summations," *Nuclear Physics*, vol. 62, pp. 211–224, 2 Feb. 1965, ISSN: 00295582. DOI: 10.1016/0029-5582(65)90864-3.

[370] A. Sehrawat, C. Srivastava, and U. Sen, "Dynamical phase transitions in the fully connected quantum ising model: Time period and critical time," *Phys. Rev. B*, vol. 104, p. 085 105, 8 Aug. 2021, ISSN: 2469-9950. DOI: 10.1103/PhysRevB.104.085105.

[371] I. Homrighausen, N. O. Abeling, V. Zauner-Stauber, and J. C. Halimeh, "Anomalous dynamical phase in quantum spin chains with long-range interactions," *Phys. Rev. B*, vol. 96, p. 104 436, 10 Sep. 2017, ISSN: 2469-9950. DOI: 10.1103/PhysRevB.96.104436.

[372] J. Lang, B. Frank, and J. C. Halimeh, "Concurrence of dynamical phase transitions at finite temperature in the fully connected transverse-field ising model," *Phys. Rev. B*, vol. 97, p. 174 401, 17 May 2018, ISSN: 2469-9950. DOI: 10.1103/PhysRevB.97.174401.

[373] P. Cejnar and P. Stránský, "Quantum phase transitions in the collective degrees of freedom: Nuclei and other many-body systems," *Physica Scripta*, vol. 91, p. 083 006, 8 Aug. 2016, ISSN: 0031-8949. DOI: 10.1088/0031-8949/91/8/083006.

[374] J. A. Muniz, D. Barberena, R. J. Lewis-Swan, D. J. Young, J. R. K. Cline, A. M. Rey, and J. K. Thompson, "Exploring dynamical phase transitions with cold atoms in an optical cavity," *Nature*, vol. 580, pp. 602–607, 7805 Apr. 2020, ISSN: 0028-0836. DOI: 10.1038/s41586-020-2224-x.

[375] B. Žunkovič, M. Heyl, M. Knap, and A. Silva, "Dynamical quantum phase transitions in spin chains with long-range interactions: Merging different concepts of nonequilibrium criticality," *Phys. Rev. Lett.*, vol. 120, p. 130 601, 13 Mar. 2018, ISSN: 0031-9007. DOI: 10.1103/PhysRevLett.120.130601.

[376] J. Lang, B. Frank, and J. C. Halimeh, "Dynamical quantum phase transitions: A geometric picture," *Phys. Rev. Lett.*, vol. 121, p. 130 603, 13 Sep. 2018, ISSN: 0031-9007. DOI: 10.1103/PhysRevLett.121.130603.

[377] R. Puebla, "Finite-component dynamical quantum phase transitions," *Phys. Rev. B*, vol. 102, p. 220 302, 22 Dec. 2020, ISSN: 2469-9950. DOI: 10.1103/PhysRevB.102.220302.

[378] S. A. Weidinger, M. Heyl, A. Silva, and M. Knap, "Dynamical quantum phase transitions in systems with continuous symmetry breaking," *Phys. Rev. B*, vol. 96, p. 134 313, 13 Oct. 2017, ISSN: 2469-9950. DOI: 10.1103/PhysRevB.96.134313.

[379] T. Hashizume, I. P. McCulloch, and J. C. Halimeh, "Dynamical phase transitions in the two-dimensional transverse-field ising model," *Phys. Rev. Research*, vol. 4, p. 013 250, 1 Mar. 2022, ISSN: 2643-1564. DOI: 10.1103/PhysRevResearch.4.013250.

[380] B. Žunkovič, A. Silva, and M. Fabrizio, "Dynamical phase transitions and loschmidt echo in the infinite-range XY model," *Philosophical Transactions of the Royal Society A: Mathematical, Physical and Engineering Sciences*, vol. 374, p. 20 150 160, 2069 Jun. 2016, ISSN: 1364-503X. DOI: 10.1098/rsta.2015.0160.

[381] A. Lerose, B. Žunkovič, J. Marino, A. Gambassi, and A. Silva, "Impact of nonequilibrium fluctuations on prethermal dynamical phase transitions in long-range interacting spin chains," *Phys. Rev. B*, vol. 99, p. 045 128, 4 Jan. 2019, ISSN: 2469-9950. DOI: 10.1103/PhysRevB.99.045128.

[382] M. Gring, M. Kuhnert, T. Langen, T. Kitagawa, B. Rauer, M. Schreitl, I. Mazets, D. A. Smith, E. Demler, and J. Schmiedmayer, "Relaxation and prethermalization in an isolated quantum system," *Science*, vol. 337, pp. 1318–1322, 6100 Sep. 2012, ISSN: 0036-8075. DOI: 10.1126/science.1224953.

[383] T. Mori, T. N. Ikeda, E. Kaminishi, and M. Ueda, "Thermalization and prethermalization in isolated quantum systems: A theoretical overview," *Journal of Physics B: Atomic, Molecular and Optical Physics*, vol. 51, p. 112 001, 11 Jun. 2018, ISSN: 0953-4075. DOI: 10.1088/1361-6455/aabcdf.

[384] M. Eckstein and M. Kollar, "Nonthermal steady states after an interaction quench in the falicov-kimball model," *Phys. Rev. Lett.*, vol. 100, p. 120 404, 12 Mar. 2008, ISSN: 0031-9007. DOI: 10.1103/PhysRevLett.100.120404.

[385] M. Moeckel and S. Kehrein, "Interaction quench in the hubbard model," *Phys. Rev. Lett.*, vol. 100, p. 175 702, 17 May 2008, ISSN: 0031-9007. DOI: 10.1103/PhysRevLett.100.175702.

[386] M. Eckstein, M. Kollar, and P. Werner, "Thermalization after an interaction quench in the hubbard model," *Phys. Rev. Lett.*, vol. 103, p. 056 403, 5 Jul. 2009, ISSN: 0031-9007. DOI: 10.1103/PhysRevLett.103.056403.

[387] B. Sciolla and G. Biroli, "Dynamical transitions and quantum quenches in mean-field models," *Journal of Statistical Mechanics: Theory and Experiment*, vol. 2011, P11003, 11 Nov. 2011, ISSN: 1742-5468. DOI: 10.1088/1742-5468/2011/11/P11003.

[388] J. Zhang, G. Pagano, P. W. Hess, A. Kyprianidis, P. Becker, H. Kaplan, A. V. Gorshkov, Z.-X. Gong, and C. Monroe, "Observation of a many-body dynamical phase transition with a 53-qubit quantum simulator," *Nature*, vol. 551, pp. 601–604, 7682 Nov. 2017, ISSN: 0028-0836. DOI: 10.1038/nature24654.

[389] S. Smale, P. He, B. A. Olsen, K. G. Jackson, H. Sharum, S. Trotzky, J. Marino, A. M. Rey, and J. H. Thywissen, "Observation of a transition between dynamical phases in a quantum degenerate fermi gas," *Science Advances*, vol. 5, 8 Aug. 2019, ISSN: 2375-2548. DOI: 10.1126/sciadv.aax1568.

[390] J. C. Halimeh, V. Zauner-Stauber, I. P. McCulloch, I. de Vega, U. Schollwöck, and M. Kastner, "Prethermalization and persistent order in the absence of a thermal phase transition," *Phys. Rev. B*, vol. 95, p. 024 302, 2 Jan. 2017, ISSN: 2469-9950. DOI: 10.1103/PhysRevB.95.024302.

[391] B. Sciolla and G. Biroli, "Quantum quenches, dynamical transitions, and off-equilibrium quantum criticality," *Phys. Rev. B*, vol. 88, p. 201 110, 20 Nov. 2013, ISSN: 1098-0121. DOI: 10.1103/PhysRevB.88.201110.

[392] G. A. Álvarez, E. P. Danieli, P. R. Levstein, and H. M. Pastawski, "Environmentally induced quantum dynamical phase transition in the spin swapping operation," *The Journal of Chemical Physics*, vol. 124, 19 May 2006, ISSN: 0021-9606. DOI: 10.1063/1.2193518.

[393] M. Heyl, A. Polkovnikov, and S. Kehrein, "Dynamical quantum phase transitions in the transverse-field ising model," *Phys. Rev. Lett.*, vol. 110, p. 135 704, 13 Mar. 2013, ISSN: 0031-9007. DOI: 10.1103/PhysRevLett.110.135704.

[394] M. Heyl, "Dynamical quantum phase transitions in systems with broken-symmetry phases," *Phys. Rev. Lett.*, vol. 113, p. 205 701, 20 Nov. 2014, ISSN: 0031-9007. DOI: 10.1103/PhysRevLett.113.205701.

[395] P. Jurcevic, H. Shen, P. Hauke, C. Maier, T. Brydges, C. Hempel, B. P. Lanyon, M. Heyl, R. Blatt, and C. F. Roos, "Direct observation of dynamical quantum phase transitions in an interacting many-body system," *Phys. Rev. Lett.*, vol. 119, p. 080 501, 8 Aug. 2017, ISSN: 0031-9007. DOI: 10.1103/PhysRevLett.119.080501.

[396] J. C. Halimeh and V. Zauner-Stauber, "Dynamical phase diagram of quantum spin chains with long-range interactions," *Phys. Rev. B*, vol. 96, p. 134 427, 13 Oct. 2017, ISSN: 2469-9950. DOI: 10.1103/PhysRevB.96.134427.

[397] S. D. Nicola, A. A. Michailidis, and M. Serbyn, "Entanglement view of dynamical quantum phase transitions," *Phys. Rev. Lett.*, vol. 126, p. 040 602, 4 Jan. 2021, ISSN: 0031-9007. DOI: 10.1103/PhysRevLett.126.040602.

[398] M. Schmitt and S. Kehrein, "Dynamical quantum phase transitions in the kitaev honeycomb model," *Phys. Rev. B*, vol. 92, p. 075 114, 7 Aug. 2015, ISSN: 1098-0121. DOI: 10.1103/PhysRevB.92.075114.

[399] U. Bhattacharya and A. Dutta, "Emergent topology and dynamical quantum phase transitions in two-dimensional closed quantum systems," *Phys. Rev. B*, vol. 96, p. 014 302, 1 Jul. 2017, ISSN: 2469-9950. DOI: 10.1103/PhysRevB.96.014302.

[400] C. Karrasch and D. Schuricht, "Dynamical phase transitions after quenches in nonintegrable models," *Phys. Rev. B*, vol. 87, p. 195 104, 19 May 2013, ISSN: 1098-0121. DOI: 10.1103/PhysRevB.87.195104.

[401] R. Jafari, A. Akbari, U. Mishra, and H. Johannesson, "Floquet dynamical quantum phase transitions under synchronized periodic driving," *Phys. Rev. B*, vol. 105, p. 094 311, 9 Mar. 2022, ISSN: 2469-9950. DOI: 10.1103/PhysRevB.105.094311.

[402] J. Naji, M. Jafari, R. Jafari, and A. Akbari, "Dissipative floquet dynamical quantum phase transition," *Phys. Rev. A*, vol. 105, p. 022 220, 2 Feb. 2022, ISSN: 2469-9926. DOI: 10.1103/PhysRevA.105.022220.

[403] R. Jafari, H. Johannesson, A. Langari, and M. A. Martin-Delgado, "Quench dynamics and zero-energy modes: The case of the creutz model," *Phys. Rev. B*, vol. 99, p. 054 302, 5 Feb. 2019, ISSN: 2469-9950. DOI: 10.1103/PhysRevB.99.054302.

[404] U. Mishra, R. Jafari, and A. Akbari, "Disordered kitaev chain with long-range pairing: Loschmidt echo revivals and dynamical phase transitions," *Journal of Physics A: Mathematical and Theoretical*, vol. 53, p. 375 301, 37 Sep. 2020, ISSN: 1751-8113. DOI: 10.1088/1751-8121/ab97de.

[405] R. Jafari and A. Akbari, "Floquet dynamical phase transition and entanglement spectrum," *Phys. Rev. A*, vol. 103, p. 012 204, 1 Jan. 2021, ISSN: 2469-9926. DOI: 10.1103/PhysRevA.103.012204.

[406] S. Vajna and B. Dóra, "Disentangling dynamical phase transitions from equilibrium phase transitions," *Phys. Rev. B*, vol. 89, p. 161 105, 16 Apr. 2014, ISSN: 1098-0121. DOI: 10.1103/PhysRevB.89.161105.

[407] F. Andraschko and J. Sirker, "Dynamical quantum phase transitions and the loschmidt echo: A transfer matrix approach," *Phys. Rev. B*, vol. 89, p. 125 120, 12 Mar. 2014, ISSN: 1098-0121. DOI: 10.1103/PhysRevB.89.125120.

[408] E. J. Torres-Herrera, M. Vyas, and L. F. Santos, "General features of the relaxation dynamics of interacting quantum systems," *New Journal of Physics*, vol. 16, p. 063 010, 6 Jun. 2014, ISSN: 1367-2630. DOI: 10.1088/1367-2630/16/6/063010.

[409] E. J. Torres-Herrera, A. M. García-García, and L. F. Santos, "Generic dynamical features of quenched interacting quantum systems: Survival probability, density imbalance, and out-of-time-ordered correlator," *Phys. Rev. B*, vol. 97, p. 060 303, 6 Feb. 2018, ISSN: 2469-9950. DOI: 10.1103/PhysRevB.97.060303.

[410] M. Schiulaz, E. J. Torres-Herrera, and L. F. Santos, "Thouless and relaxation time scales in many-body quantum systems," *Phys. Rev. B*, vol. 99, p. 174 313, 17 May 2019, ISSN: 2469-9950. DOI: 10.1103/PhysRevB.99.174313.

[411] S. Lerma-Hernández, J. Chávez-Carlos, M. A. Bastarrachea-Magnani, L. F. Santos, and J. G. Hirsch, "Analytical description of the survival probability of coherent states in regular regimes," *Journal of Physics A: Mathematical and Theoretical*, vol. 51, p. 475 302, 47 Nov. 2018, ISSN: 1751-8113. DOI: 10.1088/1751-8121/aae2c3.

[412] T. L. M. Lezama, E. J. Torres-Herrera, F. Pérez-Bernal, Y. B. Lev, and L. F. Santos, "Equilibration time in many-body quantum systems," *Phys. Rev. B*, vol. 104, p. 085 117, 8 Aug. 2021, ISSN: 2469-9950. DOI: 10.1103/PhysRevB.104.085117.

[413] H. Touchette, "The large deviation approach to statistical mechanics," *Physics Reports*, vol. 478, pp. 1–69, 1-3 Jul. 2009, ISSN: 03701573. DOI: 10.1016/j.physrep.2009.05.002.

[414] E. J. Torres-Herrera and L. F. Santos, "Extended nonergodic states in disordered many-body quantum systems," *Annalen der Physik*, vol. 529, 7 Jul. 2017, ISSN: 0003-3804. DOI: 10.1002/andp.201600284.

[415] A. Relaño, J. M. G. Gómez, R. A. Molina, J. Retamosa, and E. Faleiro, "Quantum chaos and $1/f$ noise," *Phys. Rev. Lett.*, vol. 89, p. 244 102, 24 Nov. 2002, ISSN: 0031-9007. DOI: 10.1103/PhysRevLett.89.244102.

[416] E. Faleiro, J. M. G. Gómez, R. A. Molina, L. Muñoz, A. Relaño, and J. Retamosa, "Theoretical derivation of $1/f$ noise in quantum chaos," *Phys. Rev. Lett.*, vol. 93, p. 244 101, 24 Dec. 2004, ISSN: 0031-9007. DOI: 10.1103/PhysRevLett.93.244101.

[417] L. A. Pachón, A. Relaño, B. Peropadre, and A. Aspuru-Guzik, "Origin of the $1/f^{\alpha}$ spectral noise in chaotic and regular quantum systems," *Phys. Rev. E*, vol. 98, p. 042 213, 4 Oct. 2018, ISSN: 2470-0045. DOI: 10.1103/PhysRevE.98.042213.

[418] J. M. G. Gómez, A. Relaño, J. Retamosa, E. Faleiro, L. Salasnich, M. Vraničar, and M. Robnik, "$1/f^{\alpha}$ noise in spectral fluctuations of quantum systems," *Phys. Rev. Lett.*, vol. 94, p. 084 101, 8 Mar. 2005, ISSN: 0031-9007. DOI: 10.1103/PhysRevLett.94.084101.

[419] M. S. Santhanam and J. N. Bandyopadhyay, "Spectral fluctuations and $1/f$ noise in the order-chaos transition regime," *Phys. Rev. Lett.*, vol. 95, p. 114 101, 11 Sep. 2005, ISSN: 0031-9007. DOI: 10.1103/PhysRevLett.95.114101.

[420] L. A. Colmenarez, P. A. McClarty, M. Haque, and D. J. Luitz, "Statistics of correlation functions in the random heisenberg chain," *SciPost Physics*, vol. 7, p. 064, 5 Nov. 2019, ISSN: 2542-4653. DOI: 10.21468/SciPostPhys.7.5.064.

[421] V. Khemani, S. P. Lim, D. N. Sheng, and D. A. Huse, "Critical properties of the many-body localization transition," *Phys. Rev. X*, vol. 7, p. 021 013, 2 Apr. 2017, ISSN: 2160-3308. DOI: 10.1103/PhysRevX.7.021013.

[422] R. Vosk, D. A. Huse, and E. Altman, "Theory of the many-body localization transition in one-dimensional systems," *Phys. Rev. X*, vol. 5, p. 031 032, 3 Sep. 2015, ISSN: 2160-3308. DOI: 10.1103/PhysRevX.5.031032.

[423] Á. L. Corps, J. Dukelsky, and A. Relaño, "Constants of motion characterizing continuous symmetry-broken phases," *Phys. Rev. E*, vol. 109, p. 064 102, 6 Jun. 2024. DOI: 10.1103/PhysRevE.109.064102.

[424] E. D. Denman and A. N. Beavers, "The matrix sign function and computations in systems," *Applied Mathematics and Computation*, vol. 2, no. 1, pp. 63–94, 1976, ISSN: 0096-3003. DOI: https://doi.org/10.1016/0096-3003(76)90020-5.

[425] J. D. Roberts, "Linear model reduction and solution of the algebraic riccati equation by use of the sign function," *International Journal of Control*, vol. 32, no. 4, pp. 677–687, 1980. DOI: 10.1080/00207178008922881.

[426] W. Kopylov and T. Brandes, "Time delayed control of excited state quantum phase transitions in the lipkin–meshkov–glick model," *New Journal of Physics*, vol. 17, p. 103 031, 10 Oct. 2015, ISSN: 1367-2630. DOI: 10.1088/1367-2630/17/10/103031.

[427] P. Feldmann, C. Klempt, A. Smerzi, L. Santos, and M. Gessner, "Interferometric order parameter for excited-state quantum phase transitions in bose-einstein condensates," *Phys. Rev. Lett.*, vol. 126, p. 230 602, 23 Jun. 2021, ISSN: 0031-9007. DOI: 10.1103/PhysRevLett.126.230602.

[428] Y. Guryanova, S. Popescu, A. J. Short, R. Silva, and P. Skrzypczyk, "Thermodynamics of quantum systems with multiple conserved quantities," *Nature Communications*, vol. 7, p. 12 049, 1 Jul. 2016, ISSN: 2041-1723. DOI: 10.1038/ncomms12049.

[429] J. Mur-Petit, A. Relaño, R. A. Molina, and D. Jaksch, "Revealing missing charges with generalised quantum fluctuation relations," *Nature Communications*, vol. 9, p. 2006, 1 May 2018, ISSN: 2041-1723. DOI: 10.1038/s41467-018-04407-1.

[430] P. Reimann, "Equilibration of isolated macroscopic quantum systems under experimentally realistic conditions," *Physica Scripta*, vol. 86, p. 058 512, 5 Nov. 2012, ISSN: 0031-8949. DOI: 10.1088/0031-8949/86/05/058512.

[431] N. Linden, S. Popescu, A. J. Short, and A. Winter, "On the speed of fluctuations around thermodynamic equilibrium," *New Journal of Physics*, vol. 12, p. 055 021, 5 May 2010, ISSN: 1367-2630. DOI: 10.1088/1367-2630/12/5/055021.

[432] P. Reimann, "Canonical thermalization," *New Journal of Physics*, vol. 12, p. 055 027, 5 May 2010, ISSN: 1367-2630. DOI: 10.1088/1367-2630/12/5/055027.

[433] A. J. Short, "Equilibration of quantum systems and subsystems," *New Journal of Physics*, vol. 13, p. 053 009, 5 May 2011, ISSN: 1367-2630. DOI: 10.1088/1367-2630/13/5/053009.

[434] A. J. Short and T. C. Farrelly, "Quantum equilibration in finite time," *New Journal of Physics*, vol. 14, p. 013 063, 1 Jan. 2012, ISSN: 1367-2630. DOI: 10.1088/1367-2630/14/1/013063.

[435] E. G. Lazo, M. Heyl, M. Dalmonte, and A. Angelone, "Finite-temperature critical behavior of long-range quantum ising models," *SciPost Physics*, vol. 11, p. 076, 4 Oct. 2021, ISSN: 2542-4653. DOI: 10.21468/SciPostPhys.11.4.076.

[436] M. Kac and E. Helfand, "Study of several lattice systems with long-range forces," *Journal of Mathematical Physics*, vol. 4, pp. 1078–1088, 8 Aug. 1963, ISSN: 0022-2488. DOI: 10.1063/1.1704037.

[437] R. Franzosi and M. Pettini, "Theorem on the origin of phase transitions," *Phys. Rev. Letters*, vol. 92, p. 060 601, 6 Feb. 2004, ISSN: 0031-9007. DOI: 10.1103/PhysRevLett.92.060601.

[438] F. Baroni and L. Casetti, "Topological conditions for discrete symmetry breaking and phase transitions," *Journal of Physics A: Mathematical and General*, vol. 39, pp. 529–545, 3 Jan. 2006, ISSN: 0305-4470. DOI: 10.1088/0305-4470/39/3/006.

[439] "Topological theory of phase transitions," *Journal of Physics A: Mathematical and Theoretical*, vol. 55, p. 375 002, 37 Sep. 2022, ISSN: 1751-8113. DOI: 10.1088/1751-8121/ac7f09.

[440] N. Y. Halpern, P. Faist, J. Oppenheim, and A. Winter, "Microcanonical and resource-theoretic derivations of the thermal state of a quantum system with noncommuting charges," *Nature Communications*, vol. 7, p. 12 051, 1 Jul. 2016, ISSN: 2041-1723. DOI: 10.1038/ncomms12051.

[441] M. Fagotti, "On conservation laws, relaxation and pre-relaxation after a quantum quench," *Journal of Statistical Mechanics: Theory and Experiment*, vol. 2014, P03016, 3 Mar. 2014, ISSN: 1742-5468. DOI: 10.1088/1742-5468/2014/03/P03016.

[442] F. Kranzl, A. Lasek, M. K. Joshi, A. Kalev, R. Blatt, C. F. Roos, and N. Y. Halpern, "Experimental observation of thermalization with noncommuting charges," *PRX Quantum*, vol. 4, p. 020 318, 2 Apr. 2023, ISSN: 2691-3399. DOI: 10.1103/PRXQuantum.4.020318.

[443] S. Majidy, W. F. Braasch, A. Lasek, T. Upadhyaya, A. Kalev, and N. Y. Halpern, "Noncommuting conserved charges in quantum thermodynamics and beyond," *Nature Reviews Physics*, vol. 5, pp. 689–698, 11 Oct. 2023, ISSN: 2522-5820. DOI: 10.1038/s42254-023-00641-9.

[444] E. T. Jaynes, "Information theory and statistical mechanics," *Phys. Rev.*, vol. 106, pp. 620–630, 4 May 1957, ISSN: 0031-899X. DOI: 10.1103/PhysRev.106.620.

[445] J. Khalouf-Rivera, Q. Wang, L. F. Santos, J. E. G. Ramos, M. Carvajal, and F. Pérez-Bernal, "Degeneracy in excited-state quantum phase transitions of two-level bosonic models and its influence on system dynamics," 2023. arXiv: 2303.16551.

[446] R. Islam, C. Senko, W. C. Campbell, S. Korenblit, J. Smith, A. Lee, E. E. Edwards, C.-C. J. Wang, J. K. Freericks, and C. Monroe, "Emergence and frustration of magnetism with variable-range interactions in a quantum simulator," *Science*, vol. 340, pp. 583–587, 6132 May 2013, ISSN: 0036-8075. DOI: 10.1126/science.1232296.

[447] T. W. B. Kibble, "Topology of cosmic domains and strings," *Journal of Physics A: Mathematical and General*, vol. 9, pp. 1387–1398, 8 Aug. 1976, ISSN: 0305-4470. DOI: 10.1088/0305-4470/9/8/029.

[448] W. H. Zurek, "Cosmological experiments in superfluid helium?" *Nature*, vol. 317, pp. 505–508, 6037 Oct. 1985, ISSN: 0028-0836. DOI: 10.1038/317505a0.

[449] W. H. Zurek, U. Dorner, and P. Zoller, "Dynamics of a quantum phase transition," *Phys. Rev. Letters*, vol. 95, p. 105 701, 10 Sep. 2005, ISSN: 0031-9007. DOI: 10.1103/PhysRevLett.95.105701.

[450] A. Dutta and J. K. Bhattacharjee, "Phase transitions in the quantum ising and rotor models with a long-range interaction," *Phys. Rev. B*, vol. 64, p. 184 106, 18 Oct. 2001, ISSN: 0163-1829. DOI: 10.1103/PhysRevB.64.184106.

[451] R. Puebla, O. Marty, and M. B. Plenio, "Quantum kibble-zurek physics in long-range transverse-field ising models," *Phys. Rev. A*, vol. 100, p. 032 115, 3 Sep. 2019, ISSN: 2469-9926. DOI: 10.1103/PhysRevA.100.032115.

[452] R. Islam, E. Edwards, K. Kim, S. Korenblit, C. Noh, H. Carmichael, G.-D. Lin, L.-M. Duan, C.-C. J. Wang, J. Freericks, and C. Monroe, "Onset of a quantum phase transition with a trapped ion quantum simulator," *Nature Communications*, vol. 2, p. 377, 1 Jul. 2011, ISSN: 2041-1723. DOI: 10.1038/ncomms1374.

[453] J. Simon, W. S. Bakr, R. Ma, M. E. Tai, P. M. Preiss, and M. Greiner, "Quantum simulation of antiferromagnetic spin chains in an optical lattice," *Nature*, vol. 472, pp. 307–312, 7343 Apr. 2011, ISSN: 0028-0836. DOI: 10.1038/nature09994.

[454] J. W. Britton, B. C. Sawyer, A. C. Keith, C.-C. J. Wang, J. K. Freericks, H. Uys, M. J. Biercuk, and J. J. Bollinger, "Engineered two-dimensional ising interactions in a trapped-ion quantum simulator with hundreds of spins," *Nature*, vol. 484, pp. 489–492, 7395 Apr. 2012, ISSN: 0028-0836. DOI: 10.1038/nature10981.

[455] A. Campa, T. Dauxois, and S. Ruffo, "Statistical mechanics and dynamics of solvable models with long-range interactions," *Physics Reports*, vol. 480, no. 3, pp. 57–159, 2009, ISSN: 0370-1573. DOI: https://doi.org/10.1016/j.physrep.2009.07.001.

[456] J. C. Halimeh, M. V. Damme, V. Zauner-Stauber, and L. Vanderstraeten, "Quasiparticle origin of dynamical quantum phase transitions," *Phys. Rev. Research*, vol. 2, p. 033 111, 3 Jul. 2020, ISSN: 2643-1564. DOI: 10.1103/PhysRevResearch.2.033111.

[457] S. Dusuel and J. Vidal, "Finite-size scaling exponents of the Lipkin-Meshkov-Glick model," *Phys. Rev. Lett.*, vol. 93, p. 237 204, 23 Dec. 2004, ISSN: 0031-9007. DOI: 10.1103/PhysRevLett.93.237204.

[458] W. D. Heiss, F. G. Scholtz, and H. B. Geyer, "The large N behaviour of the lipkin model and exceptional points," *Journal of Physics A: Mathematical and General*, vol. 38, pp. 1843–1851, 9 Mar. 2005, ISSN: 0305-4470. DOI: 10.1088/0305-4470/38/9/002.

[459] R. J. Lewis-Swan, S. R. Muleady, D. Barberena, J. J. Bollinger, and A. M. Rey, "Characterizing the dynamical phase diagram of the dicke model via classical and quantum probes," *Phys. Rev. Research*, vol. 3, p. L022020, 2 Jun. 2021, ISSN: 2643-1564. DOI: 10.1103/PhysRevResearch.3.L022020.

[460] L. F. Santos and F. Pérez-Bernal, "Structure of eigenstates and quench dynamics at an excited-state quantum phase transition," *Phys. Rev. A*, vol. 92, p. 050 101, 5 Nov. 2015, ISSN: 1050-2947. DOI: 10.1103/PhysRevA.92.050101.

[461] G. J. Milburn, J. Corney, E. M. Wright, and D. F. Walls, "Quantum dynamics of an atomic bose-einstein condensate in a double-well potential," *Phys. Rev. A*, vol. 55, pp. 4318–4324, 6 Jun. 1997, ISSN: 1050-2947. DOI: 10.1103/PhysRevA.55.4318.

[462] N. Y. Halpern, M. E. Beverland, and A. Kalev, "Noncommuting conserved charges in quantum many-body thermalization," *Phys. Rev. E*, vol. 101, p. 042 117, 4 Apr. 2020, ISSN: 2470-0045. DOI: 10.1103/PhysRevE.101.042117.

[463] J. A. Wheeler and W. H. Zurek, *Quantum Theory and Measurement*. Princeton University Press, 2014.

[464] J. von Neumann, "Mathematische grundlagen der quantenmechanik," in. Springer, 1932.

[465] W. H. Zurek, "Environment-induced superselection rules," *Phys. Rev. D*, vol. 26, pp. 1862–1880, 8 Oct. 1982, ISSN: 0556-2821. DOI: 10.1103/PhysRevD.26.1862.

[466] M. Lewenstein, M. F. Ciappina, E. Pisanty, J. Rivera-Dean, P. Stammer, T. Lamprou, and P. Tzallas, "Generation of optical schrödinger cat states in intense laser–matter interactions," *Nature Physics*, vol. 17, pp. 1104–1108, 10 Oct. 2021, ISSN: 1745-2473. DOI: 10.1038/s41567-021-01317-w.

[467] C. Wang, Y. Y. Gao, P. Reinhold, R. W. Heeres, N. Ofek, K. Chou, C. Axline, M. Reagor, J. Blumoff, K. M. Sliwa, L. Frunzio, S. M. Girvin, L. Jiang, M. Mirrahimi, M. H. Devoret, and R. J. Schoelkopf, "A schrödinger cat living in two boxes," *Science*, vol. 352, pp. 1087–1091, 6289 May 2016, ISSN: 0036-8075. DOI: 10.1126/science.aaf2941.

[468] G. Pieplow, C. E. Creffield, and F. Sols, "Protected cat states from kinetic driving of a boson gas," *Phys. Rev. Research*, vol. 1, p. 033 013, 3 Oct. 2019, ISSN: 2643-1564. DOI: 10.1103/PhysRevResearch.1.033013.

[469] J. Mateos, G. Pieplow, C. Creffield, and F. Sols, "Cat states in a driven superfluid: Role of signal shape and switching protocol," *The European Physical Journal Special Topics*, vol. 230, pp. 1013–1019, 4 Jun. 2021, ISSN: 1951-6355. DOI: 10.1140/epjs/s11734-021-00077-1.

[470] J. Higbie and D. M. Stamper-Kurn, "Generating macroscopic-quantum-superposition states in momentum and internal-state space from bose-einstein condensates with repulsive interactions," *Phys. Rev. A*, vol. 69, p. 053 605, 5 May 2004, ISSN: 1050-2947. DOI: 10.1103/PhysRevA.69.053605.

[471] Y. P. Huang and M. G. Moore, "Creation, detection, and decoherence of macroscopic quantum superposition states in double-well bose-einstein condensates," *Phys. Rev. A*, vol. 73, p. 023 606, 2 Feb. 2006, ISSN: 1050-2947. DOI: 10.1103/PhysRevA.73.023606.

[472] A. Nunnenkamp, A. M. Rey, and K. Burnett, "Generation of macroscopic superposition states in ring superlattices," *Phys. Rev. A*, vol. 77, p. 023 622, 2 Feb. 2008, ISSN: 1050-2947. DOI: 10.1103/PhysRevA.77.023622.

[473] L. D. Carr, D. R. Dounas-Frazer, and M. A. Garcia-March, "Dynamical realization of macroscopic superposition states of cold bosons in a tilted double well," *EPL (Europhysics Letters)*, vol. 90, p. 10 005, 1 Apr. 2010, ISSN: 0295-5075. DOI: 10.1209/0295-5075/90/10005.

[474] G. Mazzarella, L. Salasnich, A. Parola, and F. Toigo, "Coherence and entanglement in the ground state of a bosonic josephson junction: From macroscopic schrödinger cat states to separable fock states," *Phys. Rev. A*, vol. 83, p. 053 607, 5 May 2011, ISSN: 1050-2947. DOI: 10.1103/PhysRevA.83.053607.

[475] I. I. Rabi, "On the process of space quantization," *Phys. Rev.*, vol. 49, pp. 324–328, 4 Feb. 1936, ISSN: 0031-899X. DOI: 10.1103/PhysRev.49.324.

[476] ——, "Space quantization in a gyrating magnetic field," *Phys. Rev.*, vol. 51, pp. 652–654, 8 Apr. 1937. DOI: 10.1103/PhysRev.51.652.

[477] D. Braak, "Integrability of the rabi model," *Phys. Rev. Lett.*, vol. 107, p. 100 401, 10 Aug. 2011, ISSN: 0031-9007. DOI: 10.1103/PhysRevLett.107.100401.

[478] J.-Q. Liao, J.-F. Huang, and L. Tian, "Generation of macroscopic schrödinger-cat states in qubit-oscillator systems," *Phys. Rev. A*, vol. 93, p. 033 853, 3 Mar. 2016, ISSN: 2469-9926. DOI: 10.1103/PhysRevA.93.033853.

[479] J. von Neumann and E. P. Wigner, "ber das verhalten von eigenwerten bei adiabatischen prozessen," in. Springer Berlin Heidelberg, 1993, pp. 294–297. DOI: 10.1007/978-3-662-02781-3_20.

[480] L. Brillouin, "Remarques sur la mécanique ondulatoire," *Journal de Physique et le Radium*, vol. 7, pp. 353–368, 12 1926, ISSN: 0368-3842. DOI: 10.1051/jphysrad:01926007012035300.

[481] J. B. Keller, "Corrected bohr-sommerfeld quantum conditions for nonseparable systems," *Annals of Physics*, vol. 4, pp. 180–188, 2 Jun. 1958, ISSN: 00034916. DOI: 10.1016/0003-4916(58)90032-0.

[482] C. Zener, "Non-adiabatic crossing of energy levels," *Proceedings of the Royal Society of London. Series A, Containing Papers of a Mathematical and Physical Character*, vol. 137, pp. 696–702, 833 Sep. 1932, ISSN: 0950-1207. DOI: 10.1098/rspa.1932.0165.

[483] A. C. Cassidy, C. W. Clark, and M. Rigol, "Generalized thermalization in an integrable lattice system," *Phys. Rev. Lett.*, vol. 106, p. 140 405, 14 Apr. 2011, ISSN: 0031-9007. DOI: 10.1103/PhysRevLett.106.140405.

[484] Á. L. Corps, A. Relaño, and J. C. Halimeh, "Unifying finite-temperature dynamical and excited-state quantum phase transitions," Feb. 2024.

[485] M. A. Quiroz-Juárez, Á. L. Corps, R. A. Molina, A. Relaño, J. L. Aragón, R. de J. León-Montiel, and J. G. Hirsch, "Experimental observation of phase transitions of a deformed dicke model using a reconfigurable, bi-parametric electronic platform," *The European Physical Journal Plus*, vol. 138, p. 775, 9 Sep. 2023, ISSN: 2190-5444. DOI: 10.1140/epjp/s13360-023-04391-6.

[486] K. Baumann, R. Mottl, F. Brennecke, and T. Esslinger, "Exploring symmetry breaking at the dicke quantum phase transition," *Phys. Rev. Lett.*, vol. 107, p. 140 402, 14 Sep. 2011, ISSN: 0031-9007. DOI: 10.1103/PhysRevLett.107.140402.

[487] M. de Aguiar, K. Furuya, C. Lewenkopf, and M. Nemes, "Chaos in a spin-boson system: Classical analysis," *Annals of Physics*, vol. 216, pp. 291–312, 2 Jun. 1992, ISSN: 00034916. DOI: 10.1016/0003-4916(92)90178-O.

[488] A. D. Ribeiro, M. A. M. de Aguiar, and A. F. R. de Toledo Piza, "The semi-classical coherent state propagator for systems with spin," *Journal of Physics A: Mathematical and General*, vol. 39, pp. 3085–3097, 12 Mar. 2006, ISSN: 0305-4470. DOI: 10.1088/0305-4470/39/12/016.

[489] L. E. Reichl, *The Transition to Chaos in Conservative Classical Systems: Quantum Manifestations*. New York: Springer, 1992.

[490] P. Stránský, P. Hruška, and P. Cejnar, "Quantum chaos in the nuclear collective model. ii. peres lattices," *Phys. Rev. E*, vol. 79, p. 066 201, 6 Jun. 2009, ISSN: 1539-3755. DOI: 10.1103/PhysRevE.79.066201.

[491] M. Berry and J. Robbins, "Classical geometric forces of reaction: An exactly solvable model," *Proceedings of the Royal Society of London. Series A: Mathematical and Physical Sciences*, vol. 442, pp. 641–658, 1916 Sep. 1993, ISSN: 0962-8444. DOI: 10.1098/rspa.1993.0126.

[492] J. A. Mlynek, A. A. Abdumalikov, C. Eichler, and A. Wallraff, "Observation of dicke superradiance for two artificial atoms in a cavity with high decay rate," *Nature Communications*, vol. 5, p. 5186, 1 Nov. 2014, ISSN: 2041-1723. DOI: 10.1038/ncomms6186.

[493] F. Dimer, B. Estienne, A. S. Parkins, and H. J. Carmichael, "Proposed realization of the dicke-model quantum phase transition in an optical cavity qed system," *Phys. Rev. A*, vol. 75, p. 013 804, 1 Jan. 2007, ISSN: 1050-2947. DOI: 10.1103/PhysRevA.75.013804.

[494] P. Kongkhambut, H. Keßler, J. Skulte, L. Mathey, J. G. Cosme, and A. Hemmerich, "Realization of a periodically driven open three-level dicke model," *Phys. Rev. Lett.*, vol. 127, p. 253 601, 25 Dec. 2021, ISSN: 0031-9007. DOI: 10.1103/PhysRevLett.127.253601.

[495] Z. Zhiqiang, C. H. Lee, R. Kumar, K. J. Arnold, S. J. Masson, A. S. Parkins, and M. D. Barrett, "Nonequilibrium phase transition in a spin-1 dicke model," *Optica*, vol. 4, p. 424, 4 Apr. 2017, ISSN: 2334-2536. DOI: 10.1364/OPTICA.4.000424.

[496] S. J. Masson, M. D. Barrett, and S. Parkins, "Cavity qed engineering of spin dynamics and squeezing in a spinor gas," *Phys. Rev. Lett.*, vol. 119, p. 213 601, 21 Nov. 2017, ISSN: 0031-9007. DOI: 10.1103/PhysRevLett.119.213601.

[497] M. A. Quiroz-Juárez, J. Chávez-Carlos, J. L. Aragón, J. G. Hirsch, and R. de J. León-Montiel, "Experimental realization of the classical dicke model," *Phys. Rev. Research*, vol. 2, p. 033 169, 3 Jul. 2020, ISSN: 2643-1564. DOI: 10.1103/PhysRevResearch.2.033169.

[498] C. L. Johnson, *Analog computer techniques*. McGraw-Hill, Jan. 1963.

[499] A. Noordergraaf, P. D. Verdouw, and H. B. Boom, "The use of an analog computer in a circulation model," *Progress in Cardiovascular Diseases*, vol. 5, pp. 419–439, 5 Mar. 1963, ISSN: 00330620. DOI: 10.1016/S0033-0620(63)80009-2.

[500] C. Moore, "Dynamical recognizers: Real-time language recognition by analog computers," *Theoretical Computer Science*, vol. 201, pp. 99–136, 1-2 Jul. 1998, ISSN: 03043975. DOI: 10.1016/S0304-3975(97)00028-5.